AD-A007 529

HYDROBALLISTICS MODELING

John G. Waugh, et al

Naval Undersea Center
San Diego, California

January 1975

ADMINISTRATIVE INFORMATION

This report is a second printing of the book "Hydroballistics Modeling" by Dr. John G. Waugh and G. W. Stubstad. The original printing of 1000 copies, distributed by the Government Printing Office, has been exhausted for some time. To accommodate a continuous demand it is now being reprinted as NUC Technical Publication 447. Several plates in Chapter 13, which appeared in color in the original version, are in black and white for economic reasons; otherwise the book is unchanged.

Dr. Thomas Peirce of the Naval Sea Systems Command is program manager of Navy hydroballistics work; reprinting of this book was accomplished at his suggestion.

Released by
J. W. HOYT
Associate for Science

Under authority of
D. A. KUNZ, Head
Fleet Engineering
Department

UNCLASSIFIED

REPORT DOCUMENTATION PAGE		READ INSTRUCTIONS BEFORE COMPLETING FORM
1. REPORT NUMBER NUC TP 447	2. GOVT ACCESSION NO.	3. RECIPIENT'S CATALOG NUMBER AD. A007 539
4. TITLE (and Subtitle) HYDROBALLISTICS MODELING		5. TYPE OF REPORT & PERIOD COVERED Research and Development
		6. PERFORMING ORG. REPORT NUMBER
7. AUTHOR(s) John G. Waugh G. W. Stubstad		8. CONTRACT OR GRANT NUMBER(s)
9. PERFORMING ORGANIZATION NAME AND ADDRESS Naval Undersea Center San Diego, Ca. 92132		10. PROGRAM ELEMENT, PROJECT, TASK AREA & WORK UNIT NUMBERS
11. CONTROLLING OFFICE NAME AND ADDRESS Naval Sea Systems Command Washington, D. C. 20362		12. REPORT DATE January 1975
		13. NUMBER OF PAGES 353
14. MONITORING AGENCY NAME & ADDRESS(if different from Controlling Office)		15. SECURITY CLASS. (of this report) UNCLASSIFIED
		15a. DECLASSIFICATION DOWNGRADING SCHEDULE

16. DISTRIBUTION STATEMENT (of this Report)

Approved for public release; distribution unlimited.

17. DISTRIBUTION STATEMENT (of the abstract entered in Block 20, if different from Report)

18. SUPPLEMENTARY NOTES

19. KEY WORDS (Continue on reverse side if necessary and identify by block number)

Models
Missiles
Water entry
Hydroballistics

20. ABSTRACT (Continue on reverse side if necessary and identify by block number)

This report is a reprint of the hard-cover book of the same title. It is a detailed treatment of the various aspects of hydroballistics modeling. Included are discussions on theoretical and experimental modeling, prototype and modeling experiments, phenomenological studies, special experimental techniques and hydroballistics facilities, and the changing status of modeling.

DD FORM 1 JAN 73 1473 EDITION OF 1 NOV 65 IS OBSOLETE

UNCLASSIFIED

FRONTISPIECE

Missile heads used in water-entry pitch modeling.

FOREWORD

PREFACE

Realization of the ocean's importance to man has grown rapidly during the last decade, and with it has come increased activity in undersea research and development. Vehicles and weapons are appearing that may operate at speeds ranging from a mere creep to higher than presently in use, along trajectories having any orientation to the water surface, and at increasingly deeper submergence. All degrees of cavitation will be encountered, in addition to cavities composed partly of air or of highspeed exhaust gases.

The need for small-scale modeling techniques arises from the inadequacy of the three-phase, three-dimensional hydrodynamic theory and from the difficulties inherent in testing large missiles in the uncontrolled environment of the open sea. Expenditures of time and money are bound to be large in prototype testing, and the acquisition of data of adequate resolution and precision can be a formidable task.

The ultimate purpose of modeling is, of course, the practicable prediction of prototype missile behavior, an ideal that cannot always be achieved, particularly when the physical phenomena under investigation are not fully understood. Yet model studies can provide insight into little-known phenomena and prove useful in improving prototype design or in controlling the events that influence prototype behavior.

Experimental investigation of water entry began at least 75 years ago, but most of the work reported here has been done since World War II. Many specific shapes and some general configurations have been observed, usually at low velocities (500 fps or less) entering still water. These missiles, together with their entry cavities and the surrounding water, represent only a small portion of the hydrodynamic-flow regime that may be encountered in the ocean. Ambient conditions typical of the open sea and the new factors introduced by high-speed propulsion systems have not been thoroughly investigated. If modeling is to continue as a useful tool, it must widen its capabilities to keep pace with oceanography's growing needs.

It is hoped that the studies reported here, most of them conducted at the U.S. Naval Ordnance Test Station, now the Pasadena Laboratory of the Naval Undersea Research and Development Center, will provide a basis for assessing the present state of the modeling art, a springboard for future experiments, and a guide for extending the modeling technique to include other phases of hydroballistics.

J. G. W.
G. W. S.

Pasadena, California, 1972

CREDITS FOR ILLUSTRATIONS AND TABLES

Figures 1.1, 7.1, 7.2, 7.3, 7.4, 7.5, 7.6, and 7.7 taken from "Water-Entry Pitch Modeling," by John G. Waugh. Journal of Hydronautics, Vol. 2, No. 2 (1968), pp. 87-92. Reproduced by permission of the American Institute of Aeronautics and Astronautics. (Reference 96)

Figures 3.7 and 4.1 taken from "A Study of Splashes," by A. M. Worthington. New York, N.Y., the MacMillan Co., 1963. Reproduced by permission. (Reference 112)

Figure 4.2 and Tables 4.1, 4.2, and 4.3 taken from "The Impact of a Solid on a Liquid Surface," by E. G. Richardson. Proceedings of the Physical Society of London, Vol. 61, Part 4 (1948), pp. 352-66. Reproduced by permission of the Institute of Physics and the Physical Society. (Reference 68)

Figure 4.3 taken from "Fluid Flow Patterns," by Garrett Birkhoff and Thomas E. Caywood. Journal of Applied Physics, Vol. 20, No. 7 (1949), pp. 646-59. Reproduced by permission of the American Institute of Physics. (Reference 7)

Figures 17.1, 17.2, 17.4, 17.5, 17.6, 17.7, 17.8, and 17.9 taken from "The Variable-Angle Variable-Pressure Launching Tank," by J. G. Waugh. Published in "Cavitation Research Facilities and Techniques," New York, N.Y., American Society of Mechanical Engineers, 1964. pp. 118-126. Reproduced by permission. (Reference 89)

Figures 17.3, 17.10, 18.10, 18.11, 18.12, and 18.13 taken from "Techniques for Metric Photography," by J. G. Waugh, A. T. Ellis and S. B. Mellsen. Journal of the Society of Motion Picture and Television Engineers, Vol. 75, No. 1 (1966), pp. 2-6. Reproduced by permission of the Society of Motion Picture and Television Engineers. (Reference 94)

Figures 17.11, 17.12, 17.13, 17.18, 17.19, 17.20, 17.21, 17.22, 17.23, 17.24, and 17.25 taken from "The Hydrodynamics Laboratory of the California Institute of Technology," by R. T. Knapp, Joseph Levy, J. P. O'Neill and F. B. Brown. Transactions of the American Society of Mechanical Engineers, Vol. 70, No. 5 (1948), pp. 437-57. Reproduced by permission of the American Society of Mechanical Engineers. (Reference 30)

Figure 19.4 taken from "Cavitation Research Capabilities of the Lockheed Underwater Missile Facility," by Robert L. Waid. Published in "Cavitation Research Facilities and Techniques," New York, N.Y., American Society of Mechanical Engineers, 1964. pp. 127-131. Reproduced by permission. (Reference 87)

Figures 19.6, 19.7, and 19.8 taken from "The Variable-Atmosphere Wave Tank," by J. G. Waugh and A. T. Ellis. Published in "Cavitation Research Facilities and Techniques," New York, N.Y., American Society of Mechanical Engineers, 1964. pp. 114-117. Reproduced by permission. (Reference 93)

CONTENTS

PART I.
THEORETICAL MODELING

CHAPTER 1
HYDROBALLISTICS MODELING THEORY

The use of small-scale models to simulate prototype conditions is a common practice in aeronautics, ship design, and other areas of fluid mechanics. Modeling occurs when a model follows a trajectory geometrically similar to that of a prototype and reproduces the attitude of the prototype at corresponding positions along the trajectory. Modeling is accomplished by applying a force system to the model that is similar to the system acting upon the prototype (Reference 61).

The problem to be resolved in modeling is the identification of each of the involved forces as it affects the motions of the missiles. In hydroballistic phenomena of practical interest, the inertial, gravitational, and viscous forces are of primary concern. Since inertia is always important in the velocity range to be considered, the other forces are compared to it. Either the gravitational or the viscous force can be scaled simultaneously with the inertial force, but not both, unless different liquids are used in the model and in the prototype systems. Unfortunately, when the prototype liquid is water, there is at present no known liquid for use in the model system that will satisfy the requirements of both gravitational (Froude) and viscous (Reynolds) scaling.[1] A hydroballistic modeling system must be designed to scale one force ratio (i.e., one scaling or modeling parameter) and minimize the other.

Because the relative importance of Froude and Reynolds forces can be adjusted through selection of missile velocity, hydroballistics modeling is possible. At the lower, laminar-flow velocities, the Reynolds effects cannot be ignored. Either corrections must be made for the viscous forces in a Froude-scaled system or a specially restricted system must be devised. The former technique is a long-established practice in extrapolating towing-tank results to ship design. An example of a restricted system is the use, with Froude scaling, of models sufficiently large that both model and prototype velocities are above the critical Reynolds number, and viscosity effects can be neglected. Another example (Reference 39) is the modeling of high-speed maneuvers of deeply submerged submarines in the vertical plane. Here Froude scaling can be neglected and the model operating speed (if it is above the critical Reynolds number) becomes a matter of free choice.

---

[1] It is possible that aqueous polymer solutions will permit simultaneous scaling of these parameters.

Froude scaling can be successfully utilized in the higher-velocity regime because the Reynolds forces become essentially constant once turbulent flow has been established. Modeling cannot be expected in the transitional regime between laminar and turbulent flow, although it can sometimes be achieved by triggering turbulent flow artificially. The upper velocity limits of Froude scaling occur when the gravitational forces become negligible compared to those of inertia, or when the forces of compressibility, either in the missile or in the surrounding fluid, become significant. Then Mach scaling is used.

Models and prototypes that satisfy both the Froude and the Reynolds scaling laws are geometrically similar in external shape and in center of gravity (CG) location. Their masses scale as the third power and the moments of inertia as the fifth power of the ratio of missile linear dimensions (i.e., model diameter/prototype diameter). If different liquids are used in the model and in the prototype systems, the masses and moments of inertia must also be scaled directly as the respective liquid densities.

The Froude and the Reynolds scaling laws, however, require the models to operate at different velocities. Froude scaling requires smaller-than-prototype models to operate at lower-than-prototype velocities; Reynolds scaling calls for higher-than-prototype velocities with the smaller models.

The theory of modeling evolved from basic concepts of dimensional analysis, which is no more than an attempt to relate physical phenomena through ancient Greek ideas of geometrical similarity, ratio, and proportion. The extensive literature that describes both dimensional analysis and the theory of modeling has been outlined by Garrett Birkhoff (References 5, 6, and 55) and discussed by F. S. Burt (Reference 10).

The important hydroballistics modeling parameters in a Froude-scaled system are the Froude and cavitation numbers, gas-density coefficient, and Weber numbers.

The Reynolds and Mach numbers are also of interest because the validity of the modeling technique depends upon these parameters being negligible. The flexure number must be considered only if the missile becomes distorted under the load of impact or of the hydrodynamic forces.

The Froude number, F, is the ratio of the inertial and gravitational forces and is defined as

$$F = \frac{v}{(dg)^{1/2}} \qquad (1.1)$$

The cavitation number, σ, is the ratio of the static and dynamic pressures and is given by

$$\sigma = \frac{p_a + \rho_w gh - (p_g + p_v)}{\frac{1}{2}\rho_w v^2} \qquad (1.2)$$

The gas-density coefficient, ρ', is defined as the ratio of the gas density in the model system to the density of air at standard conditions of temperature and pressure.[2]

$$\rho' = \frac{\rho_m}{\rho_{std}} \qquad (1.3)$$

The Reynolds number, R, is the ratio of the inertial and viscous forces.

$$R = \frac{vd}{\nu} \qquad (1.4)$$

The Weber number, τ, is the ratio of the inertial and surface tension forces.

$$\tau = \frac{v}{(S/\rho_w d)^{1/2}} \qquad (1.5)$$

The Mach number is the ratio of the missile velocity and the velocity of sound in the fluid to be penetrated.

$$Mach = \frac{v}{c} \qquad (1.6)$$

---

[2]In the NUC studies, the reference density was that of air at 20°C and 740 torrs, i.e., the average ambient density at the Morris Dam Torpedo Range near Azusa, Calif., where prototype launchings were made.

The flexure number, f, is the ratio of inertial to flexural forces.

$$f = \frac{v^2}{n_o^2 \, \ell^2} \qquad (1.7)$$

where n_o is the fundamental transverse frequency of the missile.

In water entry or exit, it has been customary to define the parameters of the model system arbitrarily in terms of the velocity of the missile at the first contact with the air-water interface, i.e., at the moment of entry or exit. At the interface, the static head, $\rho_w gh$, is zero and, in water entry, the cavity has not yet formed. The cavitation number of the water-entry system thus reduces to

$$\sigma = \frac{p_a - (p_g + p_v)}{\tfrac{1}{2}\rho_w v_c^2} \approx \frac{p_a}{\tfrac{1}{2}\rho_w v_c^2} \qquad (1.8)$$

if $p_g + p_v$ is small compared to p_a.

The modeling constraints and the model-prototype relationships derived from the Froude-scaling law can be developed on the basis of geometrically and dynamically similar models and water as the fluid for model and prototype.

Let the ratio of the model diameter to the prototype diameter (modeling scale factor) be given by

$$\lambda = \frac{d_m}{d_p} \qquad (1.9)$$

The modeling constraints for dynamic similarity are thus

$$\ell_m = \lambda \ell_p \qquad (1.10)$$

$$m_m = \lambda^3 m_p \qquad (1.11)$$

$$I_m = \lambda^5 I_p \qquad (1.12)$$

The fluid (water) density scaling constraint is

$$\rho_{wm} = \rho_{wp} \qquad (1.13)$$

and therefore the fluid temperature scaling constraint is

$$T_{wm} = T_{wp} \qquad (1.14)$$

Since the density of water varies only slightly with temperature over the usual temperature range, the constraint of Equation 1.14 is probably not important for water-density scaling; over a temperature range of $0 - 25^\circ C$, the density of water varies only about 0.3%.

The corresponding points along the geometrically similar trajectories are identified by equal distances in diameters:

$$s_m = \lambda s_p \, ; \qquad h_m = \lambda h_p \qquad (1.15)$$

The time similitude is

$$t_m(s_m) = \sqrt{\lambda}\,t_p(s_p); \qquad t_m(h_m) = \sqrt{\lambda}\,t_p(h_p) \qquad (1.16)$$

$$s_m(t_m) = \lambda s_p(t_p); \qquad h_m(t_m) = \lambda h_p(t_p) \qquad (1.17)$$

where t_m and t_p are the time intervals required by the model and prototype to reach corresponding points.

Other model-prototype relationships are

$$v_m(t_m) = \sqrt{\lambda}\,v_p(t_p) \qquad (1.18)$$

$$a_m(t_m) = a_p(t_p) \qquad (1.19)$$

$$\zeta_m(t_m) = \zeta_p(t_p) \qquad (1.20)$$

$$\sqrt{\lambda}\,\dot{\zeta}(t_m) = \dot{\zeta}_p(t_p) \qquad (1.21)$$

$$\lambda\ddot{\zeta}(t_m) = \ddot{\zeta}_p(t_p) \qquad (1.22)$$

where v and a are the missile velocity and acceleration, and ζ represents any angle, i.e., pitch angle, θ, trajectory angle, ξ, and angle of

3

attack, α (as shown in Figure 1.1), as well as yaw, ψ, and roll, ϕ. The $\dot{\zeta}$ and $\ddot{\zeta}$ are angular velocity and angular acceleration, respectively.
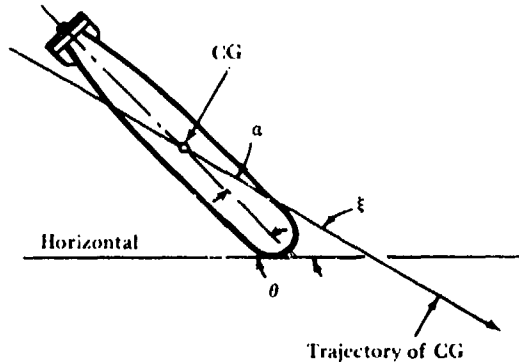
Figure 1.1. Attack, pitch, and trajectory angles; all angles are negative. (From Reference 96.)

It is evident that cavity size and shape affect the interfacial and underwater trajectory of the missile and that successful modeling of missile motion within a cavity necessarily includes modeling of the cavity. Cavity modeling requires that the ratio of the pressure forces acting to collapse the cavity to the dynamic pressure acting to open the cavity be preserved. Thus, the cavitation number must be scaled according to the Froude law; this is accomplished[3] by scaling the atmospheric pressure[4] in the model system as

$$P_{am} = \lambda P_{ap} \qquad (1.23)$$

Scaling of this type is commonly referred to as *Froude and cavitation-number scaling.* It scales static pressure on the water and cavity surfaces to the extent that pressure is constant over connected regions of the air, but it does not scale the vapor pressure of w?ter, nor does it scale the air (gas) dynamic pressure, $\frac{1}{2}\rho v_g^2$. It has been found experimentally that this dynamic pressure acts to close the water-entry cavity; hence, reducing the dynamic pressure delays cavity seal and increases cavity size by allowing a larger volume of air to enter. Modeling the water-entry cavity size requires that the gas density also be scaled:

$$\rho_m = \rho_p \qquad (1.24)$$

This extension of the Froude law is called *Froude, cavitation-number, and gas-density scaling.*

Scaling the Weber number[5] requires that the surface tension of the water be scaled as

$$S_m = \lambda^2 S_p \qquad (1.25)$$

Some reduction of surface tension in the model system can be achieved, without significantly altering the properties of the water, by adding minute quantities of aerosol to the water. A

---

[3]
$$\sigma = \left[\frac{(p_a - p_c)_p + \rho_{wp}g h_p}{\frac{1}{2}\rho_{wp}v_p^2}\right]_p = \left[\frac{\lambda(p_a - p_c)_p + \rho_{wp}g\lambda h_p}{\frac{1}{2}\rho_{wp}\lambda v_p^2}\right]_m$$

[4]In the NUC and NUC-CIT studies, 1 atmosphere pressure is defined as 740 torrs, i.e., the average ambient pressure at the Morris Dam Torpedo Range, Azusa, Calif., where prototype launchings were made.

[5]
$$\tau = \left(\frac{v_p\sqrt{\rho_{wp}d_p}}{\sqrt{S_p}}\right)_p = \left(\frac{v_p\lambda^{1/2}\sqrt{\rho_{wp}d_p\lambda}}{\sqrt{S_p\lambda^2}}\right)_m$$

4

solution of 0.1% Aerosol[6] by weight results in a lowering of the surface tension from 76 dynes/cm at 20°C to 40 dynes/cm, a reduction of 47%. This is the reduction required to scale the Weber number when λ is 1/1.38, a higher scale factor than is ordinarily used. Thus, only partial scaling of Weber number is possible in many Froude-scaled model systems. Fortunately, this partial scaling has been adequate in the water-entry model systems significantly affected by surface tension forces.

Scaling of the flexure number requires that the bulk modulus of elasticity of the prototype be equal to that of the model[7] divided by the square root of λ. If the missile is so flexible that this scaling is required, materials are available that allow scaling over a restricted range of λ.

---

[6] Aerosol OT, dioctylsodiumsulfosuccinate (Reference 2).

[7] From the flexure number $v_o^2/n_o^2 \ell^2$, $n_{o_m} = n_{op}/\lambda^{1/2}$. For a uniform free-free beam (Reference 61, pages 40-42), $n_o = (11.2/\pi)(cK/\ell^2)$ where c is the velocity of sound in the missile material, K is the radius of gyration of the beam cross-section with respect to the neutral axis, and ℓ is the length of the beam. Then $c_m = \lambda^{1/2}c_p$ where $c = (E/\rho_M)^{1/2}$, and E and ρ_M are the modulus of elasticity and density of the material, respectively. Another form of the flexure number is $\ell^2 v^2/K^2 c^2$.

CHAPTER 2

UNDERWATER-LAUNCH MODELING

Interest in the problems arising when a missile emerges from water created a need for water-exit modeling and for the modeling of underwater-launch systems (Reference 88). Examination of the physical aspects of the exit problem leads to the conclusion that it should be possible to model the underwater flight, exit, and subsequent air trajectory of a missile in a Froude — cavitation-number — scaled system, and also that the possible need for the additional constraint of gas-density scaling must be recognized.

TECHNIQUES OF MODELING

In underwater-launching systems where water is in contact with the missile during part or all of its launching phase, the character of the flow and the missile n.)tion must be modeled. If gas is ejected into the water as the missile base emerges from the launcher muzzle,[1] the gas bubble may affect the behavior of the missile and therefore it must be modeled.

In the following discussion a compressed-gas launching system is assumed in which water is in contact with the missile over its launching phase and a gas bubble is formed on missile base emergence. The following assumptions are made:

1. Both prototype and model underwater launching systems are geometrically scaled.

2. Gas expansion over the launching and gas-bubble expansion phases is free and adiabatic.[2]

3. The constraints of Froude and cavitation-number scaling (n cessary for missile-trajectory modeling) apply.

4. The effects of viscosity, surface tension, and water compressibility are negligible.

It will be shown that the additional pre-launching constraints

$$P_{gm_o} = \lambda P_{gp_o} \qquad (2.1)$$

where P_g is the gas pressure,

$$T_{gm_o} = T_{gp_o} \qquad (2.2)$$

where T_g is the gas temperature,

$$V_{m_o} = \lambda^3 V_{p_o} \qquad (2.3)$$

where V is the gas volume, and

$$\gamma_m = \gamma_p \qquad (2.4)$$

where γ is the gas specific-heat ratio, will be sufficient for modeling missile motion over the launching phase. Later it is shown that these constraints are also sufficient for modeling the

---

[1] Base emergence is considered to take place when the lower cylindrical edge of the missile clears the launcher muzzle, allowing free ejection of launcher gas into the water.

[2] Free gas expansion will not obtain over a brief regime following missile-base emergence from the launcher muzzle due to the throttling effect of the aperture between base and muzzle, and the gas bubble will not be modeled by the scaling techniques discussed. It is assumed that this regime is sufficiently brief that significant deviations in gas-bubble modeling will not be introduced.

gas bubble provided gas expansion is adiabatic or the same operating gas specific heat ratio can be assumed for both systems. If gas density is also scaled, the constraint of Equation 1.24 must be included.

The constraint of Equation 2.2 is satisfied by holding the prototype and model-launching systems at the same temperature (Equation 1.14 and subsequent discussion) and the constraint of Equation 2.3 is satisfied by geometric scaling of the launching systems. Using Equations 2.1, 2.2, 2.3, and the isothermal equation of state

$$P_g V = nR'T_g; \qquad P_g = \frac{R'}{M}\rho T_g \qquad (2.5)$$

gives

$$n_m = \lambda^4 n_p \qquad (2.6)$$

where n is the quantity of gas (in moles) in the launcher system.

At ordinary pressures, the adiabatic equation of state of a gas is given by

$$P_g V^\gamma = c; \qquad T_g V^{\gamma-1} = c' \qquad (2.7)$$

where c and c' are constants. From the pre-launching constraints (Equations 2.1, 2.2, 2.3, and 2.4), the assumed geometric similarity of the prototype and model-launching systems, and the adiabatic equation of state (Equation 2.7), it is evident that for geometrically scaled positions of the missiles in the launching systems

$$V_m = \lambda^3 V_p \qquad (2.8)$$

$$P_{gm} = \lambda P_{gp} \qquad (2.9)$$

$$T_{gm} = T_{gp} \qquad (2.10)$$

It will' be shown that missile accelerations for geometrically scaled missile positions scale directly as Equation 1.19 and hence (since initial missile velocities are zero) missile velocities scale as Equation 1.13. Since the missiles are geometrically similar, from Equation 2.9 gas pressure forces on the missile scale as λ^3. From Equations 1.13, 1.15, and 1.23, the sum of the atmospheric and hydrostatic pressures acting on the missile scales as λ and hence the force due to these pressures scales as λ^3. Assuming similarity of flow in both systems, the force required to produce the same fluid acceleration in both systems scales as λ^3. For geometrical similarity,

the friction-generating area scales as λ^2. If it is assumed that the pressure on the friction-generating area scales as λ, and the coefficient of sliding friction is the same for both systems, then the frictional force scales as λ^3. The force accelerating the missile must therefore scale as λ^3. Since the mass of the missile scales as λ^3, missile accelerations scale directly and velocities scale as $\lambda^{1/2}$. In summary, Equations 1.18, 1.19, 2.8, 2.9, and 2.10 obtain at missile-base emergence from the launcher muzzle.

For gas bubbles, neglecting fluid vapor pressure, the cavitation number σ assumes the form

$$\sigma = \frac{P_a + \rho_w gh - P_g}{\tfrac{1}{2}\rho_w v^2} \qquad (2.11)$$

It can be seen that σ is scaled at the instant of missile-base emergence from the launcher muzzle. Using gas-pressure scaling, modeling of the bubble will obtain over the regime for which gas expansion can be assumed adiabatic.

The scaling constraints above can readily be extended to include modeling of underwater-launching systems that have a diaphragm over the launcher muzzle and gas in the tube before launching. As initial boundary conditions, it is assumed that the same kind of gas is used, and its volume, temperature and pressure (hydro-static pressure at the launcher muzzle) are scaled in the prototype and model launching systems, but that diaphragm rupture takes place at first missile motion. Hence Equations 2.8, 2.9, and 2.10 are satisfied.

A similar analysis shows that missile accelerations and velocities are properly scaled (Equations 1.18 and 1.19); the cavitation number (Equation 2.11) is scaled also. Therefore, modeling of the nose bubble will obtain over the regime for which gas expansion can be regarded as adiabatic.

It is evident that after the initial gas-bubble expansion phase, heat transfer between the bubble gas and the surrounding water may cause deviations in the bubble modeling, but the gas-bubble behavior may have little effect on missile behavior after the initial expansion phase, and thus the previously discussed scaling constraints will be adequate.

The scaling of the gas specific-heat ratio (Equation 2.4) without regard to gas-density scaling offers no problems because it may be

7

accomplished by using the same gas in the model and in the prototype systems. The additional constraint of gas-density scaling (Equation 1.24), however, involves the use of different gases in the two systems.

The adjustment of gas density and specific-heat ratio in the model system to their scaled values as given by Equations 1.24 and 2.4 generally entails the use of gas mixtures. Let M_p be the molecular weight of the gas used in the prototype system (if air, $M_p = 29$) and let M_1, $M_2 \ldots$, M_r be the molecular weights of the components in the model-system gas mixture. Let n_1, $n_2 \ldots$, n_r be the respective mole fractions of the components. Then

$$\sum_{i=1}^{r} n_i = 1 \qquad (2.12)$$

and

$$M_m = \sum_{i=1}^{r} n_i M_i \qquad (2.13)$$

where M_m may be regarded as the "molecular weight" of the model-system gas mixture. From Equations 1.24, 2.5, 2.9, 2.10, and 2.13

$$\frac{M_m}{M_p} = \frac{1}{M_p} \sum_{i=1}^{r} n_i M_i = \frac{1}{\lambda} \qquad (2.14)$$

The quantity of heat necessary to raise the temperature of 1 gram molecular weight of gas by 1°C at constant volume is the molecular heat at constant volume, C_v. The quantity of heat necessary to raise the temperature of 1 gram molecular weight of gas by 1°C at constant pressure is C_p. Now let C_{v_i} and C_{p_i} be the molecular heats of the gas component of molecular weight M_i and mole fraction n_i. If th usual assumption is made that the internal e·· gy of the mixture is equal to the sum of t .ternal energies that the component gases possess separately at the same temperature, the specific-heat ratio of the gas mixture in the model system is given by

$$\gamma_m = \frac{\displaystyle\sum_{i=1}^{r} n_i C_{p_i}}{\displaystyle\sum_{i=1}^{r} n_i C_{v_i}} \qquad (2.15)$$

where γ is assumed to be constant over the range of temperatures and pressures encountered within the system. It should be noted, however, that γ generally increases with increasing pressure and decreases with increasing temperature. The following values of γ for air (taken from Reference 16) give an indication of this variation.

t, °F	Lb/in²abs			
	0	1,000	2,000	4,000
0	1.40	1.58	—	—
200	1.39	1.47	1.53	1.62
400	1.38	1.43	1.46	1.51
600	1.37	1.39	1.42	1.45

It is apparent that a significant variation of γ occurs as pressures approach the order of 1000 psi. For example, a 1/10 scale model of a prototype operating in the 1000-psi range would require pressures only on the order of 100 psi. Thus, using air in both systems would not suffice to scale in this hypothetical modeling problem.

The partial pressure p_{g_i} of each gas component is given by

$$p_{g_i} = n_i p_g \qquad (2.16)$$

where p_g is the gas-mixture pressure. That is,

$$\sum_{i=1}^{r} p_{g_i} = \sum_{i=1}^{r} n_i p_g = p_g \sum_{i=1}^{r} n_i = p_g \qquad (2.17)$$

It should be noted that the vapor pressure of the gas usually decreases with increase in molecular weight. If the vapor pressure of the gas exceeds the partial pressure at which it is to be used, it will liquefy. Also, gases of increased molecular weight become increasingly polyatomic and the specific-heat ratio decreases rapidly. Thus the number of available gases suitable for simultaneous scaling of gas density and the specific-heat ratio decreases with decrease in the modeling scale factor λ. Additional restrictions are non-toxicity, non-inflammability, and chemical inertness under modeling conditions.

8

SELECTION OF WORKING GASES

Of the gases that satisfy the constraints of gas-density and specific-heat ratio scaling where air is used in the prototype system, a mixture of xenon and Freon C-318 (octafluorocyclobutane) gives one of the smallest modeling scale factors. The value of the scale factor obtainable with this mixture can be determined from the table below.

	Air	Xenon	Freon C-318
Specific-heat ratio, γ	1.4	1.666 (Ref. 40)	1.059 (Ref. 67)
C_p, cal/mole ^oC	...	4.97 (Ref. 25)	38.353 (Ref. 67)
C_v, cal/mole ^oC	...	2.98	36.216
Molecular weight, M	(29)	131.3 (Ref. 25)	200 (Ref. 67)

Let n be the mole fraction of xenon in the binary gas mixture. Then from Equation 2.12, the mole fraction of Freon C-318 is 1 - n. From Equation 2.15 and the table above for specific-heat ratio scaling,

$$\gamma_p(air) = 1.4 = \frac{4.97n + 38.353(1 - n)}{2.98n + 36.216(1 - n)} \quad (2.18)$$

From Equation 2.18, n = 0.9393. Therefore, the mole fraction of xenon is 0.9393, and the mole fraction of Freon C-318 is 0.0607. From Equation 2.14,

$$\frac{M_m}{M_p} = \frac{1}{29} [131.3(0.9393) + 200(0.0607)]$$

$$= 4.67 = \frac{1}{\lambda} \quad (2.19)$$

The vapor pressure of Freon C-318 at ambient temperature (70°F) is 40 psia (Reference 67), which is not likely to be exceeded by scaled model-system launching-gas pressures with consequent danger of gas liquefaction.

With this gas mixture, complete scaling is possible with a modeling scale factor as small as λ = 1/4.67. For 1/5-scale modeling (λ = 1/5), the scaling would still be good: complete scaling of the specific-heat ratio and 93.4% scaling of the gas density would be attained.

Other heavy gases (Reference 67) may be applicable to modeling studies.[3] The investigator must determine a compromise between the desired degrees of scaling and the cost and availability of the gases suitable to attain them. Xenon, for example, is expensive.

Partial Scaling

Scaling of one factor at the expense of others may cause large differences between the model and prototype behavior; it is then necessary to consider a compromise partial scaling of several factors in order to obtain model data of acceptable accuracy. Partial scaling can be achieved through the selection of physical properties, and the underwater-launch system scaling can also be adjusted by altering the gas expansion during the launching phase.

It is assumed, as before, that the prototype and model systems are geometrically and dynamically scaled, and, furthermore, that the base-emergence velocity of the missile is scaled. (Since only launcher gases are involved, the subscript g is omitted from the symbol denoting gas pressure in the ensuing equations.)

The work performed by the gas in launching the missile is the sum of the kinetic energy imparted to the missile and water and the work expended in overcoming friction and expansion against hydrostatic pressure. If W is the work performed by the gas, then

$$W = \int_{V_o}^{V_1} p\,dV \quad (2.20)$$

where V_o and V_1 are the initial and final launcher-gas volumes. From Equation 2.7 and the initial boundary conditions p = p_o when V = V_o,

$$W = \frac{p_o V_o}{\gamma - 1} \left[1 - \left(\frac{V_o}{V_1}\right)^{\gamma-1} \right] \quad (2.21)$$

---

[3]Heavy gases (and liquids that would form heavy gases at reduced pressures for scaling gas density over the water surface) are available from: Union Carbide Corporation, Linde Division, New York, N.Y.; E.I. du Pont de Nemours and Co., Inc., Freon Products Division, Organic Chemicals Department, Wilmington, Delaware; Halocarbon Products Corporation, Hackensack, New Jersey; and Minnesota Mining and Manufacturing Co., Chemical Division, St. Paul, Minnesota.

If $\gamma = 1$ (isothermal expansion)

$$W = p_o V_o \ln \frac{V_1}{V_o} \qquad (2.22)$$

From Equation 2.20, the work performed by gas expansion in the prototype and model systems would be given by

$$W_p = \frac{p_{p_o} V_{p_o}}{\gamma_p - 1} \left[1 - \left(\frac{V_{p_o}}{V_{p_1}} \right)^{\gamma_p - 1} \right] \qquad (2.23)$$

and

$$W_m = \frac{p_{m_o} V_{m_o}}{\gamma_m - 1} \left[1 - \left(\frac{V_{m_o}}{V_{m_1}} \right)^{\gamma_m - 1} \right] \qquad (2.24)$$

It is obvious that under the launching constraints of Equations 2.1, 2.2, 2.3, 2.4, and 2.6, $W_m = \lambda^4 W_p$. With the assumption that the work done on (i.e., energy imparted to) the model and prototype missiles is in the same proportion, and applying the constraint of Equation 1.11, it follows that Equation 1.18 obtains and the missile velocities are Froude-scaled.

Now assume a properly scaled model system where $\gamma_m = \gamma_p$

$$W_m = \frac{p_{m_o} V_{m_o}}{\gamma_p - 1} \left[1 - \left(\frac{V_{m_o}}{V_{m_1}} \right)^{\gamma_p - 1} \right] \qquad (2.25)$$

and the same model system where $\gamma_m \neq \gamma_p$

$$W_m = \frac{p'_{m_o} V'_{m_o}}{\gamma_m - 1} \left[1 - \left(\frac{V'_{m_o}}{V'_{m_1}} \right)^{\gamma_m - 1} \right] \qquad (2.26)$$

The primed quantities in Equation 2.26 are not necessarily scaled. The final gas volume at missile-base emergence, V_{m_1}, is scaled because the same launcher is used in both systems.

If it is assumed that the energy imparted to the water and the flow pattern is negligibly affected by small variations in the missile-position – time relation during the launching phase (provided that the constraint of scaled base-emergence velocity is satisfied), Equations 2.25 and 2.26 may be equated.

That is,

$$\frac{p'_{m_o} V'_{m_o}}{\gamma_m - 1} \left[1 - \left(\frac{V'_{m_o}}{V_{m_1}} \right)^{\gamma_m - 1} \right]$$

$$= \frac{p_{m_o} V_{m_o}}{\gamma_p - 1} \left[1 - \left(\frac{V_{m_o}}{V_{m_1}} \right)^{\gamma_p - 1} \right] \qquad (2.27)$$

and the initial and final temperatures of the launcher gas are obtained from the second form of the adiabatic equation of state (Equation 2.7). For properly scaled model-launching conditions

$$T_{gm_1} = T_{gm_o} \left(\frac{V_{m_o}}{V_{m_1}} \right)^{\gamma_p - 1} \qquad (2.28)$$

A variety of combinations of non-scaled launching conditions that satisfy Equation 2.27 may now be used to approximate scaled launching conditions. The elements of the combinations depend upon the parameters considered by the investigator to be of greatest importance for scaling: the gas density, the quantity of launcher gas, its initial or final temperature, or some compromise combination thereof.

It is apparent that perfect scaling of both ρ and γ is possible only under limited circumstances; it will usually be necessary to select a partial-scaling technique. The importance of gas-density scaling is demonstrated by existing experimental evidence (e.g., Chapters 7 and 9), but experimental scaling of the gas specific-heat ratio is virtually unknown. A theoretical evaluation must be made. Inspection of Equations 2.14 and 2.15 shows that the specific-heat-ratio scaling will diverge rapidly with only slight improvement in gas-density scaling.

When the dimensions of an actual launcher and assumed initial launching conditions are substituted into Equation 2.27, various pressures, volumes, and temperatures within the system can be calculated with the aid of Equation 2.5 or 2.7. The importance of scaling γ can be assessed numerically by assigning different values in Equation 2.27 and comparing the results. The importance of scaling γ during a free expansion can be explored further by considering the effect of change in γ with the expansion of a simple spherical bubble. By examining this parallel physical system, it is possible to observe the effects of γ in the absence of the assumptions used in formulating Equation 2.27 (Reference 35).

The modeling equations indicate that a γ of less than about 1.3 in the model system will cause significant variation between the model and prototype gas expansions. Fortunately, the gas-density-scaling data suggest that partial scaling of ρ may be adequate. In the water-entry system described in Chapter 9, where gas density is one of the primary physical parameters influencing the phenomena, good modeling resulted from 80% scaling and generally usable results were obtained with only about 70%

scaling. Gas density appears to be of lesser importance in the underwater-launch system (no surface closures occur). It is possible to achieve sufficient gas-density scaling to evaluate this premise experimentally. It is probable that the partial gas-density scaling available simultaneously with a γ of at least 1.3 will be adequate to model the underwater-launch system under consideration.

A preliminary analysis such as this is based upon an estimate of the physical phenomena involved, and some of the assumptions made in formulating the theory are necessarily "ideal." The derived scaling laws should be used as guidelines for initial experimentation and should be continually reassessed in the light of accumulating physical data. Thus physical parameters within the system can be measured instead of assumed; the prototype gas expansion, for example, will in reality be neither isothermal nor adiabatic, and the specific heat ratio and gas density necessary for scaling can be established. A continuous feedback from experiment to theory tends to evolve a scaling technique that has both sound theoretical basis and physical reality.

PART II.
EXPERIMENTAL MODELING

CHAPTER 3
WATER-ENTRY PHENOMENA

Knowledge of the physical forces to be scaled is a requisite in modeling. It is often necessary, however, to begin a modeling program before this knowledge is complete, and then the investigation becomes a dual-purpose study that seeks a basis for greater understanding as well as a determination of the relative importance of the forces involved. It has been thus with water entry. The scaling laws outlined in Chapter 1 evolved as experimental knowledge grew.

In water entry, cavity formation is irrevocably blended with missile performance. The physical properties of missile, gas, and liquid together establish the forces that combine with gravity and inertia to determine the entry phenomena. It is reasonable to assume that the force exerted by the missile nose upon the water opens a cavity that continues to widen by virtue of its own inertia until gravity causes the water to return to its undisturbed position. Yet such comparatively small forces as gas flows within the cavity, minor physical properties of the liquid (surface tension, dissolved gas nuclei, etc.), and even the surface of the missile are important in determining cavity behavior. Small forces become significant at critical points of cavity closure and at missile-cavity separation

where the large, dominant forces of gravity and inertia may nearly cancel each other. By determining the occurrence of cavity separation or closure, a small, seemingly unimportant force can greatly influence cavity behavior and, hence, missile behavior. The mechanisms influencing cavity behavior have been extensively observed but are not fully understood.

The factors that might influence the water-entry phenomena, condensed from Reference 61, are listed in Table 3.1 and their dimensions in the $\rho \ell v$ system in Table 3.2.

When an airborne missile hits the water, it creates a cavity that persists and grows during the underwater trajectory, as seen in Figure 3.1. (This sequence of exposures, showing progressive stages of a missile entering the water obliquely, was printed on a rotating disk of film, using a camera with a sector-shaped slot and stroboscopic flash lamp. The camera is described in detail in Part V).

Initially, the cavity extends back to the surface of the water. As the missile travels along its trajectory, the cavity becomes longer and thinner until it closes from the surface in either of two ways: the surface of the water can close over the cavity or the cavity can "neck down" and break off at some point beneath the surface

13

TABLE 3.1. Factors Influencing Water Entry

Parameter	Amenable to Scaling
Properties of the liquid	
Density	Yes
Kinematic viscosity	No
Compressibility	No
Vapor pressure	No
Surface tension	No
Imperfections in fluidity	
Cohesion	No
Ability to support tension stress (momentarily)	No
Stress-time relaxation characteristics	No
Dissolved particles	No
Gas nuclei	No
Adhesion	Yes
Properties of the gas	
Density	Yes
Kinematic viscosity	No
External impressed pressure	Yes
Thermodynamic properties	No
Properties of the missile	
Density distribution	
Position of CG	Yes
Values of moments of inertia, total mass, etc.	Yes
Size, geometric form, and imperfections in shape	Yes
Surface condition	
Smoothness	No
Wetting and adhesion characteristics	No
Elastic properties	
Local stresses and deformations (e.g., on nose at impact)	No
General flexural deformations (e.g., those due to nose and tail lift forces)	No
Miscellaneous influences	
Impressed gravitational field	Yes
Wall effects in model tanks	Yes
Initial conditions at water impact	
Angle ξ between trajectory CG and surface	Yes
Aspect of missile at entry values of its pitch (θ), roll (ϕ), and yaw (ψ)	Yes

(Figure 3.2). The abruptness of deep closure is shown in Figure 3.3, in which a 2-inch-diameter torpedo model is photographed at 1/100-second intervals.[1] After closure, the missile continues to travel in the remaining cavity until the cavity slips away or is completely entrained by the flowing water. Remnants may persist about a dummy missile more than 100 diameters from entry. Deep closure and sudden cavity slippage occur during the launching of the 2-inch-diameter torpedo model shown in Figure 3.4.

Water entry is, then, a series of transient phenomena occurring after the quasi-steady-state airflight.

---

[1] A net prevents possible missile injury from contact with the wall.

14

TABLE 3.2. Dimensions of Quantities Occurring in Water-Entry Problems
(from Reference 61)

Property	Symbol	$\rho \ell v$ System of Units	Associated Dimensionless Number
Impose No Conditions on Scale Factors			
Density	ρ	ρ	Gas density coeff.,[a] ρ_{model}/ρ_{std}
Length	ℓ	ℓ	. . . . .
Time	t	ℓv^{-1}	. . . . .
Velocity	u	v	. . . . .
Angle		Dimensionless	
Angular velocity	. . .	$\ell^{-1} v$	. . . . .
Dynamic fluid pressure in perfect fluid	p	ρv^2	. . . . .
Temperature	T	. . .	. . . . .
Impose Special Conditions on Scale Factors			
Externally impressed pressure, vapor pressure, stress (adhesion, cohesion)	p	ρv^2	Pressure no. $p_0/\tfrac{1}{2}\rho v^2$
Bulk modulus, Young's modulus, shear modulus	. . .	ρv^2	. . . . .
Compressional wave velocity in fluid	c	v	Mach no. v/c
Kinematic viscosity	ν	ℓv	Reynolds no. $\ell v/\nu$
Surface tension	τ	$\rho \ell v^2$	Weber no. $\eta/\rho \ell v^2$
Flexibility of specimen	$1/n^2 \ell^2$	v^{-2}	Flexure no. $v^2/n^2 \ell^2$
Impressed gravitational acceleration	g	$\ell^{-1} v^2$	Froude no. $v^2/g\ell$

[a]Adjusting externally impressed pressure in model system changes density of atmosphere gas; 1-to-1 scaling of density does not hold if same gas is used in model and prototype systems. To preserve 1-to-1 scaling of gas density, a heavier gas must be used in model system.

Figure 3.1. The water-entry cavity.
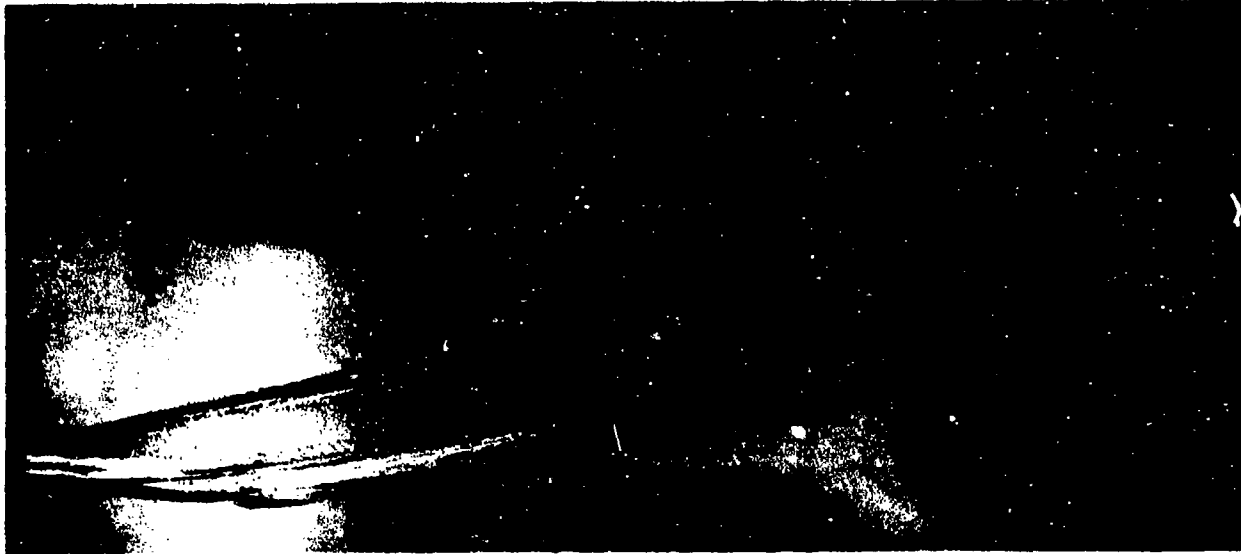
Surface closure
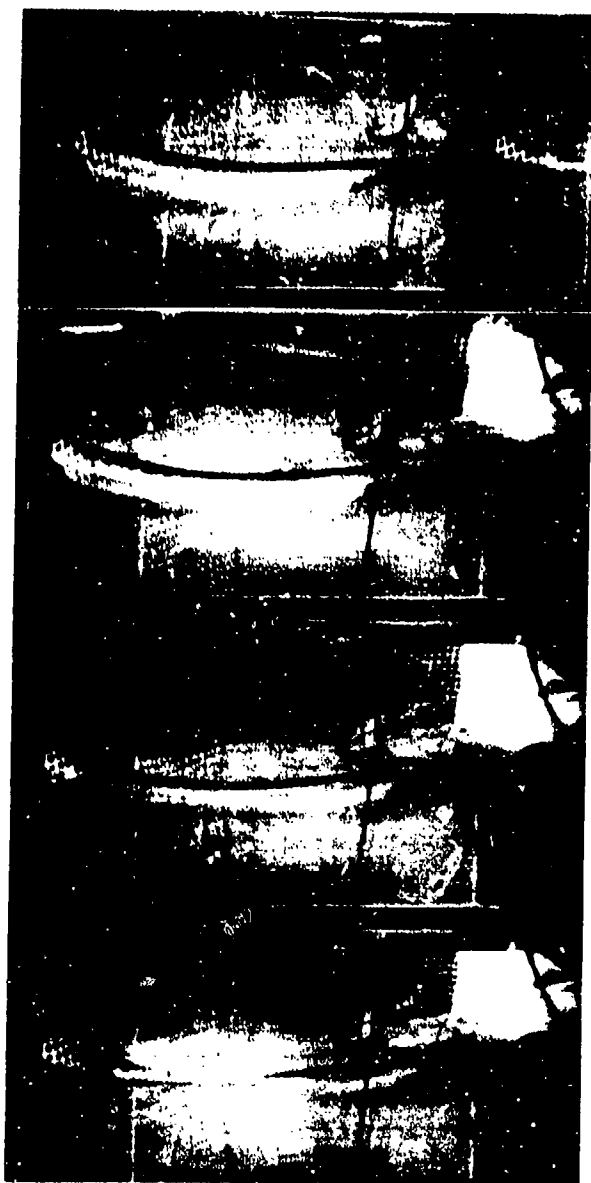

Deep closure

Figure 3.2. Water-entry cavities.

Figure 3.3. Sudden occurrence of deep closure.

Figure 3.4. Cavity behavior: deep closure, sudden strippage, and attrition.

The phenomena of water entry traditionally have been divided into four phases:

1. Impact
2. Flow formation
3. Open cavity
4. Closed cavity

To a certain degree, these phases have been studied separately, although no phase of missile trajectory is independent of preceding ones.

The velocities of the missile, both linear and angular, established during airflight have much to do with the entry phenomena because these velocities, coupled with the physical properties of the missile, determine both the inertia of the missile at impact and the orientation of the missile with respect to the water surface. Missile orientation, of course, determines the specific shape that first contacts the water.

IMPACT

Impact initiates a short-duration, high-velocity shock wave that radiates at approximately the velocity of sound in the water (Reference 10). Although the impact force is very large and may cause water-entry damage, its short duration (a fraction of a millisecond) appears to preclude its greatly influencing subsequent hydrodynamic flows in the low-velocity regime. Impact does, however, alter the missile velocity and produces a splash that may ultimately affect cavity closure. Order-of-magnitude calculations show that the compressibility of the fluid medium should have little effect on the dynamic behavior of the missile.

The sequence of photographs in Figure 3.5 (Reference 60) shows the growth of a splash during the vertical entry of an 8.6-inch sphere entering water at 24.4 fps. (The raised water profile in the vicinity of the sphere is made visible by talcum powder on the water surface.) Figure 3.6 (Reference 60) shows in silhouette the splash contour of a 4.5-inch-diameter sphere entering water at 24.4 fps. The splash sheath, which may travel four or five times missile speed

18

Figure 3.5a. Growth of a splash during vertical entry of a sphere.

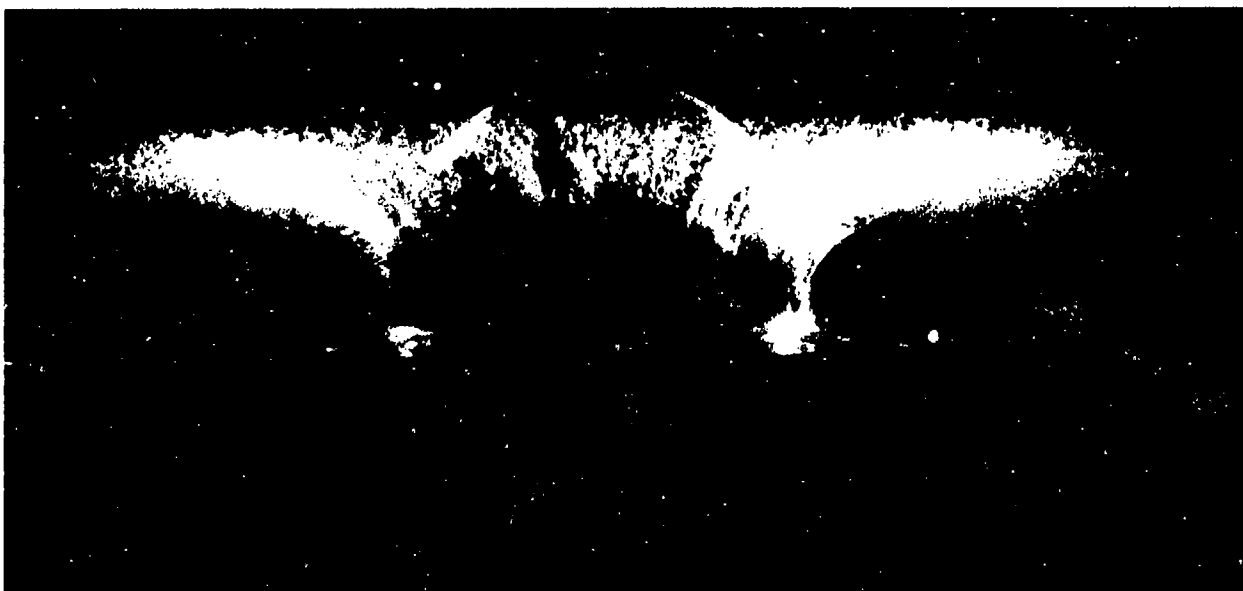Figure 3.5b. Growth of a splash during vertical entry of a sphere.

20

Figure 3.5c. Growth of a splash during vertical entry of a sphere.
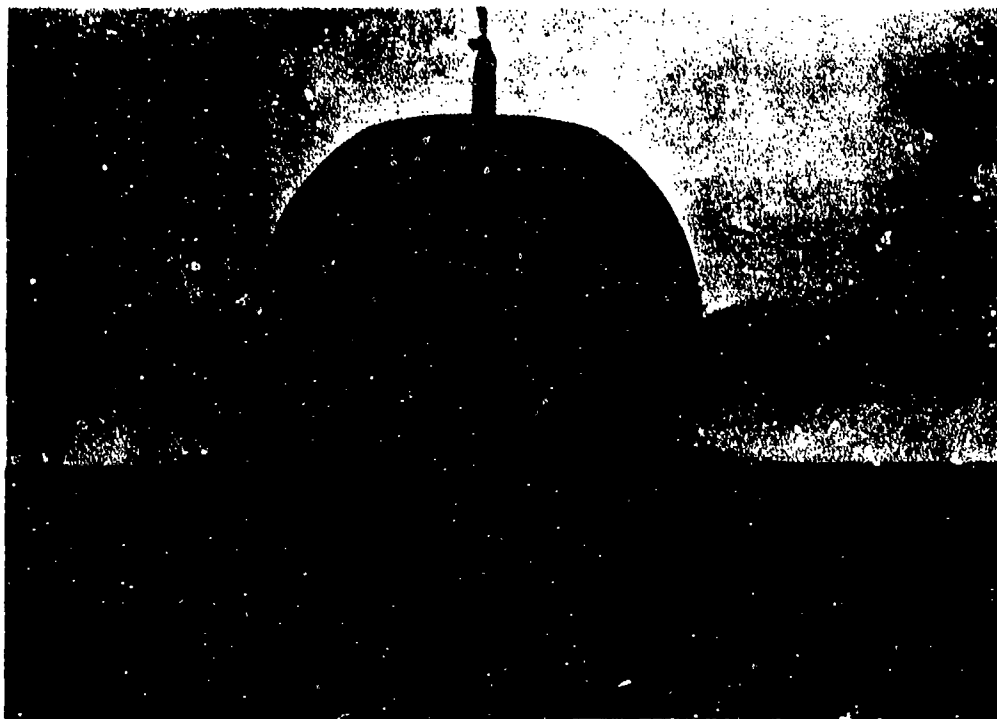
Figure 3.6. Shadowgraph of vertical entry of a sphere.

Figure 3.7. Rise of liquid surface in beaker after impact of sphere.
(From Reference 112.)

(Reference 55), leaves the spherical surface tangentially and each individual water particle continues to travel in a straight line. The curvature of the sheath does not represent the path of the individual water particle, but rather the integrated paths of many.

A slight rise in the otherwise undisturbed liquid surface beyond the splash, which occurs immediately after impact, has been attributed to the entry shock wave (Figure 3.7, from Reference 112).[2]

Another interesting manifestation of the impact force was found during the vertical entries of a right circular cylinder (Reference 101). During these launchings, circular striations normal to the direction of missile motion formed in the surface of the cavity (Figure 3.8). The striae were generated at the same frequency as the natural fundamental longitudinal vibration frequency of the missile

suspended in air, leading to the conclusion that the striae were generated by missile vibration initiated at impact, as previously suggested by Birkhoff (Reference 8).

To estimate the magnitude of the impact force, it is assumed that the missile is rigid, and that during the first instant of contact between the missile and the water, the water does not have time to flow away and, therefore, acts as if it were solid. Then the elastic peak pressure on the missile caused by the elastic deformation of the water is on the order of

$$p = \rho_w cv \sin \xi = (E \rho_w)^{1/2} v \sin \xi \quad (3.1)$$

To scale the elastic forces, model velocity must equal prototype velocity (Mach scaling) if the same liquid is used in both systems. Elastic forces in the Froud-scaled systems currently in use are not scaled because they are too small by

[2]A facsimile of Worthington's earlier edition published b' 'ongmans Green, London, 1908.
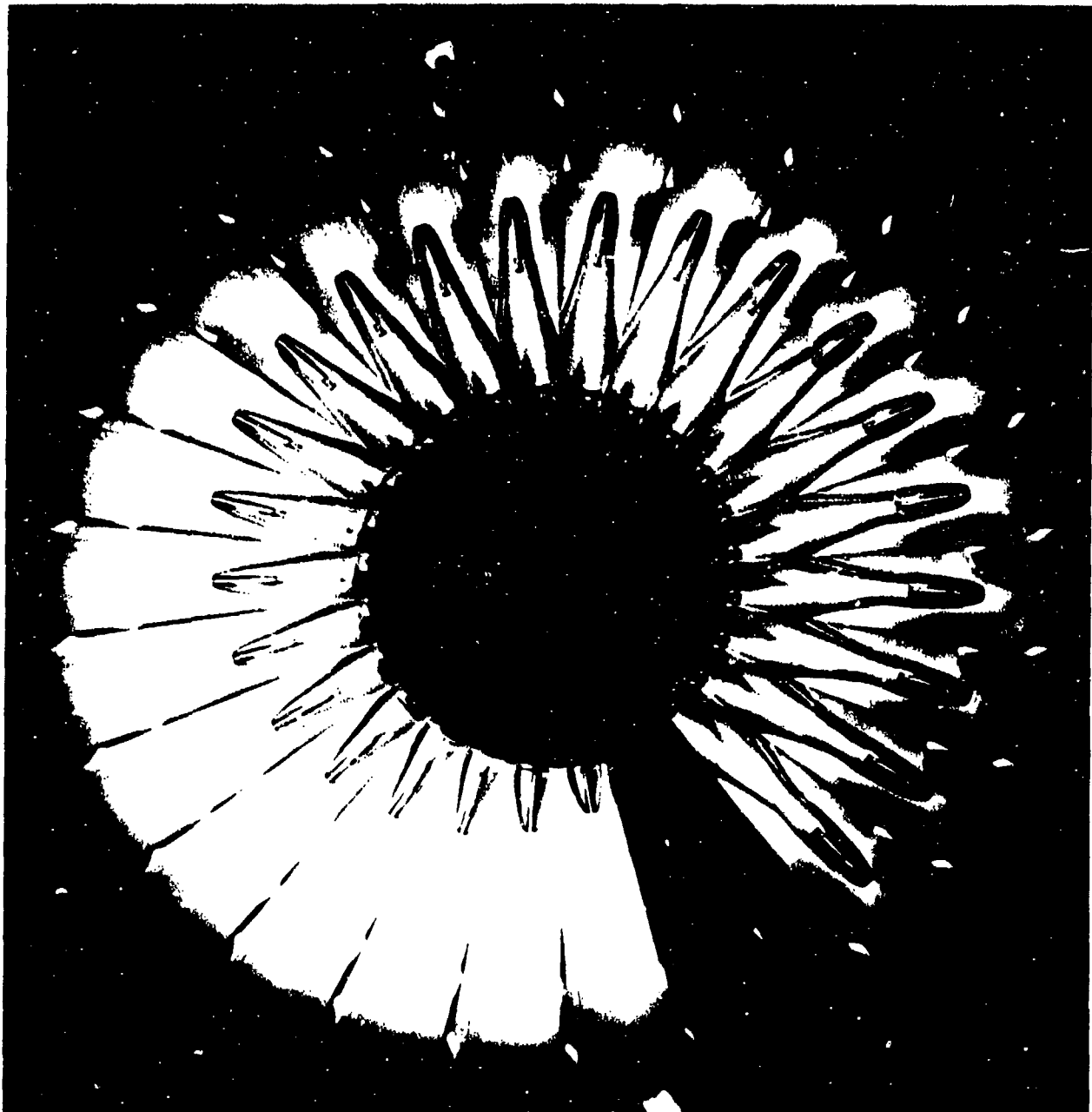
23

Figure 3.8. Cavity with circular striations.

the factor of $\lambda^{1/2}$. Failure to scale these forces has not been detrimental to modeling in the relatively low-velocity range thus far considered because their effect on the trajectory appears to be negligible, but at higher velocities this will not be the case. When the elastic forces become significant, Froude scaling must be modified by or replaced by Mach scaling.

FLOW FORMATION

Immediately after impact the water is set into motion by the missile, and a flow-forming regime ensues during which fluid pressures on the missile are considerably lower than in the impact regime, but considerably greater than in the later quasi-steady-state flow regime. This flow-formation regime is extremely complex; a
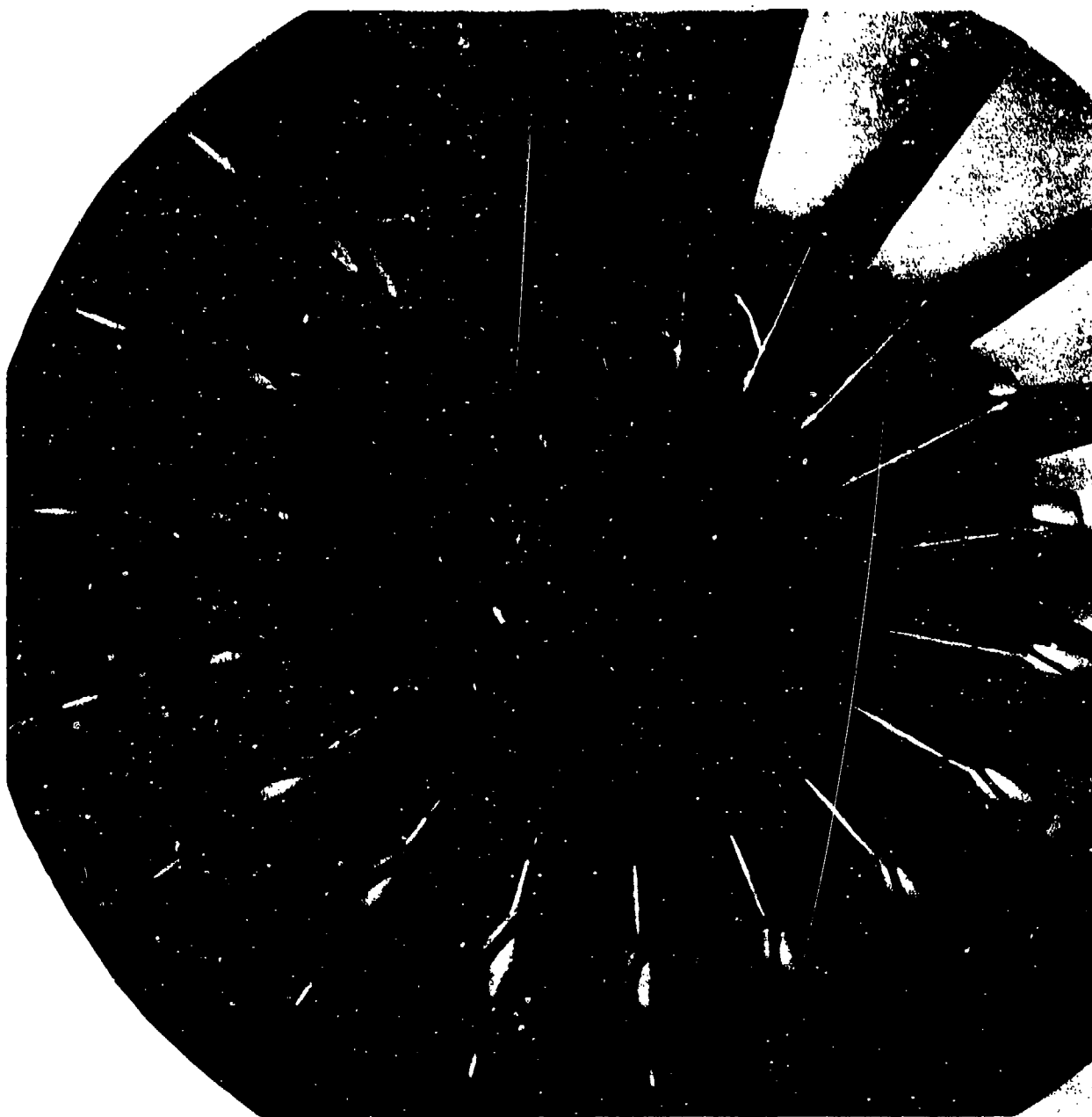
Figure 3.9. Cavity beginning to form immediately after impact.

complete theoretical description of it is not yet available. The first theoretical treatment of impact upon water was initiated by von Kármán (Reference 86). Bibliographies of work in hydrodynamic impact and water entry are included in References 52 and 83. Studies associated with or conducted at NUC are given in Chapter 8 of Reference 61 (P.Y. Chou) and in References 14, 15, 20, 21, 50, 58, and 85. Recently, hydrodynamic pressure measurements were made of

the vertical water entry of a sphere over the impact, cavity-flow, and cavity-collapse phases using submerged hydrophones (Reference 26), and missile water-entry decelerations using a telemetry system (Reference 57).

After impact, the water flows away from the missile and a cavity begins to form (Figure 3.9). The wetted surface of the missile increases rapidly until a relatively stable line of cavity separation is established (Figure 3.10).

25

Normal separation   Clinging flow

Figure 3.10. Growth of wetted surface to establish stable line of cavity separation.

This separation line may be sharply defined, irregular, malformed, or fluctuating (Figure 3.11), giving rise to clear, obscured, irregular, or distorted cavities, respectively. If the line of separation is irregular, the distance of water flow over the missile varies, producing small variations in the velocity of the water as it leaves the missile. Small velocity variations cause striations in the wall of the cavity parallel to the direction of flow, rendering the cavity translucent or even opaque. When the line of separation is so irregular as to be distorted, the velocity variation is so great as to cause large bulges in the cavity wall.

Irregular separation is frequently associated with erratic trajectory behavior (Figure 3.12 from Reference 60). When the missile is of a smooth, streamlined configuration, the fluid flow nearly conforms to the body shape, and only a thin wedge-shaped film of gas separates the liquid from the solid body (Figure 3.13).[3] This film is sometimes swept away by the water, distorting the line of cavity separation (Figure 3.14). A blunt missile shape, on the other hand, produces large clearances between missile and cavity (Figure 3.15); its separation line is sharp and clear.

The unstable condition characterized by irregular separation may be influenced by secondary forces (those arising from liquid-surface tension, missile-surface condition, gas nuclei in the water, gas viscosity, etc.), and modeling of this condition is uncertain. It is sometimes possible to trigger a normal separation artificially, by, for example, grooving the missile nose at the zone of normal separation, but great care must be exercised to assure that the cavity-tripping mechanism does not otherwise alter the flow.

A large exchange of energy occurs during the flow-forming phase of entry. Some conception of the energy ultimately imparted to the water can be gained from Figure 3.16, which shows a cavity (formed by a rifle bullet) piling up on the bottom of the tank, probably due to cavity momentum, as discussed in Reference 8, after the missile was stopped. A change in the

angular pitch velocity (whip) occurs when the resultant of the hydrodynamic force on the missile nose does not pass through the missile CG. Whip also arises from the phenomenon known as underpressure.

Hydrodynamic whip occurs during oblique entry because the lower side of the missile contacts the water first. The hydrodynamic pressure is normal to the wetted surface of the missile and, unless the contacting surface is a portion of a sphere centered on the missile CG, the resultant force produces a moment about the CG (Figure 3.17 from Reference 55). The whip from this moment causes a flat head shape to nose down and a convex head such as a hemisphere or ogive to nose up. After the nose of the missile is fully wetted, the pitching moment from this hydrodynamic-pressure force becomes zero as long as the missile is traveling with a zero angle of attack.

Another hydrodynamic factor influencing missile trajectory, underpressure, can best be explained in terms of the pressure distribution about the missile nose. The steady-state pressure on a completely wetted body is highest at the stagnation point. Farther along the body, the pressure drops to a minimum and then recovers to a nearly constant value somewhat less than stagnation pressure (Reference 73).

Now if the body is partially enveloped in a cavity, the pressure normally drops from stagnation pressure to cavity pressure at the point of separation (Reference 73). The shape of the body and its attitude in the cavity will alter the pressure distribution, but for small angles of inclination with respect to the cavity, the character of the pressure distribution is unchanged (Reference 72). Under some entry conditions, a nonsymmetric low-pressure area can thus exist ahead of the actual cavity separation point.

A low-pressure area on one side of the nose and cavity pressure on the other produces a pressure differential across the nose equal to, at most, the difference between atmospheric pressure and the vapor pressure of water. A large, long-persisting underpressure area can cause the

---

[3] A mirror inclined at 45 degrees shows the undersides of missile and cavity.
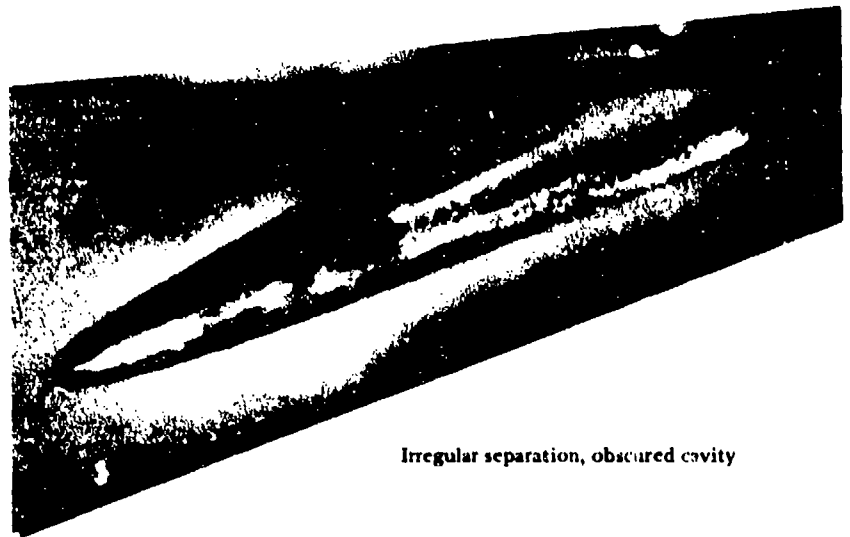
Irregular separation, obscured cavity

Sharp separation,
clear cavity

Malformed separation following minor fluctuations
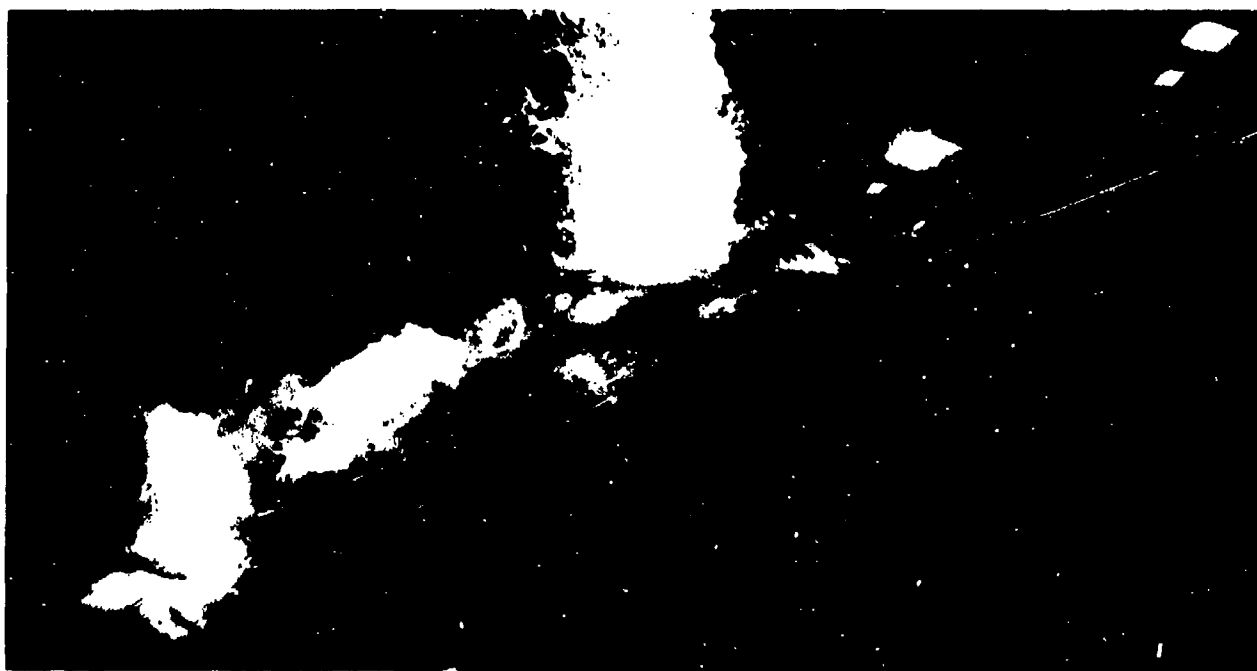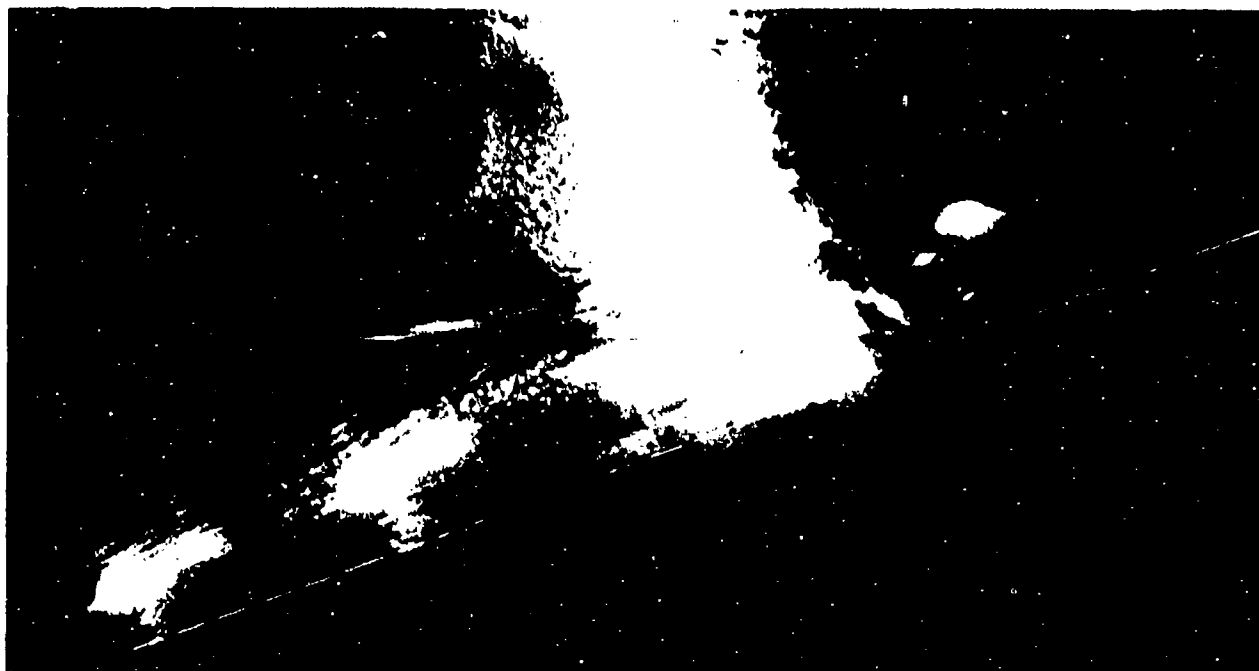
Figure 3.11. Cavity separation.

28

Figure 3.12a. Erratic trajectory caused by irregular separation.
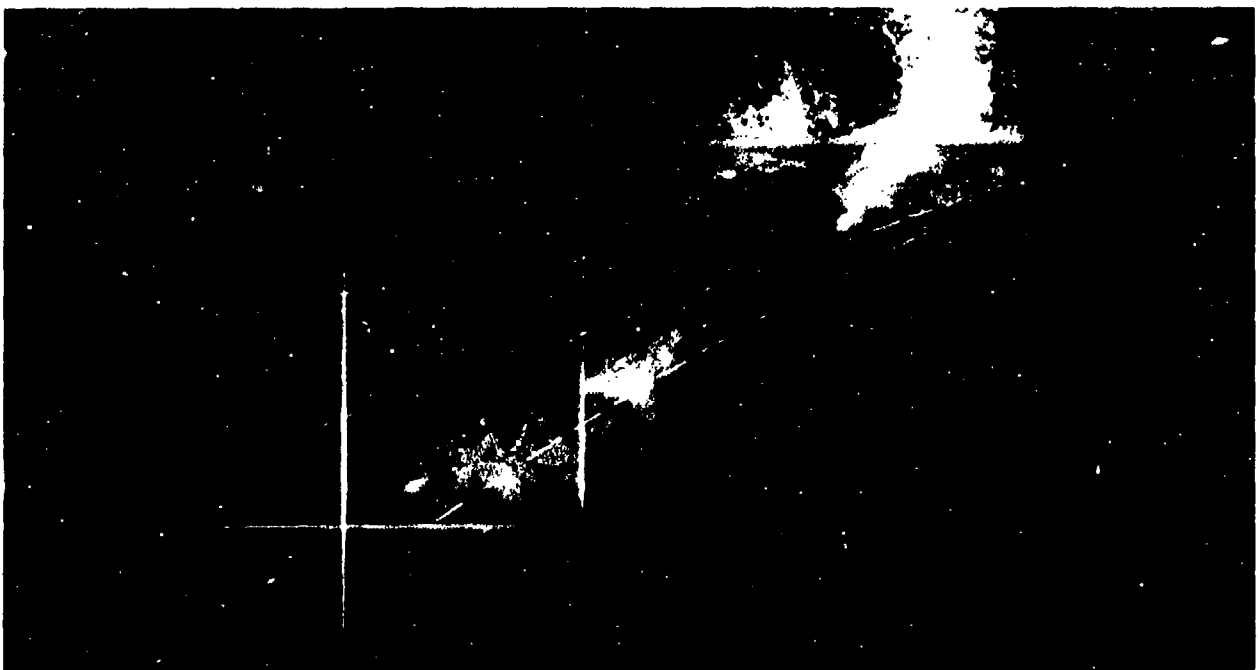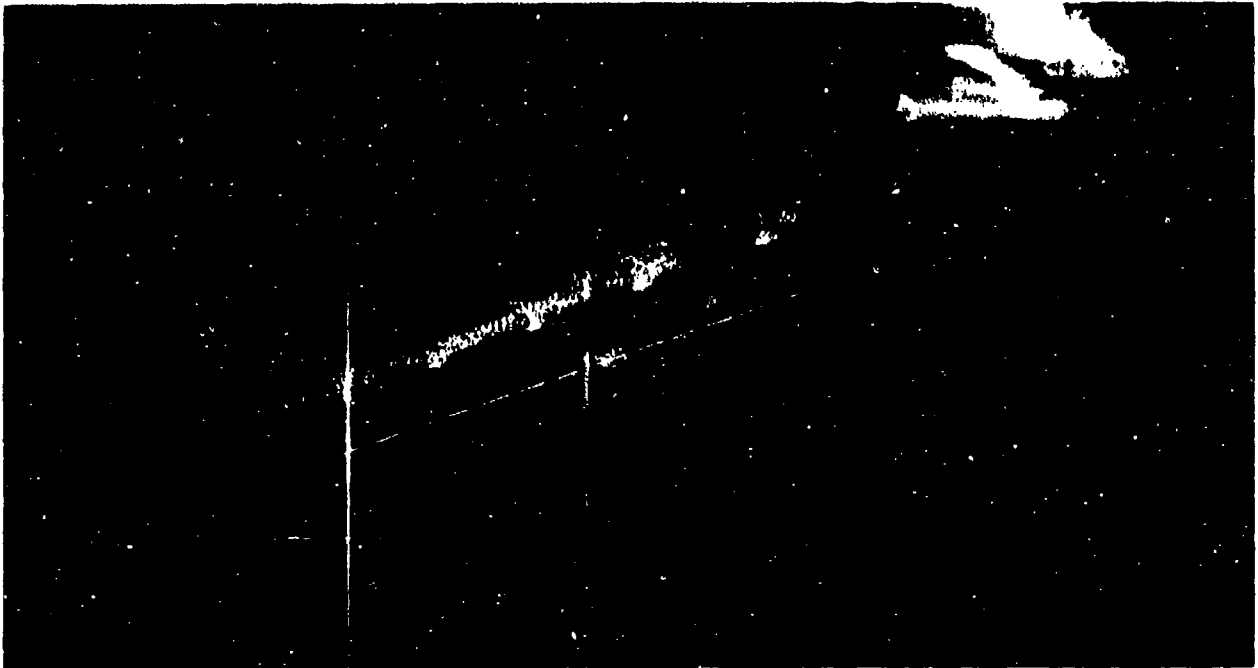
29

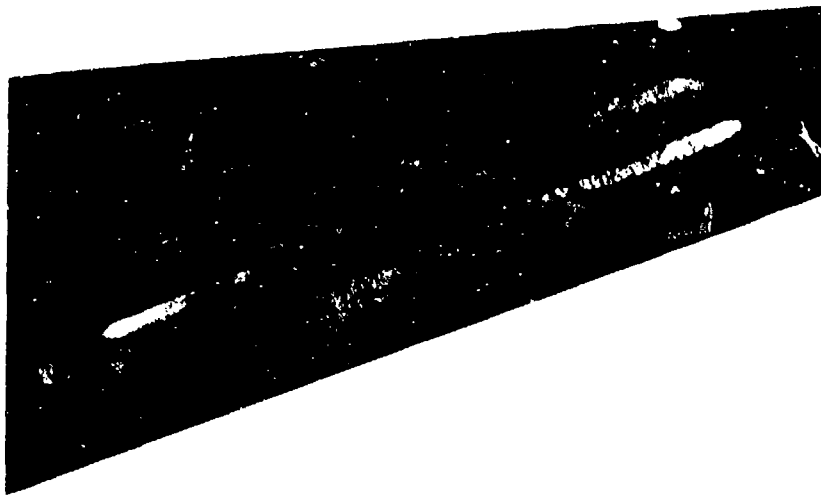Figure 3.12b. Erratic trajectory caused by irregular separation.

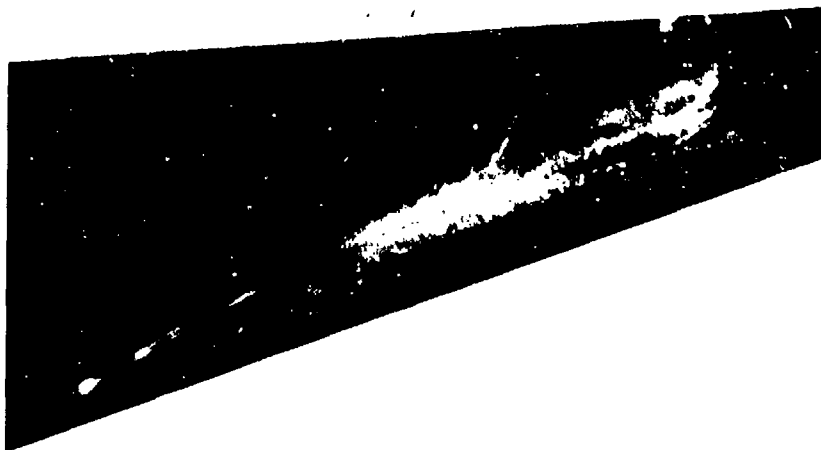Figure 3.13. Gas film separating liquid from body.

Figure 3.14. Line of separation distorted by flow clinging to streamlined body.
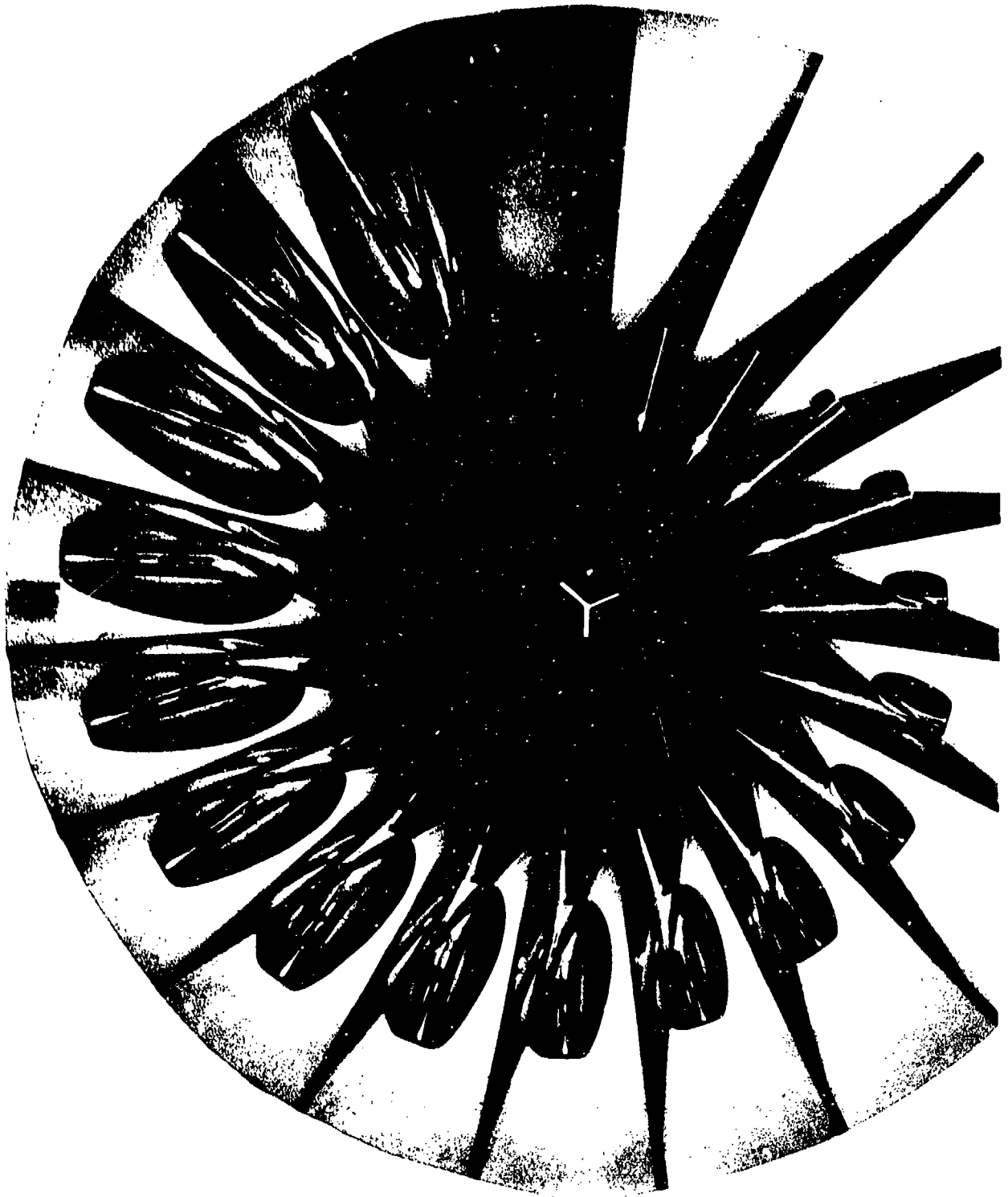
31

Figure 3.15. Flow sharply separated from blunt missile body.

Figure 3.16. Cavity formed by rifle bullet.

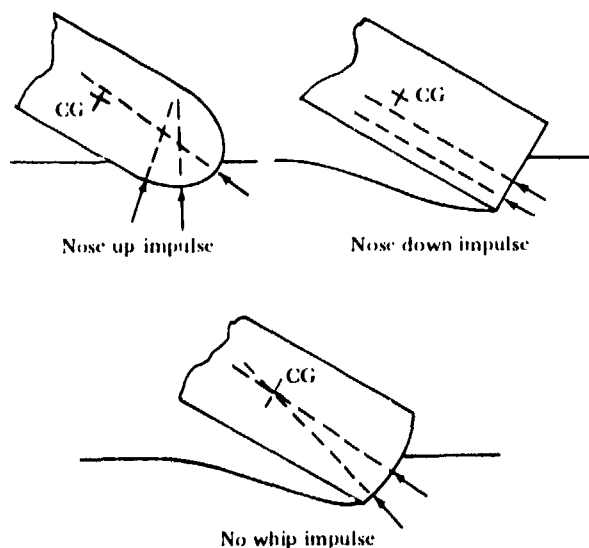Nose up impulse   Nose down impulse

No whip impulse

Figure 3.17. Whip impulse.

missile to whip so violently that diving or broaching trajectories occur (Figure 3.18 from Reference 60). Reducing the atmospheric pressure reduces the maximum pressure differential that can occur across the missile nose. Underpressure-induced whip is modeled when the atmospheric pressure in the model system is scaled.

Delayed separation, and thus the possibility of underpressure effects, will occur whenever the clearance between missile and cavity wall becomes so small that the water carries the gas in the film away faster than it can be replaced from the cavity. These narrow clearances are inherent in the flow about a streamlined body but they may also occur during oblique launchings of less streamlined shapes when the missile is oriented asymmetrically in its cavity. The gas flow in such a narrow film will occur at relatively low Reynolds numbers, increasing the
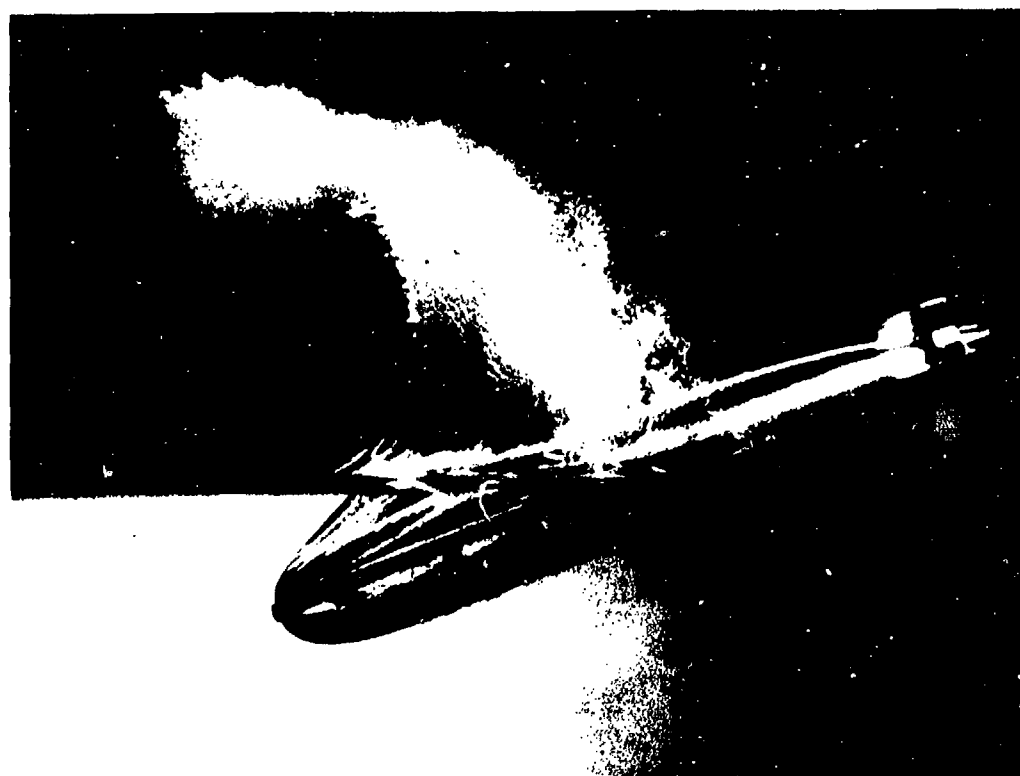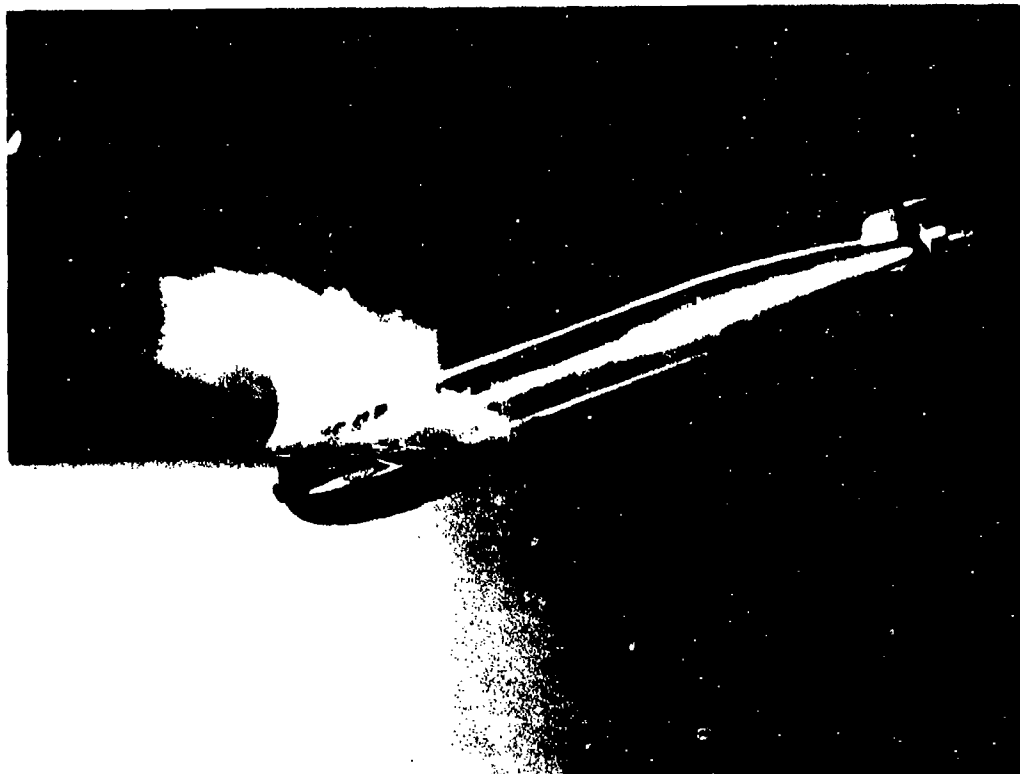
33

Figure 3.18a. Diving trajectory of torpedo model.

34

Figure 3.18b. Diving trajectory of torpedo model.

35

Figure 3.18c. Diving trajectory of torpedo model.

Figure 3.18d. Diving trajectory of torpedo model.

importance of the viscosity of the gas in determining the flow within the film. Although underpressure areas are more prevalent in small missiles, they have also been measured on 22.42-inch-diameter prototypes (Chapter 6).

In addition to Froude scaling, pressure-density or gas-density scaling is necessary for proper modeling of whip forces. Modeling of the underwater trajectory cannot be expected unless significant whip forces are properly scaled, because the whip affects missile orientation at the beginning of the underwater trajectory.

THE OPEN CAVITY

A complete mathematical description of transient water-entry cavity behavior is not yet available. Birkhoff and Isaacs (Reference 8) discuss various hydraulic flow models and propose a method for predicting (from a knowledge of its mass and cavity drag coefficient alone) the behavior of a cavity formed under vacuum conditions by any axially symmetric missile traveling with no yaw. For vertical water entries that result in the formation of open cavities (no surface seal), the cavity shapes as predicted by

Birkhoff's model are shown to correspond very well to observed cavity shapes for spheres of various sizes and materials (References 1 and 46). Scale effects in water-entry cavity behavior are discussed in References 5, 6, and 55.

During the third or open-cavity phase of water entry, the cavity remains open to the atmosphere at the surface and grows longer as the missile travels along its trajectory. Gas feeds in from above to fill the void behind the missile, giving rise to a cavity that is filled partly with gas and partly with water vapor. Cavity width is determined by the rate at which energy is imparted to the water, the wider cavity being associated with the larger energy input (Reference 46). The growth of the cavity, then, is largely determined by the shape and velocity of the missile, by the density and pressure of the atmospheric gas, and by the position of the missile in the cavity. The surface tension of the liquid, the viscosity of the liquid and the gas, and the surface condition of the missile are ordinarily of secondary importance.

Several conditions alter the texture or appearance of the cavity. Turbulence in the boundary layer ahead of cavity separation

37

increases with missile velocity and sometimes produces noticeable roughness when the boundary layer has separated to become the cavity wall Turbulent gas flows within the cavity produce pressure variations that roughen the walls. The cavity walls may be distorted by blowing splash. Re-entrant or closure jets sometimes strike the cavity wall directly or impinge upon the missile and then splash into the wall, and the simple cavity is often distorted by a secondary cavity formed by the missile tail (Figure 3.19 from Reference 111). All these cavity disturbances have been observed experimentally, and are discussed in detail in Part IV.

The orientation of the missile in the cavity influences trajectory shape. A straight trajectory approximating the continuation of the air trajectory occurs when the missile travels with only its nose in contact with the water or oscillates with its tail bounding between top and bottom cavity surfaces (Figure 3.20). If the tail remains in contact with the cavity top or bottom, a curved trajectory (either diving or upturning) results (Figure 3.21 from Reference 60). A fine-nosed missile with large underpressure area can dive with its tail riding in the cavity bottom (Chapter 8). If the missile is unstable, it may broadside (Figure 3.22).

If the resultant of the forces determining the orientation of the missile in the cavity is small, minor differences in ambient or launching conditions may change the orientation and alter the missile trajectory. It is in these instances that the art of modeling is most uncertain.

The presence of the cavity makes it difficult to measure missile position. If the cavity wall is clear, the interface acts as a reducing lens. The distortion of the missile image varies with both time and space because the curvature of the cavity wall is not constant. If the cavity wall is rough, the missile image is blurred, or even obscured.

The open-cavity phase of water entry continues until the disturbed water comes together and seals the cavity from the atmosphere.

CAVITY CLOSURE

Cavity closure occurs either at the surface, some point below, or both. The nature of the closure is determined by launching conditions and by the physical properties of the missile, the liquid, and the gas. Closure is an event of great importance because it terminates the flow of external gas into the cavity, although it is possible that fluid flow inertia may produce a slight enlargement of the cavity after closure.

The conditions determining deep cavity closure are relatively simple, being primarily the inertia of water and gravity. Momentum imparted by the missile to the water causes the cavity to open. The hydrostatic force upon the cavity and the surface tension of the liquid acting within the cavity walls tend to close the cavity. When the closure forces become dominant, the cavity will begin to narrow, form a neck, and finally close (Figure 3.23). Since the surface tension forces are usually small with respect to the hydrostatic (i.e., gravity) forces, Froude scaling of deep closure is reasonably successful.

The more complex phenomenon of surface closure, also shown in Figure 3.23, has been observed for many years without being completely explained. The force system at the cavity mouth arises from both water and gas flows. A large hydrodynamic force can occur in the cavity lip where the masses of water lie. The hydrodynamic forces in the splash are small because little water is involved. However, the splash cannot be ignored because it can modify the size of the cavity orifice, thereby significantly influencing the gas flow into the cavity. Thus, three separate flows — cavity-lip, splash, and gas — interact to produce cavity closure.[4] Empirical theory regarding cavity closure and closed cavity behavior is included in Reference 8.

The major hydrodynamic flow in the cavity lip is at first directed outward as the water flows away from the impact. Then the surface tension of the liquid, together with the hydrostatic forces, will act to restore the disturbed surface to its normal condition. The pressure forces created by the flow of the gas rushing through the cavity mouth produce a region of low pressure on the underside of the cavity lip. The higher atmospheric pressure acting from above causes the cavity to close.

The pressure produced by the gas flow is proportional to the atmospheric density. Thus,

---

[4]The resultant force from these flows determines whether or not the cavity will form. If the closure force is dominant at impact, the flow merely slips around the missile and no cavity occurs.
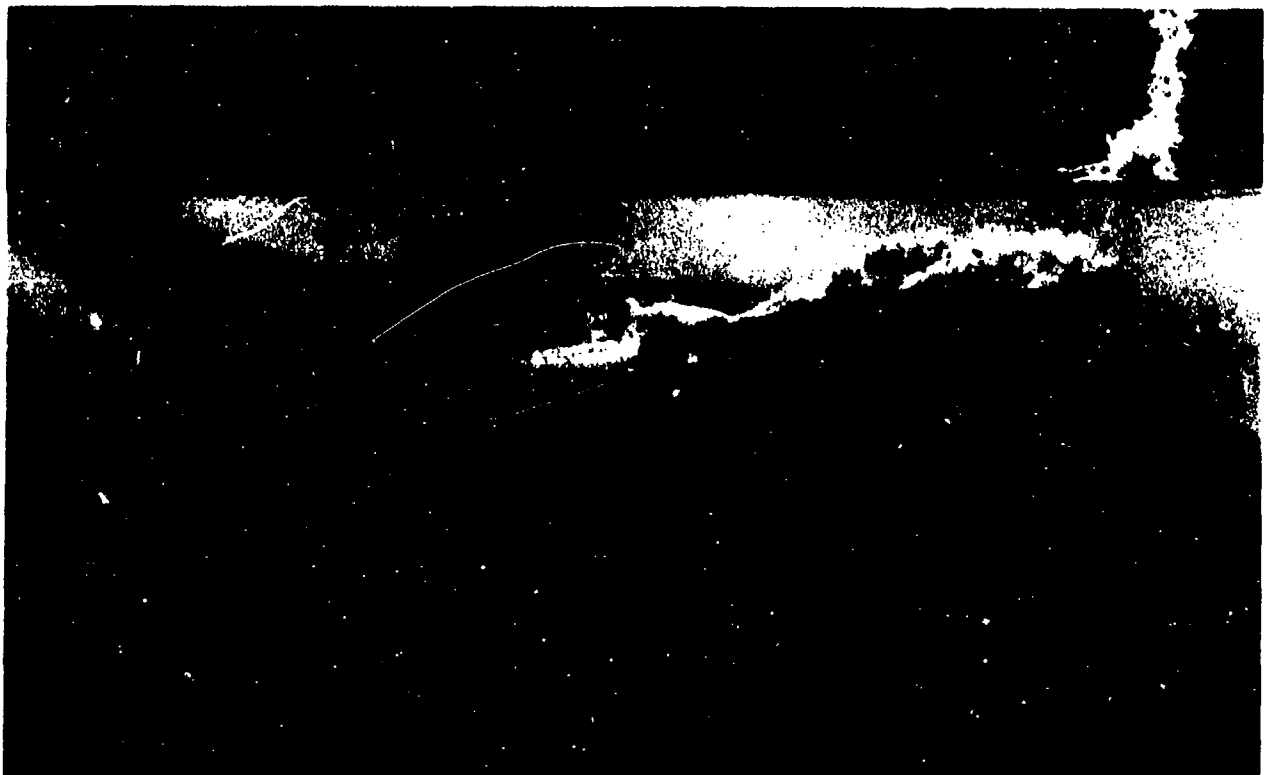
An pressure 1 atmosphere
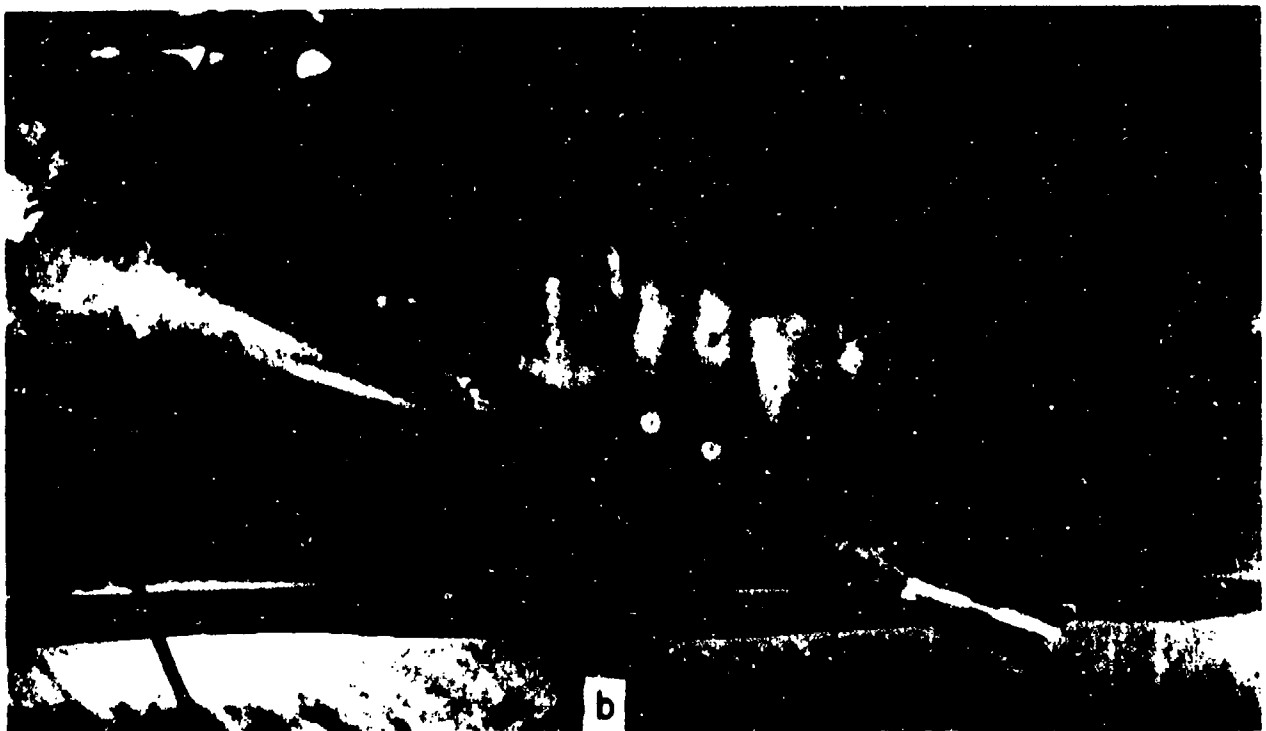
Air pressure 1/6 atmosphere

Figure 3.19. Secondary cavity formed when missile tail contacts cavity wall.

Only missile nose contacting water

Tail oscillating

Figure 3.20. Straight water-entry trajectories.

40

Figure 3.21. Examples of diving and up-turning trajectories when tail contacts cavity top or bottom.

41

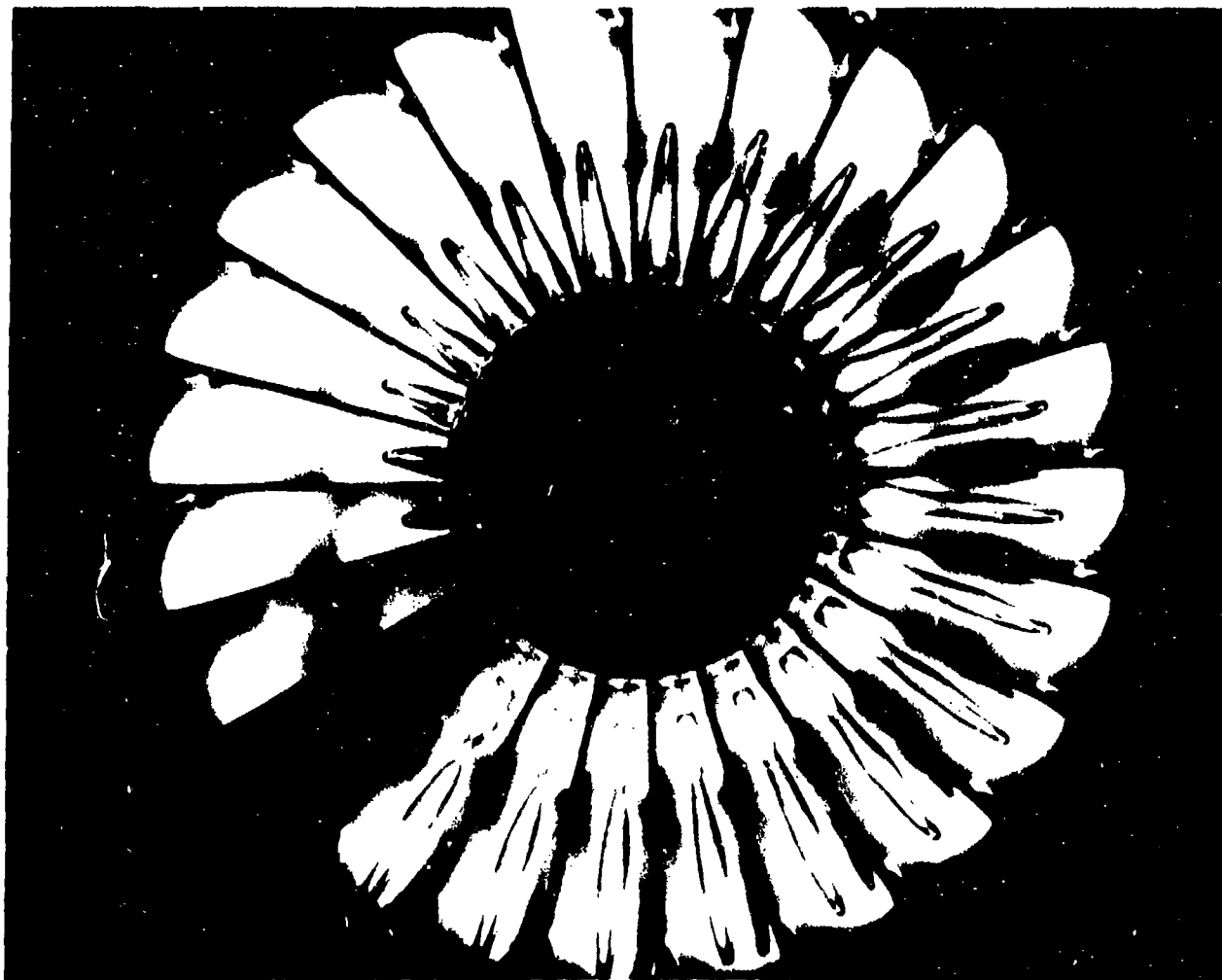Figure 3.22. Missile broadsiding after water entry.

Figure 3.23. Deep and surface cavity closure.

42

gas pressures sufficiently low to cause cavity closure are not produced on the side walls when the atmospheric density is low. Then the cavity mouth continues to widen until the hydrostatic and surface tension forces restore the surface to its normal rest condition (Figure 3.24). Under these circumstances, cavity growth is terminated by deep closure.

An indication of the pressures and forces created by the gas flow can be gained from Figure 3.25 (Reference 111), which compares the surface contours generated at two different gas pressures during two otherwise equivalent launchings of a hemisphere-head torpedo model with a flared cone tail. The 2-inch-diameter missile was 15 inches long with a trajectory water-entry angle of about 19 degrees and an entry velocity of about 120 fps. At the lower pressure, the cavity surface retains its original contour and grows rapidly at first and then more
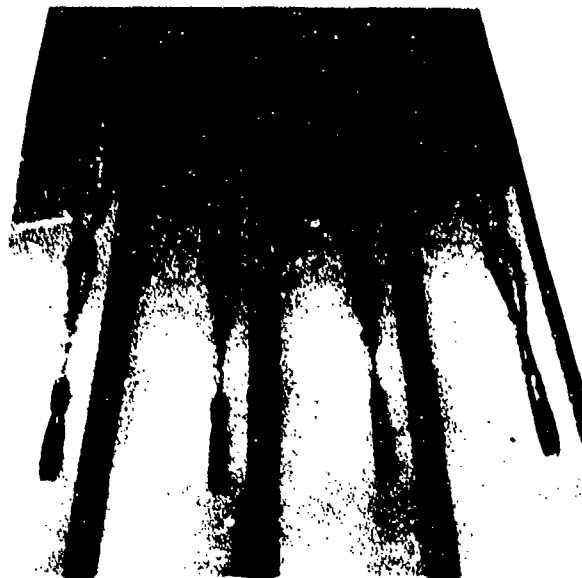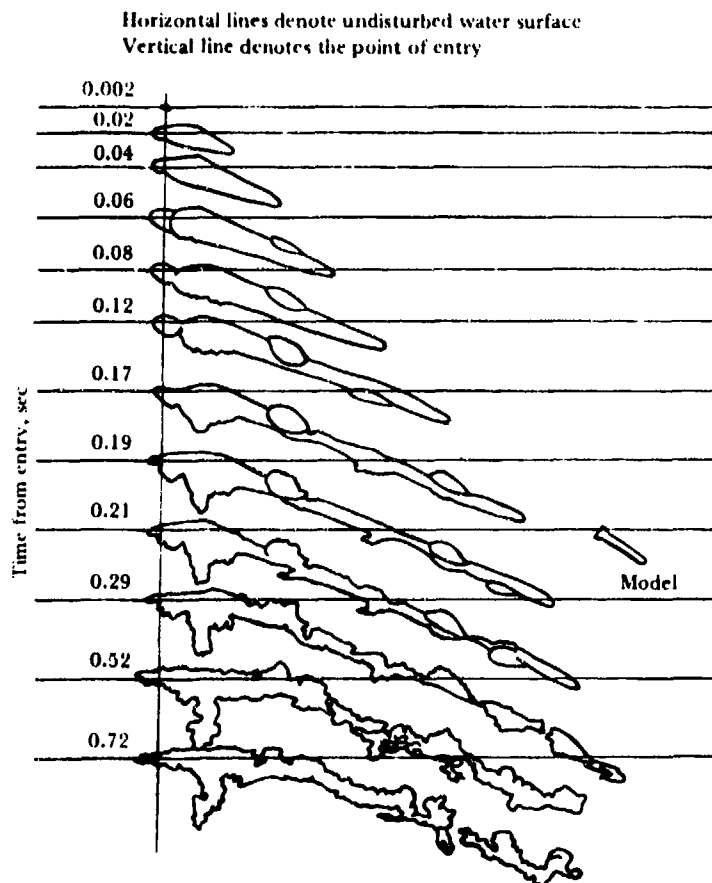

Figure 3.24. Termination of cavity growth by deep closure (right to left).

Horizontal lines denote undisturbed water surface
Vertical line denotes the point of entry

Air pressure 1 atmosphere, v_e = 120 fps, ξ = -18.7 deg

Figure 3.25a. Water-entry cavity contours.

43

slowly until about 0.2 second after water entry. Then, presumably under the influence of gravity and surface tension, the water moves in to fill the void. At the higher pressure, the motion of the surface is more complex. The contour begins to deviate from the original less than 0.06 second after entry. The general motion of the cavity wall is inward but a large rapidly growing protuberance forms beneath the cavity mouth and continues to elongate. This protuberance is probably caused by a closure jet, by air and entrained water rushing into the cavity, or by a combination of the two effects.

The sequence of photographs in Figure 3.26 shows how the cavity mouth changes as the splash and cavity grow following the vertical entry of a sphere. Above the surface, a ring of splash rises rapidly. With the passage of time, the splash falls back, thickens toward the base, and the surface-tension forces act to effect closure.

At some height, the sheath closes completely to form a dome. Above, the surface-tension forces shape the remaining ring of water into a circle of droplets. The closure dome is a fragile thing that may be destroyed by gas flow into the cavity or may be blown apart by the jet formed by closure of the cavity lips. The irregular surface of the splash sheath following vertical entry indicates that the splash is of variable thickness (Figure 3.27).

An irregular splash spoils the symmetry of surface closure and usually tends to delay it. Since water in the splash is drawn from the surface, disturbance of the surface before entry is likely to produce irregularity.

Oblique entry inherently produces an asymmetric splash, as can be seen in Figure 3.28 from Reference 60 and also in Figure 3.29. In general, surface closure follows deep closure during such launchings.
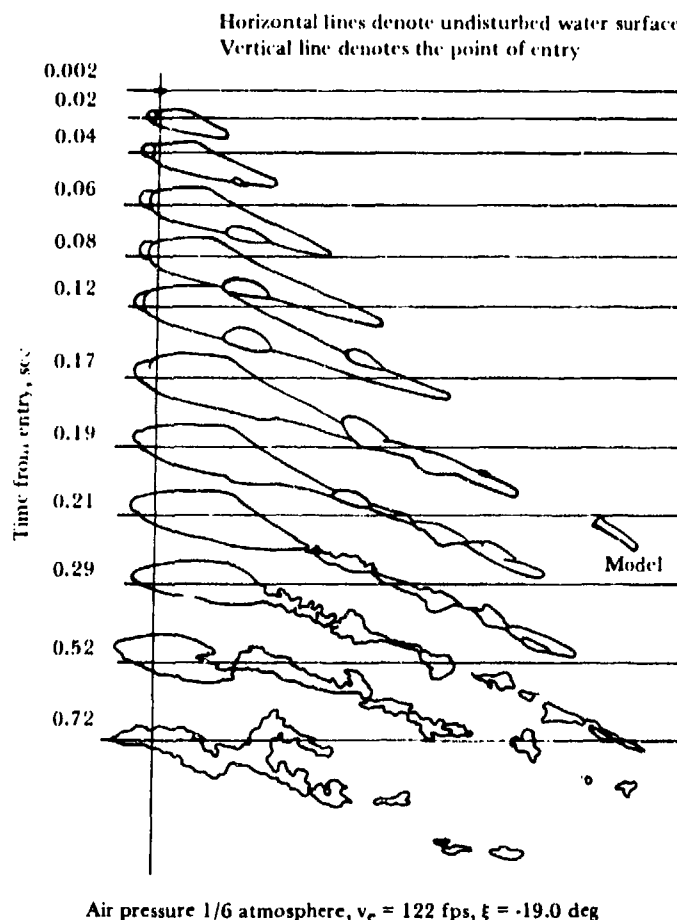

Air pressure 1/6 atmosphere, v_c = 122 fps, ξ = -19.0 deg

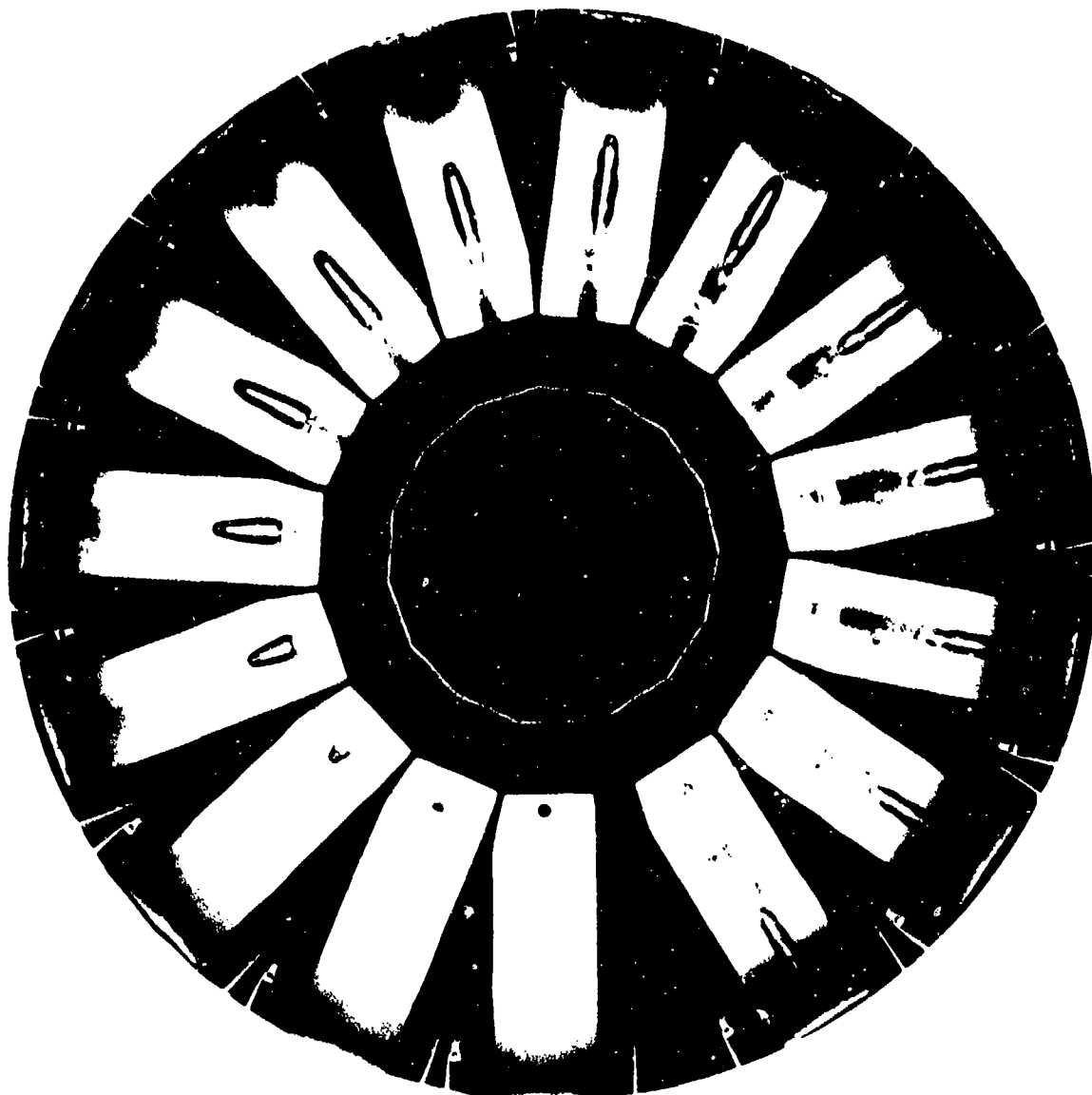Figure 3.25b. Water-entry cavity contours.

44

Figure 3.26. Cavity and splash growth after vertical entry of sphere.

Numerous forces influence surface closure and make it difficult to model. Among these forces are surface tension, the viscosity of the liquid, the viscosity of the atmospheric gas, the adhesive forces between the missile and the liquid (determined by the surface condition of the missile), gas nuclei present in the liquid, and cleanliness of the liquid surface.[5]

Fortunately, the cavity lip is usually dominant in determining surface closure. Its behavior is largely influenced by the hydrodynamic force in the main body of the liquid and the aerodynamic pressure force in the gas flow. Both forces are modeled by extending the Froude scaling laws to include gas-pressure and gas-density scaling.[6]

---

[5]Closures are also discussed in Chapters 9 and 16.

[6]If the resultant of these two forces happens to be nearly zero, the minor forces in the splash and in the cavity lip will control cavity formation. Failure to scale these may cause the model missile to enter fully wetted under conditions that produce a cavity-running prototype.
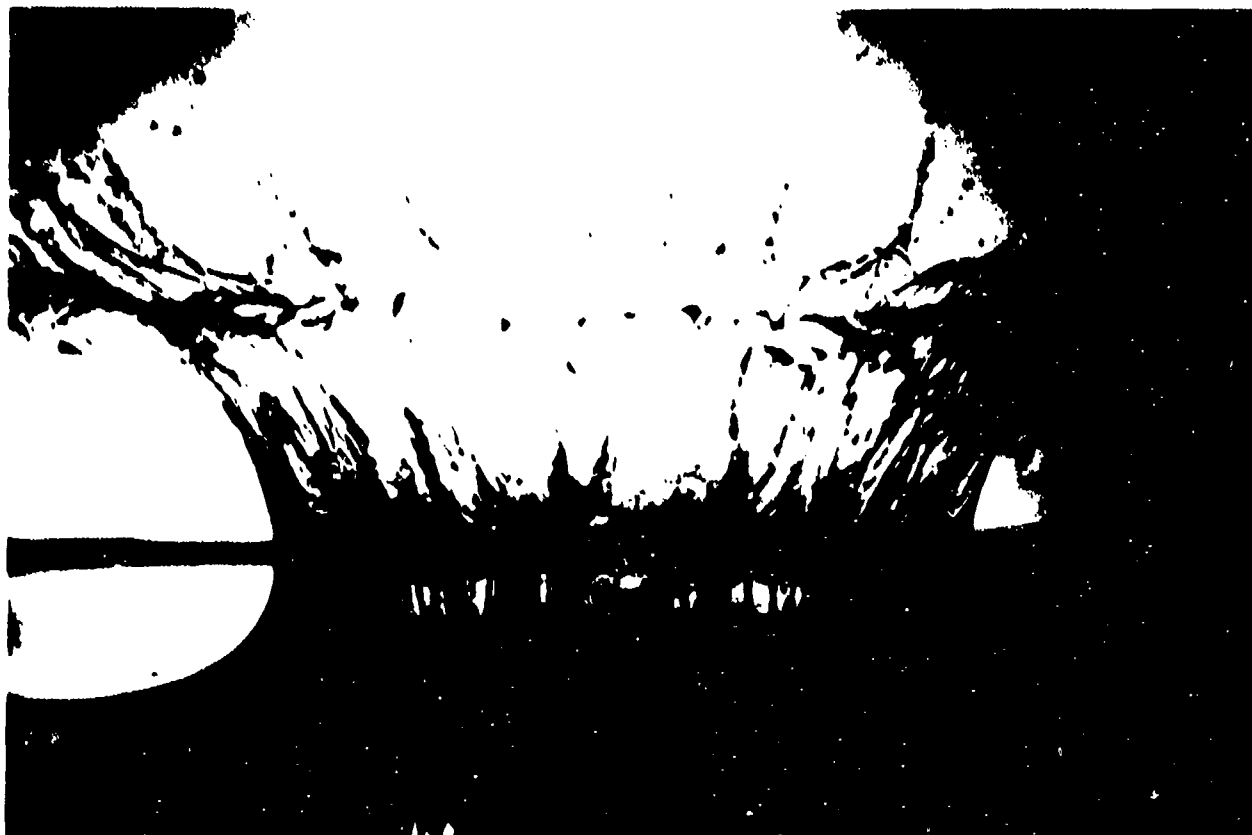
Figure 3.27. Irregularity of splash sheath thickness following vertical entry of sphere.

Jets of water, directed either up or down, are produced by cavity closure. Data indicate that the up-jets formed at deep closure are vertical or nearly so, even for non-vertical entries. According to Reference 22, this is true because the up-jet is caused by water masses colliding at deep closure as the result of the restoring action of hydrostatic pressure. For this reason, up-jets have no opportunity to form at oblique, low-angle entries. Down-jets also occur at both surface and deep cavity closure. When the water-entry angle is less than about 45 degrees, the down-jet at surface closure creates a dipole field that travels downward away from the cavity. When the entry angle is greater than 45 degrees, the down-jet is apparently dissipated in the cavity wall (Reference 8).

Closure jets usually are stronger than the re-entrant jets formed by closed cavities. As pointed out in Reference 22, the up-jet has been observed to have a velocity at deep closure that is higher than that of the missile. It is most powerful in the absence of surface closure, and becomes less powerful the earlier surface closure occurs. The down-jets following deep closure can be strong; they can deform the cavity wall or strike the missile, deflecting its trajectory, and have been known to knock the missile from the cavity. In less spectacular instances, the impinging of the jet upon the missile has decreased the apparent coefficient of drag.

THE CLOSED CAVITY

The final transient effects of water entry occur during the closed-cavity phase, when the missile-cavity system is no longer in direct contact with the atmosphere. The cavity slowly diminishes until it is entirely dispersed by the entraining action of the water (Figure 3.30 from Reference 60), or until it slips from the missile (Figure 3.31). Sudden asymmetric shedding sometimes causes gross changes in the direction of missile motion (Figure 3.32). With the disappearance of the cavity, the fourth and final phase of water entry is terminated and the fully
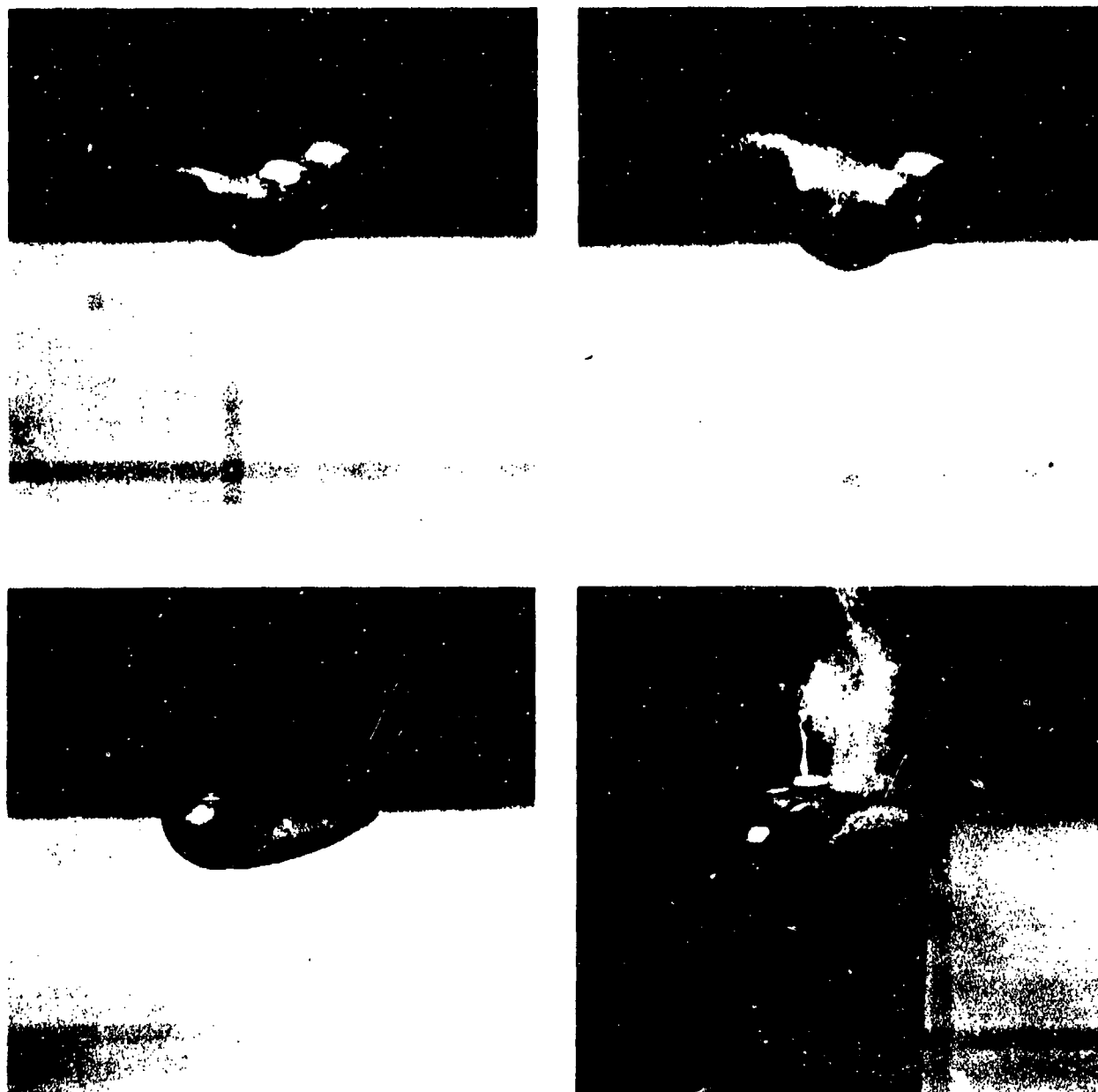
46

Figure 3.28a. Surface closure delayed by irregular splash. (Top photographs are double exposures.)

wetted or purely cavitating flows normally encountered in hydrodynamics occur. If gaseous exhausts from an internal power plant are present, the missile can travel under quasi-steady-state conditions in a cavity artificially maintained by the exhaust gases.

On rare occasions, the fourth phase of water entry does not occur. The missile may broach while it is still enveloped in a cavity or the open cavity may strip suddenly from the missile soon after it is formed, causing a marked change in the missile trajectory.
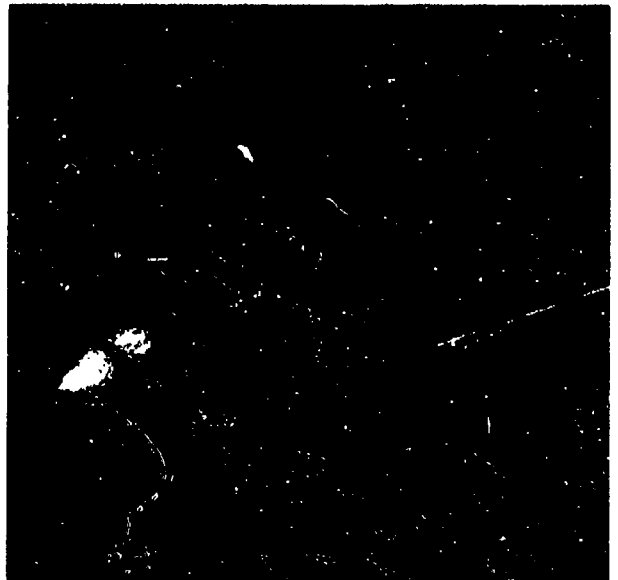
47

Figure 3.28b. Surface closure delayed by irregular splash.

Figure 3.29. Rear view of cavity produced by oblique water entry.

Figure 3.30. Cavity slowly dispersed by entraining action of water.

49

Figure 3.31. Cavity slipping from missile.

Figure 3.32. Change in missile motion caused by sudden asymmetric shedding of cavity.

CHAPTER 4
EVOLUTION OF EXPERIMENTAL HYDROBALLISTICS MODELING

Experimental hydroballistic modeling and theoretical modeling are interdependent; they have grown together in a climate of mutual support. Theoretical studies provide guidelines for experiment; discrepancies arising in the resulting data often lead to refinement of the theory.

Investigations of flow and cavity formations at water entry began in the 19th century, but the behavior of a missile during water entry was no more than a scientific curiosity until malfunction of World War II torpedoes indicated a deficiency in design information. Research received an impetus, and water-entry modeling technique grew slowly from study of the physical factors involved.

The opposite phenomenon, water exit, was discussed and a few experiments were performed at the Ordnance Research Laboratory, State College, Pa., about 1950. Decisions to develop an underwater-launched missile created an urgent accompanying need for information on the phenomena of water exit. Preliminary studies showed water exit to be not simply water entry in reverse but a process beset with problems uniquely its own (Chapter 11).

Modern water-entry research began with A. M. Worthington in the 1890's. His detailed photographs of spheres entering the water vertically (Reference 113) were unequaled for 40 years; his experimental setup was beautiful in its simplicity. His work was first published in book form in 1908 and a facsimile was published in 1963 (Reference 112).

Worthington's contribution to water-entry studies included observation of liquid drops and solid spheres entering still liquids under various conditions, and analysis of the experimental phenomena in terms of the physical forces manifested.

The experiments made with liquid drops (water or milk) into milk or water enabled him to watch the growth of the splash from the surface of the liquid and, at higher entry velocities, to observe that a cavity was also formed. The motion of the liquid originally within the falling drop and the contours of the splash revealed much information on the flow pattern and forces involved. Worthington's explanation of splash formation has remained largely unchanged for nearly 85 years.

His work with solid spheres was chiefly concerned with splash formation. He investigated the effects of entry velocity and the sphere's surface condition on the splash and, by using an oil and various glycerine mixtures instead of water, learned something of the effects of liquid density, surface tension, and viscosity upon the entry splash. Within the range of his experiments, he detected no difference between splashes formed in air and those formed in vacuum.

Worthington observed important general characteristics of water entry such as the small, rapid rise of the liquid surface at impact. He was able to explain the formation of closure jets from the flow about the cavity. Cavity flow was rendered visible in his photographs by streams of small bubbles from electrolysis. So far as is known, his photographs of a jet penetrating a closed splash dome (Figure 4.1) have yet to be duplicated in the modern laboratory.

Worthington's experience with the water entry of a smooth sphere typifies the perplexities so frequently encountered in modeling. For his series of drops, all test conditions were identical except for the two handkerchiefs used to wipe the sphere between tests. After having been wiped with one handkerchief, the sphere consistently entered with a separating splash; use

51

Figure 4.1. Closure jet penetrating splash dome. (From Reference 112.)

of the other handkerchief resulted in a clinging sheath-type splash. Yet microscopic examination showed the two pieces of cloth to be "extremely similar." As modern investigators have also learned (Reference 43 and Chapter 8), even minute variations can cause marked differences in modeling results.

Interest in the water entry of projectiles was limited until 1942, when E. G. Richardson of the Royal Aircraft Establishment in England began the study of water-entry cavity formation (Reference 68) by dropping spheres ranging in diameter from 1/5 inch to 1 inch from heights up to 126 feet above the water. Richardson introduced a fine network of bubbles to delineate the flow about the missile and the cavity,

and found that the flow pattern at the time of deep closure was in reasonable agreement with the steady-state flow pattern predicted by potential theory. He then substituted zinc chloride solution (sp. gr. = 1.75), petrol (sp. gr. = 0.71), and glycerine (sp. gr. = 1.26) for water; the flow pattern was independent of the liquid density in this range. Deep closure, however, occurred significantly later in the highly viscous glycerine.

Richardson measured transient cavity pressures and related them to cavity closure (one of the few such records that have been made). A steel disk 0.004 inch thick and 1.5 inches in diameter, mounted flush with the flat base of a hollow steel missile, transmitted cavity pressure

52

to the stylus of a scratch recorder carried within the missile. Another stylus inscribed records of the ambient hydrostatic pressure and the time. The sensitivity and response of this recorder were carefully determined to make certain that the cavity pressure records were valid. Results showed that cavity pressure was essentially atmospheric until surface closure; it then oscillated sharply before asymptotically approaching the ambient hydrostatic pressure (Figure 4.2).

Richardson also measured drag coefficients of spheres entering water at 1 and 1/5 atmosphere and entering other liquids (Table 4.1), and he measured the water-entry impact force and the added mass of a number of shapes (Table 4.2). He noted that the increased added mass obtained at higher entry speeds was reflected in the amount of water that was able to "get away" after impact in the splash. Table 4.3 summarizes the results of his ricochet studies, which indicate that the critical angle of ricochet was independent of velocity in the range studied, but that it varied with missile density.

In the early 1940's, R. M. Davies showed that the cavity and splash accompanying water entry are influenced by change in the air pressure above the liquid surface. Davies was the first to show experimentally the importance of gas density in surface closure (Reference 55, page 170).

In the late 1940's, David Gilbarg and Robert Anderson of the Naval Ordnance Laboratory, White Oak, reported a high-speed motion-picture study of the effects of atmospheric pressure upon the splash and entry cavity of spheres (Reference 22). Cavity closure at the surface was clearly a factor in determining cavity formation.[1] These investigators suggested that atmospheric density rather than atmospheric pressure largely determined the surface closure. Vertical jets were observed at the sites of both surface and deep closures, and velocities as high as 1.5 times projectile velocity were measured in a jet arising from deep closure.

Gilbarg and Anderson evaluated the Froude-scaling technique in entry cavity and splash modeling. Failure to model the cavity was attributed to lack of gas-density scaling. Splash studies, made both with and without adjusting the cavitation number in the model systems to equal that of the prototype, showed that the
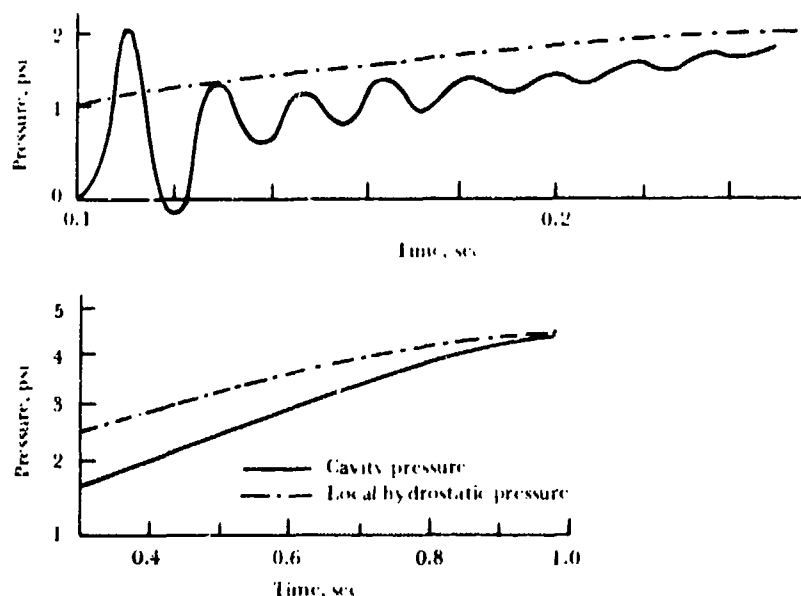

Figure 4.2. Cavity pressure as a function of time. (From Reference 68.)

---

[1] The importance of surface closure in cavity formation was first pointed out by B. D. Blackwell (Reference 55, page 170).

TABLE 4.1. Drag Coefficients of Spheres Entering Liquids
(from Reference 68)

Medium	Sphere		Mean Reynolds No.	C_D	
	Diameter, cm	Sp. Gr.		In Cavity	Fully Immersed
Steel in water	1 to 2.5	8	3×10^5	0.30	0.4
Steel in water (low pressure)	1 to 2.5	8	3×10^5	0.30	0.4
Lead in water	7	12	10^6	0.28	0.4
Steel in zinc chloride (sp. gr. 1.75)	1 to 2.5	4.5	3×10^4	0.30	0.4
Steel in petrol (sp. gr. 0.71)	1 to 2.5	+1	3×10^5	0.34	0.4
Steel in glycerine (sp. gr. 1.26)	1 to 2.5	6.5	3×10^2	0.50	0.7
Steel in water[a]	1 to 1	8	5×10^3	0.32	0.5

[a] Reference cited: Ramsauer, C. (and Dobke, G.), 1927. (Ann. Phys. Lpz., 84, 697.)

splash from the smaller spheres, scaled up to prototype size in accordance with the Froude law, decreased in height with model size. When a Freon-air mixture was used to maintain the gas density at the lower pressures, the splash height still did not scale, suggesting that surface tension was important in determining the size and shape of the splash.

The experimental studies begun by Gilbarg and Anderson were continued at NOL under the direction of Dr. Albert May. Cavity formation and closures, hydrodynamic drag, and virtual mass effects were extensively investigated (References 43, 44, 46, 47, and 48). Dr. May's data pertain to the cavity formed during the vertical entry of spheres ranging from 1/4 to 1 1/2 inches in diameter. Entry velocities were between 26 and about 80 fps. He assessed the cavity growth and closures in terms of both the physical phenomena and Froude scaling. Cavity growth and closures are not satisfactorily

modeled over this low-velocity range, the modeling failures possibly being caused by lack of viscosity or surface-tension scaling.

E. N. Harvey, J. H. McMillen, and their colleagues at Princeton University studied small steel spheres entering water at speeds ranging from 800 to 3000 fps. They found that the entry cavities formed at high velocities resembled those occurring at low velocities. In addition, elastic shock waves formed by a sphere entering water at velocities much below sonic (with respect to water) were visible in photographs by Harvey (Reference 55, page 160). Later McMillen and Albert May extended these studies at NOL to small steel spheres entering water vertically at supersonic velocities of about 7000 fps. Pressure oscillations within high-speed cavities caused noticeable pulsations in cavity size; they became more marked with increase in entry velocity (Reference 55, page 170), in agreement with the oscillation in cavity pressure

**TABLE 4.2. Water-Entry Impact and Added Mass Measurements
of 3-Inch-Diameter Missiles (from Reference 68)**

Head	Mass, gm	Specific Gravity	Entry Angle, deg	v_0/v_1 [a]	Added Mass, gm	λ at 40 m/sec [b]	λ at 4 m/sec [b]
Hemisphere	725	0.73	90	1.2	145	2.7	1.8
			64	1.25	180	3.4	...
			35	1.3	220	4.1	...
Disk	620	0.57	90	1.5	310	6.0	4.0
			64	1.4	250	4.7	...
			35	1.3	185	3.6	...
22 1/2-deg semi-angle cone	620	0.57	90	1.15	95	1.8	1.5
			64	1.15	95	1.8	...
			35	1.2	125	2.3	...
45-deg semi-angle cone	550	0.60	90	1.3	165	3.2	3.0
			64	1.2	110	2.0	...
			35	1.15	85	1.6	...
1 : 1 ogive	710	0.75	90	1.0	0	0.0	0.0
			64	1.05	35	0.6	...
			35	1.1	70	1.3^c	...

[a] v_0, v_1 = velocities just before and just after impact, respectively.

[b] $\lambda = m/c^3$ = an added mass parameter, where m (the added mass) is expressed in grams, and c (the model radius) in centimeters.

[c] This result appears anomalous.

measured by Richardson at lower velocities (References 8 and 68).

Garrett Birkhoff (Reference 6) and Birkhoff and Zarantonello (Reference 9) used experimental evidence to substantiate theoretical predictions, providing sound guidelines for exploration. They refined theory to keep pace with advancing experimental evidence. Birkhoff and Caywood (Reference 7) improved the bubble-marking technique and determined numerical velocity distributions for several flow fields. Of particular interest are their photographs showing a dipole moving down from the point of surface seal and the flow accompanying the up-jet that forms at the surface at the time of deep closure (Figure 4.3).

TABLE 4.3. Ricochet Studies
(from Reference 68)

Velocity in Path, ft/sec		Angle to Water Surface, deg		Path Length, in.	Max. Depth, diam.	Mean C_D[c]	Mean C_L[c]
v_o[a]	v_1[a]	β_o[b]	β_1[b]				
3-in. Dural Sphere, sp. gr. 2.7							
100	50	7.5	4.5	50	0.50	0.15	0.045
120	33	10.0	6.0	60	0.50	0.23	0.055
100	53	9.5	4.0	35	0.75	0.20	0.076
130	65	7.5	6.0	55	0.75	0.14	0.042
100	65	7.0	5.0	42	...	0.11	0.052
147	52	9.0	10.5	84	0.75	0.13	0.048
120	30	5.5	4.5	120	1.00	0.12	0.015
100	25	6.0	9.0	90	1.00	0.17	0.028
135	67	8.5	0.0	60	3.50	0.12	0.027
1-in. Steel Sphere, sp. gr. 7.8							
205	55	7.0	0.0	72	2.00	0.19	0.013
210	140	8.0	4.0	66	1.00	0.06	0.033
310	140	7.5	4.0	60	0.50	0.14	0.035
330	140	6.5	5.0	30	0.75	0.30	0.062
150	50	11.5	...	54	...	0.21	...
270	80	6.5	0.0	100	1.80	0.13	0.012
300	65	6.0	...	72	1.50	0.22	...
360	55	5.0	0.0	76	1.50	0.25	0.012
3-in. Ebonite Sphere, sp. gr. 1.1							
135	35	12.5	10.0	160	1.25	0.04	0.011
155	58	17.0	11.0	55	1.25	0.08	0.036
155	37	14.0	14.0	48	1.50	0.13	0.043
142	56	11.5	3.5	42	0.70	0.10	0.027
135	16	6.0	6.0	54	0.80	0.17	0.018
142	...	12.0	...	...	...	...	...
140	...	12.5	...	...	...	...	...

[a] v_o = entry velocity; v_1 = exit velocity.

[b] β_o = entry angle; β_1 = exit angle.

[c] C_D and C_L = mean drag and lift coefficients over the path

Surface closure

Figure 4.3. Flow patterns at closure. (From Reference 7.)

57

The experiments of Mason and Slichter (References 60 and 61), characterized by the type of ingenuity that marked Worthington's work, were in two categories: studies of the water entry of air-launched missiles, and special studies (also using missile shapes) of the water-entry phenomena. The latter group of experiments comprise a classic example of identification and evaluation of the physical forces influencing a phenomenon.

Slichter listed the forces that might conceivably be important (Chapter 3) and devised a series of experiments to evaluate them. He did not fall into the obvious trap of describing a force as being a magnitude or more smaller than others and, therefore, insignificant.

Slichter's work was given impetus by World War II. The Froude-scaled model of a standard U.S. aircraft torpedo (Figure 4.4, top) reproduced the trajectory of the prototype to a usable degree of accuracy; but with a slightly finer head (Figure 4.4, bottom), the prototype broached and the small (1- and 2-inch diameter) models dived with violence. When the water in the model tank was of sufficient depth, the model actually turned through 180 degrees to head in a direction up-range instead of down (Figure 4.5). The underpressure phenomena (Chapter 3) that caused the model with the finer head to dive were first identified through Slichter's experiments, which proved (1) that a low-pressure region was present, caused by the inability of the air in the cavity to maintain the gas film between the model and the cavity wall (i.e., to maintain the line of normal cavity separation), and (2) that failure to maintain normal separation caused the model to dive.

The existence of the low-pressure area was proved by the following experiment Slichter made with a 2-inch-diameter model of a torpedo launched at an entry velocity of 117 fps.

"A 0.2-in. diameter detachable disk (weight 40 mg) was inserted near the separation area, flush with the surface of the model. This disk was held in place by evacuating the model. If the disk came off during the trial run, the easily measured internal pressure was taken as greater than the external pressure on the disk, and less if the disk stayed on. In ten tries with an internal pressure of 0.02 atmosphere (absolute), the disk came off eight times and stayed on twice. With various higher internal pressures the disk invariably came off." See Figure 4.6 from Reference 61.

The tests were repeated with a light helical spring holding the disk in place, and substantially the same results were obtained.

"It was concluded that the absolute external pressure on this area almost completely vanishes during entry."
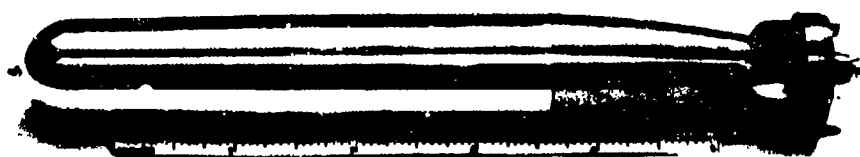
Hemisphere (standard) head
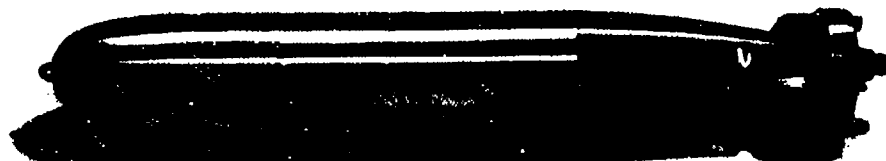
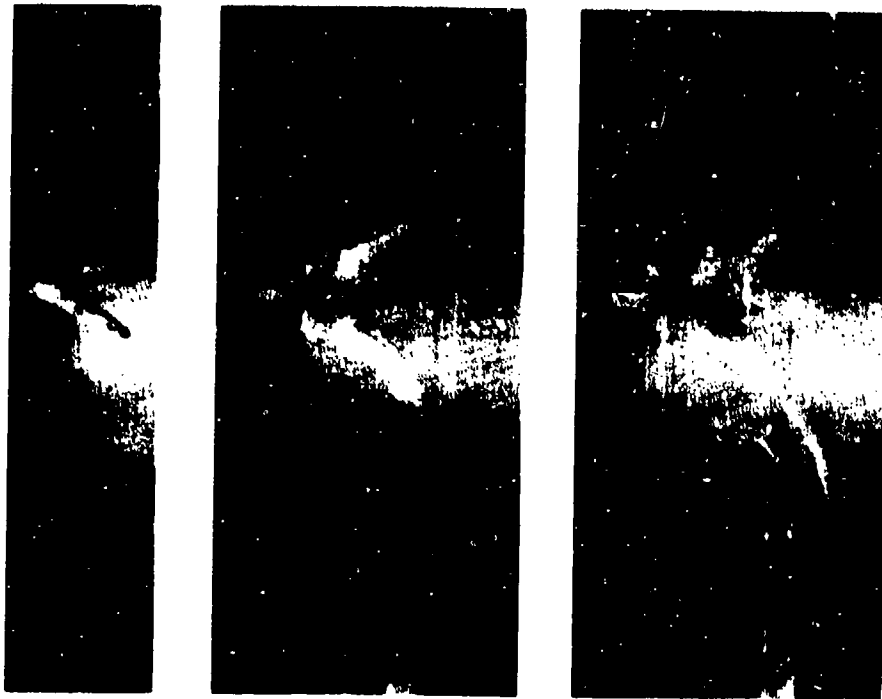Finer head

Figure 4.4. Torpedo models.

Figure 4.5. Diving trajectory, 2-inch-diameter model with finer head.

Figure 4.6. Separation of pressure disk during launching.

59

The cause of the low-pressure area was established by a series of tests with "vented" models. Small, symmetrically spaced holes were drilled in the nose of the model, saltshaker fashion (Figure 4.7), to allow air from the cavity to flow through the model and into the narrow space between the cavity wall and the model, thus preventing a low-pressure area. The differences between the lines of separation and the cavity contours of the models with and without venting are shown in Figures 4.8 and 4.9. The crease in the bottom of the cavity caused by the flow clinging to the bottom of the unvented model as the cavity was generated is noticeable in Figure 4.9. The vented model torpedo did not dive (Figure 4.10).

The importance of maintaining a gas film between the model and the cavity wall was established by showing that when cavity separation was artificially forced with rings of wire (0.005 and 0.010 inch in diameter) or with cellophane tape (0.003-inch thick) at the line of normal cavity separation, the model with the finer head followed a normal upturning trajectory.

It was apparent that the underpressure force would be greatly reduced by scaling the cavitation number. Launching facilities capable of operating at reduced atmospheric pressure were not then available; Slichter attempted to maintain the gas pressure beneath the model by raising the water temperature to 99°C, thereby increasing the vapor pressure to nearly 1 atmosphere. The expected results did not ensue, and the model dived, probably because the model was cold enough to condense the water vapor in the film as fast as it formed. This approach was abandoned without trying a heated model[2] because the Controlled Atmosphere Launching Tank at the California Institute of Technology would soon be available.

Slichter investigated the underpressure phenomena further with the finer head model and established relationships between separation angle, gas film pressure and thickness, and underpressure forces. He recognized the importance of gas viscosity, liquid surface tension, model surface finish, and the adhesion between liquid and missile in determining separation when the separation angle was small; when the entry velocity was also small, he recognized that liquid viscosity might influence separation. Slichter tried to evaluate the importance of surface tension by adding 0.01% Aerosol OT to the water to reduce the surface tension to one-third of its original value. He notes only that change in surface tension did not alter the trajectory of the hemisphere head torpedo model.

Time and funds did not allow Slichter to investigate thoroughly all the forces involved, but he examined the various elastic and compressibility forces in the system. As before, his test vehicle was a 1-inch-diameter finer head torpedo model. The compressibility of the water was altered by introducing a carefully spaced network of fine bubbles (3-mm diameter) into the water. The air content (by volume) was approximately 1 part per thousand, reducing the bulk modulus of the water by about 1/16.[3] Slichter noted only that the diving trajectory of the model was not
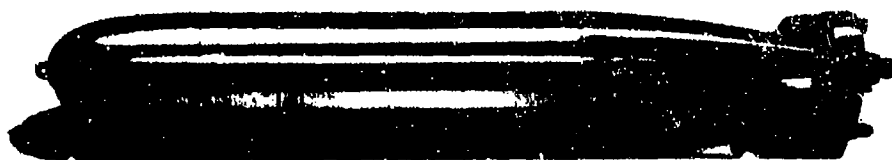

Figure 4.7. Vented model with finer head.

---

[2]Worthington experimented with smooth heated spheres and noted that flow separation was inhibited by heating. He concluded that the hot missile surface was more dust-free because dust does not settle upon surfaces heated above room temperature (Reference 112).

[3]
$$\bar{E} = \frac{E}{1 - q + qE/\gamma p_0}$$

where $\bar{E}$ = average effective bulk modulus of the mixture, E = bulk modulus of water, q = relative air content by volume, γ = a constant varying between 1.0 and 1.4 (depending upon the degree of heat interchange during compression of the air), and p_0 = atmospheric pressure.
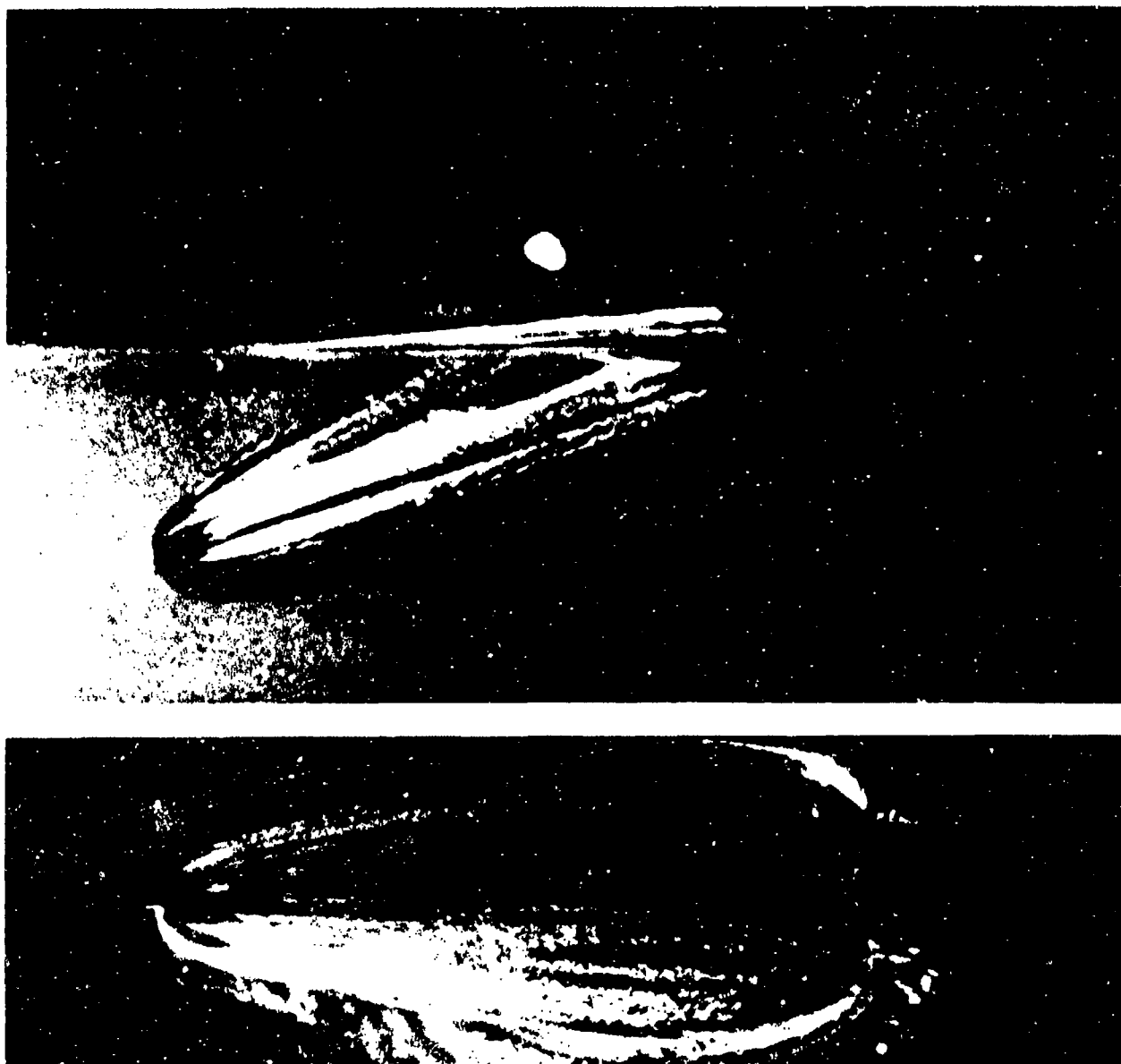
Figure 4.8. Normal cavity generated by vented model.

altered by this modification or by changing the
elasticity of the model with a nose made of a
1/16-inch-thick layer of soft rubber supported
by a metal frame. He felt that further investiga-
tion of the elasticity of the missile and of the
effects of a frangible nose cap might prove
valuable in solving missile-entry problems.

Slichter also tried altering the elasticity of
the liquid by launching the model into water

covered by a layer of acetone "several inches
thick". Although several other properties in
addition to the elasticity were changed by this
procedure,[4] the trajectory was not noticeably
affected.

Slichter established the importance of mis-
sile flexure by showing that the trajectory of the
hemisphere head model was markedly altered by
deliberately offsetting the afterbody and shroud

[4]Some properties of acetone with respect to those of water are as follows: surface tension 1/3, compressibility 2.1,
kinematic viscosity 0.38, density 0.79, and velocity of sound 0.81.

61
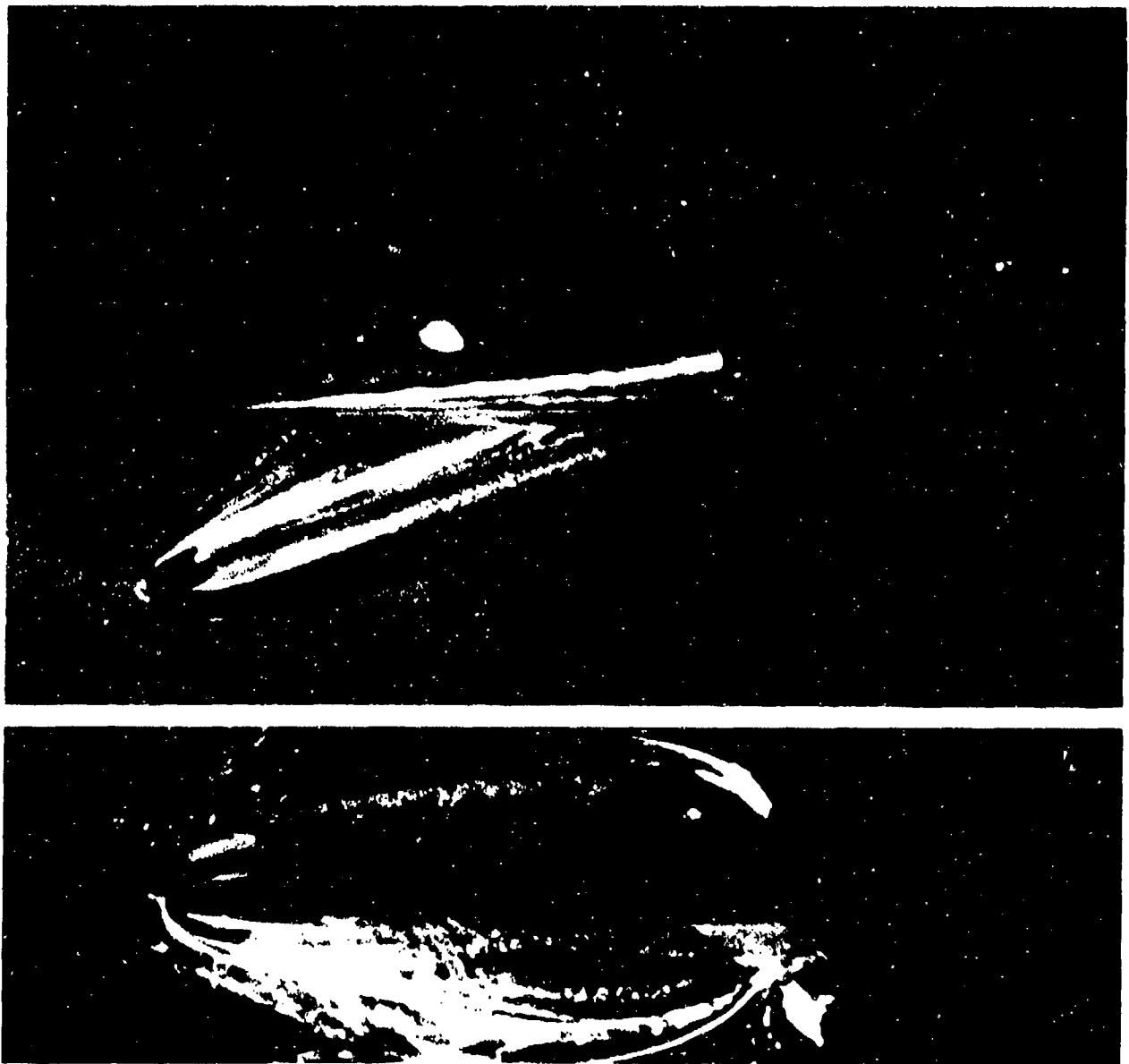
Figure 4.9. Crease along bottom, distorting cavity of unvented model.

ring by only 1.5 degrees. He demonstrated that the oblique trajectory of a torpedo generally turns upward as missile density is decreased. A similar effect was obtained when missile density was held constant and entry velocity increased.

In Slichter's experiments with spheres, he measured the rotation of an obliquely entering sphere to see whether the shear force at impact would perturb a small missile; he concluded that the shear force was insignificant. Using bubbles to mark the flow field, he studied the impact of a sphere and several other mathematically tractable shapes upon the water surface (Figures 4.11 through 4.14).

After Slichter laid the foundations of understanding and demonstrated several techniques, experimenters under the direction of R. T. Knapp at the Controlled Atmosphere Launching Tank at CIT noted that the trajectory modeling of a fine-nosed shape was greatly improved by reducing atmospheric pressure and, furthermore, that the best modeling was

Figure 4.10. Nondiving vented model.

obtained at the atmospheric pressure that scaled the cavitation number one-to-one (References 37 and 38).[5]

Another interesting study at the CIT tank (Reference 36) showed the effects of variation in Froude and cavitation numbers upon the behavior of a 2-inch-diameter torpedo model. The data showed the trajectory to be very sensitive to change in cavitation number; Froude number influence was more complex. Sometimes the trajectory was almost independent of Froude number; at other times a small change in Froude number would change a diving trajectory into a broach. In general, sensitivity to Froude number was noted when a small resultant force determined model orientation in the cavity.

Concurrently with the early model studies, prototype missile launchings were made at the NUC Morris Dam Torpedo Range (Part V). Data

were obtained on air and underwater trajectories, entry whip, and the time of first contact between missile tail and cavity. The missile attitude during underwater flight was also recorded for a few launchings. Some underwater drag data were taken, and the effect of missile shape was studied by successively varying nose and tail contours, shroud ring, fin, propeller design and placement, and the overall length of the missile (References 56 and 59).

Part III of this book presents more recent studies. The water-entry phenomena from initial whip through cavity attrition have been inspected in detail, and many of the secondary forces originally listed by Slichter have lent interest and an aura of the unexpected to the experimental results. Preliminary studies of water exit and earth entry are also included.

---

[5]Extensive studies of water entry were made at the Alden Hydraulic Laboratory (now Alden Research Laboratories), Worcester Polytechnic Institute, Worcester, Mass., and by the British Admiralty at its laboratories in Teddington, Middlesex, U.K.

Figure 4.11. Flow field immediately after impact of 8.6-inch-diameter sphere.

Figure 4.12. Flow field established by vertical entry of 90-degree cone.
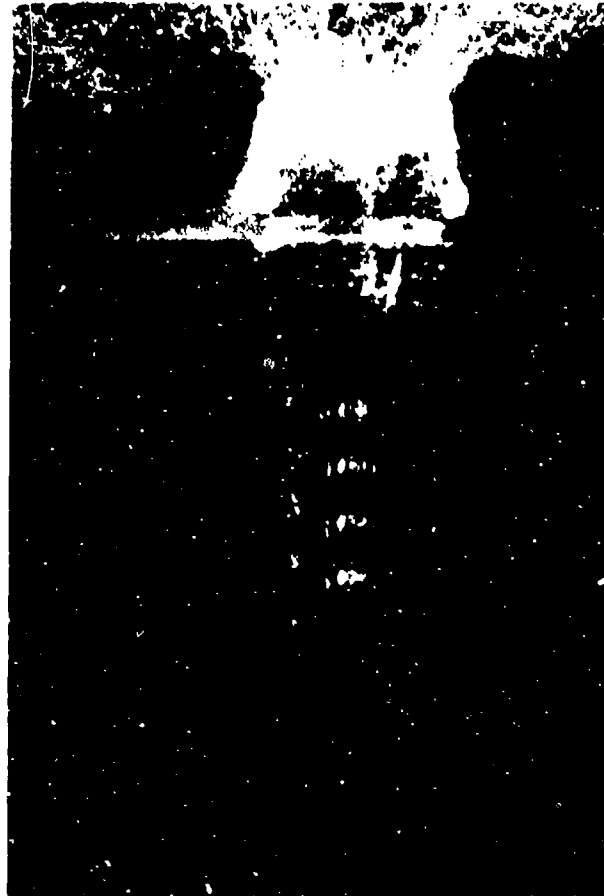
Figure 4.13. Flow field established by vertical entry of 2-inch-diameter sphere.

Figure 4.14. Flow field established by oblique entry of model.

PART III.
PROTOTYPE AND MODELING EXPERIMENTS

CHAPTER 5
FULL-SCALE WHIP AND DECELERATION AT WATER ENTRY

The value of modeling lies in the assistance it gives to the prediction of full-scale missile behavior. Various physical influences encountered when a torpedo (prototype or model) hits the water require scrutiny, measurement, and analysis in order that they may be applied to the modeling process and so increase its worth to the engineering development of underwater missiles.

Whip and deceleration depend upon the water-entry conditions and upon the missile shape and dynamic parameters. The studies discussed here (first reported in References 91, 97, and 98) are concerned with the effect of head shape on the whip and water-entry deceleration of full-scale missiles. The program was planned primarily to obtain data that could be directly applied to service-missile design, and it was also anticipated that it could be used later to investigate whip modeling.

The ultimate trajectory of a missile undergoing water entry is markedly influenced by its behavior in the cavity stage. Whip, $\Delta\dot\theta$, the change in missile pitch velocity while the tip of the nose is being wetted, may be attributed to the high shock at water impact and to the forces associated with the establishment of flow. It is probably the most important single factor in determining the underwater trajectory of a missile. Whip influences the position of the missile in the water-entry cavity, which in turn largely determines whether the underwater trajectory will be upturning, downturning, or straight. Deceleration of the missile in the cavity not only influences the underwater trajectory and angular momentum but may be so severe as to cause damage to the shell and to the missile's internal mechanism.

Two separate mechanisms contribute to whip during oblique entry. The more important one results from the lower part of the nose being wetted first, giving rise to unbalanced forces that may be quite large. The forces come not only from fluid pressure but also from reduced pressure in the nose undercavity (underpressure effect). The torque thus applied about the CG produces the change in pitch velocity known as whip. The other whip-producing mechanism occurs when the missile enters the water with an attack angle, α. Then the drag forces producing the change in the axial velocity contribute a whip moment about the CG.

The whip is linearly dependent on the water-entry velocity, v, because the forces on the head are proportional to v^2, and the time during which these forces are unbalanced (acting

69

on the lower side of the head only) varies as $1/v$. The impulse thus will vary as v. For spherically tipped heads (assuming small attack angles), there should be a linear dependence of whip upon angle of attack. Calculation of the whip requires a knowledge of the instantaneous pressure distribution over the missile nose during water entry; this, at present, is unavailable.

After water impact and the establishment of flow, the missile ordinarily travels several lengths beneath the water surface with only its nose in contact with the water. During this time, the drag force does not usually act through the CG; the moment, depending upon the head configuration and the amount of angle of attack, is directed toward either increasing or decreasing the pitch angle of the missile. The angular acceleration produced by the drag moment thus either adds to or subtracts from the whip.

To implement the investigation of whip and deceleration at water entry, 14 full-scale heads (Figure 5.1) were attached to an aircraft torpedo afterbody. The geometry of the ogive, spherogive, and plate-ogive heads is shown in Figure 5.2. The ogival portion of the spherogive and the plate ogive heads is designated by expressing the radius of the generating curve in projectile diameters. The spherical portion is expressed in terms of the half-sphere angle, i.e., the angle subtended by the generating curve of the spherical nose measured from the tip of the nose to the point of junction with the ogival curve.

In the nomenclature used to designate the plate-ogive heads, the flat-plate radius, P, is given by

$$\frac{P}{2R_p} = 0.5 - \frac{R_o}{2R_p} \qquad (5.1)$$

where R_o is the ogival radius and R_p is the projectile radius. Thus, the plate 0.1-diameter ogive head has a plate radius of 0.4 diameter. The tolerances on the ogive, spherogive, and plate-ogive head dimensions were held to ±0.001 diameter of the nominal values.

Heads h, i, j, and k (shown in Figure 5.1) are modifications of a cone of 8.4 ±0.05-degree generating angle. Head h is a truncated cone with a plate of 0.500 ±0.002 diameter. The flat plate may be regarded as a segment of a sphere of infinite radius. Head i differs from Head h in
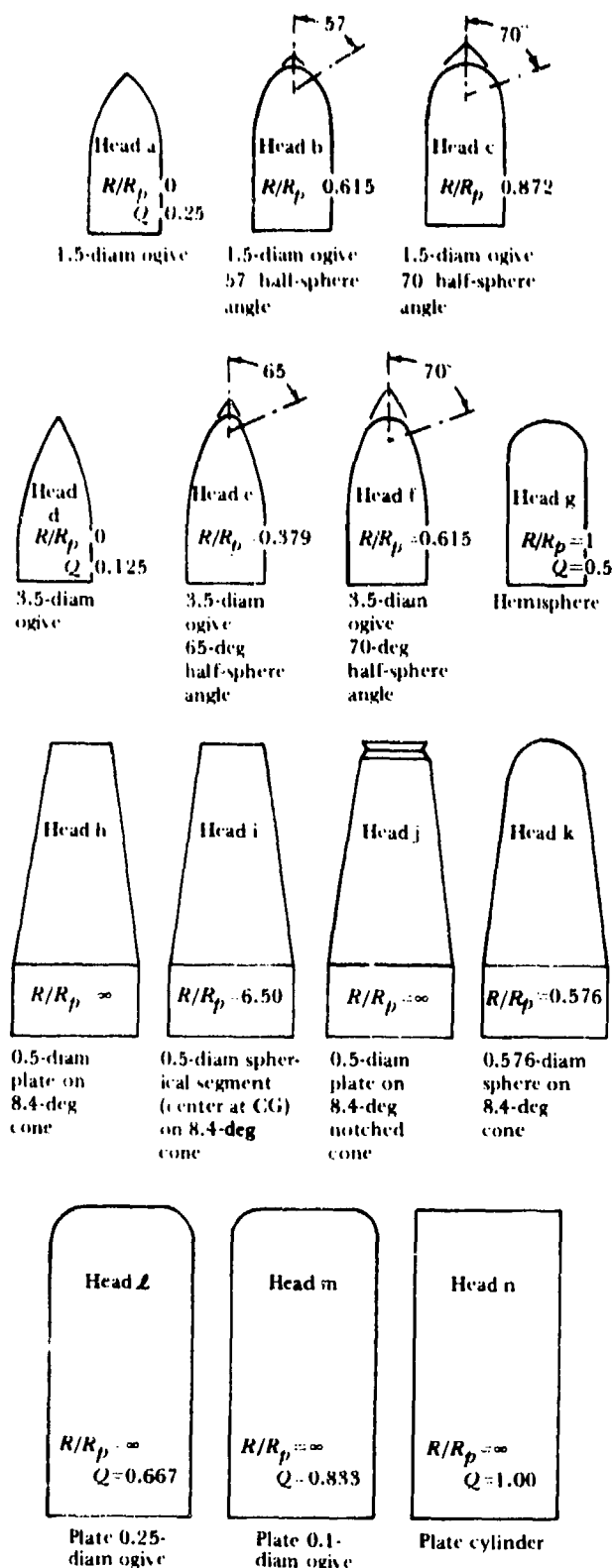
Figure 5.1. Full-scale head shapes used in underwater trajectory studies.

70
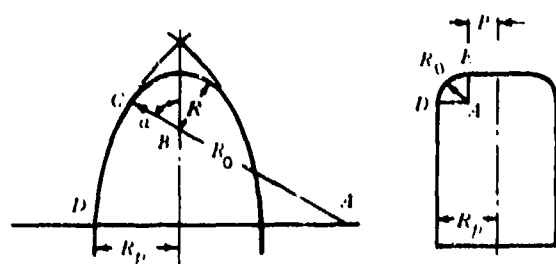
A   Center of curvature of ogive
B   Center of curvature of sphere
C   Junction of sphere and ogive
D   Junction of ogive and cylinder
E   Junction of ogive and plate
P   Plate radius
R   Sphere radius
R_0 Ogival radius
R_p Body or projectile radius
a   Half-sphere angle

Figure 5.2. Geometry of ogive, spherogive and plate-ogive heads.

Figure 5.3. Radius of sphere versus cavity diameter.

that a segment of a sphere centered at the missile CG was substituted for the flat plate. The spherical radius is 6.5 times the projectile radius. Head j differs from Head h in that an annular groove was added just aft of the nose flat. Head k has a spherical-cap nose with a radius of 0.576 ±0.002 of the projectile radius and meets the conical section tangentially.

SELECTION OF HEAD SHAPES

It was expected that water entry would take place under conditions of well-developed cavitation and that cavity separation would affect missile performance. Since water-entry cavity separation should approximate steady-state cavity separation, the results of steady-state cavity studies on 1.0-, 2.3-, and 5.0-diameter ogives and spherogives (Figure 5.3) were used as a guide in the selection of head spheres.[1] These data indicate that when the spherical segment is large in comparison with the ogive, cavity separation takes place on the sphere, and cavity growth is controlled by sphere size. When the spherical segment is small in comparison with the ogive, cavity separation occurs on the ogive and cavity growth is independent of sphere size. The critical sphere

size dividing the two regimes varies with different spherogive families. There appears to be a linear relationship (shown as a solid line in Figure 5.3) between sphere size and maximum bubble diameter when cavitation occurs on the spherical portion of the nose.

The 1.5- and 3.5-diameter ogive families were selected for extensive water-entry behavior studies. The maximum diameters of the cavities forming on the ogive were estimated (by parabolic interpolation of those forming on the 1.0, 2.3, and 5.0-diameter ogives) to be 1.60 and 1.34 diameters. When these dot-dash lines are extended to meet the solid line, the points of junction give the critical sphere radii of 0.40 and 0.30 diameter, respectively, for these ogives. The corresponding half-sphere angles are approximately 66 and 70 degrees.

---

[1] Figure 5.3 is taken from Reference 33. It shows the original data; the dot-dash lines for the 1.5- and 3.5-diameter ogives and lettered points were added subsequently.

71

Cap sizes below and above the critical value (57 and 70 degrees) were selected in the 1.5-diameter sphere-ogive family in order to compare water-entry performance in the presence of both spherical and ogival separation. The critical sphere size (70 degrees), where variation in angle of attack would result in varying degrees of separation on both the spherical and ogival portions, and the subcritical 65-degree cap sizes were chosen for the 3.5-diameter family. The points representing these heads are identified in Figure 5.3 by their letter designations.

The plate-ogive heads were selected in such a manner as to extend the ogive-head data over the entire range $0 \leq R_o/R_p \leq \infty$. Because pure ogives are not possible in the range $0 \leq R_o/R_p < 1$, a modification was introduced in the form of a flat plate.

In order to present the ogive–plate-ogive data graphically, the arbitrary parameter.

$$Q = \frac{1}{1 + R_o/R_p} \qquad (5.2)$$

was used. This parameter has the more convenient range $0 \leq Q \leq 1$. The value of Q for the hemisphere head is 0.5 and lies in the middle of the range.

Test shapes corresponding to Q values of 0.667, 0.833, and 1.000 were selected: the plate 0.25-diameter ogive, the plate 0.1-diameter ogive, and the plate cylinder, respectively.

Cones of 8.4-degree generating angle were selected primarily because they approximated the contours of rocket ordnance. Head h, a truncated cone, was of interest because it was likely to experience low whip and reasonably low water-entry deceleration. Low whip was expected because nose-down forces generated as the disk was wetted would tend to be canceled by nose-up forces on the conical section (Figure 5.4). Head i was chosen in order to ascertain the effect a curved nose would have on the whip of a missile if it were so designed that the nose forces passed through the CG of the torpedo, thereby producing no moment. Since the shear forces on the curved nose should be very small in comparison with the inertial forces, it was hoped that the contributions of the flat plate and conical section of the head to the whip could be estimated from a comparison of the whips of Heads h and i.
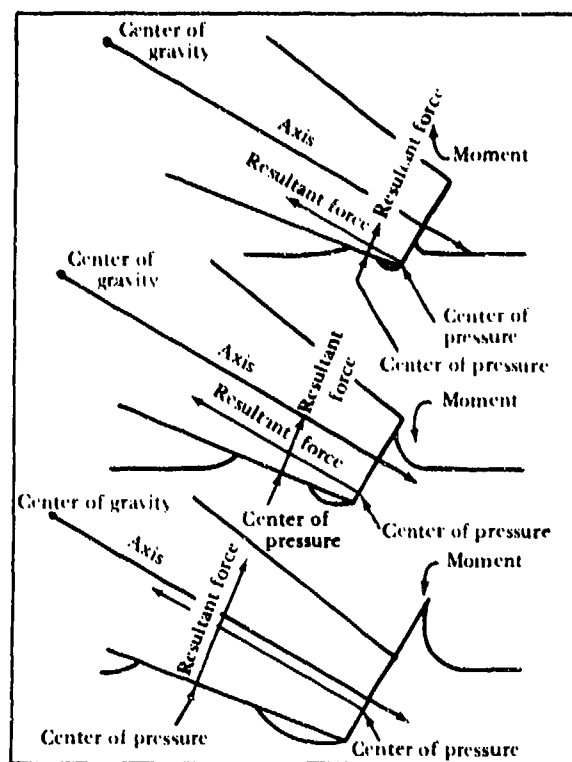
Figure 5.4. Water entry, Head h.

Interest in the configuration designated Head j was prompted by studies of water-running bodies. A sharp-edged separation ring or groove in the head of a Henschel body causes the flow to separate from the body at the discontinuity, surrounding it with a cavity. The size of the cavity is controlled by choice of head shape. A conical midsection with a flared skirt at the rear causes the body to oscillate back and forth in the cavity, thereby stabilizing the underwater trajectory. Of particular interest in Head j was its underwater trajectory performance; its water-entry behavior was expected to be similar to that of Head h.

EXPERIMENTAL CONDITIONS

The full-scale dummy torpedoes used in this study of whip and deceleration at water entry were launched into the fresh water of the NUC Morris Dam Torpedo Range (Part V). The trajectory angle at water entry was about 20 degrees. Nominal entry velocities were both 400 and 500 fps for all except the two bluntest heads (m and n were restricted to 400 fps to

72

avoid damage from the high water-entry deceleration forces). At these velocities, $\sigma < 0.03$ and comparison of this low cavitation number with the results of other investigations (References 31, 32, and 33) indicated that water entry would take place under conditions of well-developed cavitation.

Table 5.1 lists the ballistic parameters of torpedoes with the different head configurations. All were 22.42 inches in diameter, and the CG was always within 0.01 inch of the longitudinal axis of symmetry. Because of the considerable variation in head shape and the consequent variation in weight and weight

TABLE 5.1. Ranges of Ballistic Parameters of Torpedo Dummies

Head	Length of head, [a] in.	Length torpedo dummy, [b] ft	Weight torpedo dummy, lb	Distance CG from nose, in.	Distance CB from nose, in.	Buoyancy of torpedo dummy, lb	Moment of inertia of torpedo dummy, [c] slug-ft^2
a	51.7	12.8	1,480–1,520	71.1	70.5–71.1	168–208	748–756
b	51.7	12.8	1,514–1,663	71.1–72.9	69.6	65–214	719–851
c	51.7	12.8	1,526–1,549	71.1–72.1	68.9–69.0	204–227	789
d	51.7	12.8	1,461–1,565	71.1	75.3	21–125	693–766
e	51.7	12.8	1,457–1,494	71.1	68.1–71.9	160–192	711–719
f	51.7	12.8	1,614–1,680	71.1	70.2–70.3	70–98	803–821
g	51.7	12.8	1,526–1,527	69.5–70.0	67.5	268–269	771
h	51.7	12.8	1,397–1,470	71.1–73.3	72.1–72.9	136–209	682–737
i	51.7	12.8	1,496–1,555	73.0	73.2	59–118	752–764
j	51.7	12.8	1,537–1,559	71.1	68.0–71.1	49–77	766–814
k	51.7	12.8	1,430–1,513	71.1–72.9	72.9–73.4	124–176	707–736
ℓ	45.6	12.2	1,582–1,590	63.7	63.7	150–158	743
m	42.3	12.0	1,544–1,558	63.7	68.3	182–196	694
n	42.3	12.0	1,547–1,552	63.8	68.2	153–193	694

[a]Distance from nose to joint ring.

[b]Distance from nose to tail plug.

[c]About a transverse axis through CG.

73

distribution, it was impossible to adjust all the body parameters to the same nominal values. In order to compare the data, corrections were necessary; the actual range of values is shown in Table 5.1.

The whip data were corrected to a moment of inertia of 800 slug-ft^2 and an entry velocity of 500 fps. The water-entry deceleration was corrected to a torpedo weight of 1,500 pounds.[2] Because the linear velocity of the missile at the end of the whip phase was within 2.5 percent of the entry velocity, the entry velocity was used in reducing the whip data. Torpedo yaw at water entry was small and therefore was neglected.

Whip, pitch, velocity, and deceleration at water entry was recorded with a flare camera (described with other equipment and facilities in Part V). The slope of the velocity-time curve obtained from the range position data gives the deceleration (Figure 5.5). The angle made by lines joining synchronous flare-image pairs with the torpedo line of flight gives the angle of attack. Since the line of flight does not change perceptibly, the rate of change in angle of attack is equal to the rate of change in pitch. Therefore, the pitch velocity can be obtained from the slopes of the angle-of-attack-versus-time curves (Figure 5.6). Water-entry angles of attack of varying degrees were obtained by attaching to the muzzle of the launcher tube steel extensions which induced asymmetric blast, thereby imparting a pitch velocity to the torpedo.

Whip data for Heads a and d are shown in Figure 5.7 together with regression lines fitted to the data by the method of least squares. For
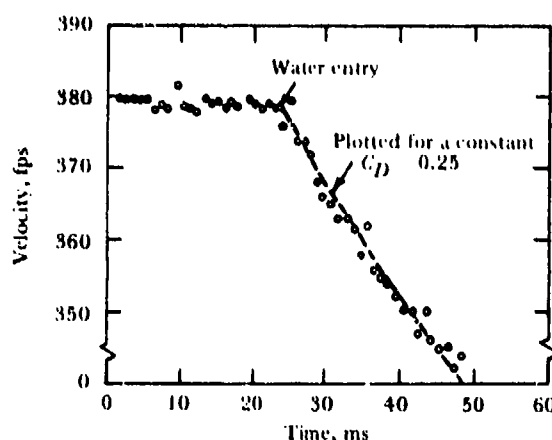
Figure 5.5. Deceleration during water entry.
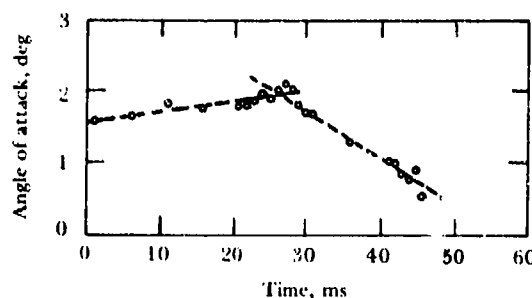
Figure 5.6. Pitch velocity during water entry.

all head shapes, it was found that the whip is a linearly increasing function of the angle of attack for the range of angles studied. Regression lines fitted to the data for all heads are shown below, where a is in degrees and $\Delta\dot\theta$ is in

---

[2] To correct whip to the nominal entry velocity of 500 fps (Reference 106):

$$\Delta\dot\theta_1 = \frac{500}{v}\Delta\dot\theta$$

To correct whip to the nominal moment of inertia of 800 slug-ft^2:

$$\Delta\dot\theta_2 = \frac{I}{800}\Delta\dot\theta$$

To correct water-entry deceleration to the nominal missile weight of 1,500 pounds:

$$a_1 = \frac{m}{1500}a$$

Measured values of entry velocity, moment of inertia, whip, weight, and deceleration are v, I, $\Delta\dot\theta$, m, and a, respectively. The desired corrected whips and deceleration are $\Delta\dot\theta_1$, $\Delta\dot\theta_2$, and a$_1$. These relationships are discussed in References 91 and 106.

74

Head a. $\Delta\theta = 13.9\alpha + 175$

Head d. $\Delta\theta = 22.5\alpha + 151$
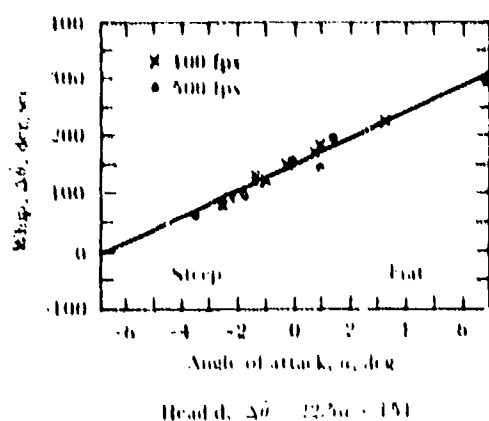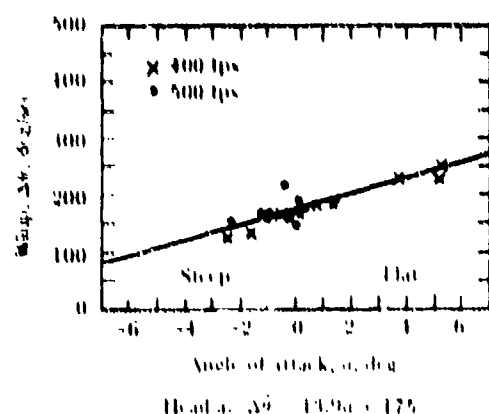
Figure 5.7 Angle of attack dependence of whip. Data corrected for 500 fps entry velocity and 800 slug ft² moment of inertia.

degrees per second. It is difficult to evaluate whip performance from these data because the change in whip with

Head a.	$\Delta\theta = 13.9\alpha + 175$
Head b.	$\Delta\theta = 19.0\alpha + 150$
Head c.	$\Delta\theta = 15.8\alpha + 113$
Head d.	$\Delta\theta = 22.5\alpha + 151$
Head e.	$\Delta\theta = 21.2\alpha + 134$
Head f.	$\Delta\theta = 16.3\alpha + 88$
Head g.	$\Delta\theta = 10.2\alpha + 133$
Head h.	$\Delta\theta = 12.7\alpha + 62$
Head i.	$\Delta\theta = 13.9\alpha + 57$
Head j.	$\Delta\theta = 13.0\alpha + 49$
Head k.	$\Delta\theta = 15.4\alpha + 81$
Head ℓ.	$\Delta\theta = 5.0\alpha + 65$
Head m.	$\Delta\theta = 2.3\alpha + 24$
Head n.	$\Delta\theta = 1.02\alpha - 18$

entry attack angle (i.e., attack sensitivity) varies greatly among the different head shapes. To

compare whip at –4, 0, and +5 degrees and at 500-fps velocity, the whips and attack sensitivities of the ogives and spherogives are plotted in Figure 5.8 as functions of the ratio of spherical-cap radius to body radius.

For the same value of R/R_p, the 1.5-diameter spherogive family (Heads a, b, c) shows greater whip than the 3.5-diameter family (Heads d, e, f) at both zero and –4-degree entry angle of attack and, except for smaller values of R/R_p, the +5-degree curves follow the same trend. The high attack sensitivity of the 3.5-diameter ogive causes the observed reversal in the whips of the pure ogive heads. Head c, with only a small spherical cap, also shows a high attack sensitivity.

The whips and attack sensitivities of the ogive, plate-ogive series (Heads d, a, g, ℓ, m, n) are shown in Figure 5.9 as functions of the parameter Q (Equation 5.2). A hypothetical "needle" ogive head of infinite radius ($R_0 = \infty$) should have zero whip, and this whip was included in the 0-degree curve to provide a limit point for $Q = 0$. The distances of the CG from the nose were about 70 inches for the hemisphere (Head g) and the ogives and 64 inches for the plate ogives. (The CG position affects the whip and attack sensitivity.) The data could not be corrected to a standard CG position because the exact relationships were unknown; the ogive and plate-ogive data should be compared only for trends.

The general shape of the whip functions is similar for the attack angles studied. The attack sensitivity of the plate-ogive series decreased with increasing Q (decreasing R) to a minimum value of essentially zero for the plate cylinder (Head n) and its whip can be assumed to be independent of the angle of attack within the range of entry angles investigated. For the hemisphere head (Head g), the contour contacting the water remains unchanged by the angle of attack, and only the whip-producing drag force lever arm differs. A theory developed on this basis for the attack sensitivity of the hemisphere head shows good agreement with the experimental evidence (Reference 91).

The cone heads h, i, and j show small differences in whip and, as might be expected from the behavior of the hemisphere and plate heads, the whip of Head k is greater than that of the other cone heads (Figure 5.7). The contribution of the conical section of the plate-cone
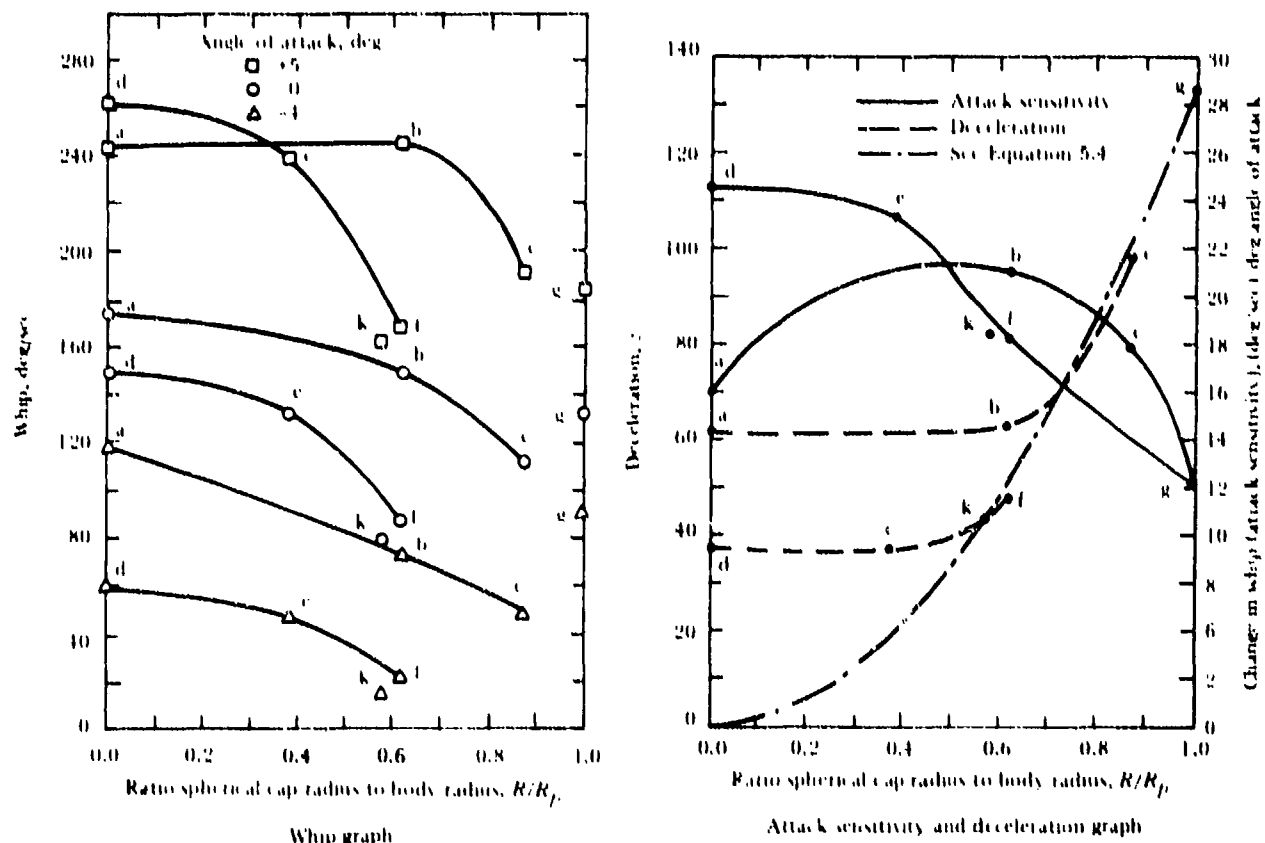
Figure 5.8. Whip, attack sensitivity, and deceleration of water entry as functions of spherical cap radius, spherogive heads. Entry velocity 500 fps.
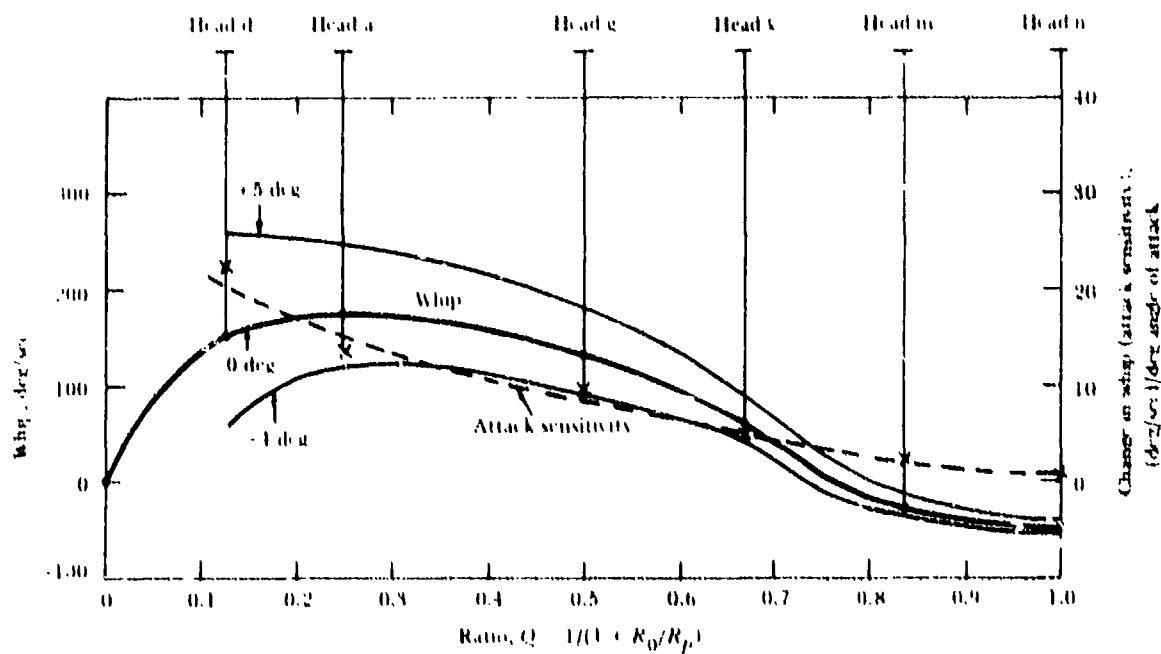

Figure 5.5. Whip at -4, 0, and -5 degree angle of attack and attack sensitivity at 500 fps entry velocity.

heads to the whip can be estimated by comparing the data of Heads h and j with results obtained from Head i, where forces acting on the spherical portion of the head have no moment. The similarity in performance indicates that the flat plate had little effect on the whip; the whip of these heads was produced largely on the conical surface.

Mean water-entry decelerations were measured during the time from nose contact to tail submergence, and the corresponding mean entry velocities were also determined for use in drag-coefficient calculations and in the subsequent deceleration curves.

The deceleration, corrected to a missile weight of 1,500 pounds, was plotted on a logarithmic scale as a function of the water-entry velocity. On the hypothesis that the deceleration would be of the form

$$a = cv^2 \tag{5.3}$$

(where a is the deceleration, v the water-entry velocity, and c a constant characteristic of the head), parabolic regression curves of the type given by Equation 5.3 were fitted to the data by the method of least squares. These regression curves appear in the logarithmic plots as straight lines with a slope of two. The good agreement of the data with these lines shows the validity of the assumption that the cavity drag is proportional to v^2.

A typical plot of water-entry deceleration (Head a) is shown in Figure 5.10; the formulas for all 14 heads are given below, where v is in feet per second and a is in gravitational units. The drag coefficient for the hemisphere (Head g) was 0.30, the same as that measured for a hemisphere-head dummy aircraft torpedo at entry velocities of about 400 fps (Reference 106)[3]. It is in good agreement with the results of water-tunnel tests (Reference 32) and with integrated experimentally obtained pressure distributions (Reference 56 and 73). Other investigations showed that for Head k, cavitation occurs on the spherical cap, and its drag coefficient based on the cross-sectional area of the sphere is 0.32. The agreement between the drag

Head a. $a = 2.47 \times 10^{-4} v^2$; $C_D = 0.14$
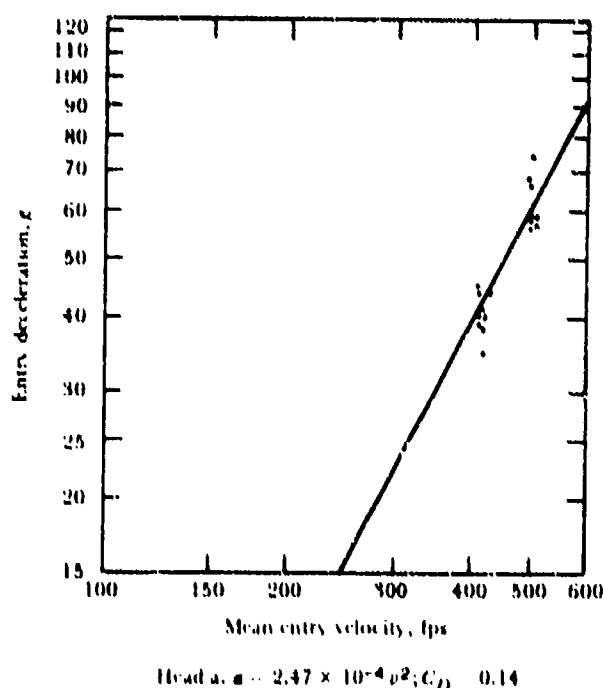
Figure 5.10. Deceleration as a function of mean velocity at water entry.

coefficients indicates that drag forces other than those acting on the spherical cap are small. The drag coefficients for the 1.5- and 3.5-diameter ogive heads show good agreement with results obtained from integration of experimentally obtained pressure distributions (Reference 56).

Head a. $a = 2.47 \times 10^{-4} v^2$; $C_D = 0.14$
Head b. $a = 2.50 \times 10^{-4} v^2$; $C_D = 0.14$
Head c. $a = 3.93 \times 10^{-4} v^2$; $C_D = 0.22$
Head d. $a = 1.50 \times 10^{-4} v^2$; $C_D = 0.09$
Head e. $a = 1.47 \times 10^{-4} v^2$; $C_D = 0.08$
Head f. $a = 1.90 \times 10^{-4} v^2$; $C_D = 0.11$
Head g. $a = 5.33 \times 10^{-4} v^2$; $C_D = 0.30$
Head h. $a = 3.84 \times 10^{-4} v^2$; $C_D = 0.22$
Head i. $a = 3.55 \times 10^{-4} v^2$; $C_D = 0.20$
Head j. $a = 3.65 \times 10^{-4} v^2$; $C_D = 0.21$
Head k. $a = 1.89 \times 10^{-4} v^2$; $C_D = 0.11$
Head ℓ. $a = 7.85 \times 10^{-4} v^2$; $C_D = 0.44$
Head m. $a = 11.05 \times 10^{-4} v^2$; $C_D = 0.62$
Head n. $a = 14.71 \times 10^{-4} v^2$; $C_D = 0.83$

[3] The C_D of the aircraft torpedo, based on its maximum cross-sectional area, was 0.25. The radius of the nearly hemispherical cap of the torpedo was 10.30 inches. The value of 0.30 was obtained when the C_D was calculated on the basis of the projected area of the sphere.

If it is assumed that water contact is restricted to the spherical cap of the spherogives and that the area of contact is proportional to the square of the cap radius, then from the basic drag equation and from Newton's Second Law (Reference 91),

$$a = a_0\left(\frac{R}{R_p}\right)^2 \qquad (5.4)$$

where a_0 is the deceleration of the hemisphere head.

This parabolic relationship is shown as a dot-dash curve in the righthand graph of Figure 5.8. Heads c, f, and k lie close to the parabola; Heads a, b, d, and e (which are either pure ogives or have small spherical caps) show deviation. Evidently, cavitation occurs on the ogival portion of these heads as originally predicted from the water-tunnel data. For cap sizes above the critical, the deceleration curves for both spherogive families appear to follow the parabolic curve. For cap sizes below the critical, there is a departure from the curve, the 1.5-diameter spherogive family having higher deceleration than the 3.5-diameter family, as would be expected from the data of Figure 5.3.

The drag coefficients of the ogive and plate-ogive heads and drag coefficients determined by integrating the pressure distributions of ogives and plate ogives for $\sigma = 0$ and $\sigma = 0.05$ (Reference 73) are plotted as a function of Q in Figure 5.11. The deviation of the Head d (3.5-diameter ogive) drag coefficient from the dotted curve indicates that skin friction is more important in determining the drag coefficient of finer noses. The contribution of the skin friction to the Head d drag coefficient was estimated as 0.0085, which would account for about half the discrepancy.

The drag coefficient of the plate-cylinder head is 0.83, in good agreement with the value of 0.82 derived from free-streamline theory (Reference 65) and with the value 0.80 calculated from pressure distributions measured in the California Institute of Technology water tunnel (Reference 32).

Heads h, i, and j showed similar water-entry decelerations, in keeping with the High-Speed Water-Tunnel data (References 31, 32, and 33) that indicate cavity separation on the plate or spherical cap. The drag coefficients of the plate-cone Heads h and j, expressed on the basis of the plate area, were 0.88 and 0.84, respectively. These corrected drag coefficients show good agreement with that of 0.83 obtained for a
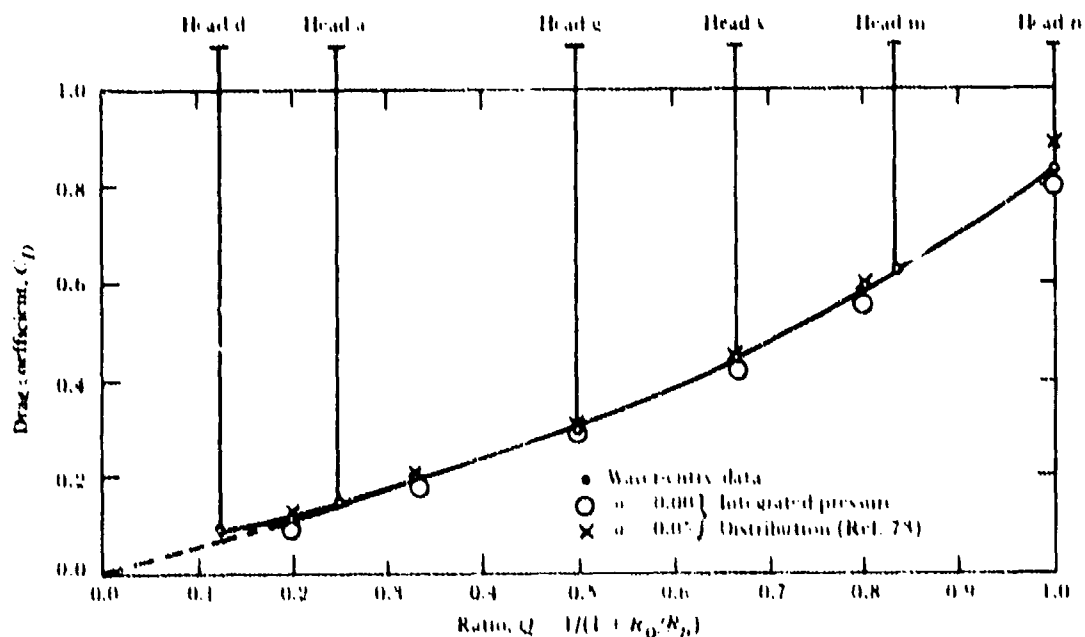
Figure 5.11. Drag coefficients, ogive and plate-ogive heads

full-diameter plate head on another dummy aircraft torpedo launched under similar conditions, and with the value 0.82 derived from the free-streamline theory (Reference 65). The annular groove of Head j evidently has little effect on water-entry deceleration. The corrected drag coefficient of 0.80 for Head i indicates that the slight curvature of the spherical nose had little effect on the water-entry deceleration and that other drag forces acting on the nose are small.

Underwater trajectories, recorded while water-entry whip and deceleration data were being obtained, were determined from the hydrophone array shown in Figure 5.12 and described in Part V. Hydrophones recorded the position of the missile at several known times during underwater flight, and nets were stationed from 530 to 780 feet from the entry point at intervals of 50 feet and supported at the surface by wire cable floated by corks. The nets were light enough not to impede the flight of the missiles, and the location of the holes made in them provided additional data.

The data for Head j (Henschel type) at the nominal 400- and 500-fps entry velocities are taken from Reference 95 as examples of stable underwater trajectories. The relative launching conditions are shown in Table 5.2, elevation and plan views of the trajectories in Figures 5.13 and 5.14, and vertical and lateral deviation from the extended air trajectory after 100 feet of underwater travel in Figures 5.15 and 5.16. Additional data are available in Reference 95.

Some general trends were apparent in the trajectory data obtained with the 14 head shapes. The first 100 feet of underwater trajectory was not appreciably affected when (other entry conditions being equal) the water-entry velocity was increased from 400 to 500 fps. Apparently, gravitational and buoyancy forces are of minor consequence over this velocity range. (A detailed explanation is available in Reference 95.) Farther along, the trajectory was influenced by gravity and buoyancy forces and these forces became more predominant after the torpedo had lost most of its velocity.
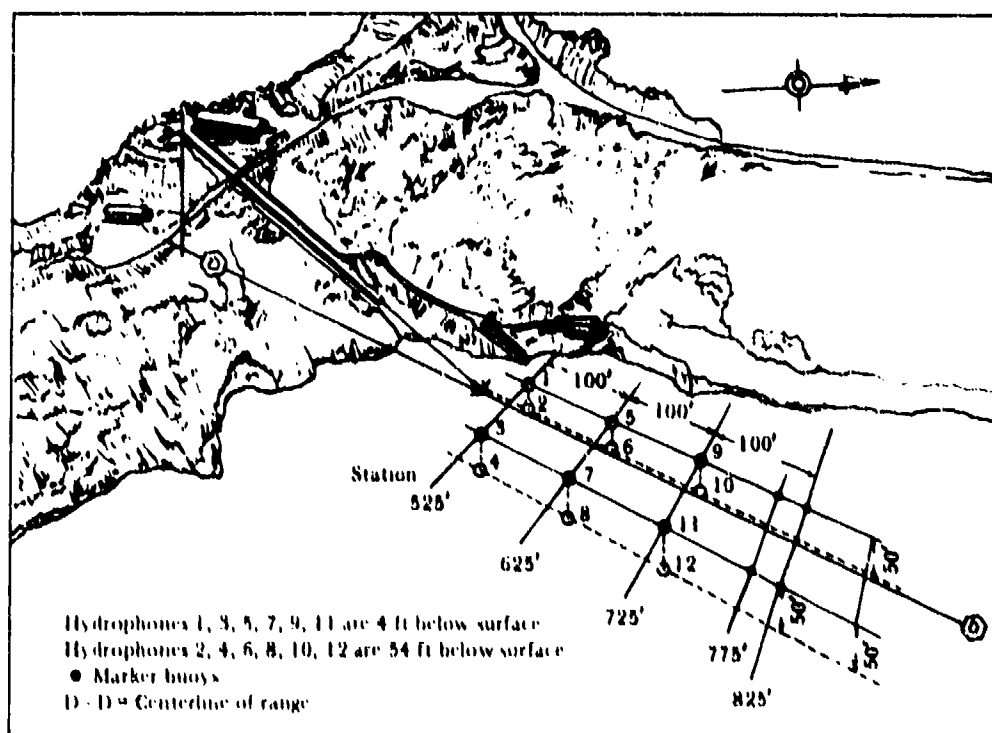
Figure 5.12. Fixed-angle launcher site, hydrophone locations.

79

TABLE 5.2. Launching Conditions, Head j

Curve No. (Fig. 5.13 and 5.14)	Angle of Attack, deg	Whip, deg/sec	Pitch Velocity, deg/sec [a]	Yaw, deg	Water-Entry Velocity, fps
1	5.8	94	100	1.4	394
2	4.4	79	96	-1.0	400
3	1.7	0	......	-1.9	395
4	0.7	.....	......	-1.7	414
5	......	......	......	-1.7	399
1	-.6	161	176	-1.0	507
2	3.5	105	70[b]	-1.0	507
3	......	......	......	-2.5	507
4	2.7	77	92	0.0	504
5	1.1	54	40	0.5	502
6	0.8	63	72	2.1	500
7	0.6	58	91	-1.0	506
8	0.2	......	......	-0.5	471
9	-0.2	42	24	-0.7	506
10	-0.8	40	28	0.7	511
11	-2.2	33	20	0.4	508

[a]Pitch velocity just after whip has taken place.

[b]Pitch velocity subject to error because of lack of information on roll.
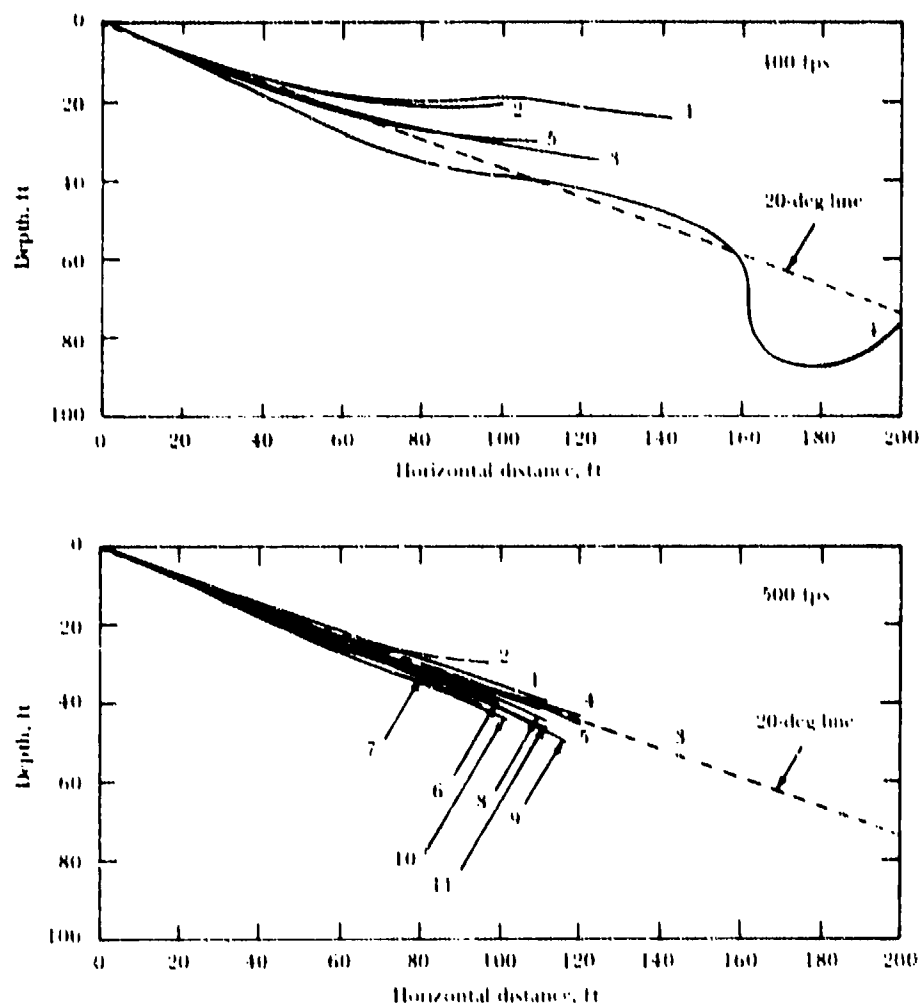
Figure 5.13. Elevation, Head of underwater trajectory.

With the ogive and spherogive configurations, the trajectory rapidly became more shallow with increase in entry angle of attack. The data indicated "critical" angle of attack[4] values, and there was fair agreement between the experimental and calculated values of critical pitch. For plate-cone configurations, the data were less defined, although there was a suggestion of critical angle of attack. With the plate-ogive configurations, there was evidence of a critical angle of attack and, in contrast to the ogive-spherogives, evidence of an increase in maximum depth of dive with increase in attack angle.

Several of the full-scale missiles used in this study of whip and deceleration at water entry also served as prototypes in subsequent studies of water-entry pitch modeling (Chapter 7). The data obtained, although not directly related to the modeling of their behavior, could have direct application to missile design and could also point up areas in missile water-entry behavior that should be studied through correlation with models.

----

[4] By "critical" is meant that angle of attack at which the trajectory changes from unturning to downturning or vice versa.

81
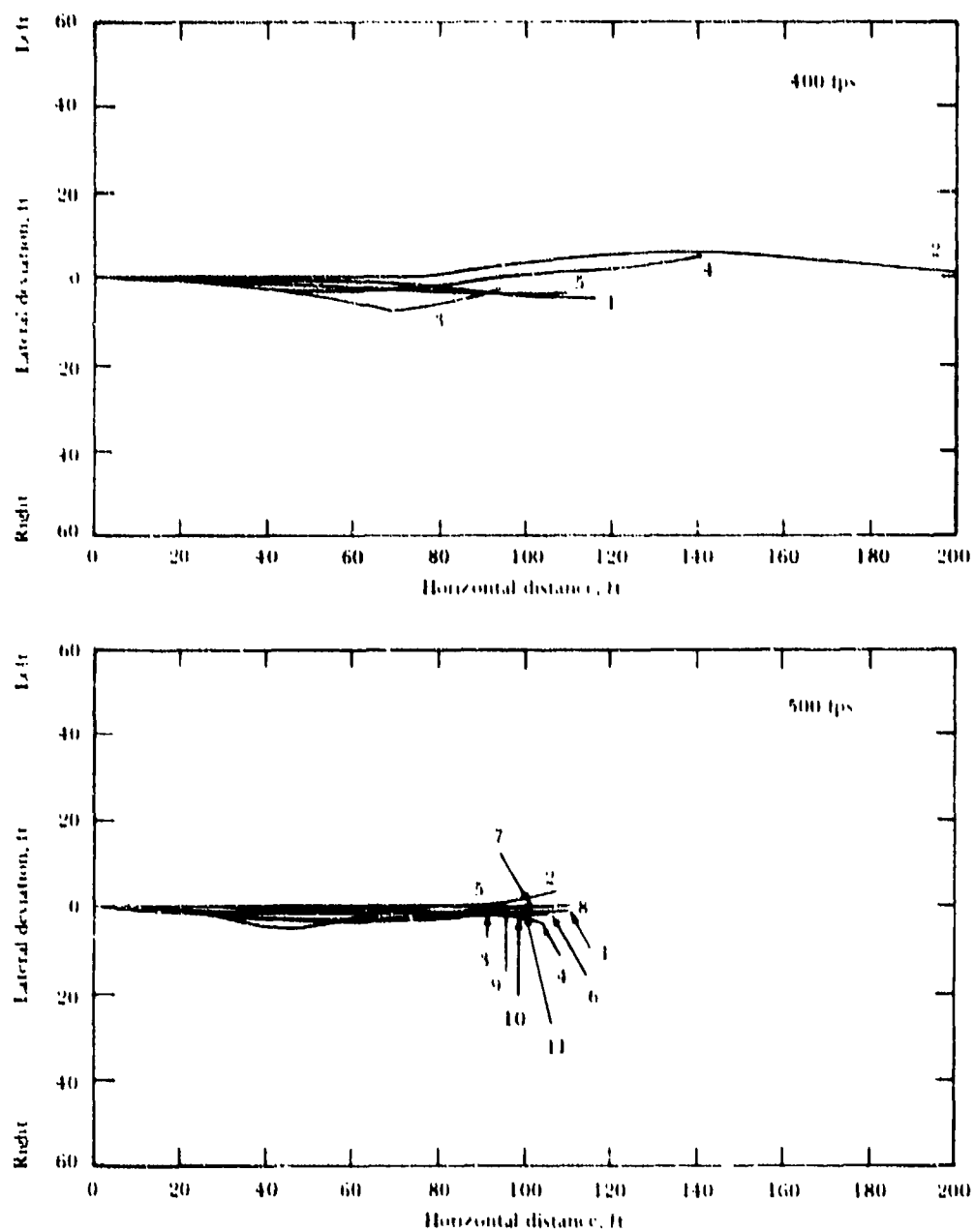
Figure 5.14. Plan view, Head 1 underwater trajectory.
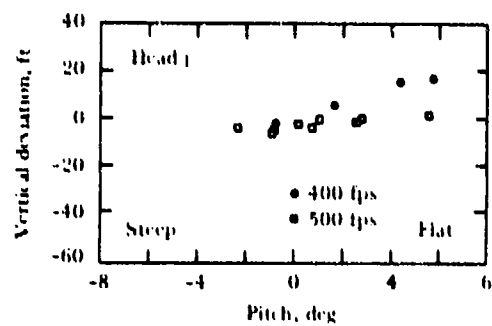
Figure 5.15. Vertical deviation at 100 feet, Head j.
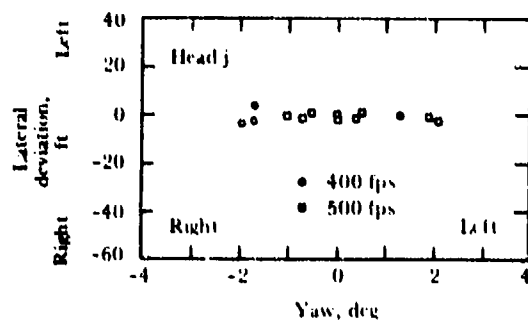
Figure 5.16. Lateral deviation at 100 feet, Head j.

CHAPTER 6
WHIP AND UNDERPRESSURE

During early modeling studies of oblique water entry of missiles, it was observed that Froude scaling alone did not accomplish modeling, the model generally tending toward a more downward trajectory than the prototype; in some instances the model dived while the prototype turned upward and broached. L. B. Slichter (Reference 61) investigated this anomalous behavior and established that portions of the underside of the model may be subjected to less than atmospheric pressure during water entry. In that event, atmospheric pressure acting on the upper side of the model nose could, in opposition to the reduced pressure areas beneath it, generate a moment large enough to overbalance the water-pressure forces completely and produce a nose-down whip and diving trajectory.

Slichter's studies were confined to small models, but the inference is plain: if this reduced-pressure or under-pressure effect obtains for models, it must also obtain for full-scale missiles. The magnitude of the under-pressure effect was not known at that time, but it was clear that the effect would have to be scaled if correlation was to occur, and that Froude scaling alone was insufficient.

A hypothetical explanation of the generation of underpressure areas is that a cavity forms beneath the missile nose when it enters water obliquely. While it is first forming, the cavity is open to the atmosphere and is composed of water vapor and air, but as the missile penetrates farther into the water, the cavity is sealed off from outside air but continues to grow, with the result that the gas pressure inside it is lowered, and the pressure on the lower side of the nose is reduced to less than atmospheric.

Supporting evidence for the hypothesis can be seen in Figure 6.1, which shows photographically and diagrammatically the oblique water entry of a 2-inch-diameter plate-cylinder-head model (entry velocity 128 fps, trajectory angle 20 degrees, and atmospheric pressure over the water surface). An undercavity of air and water vapor has been sealed off by the splash lip impinging on the lower side of the cylinder. According to the hypothesis stated above, the cavity expanded after it was sealed off from the outside air, thereby reducing the gas pressure within it to below atmospheric pressure. The splash lip is even more apparent in Figure 6.2, which shows a flat-plate model entering water
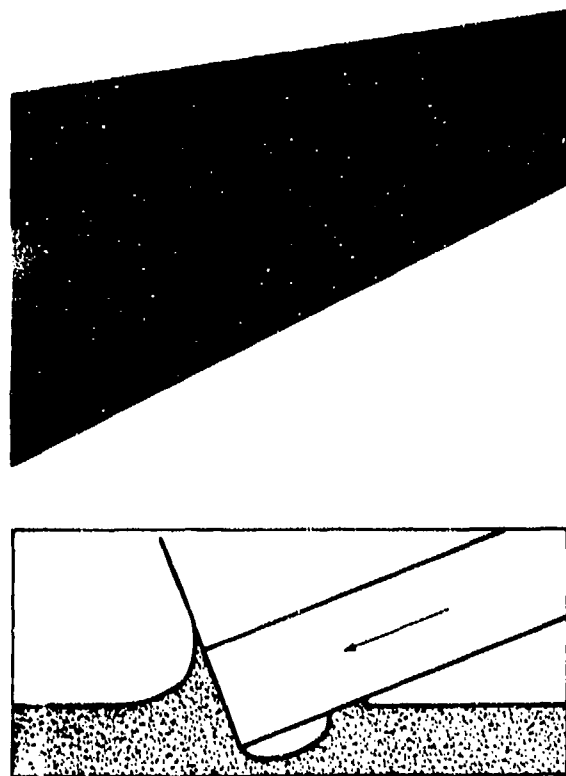
Figure 6.1. Oblique water entry of plate-cylinder head.

84
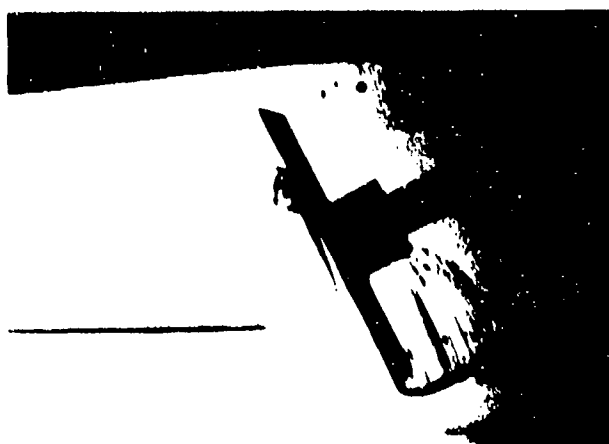
Figure 6.2. Oblique water entry of flat plate.

obliquely. The sides of the flat plate are in contact with the glass walls of the tank, there is no flow around the sides of the plate, and the flow is essentially two-dimensional. The splash lip that would form the undercavity seal if a rectangular-head configuration were used appears as a cusp behind the plate.

If the assumptions of the hypothesis are correct, venting the undercavity to the atmosphere should equalize cavity and ambient air pressure, thereby reducing or nullifying the underpressure effect. Such venting can be accomplished by modifying the missile head, and if the other water-entry characteristics of the head are changed only slightly, vented and unvented heads can then be launched under similar conditions to determine whether a significant underpressure exists at service-missile scale. Model heads with different degrees of venting can be launched under similar conditions at atmospheric pressure to provide information on the correlation of the underpressure effect with undercavity behavior. Finally, reducing the air pressure over the water surface should also reduce the underpressure effect. The launching of an unvented model head at different ambient air pressures but with otherwise similar conditions should not only provide information on the correlation of the underpressure effect with cavity behavior but should also indicate whether reduced air pressure could be used to scale the underpressure effect. The NUC studies described below include published (References 99 and 100) and unpublished data.

Prototype missiles selected for study consisted of vented plate and unvented plate-cylinder heads attached to a torpedo after body (Figure 6.3). Duralumin 2-inch-diameter models were built with different degrees of venting achieved by varying the cylinder length. The

Plate-cylinder head

Vented-plate head
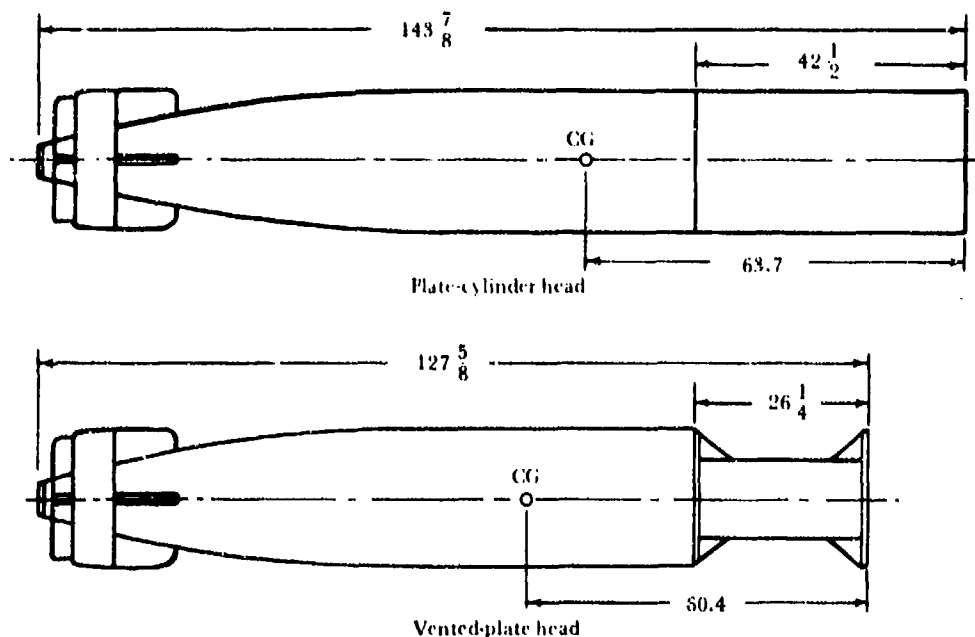
Figure 6.3. The 22.42-inch-diameter prototype. (Dimensions are in inches.)

85

head shapes (designated A through H) and their dimensions are shown in Figure 6.4. (The application of Head H is described later, in connection with Figure 6.20.) These heads, as well as a plate-cylinder head, were attached to model afterbodies, as shown in Figure 6.5.

Prototype and model parameters are shown in Table 6.1. Variations in head configuration and the consequent weight and weight-distribution differences made it impossible to adjust the body parameters to bring them into complete agreement within each set of tests. However, the distance of the CG from the nose of the missiles was held constant (by adjustment of internal weights) within each set, and in all instances the CG was located on the longitudinal axis of symmetry. Corrections were applied for the small variations in moment of inertia.[1] No

attempt was made at correlation; the sets of tests were independent of each other.

Whip was arbitrarily defined as the change in pitch velocity between water contact and the complete submergence of the nose plate; this definition proved to be physically reasonable upon inspection of the pitch-velocity time functions (Figure 6.6). Whip so defined is equal to the corrected pitch velocity at the time of complete nose-plate submergence because all data are corrected to zero pitch velocity at water contact.

To investigate the effects of venting on whip, full-scale dummy torpedoes and 2-inch-diameter models were subjected to test launchings. The prototypes were launched into fresh water at the NUC Morris Dam Torpedo Range (Figure 5.12). The torpedo with the plate-cylinder head was launched 12 times from the Fixed-Angle Launcher (FAL), the torpedo with the vented head 21 times from the Variable-Angle Launcher (VAL). The trajectory angles at water entry ranged from 20 to 22 degrees; the nominal launching velocity was 400 fps. To study the correlation of the underpressure effect with cavity behavior and the degree of venting, the model afterbody shown at the top of Figure 6.5 was launched with Heads A to G into the Open Launching Tank at the NUC Hydroballistics Laboratory. The entry angle was 20.35 degrees, the entry velocity was 137.5 fps, and the atmospheric pressure was ambient. To study the effects of atmospheric pressure and water surface tension on whip, launchings using only the fully vented model (Head A with the afterbody shown at the top of Figure 6.5) and the unvented model (shown at the bottom of Figure 6.5) were made later in the NUC Variable-Atmosphere Variable-Pressure (VAVP) Launching Tank (described in Part V). The entry angle was 20 degrees, pressures ranged from 0.1 to 1.5 atmospheres, and launching velocities were 80 to 81 fps. Velocities were measured with a photocell timer and whips were measured with the optical whip recorder (Part V).

Actual launching conditions for all missiles are listed in Table 6.1. The effects of yaw at water entry were neglected because in most cases the yaw was very small (less than a degree) and the maximum angle recorded was
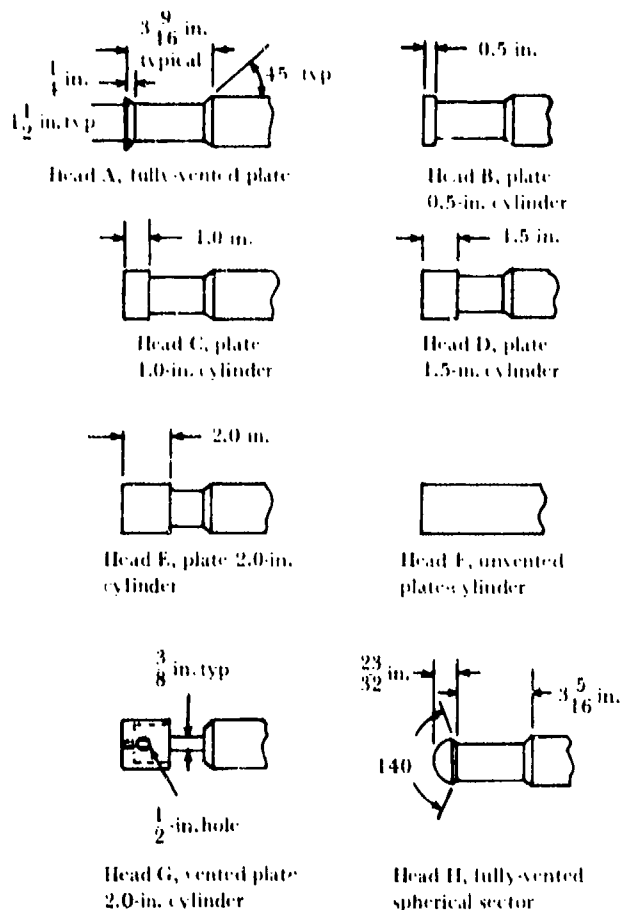
Figure 6.4. Head shapes of 2-inch-diameter models.

___

[1] See footnote 2, Chapter 5.
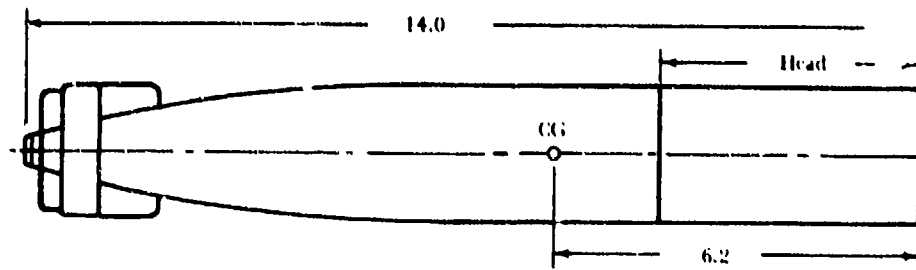
For venting studies in Open Tank.
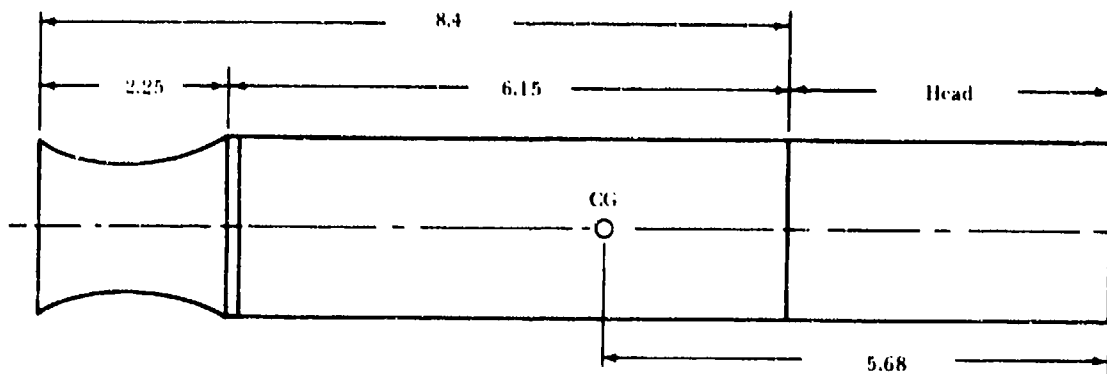
For atmospheric pressure and water surface tension studies in VAVP Tank.

Figure 6.5. Two-inch-diameter model afterbodies with plate-cylinder heads. (Dimensions in inches.)
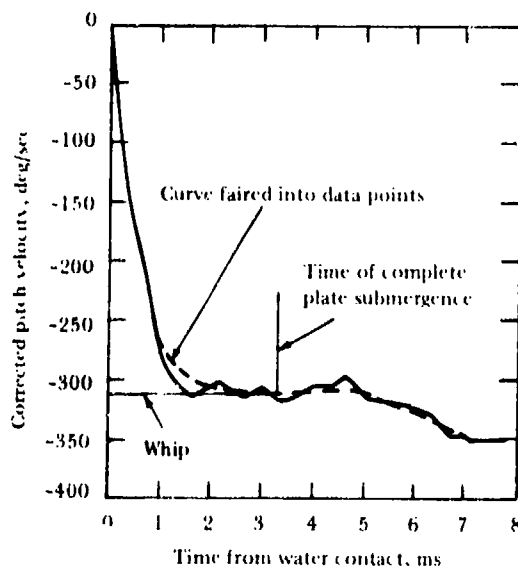
Figure 6.6. Typical water-entry pitch velocity–time plot, 2-inch plate cylinder, Head E.

1.8 degrees. For comparison of results, prototype data were corrected to a nominal water-entry velocity of 400 fps and moment of inertia of 800 slug-ft^2; model data in the first set were corrected to 137.5 fps and 21.3 lb-in^2. All data were corrected to zero pitch velocity at water contact.

Plate submergence was defined in terms of the geometry of thè static model system (Figure 6.7). The water-contact velocity was used to calculate the time of plate submergence and was also used in the whip calculations because experimental evidence showed that the velocity decreased only 2.5% between contact and total plate submergence. The whip was measured from the fitted curve.

Prototype whip as a function of attack angle is shown in Figure 6.8. In spite of the large scatter in the data, it is apparent that the missile's negative whip is reduced by venting, as predicted by the underpressure hypothesis. The

87

Undisturbed water level   Half submergence

Undisturbed water level   Full submergence
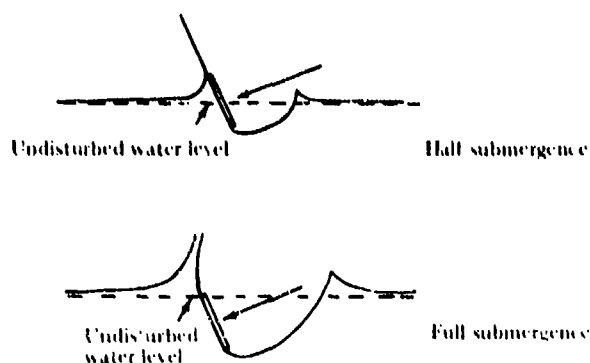
Figure 6.7. Plate at half and full submergence.
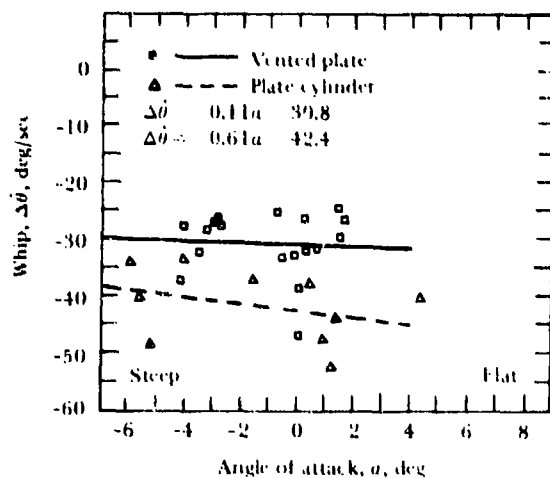
Figure 6.8. Dependence of whip on angle of attack. Water-entry velocity 400 fps, 20-degree water-entry angle.

Figure 6.9. Whip versus angle of attack, plate and plate-cylinder heads.

test data also prove that the phenomenon of underpressure exists with full-scale missiles as well as with models.

The whip of the plate-cylinder model becomes increasingly negative as the cylindrical section is lengthened (Figure 6.9), which can reasonably be attributed to underpressure because actual impact of the flow upon the underside of the cylinder would naturally result in positive whip-producing forces. The vent hole in the 2-inch cylinder head reduced the whip considerably, but venting was not complete, approximating instead that of a cylinder somewhat less than 1 inch in length.

The whip as a function of distance traveled beyond water contact is plotted in Figure 6.10. These averaged curves show that evidence of underpressure in the whip functions of the

vented missiles ceased at about one-half plate submergence regardless of cylinder length; the whip function of the unvented head indicated that underpressure continued almost until total plate submergence.

Duplicate launchings of models with Heads A through G were photographed with the rotating disk camera; side views of Heads A, E, and F launchings are shown in Figure 6.11. It is apparent that half-plate submergence corresponded approximately to the complete entry of the 2-inch cylindrical body section and that the CG crossed the interface at about the time of

The photographs of Figure 6.12 show that small secondary cavities formed as the midsections of the vented models crossed the interface but did not form during the launching of the unvented missile. The cylindrical section of the unvented head remained in contact with the water as the upper half of the plate face was

88

TABLE 6.1. Ballistic Parameters and Launching Conditions,
Plate-Cylinder and Vented-Plate Missiles

Parameter	Full scale (22.42 in.)		Small scale (2 in.) Open tank		Small scale (2 in.) VAVP tank	
	FAL Plate cylinder	VAL Vented plate	Plate cylinder [a]	Vented plate [b]	Plate cylinder [c]	Vented plate [d]
Ballistic						
Weight, lb	1547-1552	1481-1502	1.081	1.170-1.174	1.100	1.172
Length of missile, in.	143.9	127.6	14.0	14.0	12.0	14.0
Distance of CG from nose, in.	63.7	60.1-60.6	6.20	6.20	5.68	6.20
Moment of inertia about transverse axis through CG	694 slug-ft^2	503.5 slug-ft^2	20.22 lb-in^2	20.22-21.90 lb-in^2	18.35 lb-in^2	20.22 lb-in^2
Launching						
Trajectory entry entry angle, deg	20-22	20-22	20.35	20.35	20.0-20.5	20.0-20.5
Angle of attack, deg	-5.9 to +6.8	-4.1 to +4.3	-0.75 to +1.15	-1.35 to +1.15	±0.25	±0.25
Velocity, fps	400	400	137.5	137.5	80-81	80-81
Atmospheric pressure, atm	Ambient	Ambient	Ambient	Ambient	0.1 to 1.5	0.1 to 1.5
Water surface tension, dynes/cm	Normal[e]	Normal[e]	Normal[e]	Normal[e]	Normal[e] (also 28.7)	Normal[e]

[a] Afterbody at top of Figure 6.5 with Head F.

[b] Afterbody at top of Figure 6.5 with vented head (except Head H).

[c] Plate cylinder head model at bottom of Figure 6.5.

[d] Afterbody at top of Figure 6.5 with Head A.

[e] Normal = 75.6 dynes/cm.
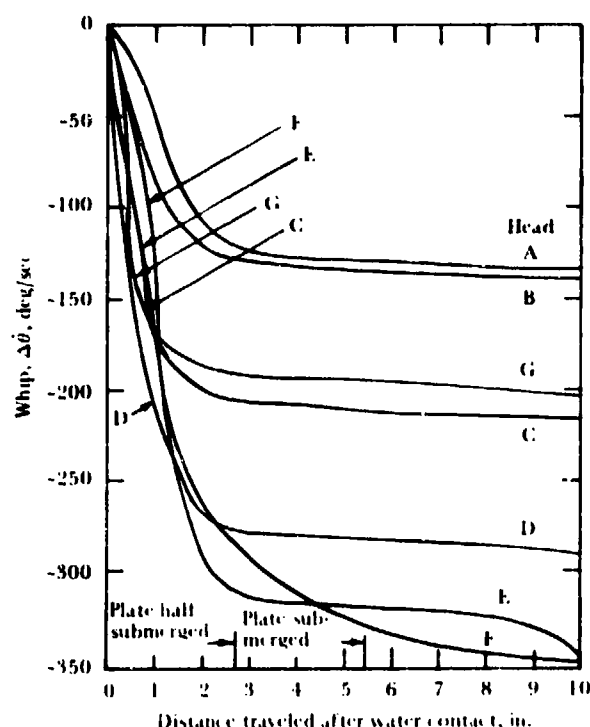
Figure 6.10. Water-entry whip, plate and plate-cylinder heads.

wetted, and the missile was fully engulfed by the cavity soon after the CG crossed the interface.

It is interesting to compare the whips of the vented full-scale and model heads. The CG's are situated on the axis of symmetry of both missiles, and the hydrodynamic forces on the plate must act normally to the plate (except for slight shearing forces). Thus, the moments of the hydrodynamic forces about the CG will not be influenced by the distance of the CG aft of the nose. According to the hypothesis, these fully vented missiles should experience no moment from underpressure and, moreover, the whip should also be independent of the lateral CG location. Because the whip varies as the fourth power of the plate diameter (Reference 97), directly as the entry velocity, and inversely as the moment of inertia, the whip at zero pitch scaled from the 2-inch model to the 22.4-inch prototype would be

$$-128.2\left(\frac{22.4}{2}\right)^4\left(\frac{400}{137.5}\right)\left(\frac{21.3}{800 \times 32.2 \times 144}\right)$$

$$= -33.7 \text{ deg/sec} \qquad (6.1)$$

The experimentally obtained whip for the full-scale vented-plate head is -30.8 deg/sec. The difference between experimental and scaled whip is within the scatter of the data.

Atmospheric pressure also affects the whip of the plate-cylinder model, being about five times as great at 1.5 atmosphere as at 0.1 atmosphere (Figure 6.13). It increased steadily with time until the plate was approximately half submerged, then decreased for a millisecond or two before increasing again.

Photographs of cavity growth (Figure 6.14) reveal two interesting features. First, the size of the undercavity increases with decrease in pressure, as illustrated in Figure 6.15, in which the increase in cavity size with decrease in pressure for comparable distances of missile penetration is apparent. Second, small protuberances are created along the bottom of the undercavity with increase in pressure. They reduce to almost nothing at 0.1 atmosphere, indicating that the undercavity vents, at least partially soon after the missile enters the water. The small differences can be considered important because duplicate cavities resulted from the same entry conditions (Figure 6.16). It is possible that wetted underpressure areas may exist that are not within the undercavity.

Figure 6.17 shows that change in ambient air pressure does not significantly affect the whip of the fully vented plate model (Head A). The ballistic parameters and conditions are given in the last column of Table 6.1. Compared with the unvented plate-cylinder model, this configuration experienced a relatively small whip at air pressures ranging from 0.1 to 0.5 atmosphere, indicating that the underpressure effect in that environment is negligible.

Launchings made with the vented model were repeated with an unvented hemisphere-head model, using approximately the same ballistic parameters. The negative whip of this configuration, like that of the unvented plate cylinder, increased greatly with atmospheric pressure, being +250 deg/sec at 0.1 atmosphere and ranging to -400 deg/sec at 1.5 atmospheres. The whip at 1.5 atmospheres was not reproducible. A similar variance in whip was noted at 1.0 atmosphere, a lesser variance at 0.7, and none at 0.4 or 0.1 atmosphere. At the higher pressure conditions, a change in angular velocity comparable to whip sometimes occurred in the yaw plane.

90
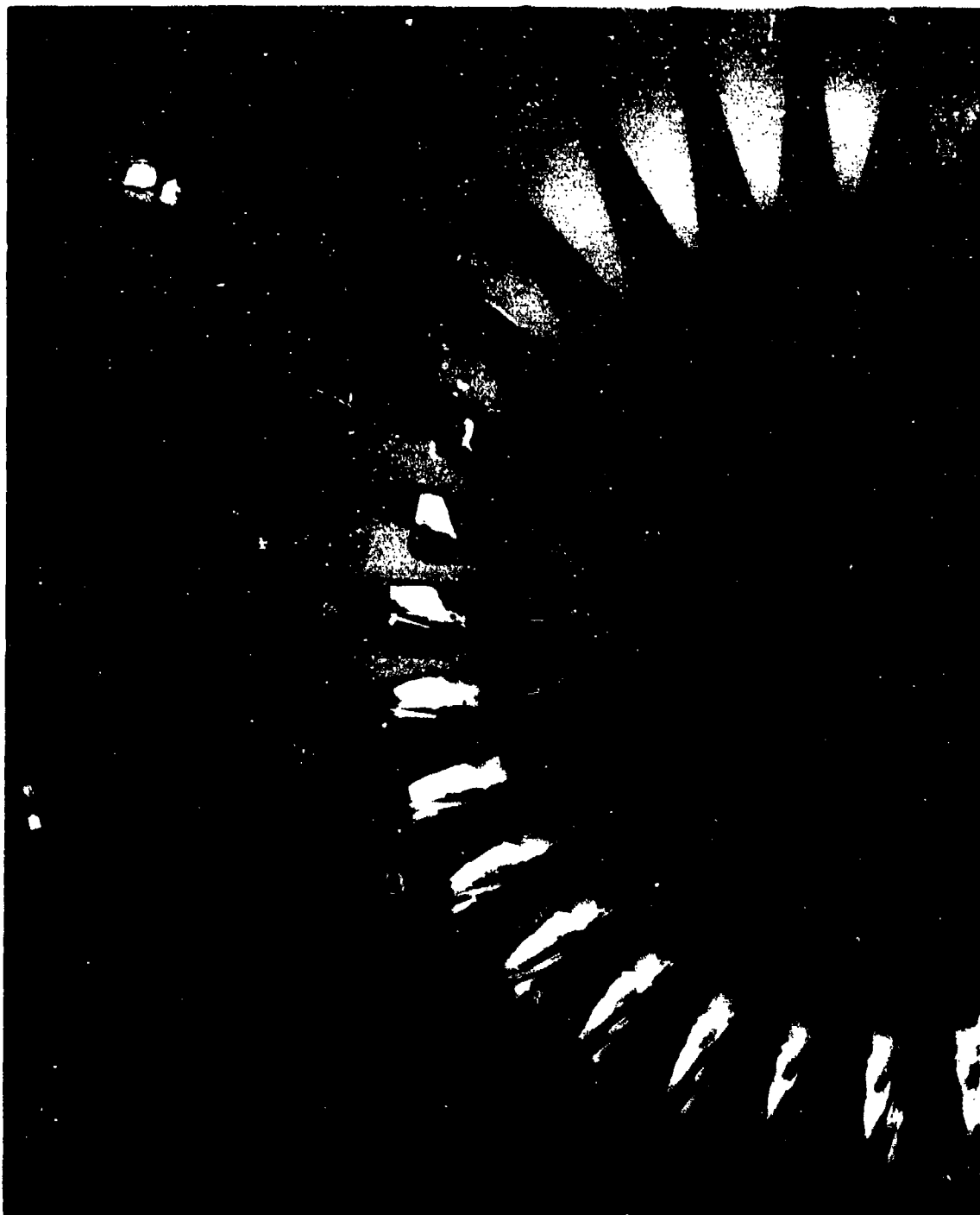
Head A, fully vented plate cylinder

Figure 6.11a. Water entry cavities as affected by venting.

Head E, plate 2-inch-diameter cylinder

Figure 6.11b. Water entry cavities as affected by venting.
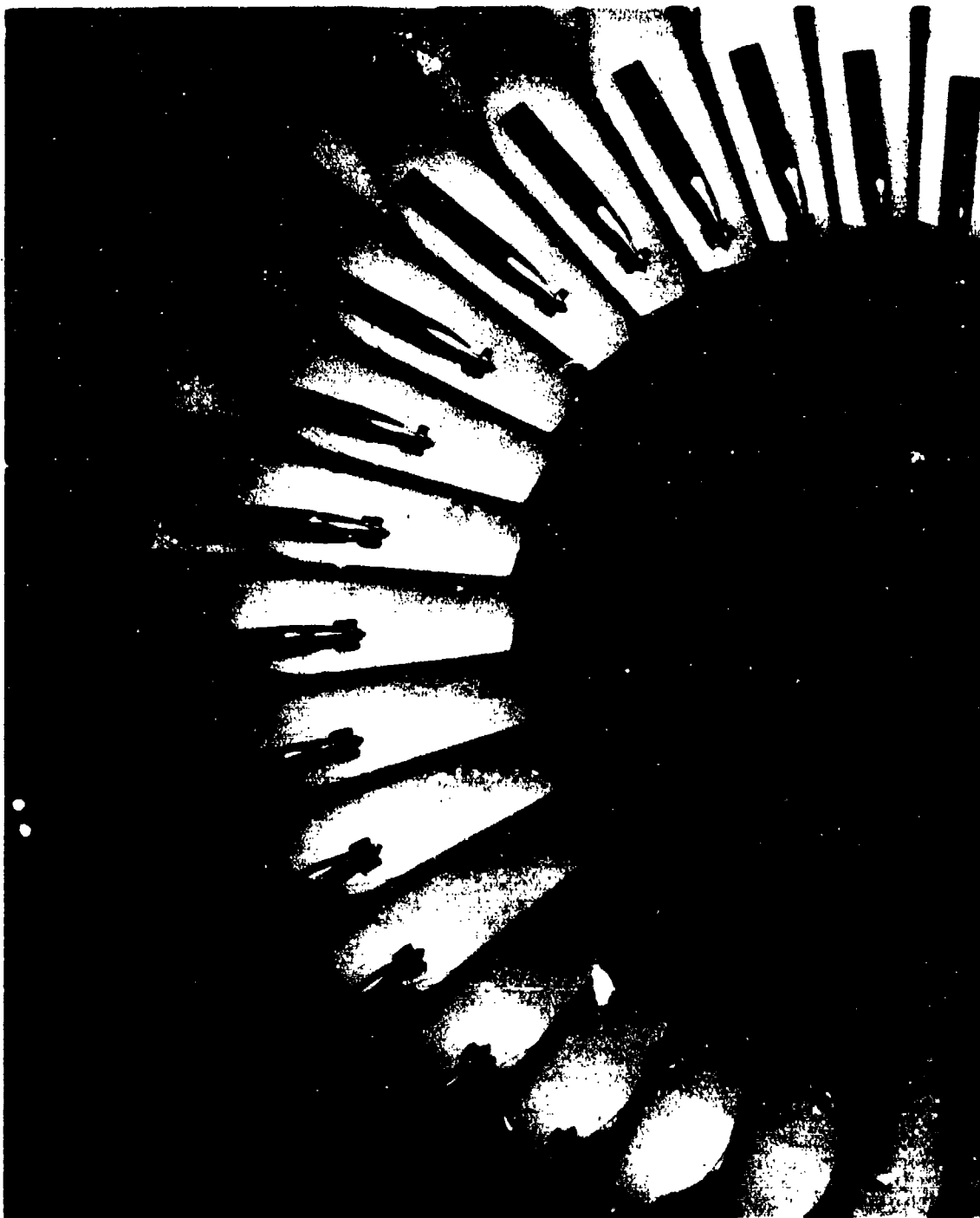
Head F, unvented plate cylinder

Figure 6.11c. Water entry cavities as affected by venting.

93
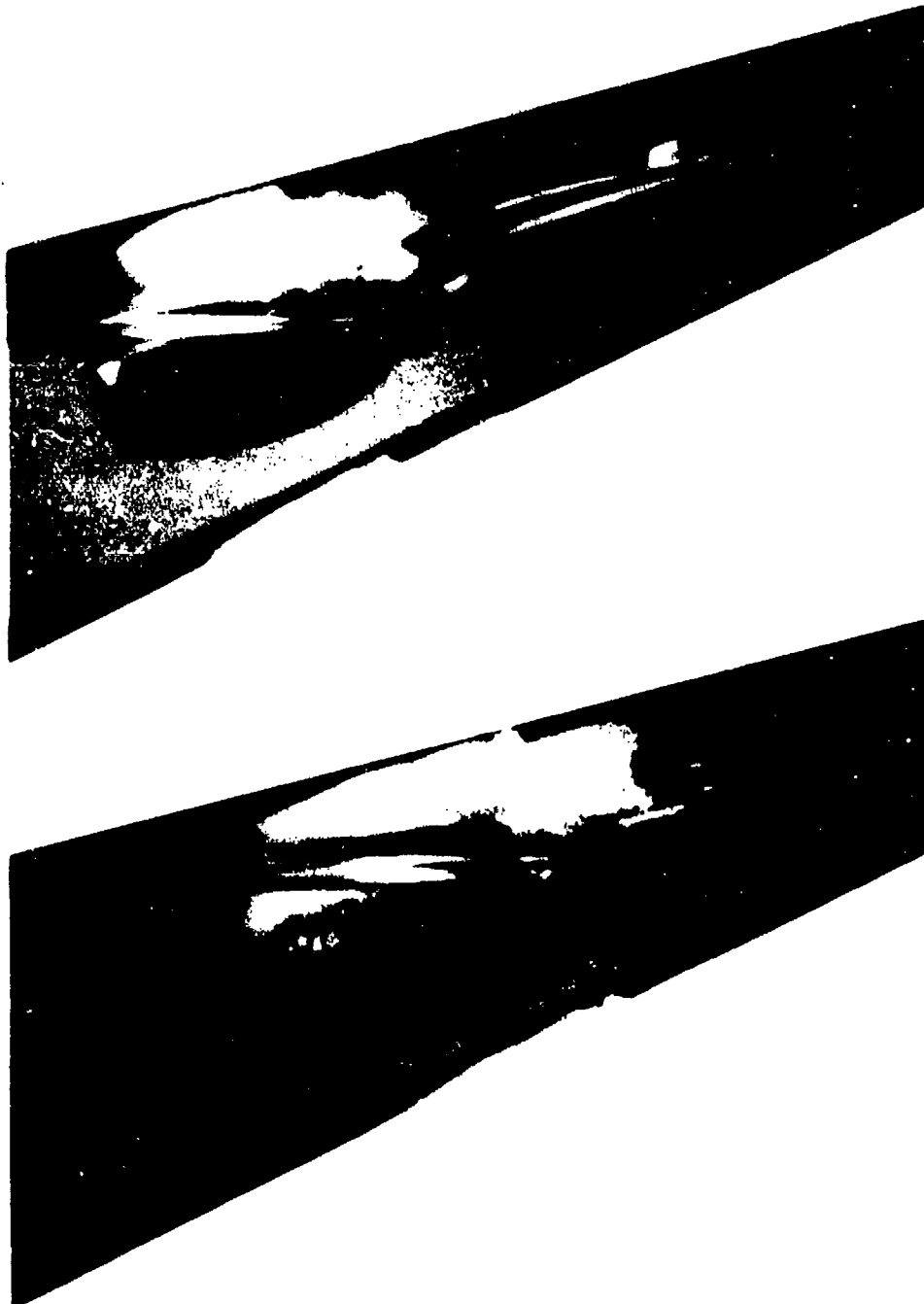
Head A. fully vented plate cylinder

Figure 6.12a. Secondary water-entry cavities as affected by venting.
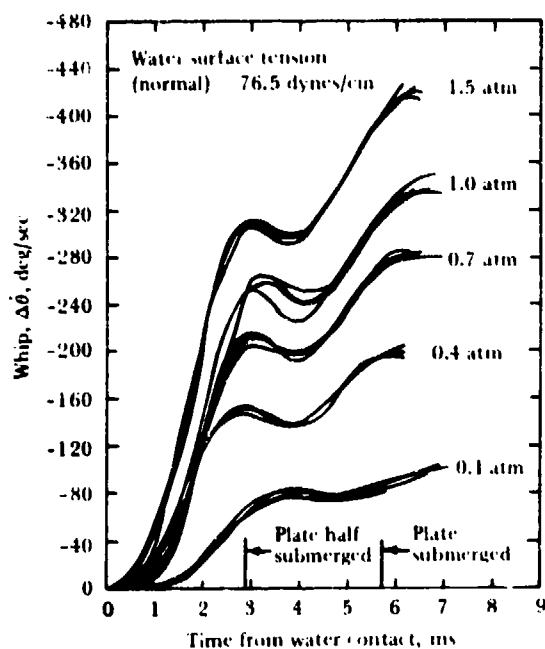
94
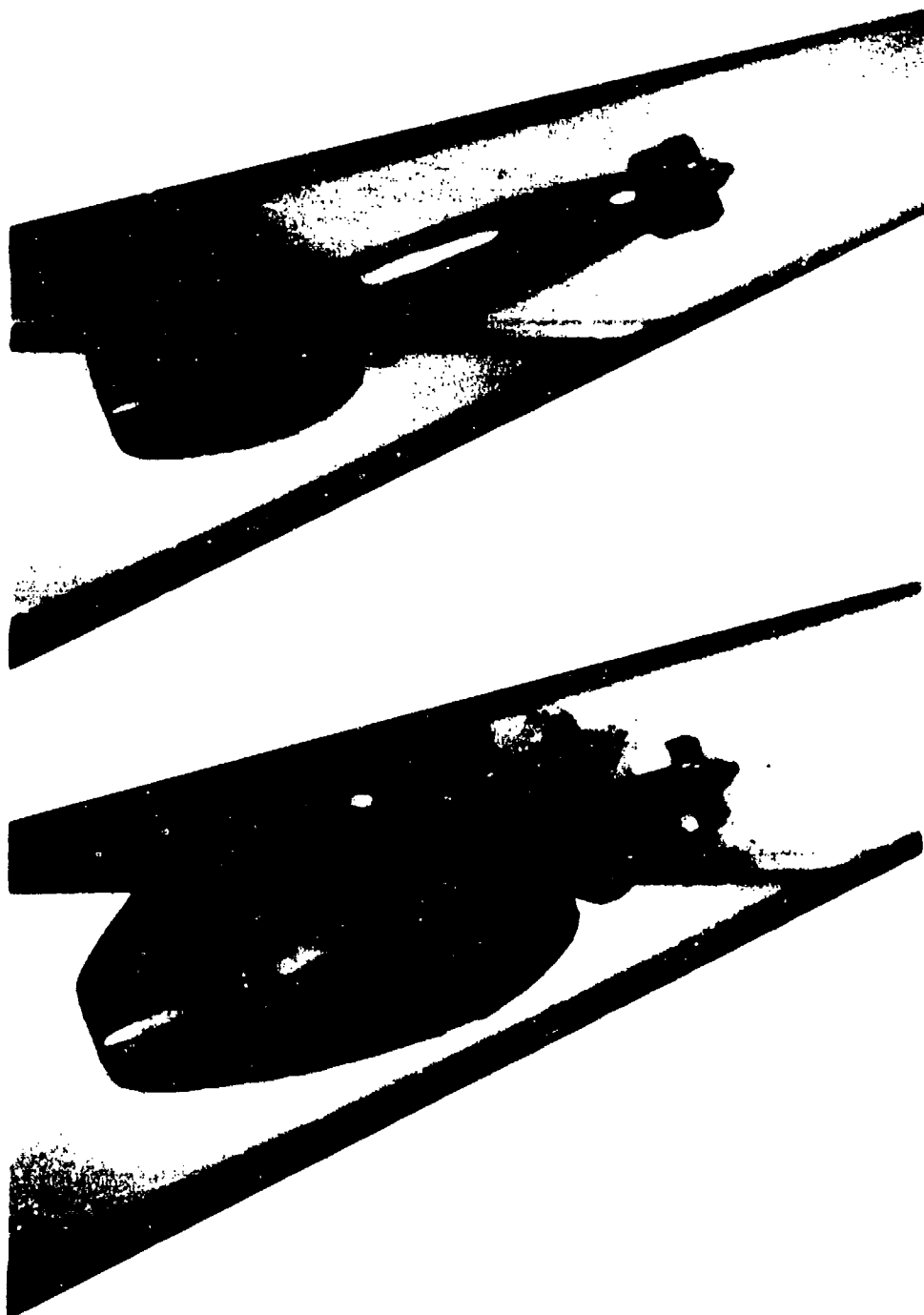
Head E, plate 2-inch-diameter cylinder

Figure 6.12b. Secondary water-entry cavities as affected by venting.

Head F, unvented plate cylinder

Figure 6.12c. Secondary water-entry cavities as affected by venting.

Figure 6.13. Whip versus time, unvented plate cylinder (Head F), at varied air pressures.

Cavity photographs of the unvented hemisphere head model at different atmospheric pressures made simultaneously with whip records show marked variation in cavity shape with air pressure. Reproducible whip was associated with a stable cavity and normal separation. Unstable cavities, sometimes with erratic separation, occurred at the higher atmospheric

pressures (Figure 6.18). Considerable irregularity and lack of reproducibility were apparent during launchings at 1.0 atmosphere (Figure 6.19). The stable, symmetric cavity formed at reduced pressure (0.1 atmosphere) is illustrated in Figure 6.20.

A spherical sector (Figure 6.4, Head II) was installed on the afterbody shown at the top of Figure 6.5 and this missile was launched at 0.1 and at 1.0 atmosphere. Stable, reproducible cavities were formed at both pressure conditions and the two cavities looked much alike (Figure 6.21).

The effect of surface tension upon the whip of the plate-cylinder model was also recorded (Figure 6.22). Launchings were made under the same conditions as those shown in Figure 6.13, except that the water surface tension was reduced to 28.7 dynes/cm by Aerosol.[2] Comparison of the two sets of runs shows little difference in the magnitude of the whip functions, but their reproducibility in similar launching conditions was less at the lower surface tension.

It was concluded from these tests that underpressure significantly affects the water-entry whip of both prototype service missiles and small models and would have to be scaled if water-entry trajectory modeling is to occur. For such an accomplishment, it would be necessary to scale the gas pressure over the water surface in the model systems.

---

[2]Less than 0.1% by weight of Aerosol OT (Reference 2); hence not significantly affecting the water density or the vapor pressure.

97

1.5 atmospheres

Figure 6.14a. Cavity growth as affected by atmospheric pressures, unvented plate cylinder, Head F.

98
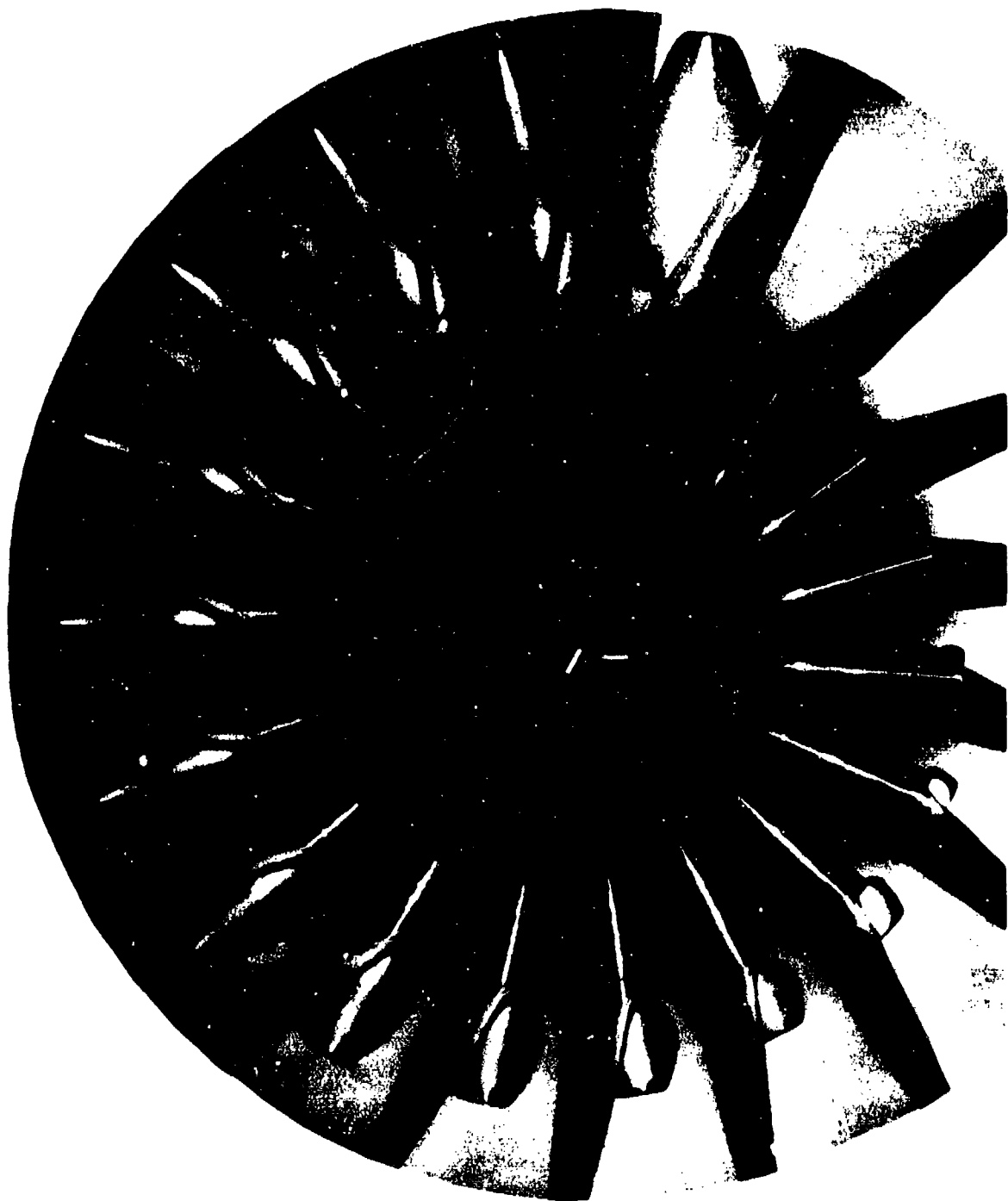
1.0 atmosphere

Figure 6.14b. Cavity growth as affected by atmospheric pressures, unvented plate cylinder, Head F.
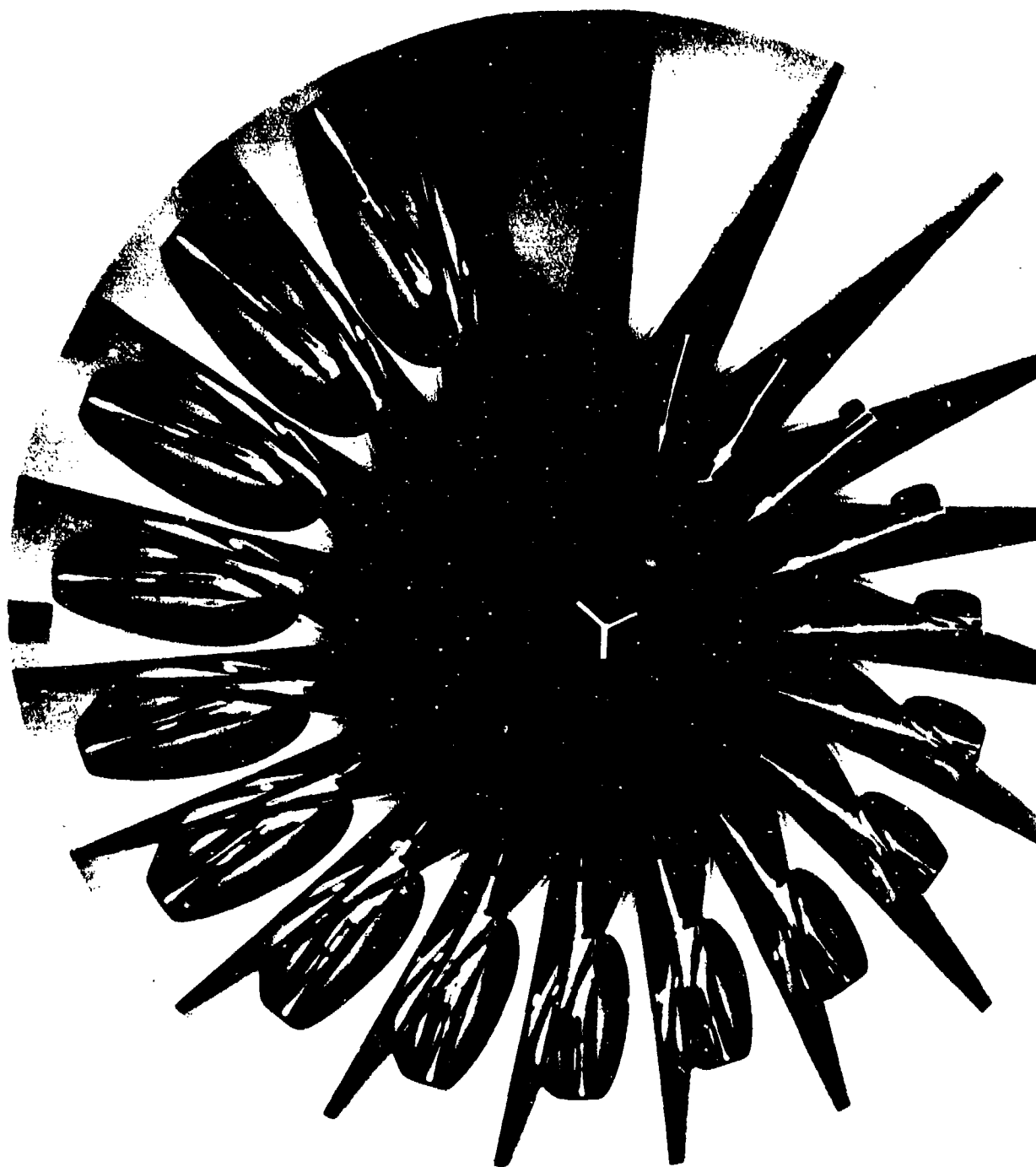
0.1 atmosphere

Figure 6.14c. Cavity growth as affected by atmospheric pressures, unvented plate cylinder, Head F.
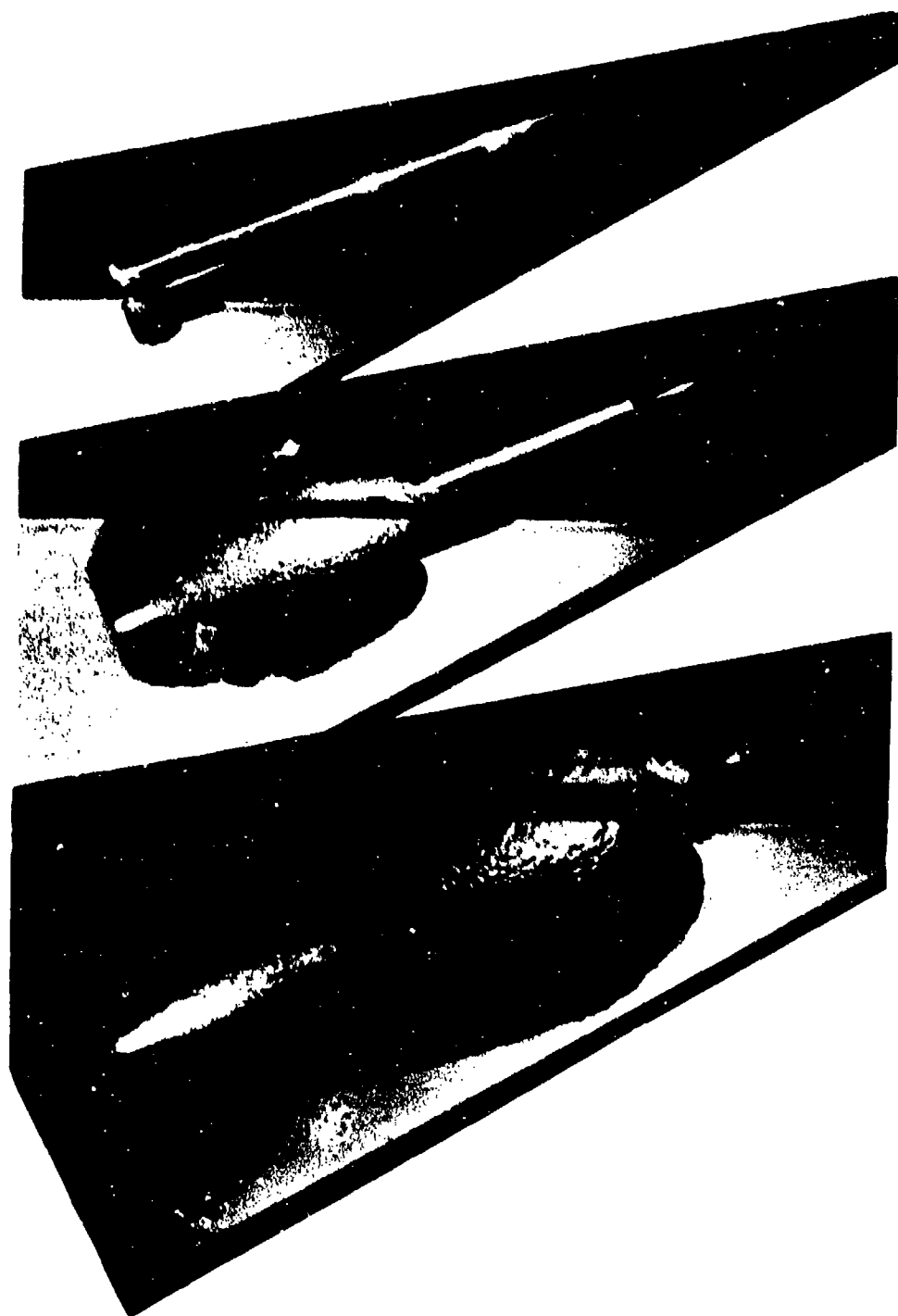
1.5 atmospheres

Figure 6.15a. Enlargements of water-entry cavities of Figure 6.14.

101

1.0 atmosphere

Figure 6.15b. Enlargements of water-entry cavities of Figure 6.14.

102

0.1 atmosphere

Figure 6.15c. Enlargements of water-entry cavities of Figure 6.14.

103
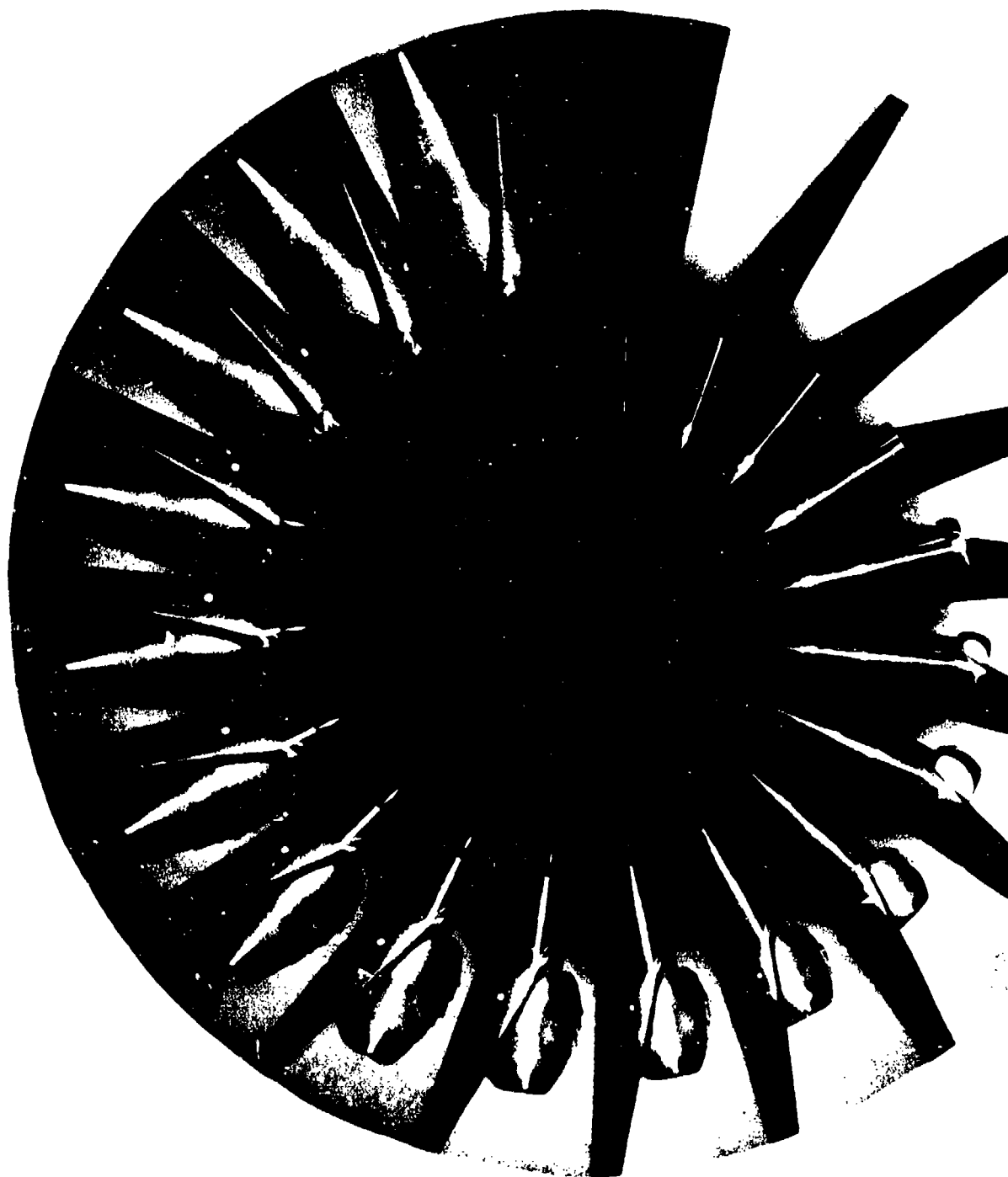
Run No. 1

Figure 6.16a. Identical cavities formed under equal entry conditions, unvented plate cylinder, Head F, 1.0-atmosphere air pressure.
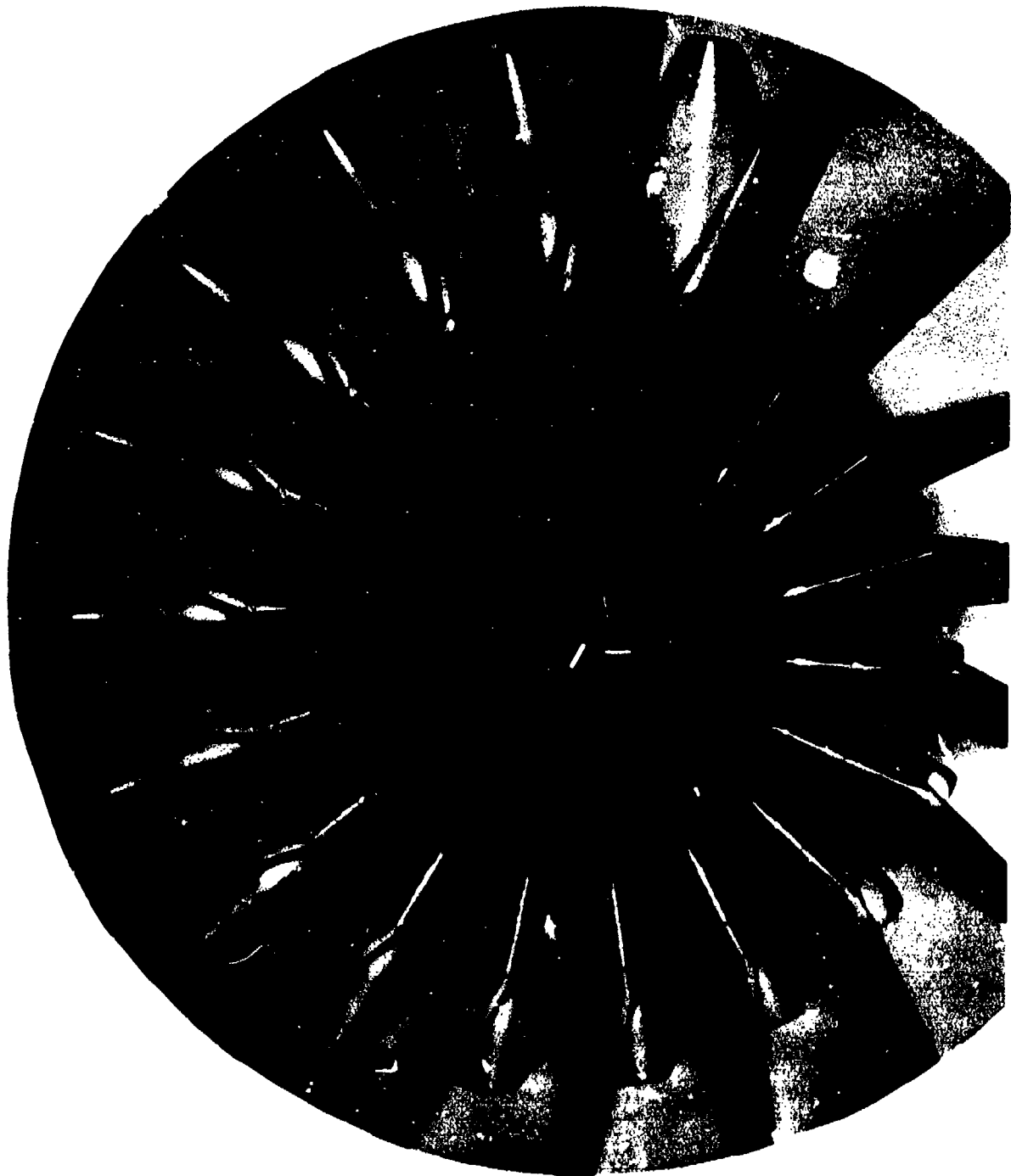
Run No. 2

Figure 6.16b. Identical cavities formed under equal entry conditions, unvented plate cylinder, Head F, 1.0-atmosphere air pressure.
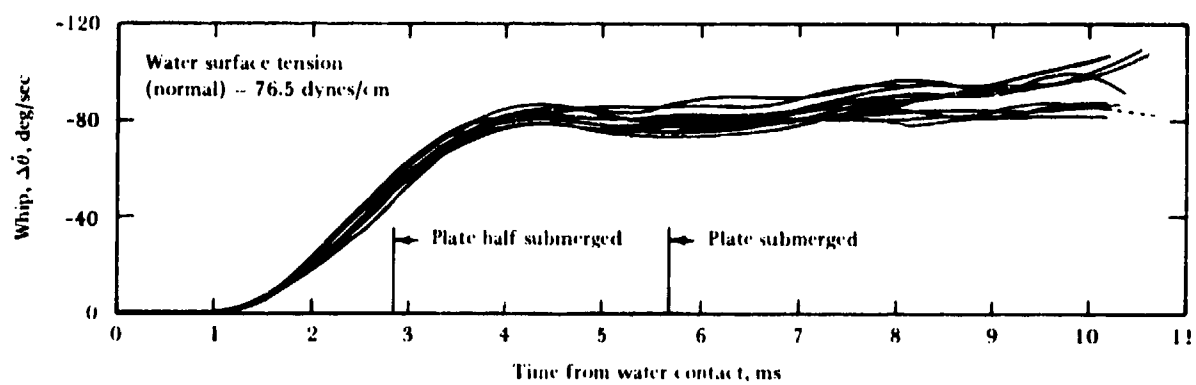
Figure 6.17. Whip versus time, fully vented plate (Head A), at varied air pressures.
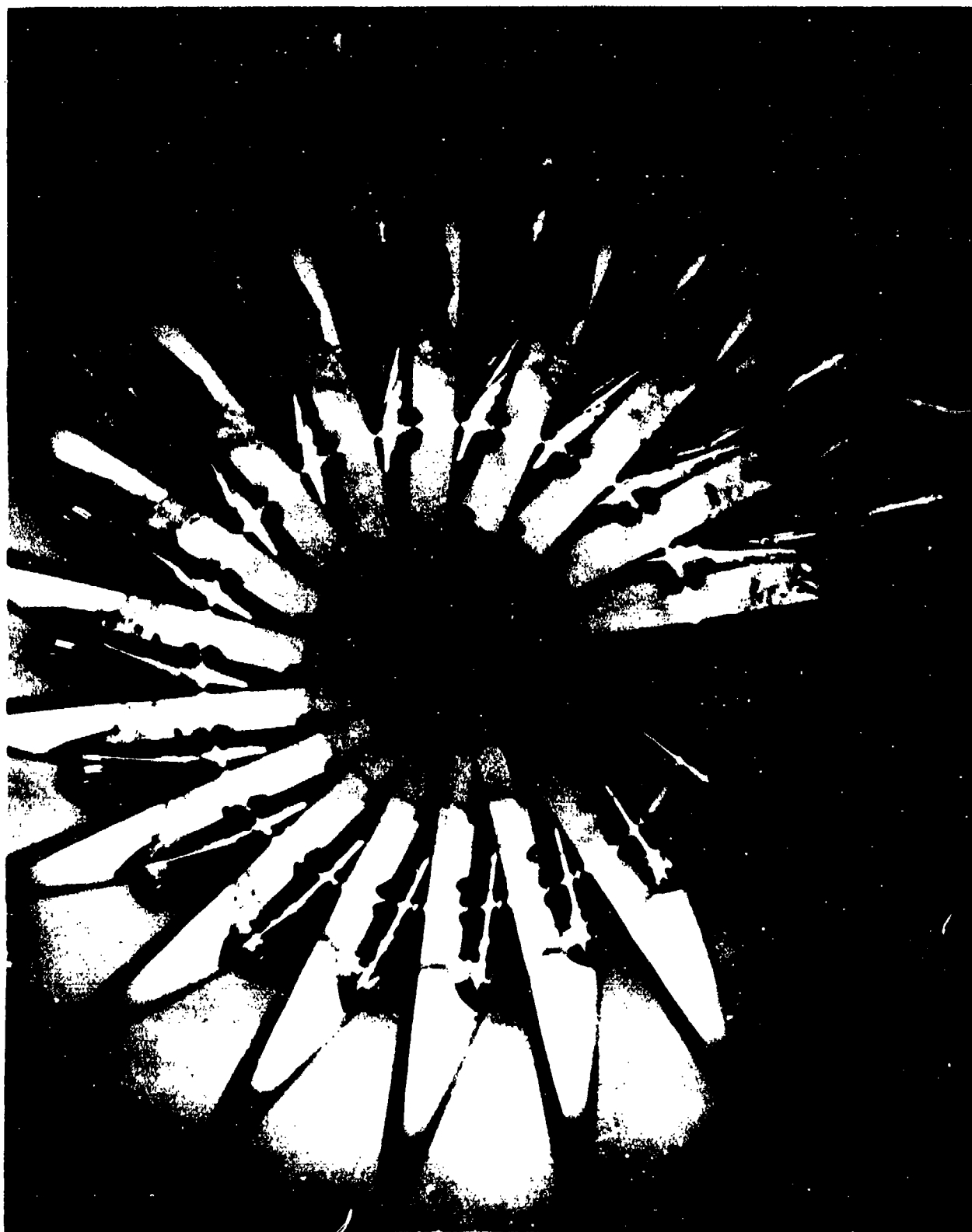
Figure 6.18. Unstable cavity separation, unvented hemisphere head model entering water at 1.0 atmosphere air pressure.
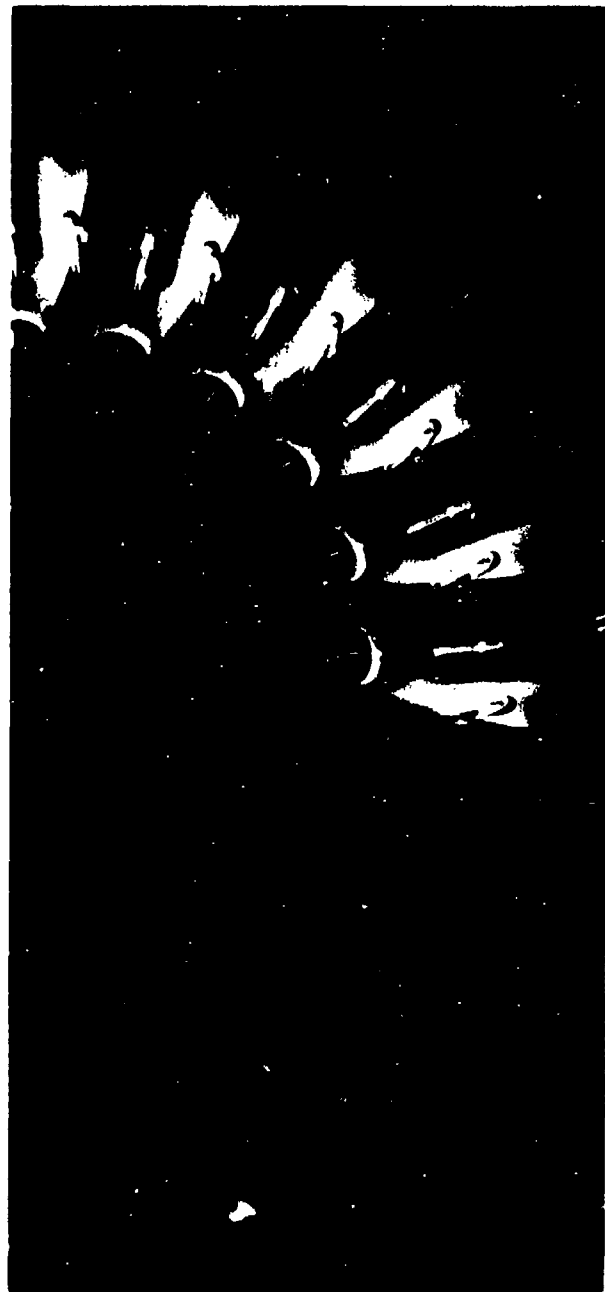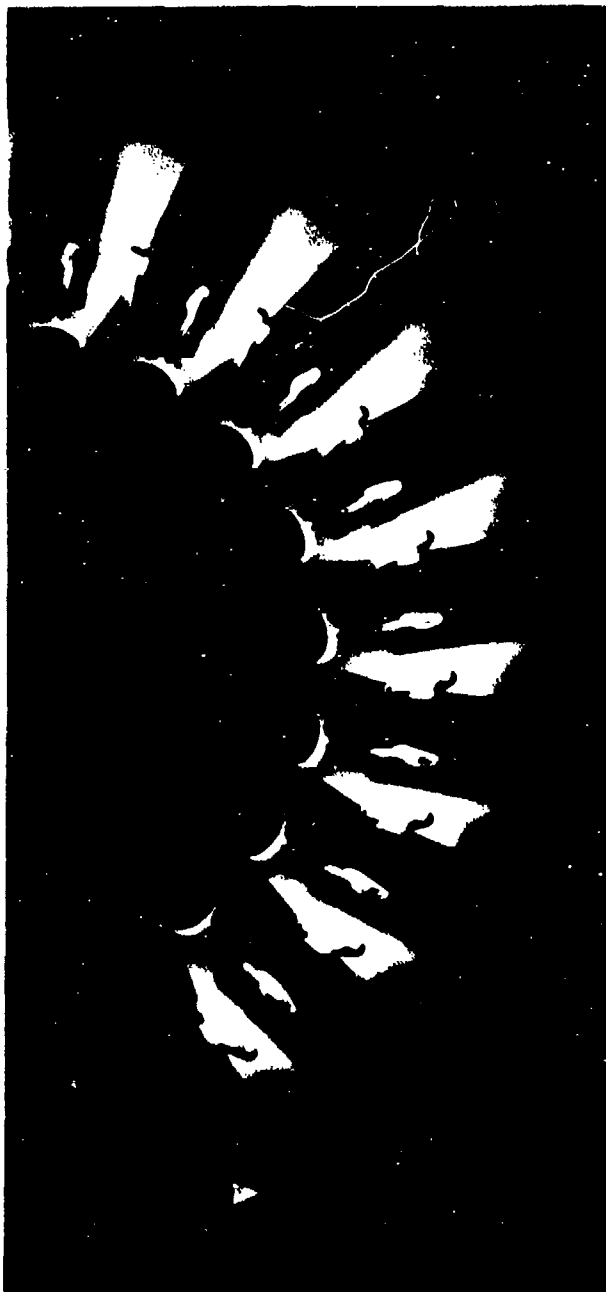
Figure 6.19. Unreproducibility of unstable cavities under similar launching conditions, unvented hemisphere head model, 1.0-atmosphere air pressure.
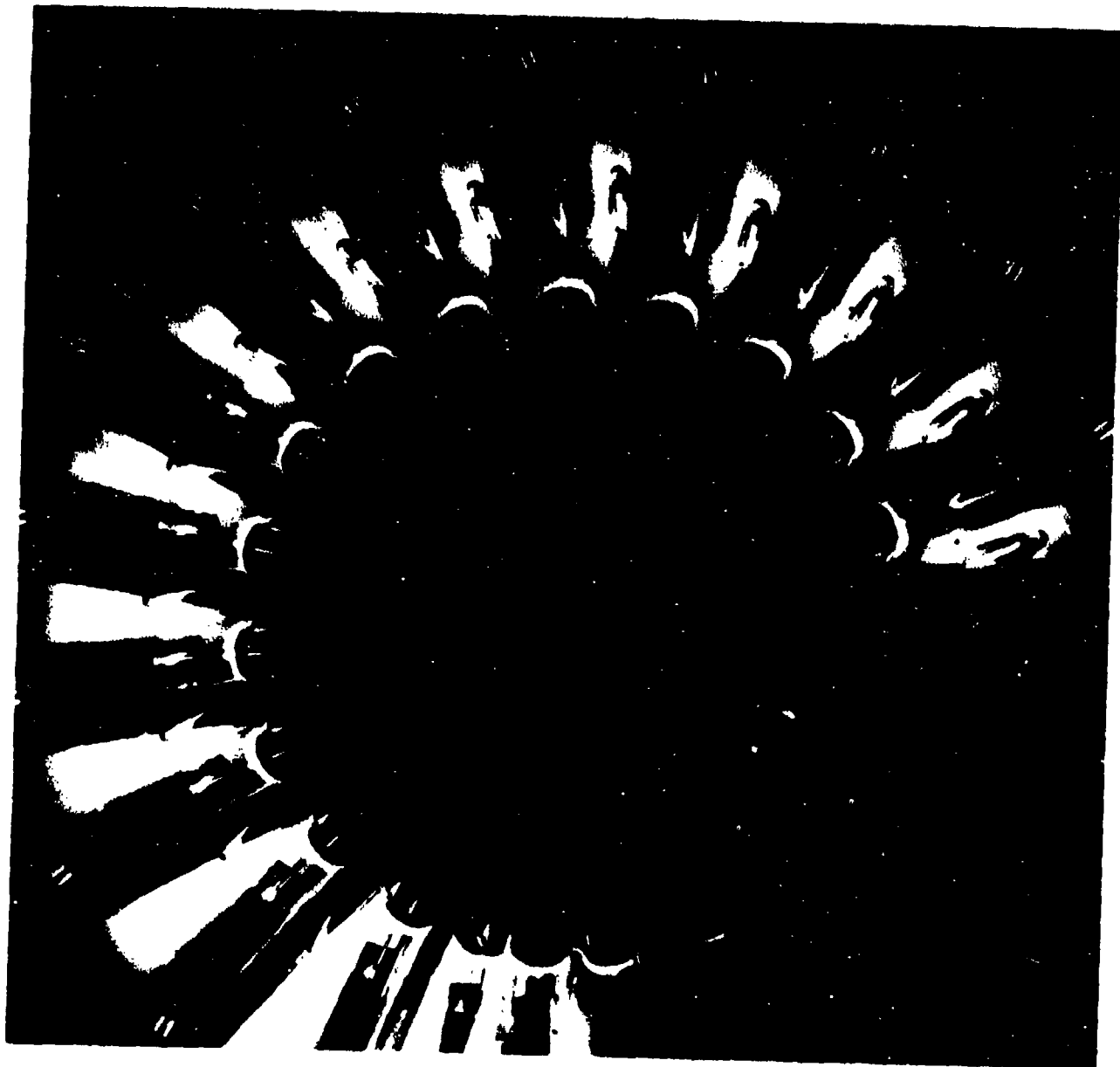
Figure 6.20. Stable, symmetrical cavity, unvented hemisphere head model, 0.1-atmosphere air pressure.

1.0 atmosphere

Figure 6.21a. Stable cavity, fully vented spherical sector, Head H.

110
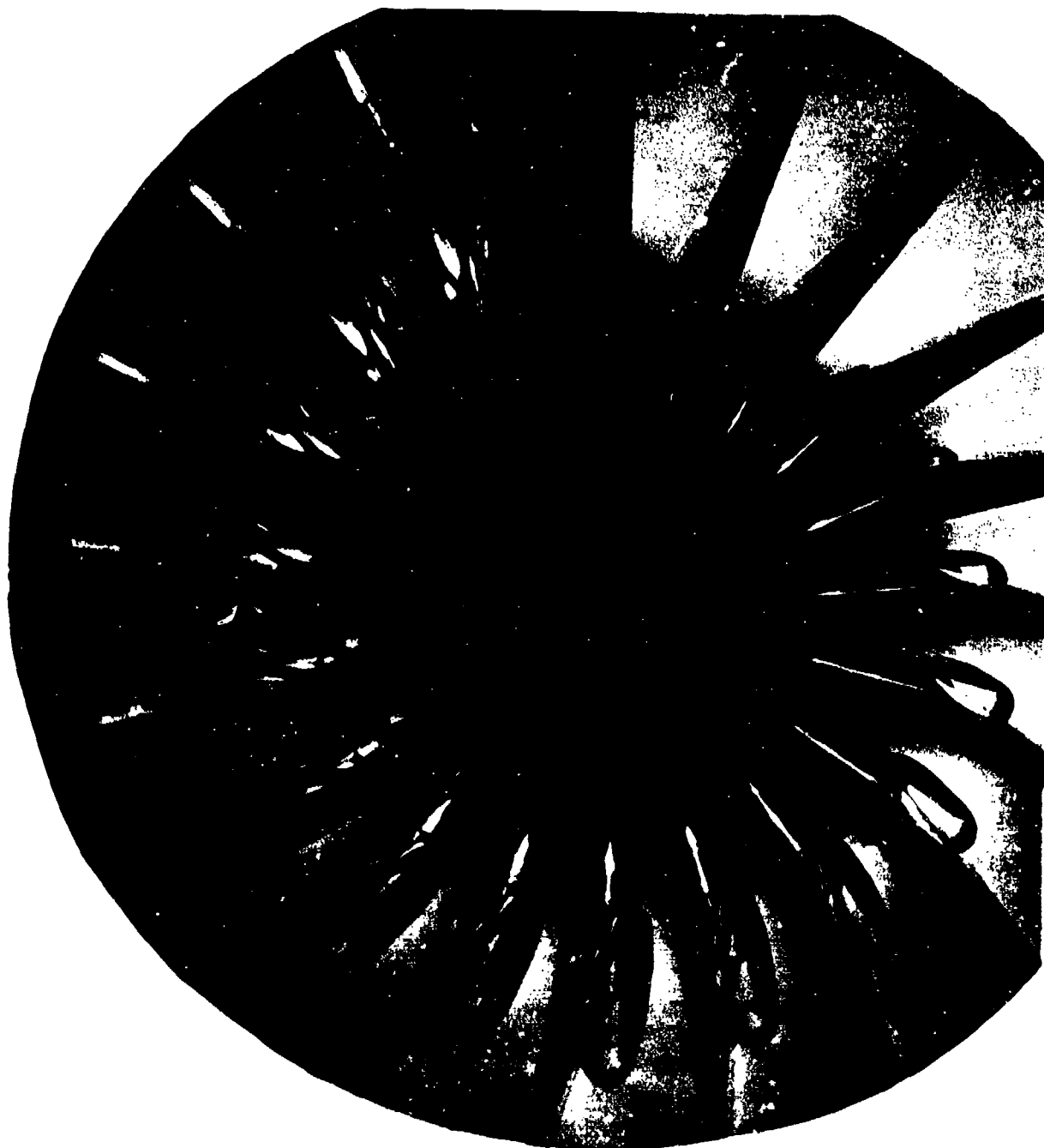
0.1 atmosphere

Figure 6.21b. Stabo-cavity, body-sectioned sphere-reactor Head II.
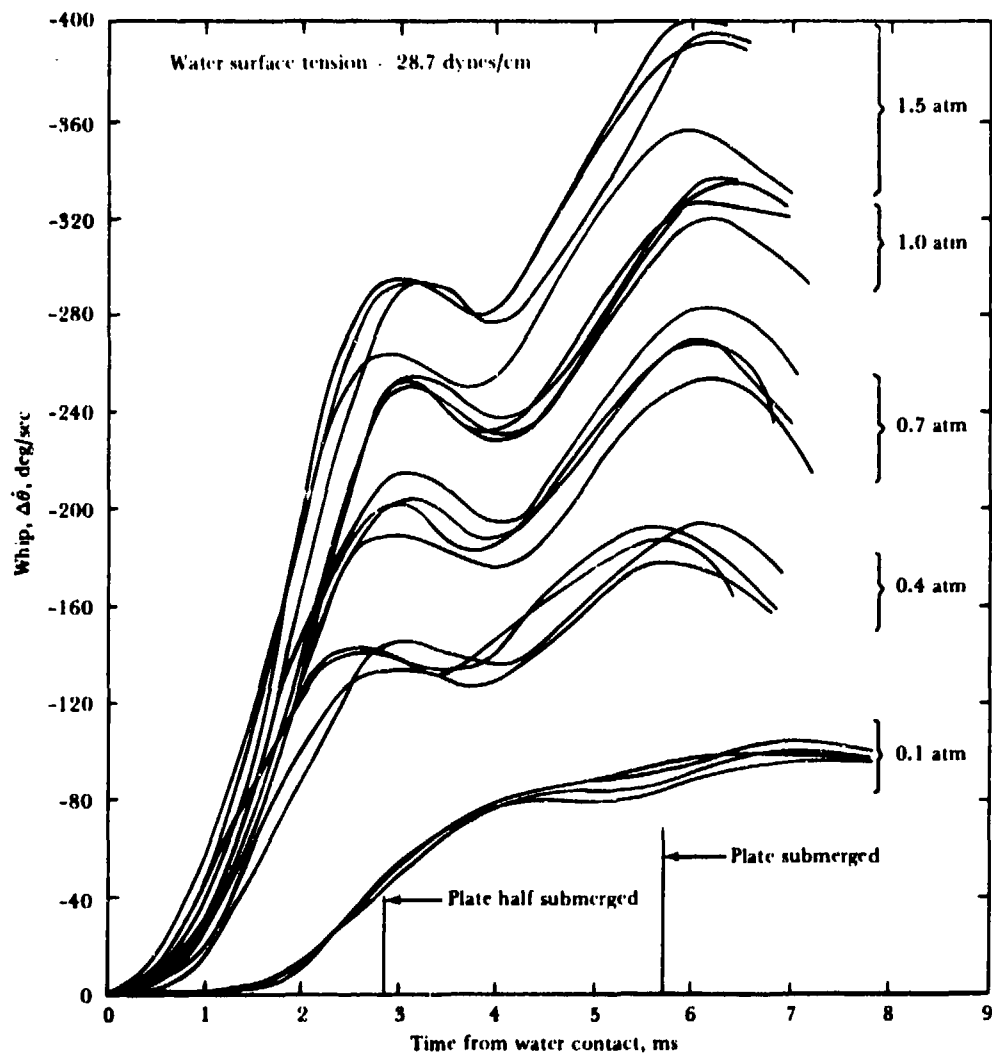
Figure 6.22. Whip versus time, unvented plate cylinder (Head F), at varied air pressures and reduced surface tension.

112

Water-entry theory (Chapter 2) indicates that water-entry pitch behavior may be properly modeled with one-to-one Froude and cavitation number and gas-density scaling. The experimental investigation described in this chapter was designed to test the theory. The oblique water-entry pitch behavior of fully cavitating missiles over approximately one missile length of water penetration was studied (Reference 96).[1] One-to-one Froude scaling alone was not evaluated because earlier tests (Chapter 4) had demonstrated this technique to be inadequate. Its failure was traced, at least in part, to nonmodeling of the pressure distribution in the separation area beneath the missile nose immediately after water impact (underpressure effect, Chapter 6).

Full-scale water-entry pitch data from six of the missiles used in the studies discussed in Chapter 5 (Heads a, d, g, ℓ, m, and n of Figure 5.1) were compared with results from 2-inch-diameter models using one-to-one Froude and cavitation-number scaling. Partial gas density scaling was also investigated.

The 2-inch models were geometrically and dynamically similar to the prototype missiles except that a cylindrical afterbody with a simple tail (Figure 7.1) was used because the studies were to be made, at most, over one missile length of water penetration in which the tail did not contact the cavity wall. All the heads were 3.6 inches long; all the missiles were 12 inches in overall length. The models had movable internal weights that allowed the masses, CG's, and moments of inertia to be adjusted as required by dynamic similarity.

Prototype and model parameters are listed in Table 7.1. The prototypes were launched into fresh water at the NUC Morris Dam Torpedo Range and the models were launched into the NUC Variable-Angle Variable-Pressure Launching Tank. These facilities and their equipment are described in detail in Part V.

Models were launched into fresh water at a nominal water-contact velocity of 119.6 fps and with 1/11 atmosphere air or gas pressure. The nominal trajectory angle at water contact was -20.5 degrees, and the accompanying angles of attack and yaw were so small as to be taken as nominally zero. Water-entry pitch and yaw data were obtained at intervals of 0.8 ms if the change in water-entry pitch was low and 0.4 ms if the change was high. Simultaneous sideview camera data were also obtained, permitting analysis of the missile water-entry pitch, water penetration, and cavity development.

For the plate-cylinder-head model, data could be recorded over only about 4 diameters of water penetration. Different programming of the launching equipment allowed the range of penetration to be extended to 5 or 5 1/2 diameters, but water-contact pitch and pitch-velocity data could not be obtained for these launchings. Since the water-contact conditions were nearly constant for successive launchings, the values obtained previously were used to correct the extended-range launching data. Prototype and model launching conditions are summarized below:

	Prototype	Model
Velocity	400 fps (nom.)	119.6 fps

---

[1] Spatial limitations on the model launching tank precluded modeling the underwater trajectory.

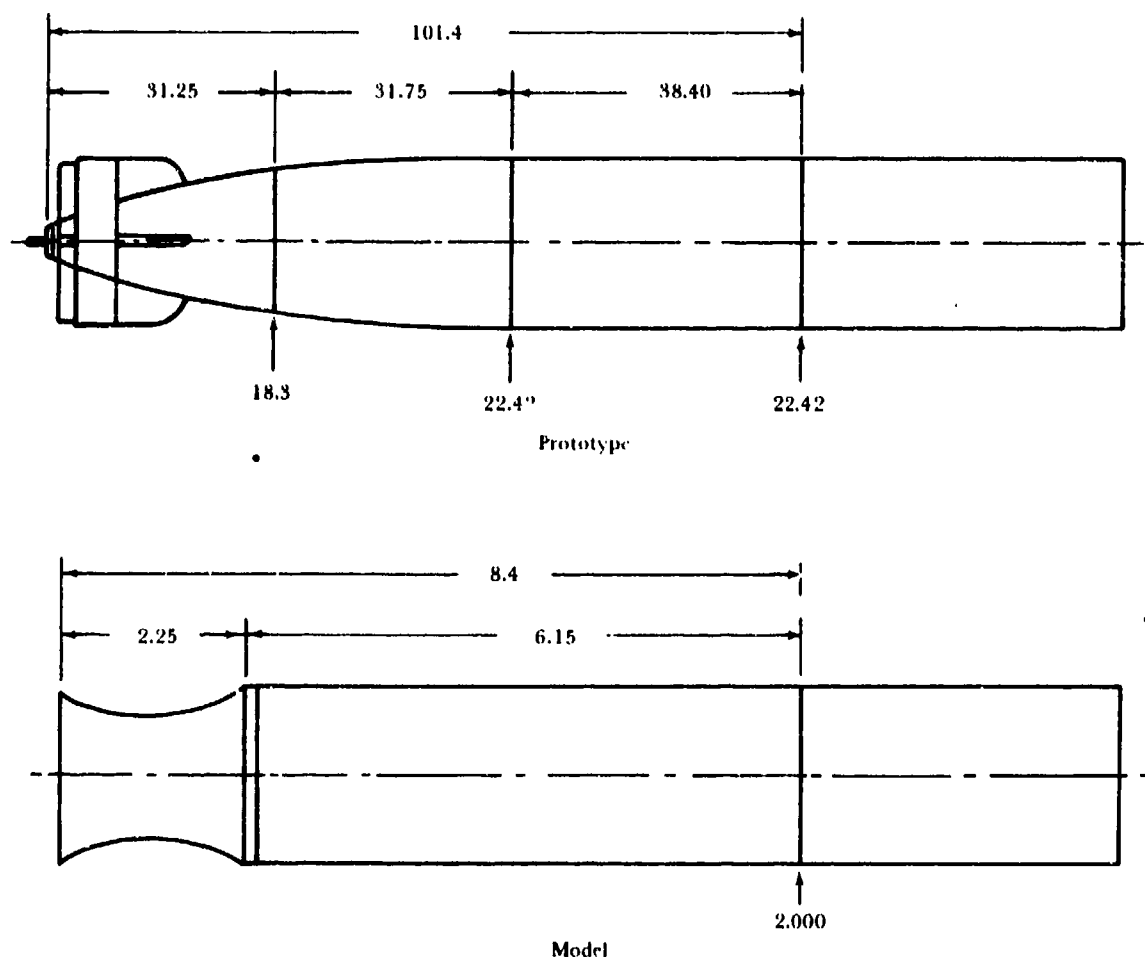Figure 7.1. Experimental configurations with Head n. Dimensions are in inches. (From Reference 96.)

	Prototype	Model
Ambient air pressure	Atmospheric	1/11 atm.
Trajectory angle	-20.5 to -20.9 deg	-20.5 deg
Angle of attack	-1.6 to +1.4 deg	-0.20 to +0.55 deg
Yaw angle	±2.3 deg	±0.5 deg

Table 7.2 gives further data; the angles were defined in Chapter 1 (Figure 1.1). The effect of yaw on the water-entry pitch behavior appears to be small, and this parameter was not considered in the modeling studies.

It was not always possible to scale prototype water-contact velocity and pitch velocity accurately, and corrections for scaling discrepancies were made in order to compare model and prototype data, the corrections being made

for the purpose of assessing the modeling technique and not to overcome the limitations of the equipment. These corrections are derived in Reference 96.

The gas density could not be scaled completely (one to one) because a sufficiently heavy gas was not available; a partial scaling of 0.7 to 0.8 was achieved.

Freon 114B2 (dibromotetrafluoroethane) (Reference 67) with a density nine times greater than that of air under the same conditions of temperature and pressure, was used to achieve partial gas-density scaling. Were it not for the presence of water vapor in the tank, it should be theoretically possible to obtain a gas-density coefficient of 9/11 at 1/11 atmosphere. From Dalton's law of partial pressures, the gas-density coefficient for equilibrium gas-water-vapor mixtures at 1/11 atmosphere in the presence of

114

TABLE 7.1. Prototype and Model Parameters

Parameter	Diameter, in.	Length, in.	Mass, lb.	Distance from Nose to CG, in.	Moment of Inertia about Transverse Axis through CG	Contour Tolerance in. on Radius
Head d, 3.5-diameter ogive (Figure 7.2)						
Prototype	$22.42 \, ^{+0.020}_{-0.010}$	$154 \pm 1/8$	$1,560 \ldots 1,565 \pm 1/2$	$71.1 \pm 1/4$	745 ± 5 slug ft²	0.040
Model						
Required by Froude scaling	2.0000	---	1.108	6.343	19.51 lb in²	---
Actually used	2.0000 ± 0.0002	12.0	1.112 ± 0.005	6.35 ± 0.01	19.64 ± 0.15 lb in²	$+0.000 - 0.001$
Head a, 1.5-diameter ogive (Figure 7.3)						
Prototype	$22.42 \, ^{+0.020}_{-0.010}$	$154 \pm 1/8$	$1,495 \ldots 1,496 \pm 1/2$	$71.1 \pm 1/4$	756 ± 5 slug ft²	0.040
Model						
Required by Froude scaling	2.0000	---	1.061	6.343	19.80 lb in²	---
Actually used	2.0000 ± 0.0002	12.0	1.096 ± 0.005	6.35 ± 0.01	19.99 ± 0.15 lb in²	$+0.000 - 0.001$
Head g, hemisphere (Figure 7.4)						
Prototype	$22.42 \, ^{+0.020}_{-0.010}$	$154 \pm 1/8$	$1,526 \pm 1/2$	$69.5 \pm 1/4$	771 ± 5 slug ft²	0.040
Model						
Required by Froude scaling	2.0000	---	1.083	6.200	20.19 lb in²	---
Actually used	2.0000 ± 0.0002	12.0	1.084 ± 0.005	6.20 ± 0.01	20.12 ± 0.15 lb in²	$+0.000 - 0.001$
Head e plus 0.25-diameter ogive (Figure 7.5)						
Prototype	$22.42 \, ^{+0.020}_{-0.010}$	$154 \pm 1/8$	$1,583 \ldots 1,586 \pm 1/2$	$63.7 \pm 1/4$	743 ± 5 slug ft²	0.040
Model						
Required by Froude scaling	2.0000	---	1.124	5.683	19.46 lb in²	---
Actually used	2.0000 ± 0.0002	12.0	1.130 ± 0.005	5.68 ± 0.01	19.46 ± 0.15 lb in²	$+0.000 - 0.001$

115

TABLE 7.1. Prototype and Model Parameters (continued)

Parameter	Diameter, in.	Length, in.	Mass, lb.	Distance from Nose to CG. in.	Moment of Inertia about Transverse Axis through CG	Contour Tolerance in. on Radius
Head m, plate 0.1-diameter ogive (Figure 7.6)						
Prototype	22.42 +0.020 −0.010	144 ± 1/8	1,544–1,545 ± 1/8	63.7 ± 1/4	694 ± 5 slug ft^2	0.040
Model						
Required by Froude scaling	2.0000	- - -	1.097	5.683	18.18 lb in^2	- - -
Actually used	2.0000 ± 0.0002	12.0	1.103 ± 0.005	5.68 ± 0.01	18.37 ± 0.15 lb in^2	+0.000 − 0.001
Head n, plate cylinder (Figure 7.7)						
Prototype	22.42 +0.020 −0.010	144 ± 1/8	1,551–1,552 ± 1/2	6.37 ± 1/4	694 ± 5 slug ft^2	- - -
Model						
Required by Froude scaling	2.0000	- - -	1.100	5.683	18.18 lb in^2	- - -
Actually used	2.0000 ± 0.0002	12.0	1.109 ± 0.005	5.68 ± 0.01	18.35 ± 0.15 lb in^2	- - -

[a] 1,480 lb for one prototype launching.

116

TABLE 7.2. Launching Conditions, One-to-One Froude and Cavitation-Number Scaling (F, σ Model Data)

Prototype			Model		
Velocity, fps	Trajectory Angle, deg	Angle of Attack, deg	Velocity, fps	Trajectory Angle, deg	Angle of Attack, deg
Head d, 3.5-Diam. Ogive (Fig. 7.2)					
416	-20.6	-1.4	117.5	-20.30	0.42
418	-20.7	-0.3	119.2	-20.30	0.22
416	-20.7	0.7	118.9	-20.30	0.34
419	-20.7	-1.0	120.6	-20.30	0.19
Head a, 1.5-Diam. Ogive (Fig. 7.3)					
446	-20.7	-0.2	120.3	-20.30	0.47
430	20.9	0.2	120.3	-20.30	0.55
425	-20.8	0.8	120.5	-20.30	0.53
430	-20.7	-0.5	121.8	-20.30	0.37
Head g, Hemisphere (Fig. 7.4)					
415	-20.7	-0.2	120.8	-20.30	0.07
411	-20.7	-0.6	120.2	-20.30	0.01
412	-20.6	0.2	119.0	-20.30	0.15
			118.2	-20.30	-0.20
Head ℓ, Plate 0.25-Diam. Ogive (Fig. 7.5)					
430	-20.5	-0.2	119.8	-20.30	0.17
428	-20.6	0.2	120.5	-20.30	0.13
417	-20.7	-0.9	120.6	-20.30	0.16
421	-20.6	0.2	120.9	-20.30	0.07
Head m, Plate 0.1-Diam. Ogive (Fig. 7.6)					
394	-20.9	-0.9	122.4	-20.30	-0.17
398	-20.8	1.4	119.6	-20.30	0.23
398	-20.8	0.9	118.9	-20.30	0.41
			119.3	-20.30	0.33

117

TABLE 7.2. Launching Conditions, One-to-One Froude and Cavitation-Number Scaling (F, σ Model Data) (Continued)

	Protype			Model	
Velocity, fps	Trajectory Angle, deg	Angle of Attack, deg	Velocity, fps	Trajectory Angle, deg	Angle of Attack, deg
Head n, Plate-Cylinder (Fig. 7.7)					
400	-20.8	1.0	117.8	-20.30	-0.04
401	-20.8	0.4	120.6	-20.30	-0.18
403	-20.8	1.4	121.0	-20.30	-0.06
401	-20.8	-1.6	119.7	-20.30	-0.13
			119.6	-20.20	(a)
			120.0	-20.20	(a)
			122.1	-20.20	(a)
			122.4	-20.20	(a)

[a] Angle of attack not known but probably between -0.5 and 0.5 deg.

water is 0.69 at 20°C and 0.79 at 10°C;[2] an appreciable gain in partial scaling could be realized by chilling the water. Therefore, the tank water was chilled to 10°C for the launchings that involved gas-density scaling. Experimental gas-density coefficients differed from the theoretical value because of air leakage and because of difficulties in metering the heavy gas and controlling tank pressure.

Prototype data (Chapter 5) were corrected to a nominal water-contact velocity of 400 fps. Model data involved such small deviations in water-contact velocities that no correction was made from the scaled nominal value (119.6 fps). Both model and prototype water-entry pitch data were corrected to zero water-contact pitch velocity and are shown in Figure 7.2 to 7.7 as the change in pitch after water contact. The model and prototype time scales are in the ratio of $1 : \sqrt{11.2}$. With one-to-one Froude and cavitation-number scaling (F, σ model data), water-entry pitch correlation to within the accuracy of the prototype data was obtained for

five of the six head configurations. For the sixth, the plate 0.1-diameter ogive head (Head m), the model's change in nose-down pitch was about half that of its prototype. A smaller whip is experienced by this head, and consequently the pitch-inducing force, which is the resultant of hydrodynamic and underpressure forces, must be smaller. The hydrodynamic component of the pitch-inducing force on the Head m configuration is also comparatively small and in the same direction as the underpressure force (Chapter 5). This head would thus naturally be more sensitive to non-modeling of the underpressure force because that force contributes a more significant fraction of the total whip.

The dispersion of the model data curves also indicates the sensitivity of Head m, and this conclusion seems to be substantiated further when gas-density scaling is added.

One-to-one Froude and cavitation-number and gas-density scaling (F, σ, ρ model data) was used for three configurations — Heads g, m, and

---

[2]Water-vapor pressures are 17.54 and 9.20 torrs at 20°C and 10°C, respectively.
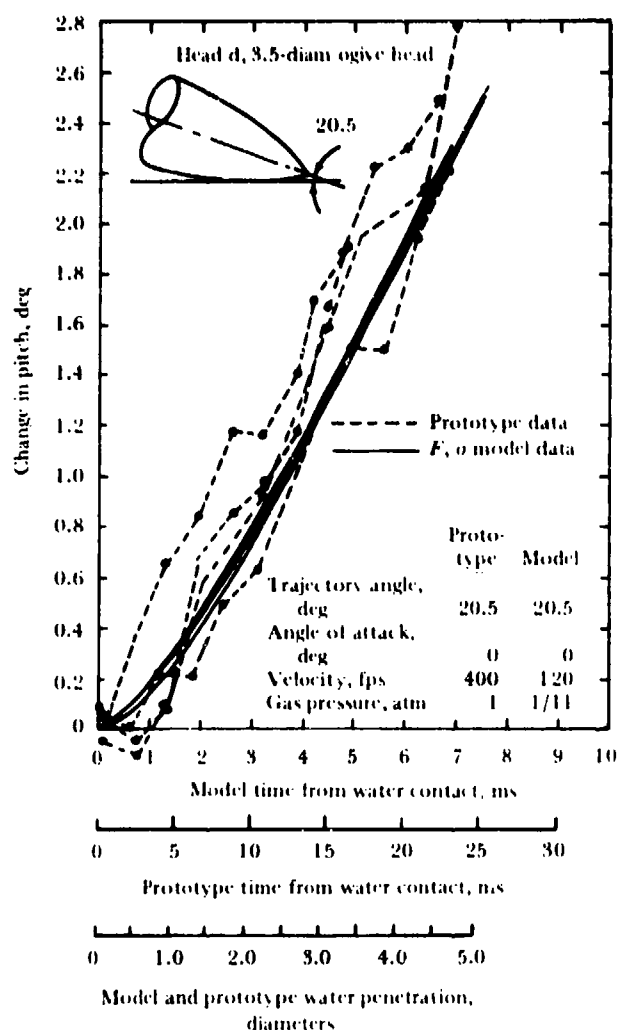
Figure 7.2. Prototype and model water-entry pitch data, Head d. (From Reference 96.)
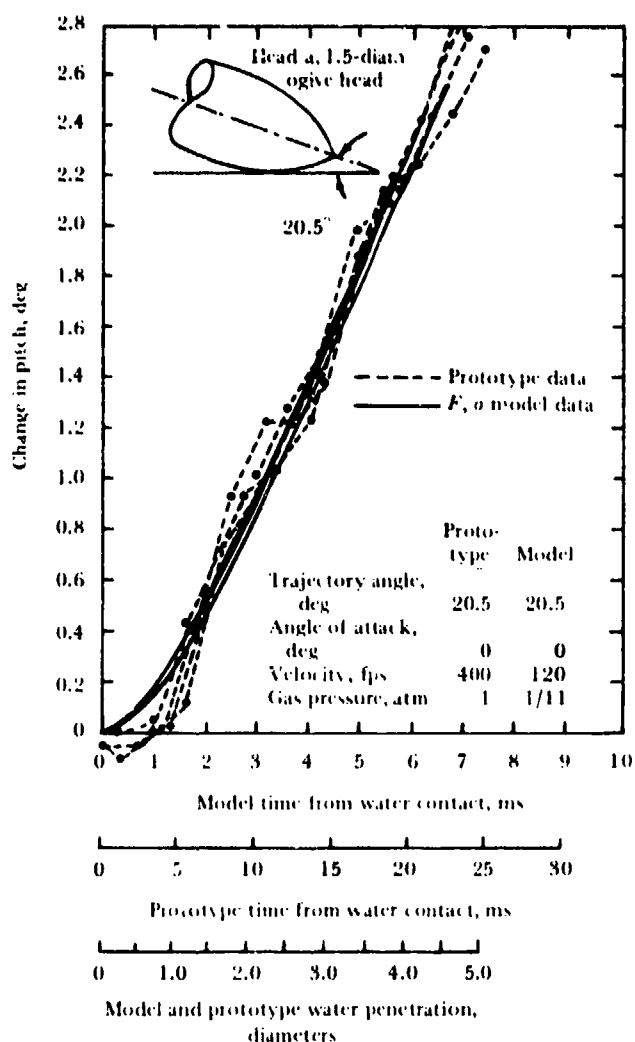
Figure 7.3. Prototype and model water-entry pitch data, Head a. (From Reference 96.)

n (Table 7.3 and dot-dash curves on Figures 7.4, 7.6, and 7.7). Water-entry correlation to within the accuracy of the prototype data was obtained for all heads when 0.7 gas-density scaling was used. It is significant (although expected on the basis of theory) that modeling of the Head m configuration was obtained without any reduction in the correlation obtained for the other two configurations in the absence of gas-density scaling.

The tests indicate that water-entry pitch modeling with one-to-one Froude and cavitation scaling was adequate for the head configurations that showed considerable change in water-entry pitch, but correlation failed when the change

was small unless gas-density scaling was also used.

Model and prototype water penetration was measured, and plotted (in diameters) for comparison with the respective model and prototype time scales. In no case did the penetration data for corresponding scale times deviate more than 7% in a penetration range of about 5 diameters. Missile penetration is indicated in Figures 7.2 to 7.7 by a third scale (the other two being model and prototype times) constructed by plotting the averages of the model and prototype penetration in diameters for corresponding scaled times. The deviation of experimental data from the averaged penetration scale

119
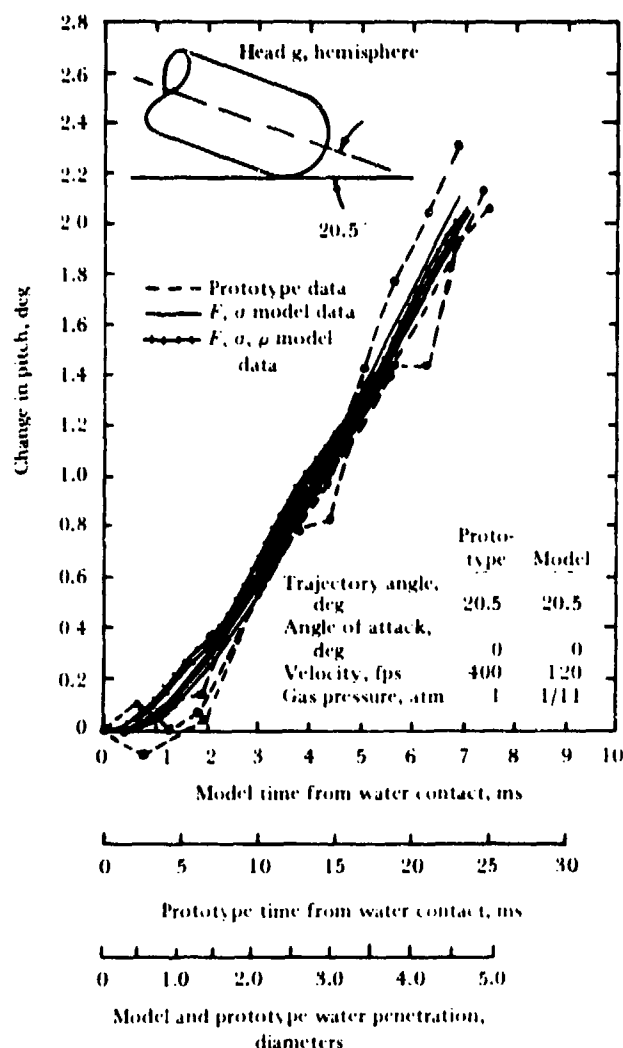
Figure 7.4. Prototype and model water-entry pitch data, Head g. (From Reference 96.)
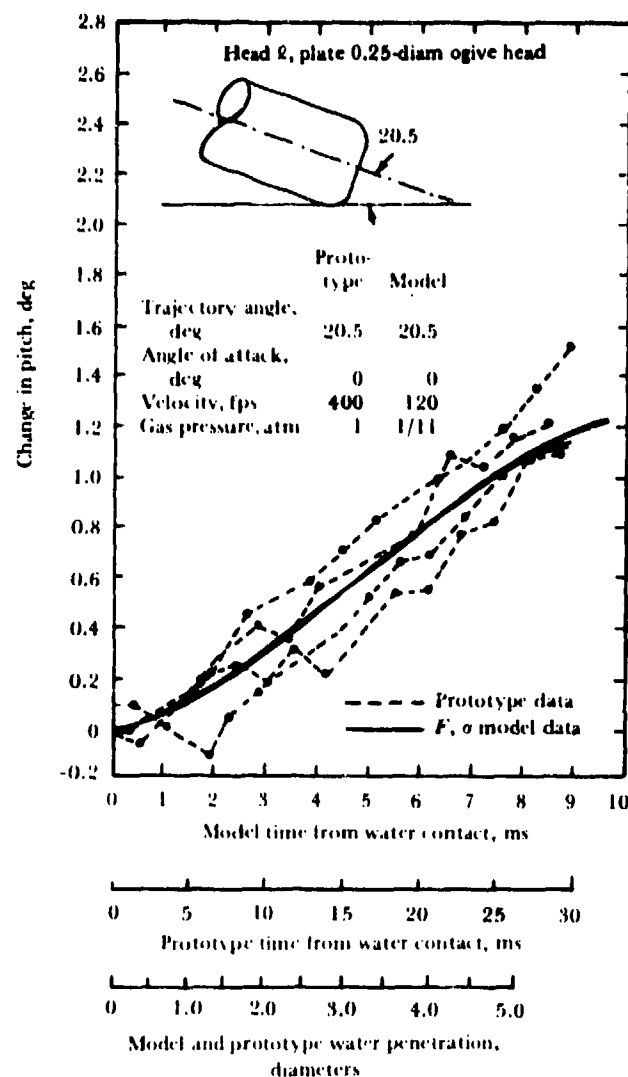
Figure 7.5. Prototype and model water-entry pitch data, Head l. (From Reference 96.)

is, at most, 3.5%. The data for extended-range launchings made with the plate-cylinder head are shown in Figure 7.7 for a range of 4 to about 5.5 diameters of water penetration.

One-to-one Froude and cavitation-number and gas-density scaling models some of the initial boundary conditions that are necessary in order that the subsequent underwater trajectory can be modeled; other studies (Chapters 8 and 9) indicate that this technique models water-entry cavities for at least 20 diameters of underwater flight. Thus, this scaling technique simultaneously models the water-entry and underwater trajectory of a cavity-running missile.

It is of interest to compare the change in model pitch resulting from the addition of gas-density scaling. With Head m, pitch correlation did not occur without gas density scaling. Head n's pitch change became slightly more negative but still lay within the scatter of the prototype data; that of Head g was little altered except for becoming slightly more positive during the first diameter of underwater travel.

The exact mechanism by which gas density alters pitch is unknown beyond the fact that change in gas density probably affects the undercavity separation. Extrapolation of cavity studies (Chapter 9) suggests that the undercavity
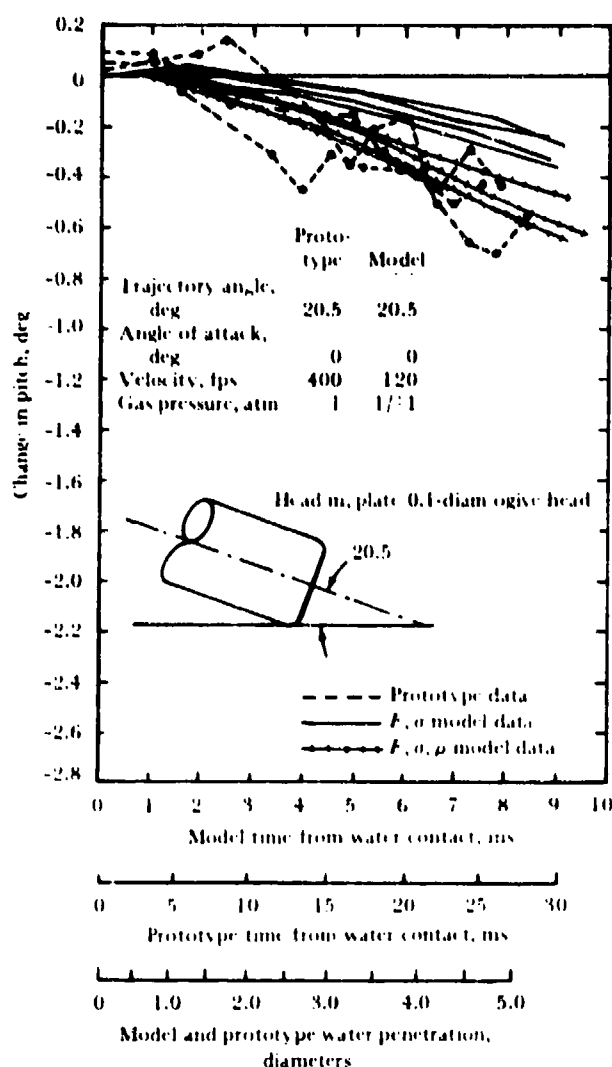
Figure 7.6. Prototype and model water-entry pitch data, Head m. (From Reference 96.)

Figure 7.7. Prototype and model water-entry pitch data, Head n. (From Reference 96.)

might close earlier, be smaller, or last longer, but those suppositions cannot be verified because the cavity photographs taken simultaneously with the pitch records lack sufficient detail.

Three launchings were made with the 0.1-diameter plate ogive (Head m) missile to investigate the effect of decreasing the gas density in the model system. An atmosphere of helium (density approximately one seventh that of air) was substituted for air. An ambient

pressure of 0.1 atmosphere was maintained during all launchings. The pitch change of the model in the helium atmosphere was just perceptibly more positive than that of the model in air; the change in the gas density coefficient ($\rho' = 0.1$ to $\rho' = 0.014$) was insignificant. However, the pitch data from the helium launchings showed more scatter, suggesting that the undercavity was less stable in helium. The relationship between pitch change and undercavity formation warrants further investigation.

TABLE 7.3. Model Launching Conditions,
One-to-One Froude and Cavitation-
Number and Gas-Density Scaling
(F, σ, ρ Model Data)[a]

Velocity, fps	Trajectory Angle, deg	Angle of Attack, deg	Gas-Density Ratio
Head g, Hemisphere (Fig. 7.4)			
119.8	-20.30	-0.33	0.75
119.8	-20.30	-0.41	0.76
119.9	-20.30	-0.49	0.68
122.9	-20.30	-0.40	0.65
Head m, Plate 0.1-Diam. Ogive (Fig. 7.6)			
122.2	-20.30	-0.62	0.59
121.9	-20.30	-0.67	0.80
122.1	-20.30	-0.62	0.84
121.7	-20.30	-0.80	0.82
Head n, Plate-Cylinder (Fig. 7.7)			
120.8	-20.30	-0.82	0.71
120.3	-20.30	-0.80	0.82
120.9	-20.30	-0.90	0.80
119.6	-20.30	-0.83	0.82

[a]Prototype data are in Table 7.2

UNDERWATER TRAJECTORY MODELING

Water-entry pitch modeling, discussed in the previous chapter, proved feasible, automatically satisfying the initial conditions for modeling the subsequent missile underwater trajectory. It thus becomes necessary to determine to what extent additional conditions such as cavity behavior and the character of the flow (laminar or turbulent) affect model behavior. It is evident that the model must be completely geometrically scaled if the missile underwater trajectory is to be modeled.

The experimental program detailed in this chapter was specifically planned to test the effect of one-to-one Froude scaling in conjunction with varying prototype velocity, cavitation number, boundary-layer condition, and water surface tension in water-entry modeling (Reference 110). Less attention was paid to the details of water-entry behavior and more emphasis was placed on the underwater trajectory and phenomena related to it. Launching conditions and missile shape were selected to include regions where modeling failures might be expected (References 36, 37, and 38), and the range of entry attack angles was wider than any that had been used before.

Gas-density scaling was not included. Its importance was not known at the time, and the large volume of the CIT Controlled-Atmosphere Launching Tank, in which model water-entry and underwater trajectory tests were conducted, would have made such scaling difficult.

Head f, the 3.5-diameter 70-degree spherogive shown in Figure 5.1, was chosen for this study because it had a fine nose shape that was known to be extremely sensitive to variation in entry condition. As discussed in Chapter 5, water-tunnel tests indicated that cavity separation might occur either on the spherical portion or on the ogive, tending to make this shape

sensitive to small secondary forces. Prototype and model missiles are shown in Figure 8.1 and their physical properties listed in Table 8.1. The model was scaled in accordance with the Froude law to be dynamically and geometrically similar to the prototype.

The prototype was launched from the NUC Variable-Angle Launcher at nominal entry velocities of 200 and 400 fps. The model was launched in the CIT Controlled-Atmosphere Launching Tank at velocities of 60 and 120 fps, corresponding to Froude scaling of the prototype, and at 60 fps (scaled) and 80 fps (non-scaled) in the NUC Variable-Angle Variable-Pressure Launching Tank. All tests were made with a nominal air trajectory angle of 22 degrees. The angle of attack of the prototype at water entry varied between 0 and +6 degrees (nose up with respect to the trajectory); the angle of attack of the model varied between -3 (nose down) and +6 degrees (nose up). All prototype tests were made at full atmospheric pressure; the model tests were made at air pressures of 1, 1/11, and 1/21 atmosphere. For several of the launchings, the nose of the model was artificially roughened with grains of sand. Five launchings were made in the smaller VAVP launching tank, with the surface tension reduced to 40 dynes/cm. Entry conditions of the individual launchings are shown in Tables 8.2, 8.3, and 8.4.

Initial tests demonstrated the significance of boundary-layer flow on water-entry behavior, a factor previously hoped to be negligible since only a small portion of the missile surface is wetted during the cavity phase of the trajectory. It was found that Froude and cavitation-number modeling did not result in correlation without a turbulent boundary layer. Both the Reynolds number and the roughness were sufficient to

2-inch-diameter model
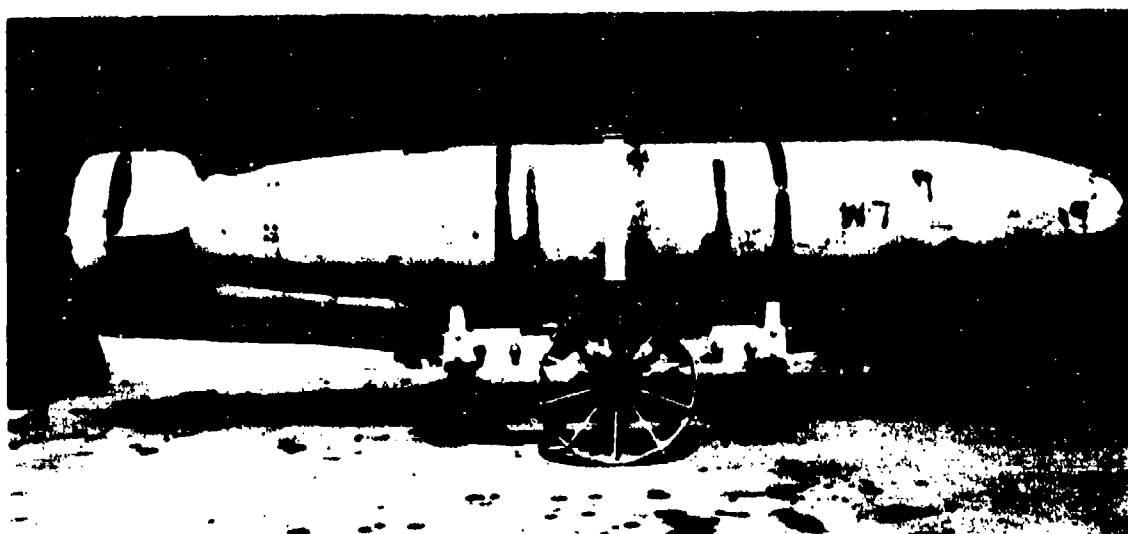
22.42-inch-diameter prototype
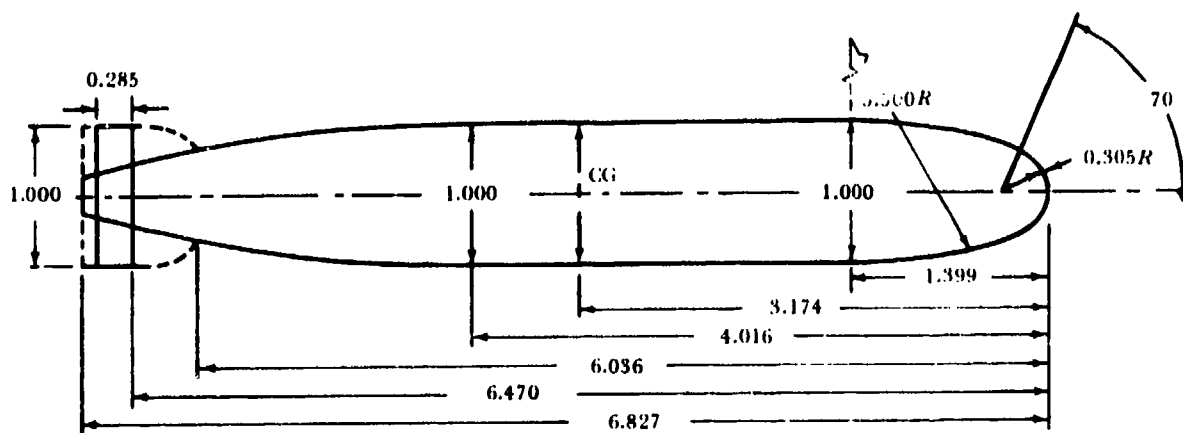
Dimensions in diameters

Figure 8.1. Model and prototype with a 3.5-inch-diameter, 70-degree spherogive nose.

TABLE 8.1. Model an' .otype Dimensions

Parameter	Prototype [a]	Model Required by Froude Scaling	Model Actually Used
Diameter, in.	22.42 +0.020 -0.010	2.000	2.001 ±0.0002
Length, in.	152-1/8 ±1/8	13.654	13.645 ±0.005
Weight, lb	,-t .veen 1640 .md 1675 ±1/2	1.186	1.190 ±0.005
Distance from CG to nose tip, in.	between 71 and 73-1/8 ±1/4	6.522	6.514 ±0.02
Moment of inertia about transverse axis through CG	between 770.9 and 798.1 ±5 slug ft^2	0.1436 lb ft^2	0.1436 ±0.001 lb ft^2
Contour Tolerance, in. on radius	±0.040	- - - - - -	±0.001
Surface roughness, μ in.	40 - 60	- - - - - -	12

[a] Internal mechanism not the same fo. all prototype launchings; weight, CG location, and moment of inertia therefore varied slightly.

insure a turbulent boundary layer on the proto-type, but the model surface was smooth and the Reynolds number relatively low, the transition from laminar to turbulent boundary layer occurring at some velocity between 60 and 120 fps, probably above 80 fps. Consequently, a turbulent boundary layer was induced artificially for the 60-fps launching velocity by roughening the surface of the model nose with grains of sand cemented to it. The degree of surface roughness cannot be scaled from that of the prototype because boundary-layer thickness is a function of Reynolds number and cannot be scaled as an ordinary linear dimension of a Froude scaled system. The sand-grain diameter

required (0.030 ± 0.002 inch) was estimated from the relationship (Reference 74, page 40):

$$\frac{\delta}{\ell} = 0.37\left(\frac{v\ell}{\nu}\right)^{-1/5} = 0.37 \, (R_\ell)^{-1/5} \qquad (8.1)$$

where for a smooth, flat plate at zero incidence, δ is the boundary-layer thickness in turbulent flow, ℓ is the length of the plate, and R_ℓ is the Reynolds number related to the length of the plate.

Equal Froude and cavitation-number scaling produced valid correlation when a turbulent boundary layer was artificially induced; the

125

<table>
<tbody>
<tr><td>

TABLE 8.2. Prototype Launchings, Variable-Angle Launcher [a]

Air Trajectory Angle, deg	Entry Pitch Angle, deg	Entry Velocity, fps
20.2	-0.7	414
23.0	+1.1	200(nom)
22.8	+1.0	193
22.5	-0.3	197
20.0	-0.1	200(nom)
20.0	+0.1	195
22.5	+0.8	201
22.2	+0.4	202
22.2	+2.1	200
22.2	+1.7	202
22.1	+2.2	207
22.2	+1.6	209
21.6	+1.9	213
21.5	+0.3	206
22.6	+2.8	204
22.7	+2.7	198
23.7	+2.5	183
23.7	+2.4	198
23.5	+5.8	189
23.3	+3.0	187
23.2	+2.7	214
20.0	+5.9	194

[a] Angles measured to ± 1 deg, velocity measured to ± 5 fps

</td><td>

TABLE 8.3. Model Launchings, Variable-Angle Variable-Pressure Launching Tank [a]

Entry Velocity, fps ±1/2 fps	Air Pressure, atm	Roughness, Type (Figure 8.3)	Surface Tension, dynes/cm
80.8	1/11	B	76
81.2	1/11	..	76
81.4	1	..	76
61.4	1	..	76
61.2	1/11	..	76
61.4	1/11	B	76
61.8	1	B	76
80.8	1	B	76
60 (nom)	1/11	..	76
61.2	1/11	..	76
61.7	1	..	76
61.4	1	B	76
61.7	1	B	76
61.4	1	B	76
81.0	1	B	76
81.2	1	B	76
81.7	1	B	76
81.0	1/11	..	76
80.7	1	..	76
81.0	1/11	B	76
81.3	1/11	B	76
61.2	1/11	B	76
61.4	1/11	B	76
61.5	1	B	39.8
60 (nom)	1	B	39.8
62.4	1	B	41.8
62.1	1	B	39.2
61.7	1/11	B	40.1

[a] Nominal entry angles: 30-deg air trajectory, -0.5-deg entry pitch. Actual entry angles, ±0.5 deg of nominal angles.

</td></tr>
</tbody>
</table>

smooth model did not reproduce prototype behavior. When the entry velocity of the model was increased until a turbulent boundary layer occurred naturally, the presence of the roughness made no difference in model behavior; the model with and without roughness reproduced the prototype trajectory.

126

TABLE 8.4. Model Launchings, Controlled Atmosphere Launching Tank

Air Trajectory Angle, deg	Entry Angle of Attack, deg	Tolerances on Angles, deg	Entry Velocity, fps ±½ fps	Entry Pitch Velocity, deg/sec	Air Pressure, atm	Roughness, Type (Figure 8.3)
23.3	+2.2	1	59.3	...	1	..
22.4	+1.3	1	61.3	-5	1/11	..
22.7	+0.2	1	60.3	-5 to -10	1/11	..
22.4	+0.2	1	60.4	+10	1/11	..
23.1	+0.4	1	59.6	+20	1/11	..
22.3	-2.4	1	60.0	-10	1/11	..
22.6	-1.0	1	60.5	-10	1/11	..
22.4	+0.2	1	61.0	+15	1/11	..
22.2	+1.4	1	60.6	+10	1/11	..
22.5	-12.5	1	60.6	+25	1/11	..
22.3	+2.1	1	60.2	0	1/11	..
21.4	+3.5	1	61.1	+10	1/11	..
21.3	+4.2	1	60.6	-10	1/11	..
21.2	+4.2	1/2	60.1	-5	1/11	..
21.3	+5.0	1/4	60.1	0	1/11	..
20.8	+1.0	1/2	60.6	0	1/21	..
20.8	+1.1	1/2	60.9	+10	1/21	..
21.3	+5.4	1/4	60.3	-5	1	..
20.6	+4.4	1/4	60.6	-10 to -15	1	..
20.6	+2.6	1/4	60.0	0	1	..
20.6	+0.8	1/2	60.6	0	1	..
21.1	+2.1	1	60 (nom)	...	1/11	A
20.9	+1.9	1/2	60.1	0	1/11	A
21.0	+1.2	1/4	60.8	+5	1/11	B
22 (nom)	+1.5 (approx)	...	60 (nom)	...	1/11	B
20.8	+1.6	1/2	59.9	+10	1/11	B
20.0	0.0	1/4	120.2	-10	1/11	..
19.9	-0.3	1/4	120.0	-10 to -15	1/11	..
17.7	-2.9	1/4	122.4	-25	1/11	..
21.0	+1.5	1/2	60.0	-10	1/11	B

127

TABLE 8.4. Model Launchings, Controlled Atmosphere Launching Tank (continued)

Air Trajectory Angle, deg	Entry Angle of Attack, deg	Tolerances on Angles, deg	Entry Velocity, fps ±½ fps	Entry Pitch Velocity, deg/sec	Air Pressure, atm	Roughness, Type (Figure 8.3)
21.0	+1.6	1/2	60.4	-10	1/11	B
21.2	+5.4	1/2	60.2	-10	1/11	B
21.2	-0.5	1/2	120.5	. . .	1/11	B
21.1	-1.0	1	120.0	-30	1/11	B
21.6	+6.2	1/4	60.7	-5	1/11	B
21.3	-0.2	1/2	119.8	-10	1/11	B
21.5	-0.4	1/4	121.0	-5	1/11	..
21.5	-0.6	1/2	120.6	-10	1/11	..
21.6	+1.9	1/4	60.2	+5	1/11	C
21.5	+5.4	1/2	60.3	-15	1/11	D
21.1	+5.2	1/2	60.1	-10	1	D
21.3	+5.2	1/4	60.2	-25	1/11	E
19.0	-1.0	1	60.8	-15	1	B
19.9	+0.1	1	60.2	-20	1	B
19.0	-0.9	1	60.2	-15	1	B
19.1	-1.0	1	60.8	-15	1	B
20.1	-0.2	1/2	120.5	-15	1	B
20.2	-0.1	1/2	121.0	-20	1	B
20.0	-0.1	1/2	120.9	. . .	1	B

Because of the uncertainties associated with causing a turbulent boundary layer artificially, it is preferable to conduct modeling experiments at entry velocities that will cause the turbulent boundary layer to occur naturally.

Entry velocities: 200 fps (prototype) and 60 fps (model). Figure 8.2 compares the trajectories of the smooth model at air pressures of 1, 1/11, and 1/21 atmosphere with the prototype trajectories during launchings having approximately the same entry pitch angles. Although the model trajectories occurring at 1/11 atmosphere (equal cavitation number in model and prototype systems) are in best agreement with those of the prototype, the model ceases to approximate the behavior of the prototype after 35 diameters of underwater travel. Furthermore, the prototype trajectories are concave upward; the model trajectories are convex.

The effect on trajectory of artificially inducing a turbulent boundary layer was investigated by roughening the model noses in several different ways (Figure 8.3). Figure 8.4 compares several prototype trajectories with those of 1/11-atmosphere models having variously roughened noses; entry angles of attack were comparable in the range from -0.3 to +2.8 degrees. Roughness A did not alter the model trajectory appreciably. The increased area

128
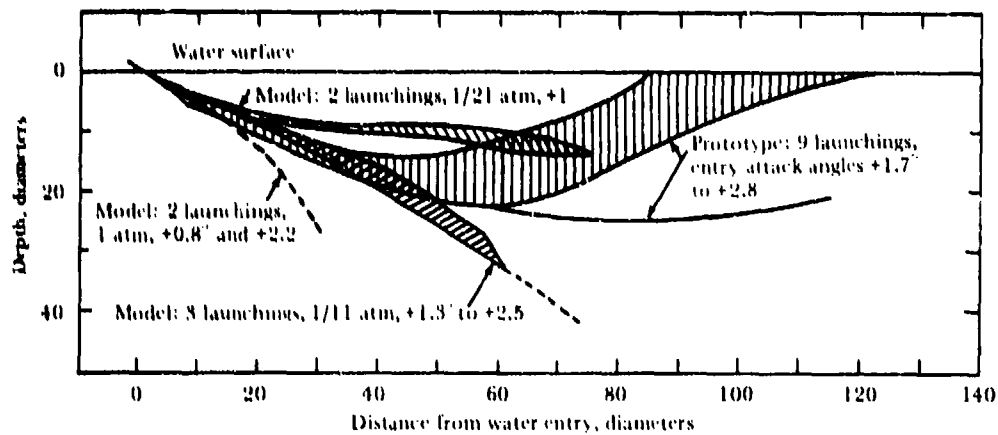
Figure 8.2. Underwater trajectories. Entry velocities 60 fps for Froude-scaled smooth-nosed model, 200 fps for prototype.

Type A   Type A   Type B

A. Circular cap of sand on spherical tip

B. Larger circular cap of sand on spherical tip

C. Two rings of sand on ogive

D. Three rings of sand on ogive

E. Three rings of sand plus band of grains placed at random on ogive

Type C, D and E
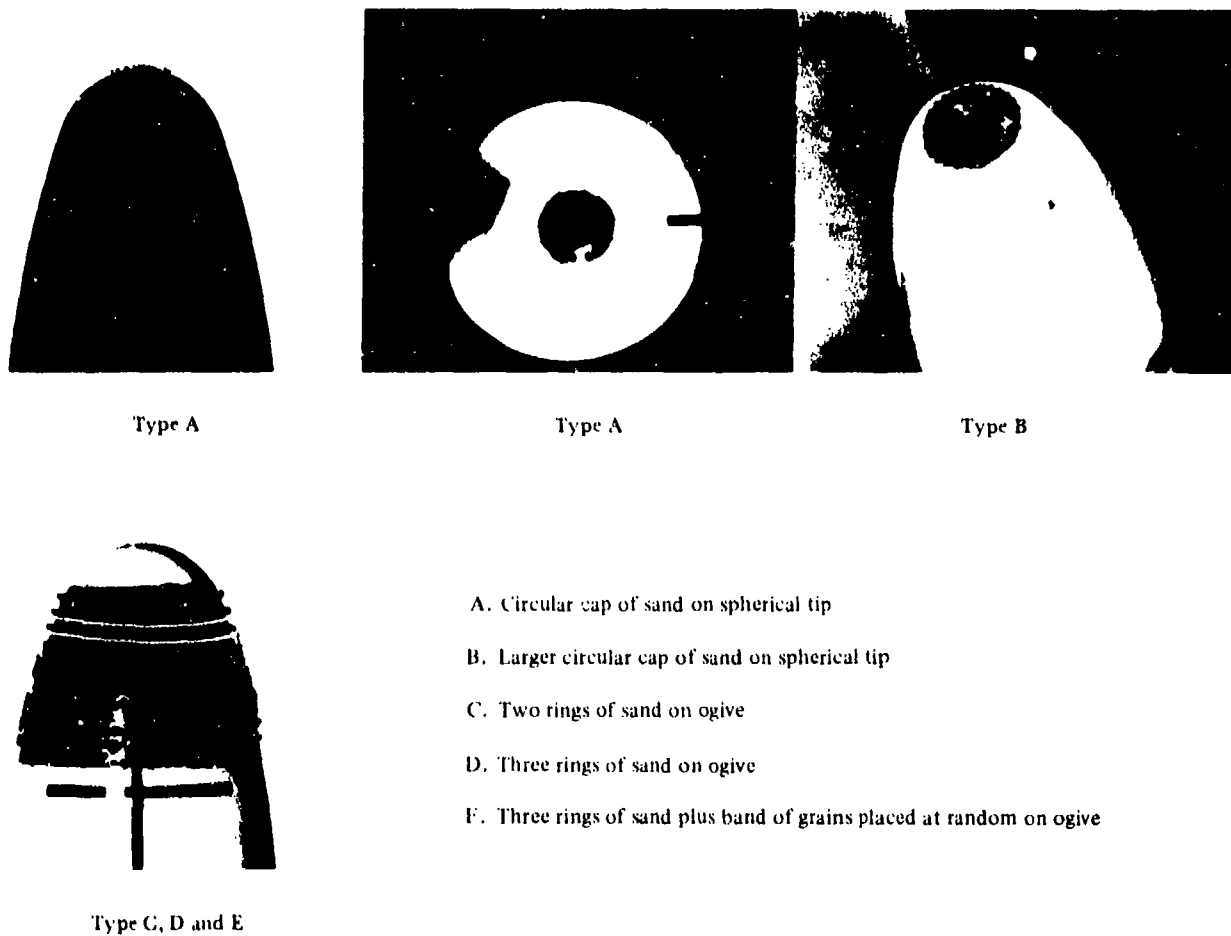
Figure 8.3. Location of roughness (0.030-inch-diameter regularly spaced grains of sand) applied to model nose.

129

Roughness types A and C
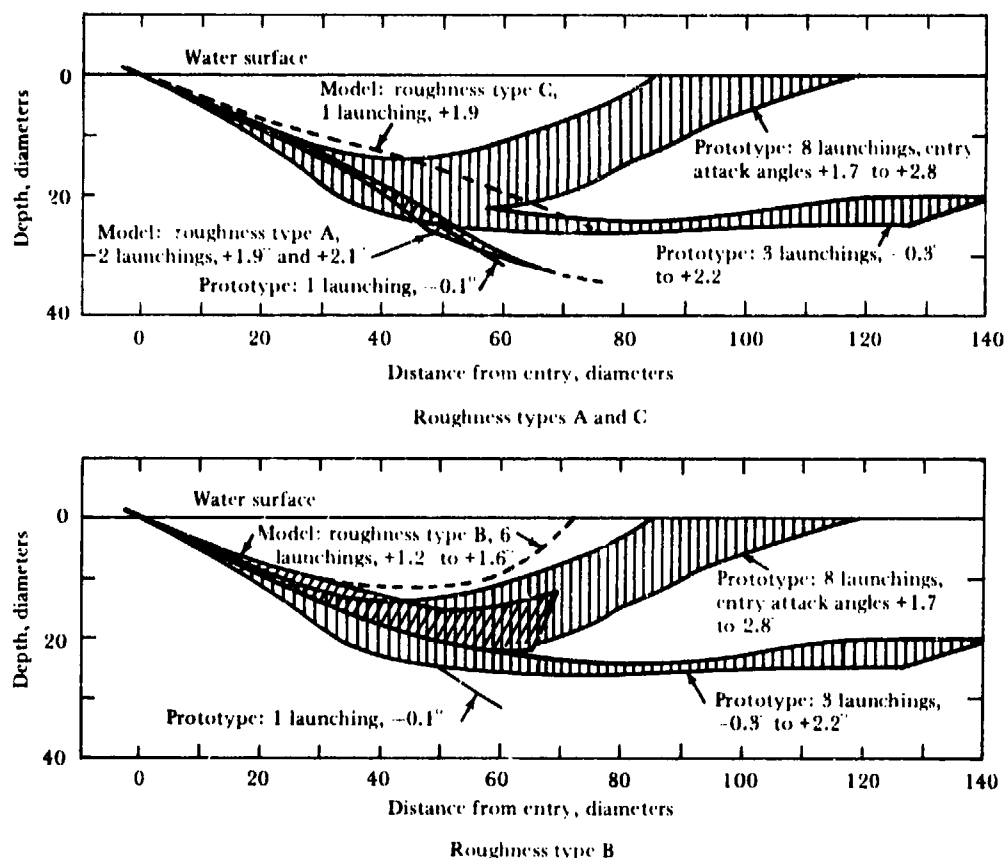
Roughness type B

Figure 8.4. Underwater trajectories. Entry velocities 60 fps for Froude-scaled roughened model, 200 fps for prototype.

of roughness B resulted in model trajectories that curved slightly upward, and, within the accuracy of the prototype data, reproduced the prototype trajectory. Roughness C did not permit valid modeling. Data on roughnesses D and E were not obtained in this range.

Although no large differences occurred in the cavities of the smooth model and in those of the models with various roughnesses, detailed photographs of the cavities show that the bottom of the cavity made by the smooth model was scalloped and the cavity of the roughened (type B) model was not (Figure 8.5). The scalloping was probably caused by an irregular fluctuating separation of the flow from the bottom of the model; failure to model flow separation could cause the observed discrepancy between the prototype and the smooth model in the Froude- and cavitation-number-scaled system. The scalloping almost disappeared when the velocity of the smooth model was increased

to 80 fps (Figure 8.6). Roughnesses A and B did not affect the drag as long as the model remained in the cavity. Roughnesses C, D, and E increased the drag (Figure 8.7). Thus, the roughness that produced valid modeling (type B) and the roughness that failed to perturb the trajectory of the smooth model (type A) did not alter the drag of the model.

When the entry attack angles were increased to +5.2 to +6.2 degrees, the model trajectories curved downward, the types B- and D-roughened models deviating from the prototype trajectory after 40 diameters of underwater travel and the type E-roughened model deviating after 60 diameters (Figure 8.8).

The failure of the roughened model to reproduce the prototype trajectories having large nose-up entry pitches may be attributed to several factors. First, it was necessary to induce a nose-up pitch velocity of about 50 deg/sec during the prototype airflight in order to obtain

130

Smooth model

Model with type B roughness

Figure 8.5. Cavities of smooth and roughened models compared 47 ms after
water entry. Entry velocity 60 fps, air pressure 1/11 atmosphere.

the flat entry attack angles, but the model had a nose-down pitch velocity of 10 to 21 deg/sec. The behavior of this sensitive nose shape is likely to be affected by that amount of difference in entry pitch velocity.

Second, it is difficult to induce a turbulent layer artificially without significantly altering some other aspect of the flow about the missile. When the entry angle of attack was so flat that the ogival portion of the nose entered the water before the spherical tip, satisfactory correlation could not be induced with either roughness on the tip or roughness on the ogive. Sand on the nose tip apparently failed to trigger a turbulent boundary layer, and sand on the ogive increased the drag, thereby decreasing the model velocity more rapidly. The lower velocity caused the boundary layer flow to revert to laminar flow earlier in the trajectory and also produced a steeper trajectory, probably because of the

greater influence of nose underpressure at reduced velocity.

Third, at the greater nose-up angles of attack, where separation occurs on the ogive, the separation angle is small, making this region particularly sensitive to scaling parameters. It is possible that the correlation failure was caused by improper cavity-separation modeling due to non-scaling of gas density.

The pitch of the torpedo with respect to the horizontal was recorded as a function of time during several of the prototype launchings. The only comparable model launching (1/11-atmosphere air pressure, type B roughness) was compared to the prototype results. The model reproduced the orientation of the prototype as well as its path (Figure 8.9).

Several tests were made with the type B roughened-nose model at full atmospheric pressure and 0-degree entry attack angle to see

131

Smooth model

Model with type B roughness
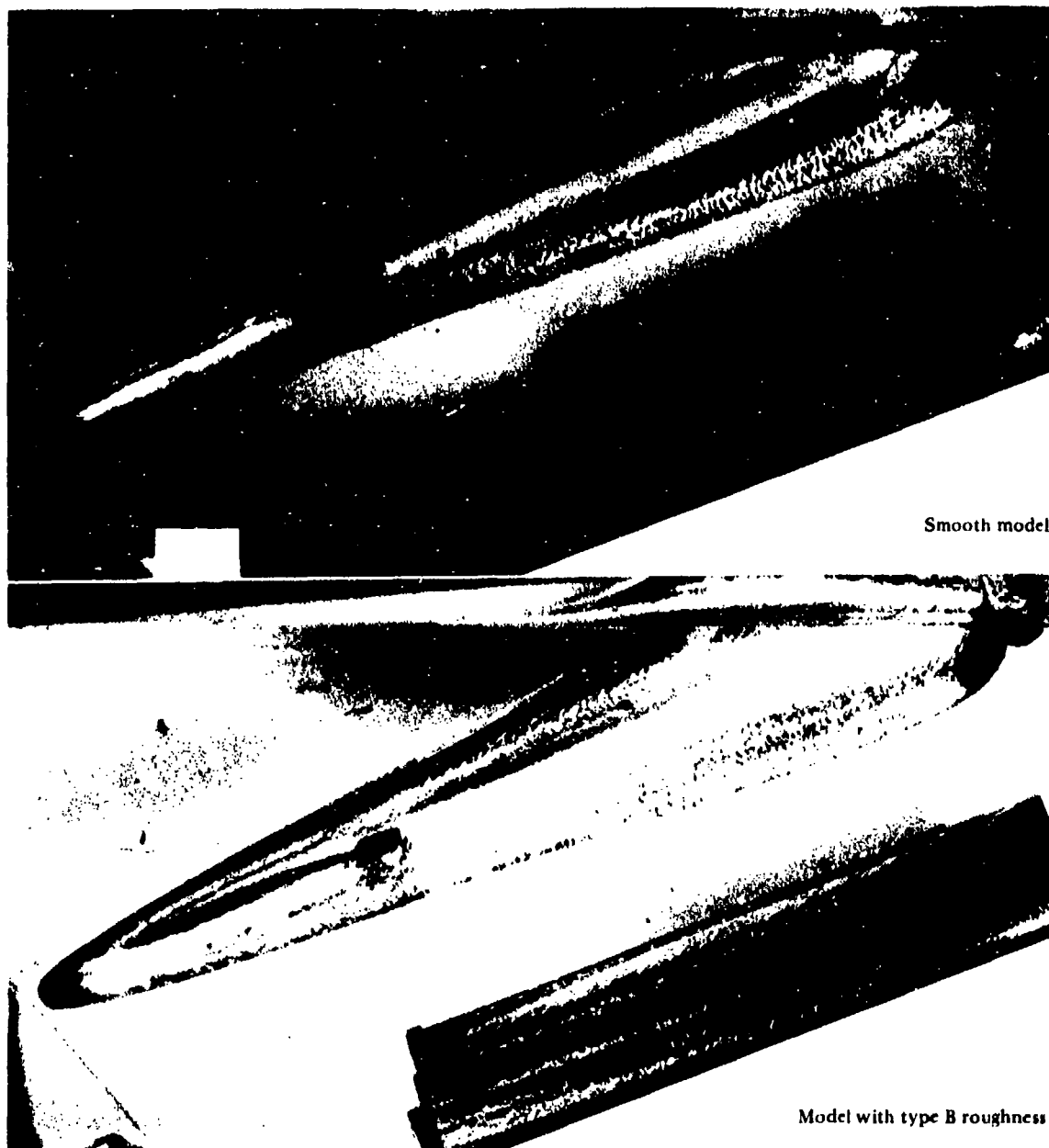
Figure 8.6. Cavities of smooth and roughened models compared 38 ms after water entry. Entry velocity 80 fps, air pressure 1/11 atmosphere.

whether Froude scaling alone would be adequate. During half of the launchings, the entry cavity stripped from the model and trailed from the shroud ring after only 1 1/2 or 2 lengths of underwater travel (Figure 8.10). The model trajectory deviated sharply from that of the prototype when the model remained in its cavity and it was erratic when early stripping occurred (Figure 8.11). The early loss of the cavity was associated with a marked decrease in drag (Figure 8.12), but as long as the cavity did not strip from the roughened model, the roughness made no detectable difference in the cavity at full atmospheric pressure (Figure 8.13). Evidently, Froude scaling alone is inadequate.

132
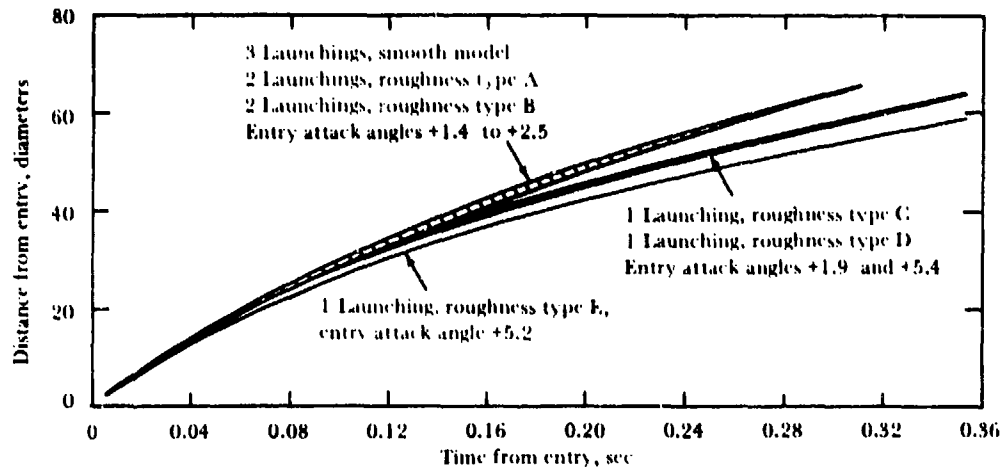
Figure 8.7. Effect of model roughness on drag. Entry velocity 60 fps, air pressure 1/11 atmosphere.
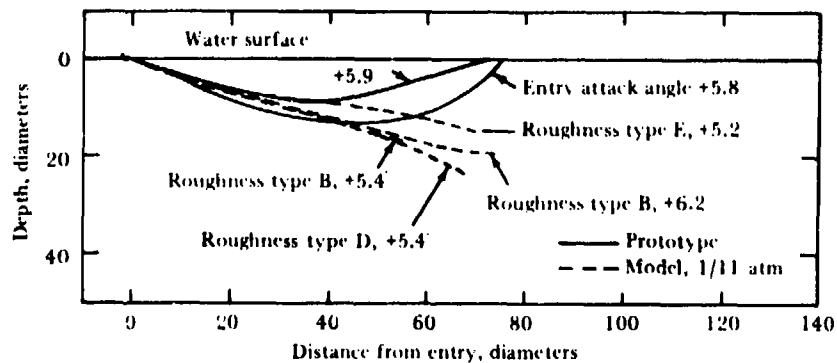
Figure 8.8. Effect on trajectory of increasing entry angle of attack. Entry velocity 60 fps for Froude-scaled roughened models, 200 fps for prototype.
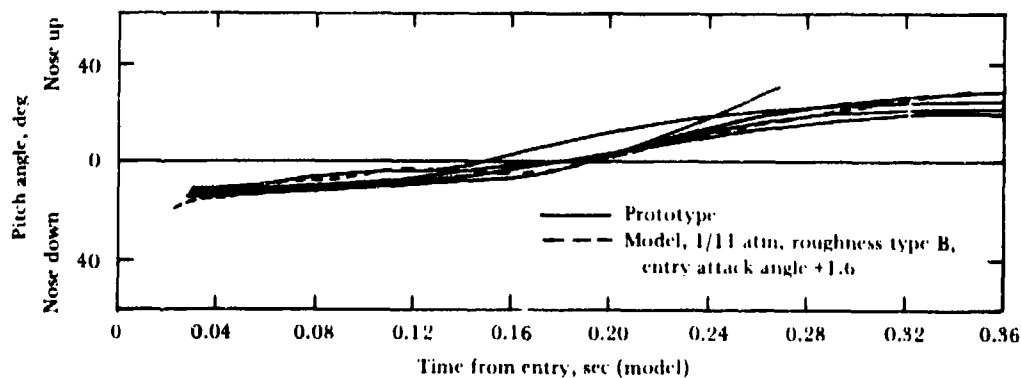
Figure 8.9. Pitch of model and prototype compared as a function of time. Entry velocity 60 fps for Froude-scaled model, 200 fps for prototype. Equal cavitation numbers.

133

Figure 8.10. Entry cavity stripping from model early in underwater travel. Entry velocity 60 fps, air pressure 1 atmosphere, roughness type B.

134
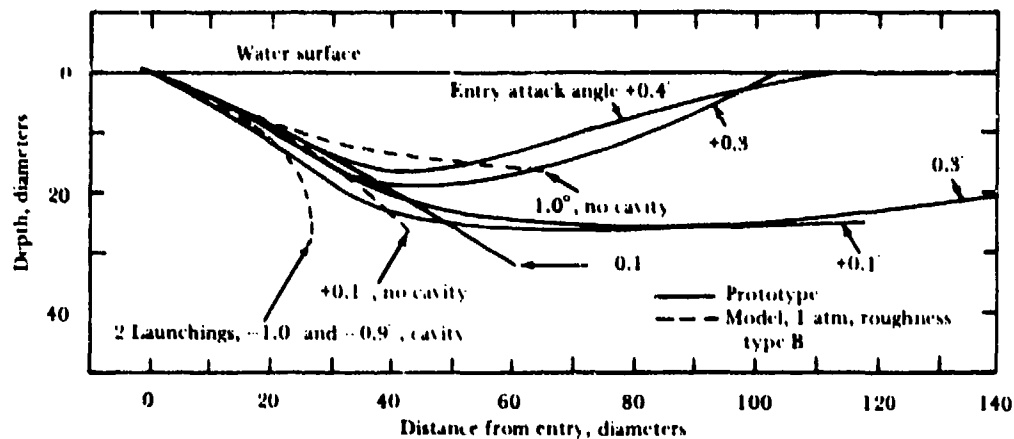
Figure 8.11. Effect of early cavity stripping on model underwater trajectory. Entry velocity 60 fps for Froude-scaled model, 200 fps for prototype. Air pressure 1 atmosphere.
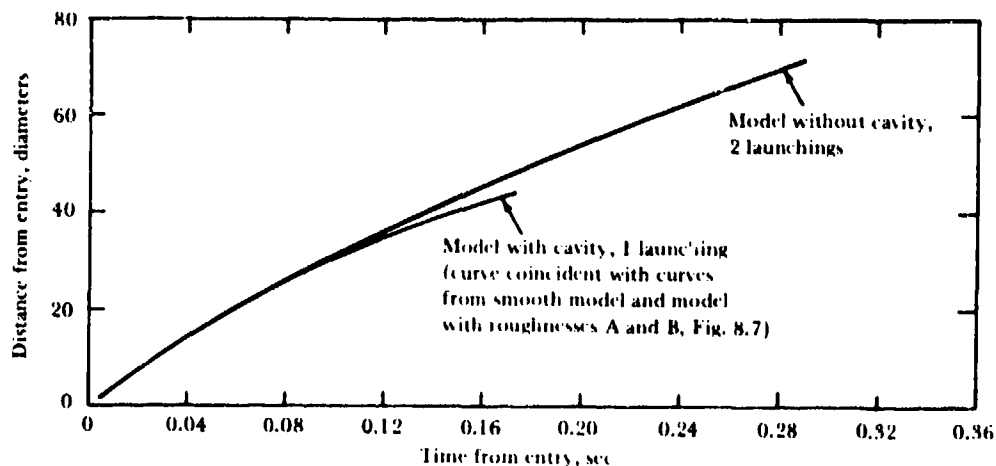
Figure 8.12. Effect of early cavity stripping on model drag. Entry velocity 60 fps, air pressure 1 atmosphere.

Entry Velocities: 400 fps (prototype) and 120 fps (model). Only one launching was made at 400 fps. Figure 8.14 compares its trajectory with both smooth and type B-roughened model trajectories at 120 fps. All model tests were made with an air pressure of 1/11 atmosphere. At this velocity, the models with the rough nose and the models with the smooth nose reproduced the trajectory of the prototype to within 3 diameters during 70 diameters of underwater travel.

Figure 8.15 compares the fragmentary pitch record obtained during the prototype test

with the results from the model launchings. The prototype curve was aligned with the model curves by sliding it horizontally until the first recorded pitch angle equaled the pitch of the model. Then the pitch of the prototype as a function of time differed 6 degrees or less from that of the model during the ensuing 0.27 second (0.9 second in the prototype system). The scatter of pitch data for several prototype runs having nearly identical trajectories is evident in Figure 8.9.

When the rough-nosed model was launched at full atmospheric pressure, the model remained

135

Smooth model

Model with type B roughness
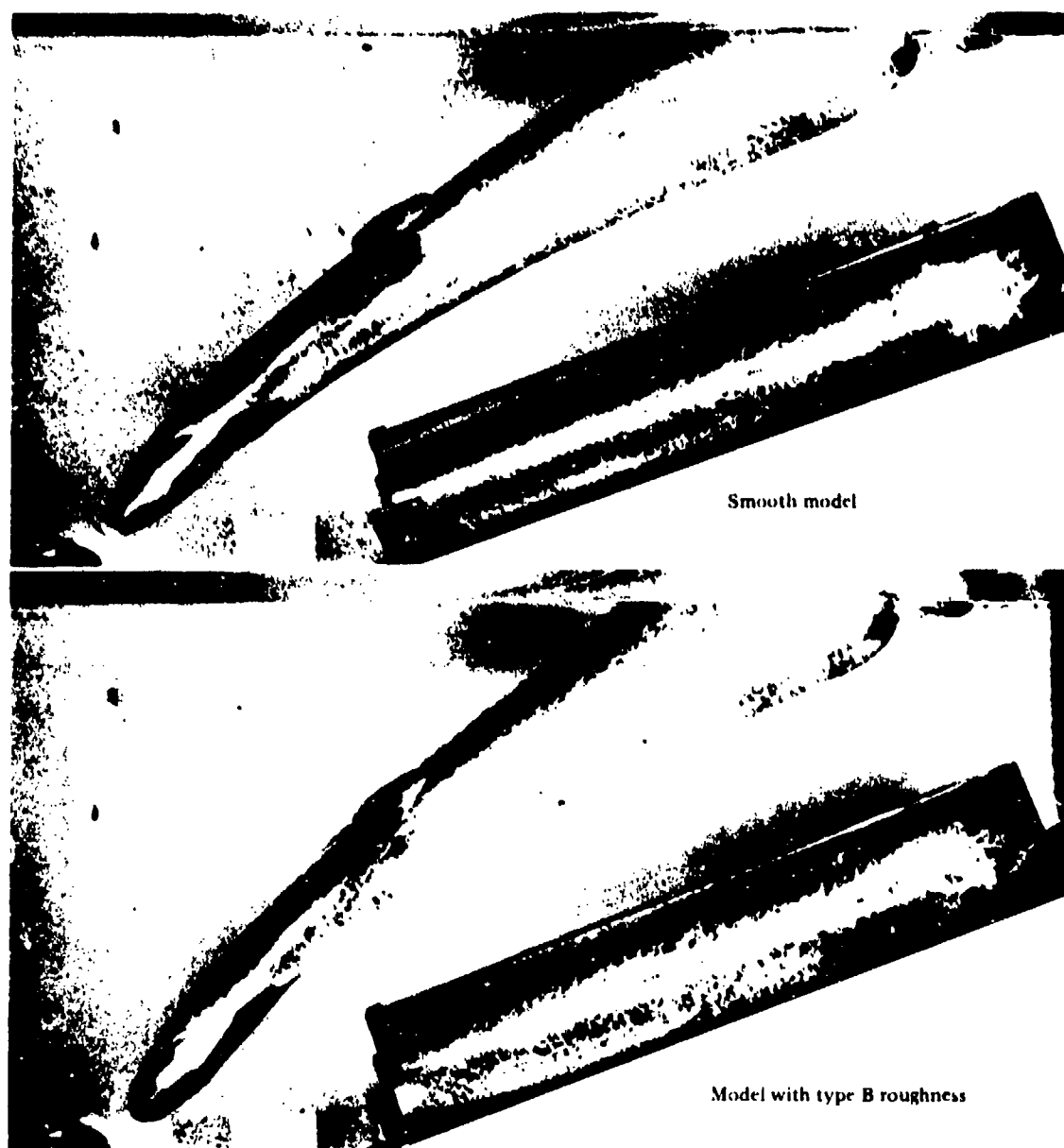
Figure 8.13. Similarity of smooth and roughened model cavities at full atmospheric pressure.

in the cavity and the trajectory deviated from that of the prototype, proving that Froude scaling alone was inadequate.

When type B-roughened models shed their cavities after only 1 1/2 or 2 lengths of underwater travel during full-pressure launchings, further investigation was instituted. The smooth model did not leave its cavity during entries at 60, 80, and 120 fps; neither did the roughened model launched at 1/11 atmosphere. When the roughened model was launched at full atmospheric pressure (eight times at 60 fps, four times at 80 fps, and three times at 120 fps), the cavity stripped during half of the 60- and 80-fps launchings and did not strip at all at 120 fps.

To investigate its possible contribution to cavity stripping, the surface tension of the water was reduced from 76 to 40 dynes/cm by adding
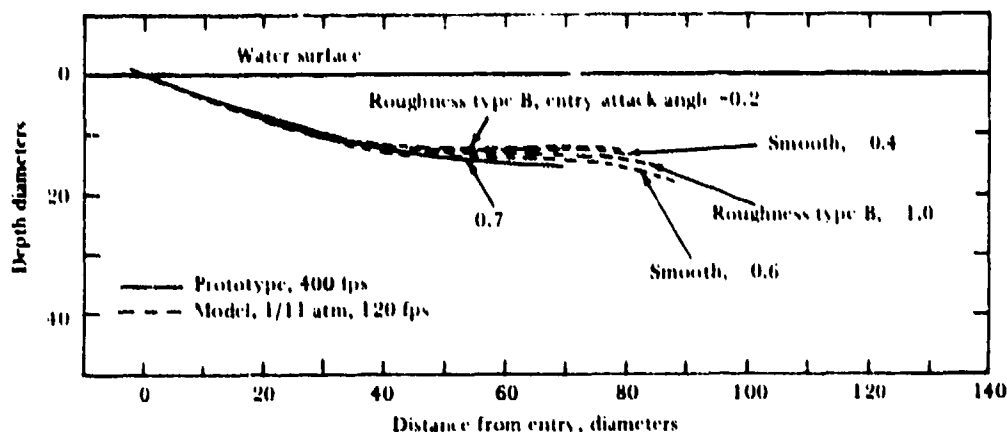
Figure 8.14. Underwater trajectory of prototype compared with trajectories of Froude-scaled smooth and roughened models. Equal cavitation numbers.
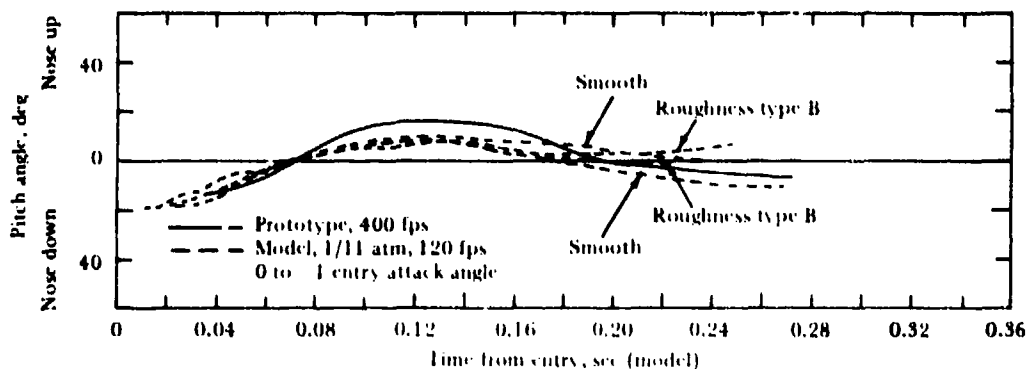
Figure 8.15. Pitch prototype compared with pitch of Froude-scaled smooth and roughened models.

Aerosol OT[1] (Reference 2) to obtain partial scaling (a reduction of 1/121 is required for modeling, but no known liquid is capable of meeting this requirement). During four launchings of the roughened model at an entry velocity of 60 fps and full atmospheric pressure, none of the cavities stripped, indicating that surface-tension forces were at least partially responsible for the phenomenon. Figure 8.16 shows a stripped cavity and compares normal entry cavity in water with one in the Aerosol solution; there is very little difference.

One launching into the Aerosol solution with the tank air pressure reduced to 1/11 atmosphere showed no change in the shape of

the cavity with change in surface tension (Figure 8.17).

At the trajectory angle used in these tests, the spherical portion of the nose contacts the water first if the entry attack angle is steeper than 0 to -1 degree; if the angle of attack is flatter than +3 or +4 degrees, the ogive contacts first. In the intermediate attack-angle range, the contact is at the junction between sphere and ogive. At an air pressure of 1/11 atmosphere, the entry attack angle appears to influence the trajectory of the model (Figure 8.18). Available data are insufficient to show whether or not a similar trend exists at full atmospheric pressure.

---

[1] Solution concentration less than 0.1% Aerosol by weight.

137

Water surface tension 76 dynes/cm, stripped cavity.

Water surface tension 76 dynes/cm, normal cavity.

Dilute Aerosol solution, surface tension 40 dynes/cm.

Figure 8.16. Entry cavities of roughened models in water and in Aerosol solution. Entry velocity 60 fps, full atmospheric pressure, roughness type B.

138
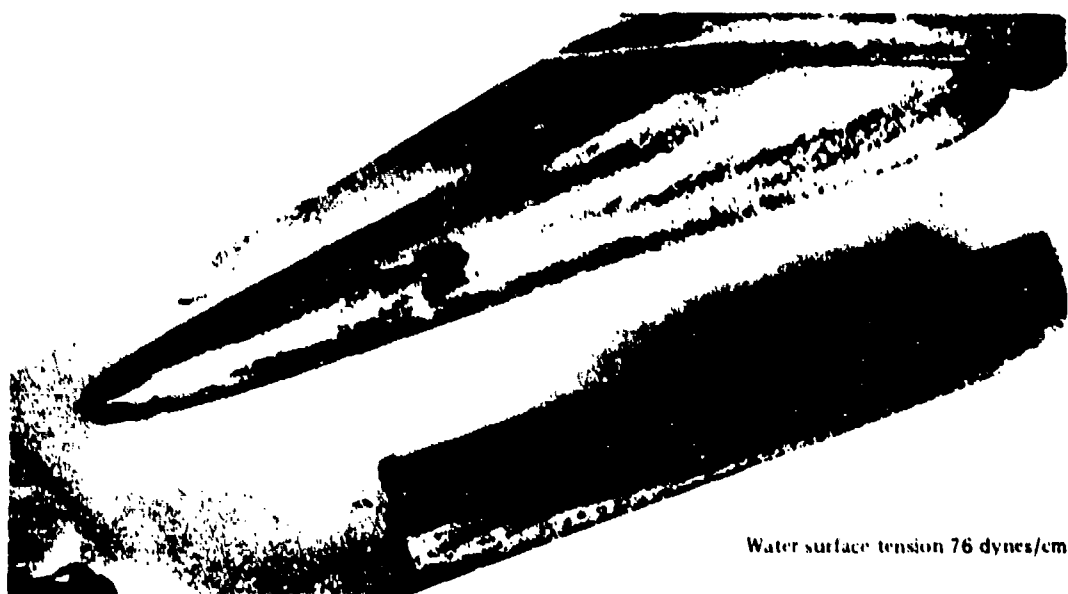
Water surface tension 76 dynes/cm
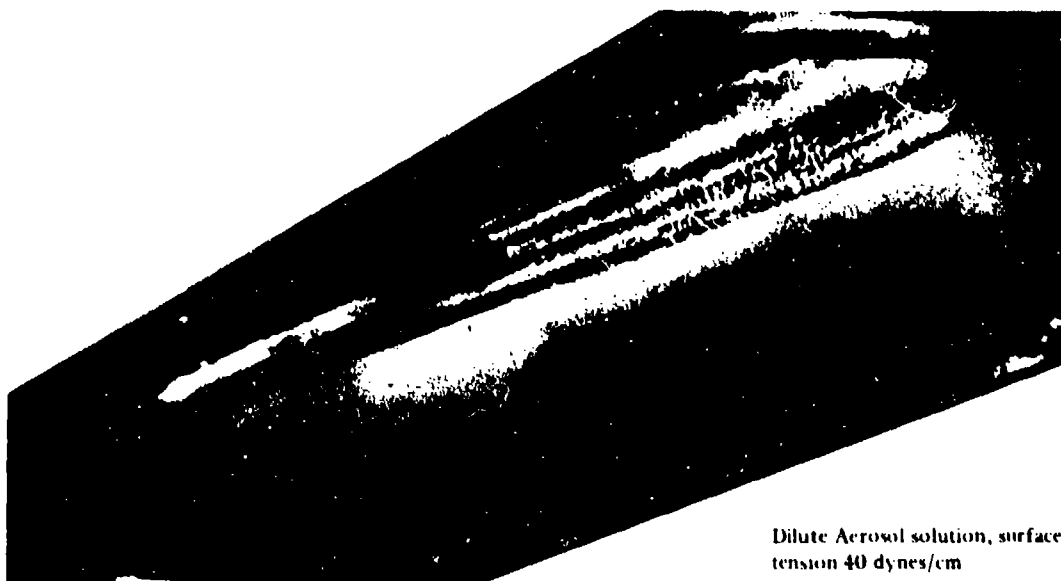
Dilute Aerosol solution, surface tension 40 dynes/cm

Figure 8.17. Entry cavities of roughened model in water and in Aerosol solution. Entry velocity 60 fps, air pressure 1/11 atmosphere, roughness type B.

Model velocity as a function of time was not significantly affected by change in entry attack angle, indicating that model orientation in the cavity and the degree of contact between model and water had little effect upon drag. This was observed at both the 1- and 1/11-atmosphere pressure conditions (Figure 8.19).

The effect of change in air pressure on underwater trajectory depended upon model angle of attack at water contact. At an angle of

approximately +2 degrees, the trajectory became flatter as the air pressure decreased; at angles from +4 to +6 degrees, the trajectory became steeper with decrease in air pressure (Figure 8.20). Photographs of four of the Figure 8.20 launchings are shown in Figure 8.21. The entry cavity and the orientations of the model in the last three parts of Figure 8.21 are similar at the outset, but the subsequent trajectories show considerable variation, probably as the result of differences in flow separation about

139
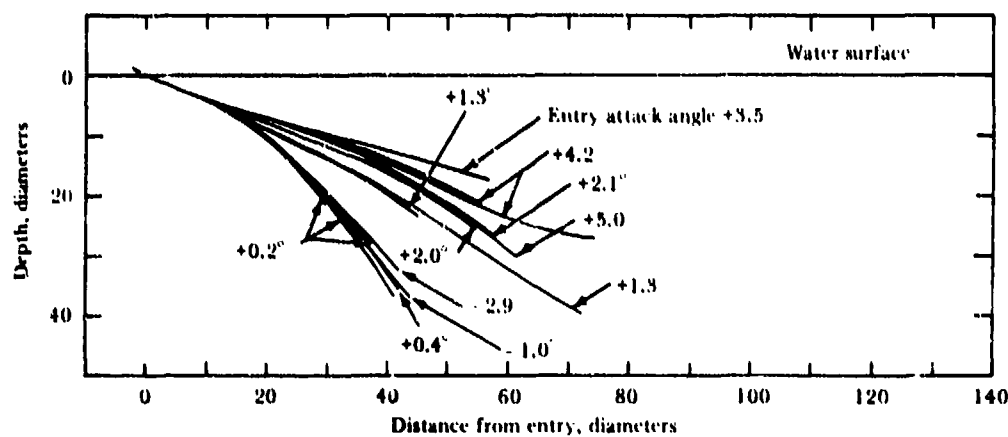
Figure 8.18. Influence of entry angle of attack on trajectory of smooth model.
Entry velocity 60 fps, air pressure 1/11 atmosphere.

the nose. The lines of separation around the nose are not apparent.

Tail contact with the bottom of the cavity was not sufficient to prevent a downturning trajectory, indicating that nose forces were stronger than tail forces. The deceleration of the model was almost the same whether the tail initially contacted the water at entry or 70 ms later (Figure 8.22).

The air pressure in the model system also made little difference in the velocity-time function (Figure 8.23). The 1- and 1/11-atmosphere curves are the averages of the individual tests plotted in Figure 8.19 compared with the results of two launchings at 1/21 atmosphere.

Increasing the entry velocity flattened the trajectory (Figure 8.24) and affected the deceleration of the model. The average drag coefficient during the first 26 diameters of underwater travel was 0.17 for an entry velocity of 60 fps and 0.12 for an entry velocity of 120 fps. The value of 0.12 is in good agreement with the value of 0.11 measured for the

prototype (entry velocity of 400 fps) during the first length of underwater travel.

In drawing a conclusion from the results of these underwater trajectory studies, it must be remembered that the experiments with this particular missile were carried out under rather restricted conditions. Care should be exercised in extrapolating from its behavior.

It was found that one-to-one Froude and cavitation-number scaling is sufficient to reproduce the trajectory of the prototype and its attitude in space if the velocity of the model is great enough to cause a turbulent boundary layer in the flow. The addition of gas-density scaling may be necessary for the modeling of some types of missiles.

The effect of surface tension on one-to-one Froude and cavitation number scaling is insignificant. The uncertainty of inducing a turbulent boundary layer by artificial means makes it preferable to conduct modeling experiments at entry velocities that will naturally result in turbulence in the boundary layer.

140
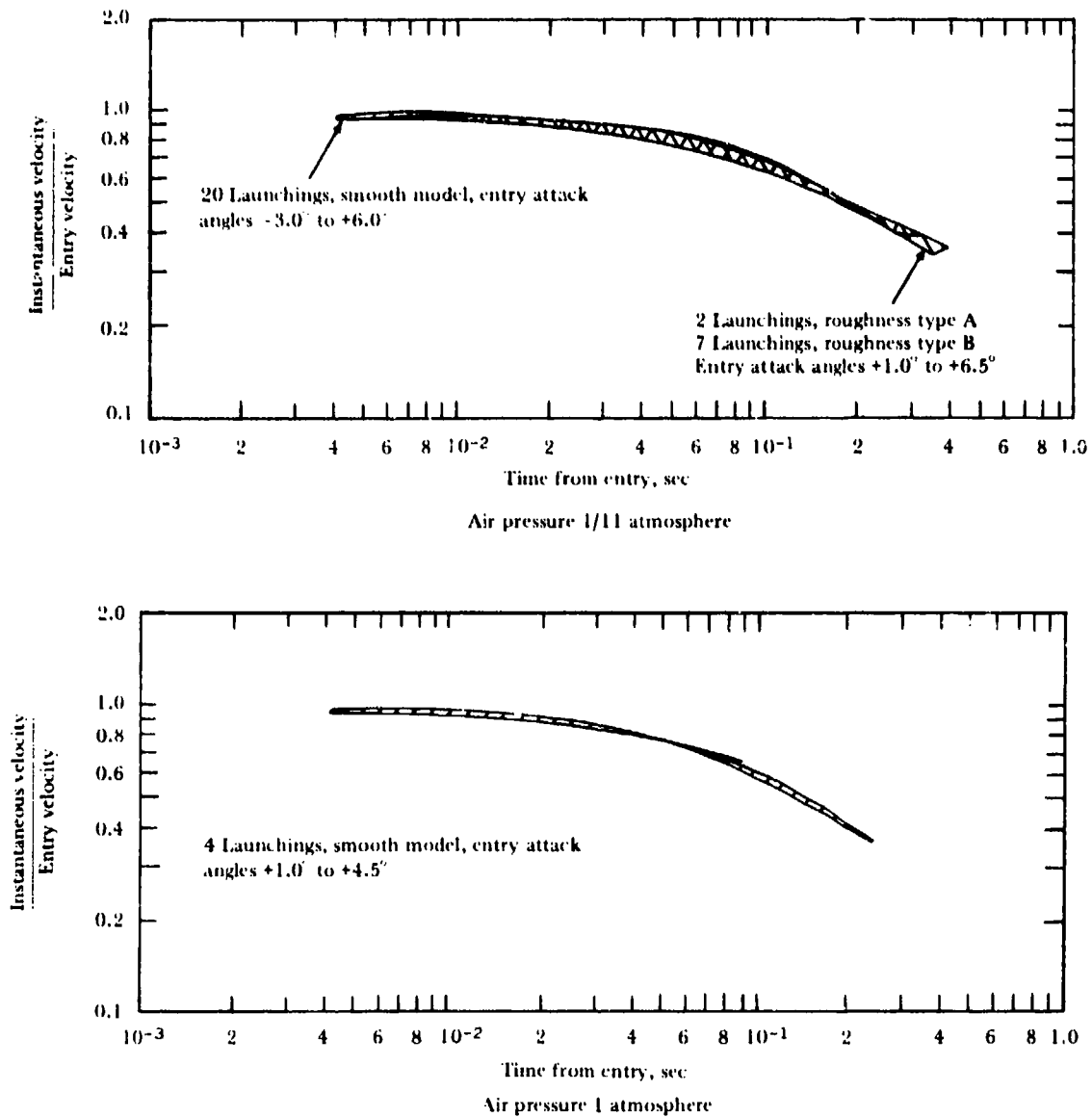
Figure 8.19. Ratio of instantaneous velocity to entry velocity as a function of time. Entry velocity 60 fps.

141
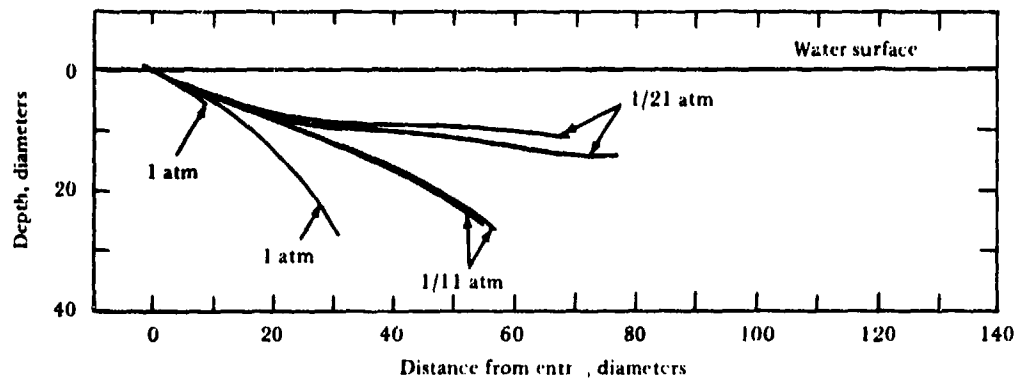
Entry attack angles +1 to +2.5 degrees
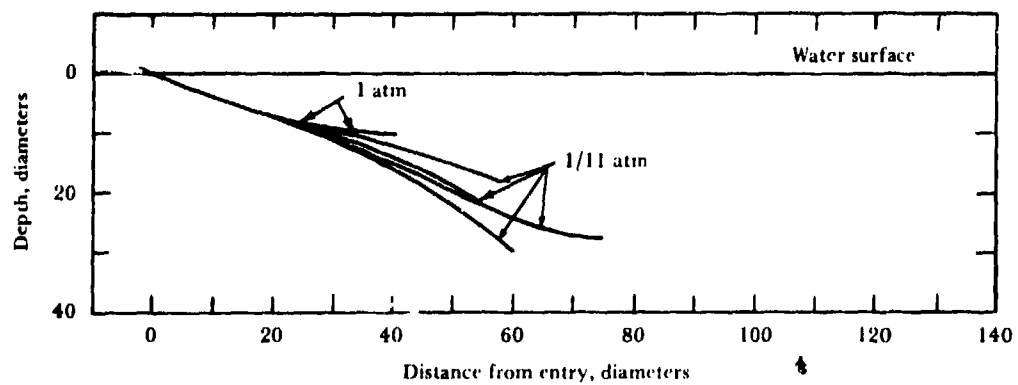
Entry attack angles +4 to +6 degrees

Figure 8.20. Effect of change in air pressure on trajectory of smooth model.

142

1/11 atmosphere, entry attack angle +2.5 degrees

1 atmosphere, entry attack angle +2.2 degrees

1/11 atmosphere, entry attack angle +5.0 degrees
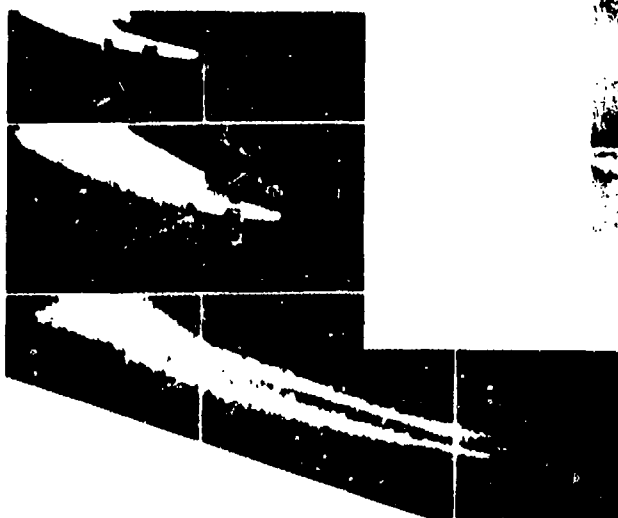
1 atmosphere, entry attack angle +5.4 degrees

Figure 8.21. Entry cavities of smooth model at various air pressures and entry attack angles (31, 52, and 167 ms after water entry).

143
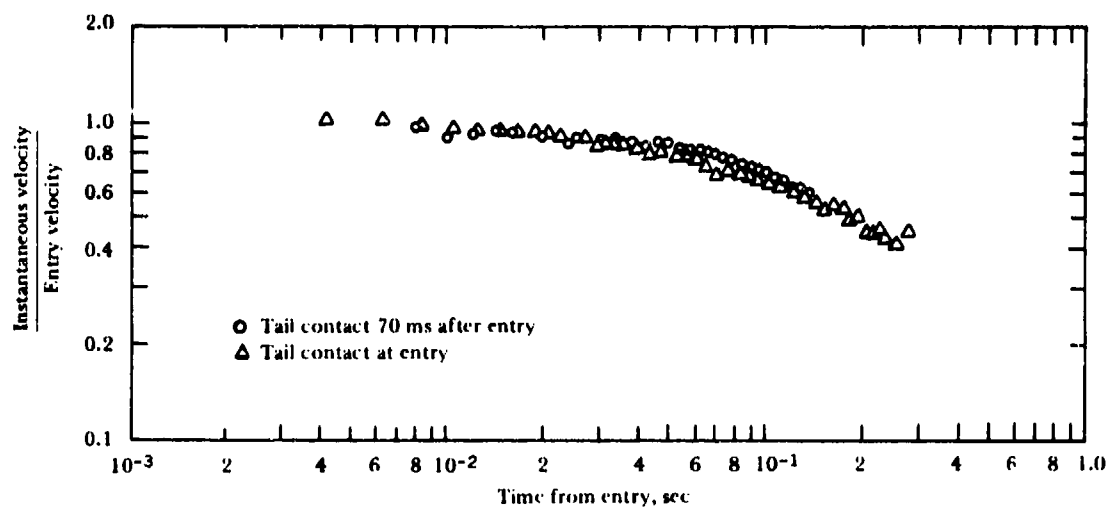
Figure 8.22. Effect on velocity-time function when tail of smooth model contacts bottom of cavity. Entry velocity 60 fps, air pressure 1/11 atmosphere.
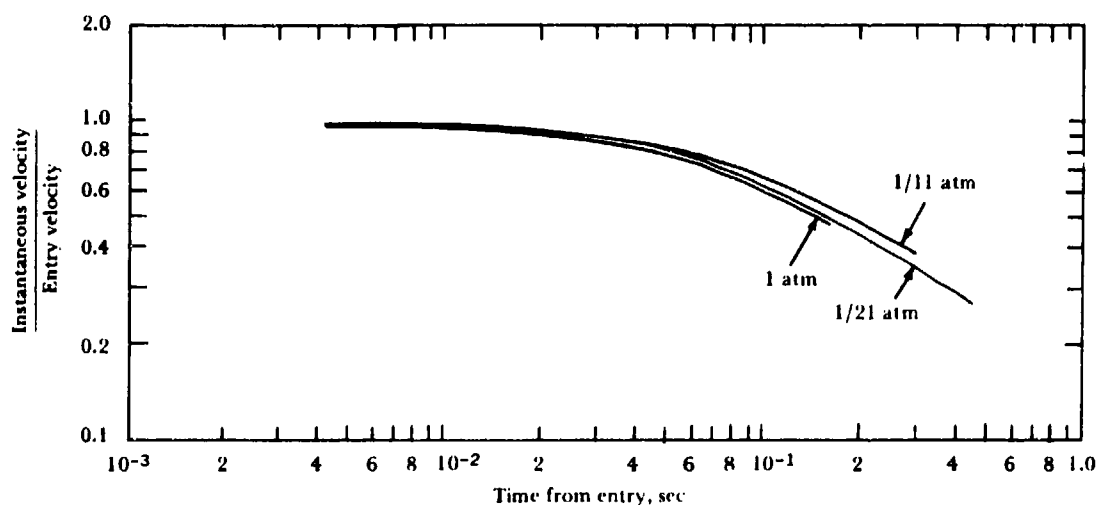
Figure 8.23. Effect of air pressure on velocity-time function of smooth model. Entry velocity 60 fps.
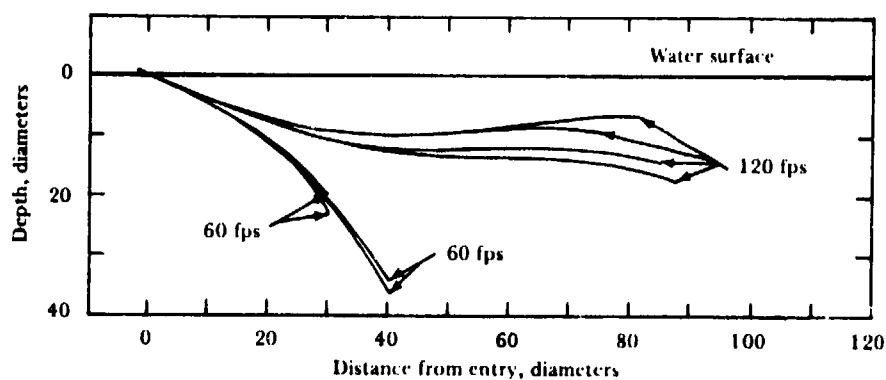
Figure 8.24. Effect of increased entry velocities on trajectories of smooth model. Entry attack angles - 0.6 to +0.4 degrees, air pressure 1/11 atmosphere.

144

WATER-ENTRY CAVITY MODELING

The behavior of a missile is noticeably affected by the size and shape of the cavity enveloping it during high-speed water entry. Modeling of the cavity is an essential part of modeling missile behavior.

As mentioned in the first chapter, one-to-one Froude and cavitation-number scaling does not scale air density. Static pressures on the water and on cavity surfaces are scaled only to the extent that pressure is constant over connected regions of air; the air (gas) dynamic pressure, $\frac{1}{2}\rho v_g^2$ is not scaled. Therefore, the pressure tending to close the cavity is reduced and cavity seal is delayed, possibly permitting more air to enter and the cavity size to be increased. For these reasons, the modeling of cavity size may require gas-density scaling.

Although one-to-one scaling of only the Froude and cavitation numbers had been reasonably successful in modeling oblique water-entry motion (Chapter 7) and underwater trajectory behavior (Chapter 8 and Reference 38), no systematic data on the size and shape of the cavity were obtained, nor were the few instances of failure to model the trajectory fully explained. Thus the need arose to examine scaling techniques for modeling the water-entry cavity in some detail, so that both the role of the cavity in determining missile performance and the sensitivity of the cavity to scaling conditions might be established.

EXPERIMENTAL PROGRAM

The experimental program conducted at the NUC Hydroballistics Laboratory in the Variable-Angle Variable-Pressure Launching Tank sought to investigate the importance of gas-density scaling in conjunction with Froude- and cavitation-number scaling in water-entry cavity modeling. Three models were used: a 2-inch-diameter model to represent the prototype missile, and 1-inch and 1/2-inch-diameter models geometrically and dynamically similar to the prototype. The relatively uncomplicated vertical cavity was investigated first (Reference 101); the knowledge and experience so gained were then focused on the more complex problems of the oblique cavity (Reference 102).

For the vertical-entry modeling studies, a missile with a simple shape, a hemisphere head, a cylindrical body section, and a spool-shaped tail (Figure 9.1) was selected because previous investigations (References 22 and 46) had shown that change in atmospheric density caused large differences in the vertical water-entry cavity of a sphere. Thus gas-density effects could be expected with the blunt-nosed hemisphere head. This configuration also has the advantage of relative stability at water entry, which reduces the chance of the density effect being obscured by small fluctuations of the cavitation number or by differences in missile attitude at water entry. The spool-shaped tail was designed to exert a stabilizing effect on the missile during its underwater trajectory. Nominal water-entry velocities were 120 fps for the 2-inch-diameter prototype missile, 85 fps for the 1-inch model, and 60 fps for the 1/2-inch model. An arbitrary length-to-diameter ratio of six was used.

For the oblique-entry modeling studies, two missile shapes were required to generate the two kinds of cavities that seemed to be potentially sensitive to gas-density scaling. A narrow cavity that tends to close quickly at the water surface was generated by a missile consisting of a truncated cone having a 10.5-degree generating angle and a 0.313-diameter plate (Figure 9.2). The second cavity is one that forms when the missile enters the water at a shallow angle and quickly contacts the top cavity lip, the lip
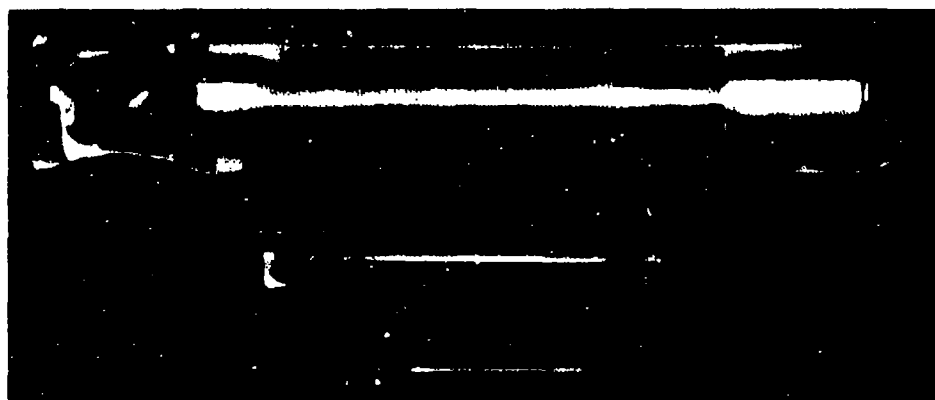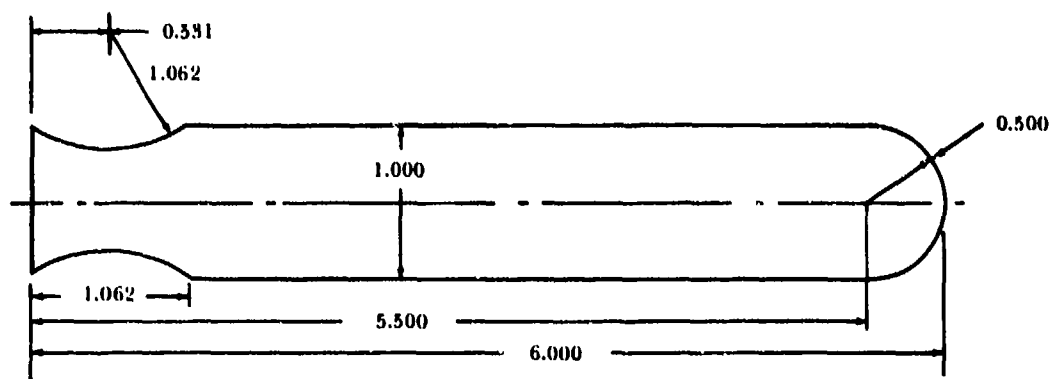
Figure 9.1. Hemisphere missile for vertical water-entry modeling. Dimensions in diameters.

having a narr... cross section and relatively low inertia. The missile fabricated to generate this cavity had a simple plate-cylinder nose shape, with a cylindrical body and tail (Figure 9.3). Missile dimensions and parameters are shown in Table 9.1.

For the initial study, the simplest of entry cavities was preferred – an axially symmetric cavity formed when the trajectory and axis of the missile are vertical at water entry. The effects of four scaling conditions on the vertical-entry cavity modeling of the hemisphere missile were studied.

The 2-inch-diameter hemisphere prototype was tracked at least 25 diameters after water entry, the 1-inch-diameter model for 35 diameters and the 1/2-inch-diameter model for 45 diameters. The prototype was photographed at 0.0025-second intervals. The smaller models were photographed at intervals of 0.00167 and 0.00125 second, respectively, which scale approximately as $\lambda^{1/2}$.

The oblique-entry cavities were investigated under the following conditions:

Scaling Condition	Froude No., F	Cavitation No., σ	Gas-Density Coefficient, ρ'
1. One-to-one Froude-number, cavitation-number, and gas-density scaling	51.8	0.073	0.8
2. One-to-one Froude-number and cavitation-number scaling	51.8	0.073	0.4λ
3. One-to-one Froude-number and gas-density scaling	51.8	0.146/λ	0.8

The truncated-cone missiles were photographed during the first 20 diameters of their underwater trajectory. The plate-cylinder missiles were photographed either during the

146
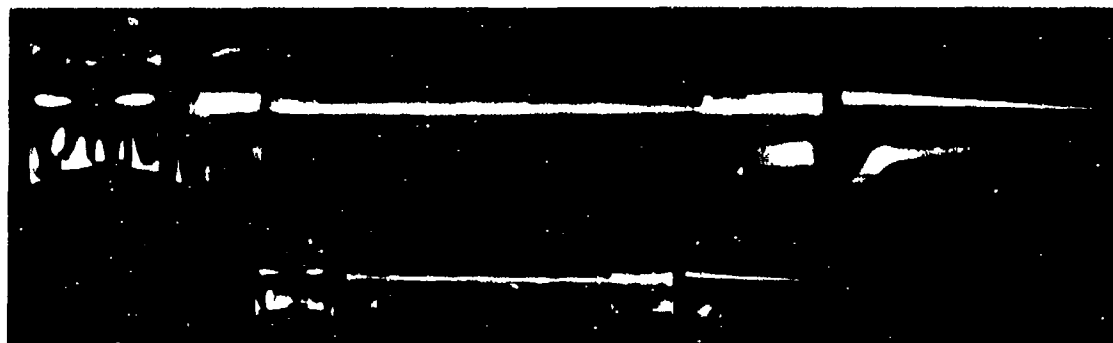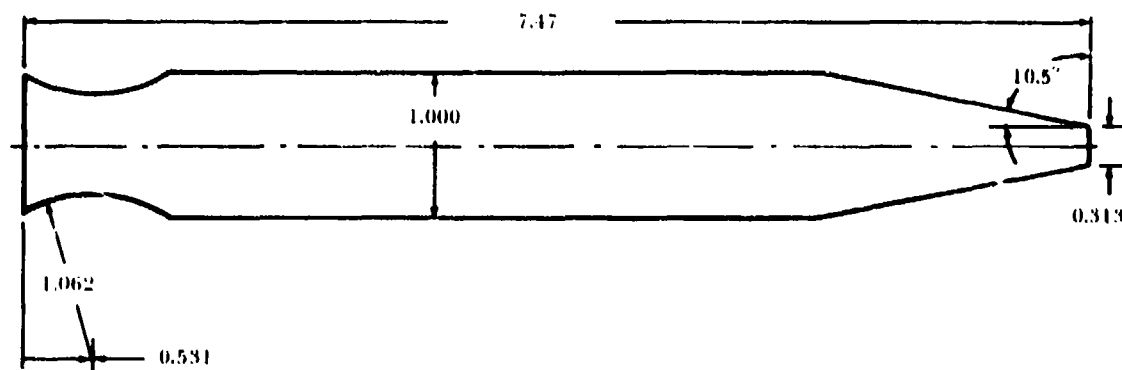
Figure 9.2. Truncated-cone missile for oblique water-entry modeling. Dimensions in diameters.
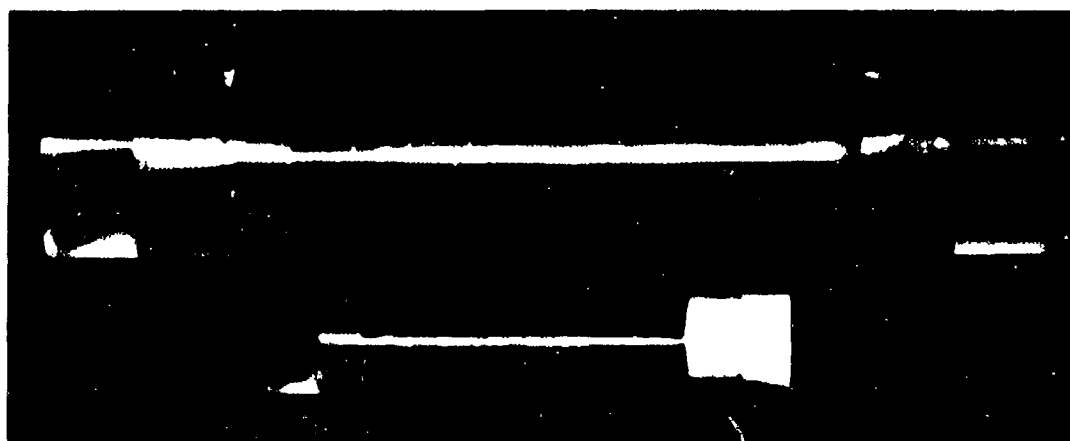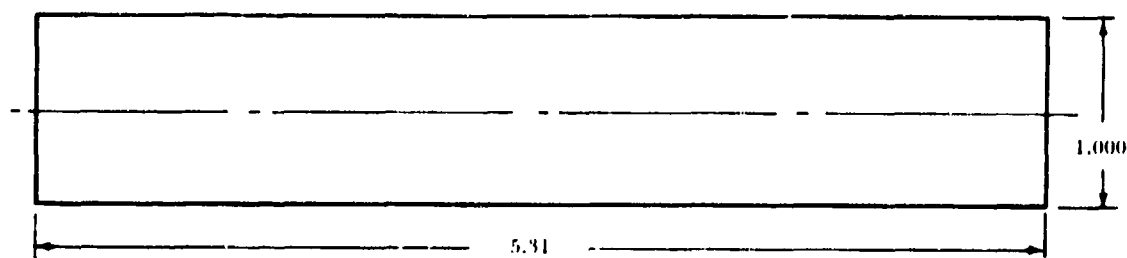
Figure 9.3. Plate-cylinder missile for oblique water-entry modeling. Dimensions in diameters.

147

TABLE 9.1. Prototype and Model Parameters

Parameter	Hemisphere Missile					Truncated-Cone Missile			Plate-Cylinder Missile		
	2-in.-Diam. Prototype	1-in.-Diam. Model		1/2-in.-Diam. Model		2-in.-Diam. Prototype	1-in.-Diam. Model		2-in.-Diam. Prototype	1-in.-Diam. Model	
		Required by Froude Scaling $\lambda = 1/1.999$	Actual Parameters	Required by Froude Scaling $\lambda = 1/4.012$	Actual Parameters		Required by Froude Scaling $\lambda = 1/1.999$	Actual Parameters		Required by Froude Scaling $\lambda = 1/1.999$	Actual Parameters
Diameter, in.	1.998	0.999	0.999	0.498	0.498	1.998	0.999	0.999	1.998	0.999	0.999
Length, in.	12.016	6.011	6.005	2.995	3.007	14.95	7.48	7.46	10.61	5.31	5.31
Weight, lb	1.128	0.139	0.141	0.017	0.017	1.304	0.163	0.167	1.045	0.131	0.130
Distance of CG from nose, in.	5.90	2.95	2.92	1.47	1.47	7.97	3.99	3.93	5.35	2.70	2.65
Moment of inertia,[a] lb in²	15.61	0.489	0.49	0.015	0.015	21.44	0.672	0.672	12.59	0.394	0.389
Cone angle	...	...	...	...	...	10°30'	10°30'	10°24'	...	...	...
Diameter of nose flat, in.	...	...	...	...	...	0.619	0.310	0.318	1.998	0.999	0.999

[a] About a transverse axis through the CG.

148

first 15 diameters or during the interval between 20 and 30 diameters of their underwater travel. Whip data were obtained when the first 15 or 20 diameters of travel were recorded.

As in the vertical water-entry studies, the models were photographed at shorter time intervals than the prototypes, the ratio approximating $\lambda^{1/2}$. The truncated-cone prototype was photographed at 0.0033-second intervals and the plate-cylinder prototype at 0.005-second intervals. Some tests were conducted at even shorter intervals to permit more detailed studies of cavity behavior. Water entry was defined as the first contact between the missile and the water surface. All events were timed from water entry and all positions measured with respect to it.

Figure 9.4 is a typical print from the rotating-disk camera (described in Part V) illustrating the vertical water entry of the 1-inch-diameter hemisphere model launched with a water contact velocity of about 85 fps, gas pressure of 1/4 atmosphere, and gas-density coefficient of 0.8. To preclude any ambiguity in the terms "surface closure" and "deep closure," they are identified in Figure 9.4. Surface closure is the closure of the water surface itself and not the dome of the splash; deep closure is any permanent break in the cavity beneath the water surface.

The following measurements were made from the photographs: (1) the time and position of cavity closure, (2) the cavity diameter at the missile tail, and (3) the projected cavity area in a vertical plane containing the cavity axis of symmetry. The missile positions and the cavity parameters listed and illustrated in Figure 9.5 were measured for each oblique launching and obtained as functions of time. Lack of information on yaw made it impossible to determine missile underwater pitch angles; angles of inclination (see Nomenclature) as shown in Figure 9.5 were measured. For coincident trajectory and object planes, sideview photographs show missile inclination. In vertical trajectories, the indeterminate trajectory plane is taken to be the object plane chosen for photography. The model data were scaled up to prototype size, making the curves and photographs of the small and large missiles directly comparable.

Gas densities are described in terms of the gas-density coefficient ρ', which is the ratio of the density of the gas, at the temperature and pressure of the model system, to that of a standard, defined as the density of air at 20°C and 740-torr pressure. The desired densities were obtained by mixing air with two heavy gases - Freon 12 (dichlorodifluoromethane) and Freon 114B2 (dibromotetrafluoroethane) which have densities, respectively, four and nine times greater than air under the same conditions of temperature and pressure (Reference 67). A gas-density coefficient of 0.8 was used as the experimental baseline atmospheric density. Helium was added to air to reduce its gas-density coefficient to 0.8 for the full atmospheric pressure launchings.

To determine the extent to which prototype cavities having a gas-density coefficient of 1.0 could be predicted from a modeling system having a gas-density coefficient of 0.8, vertical launchings of the hemisphere missile were also made at atmospheric pressure and a gas-density coefficient of 1.0.

To determine whether the air content of the water altered the entry cavity, it was varied for several launchings of the prototype hemisphere missile. Cavity size and shape were not affected, but the cavity wall became roughened when the air content of the water exceeded the equilibrium concentration with air at atmospheric pressure. Since well-defined cavity contours were important to modeling, this equilibrium concentration was carefully maintained during all tests.

EXPERIMENTAL RESULTS: VERTICAL CAVITY

The three sizes of hemisphere head missiles formed reproducible cavities as long as the gas-density coefficient was 0.8 or higher. Surface closure always occurred before deep closure. When the gas-density coefficient was decreased by lowering the atmospheric pressure, cavity closure became erratic under presumably equal entry conditions. Surface closure was late, and in some instances followed deep closure or failed to occur during the recorded trajectories.

Cavity closure is extremely important in determining cavity history because (1) the mass of gas in the cavity cannot appreciably increase after the cavity closes, and (2) the persistence of the cavity about the missile is largely determined by the time and place of deep closure.

As shown in Figure 9.4, the seal that formed at the top of the cavity was always flat
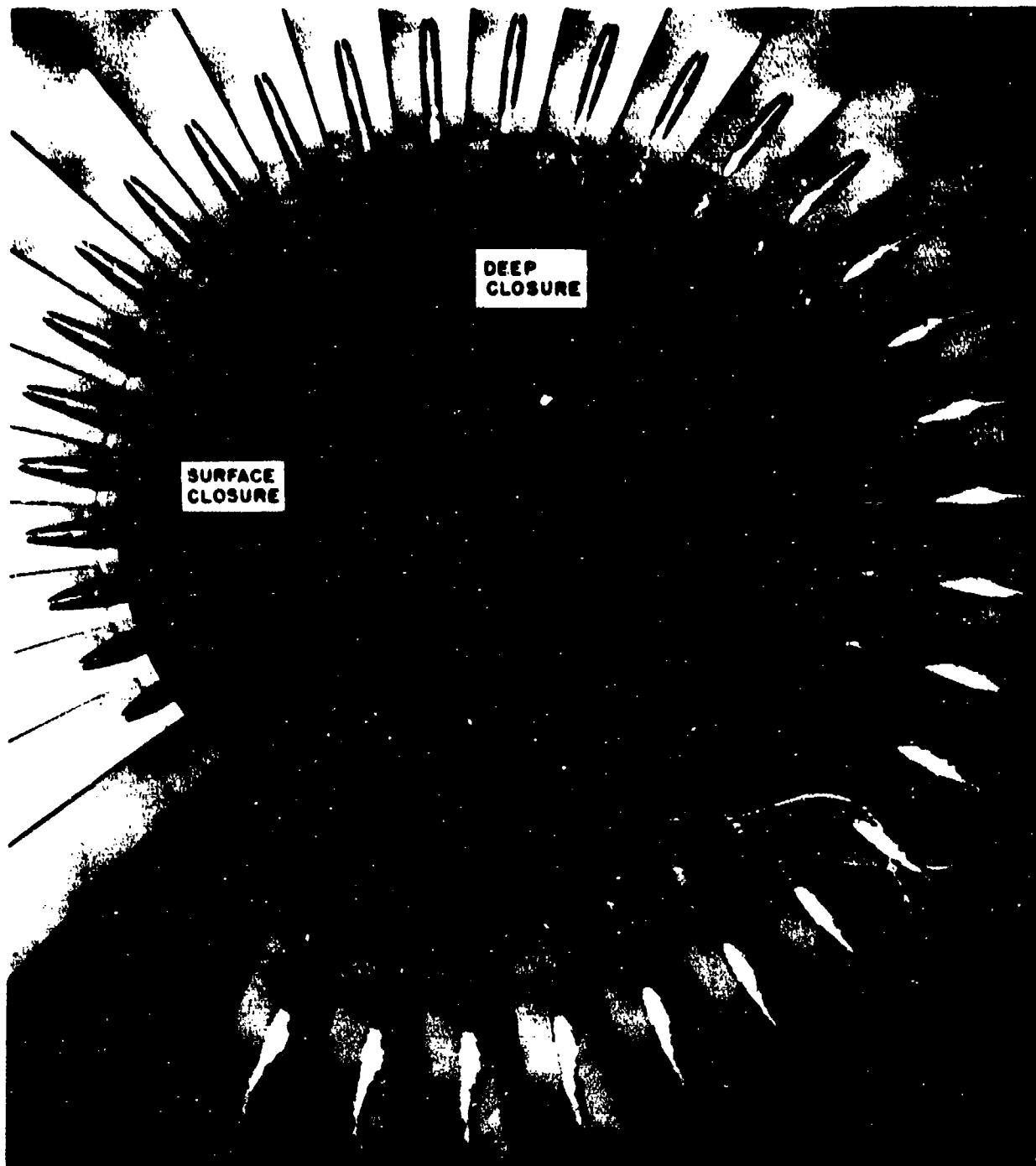
Figure 9.4. Vertical water-entry cavity of 1-inch-diameter hemisphere missile.

a — Width of cavity mouth
b — Diameter of cavity at missile tail
c, d — Cavity lips
e — Cavity cusp
f — Inclination of missile axis

Truncated-cone missile

a — Width of nose cavity mouth
b — Width of tail cavity mouth
c — Length of cavity
d — Diameter of nose cavity
e — Diameter of tail cavity
f — Inclination of missile axis
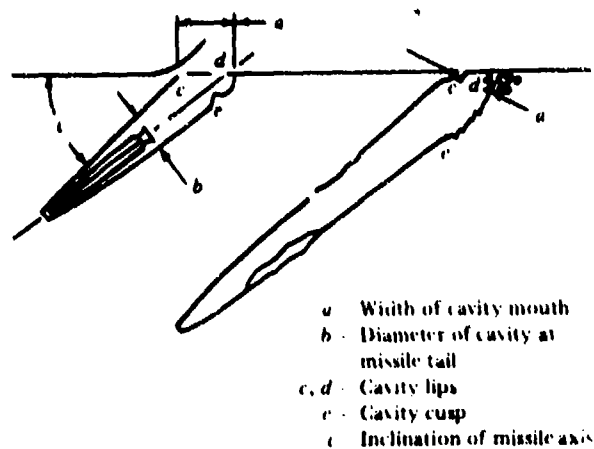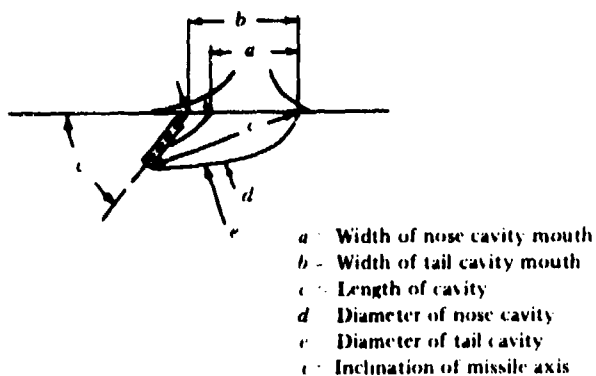
Plate-cylinder missile

Figure 9.5. Oblique water-entry cavity parameters measured from photographic data.

and essentially parallel to the water surface. The depth of the cavity top was measured and plotted as a function of time after water entry. In many instances, several deep closures occurred during a single launching.

Figures 9.6 to 9.8 compare the closures obtained with one-to-one Froude- and cavitation-number scaling or Froude-number and gas-density scaling with the closures obtained when all three — Froude and cavitation numbers and gas density — are scaled simultaneously. With gas-density scaling, both surface closure and deep closure modeling are obtained, whether or not the cavitation number is scaled; surface-closure modeling is slightly improved when cavitation-number scaling is included.

Without gas-density scaling, modeling does not occur.

To find out what happens when only gas density or only gas pressure is varied, an additional series of launchings was made with the 2-inch prototype missile. Figure 9.6 compares gas-density coefficients of 0.4 and 0.8. Figure 9.7 compares gas pressures $\sigma = 0.146$ and $\sigma = 0.073$. Increase in gas density at constant pressure accelerates cavity surface closure, with a reduction in projected cavity area. Reduction in gas pressure at constant gas density only slightly affects surface and deep closure and projected cavity area.

The ratio of the difference in depth to the difference in time between the surface and the first deep closure (Figures 9.6 to 9.8) provides an index of cavity modeling. If the ratio for the 2-inch-diameter missile with one-to-one Froude and cavitation-number and gas-density scaling is taken as the prototype modeling condition, an empirical closure parameter ω which compares cavity-closure modeling under the different scaling conditions, can be defined as follows:

$$\omega = \left(\frac{\lambda^{-1}\,\Delta h}{\lambda^{-1/2}\,\Delta t}\right)\Big/\left(\frac{\Delta h_p}{\Delta t_p}\right)_* =$$

$$= \left(\frac{\Delta h}{\lambda^{1/2}\,\Delta t}\right)\Big/\left(\frac{\Delta h_p}{\Delta t_p}\right)_* \qquad (9.1)$$

where Δh is the difference in depth and Δt is the difference in time between surface and the first deep closure. Depth and time in the numerator of Equation 9.1 have been scaled to prototype conditions, and the denominator $(\Delta h_p/\Delta t_p)^*$ represents the ratio for the prototype modeling condition. Subscripts are not used in the numerator because ratios for both prototype and models are used. For cavity closure modeling, $\omega = 1$. From Figure 9.9, where ω is plotted as a function of gas pressure and scaling conditions, it is evident that one-to-one gas-density scaling is necessary for modeling the closure parameter and that one-to-one cavitation-number scaling is of relatively little importance.

The magnitude of the cavity diameter at the missile tail[1] appeared to be little changed by

---

[1] Measured only when the tail was not in contact with the cavity wall.

151
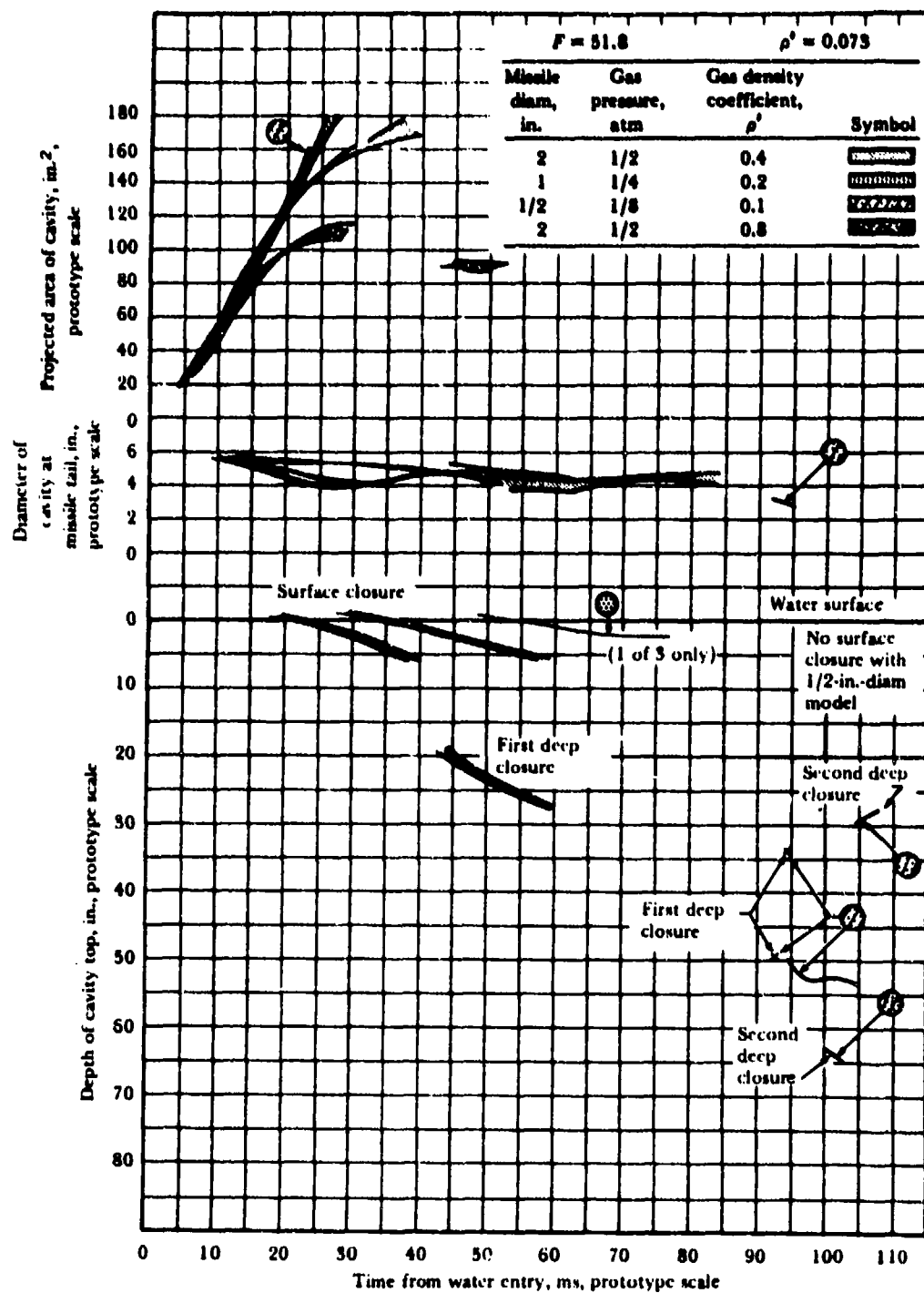
Figure 9.6. Cavity parameters of hemisphere missile with one-to-one Froude and cavitation-number scaling. $\xi = 90$ degrees.

152
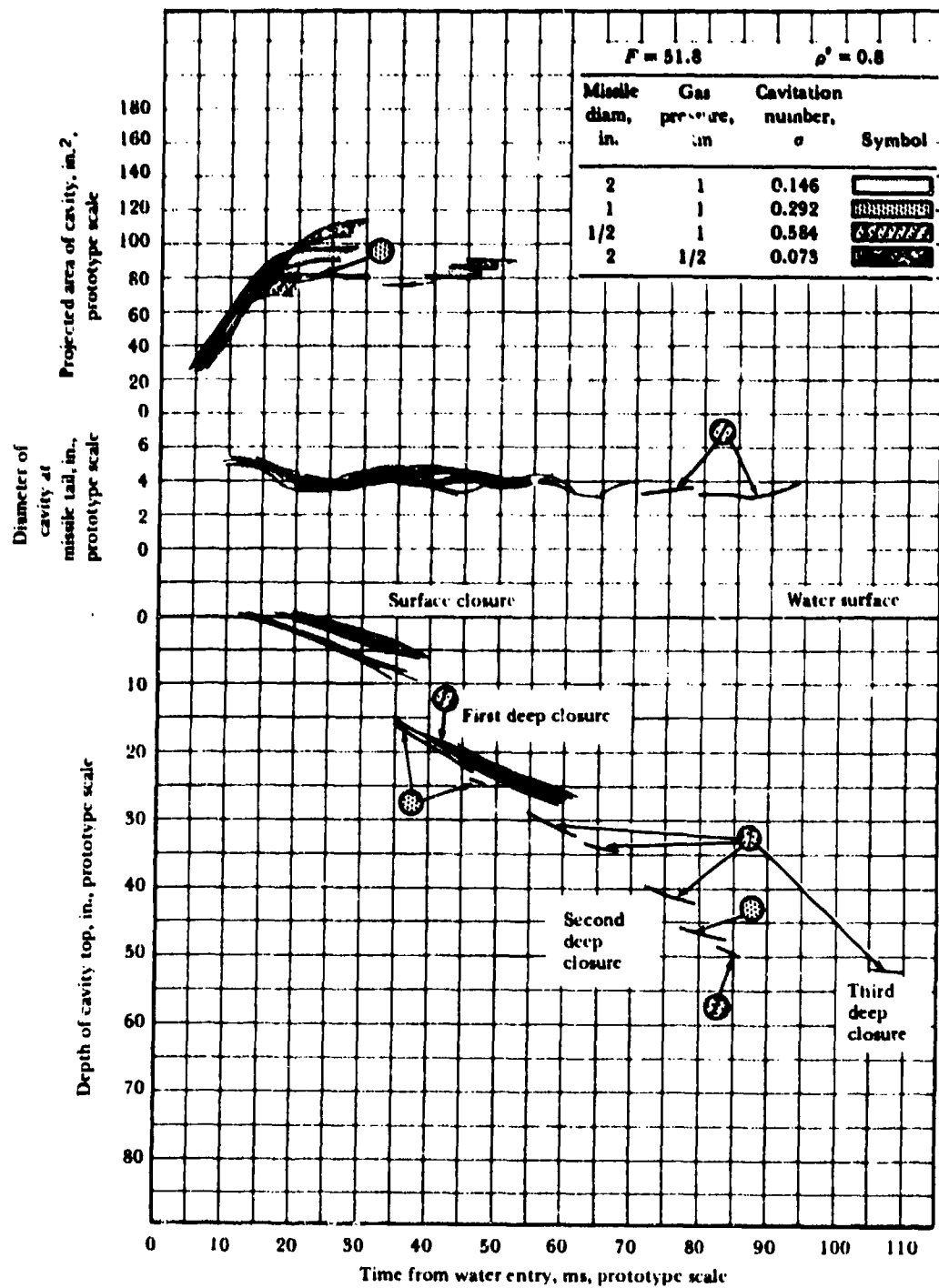
Figure 9.7. Cavity parameters of hemisphere missile with one-to-one Froude and gas-density scaling. $\xi = 90$ degrees.

153
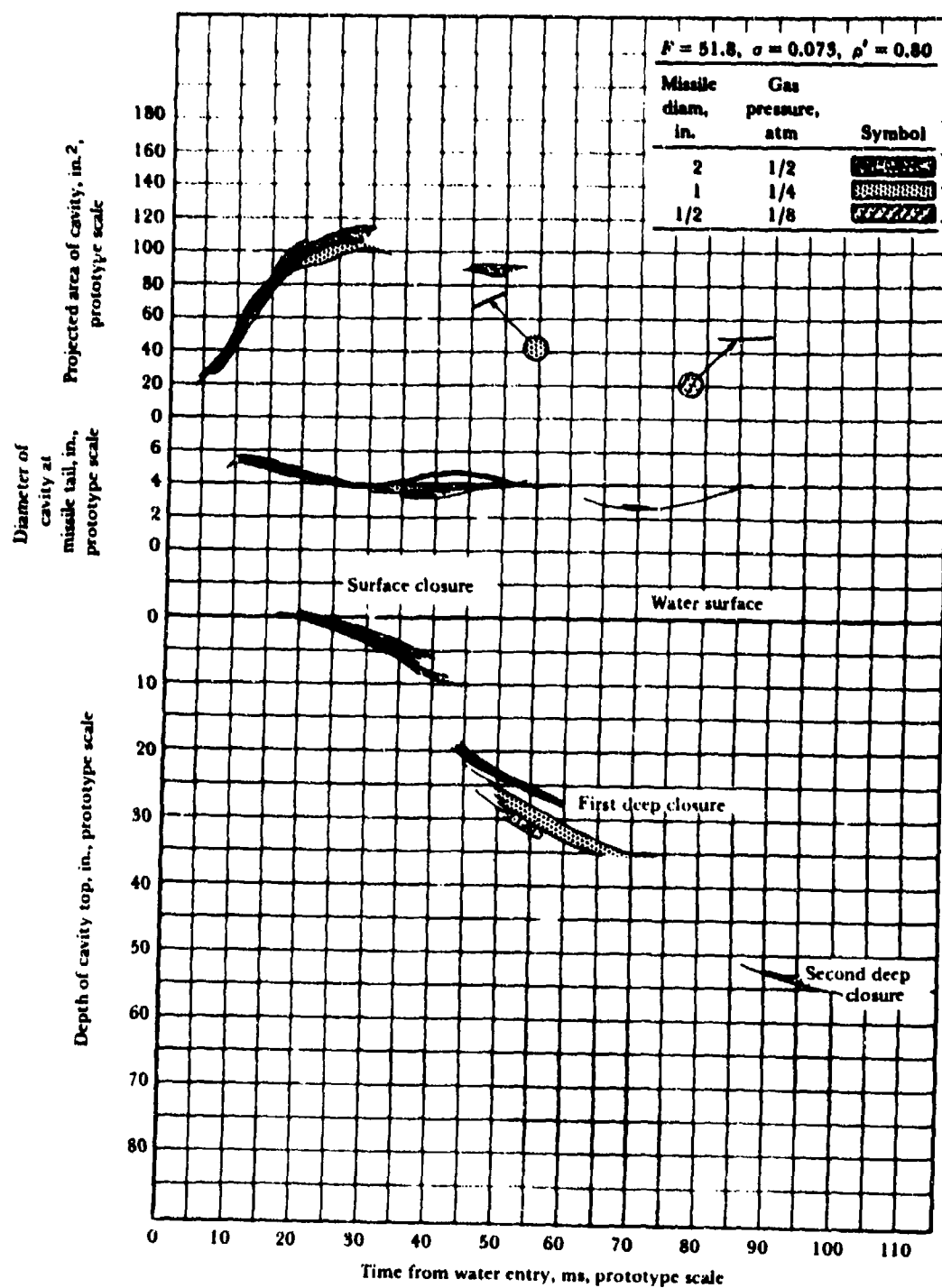
Figure 9.8. Cavity parameters of hemisphere missile with one-to-one Froude and cavitation-number and gas-density scaling. $\xi = 90$ degrees.

154
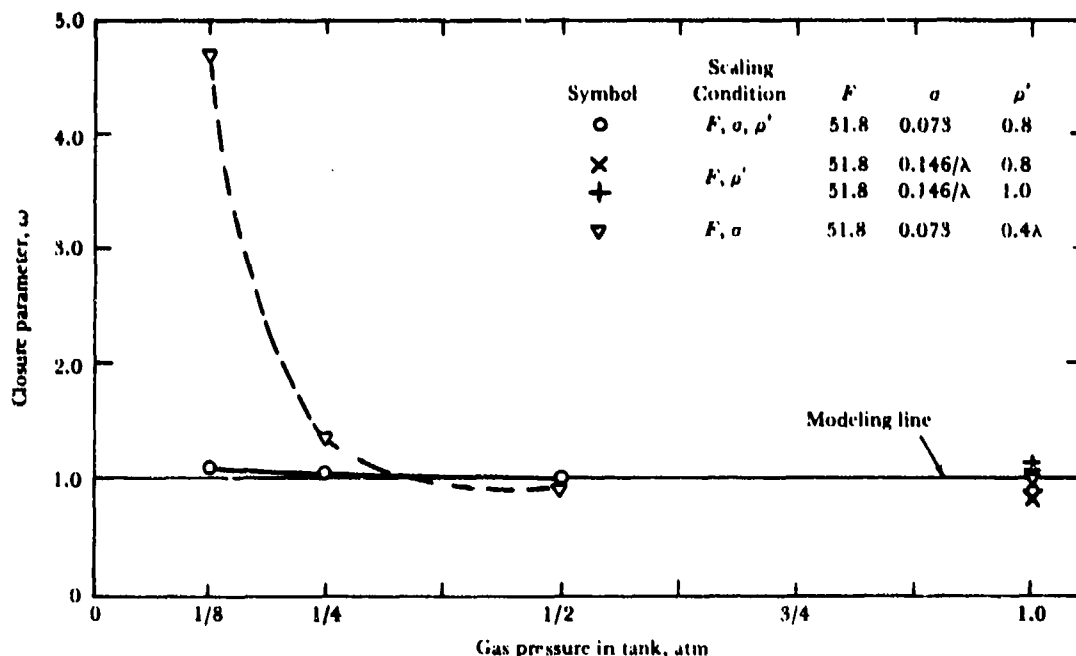
Figure 9.9. Importance of gas-density scaling in modeling cavity closure of hemisphere missile. ξ = -90 degrees.

the various scaling conditions; the cavity diameter curves never deviated more than one missile diameter from the prototype condition.

Small oscillations in the cavity diameter-time curves were not modeled by any scaling condition. However, it was observed that:

1. Oscillation occurred only after the cavity was closed from the atmosphere above the water surface.

2. The period of the oscillation increased with

   a. Increase in missile diameter at constant Froude number
   b. Decrease in gas density
   c. Decrease in gas pressure

For geometrically similar cavities, the cavity volume ratio is equal to λ times the projected area ratio. After deep closure, the cavity area remaining about the missile was measured. When the gas-density coefficient was 0.8 or higher, the cavities made by the three hemisphere missiles were sufficiently similar (Figure 9.10) that the relationship between cavity volume and area ratios could be assumed. When the gas-density coefficient was not scaled, the cavities were initially similar but became quite different in shape later in the trajectory (Figure 9.11); no direct comparison of volume could be made.

Figures 9.6 to 9.8 show that fair modeling of cavity volume was achieved by one-to-one scaling of Froude number and gas density, and that excellent modeling resulted when the cavitation number was also scaled. Successful modeling of cavity volumes, with 1-inch and 1/2-inch diameter spheres in a one-to-one Froude and cavitation-number and gas-density scaled system, was reported in Reference 46.

Equations 1.9, 1.16, and 1.17 indicate that the underwater trajectory (here, water penetration distance) will be modeled if the distance, expressed in diameters, is the same when the corresponding times of penetration scale as $\lambda^{1/2}$. Measurements of penetration distances corresponding to 0.05 second in the prototype scale (about 24 diameters of penetration, the greatest distance for which modeling comparison could be made), indicate that good underwater trajectory modeling was obtained for all modeling conditions.

EXPERIMENTAL RESULTS: OBLIQUE CAVITY

Truncated-Cone Missile

The narrow water-entry cavity produced by the truncated-cone missile was found to be extremely sensitive to gas-density scaling. The

155

Scaling condition	2-in.-diam prototype	1-in.-diam model (enlarged)	1/2-in.-diam model (enlarged)
F 51.8 ρ' 0.8			
σ	0.146	0.292	0.584
Cavity length scaled to prototype dimensions, in.	15.0	14.4	13.6
L/D_{max}	3.13	3.18	3.15
F · 51.8 ρ' = 1.0			
σ	0.146	0.292	0.584
Cavity length scaled to prototype dimensions, in.	14.1	13.2	14.4
L/D_{max}	3.18	3.08	3.29
$F = 51.8$ $\sigma = 0.073$ $\rho' = 0.8$			
Cavity length scaled to prototype dimensions, in.	14.8	14.6	14.4
L/D_{max}	3.06	3.05	3.14

Figure 9.10. Shape of hemisphere missile vertical water-entry cavity, gas density scaled.

cavities that formed at low and at high densities in otherwise equal systems were entirely different in character, as illustrated in Figure 9.12 (cavitation number $\sigma = 0.073$) and in Figure 9.13 (cavitation number $\sigma = 0.146$). At low densities, the cavities are extremely large and still growing at the end of the photographic records; at high densities the cavities close at the surface and soon begin to disappear. Comparison of the two pictures in each figure shows clearly that change in gas-density coefficient and not change in cavitation number is responsible for the change in cavity character.

Shifting the gas-density coefficient from 0.11 to 0.195 made a difference in the surface closure of the truncated-cone missile cavities, as shown in Figure 9.14. Increasing the gas-density coefficient retarded the growth of the cavity

Scaling condition	2-in.-diam prototype	1-in.-diam model (enlarged)	1/2-in.-diam model (enlarged)
F 51.8 σ 0.79			
ρ'	0.4	0.2	0.1
Cavity length scaled to prototype dimensions, in.	13.7	14.8	16.0
L/D_{max}	2.61	2.78	2.78
F 51.8 σ 0.073			
ρ'	0.4	0.2	0.1
Cavity length scaled to prototype dimensions, in.	36.7	40.5	38.4
L/D_{max}	8.54	4.54	3.73

Figure 9.11. Shape of hemisphere missile vertical water-entry cavity, gas density not scaled.

mouth at the water surface. The growth rate is extremely sensitive to gas-density changes in the range of $0.4 < \rho' < 0.8$; above and below this range, the sensitivity is less. No variation in missile attitude occurred during the range of test variables.

The cavity diameter at the missile tail as a function of time is another measurement shown in Figure 9.14. This parameter is not so dependent upon gas density as is surface closure. In the range $0.8 < \rho < 1.95$, the cavity diameter decreases 17%, but below 0.8 the diameter is almost independent of ρ' (Figure 9.15). The time between water entry and the missile tail's first contact with the cavity wall indicates a dependence upon gas density similar to that

157

$\rho' = 0.11$
37 ms after water entry

$\rho' = 1.95$
37 ms after water entry

Figure 9.12. Effect on truncated-cone prototype cavity of change in gas-density coefficient when $\sigma = 0.073$, $\xi = -39°$.

$\rho' = 0.17$
40 ms after water entry

$\rho' = 3.48$
42 ms after water entry
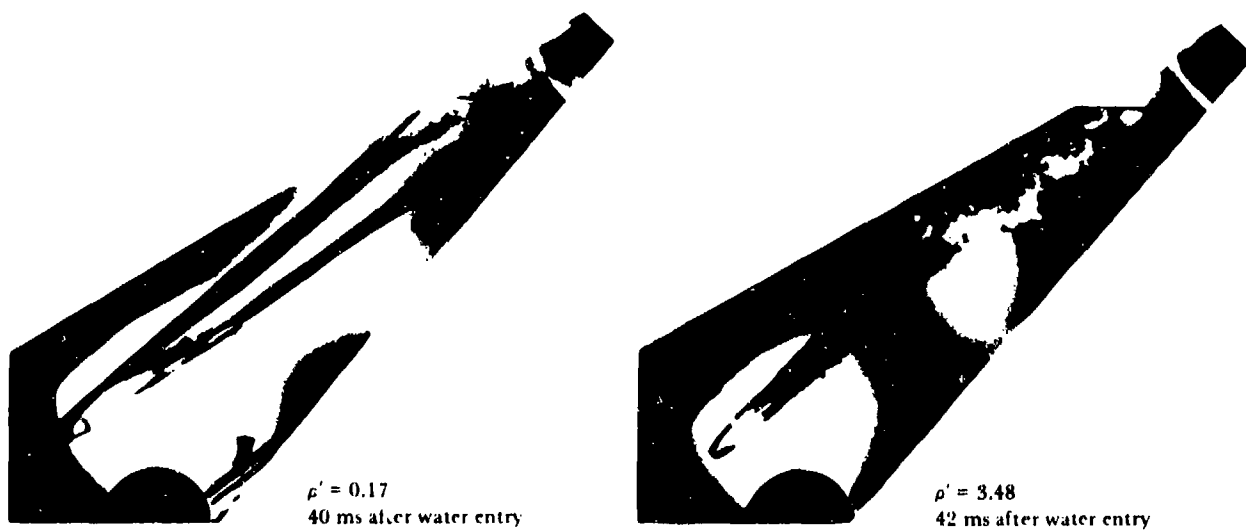
Figure 9.13. Effect on truncated-cone prototype cavity of change in gas-density coefficient when $\sigma = 0.146$, $\xi = 39°$.

158
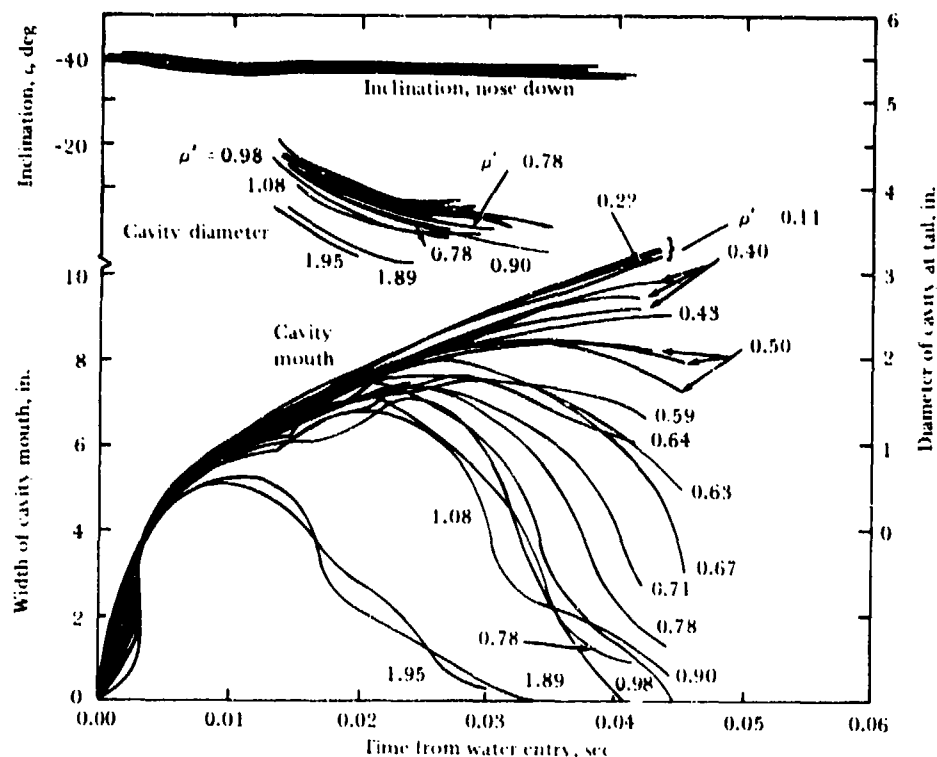
Figure 9.14. Effect on truncated-cone prototype cavity of variation in gas-density coefficient from 0.11 to 1.95. F 51.8, σ 0.073, ξ 39 degrees.

shown by the cavity diameter: tail contact occurs earlier with decrease in cavity width.

The response of the 1-inch model water-entry cavities to change in gas density (Figures 9.16 and 9.17) was similar to that of the prototype. No significant change in the diameter at the missile tail was observed for a gas-density range of 0.1 to 0.8 and cavitation numbers 0.073 and 0.292.

The narrow oblique cavity responded in much the same way as the vertical cavity to the various scaling techniques; i.e., one-to-one scaling of the Froude and cavitation numbers and the gas-density coefficient modeled the cavity to a high degree of accuracy. Failure to scale the cavitation number did not prevent good modeling, but when the gas-density coefficient was not scaled, modeling did not occur.

Figures 9.18 to 9.21 are a series of cavity photographs paired with surface-closure curves for the respective cavities. These are discussed below according to the scaling conditions they represent.

When all three factors were scaled, cavities that formed under equal conditions looked very

much alike, and cavity-mouth curves showed that an excellent degree of modeling was obtained. Closure curves and photographs illustrating the conditions $\rho' = 0.1$ and $\rho' = 0.8$ are shown in Figures 9.18 and 9.19, respectively.

For the scaling that included only Froude number and gas-density coefficient, a good degree of modeling also was obtained (Figure 9.20).

Figure 9.21 shows the effect of one-to-one scaling of the Froude and cavitation number upon the truncated-cone cavities. Here $\rho' = 0.4$ for the prototype and 0.2 for the model. Both the photographs and the cavity-mouth curves show that the prototype cavity mouth is beginning to close at the end of the photographic record, while the mouth of the model cavity is still growing. The data show that satisfactory modeling of surface closures does not result when ρ' is not scaled.

The change in missile attitude at water entry, measured from the whip records, was found to be independent of scaling conditions. The change in missile yaw angle was negligible. From the data available, the undercavity seems

159
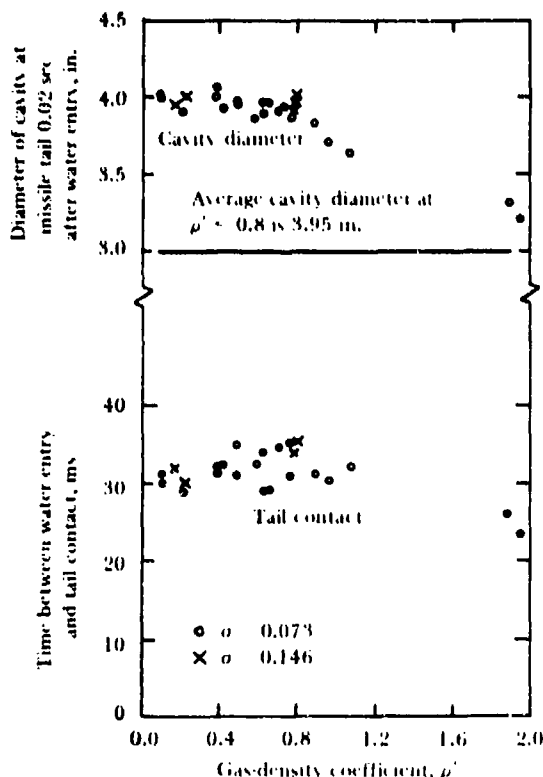
Figure 9.15. Effect of gas-density coefficient on truncated-cone prototype cavity diameter. F 51.8, f 39 degrees.

to be insensitive to scaling condition. The slope of the cone appears to prevent elongation of the undercavity with decreasing atmospheric pressure, thereby preventing a reduction in whip similar to that experienced by the plate-cylinder missile (Chapter 6). The whip of this head shape might profitably be studied over a wide range of entry conditions; it is unusual to find whip independent of cavitation number.

Reference 102 indicates that the first 20 diameters of trajectory are independent of gas density in the range $0.11 < \rho' < 1.95$ but may be affected by gas densities above $\rho' = 2.0$. The inclination of the missile axis was also found to be independent of scaling conditions during the first 20 diameters of underwater travel.

Plate Cylinder Missile

In contrast to the truncated-cone missile, the plate-cylinder missile showed greater trajectory and attitude sensitivity to gas-density varia-

tions. Further, it was sensitive to changes in cavitation number; the truncated-cone missile was not.

The pitch of the plate-cylinder prototype increased with both gas-density coefficient and cavitation number, as shown in Figure 9.22, where the change in pitch is plotted as a function of time, and in Figure 9.23, where the change in pitch after 5 ms of underwater trajectory is presented as a function of the gas-density coefficient. Approximately equal increases in negative pitch were caused by changing the gas-density coefficient from 0.1 to 0.8 at a constant cavitation number of 0.073, and by changing the cavitation number from 0.073 to 0.146 at a constant gas-density coefficient of 0.8. The time between water entry and first contact between missile tail and top cavity wall decreased at higher gas-density coefficients and cavitation numbers, in keeping with the concurrent increase in negative pitch (Figure 9.24).

Increase in negative whip (i.e., pitch) with cavitation number had been observed in the oblique water entry of a 2-inch-diameter model with a plate-cylinder nose (Chapter 6), and some indication of increase in negative pitch with increase in gas-density coefficient also appears in the plate-cylinder data shown in Figure 7.7.

Flow separation is probably influenced by the density of the ambient gas. Because cavity closure is accelerated by increasing gas density, it is possible that undercavity sealing also occurs earlier, causing the undercavity to be smaller. This would increase the wetted underpressure area and explain the observed increase in negative pitch with gas-density coefficient.

During the first 15 diameters of underwater travel, the trajectory of the plate-cylinder prototype was independent of launching conditions. After approximately 20 diameters, the trajectory became flatter with decreasing gas-density coefficient or cavitation number, resulting in a vertical spread of three diameters in the trajectories after 28 diameters of horizontal travel. Figure 9.25 shows the relationship between missile trajectory and the inclination of the missile axis, which changes 9 degrees after 15 diameters of travel, although the trajectories at this point are very nearly the same. After 28 diameters of travel (Figure 9.26), the trajectories deviate only three diameters but the spread of the inclination curves is 40 degrees. The extreme sensitivity of the missile inclination

160

$\rho' = 0.81$
49 ms after water entry

$\sigma = 0.292$

$\rho' = 0.10$
52 ms after water entry

$\rho' = 0.21$
52 ms after water entry

$\rho' = 0.47$
50 ms after water entry

$\rho' = 0.81$
50 ms after water entry

$\sigma = 0.073$
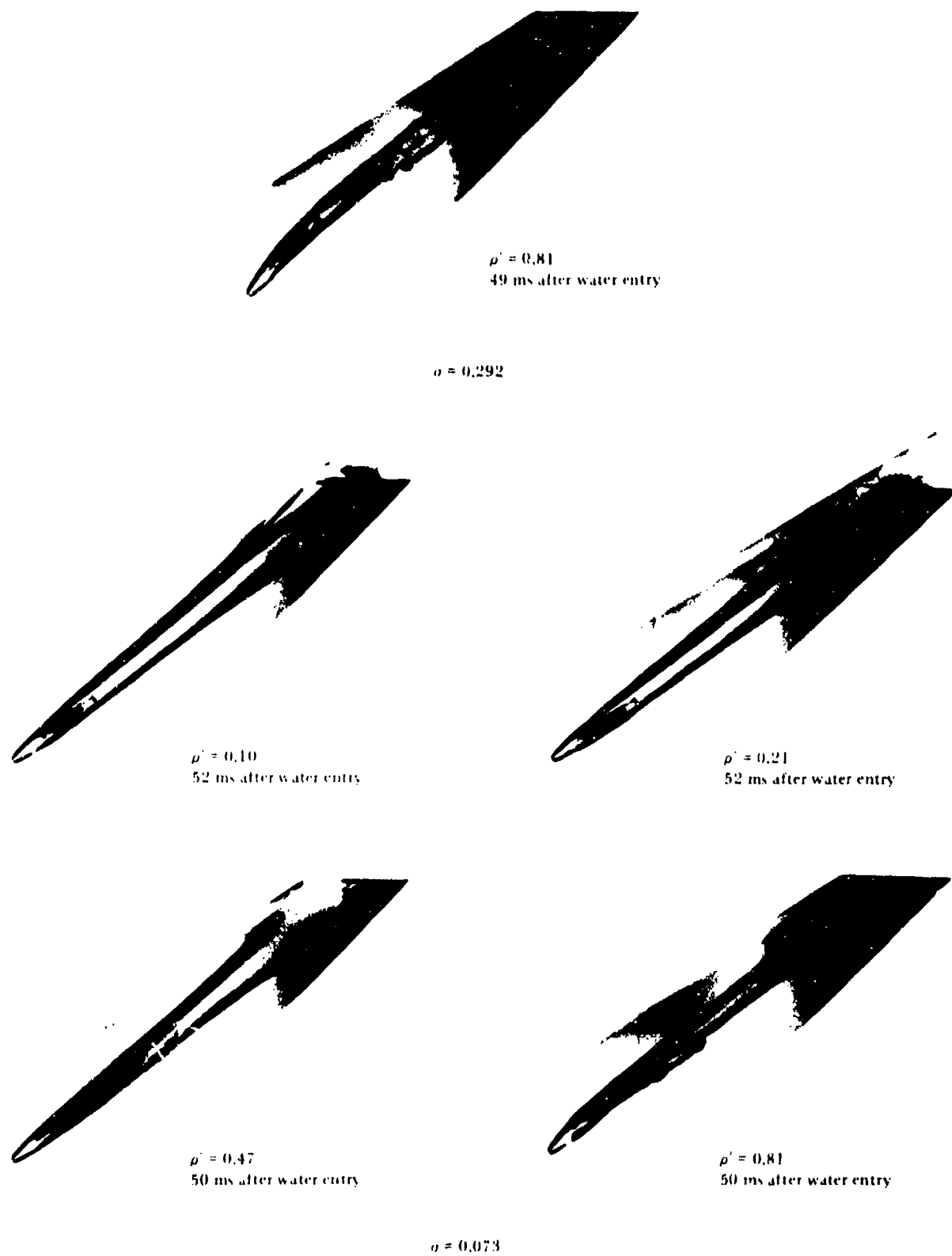
Figure 9.16. Typical truncated-cone model cavities. $F = 51.8, \xi = 39$; time in prototype scale.
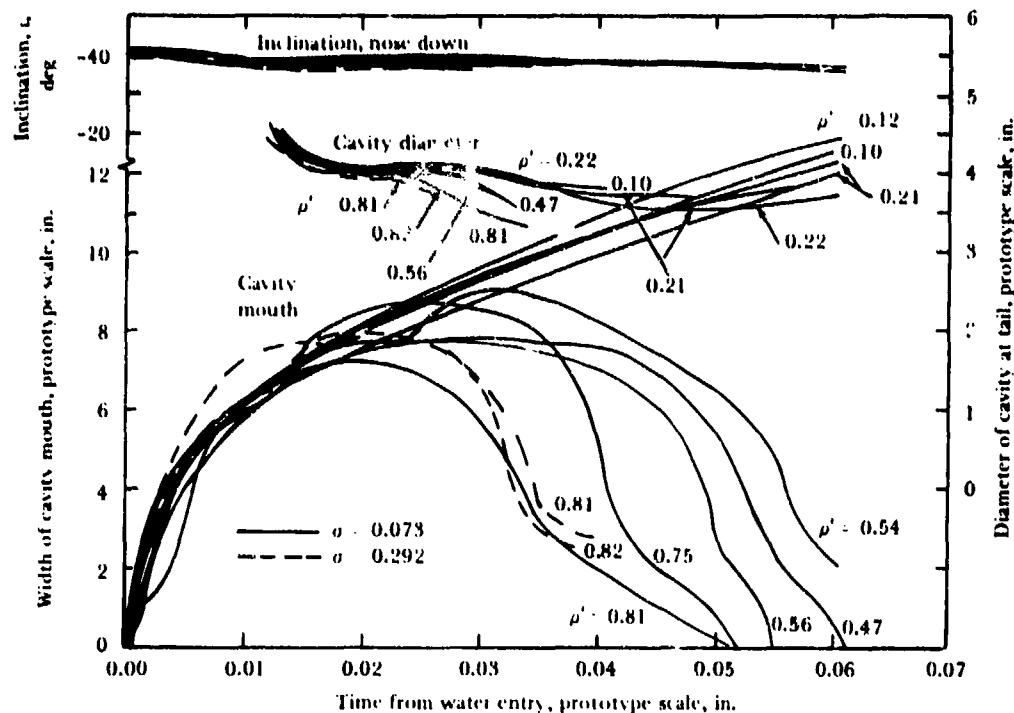
Figure 9.17. Effect on truncated-cone model of variation in gas-density coefficient from 0.10 to 0.82. Γ 51.8, ξ 39 degrees.

to changes in launching conditions is apparent in Figure 9.27.

The cavities formed by the plate-cylinder prototype under the various launching conditions were similar in appearance, all so wide that surface closure did not occur during the photographic record. Typical cavities, formed under various scaling conditions during the second series of launchings, are shown in Figure 9.28. Three photographs from each launching show that the cavities were still similar in appearance after 20 diameters of travel, and that differences appeared only as the cavities began to close about the missile, evidencing variations that probably affected missile position. Even rather small differences in the cavity assume significance because the cavities from duplicate launchings were so similar that their photographs at the same times after water entry appear to be two prints of the same negative (Figure 9.29).

Figure 9.30 reproduces average parameter curves for each launching condition. The width of the cavity mouth is the only parameter significantly affected by launching conditions, showing a maximum variation of 10% when the

gas-density coefficient was changed from 0.1 to 0.8.

Both trajectory and cavity of the plate-cylinder prototype were independent of launching conditions during the early portion of the trajectory, where model data were also obtained. All scaling techniques investigated resulted in modeling both cavity and trajectory.

Figure 9.31 presents typical photographs of the model and prototype cavities, taken at the same time after water entry. All the cavities are almost identical in appearance, except for the differences in cavity texture and the varying degrees of tail contact. The textures of the cavity wall are similar when the gas-density coefficient is scaled. At a constant cavitation number of 0.073, the walls of both model and prototype cavities are opaque when $\rho' = 0.8$ and transparent when $\rho' = 0.1$; at a constant gas-density coefficient of 0.8, the cavities were opaque at all cavitation numbers investigated. The clearing of the cavity wall is apparently an effect of gas density rather than of cavitation number.

Most of the launchings of the 1-inch-diameter plate-cylinder model were made with

162
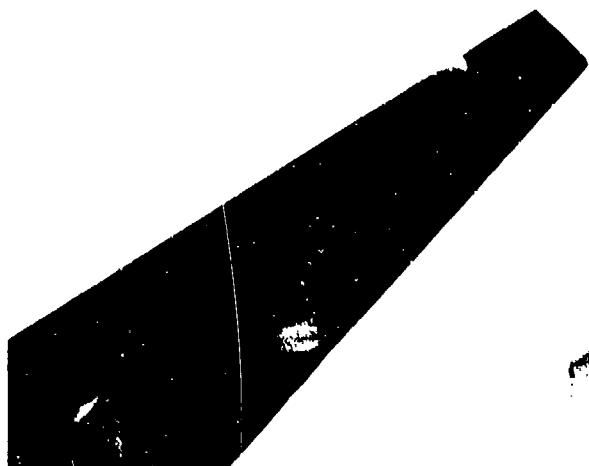
Prototype
33 ms after water entry

Prototype
32 ms after water entry
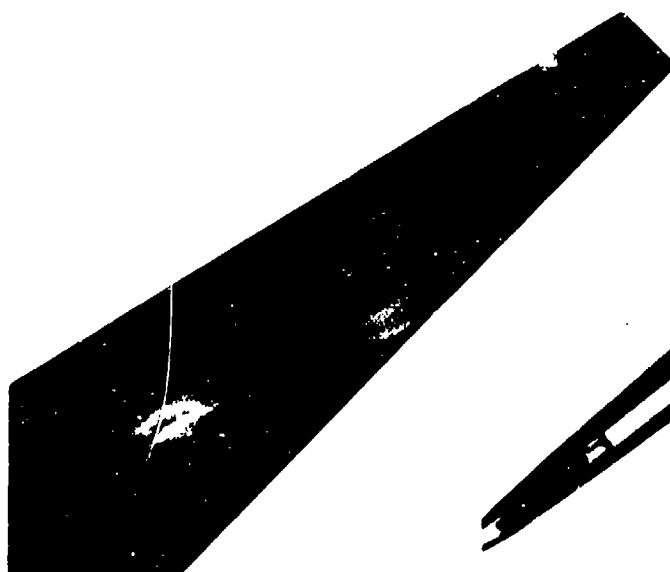
Prototype
47 ms after water entry

Model
44 ms after water entry

Figure 9.18a. Shape of truncated-cone missile oblique-entry cavities with $F = 51.8$, $\sigma = 0.073$, $\rho' = 0.1$, $\xi = 39$. Time in prototype scale.

163
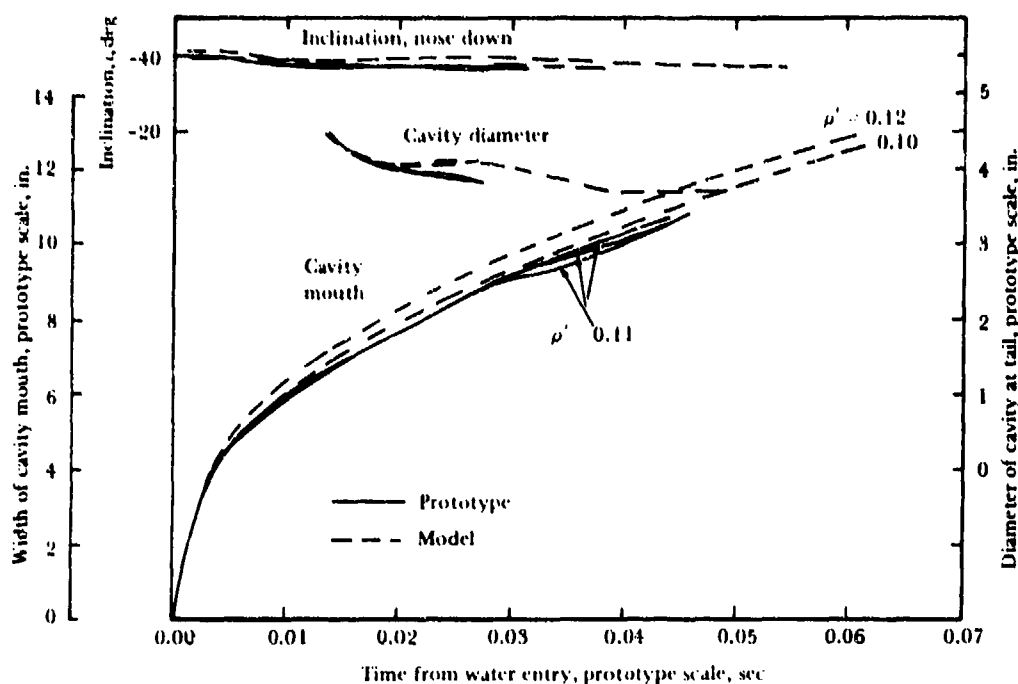
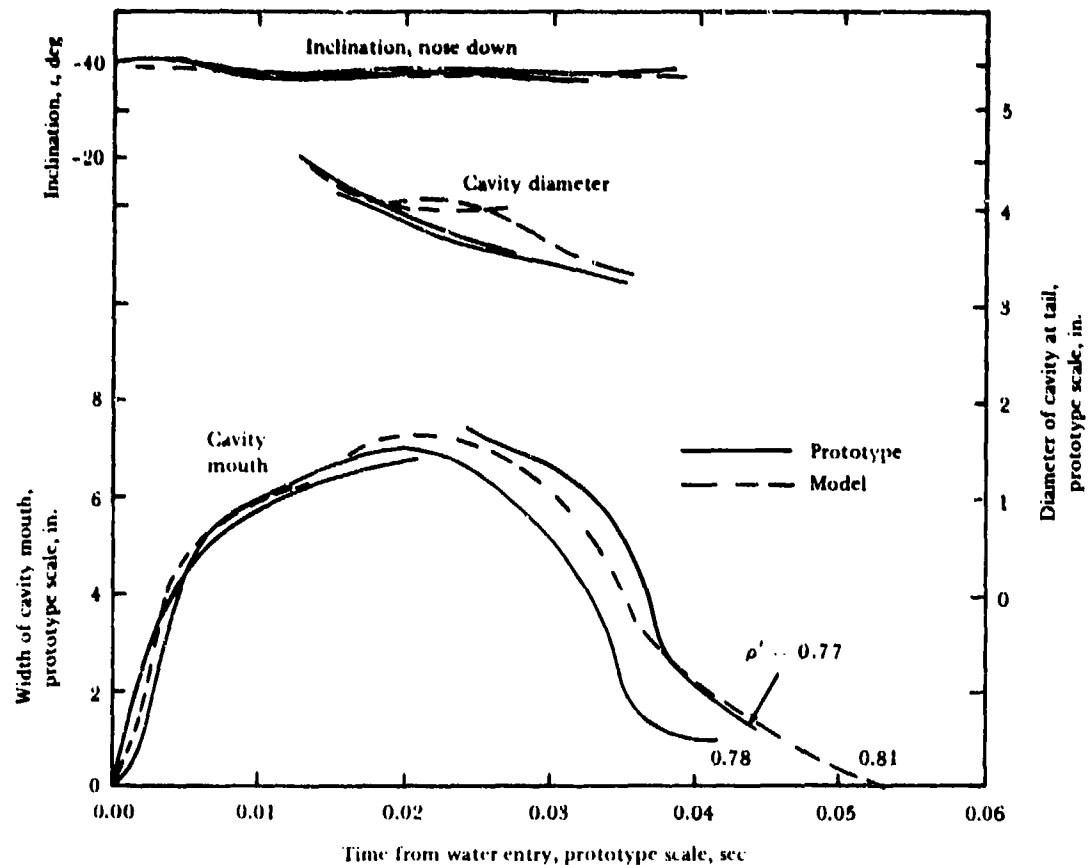Figure 9.18b. Curves for Figure 9.18a cavity parameters.

some initial nose-down pitch (Reference 102), which tended to make tail contact earlier and more violent. This in turn exaggerated the size of the tail cavity and frequently caused the tail bulge to break through the water surface (Figure 9.32). When this occurred, both the nose and tail cavities were measured. Cavity parameter curves from three launchings at the condition $F = 51.8$, $\sigma = 0.073$, and $\rho' = 0.8$, presented in Figure 9.33, show that the behavior of the nose cavities was independent of tail-cavity formation.

Average curves, presenting only model nose-cavity data from each scaling condition, are compared with each other in Figure 9.34; they can be compared with the corresponding prototype curves in Figure 9.30. The cavities formed by model and prototype under equal scaling conditions differ less than the cavities formed by the same missile under various launching conditions.

DISCUSSION OF RESULTS

This investigation showed that narrow water-entry cavities formed by the vertically launched hemisphere missile and the obliquely

launched truncated-cone missile were sensitive to variation in gas density. Gas-density scaling is necessary to obtain modeling. Modeling of the hemisphere cavity is somewhat improved by the addition of cavitation-number scaling. Accuracy in prediction of full-size cavities of this type is greatly improved by gas-density scaling. Good water-penetration-distance modeling was obtained for all modeling conditions studied.

Cavitation number may prove more important in scaling cavities formed by other missiles or cavities formed by these missiles under different entry conditions. Furthermore, modeling of later missile motion requires that the cavitation number be scaled (Chapter 8). The general insensitivity of the truncated-cone missile to change in cavitation number is probably related to the constant whip at water entry.

The plate-cylinder prototype data show that both cavitation number and gas-density coefficient influence the cavity, trajectory, and attitude of this obliquely launched missile beyond 15 diameters of underwater travel; hence, modeling cannot be expected unless both parameters, in addition to the Froude number, are scaled.

164

Prototype
35 ms after water entry

Model
33 ms after water entry

Prototype
49 ms after water entry
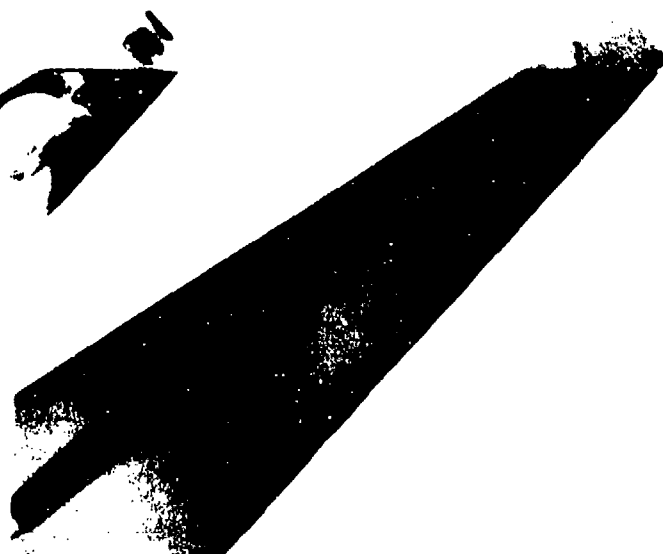
Model
48 ms after water entry

Figure 9.19a. Shape of truncated-cone missile oblique-entry cavities with $F = 51.8$, $\sigma = 0.073$, $\rho' = 0.8$, $\xi = 39°$. Time in prototype scale.

165

Figure 9.19b. Curves for Figure 9.19a cavity parameters.

The studies demonstrated that gas-density scaling, in conjunction with Froude and cavitation-number scaling, is generally necessary for water-entry cavity modeling, which is necessary for modeling the behavior of the missile in its underwater trajectory in the cavity. Since cavitation-number scaling in conjunction with Froude-number scaling is required for modeling missile oblique water-entry motion, cavitation-number scaling and gas-density scaling in conjunction with Froude-number scaling are probably required for simultaneous modeling of missile behavior during water entry and during underwater trajectory in the cavity.

166
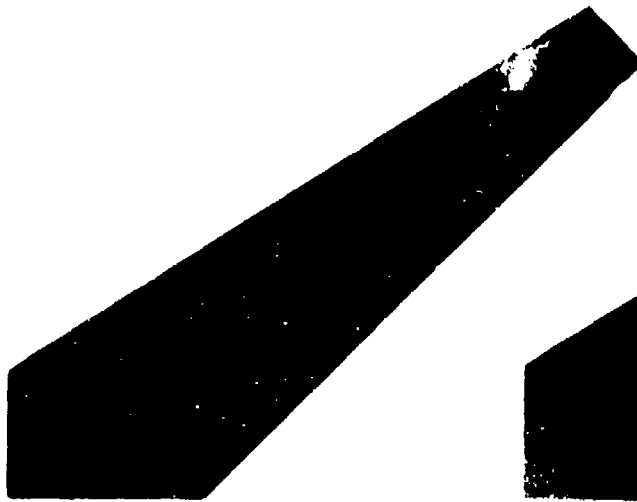
Prototype
37 ms after water entry
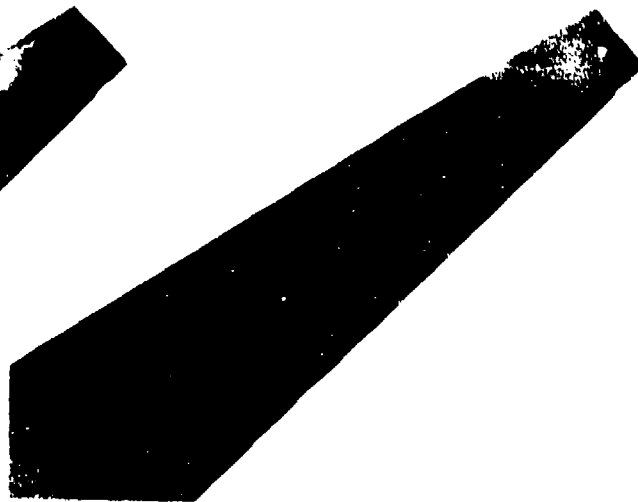
Model
35 ms after water entry

Prototype
47 ms after water entry

Model
46 ms after water entry

Figure 9.20a. Shape of truncated-cone missile oblique-entry cavities with $F = 51.8$, $\sigma = 0.146$, for the prototype and 0.292 for the model, $\rho' = 0.8$, $\xi = 39°$. Time in prototype scale.

167
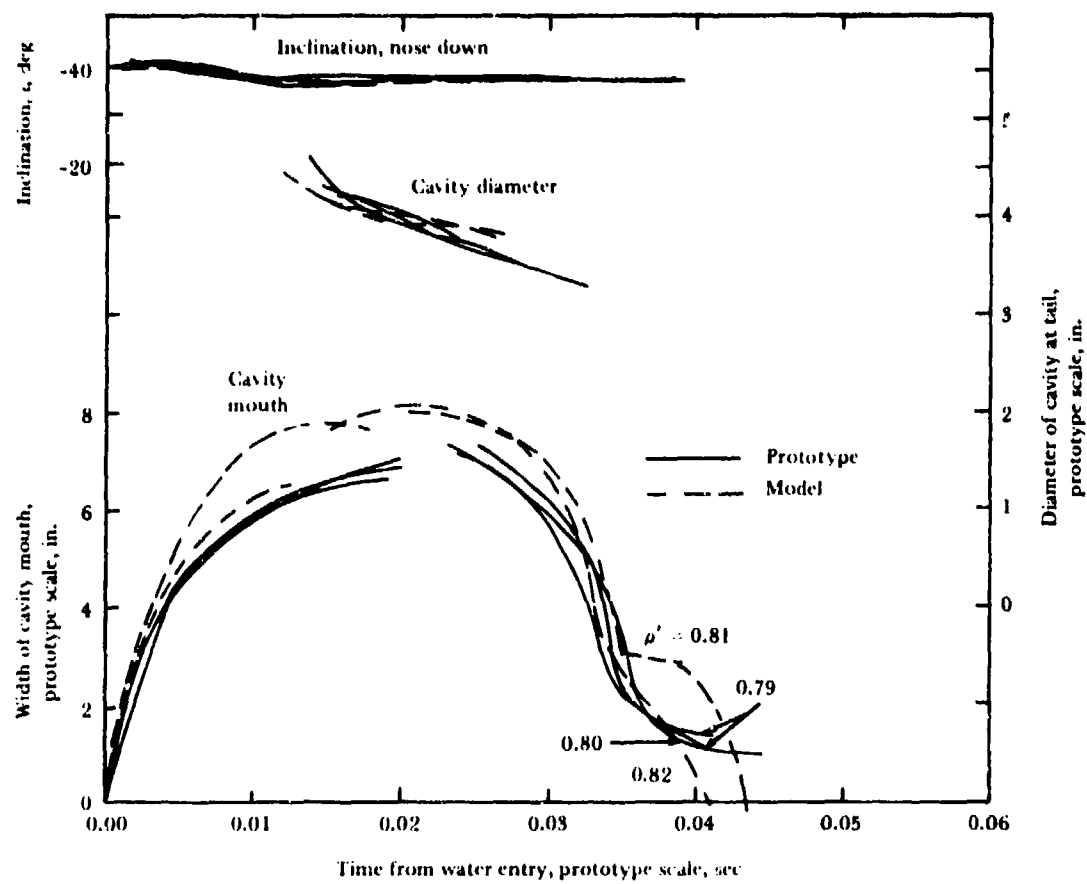
Figure 9.20b. Curves for Figure 9.20a cavity parameters.
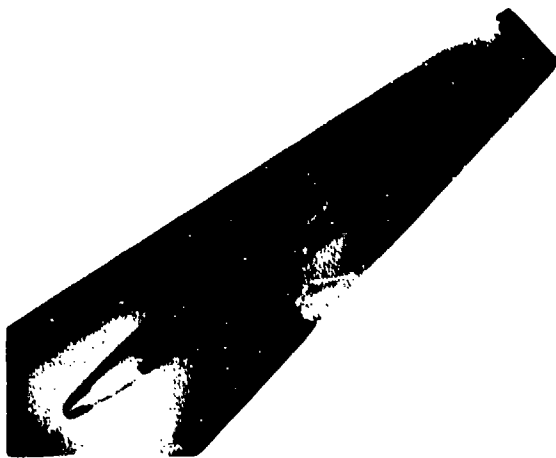
168

Prototype
35 ms after water entry
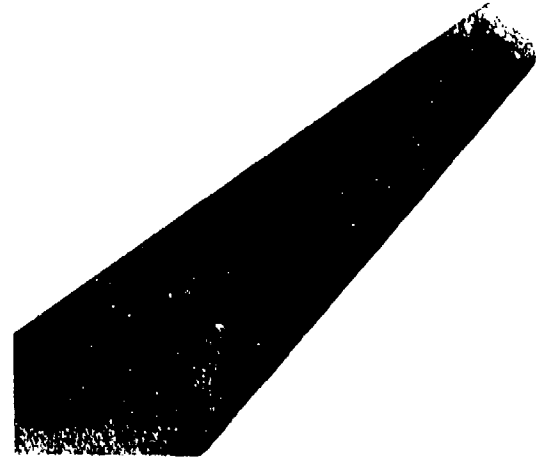
Model
35 ms after water entry

Prototype
49 ms after water entry

Model
49 ms after water entry

Figure 9.21a. Shape of truncated-cone missile oblique-entry cavities with $F = 51.8$, $\sigma = 0.073$, and $\rho' = 0.4$ for the prototype, and 0.2 for the model, $\xi = -39°$. Time in prototype scale.

169
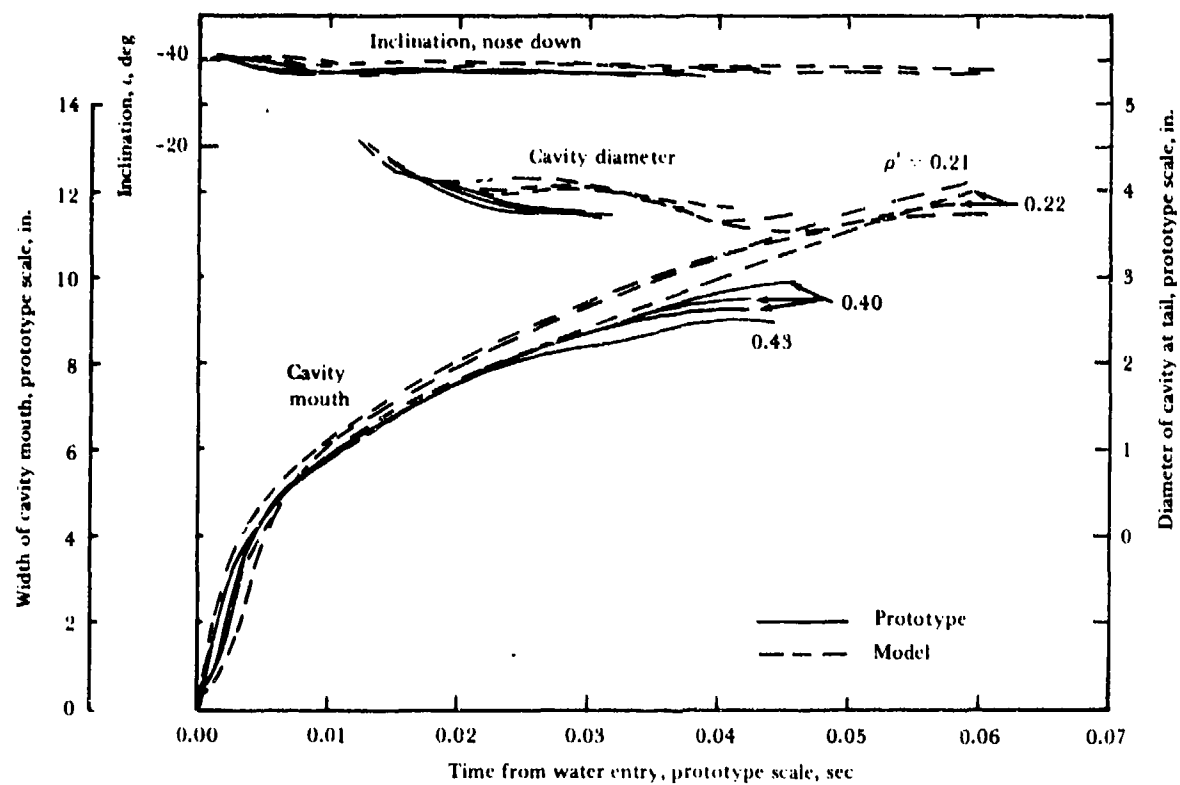
Figure 9.21b. Curves for Figure 9.21a cavity parameters.
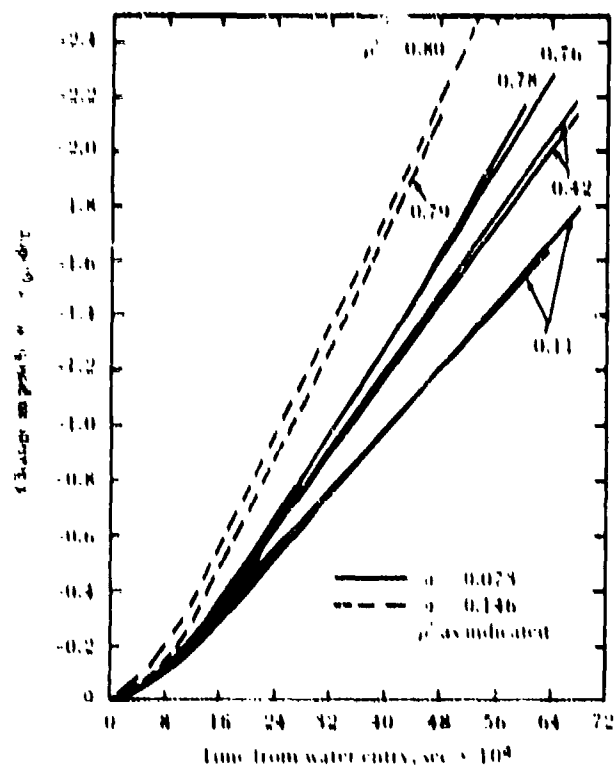
Figure 9.22. Change in pitch after water entry of plate-cylinder prototype, with F = 51.8, t = 20 degrees.
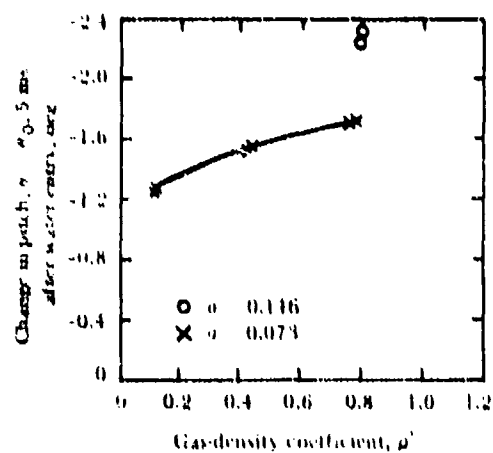
Figure 9.23. Change in pitch 5 ms after water entry of plate-cylinder prototype. F = 51.8, t = 20 degrees.

Figure 9.24. Time between water entry of plate-cylinder prototype and first contact of tail with cavity wall. F = 51.8, t = 20 degrees.
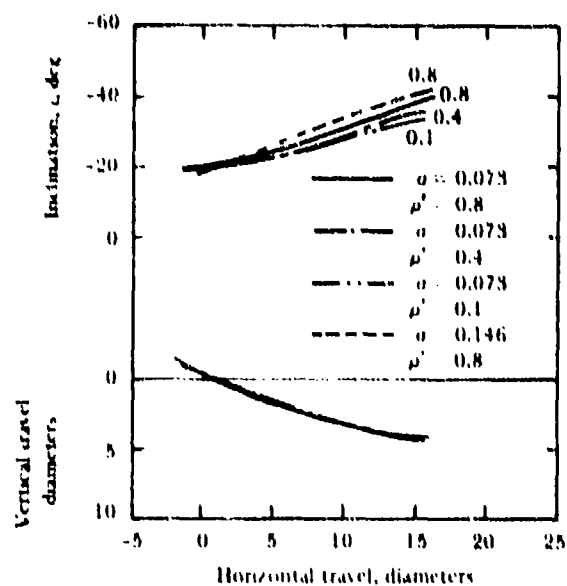
Figure 9.25. Trajectory of plate-cylinder prototype during first 15 diameters of underwater travel. F = 51.8, t = 20 degrees.

Figure 9.26. Trajectory of plate-cylinder prototype between 20 and 28 diameters of underwater travel. F 51.8, ↓ 20 degrees.
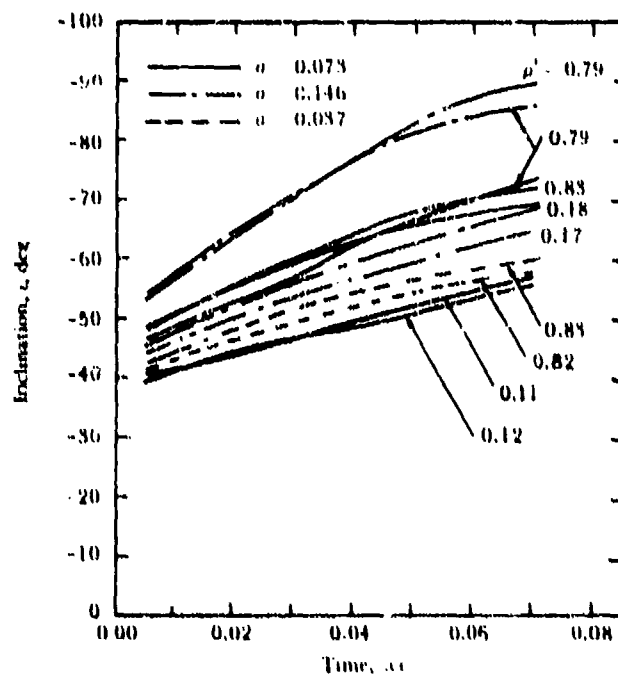
Figure 9.27. Effect of scaling condition on inclination of plate-cylinder prototype. F 51.8, ↓ 20 degrees.

172

F = 51.8
σ = 0.146
p' = 0.17

F = 51.8
σ = 0.036
p' = 0.82

F = 51.8
σ = 0.073
p' = 0.11

F = 51.8
σ = 0.073
p' = 0.63

F = 51.8
σ = 0.146
p' = 0.79
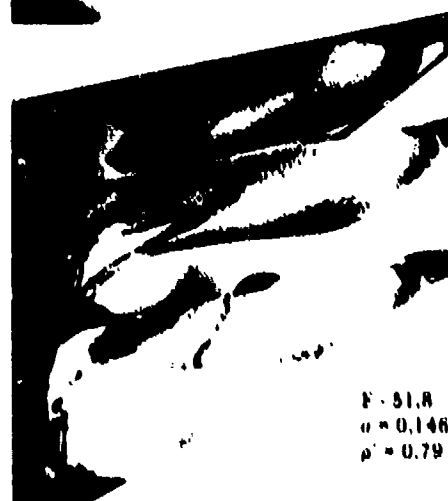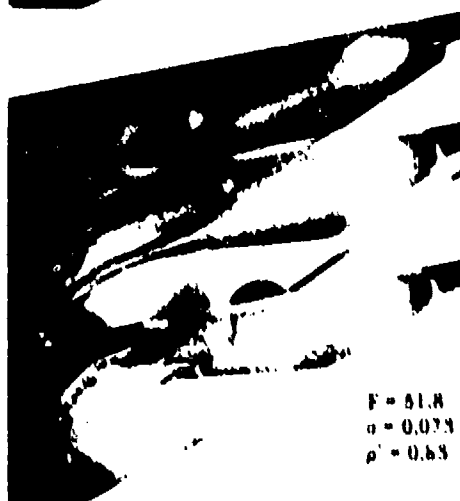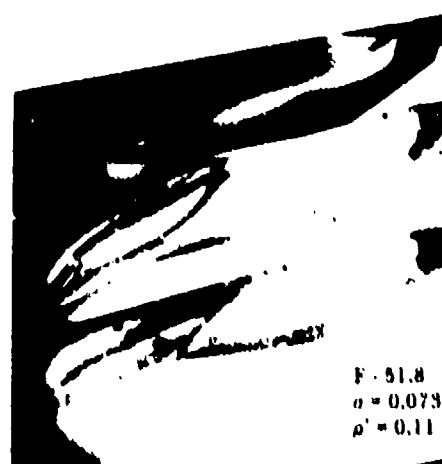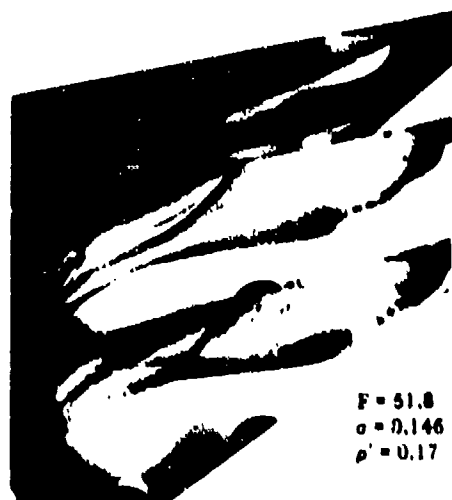
Figure 9.28. Effect of scaling condition on plate-cylinder prototype cavity, θ = 80°. Photographed about 120, 170, and 190 ms after water entry.

F - 51.8
σ = 0.146
ρ' = 0.79
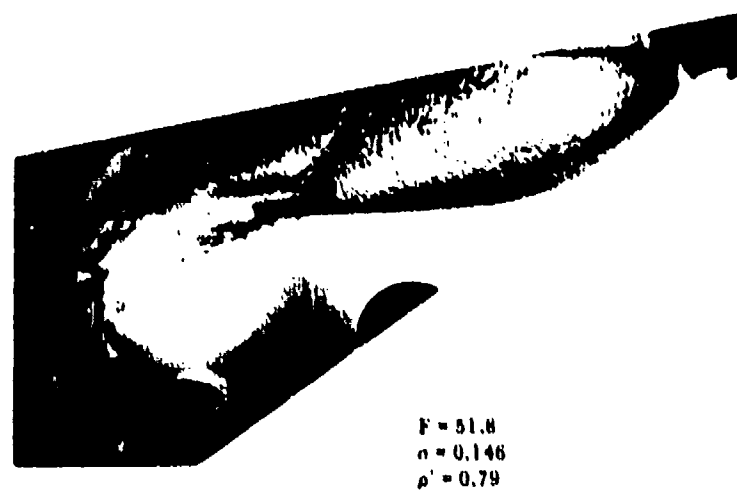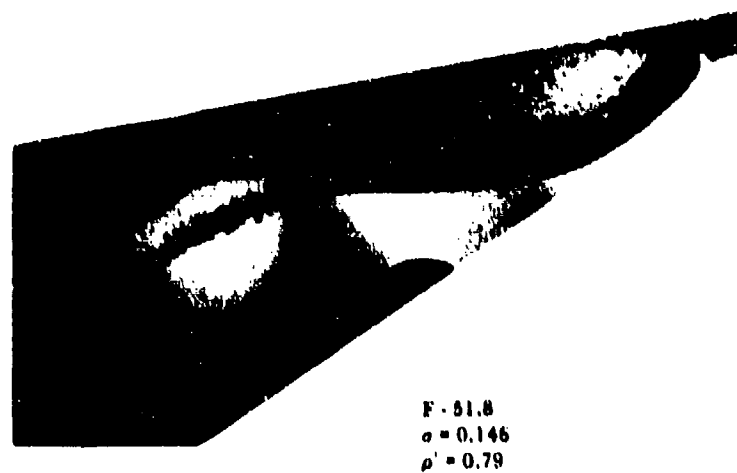
F = 51.8
σ = 0.146
ρ' = 0.79

Figure 9.29. Cavity similarity of two plate-cylinder missile launchings under the same conditions. ξ = 20".

174
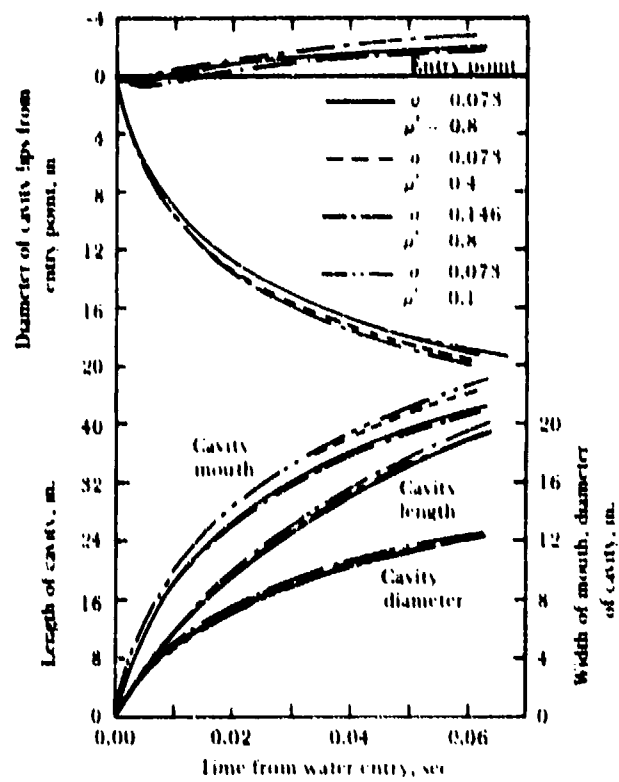
Figure 9.30. Effect of launching conditions on plate-cylinder prototype cavities. $F = 51.8$, $t = 20$ degrees.

175
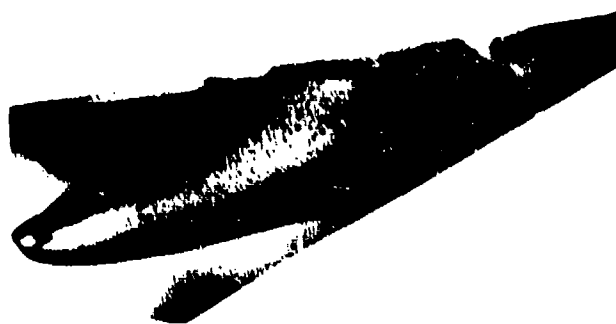
Prototype
57 ms after water entry

Model
57 ms after water entry

$\rho' = 0.8$

Prototype
57 ms after water entry

Model
57 ms after water entry

$\rho' = 0.1$

Figure 9.31. Effects of scaling conditions on plate-cylinder missile cavities,
F = 51.8, σ = 0.073, ξ = 20°. Time in prototype scale
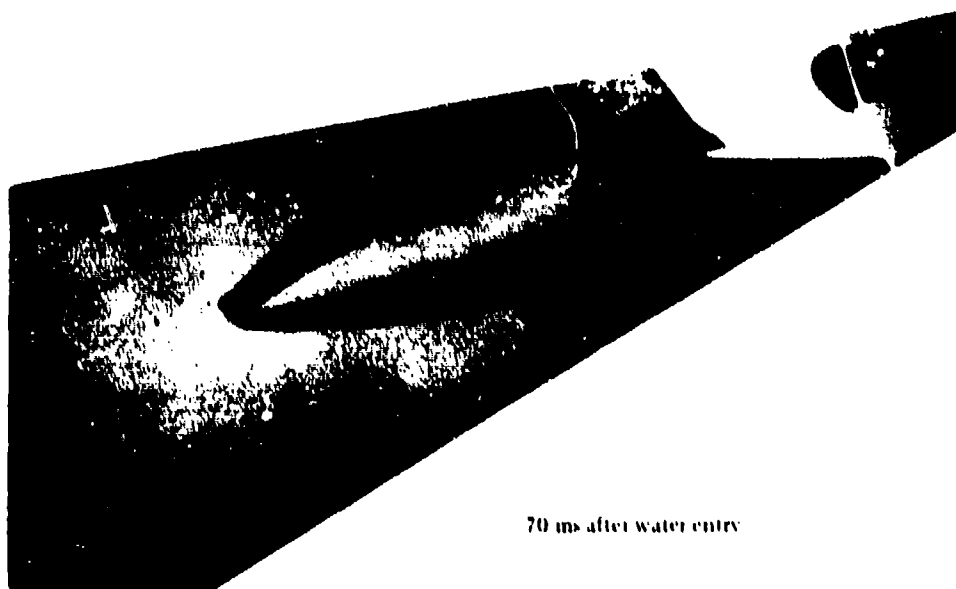
70 ms after water entry

Figure 9.82. Tail cavity of plate-cylinder model breaking water surface, with t = 20 . Time in prototype scale.
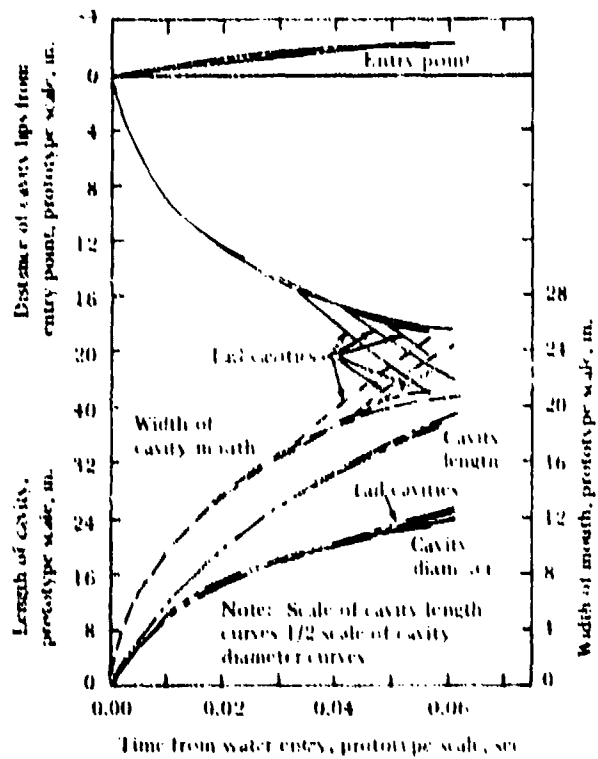
Figure 9.83. Plate-cylinder model nose-cavity behavior versus tail-cavity behavior, with F = 51.8, σ = 0.073 ρ' = 0.8, t = 20 degrees.
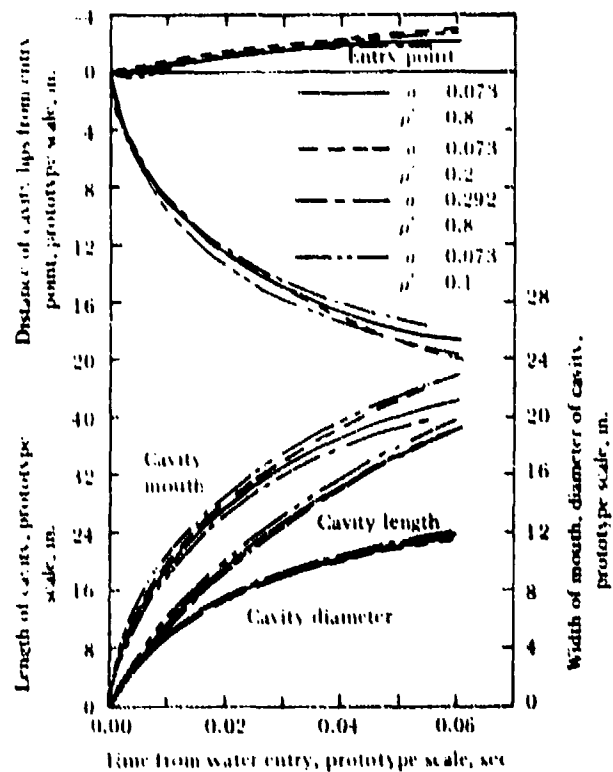
Figure 9.84. Effect of scaling condition on plate-cylinder model nose-cavity parameters, with F = 51.8, t = 20 degrees.

177

CHAPTER 10
EXPLORATORY EARTH-ENTRY STUDIES

The major forces affecting a missile in earth-entry would presumably be similar to those in water entry and consist of deceleration forces, cross-forces on the head and stabilizing forces on the body and tail. It was of interest to apply the techniques developed in water-entry studies to earth-entry studies in the NUC Hydroballistics Laboratory. They consisted of launches into clean ungraded beach sand, a simple soil of fairly homogeneous composition, which yielded data on missile sand-entry whip (change in pitch velocity) and "splash."

A box of sand was placed in the Open Launching Tank (Figure 10.1). Two nested boxes were used (Figure 10.2), the outer one constructed of 3/4-inch plywood over a 2-inch angle-iron frame with a plate-glass window on one side. The lid had an opening in the upper
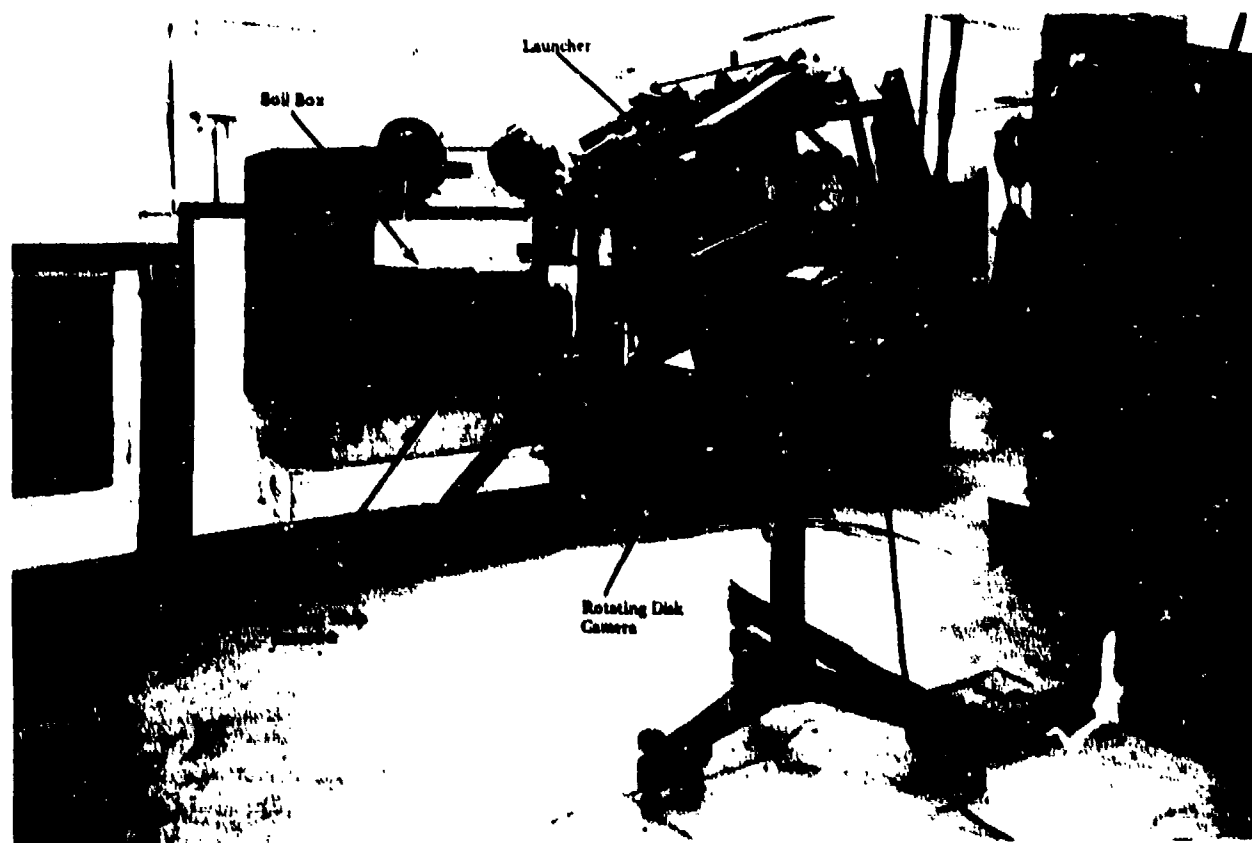
Figure 10.1. Laboratory setup for earth-entry studies.
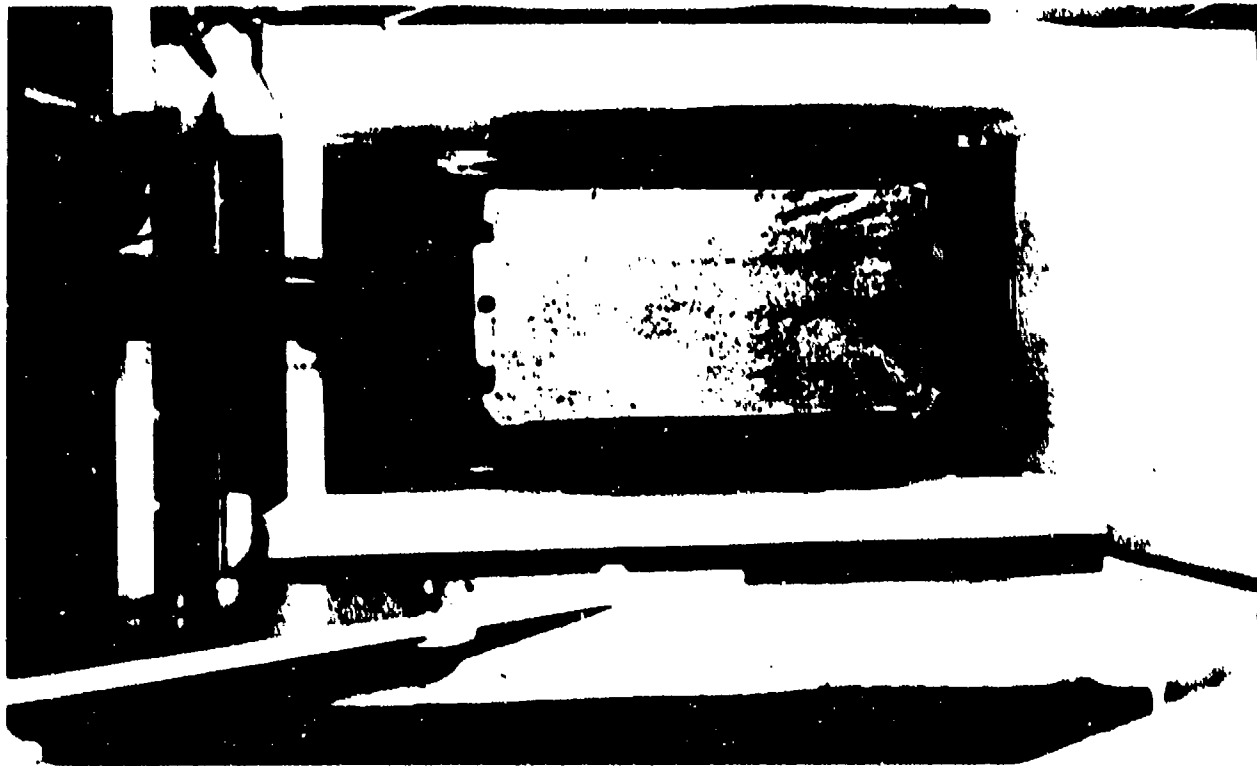
Figure 10.2. Nested test boxes.

front to allow missile entry and to admit light for the optical whip recorder (Part V). The interior was painted white to reflect light for photography. The inner box was made of sheet metal, 24 inches long, 12 inches wide, and 12 inches deep.

The sand was sifted through ordinary window screen. For dry sand tests, the inside box was filled to the top, packed down, and the excess sand scraped off to leave a smooth level surface. For wet sand tests, the hard-packed sand was thoroughly soaked with water, allowed to stand for some time, and the surface rewetted just before firing. This procedure was followed so that the condition of the sand would remain reproducible.

The missile was a cylinder 6 inches long and 1 inch in diameter with a 1-diameter ogive nose (Figure 10.3). It was made of case-hardened steel hollowed out to reduce the weight to 0.5 pound, with a small rear mirror for the whip records (Part V). The center of gravity was 3.28 inches from the tip of the nose; the moment of inertia was 1.86 lb in^2.

The missile was propelled into the sand at a nominal velocity of 100 fps from a catapult launcher (Part V). The velocity was measured by an electronic chronograph actuated by two photocell pickups; the whip of the missile at entry was recorded by the optical whip recorder.

Tests were made at 20- and 30-degree entry angles into both dry and wet sand. For each condition, three launchings were made: two for whip records and one for splash. Prior to launching, the missile was coated with a thin layer of machinist's Prussian blue; any color remaining on its surface at recovery was considered evidence of cavity formation. After each shot, the sand was removed with great care in order not to disturb the missile because its final position in the box supplied information on depth of penetration, approximate trajectory, and average deceleration.

Similar launchings were made into water to allow direct comparisons between water- and sand-entry splash characteristics.

Figures 10.4, 10.5, and 10.6 show the launching of the missile along a 30-degree
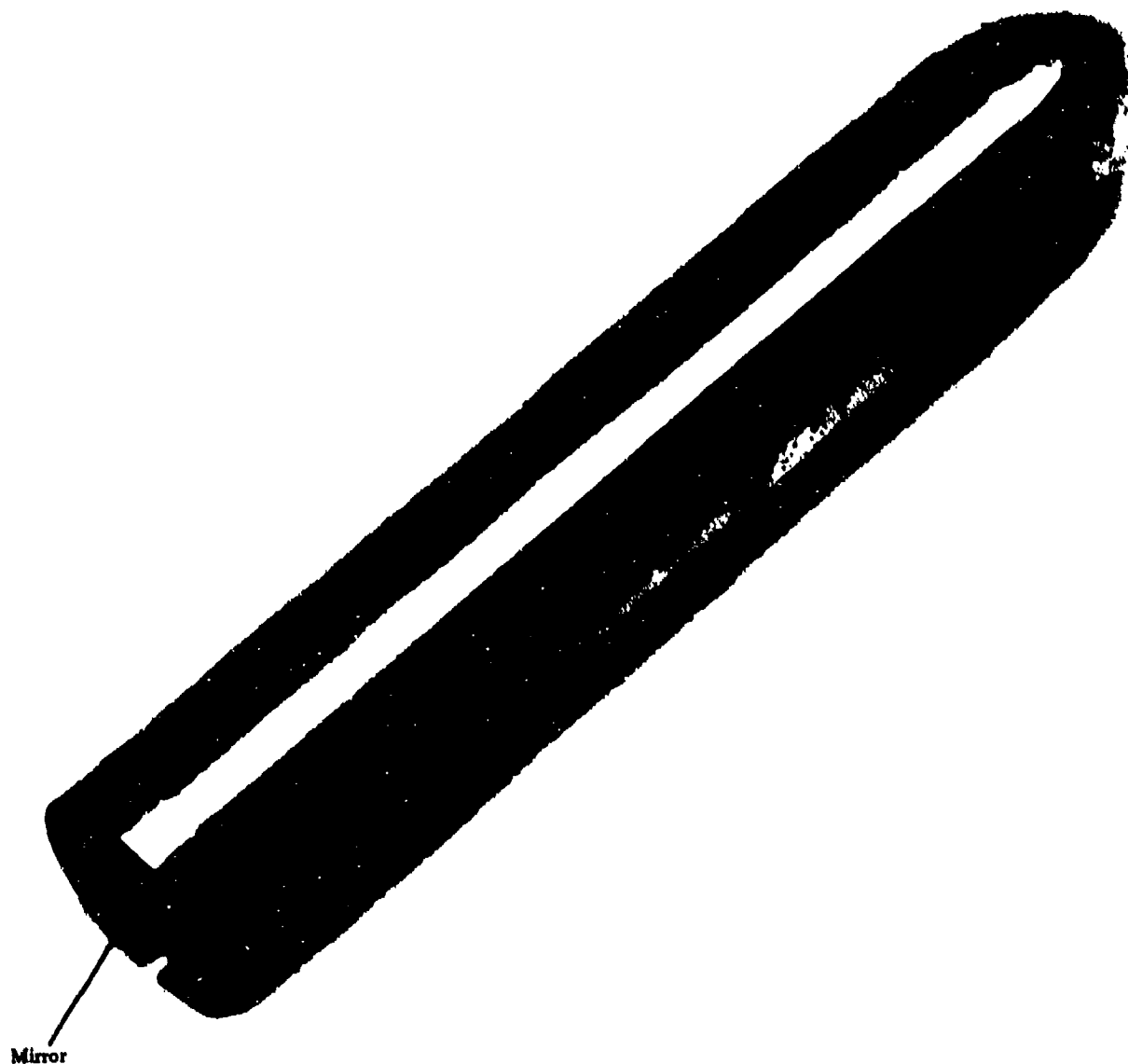
179

Figure 10.3. One-inch-diameter missile with mirror for whip records.

trajectory into wet sand, dry sand, and water, respectively. Similar splash contours occurred when the missile entered wet or dry sand, and there was little difference between them and the water-entry splashes. Figure 10.7 shows the surface of wet sand after the missile was fired into it; Figure 10.8 shows the final position of the missile after the sand had been removed.

After all launchings into sand, the Prussian blue was gone from the ogive nose and the lower rear of the model, but the color on the remaining portions was practically undisturbed, indicating that the model must have been enveloped in a cavity during most of the flight. The color pattern remaining after a 30-degree launching into dry sand is shown in Figure 10.9.
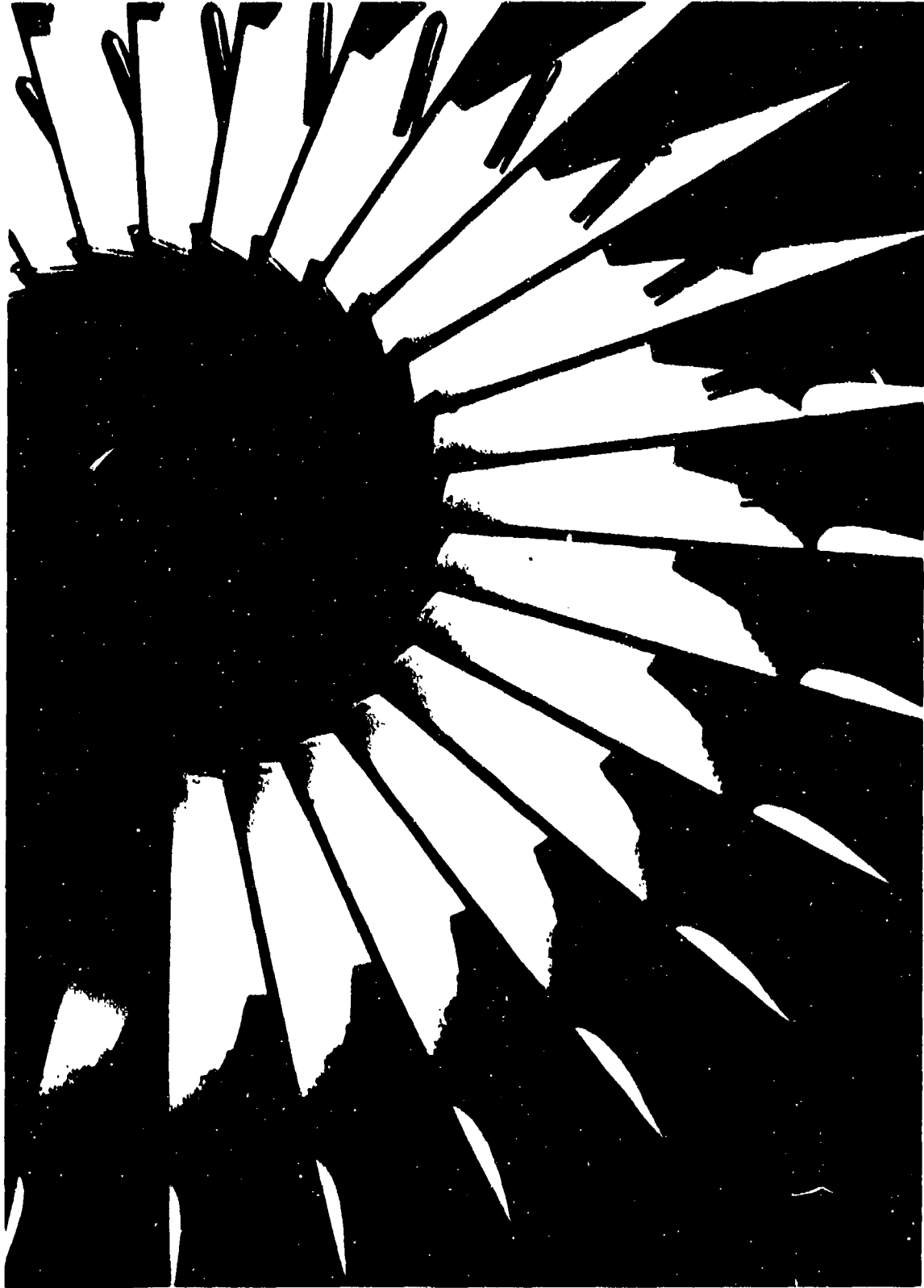
Figure 10.4. Missile entering wet sand at 30 degrees, 100 fps.

Figure 10.5. Missile entering dry sand at 30 degrees, 100 fps.
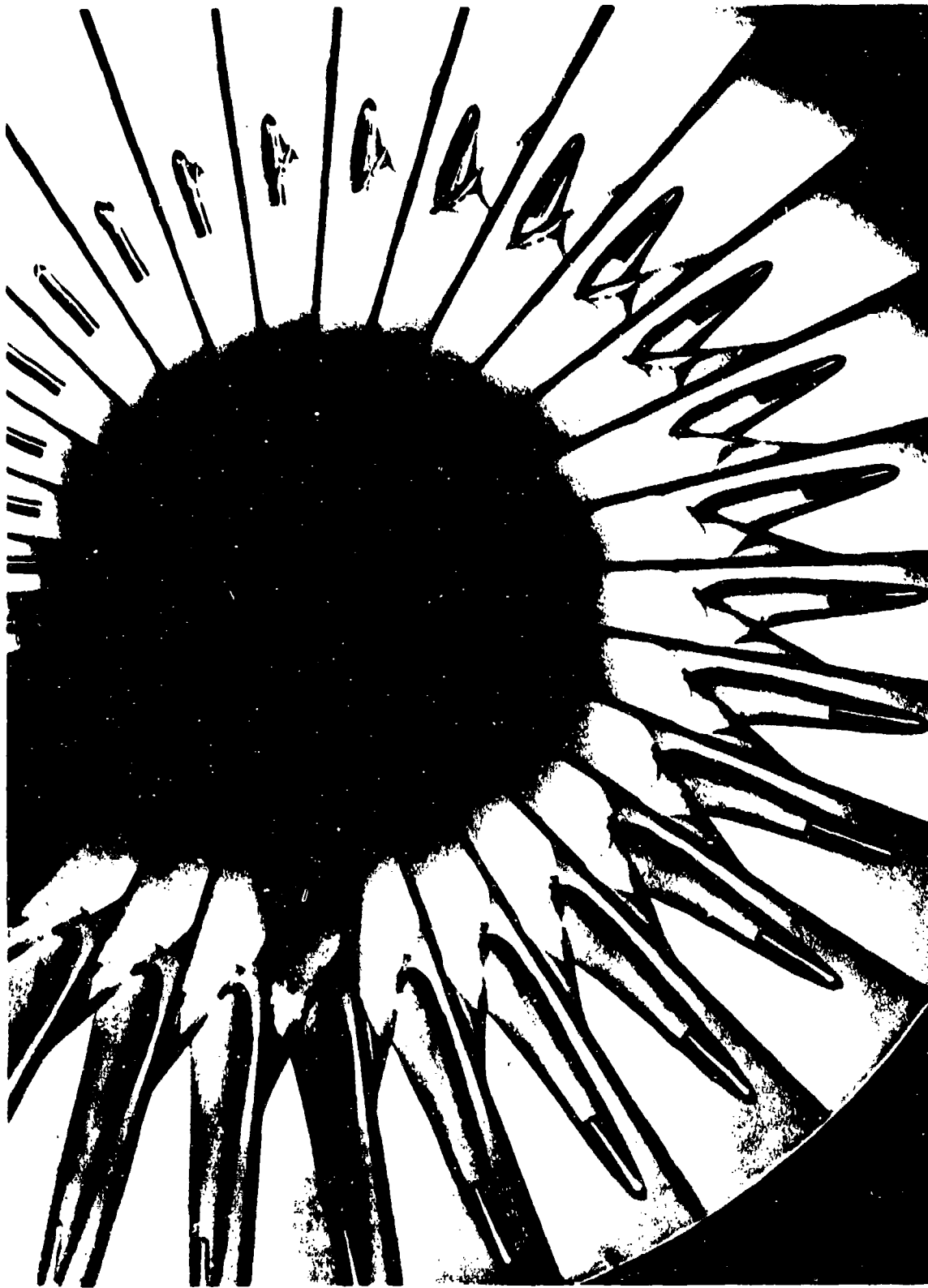
Figure 10.5. Missile entering water at 90 degrees, 100 fps.
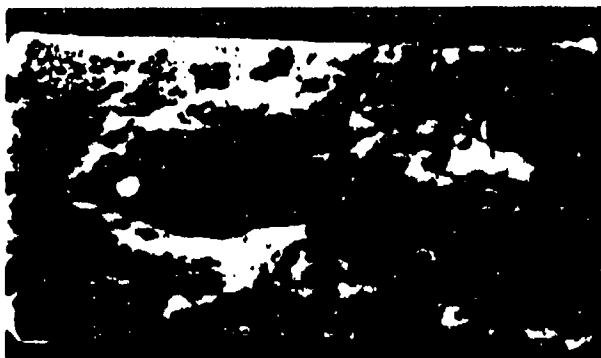
Figure 10.7. Surface of wet sand after missile impact at 30 degrees.
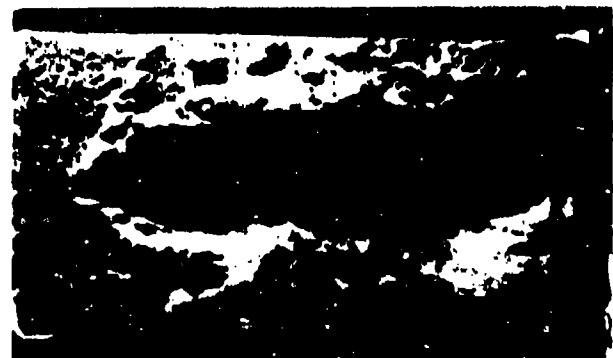
Figure 10.8. Sand removed to show missile.
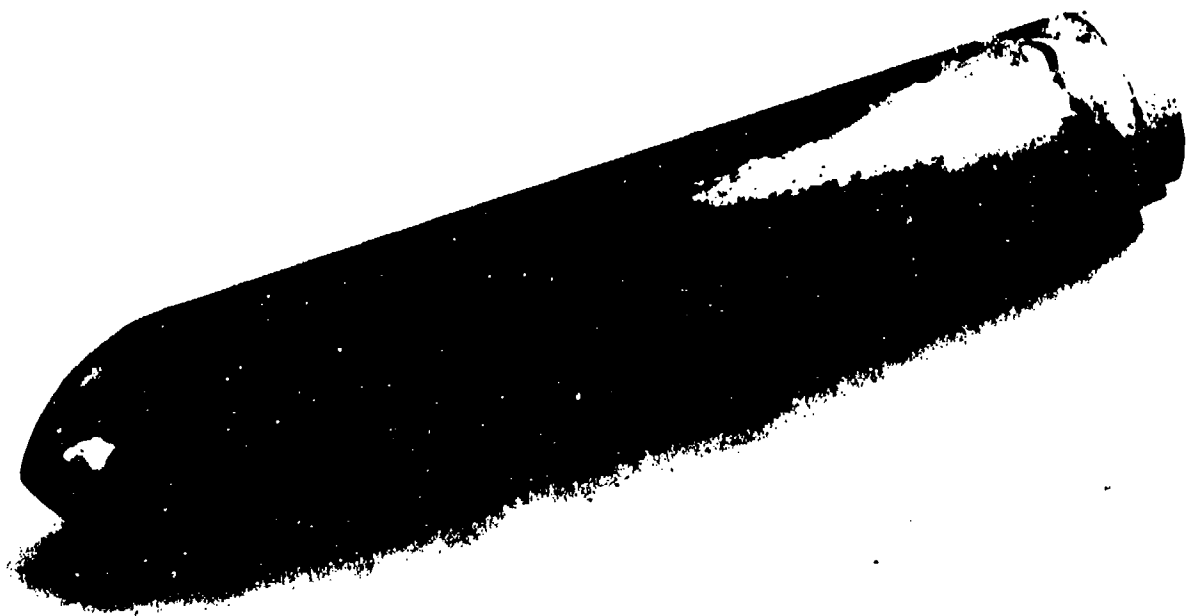
Figure 10.9. Erosion of 1-inch-diameter missile bottom by dry sand.

Measurements indicated that sand separation on the head took place about 0.8 projectile diameter aft along the underside of the missile, where lateral motion of the sand was restricted. Water-tunnel tests show separation 0.85 diameter aft when a cavity forms on this missile head shape in water (Reference 33). Since both sand and water can be assumed to leave the surface of the missile tangentially at separation, it is reasonable to expect the forward portions of the sand and water cavities to be similar in shape.

The missile experienced a positive (nose-up) whip at earth entry. In both wet and dry sand, the whip was greater at the 30-degree than

at the 20-degree trajectory angle (Figure 10.10). Calculations of the expected whip of this missile, based on tests of large-scale missiles in water and corrected for the density of the sand, gave a whip of 450 deg/sec.

Complete whip records were not obtained because the trace of the light ray reflected from the missile tail mirror of the optical whip recorder (Part V) moved off the camera lens before the whip-producing regime terminated. However, the pitch velocity curves of Figure 10.10 indicate that the whip is more than 1,500 deg/sec for the 20-degree entry and 2,000 deg/sec for the 30-degree entry.
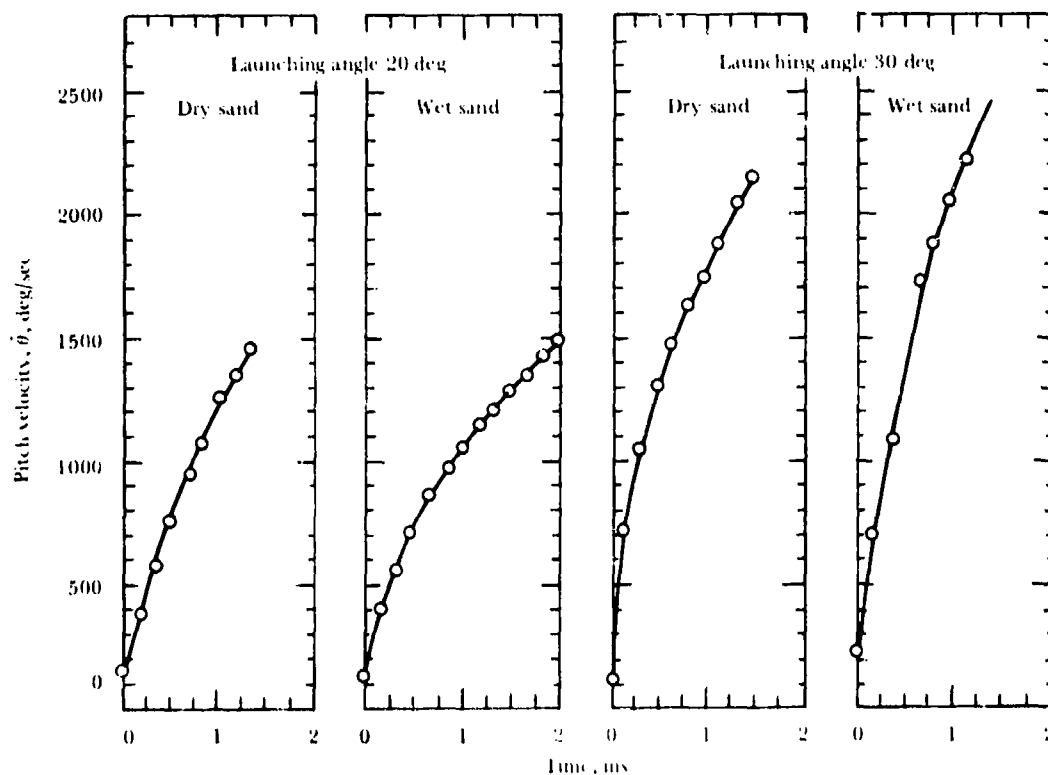
Figure 10.10. Whip measurements, Earth Entry Studies.

CHAPTER 11
WATER-EXIT STUDIES

The phenomena that occur when a missile exits from water into air differ from those that occur in water entry, and water exit cannot be regarded as water entry in reverse. The hydrodynamic flow pattern, varying as it does during exit, causes torques and forces that have no counterpart in water entry. The water-air interface "sees" a combined missile-cavity shape, causing even the missile configuration to be a variable. When water-exit is oblique, the force pattern is likely to be asymmetrical, causing a refraction of the missile trajectory and changes in orientation and angular velocity. Thus the water-exit behavior of a missile depends on many factors such as missile shape, ballistic parameters, velocity, trajectory angle, orientation, and the cavity.

The structural-strength requirements of a water-exit missile also differ from those of a water-entry vehicle. Instead of impact as at entry, there is an abrupt reduction of forces on the missile; these are likely to be asymmetrical and cause perturbations.

Studies were made of the ways in which change in trajectory angle and cavitation number affect the flight of 2-inch-diameter missiles exiting from still water into air. Repeatable perturbations, however, did not occur under presumably equal exit conditions; evidently some factors must have shown random fluctuations. Since studies of random phenomena must be statistical in nature, the number of launchings needed to predict missile performance depends upon the confidence level desired. Rather than concentrating on a few test conditions for statistical analysis, a wide range of conditions was investigated less thoroughly in order to obtain a picture of overall missile performance.

EXPERIMENTAL PROGRAM

The studies (References 103, 104, and 105) were made at the NUC Hydroballistics Laboratory in the Variable-Angle Variable-Pressure Launching Tank. Three missiles were used. The first (used most extensively) was a simple body having a grooved hemisphere head with a probe, a cylindrical midsection, and a spool-shaped tail. The second missile had a truncated-cone nose with a probe and a torpedo-type tail. The third missile, a composite of the other two, combined grooved hemisphere head with torpedo tail. Probes concentric with the missile axes were installed to permit good attitude measurements when the missiles themselves were obscured by cavitation.

The missile configurations are shown in Figure 11.1; their parameters are given in Table 11.1.

A specially designed underwater launcher was used to propel the missile without imparting any angle of attack or yaw or angular velocity, and, in addition, without introducing air or any extraneous substances such as hydraulic fluid or grease (Part V).

In order to remove any effects of abnormally high air content in the water on cavity behavior, the air content was reduced to below that of water at 20°C in equilibrium with air at 1-atmosphere pressure. De-aeration was accomplished by bubbling air through the water for at least an hour at 0.1 atmosphere. Tests with a Van Slyke manometric gas analyzer (Reference 62) showed that the air content of the de-aerated water was reduced to at least two thirds that of water at 20°C in equilibrium with air at 1-atmosphere pressure.
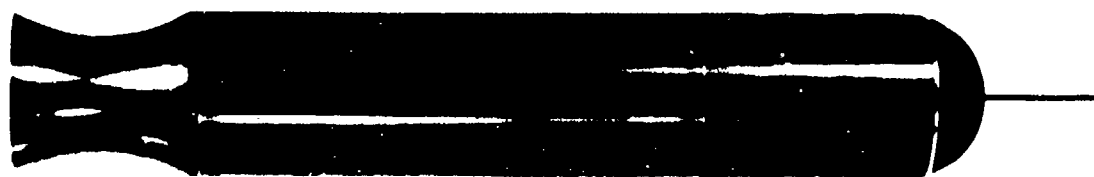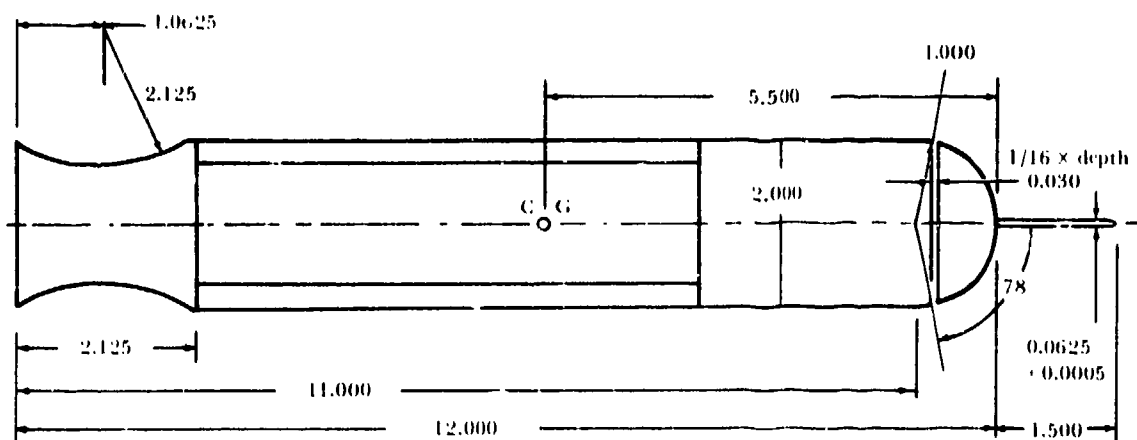
Hemisphere

Truncated cone

Composite

Figure 11.1. Missile configurations. Dimensions in inches.

TABLE 11.1. Missile Parameters

Parameter	Hemisphere	Truncated Cone	Composite
Diameter, in.	$2.000 \begin{smallmatrix}+0.000\\-0.001\end{smallmatrix}$	$2.000 \begin{smallmatrix}+0.000\\-0.001\end{smallmatrix}$	$2.000 \begin{smallmatrix}+0.000\\-0.001\end{smallmatrix}$
Length, [a] in.	12.004 ± 0.040	12.845	12.90
Mass, lb	1.275 ± 0.001	1.327 - 1.332	1.268 - 1.275
Distance from CG to nose, [a] in.	5.50	5.00	5.38
Moment of inertia, [b] lb-in^2	12.018	18.33	15.104

[a] Excluding probe.

[b] About a transverse axis through the CG.

Sideview water-exit data were obtained with a rotating-disk camera (Part V) and Edgerton-type stroboscopic flash lamps adjusted to give multiple exposures at a frequency of 250 per second, i.e., at an interval of 4 ms between frames. The rotating-disk camera was positioned so that its axis was normal to the plane of the tank window and passed through the point of intersection of the water surface and the projected tank centerline. The range of missile positions over the exposure sequence was adjusted by means of a time-delay apparatus that triggered the flash lamps at an appropriate time after launcher actuation.

Several launchings were made at trajectory angles of 75 and 90 degrees, using two cameras. Perturbations occurred in both planes and were generally of comparable magnitude and randomness.

The photographic data were reduced and plotted as functions of time from water exit. Missile position was measured at the junction of the probe and the missile nose. The time of water exit is defined as the instant at which the junction of the probe and the missile intersects the plane of the undisturbed water surface. Figure 11.2 presents data from a typical launching.

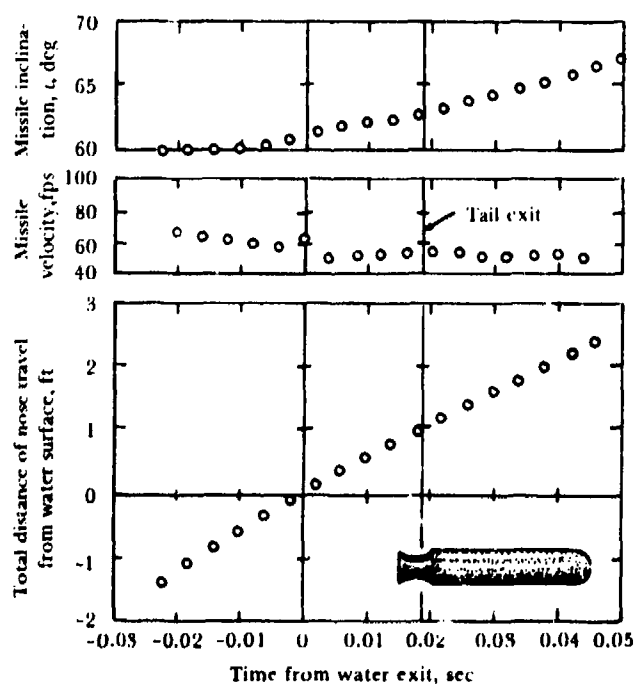One-to-one Froude- and cavitation-number scaling was assumed for modeling water exit in

Figure 11.2. Data from typical underwater launching of hemisphere missile.

the turbulent-flow regime where Reynolds-number scaling could be ignored. Gas-density scaling, although required for some conditions in water-entry modeling (Chapters 7 and 9), could be ignored here because, at exit, the system of forces acting upon the missile is made up of large water forces established during the underwater trajectory. The density of the water is on the order of 10^3 to 10^4 times that of the tank atmosphere. Thus, inertial and aerodynamic pressure-reduction forces that are directly dependent upon the atmospheric density are not apt to be significant in altering a force system already established by the water. It was found experimentally that variations in the gas-density coefficient, p', from 0.20 to 1.18 made no significant difference in the water-exit perturbation.

An exit velocity of 60 fps, the limit of the launcher mechanism, was used. This velocity was slightly below that necessary to produce turbulent flow over a hemispherical missile nose (Reynolds number 9.7 x 10^5, Reference 23). The consistent results obtained when a 2-inch model with its nose artificially roughened (Chapter 8) was operated in a 50- to 60-fps water-entry velocity range prompted the decision to use a missile with a roughened nose for these tests.

However, preliminary tests of a hemisphere missile without groove or probe showed that 60-fps exit velocity did not produce turbulent flow; instead, it gave rise to sporadic disturbances ahead of the zone of cavity separation that caused erratic cavities in some instances and hence large exit perturbations.

Turbulent flow was triggered artificially by providing a concentric groove cut in the missile nose at the approximate zone of cavity separation, as shown at the top of Figure 11.1. The groove helped to stabilize the cavity and prevent erratic cavity formation.

Launchings of the hemisphere missile with groove and probe were made over a wide range: the trajectory angle was varied from 90 degrees (vertical) to 15 degrees above the horizontal in 15-degree increments, and the cavitation numbers were selected to give flow regimes varying from nearly fully wetted to fully enveloping

cavitation. The test conditions consisted of all combinations of the following parameters:

Trajectory launching angle, ξ, deg	90, 75, 60, 45, 30, 15
Cavitation number[1] σ	0.576, 0.431, 0.289, 0.106, 0.045
Water-exit velocity, v_e, fps	53 to 63

At least three launchings were made at each test condition.

EXPERIMENTAL RESULTS

Hemisphere Missile

The hemisphere missile trajectories were not greatly perturbed by water exit. A maximum spread of about 1/6 foot (one missile diameter) occurred after about 2 1/2 feet of air travel (Figure 11.3).

Perturbations in missile attitude occurring at water exit were observed under all degrees of cavitation and at all trajectory angles investigated. At first glance, the magnitude and direction of the perturbations appeared random, but they assumed a pattern when interpreted in terms of flows about the missile. The system of water-exit forces is complex, and the net effect
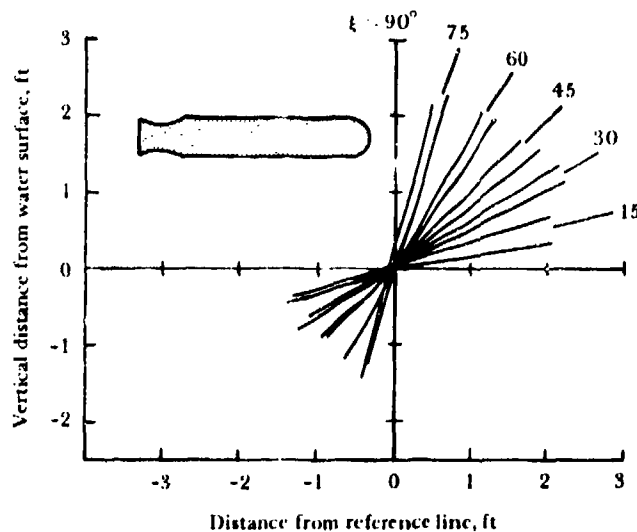

Figure 11.3. Trajectories of hemisphere missile.

of these forces upon the missile is delineated by the shape of the cavity, wake, water surface, and splash. From study of these, it is possible to predict the nature of the perturbation (Reference 105).

The water-exit perturbation of the hemisphere missile was dependent upon both the cavitation number and the trajectory angle, the cavitation number being by far the more important variable. Typical flow patterns could be associated with each cavitation number. They were modified by the superimposed variation of trajectory angle, but they were recognizable at all trajectory angles.

A general similarity was observed in the flow patterns of the hemisphere missile at all test conditions. Cavitation of varying degrees ranging from nearly fully wetted flow to fully

enveloping cavitation occurred during all underwater flights. At nose emergence, a small amount of water exited on top of the missile nose and accelerated ahead of the missile (Figure 11.4). At the water surface, most of the cavity was wiped from the missile and stayed behind in the water at all cavitation numbers except one: $\sigma = 0.289$ (Figure 11.5). At this cavitation number, the cavity was rapidly collapsing forward just prior to exit, the forward motion apparently giving it sufficient momentum to break through the water surface and exit with the missile. This condition was noted at all trajectory angles (Figure 11.6) and was generally associated with a small exit perturbation. Also, during all launchings, a portion of the tail cavity followed the missile through the interface to disintegrate violently

Trajectory Angle, ξ, deg

| 90 | 75 | 60 | 45 | 30 |

15

Full cavity, $\sigma = 0.045$

Trajectory Angle, ξ, deg

| 90 | 75 | 60 | 45 | 30 |

15

Partially wetted flow, $\sigma = 0.576$
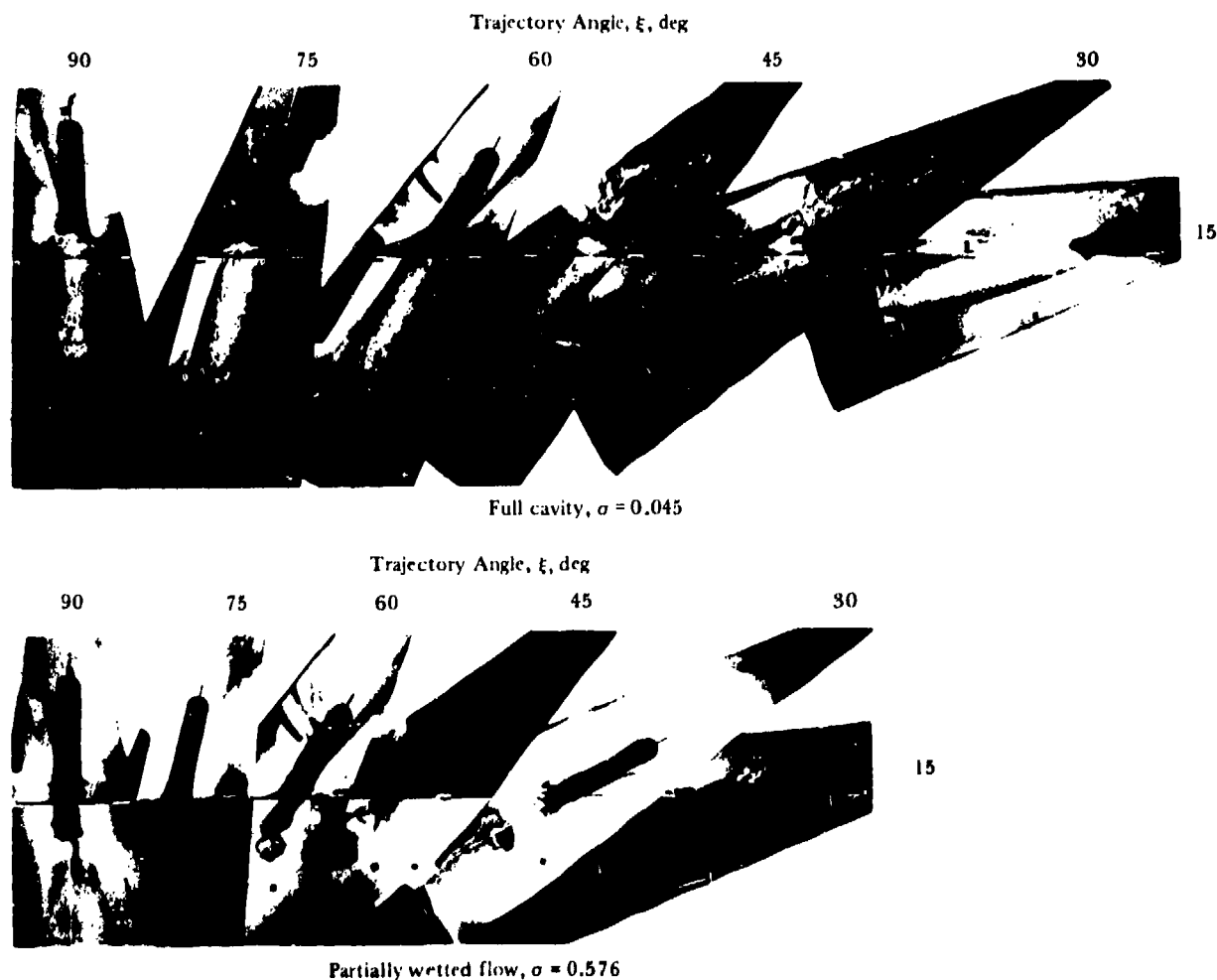
Figure 11.4. Cavitation variations, water exit of hemisphere missile.

190

-1.1   +2.9   +6.9   +10.9   +14.9   +18.9

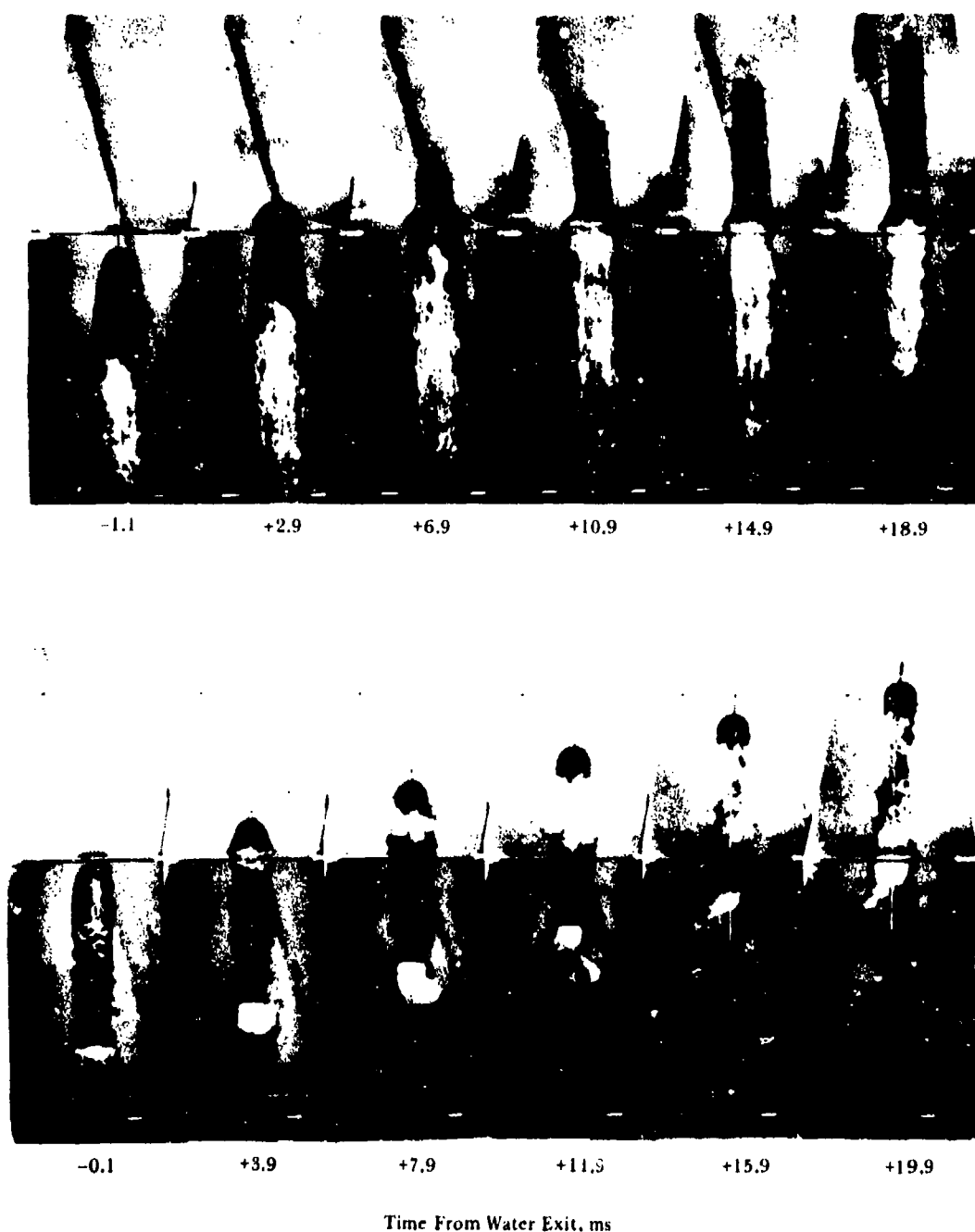-0.1   +3.9   +7.9   +11.9   +15.9   +19.9

Time From Water Exit, ms

Figure 11.5. Hemisphere missile at water exit, $\xi = 90°$. Top: cavity left behind ($\sigma = 0.106$). Bottom: cavity exits with missile ($\sigma = 0.289$).

after exit (Figure 11.7). The violence of cavity disintegration appeared to be about the same at all cavitation numbers (Figure 11.8). The differing aspects of the flow pattern occurring at each cavitation number are discussed in Reference 105.

The water-exit perturbations observed can be divided into two types: (1) those arising when the missile exits in a fully developed cavity (top of Figure 11.5) and (2) those arising when the missile exits under conditions of partially wetted flow (bottom of Figure 11.5). The latter

191

Trajectory angle

90°   75°   60°   45°

30°

15°
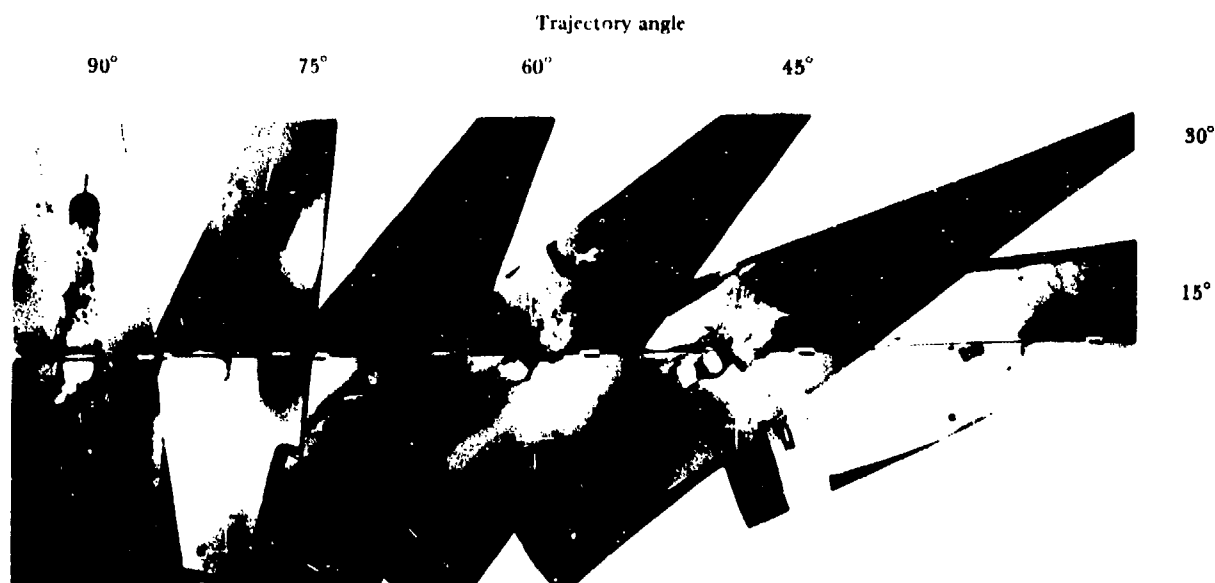
Figure 11.6. Hemisphere missile nose-cavity exit ($\sigma = 0.289$).

16.2   20.2   24.2   28.2   32.2   36.2   40.2   44.2   48.2

Time From Water Exit, m·
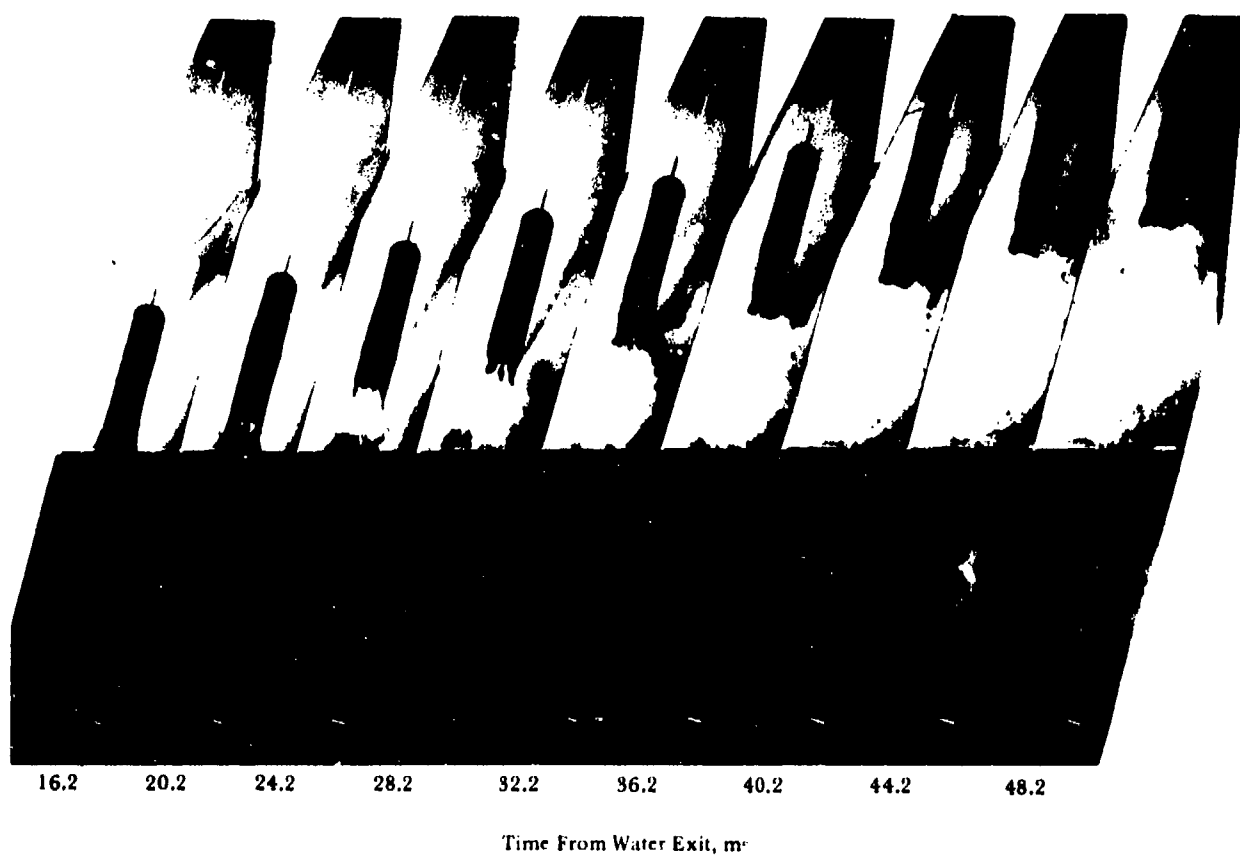
Figure 11.7. Disintegration of hemisphere missile tail cavity at exit, $\sigma = 0.576$, $\xi = 75°$.

192

Cavitation No.

0.576   0.431   0.289   0.106   0.045
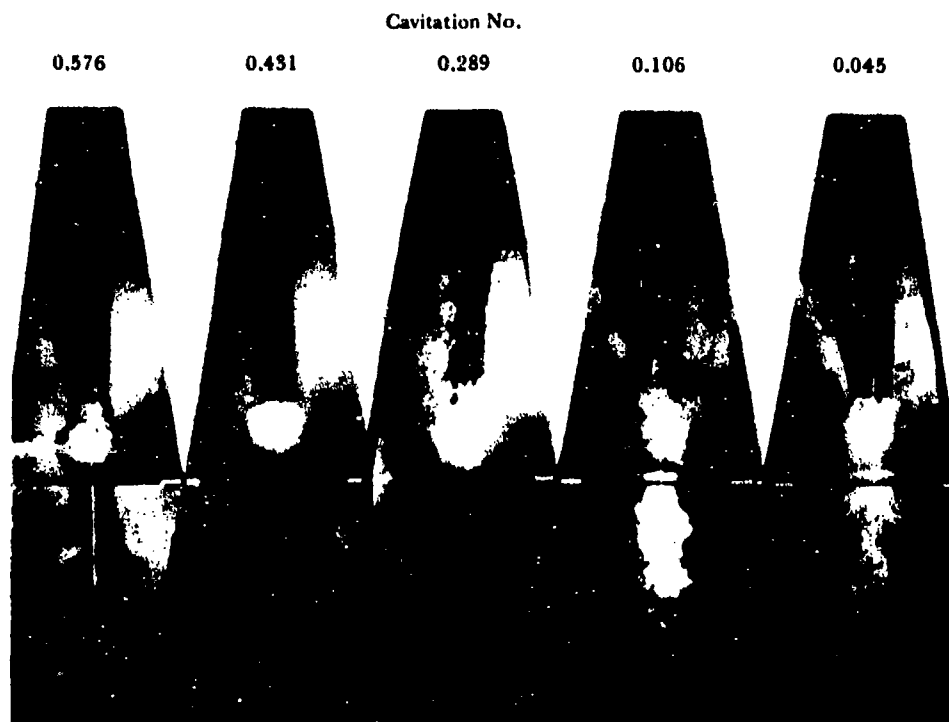
About 28 ms after water exit

Cavitation No.

0.576   0.431   0.289   0.106   0.045
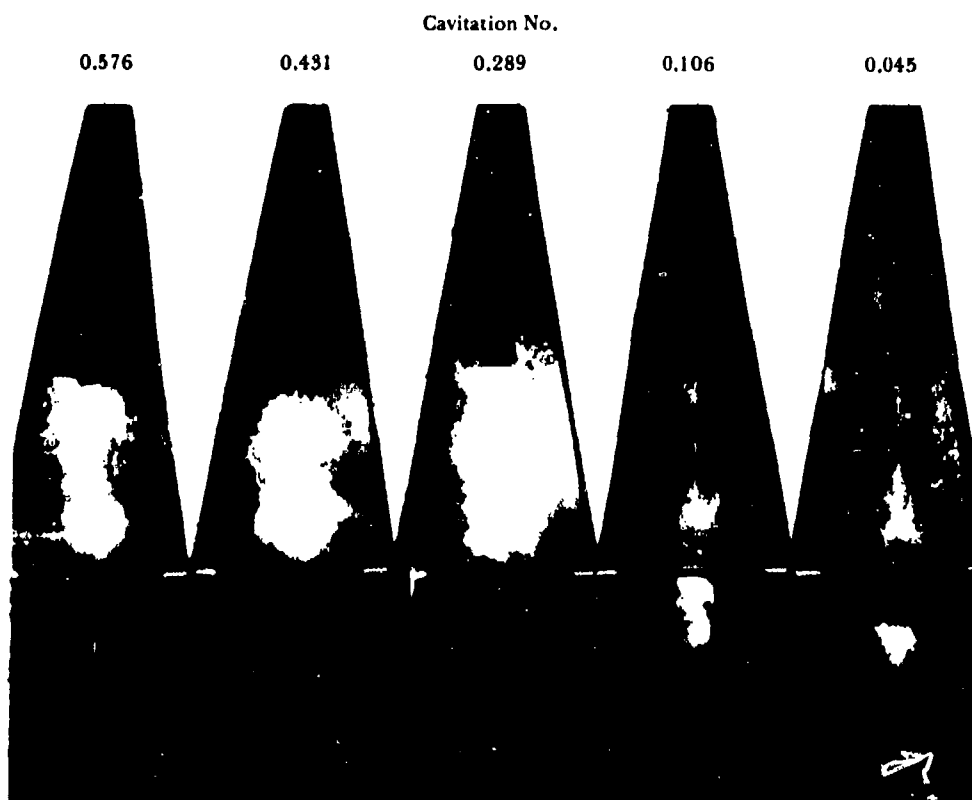
About 42 ms after water exit (one missile length of airflight)

Figure 11.8. Effect of cavitation number on disintegration of hemisphere missile tail cavity, $\xi = 90°$.

193

type of perturbation is modified by the degree of partial wettedness. When exit occurred in a full cavity (σ = 0.106 and 0.045), the perturbation was predominantly positive (nose-up); the partially wetted condition (σ = 0.576, 0.431, and 0.289) was more apt to be associated with a negative (nose-down) perturbation. At σ = 0.431, where the cavity was particularly unstable and tended to disrupt the water surface during exit, the scatter in the perturbation was so great that the perturbation ranged from extremely positive to extremely negative during presumably duplicate launchings.

Figure 11.9 summarizes the perturbations observed at the various trajectory angles at nose exit, tail exit, and 45 ms after nose exit as functions of cavitation number. The range of perturbation as a function of cavitation number occurring at any given trajectory angle increased slowly as the trajectory became more oblique until the 45-degree trajectory angle was reached. Then the range became noticeably larger and

continued wide at the 30- and 15-degree conditions. The perturbation curves for the oblique trajectory angles were all of similar shape and tended to become more negative as the trajectory angle became more shallow.

The photographic records reveal the nature of the mechanisms causing water-entry perturbations. When exit occurred in the presence of fully developed cavitation, the perturbation was influenced by the flow ahead of the zone of cavity separation and by the degree of isolation maintained by the cavity between the missile and the water surface. When the base of the missile was partially wetted, the flow pattern was more difficult to interpret. However, the flow was delineated to some extent by a ring of vortex cavitation shedding from the missile base. It is possible that the perturbation was caused by the shedding of the vortex (Reference 80). The position of the shed vortex indicates the direction of missile perturbation. If the vortex ring trailed from the left of the missile tail
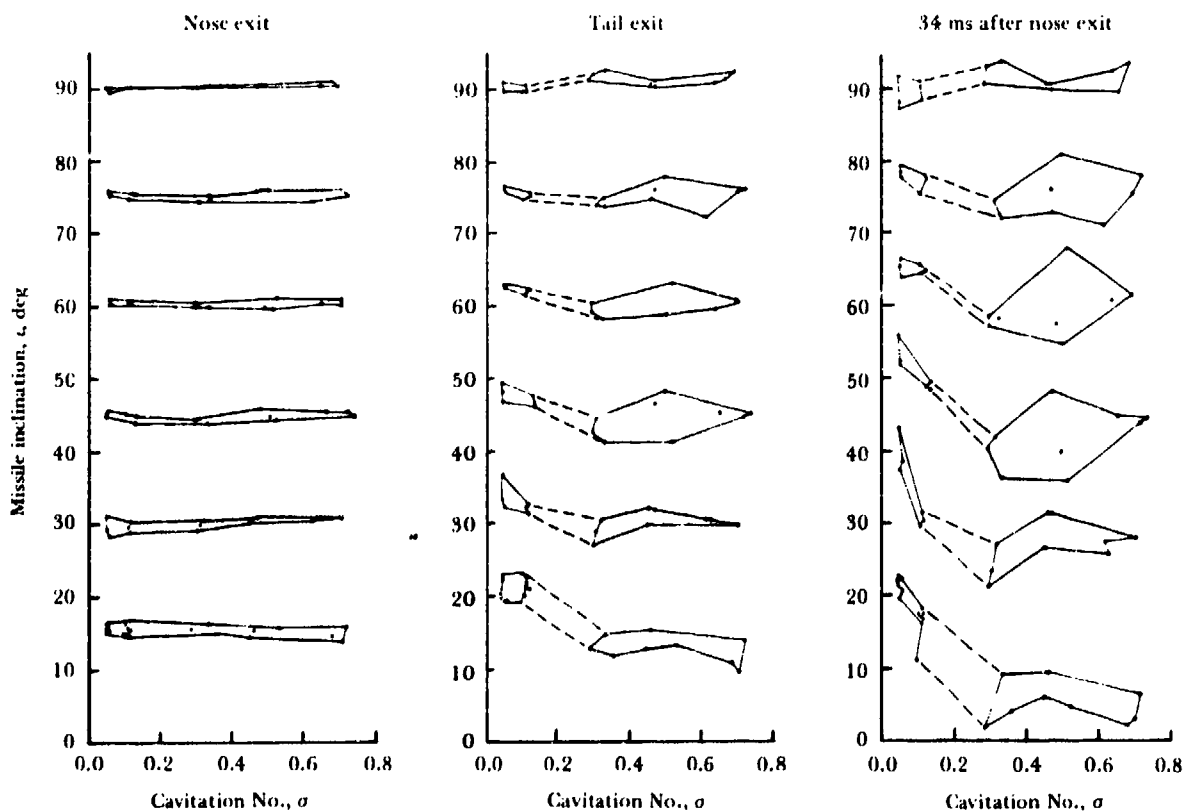

Figure 11.9. Summary of hemisphere missile water-exit perturbations at various trajectory angles.

194

during exit, the perturbation was negative; a right-trailing vortex caused a positive perturbation (Figure 11.10).

The great randomness in perturbation characteristic of tne oblique launchings made at $\sigma = 0.431$ occurred because the weak cavitation system produced unrepeatable hydrodynamic flow patterns during both the underwater trajectory and the water exit.

At the 90-degree trajectory angle, the perturbation was small and seemed to grow predominantly from conditions established prior to exit. ¨ ¿ trends and behavior patterns typical of the oblique trajectory angle did not appear. Figure 11.11 shows parts of five launchings, one at each cavitation number, made at the 90-degree trajectory angle. The missile attitude as a function of time and approximate distance from water exit is shown in Figure 11.12.

At the 75-degree trajectory angle (Figures 11.13 and 11.14), the scatter at the two higher cavitation numbers was so great that the perturbations overlapped those at the three lower numbers. At $\sigma = 0.289$ (partially wetted) the perturbation was negative, and at $\sigma = 0.045$ and $\sigma = 0.106$ (fully cavitating), the perturbation was positive. Two launchings from each of the partially wetted conditions are included in Figure 11.13 to show how variation in perturbation grows from differences in the underwater and exit-flow patterns.

Detailed data from the 60-degree trajectory angle are presented in Figures 11.15 and 11.16. The scatter at the $\sigma = 0.431$ condition was so great that these perturbations overlapped the other data. Otherwise, the perturbation occurring under fully developed cavitation was positive with respect to the partially wetted flow perturbation.

The range of perturbations observed at 45-degree trajectory angle was noticeably wider than at the steeper angles (Figures 11.17 and 11.18). Scatter still occurred at $\sigma = 0.431$ and to a lesser degree at $\sigma = 0.289$, but the difference between the fully cavitating perturbation and that of the partially wetted flow condition was great enough that the data from $\sigma = 0.431$ no longer overlapped the other results. The flow pattern determining the perturbation at $\sigma = 0.431$ was particularly well delineated (Figure 11.17). Strong differences occurred both in the wake and in the ring of cavitation shedding from the nose cavity.

The large scatter typical of the data at $\sigma = 0.431$ for the steeper oblique trajectory angles did not occur at the 30-degree trajectory angle (Figures 11.19 and 11.20). An extremely large nose-up perturbation occurred at $\sigma = 0.045$, but at $\sigma = 0.106$ the growth of the perturbation was checked by the missile dragging in the water during exit.

At the 15-degree trajectory angle, the obliqueness of the trajectory was most important in determining the perturbation (Figures 11.21 and 11.22). The partially wetted missile dragged heavily in the water during exit; even the full cavity did not completely protect the missile from water contact. The nose-up motion of the missile was arrested at $\sigma = 0.045$ and reversed at $\sigma = 0.106$, and a nose-down perturbation occurred at all the higher cavitation numbers.

The randomness in water exit observed during this study may have been caused by (1) unstable cavity flows, (2) missile shape, or (3) Reynolds-number effects either in the form of unstable cavity separation or in cavitating vortices that shed into the wake and thereby increase its activity. Each of these three conditions was examined in detail and further launchings were made to illuminate the last two of the three problem areas.

The blunt missile base used in these studies was expected to have a large underwater drag, but the large and random exit perturbations were not foreseen. The possibility that the probe exerts an adverse effect upon cavity formation by feeding sporadic vortices into the boundary layer ahead of the cavity separation zone, altering the pressure distribution sufficiently to distort the line of cavity separation and changing the cavity configuration, was studied. Without a probe (first part of Figure 11.23), the ungrooved hemisphere missile was enveloped in a clear cavity that did not fluctuate significantly with time ($v_e = 56.7$ fps, $\sigma = 0.052$). With a probe (second and third parts of Figure 11.23), the cavity was either rough and opaque, fluctuating slightly with time ($v_e = 63.3$ fps, $\sigma = 0.038$) or erratic and flapping, with large protuberances in the wall and a shifting line of separation.

It had been hoped that the 60-fps exit velocity would be adequate to prevent transition from laminar to turbulent flow and thereby avoid Reynolds-number effects, but full turbulence apparently did not occur in the flow ahead
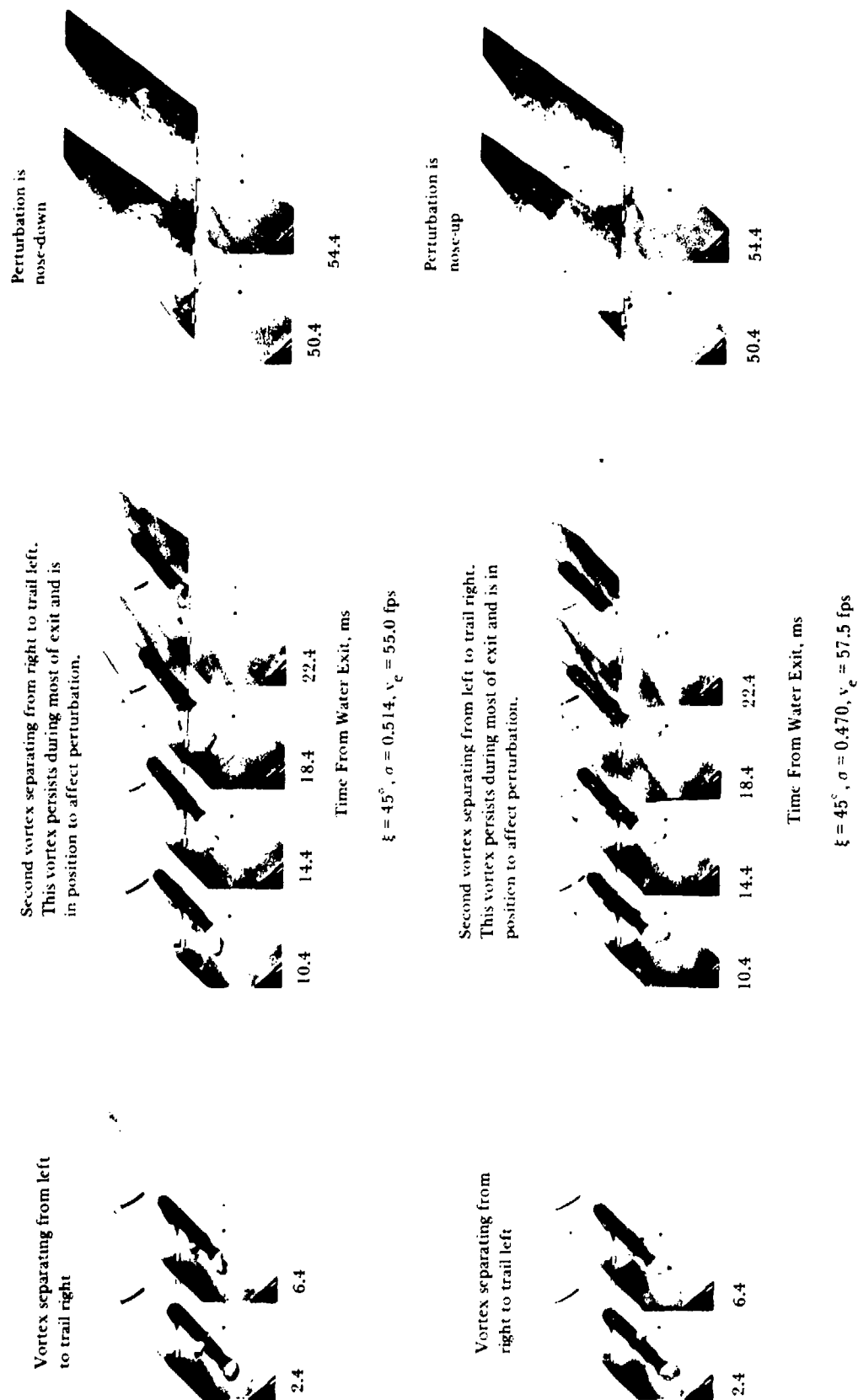
Vortex separating from left to trail right

2.4   6.4

Second vortex separating from right to trail left. This vortex persists during most of exit and is in position to affect perturbation.

10.4   14.4   18.4   22.4

Time From Water Exit, ms

$\xi = 45°$, $\sigma = 0.514$, $v_e = 55.0$ fps

Perturbation is nose-down

50.4   54.4

Vortex separating from right to trail left

2.4   6.4

Second vortex separating from left to trail right. This vortex persists during most of exit and is in position to affect perturbation.

10.4   14.4   18.4   22.4

Time From Water Exit, ms

$\xi = 45°$, $\sigma = 0.470$, $v_e = 57.5$ fps

Perturbation is nose-up

50.4   54.4

Figure 11.10. Left-right convention identifying vortex patterns in hemisphere missile launchings.

196
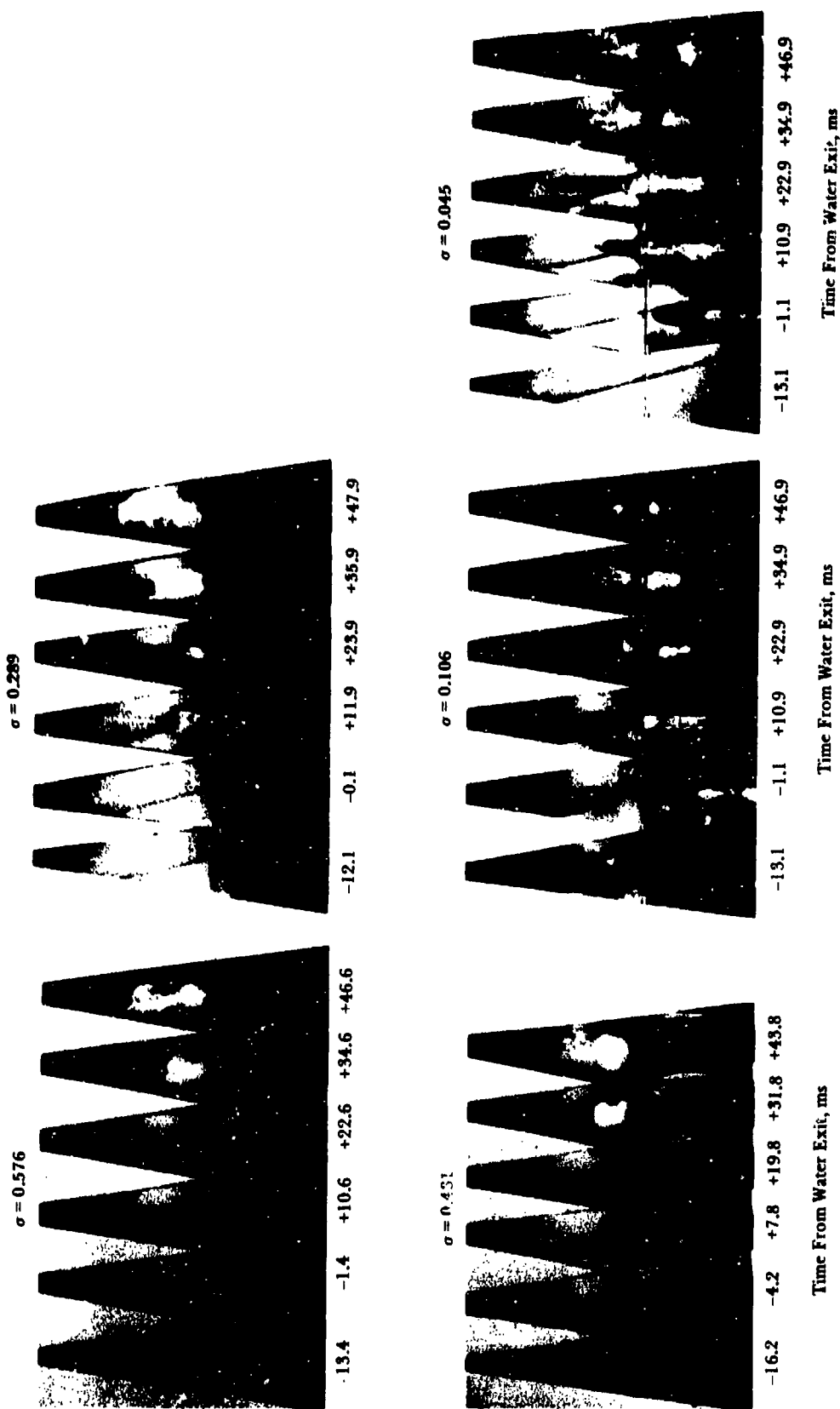
Figure 11.11. Small perturbations in hemisphere missile water exit, $\xi = 90°$.

197
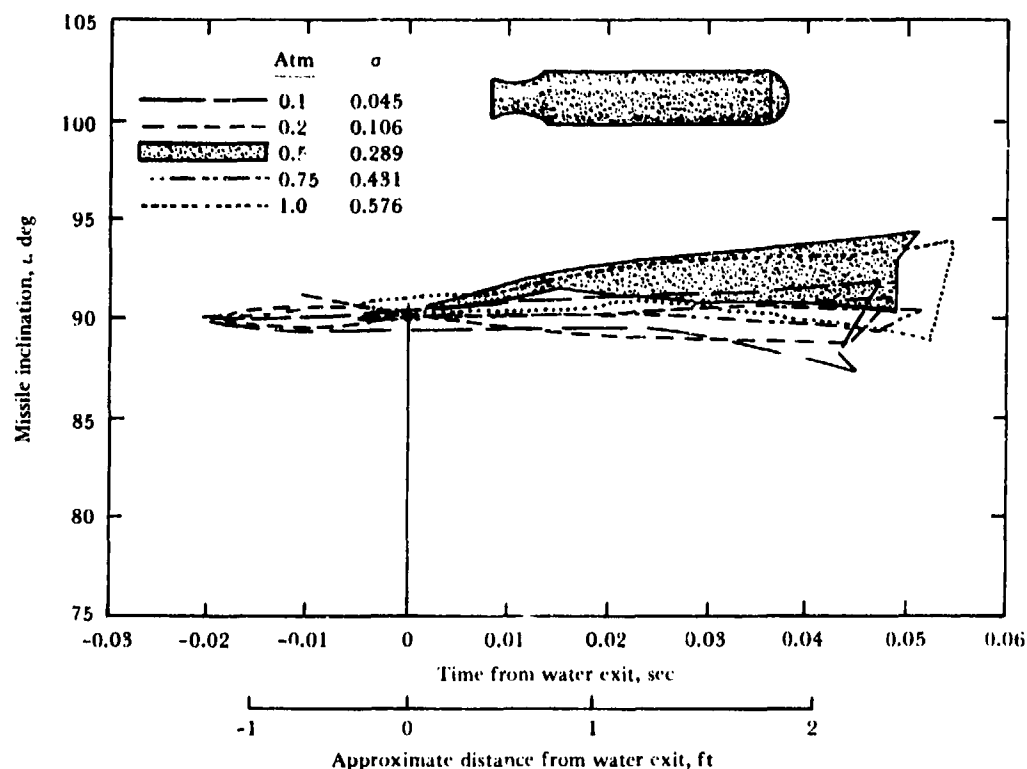
Figure 11.12. Plots of hemisphere missile water exits of Figure 11.11, ξ = 90 degrees.

of the zone of cavity separation. The viscosity effects manifested themselves either in the form of unstable cavity separation and shape or in large, sporadic vortices shedding into the wake. The addition of the nose probe, which was necessary if adequate missile attitude data were to be taken, seemed to increase the instability of the hydrodynamic flow still further.

The flow over the missile nose was made visible with nigrosine dye paste introduced through slots in the probes. During launching and subsequent underwater trajectory, the dye streamed from the slots, marking the flow along the probe and over the missile nose. Minute vortices were visible in the dye trace and a zone of separation seemed to occur at the base of the probe (Figure 11.24). Adding a nylon fairing to the probe to fill the approximate zone of separation tended to stabilize the cavity (Figure 11.25), suggesting that the erratic cavity formation was being caused by disturbances in the flow introduced by separation of the probe boundary layer. Using a fairing to eliminate erratic cavities is not feasible because the shape of the separation zone varies as the missile

velocity decreases along the trajectory. Moreover, a fairing would defeat the original purpose of the probe, which was to obtain accurate missile-attitude data.

Truncated-Cone Missile

When the truncated-cone missile was launched (Figure 11.1 and Table 11.1), its nose shape provided an immediate discontinuity for cavity separation, and its faired torpedo-type tail stabilized the flow about the missile afterbody. The missile was launched with (1) the standard 1 1/2-inch probe, (2) the standard probe shortened to 1 inch, and (3) no probe. All launchings were made at a 45-degree trajectory angle, some at 70 fps and some at the maximum obtainable velocity of about 80 fps. Typical photographs of missile launchings with the standard probe were made at constant Froude number and several different cavitation numbers (Figure 11.26). Missile water-exit perturbations can be seen in Figure 11.27.

At σ = 0.195, perturbations from 12 launchings ranged from 0 to -1/2 degrees, a perturbation of low magnitude. The photographs showed

198

σ = 0.576 (nom.)

−15.8 −3.8 +8.2 +20.2 +32.2 +44.2

σ = 0.576 (nom.)

−15.7 −3.7 +8.3 +2.03 +32.3 +44.3

· = 0.431 (nom.)

−13.7 −1.7 +10.3 +22.3 +34.3 +46.3

σ = 0.431

−16.5 −4.5 +7.5 +19.5 +31.5 +43.5

σ = 0.289

−14.9 −2.9 +9.1 +21.1 +33.1 +45.1

σ = 0.289

−13.4 −1.4 +10.6 +22.6 +34.6 +46.6

σ = 0.106

−14.8 −2.8 +9.2 +21.2 +33.2 +45.2

σ = 0.045

−12.6 −0.6 +11.4 +23.4 +35.4 +47.4
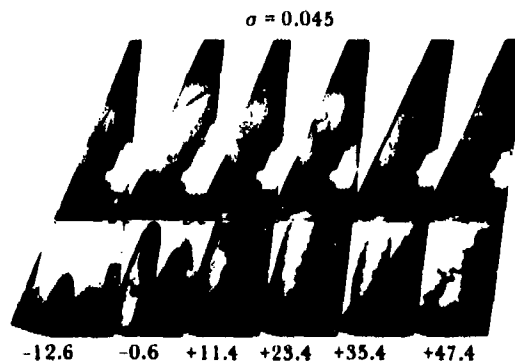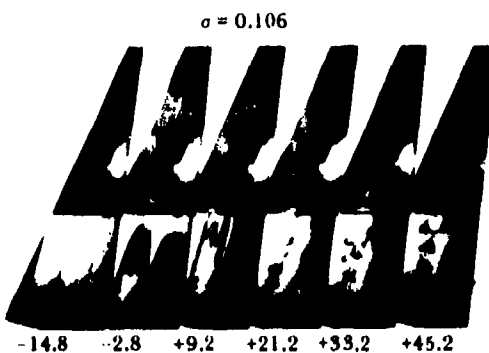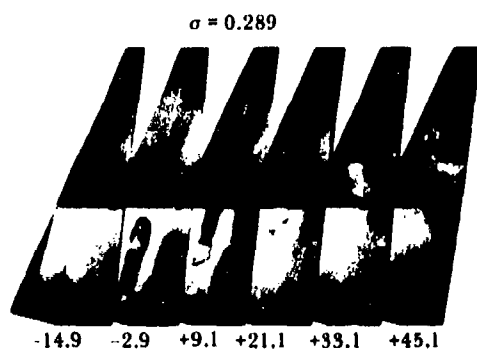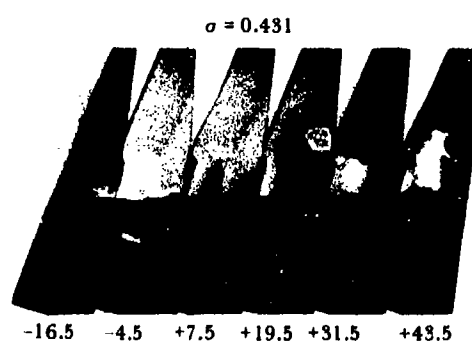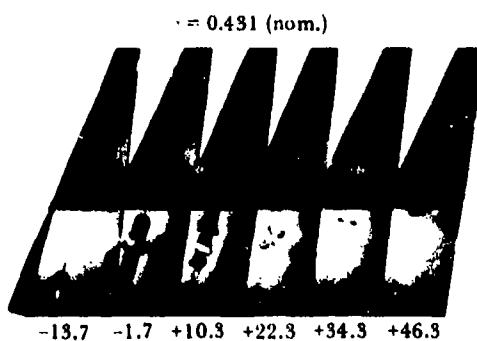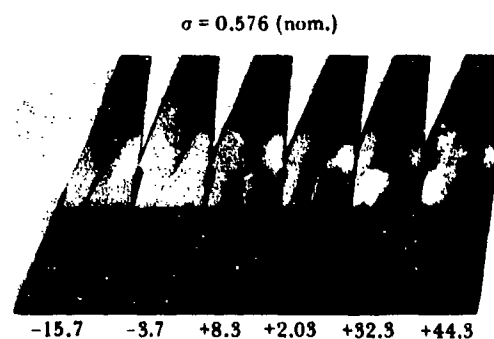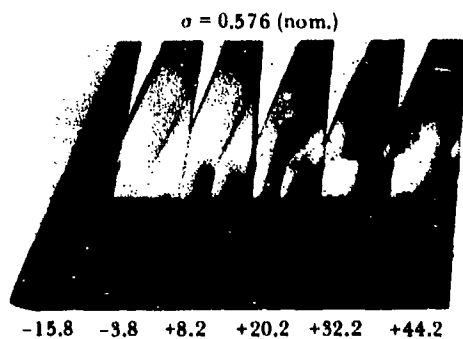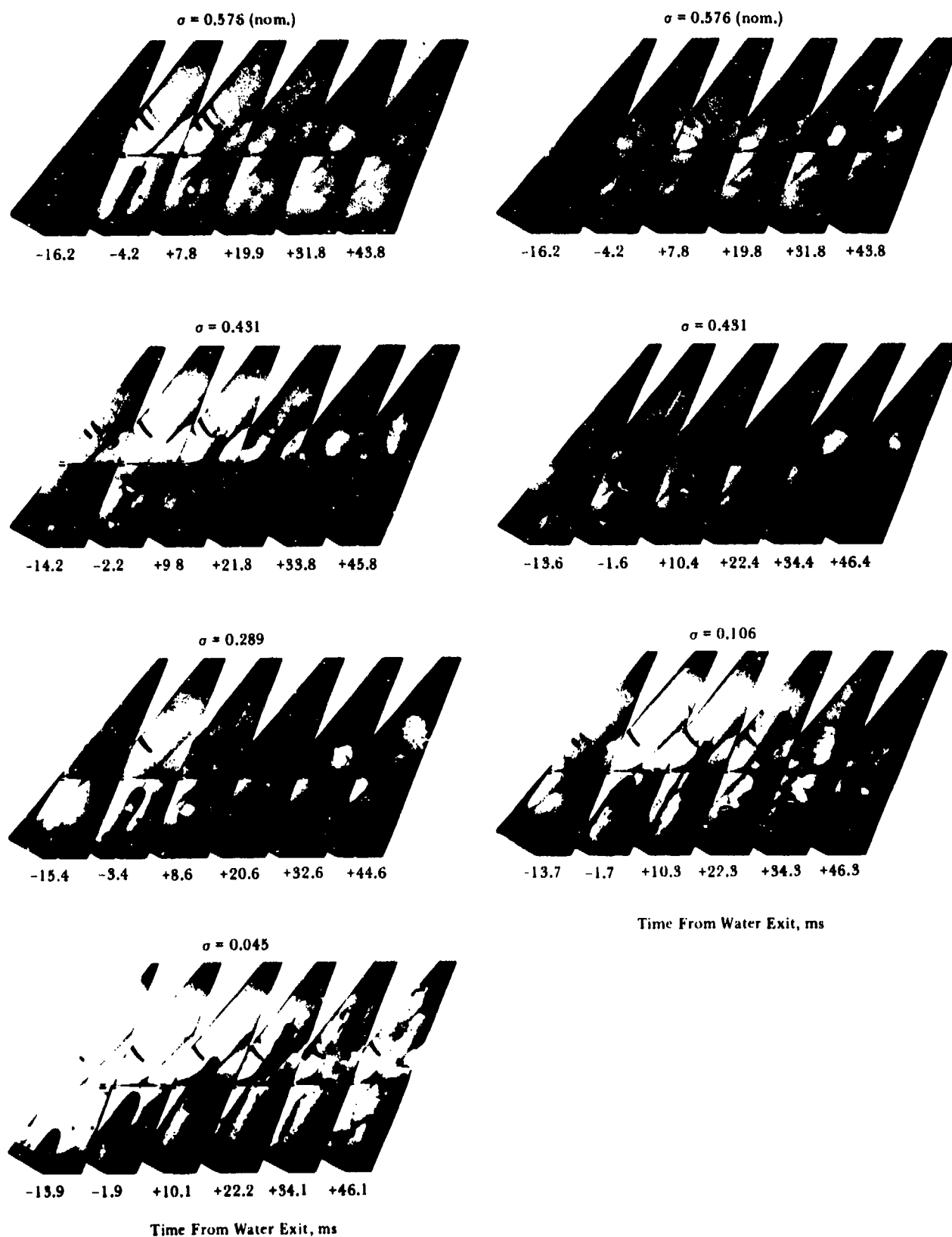
Time From Water Exit, ms

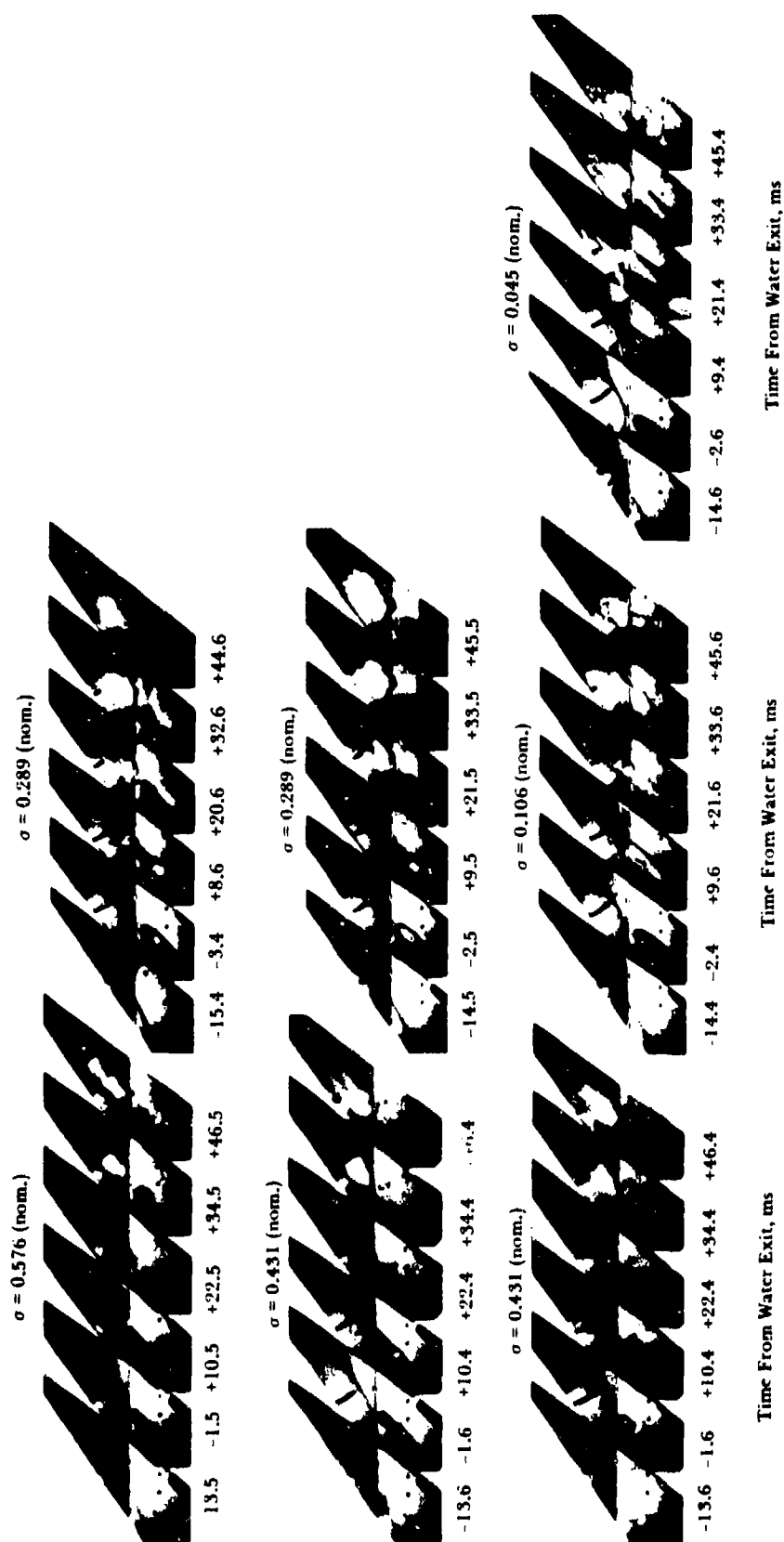Time From Water Exit, ms

Figure 11.13. Perturbations in hemisphere missile water exit, $\xi = 75°$.

199
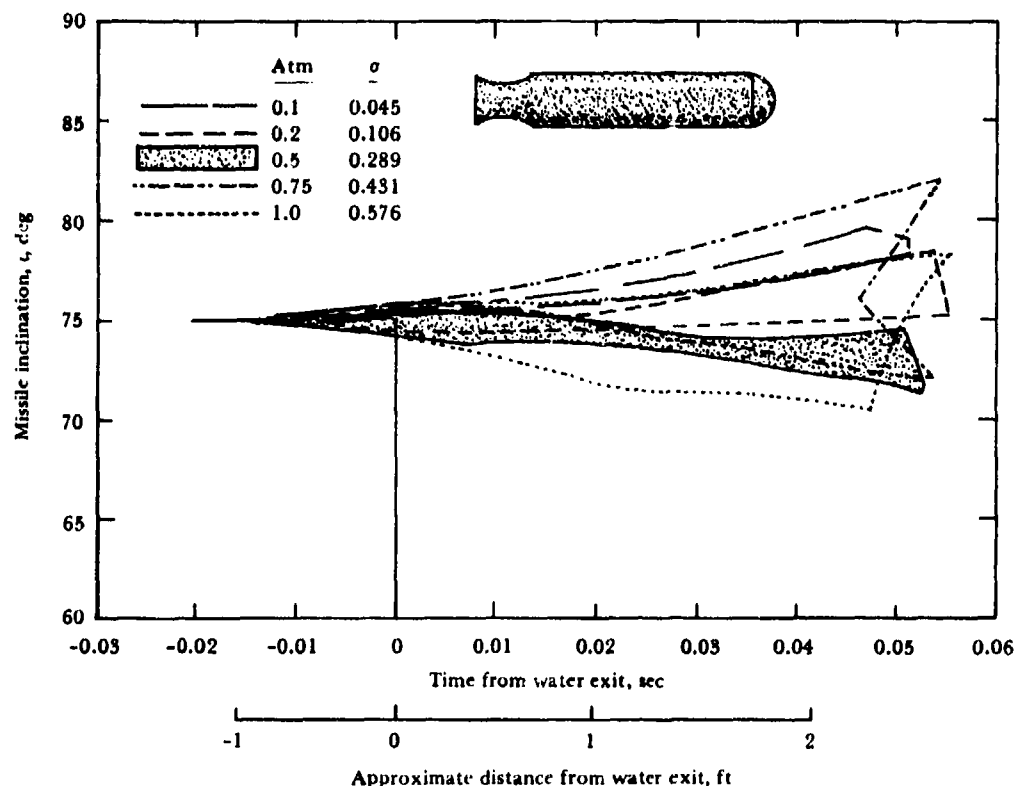
Figure 11.14. Plots of hemisphere missile water exits of Figure 11.13, ξ = 75 degrees.

the nose cavity rapidly collapsing forward as the missile approached the water surface, and, during exit, bursting through the surface instead of remaining behind in the water. The velocity field generated by the collapsing cavity apparently prevented interaction between the missile and the water surface.

The large scatter occurring in the perturbation at σ = 0.078 appeared to be caused by interaction between the water surface and the tail fins or by the flat nose cutting into the water surface and pushing water ahead.

The presence of the probe caused no significant difference either in the perturbation (Figure 11.27) or in the flow patterns about the missile (Figure 11.28), in contrast to the hemisphere missile, which experienced a change in flow pattern when the probe was added. Apparently, any disturbance in flow introduced by the probe was overridden by the large disturbance created by the nose flat.

A 10% variation in exit velocity did not cause any significant variation in either perturbation or flow pattern.

Composite Missile

The grooved hemisphere head was combined with the torpedo tail to make a composite missile (Figure 11.1 and Table 11.1), and a few launchings were made at the 45-degree trajectory angle, at water-exit velocities ranging from 60 to 75 fps, and at various cavitation numbers. Typical photographs of water exit are presented in Figure 11.29, and the missile attitude is shown as a function of cavitation number in Figure 11.30. Figure 11.31 illustrates the smooth separation of the vortices from the tapered missile tail.

The composite missile's behavior was similar to that of the truncated-cone missile. Scatter occurred in the exit perturbations, but it was of lesser magnitude and the randomness was not detectable until late in exit, suggesting that it was not nose-induced.

SUMMARY

The following conclusions can be drawn from the water-exit study.

200

σ = 0.575 (nom.)

-16.2   -4.2   +7.8   +19.9   +31.8   +43.8

σ = 0.576 (nom.)

-16.2   -4.2   +7.8   +19.8   +31.8   +43.8

σ = 0.431

-14.2   -2.2   +9 8   +21.8   +33.8   +45.8

σ = 0.431

-13.6   -1.6   +10.4   +22.4   +34.4   +46.4

σ = 0.289

-15.4   -3.4   +8.6   +20.6   +32.6   +44.6

σ = 0.106

-13.7   -1.7   +10.3   +22.3   +34.3   +46.3

Time From Water Exit, ms

σ = 0.045

-13.9   -1.9   +10.1   +22.2   +34.1   +46.1

Time From Water Exit, ms
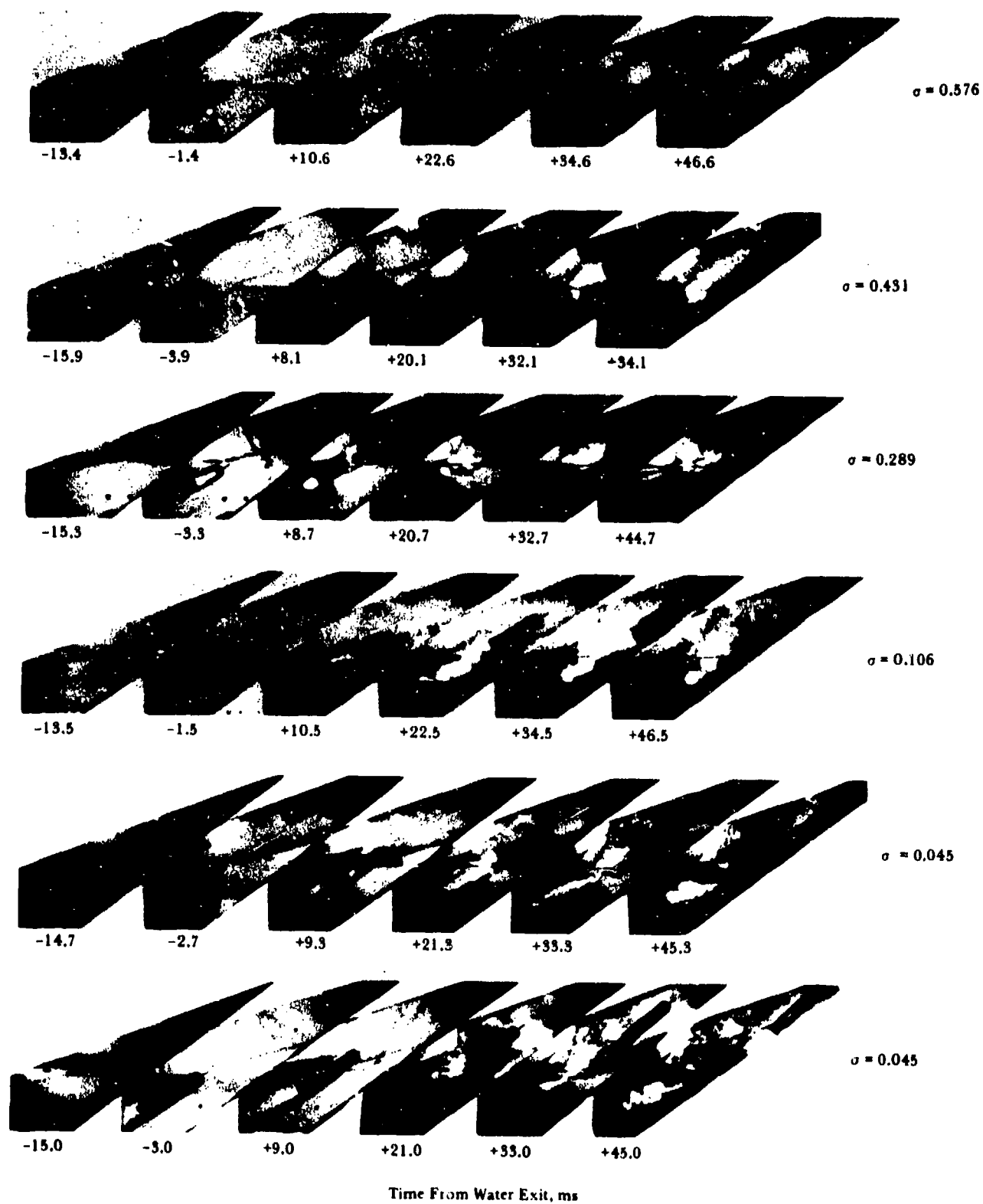
Figure 11.15. Perturbations in hemisphere missile water exit, ξ = 60°.

201
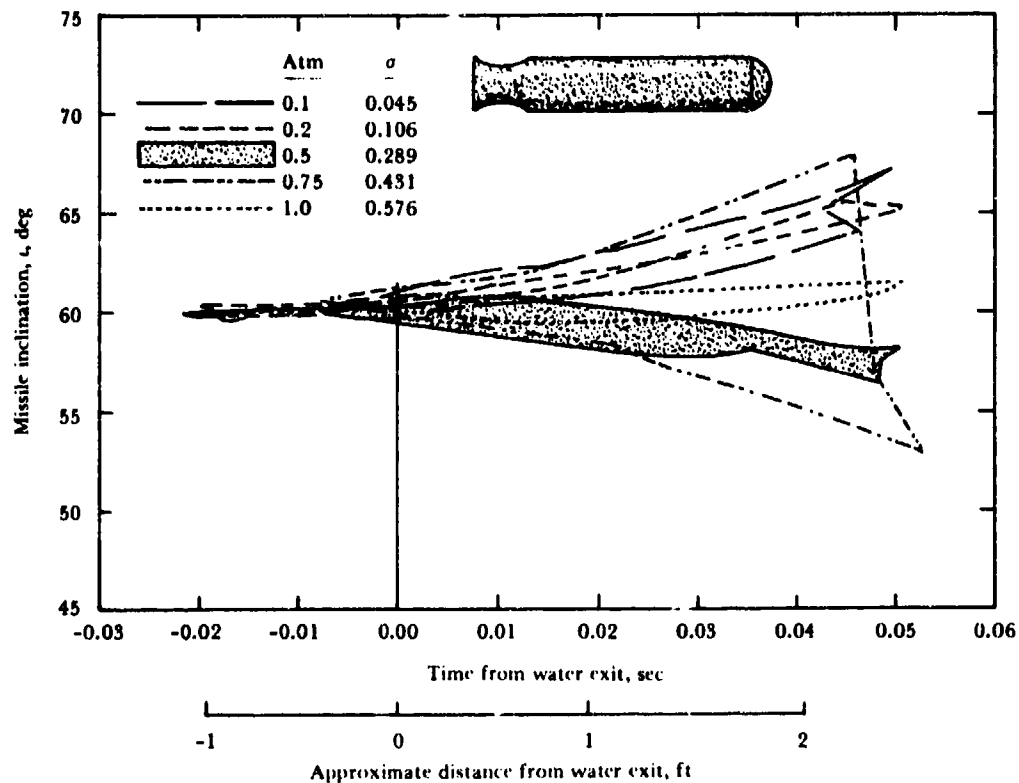
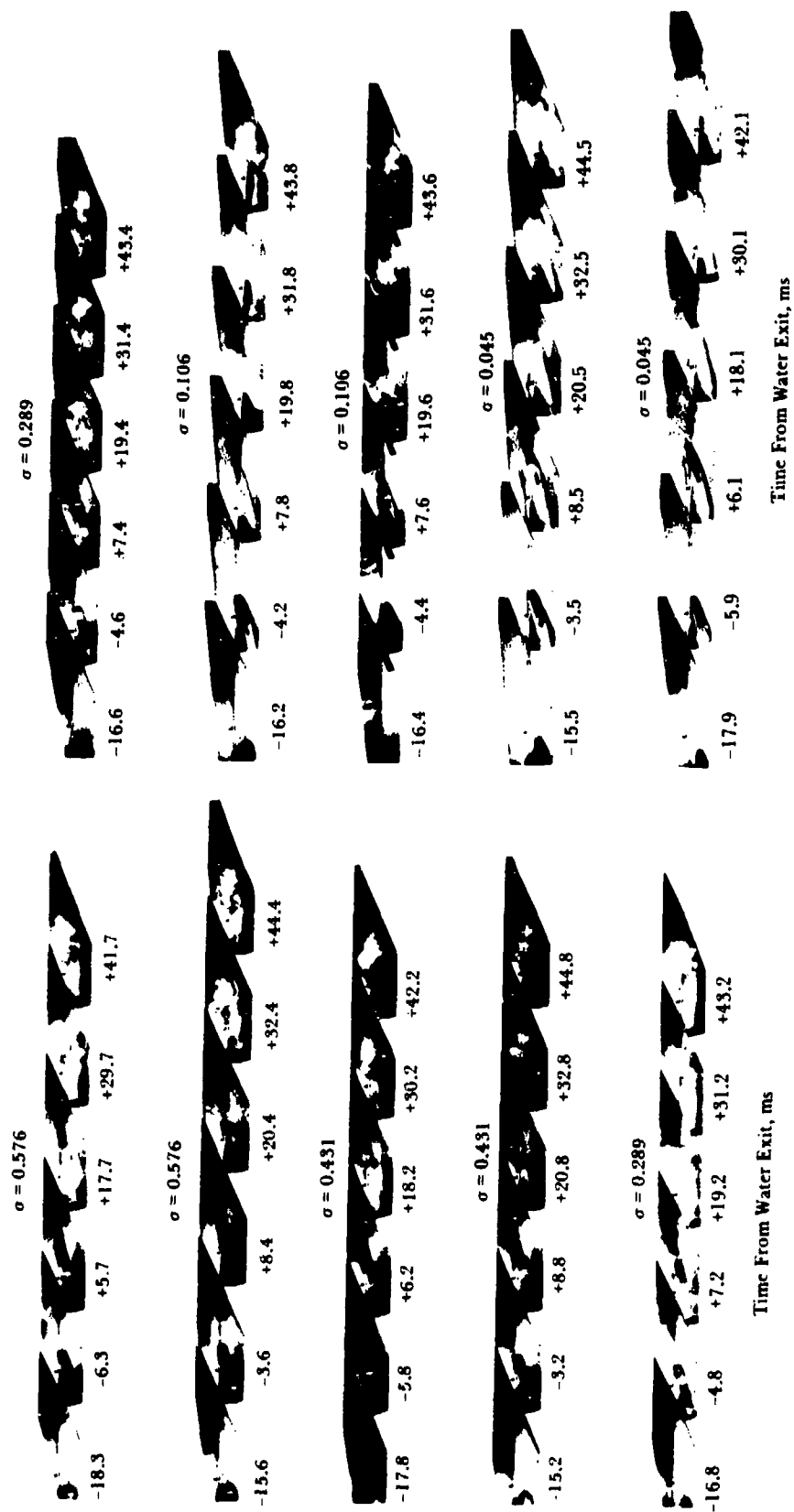Figure 11.16. Plots of hemisphere missile water exits of Figure 11.15, ι = 60 degrees.

1. The trajectories of the missiles were not greatly disturbed at water exit. A maximum deviation of about 1/2 diameter occurred after 15 diameters of air travel.

2. Water-exit perturbations in missile attitude were observed under conditions of flow ranging from nearly fully wetted to completely enveloping cavitation and at all trajectory angles investigated (15 to 90 deg. s with respect to the water surf r

3. Cavitation number we ure important in determining the magnitude and direction of the perturbation than was the trajectory angle. When the missile exited under conditions of fully developed cavitation, the perturbation was predominantly positive (nose up); when exit occurred under conditions of partially wetted flow, the perturbation tended to be negative (nose down). Maximum perturbations of ±13 degrees were recorded after about 13 diameters of air travel. The

perturbations of the standard missile measured during this study are summarized in Figure 11.9. The perturbation range at any given trajectory angle was less when the trajectory was steeper than 45 degrees.

4. Repeatable water-exit perturbations did not arise from presumably duplicate launchings.

5. A faired torpedo-type tail greatly reduced the magnitude and randomness of perturbations occurring when the missile base was wetted.

6. An artificially maintained cavity, or a cavity collapsing under controlled conditions, or both, may be a way to limit the magnitude and randomness of the exit perturbation.

7. The basic design rule for minimizing water-exit perturbations is that care must be taken to avoid anything — missile shape or ambient condition — that tends either to produce an unstable hydrodynamic flow pattern or to magnify one that has occurred.

202

$\sigma = 0.576$ (nom.)

$\sigma = 0.289$ (nom.)

13.5   −1.5   +10.5   +22.5   +34.5   +46.5   −15.4   −3.4   +8.6   +20.6   +32.6   +44.6

$\sigma = 0.431$ (nom.)

$\sigma = 0.289$ (nom.)

−13.6   −1.6   +10.4   +22.4   +34.4   +46.4   −14.5   −2.5   +9.5   +21.5   +33.5   +45.5

$\sigma = 0.431$ (nom.)

$\sigma = 0.106$ (nom.)

−13.6   −1.6   +10.4   +22.4   +34.4   +46.4   −14.4   −2.4   +9.6   +21.6   +33.6   +45.6

Time From Water Exit, ms   Time From Water Exit, ms

$\sigma = 0.045$ (nom.)

−14.6   −2.6   +9.4   +21.4   +33.4   +45.4

Time From Water Exit, ms

Figure 11.17. Perturbations in hemisphere missile water exit, $\xi = 45°$

203
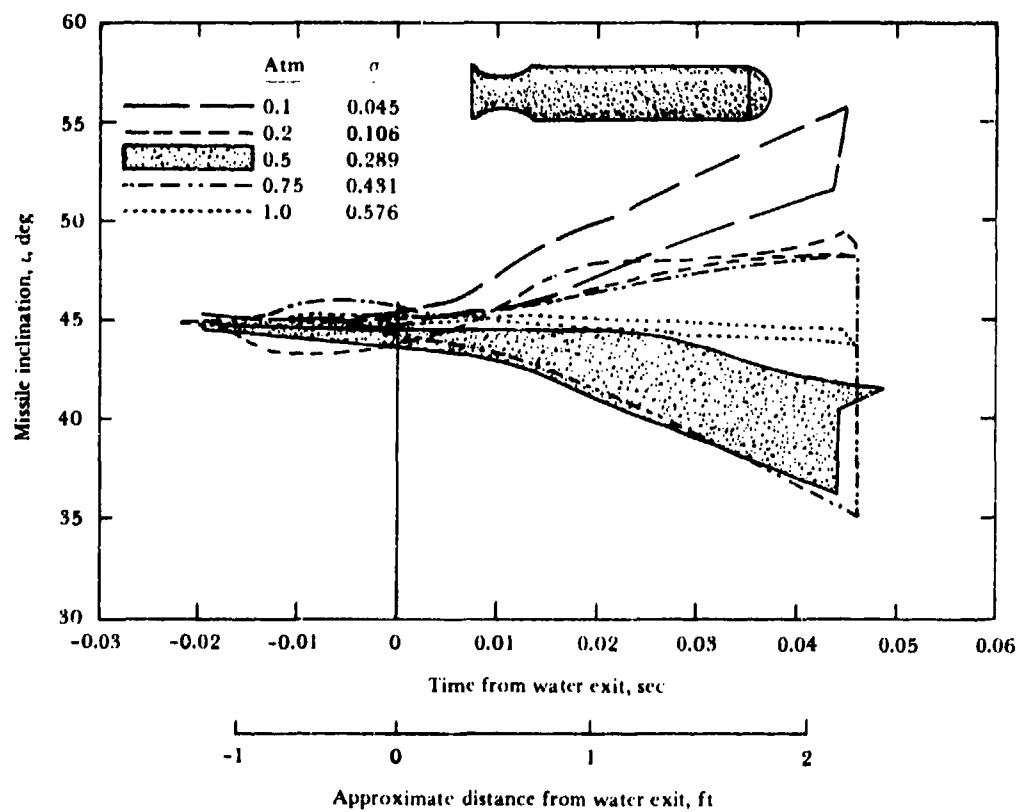
Figure 11.18. Plots of hemisphere missile water exits of Figure 11.17, $\xi = 45$ degrees.

$\sigma = 0.576$

−13.4   −1.4   +10.6   +22.6   +34.6   +46.6

$\sigma = 0.431$

−15.9   −3.9   +8.1   +20.1   +32.1   +34.1

$\sigma = 0.289$

−15.3   −3.3   +8.7   +20.7   +32.7   +44.7

$\sigma = 0.106$

−13.5   −1.5   +10.5   +22.5   +34.5   +46.5

$\sigma = 0.045$

−14.7   −2.7   +9.3   +21.3   +33.3   +45.3

$\sigma = 0.045$

−15.0   −3.0   +9.0   +21.0   +33.0   +45.0

Time From Water Exit, ms

Figure 11.19. Perturbations in hemisphere missile water exit, $\xi = 30°$.

205
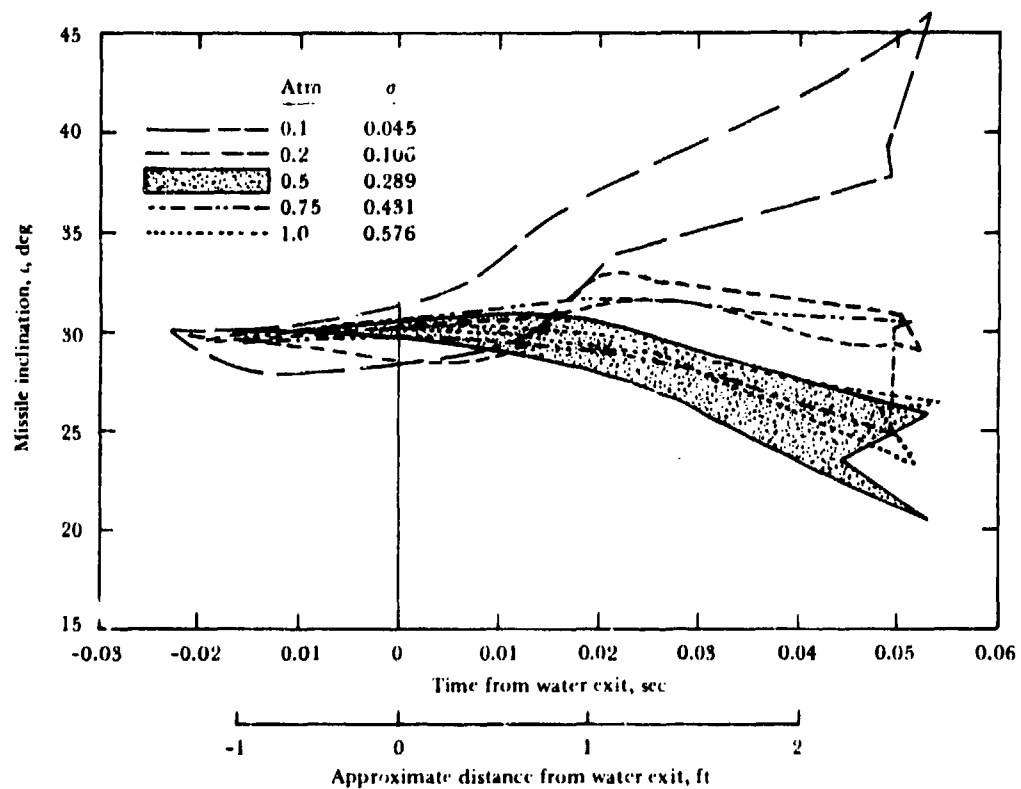
Figure 11.20. Plots of hemisphere missile water exits of Figure 11.19, $\xi = 30$ degrees.

Figure 11.21. Perturbations in hemisphere missile water exit, $\xi = 15°$.
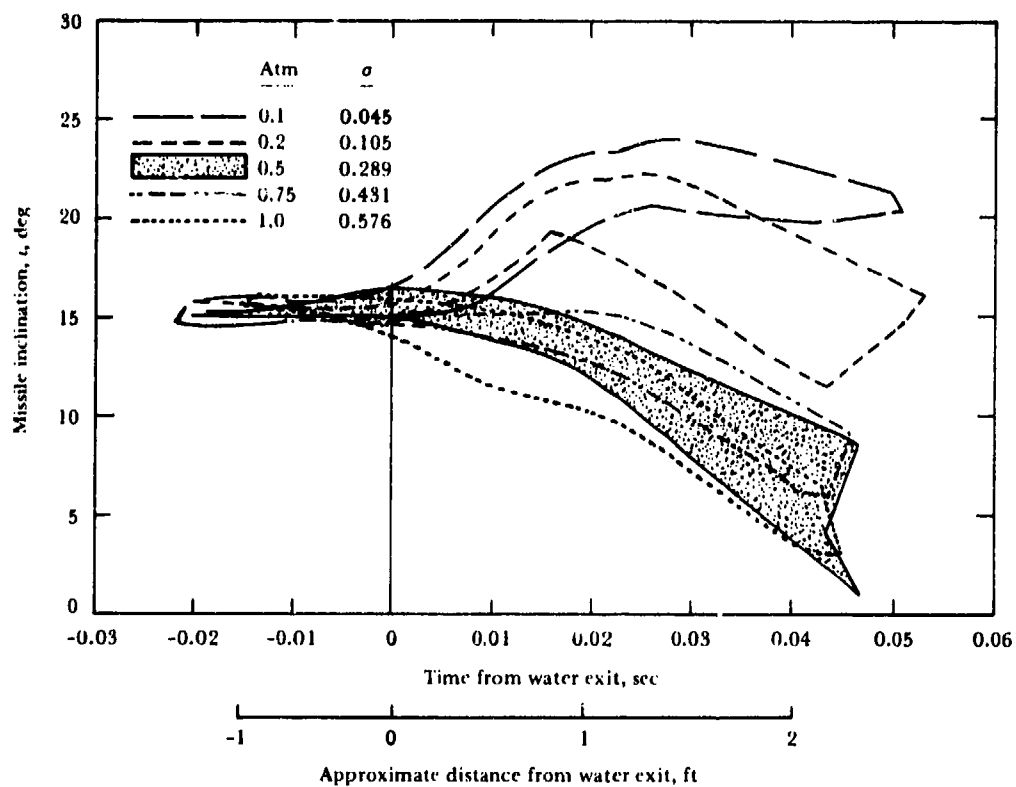
Figure 11.22. Plots of hemisphere missile water exits of Figure 11.21,
$\xi = 15$ degrees.

208

Without probe
$v_c = 56.7$ fps
$\sigma = 0.052$
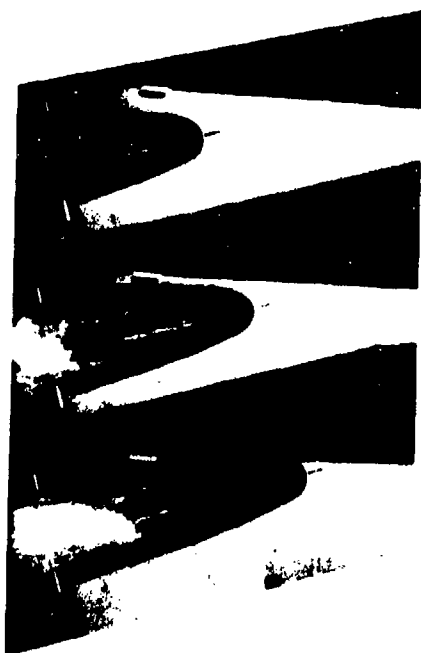
With probe
$v_c = 63.3$ fps
$\sigma = 0.038$
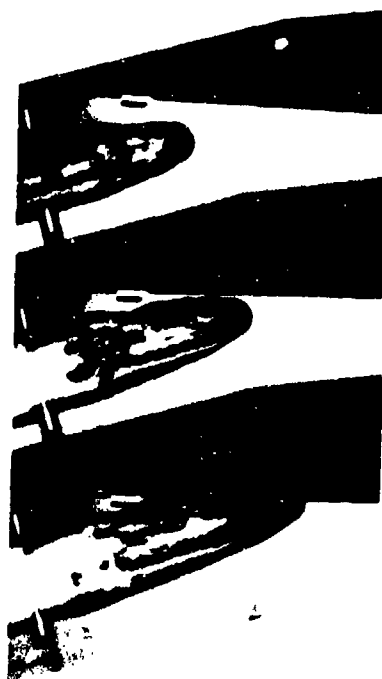
With probe
$v_c = 63.3$ fps
$\sigma = 0.045$

Figure 11.23. Effect of probe on ungrooved hemisphere missile cavity configuration, $\xi = 30°$.
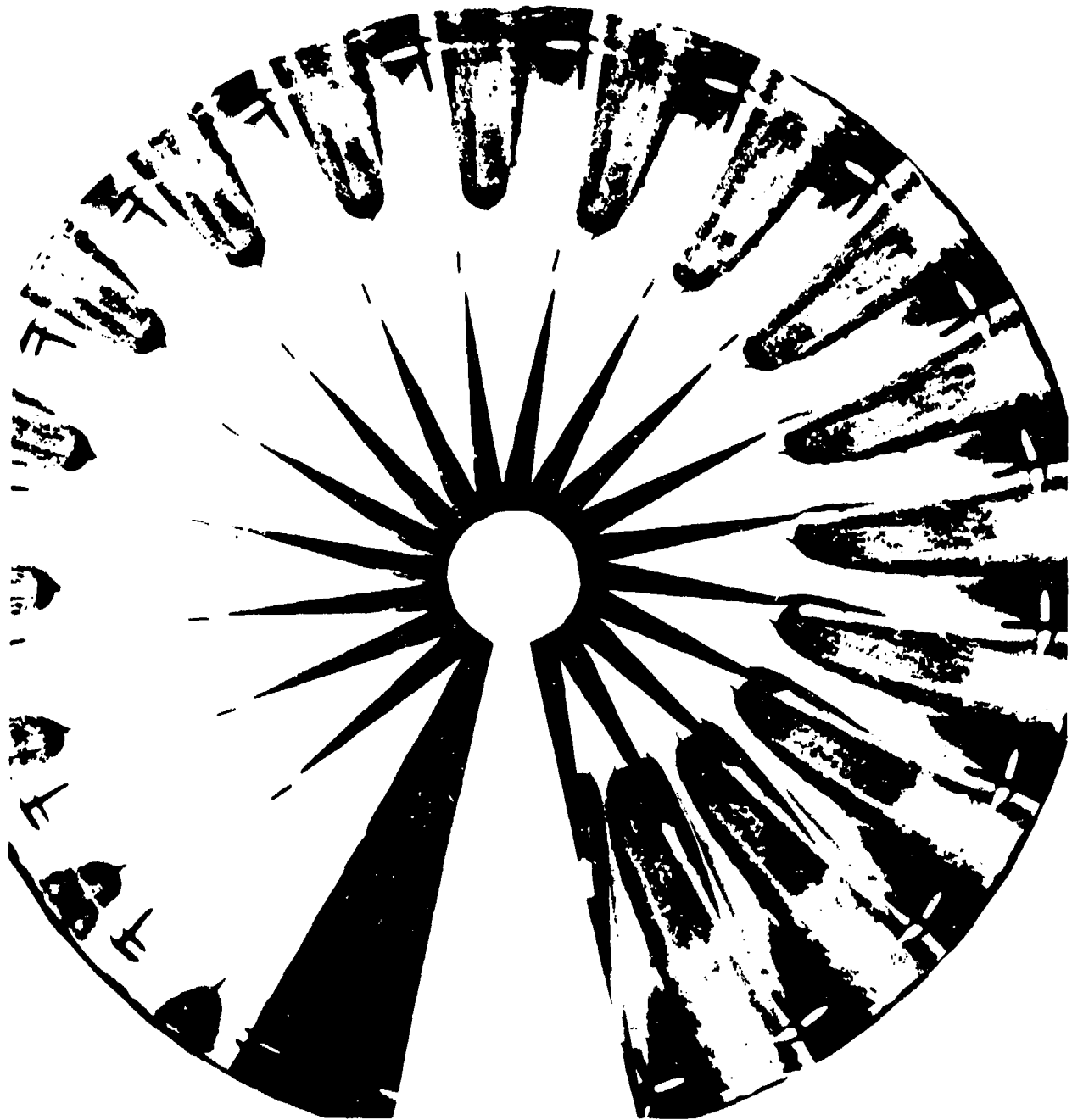
Figure 11.24. Dye trace from slotted probe marking large zone of separation on ungrooved hemisphere missile nose.

Figure 11.25. Cavity stabilized by nylon fairing on ungrooved hemisphere missile nose.

$\sigma = 0.451$

$\sigma = 0.078$

$\sigma = 0.195$

$\sigma = 0.033$
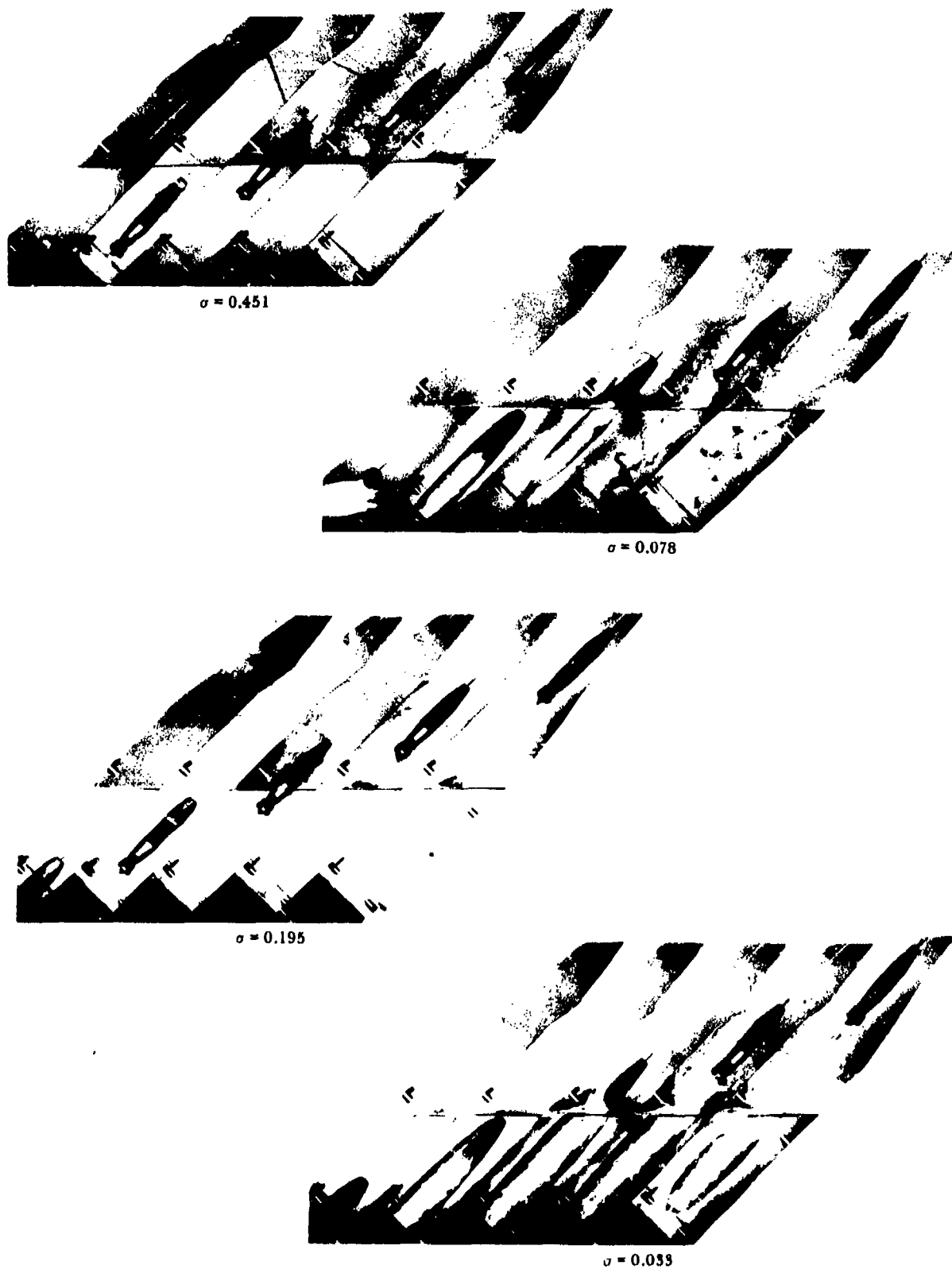
Figure 11.26. Effect of cavitation number on flow pattern and water exit of truncated-cone missile, $\xi = 45°$, $v_c = 68$ to 73 fps.

212
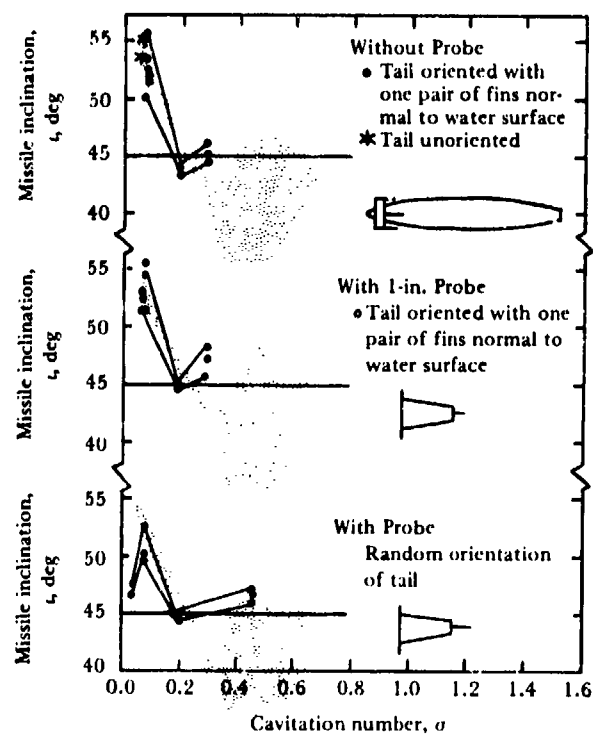
Figure 11.27. Truncated-cone missile perturbations compared with hemisphere missile perturbation range (shaded areas). $\xi = 45$ degrees.

213

Standard probe (1 1/2 in.)

1-in. probe

No probe

$\sigma = 0.195$

Standard probe (1 1/2 in.)

1-in. probe

No probe

No probe

$\sigma = 0.078$
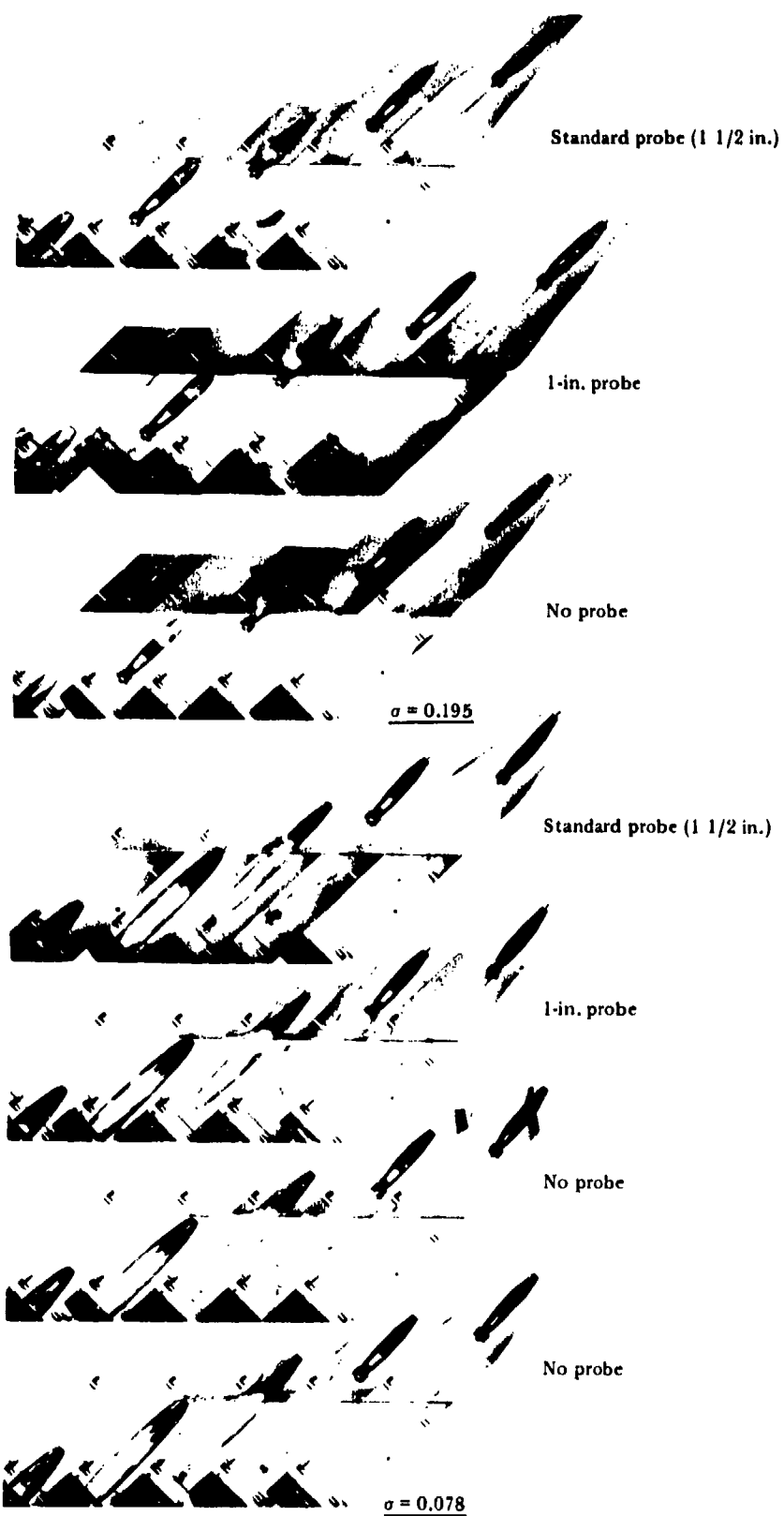
Figure 11.28. Effect of probe length on flow pattern and water exit of truncated-cone missile, $\xi = 45°$, $v_e = 70$ to 73 fps.

214

$v_c = 60$ fps
$\sigma = 0.045$

$v_c = 64$ fps
$\sigma = 0.091$

$v_c = 73$ fps
$\sigma = 0.194$

$v_c \approx 77$ fps
$\sigma = 0.261$

$v_c = 75$ fps
$\sigma = 0.369$
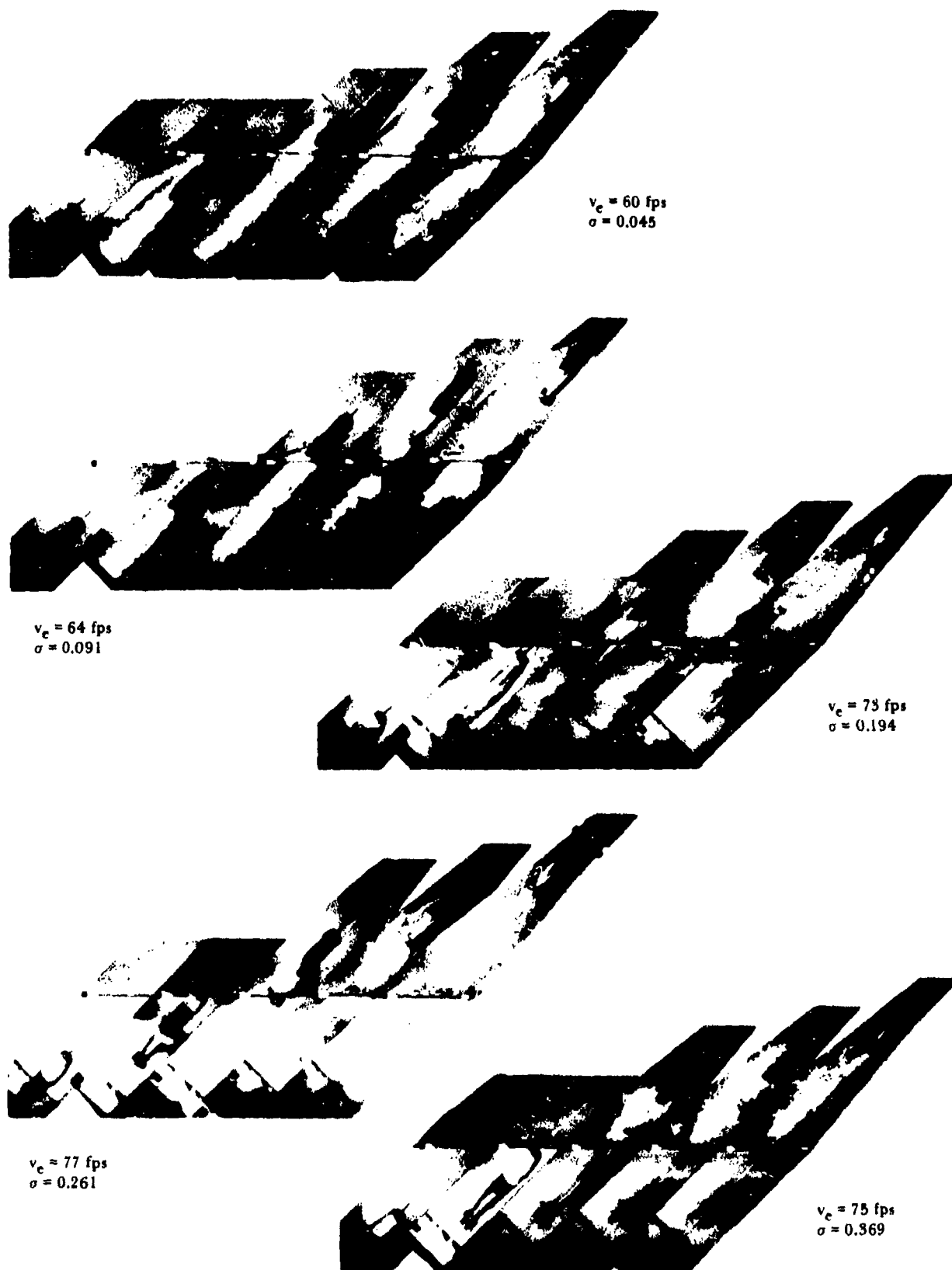
Figure 11.29. Effect of cavitation number on flow pattern and water exit of composite missile, $\xi = 45°$.

215
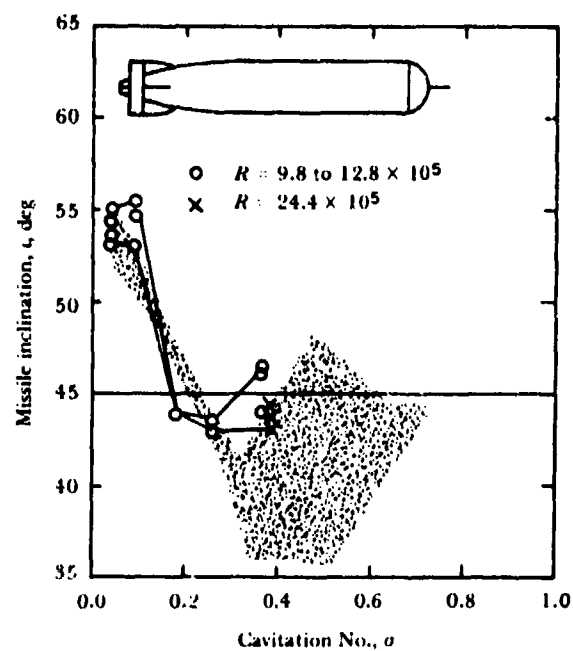
Figure 11.30. Comparison of missile inclination about 2½ feet after water exit, composite missile versus hemisphere missile (shaded area) as affected by cavitation number. ξ = 45 degrees.

Figure 11.31. Smooth separation of vortices from tapered tail of composite missile. ξ = 45°, σ = 0.369, v_e = 75 fps.

PART IV.
PHENOMENOLOGICAL STUDIES

CHAPTER 12
WATER-ENTRY SPLASH CONTOURS[1]

The contour of a missile's water-entry splash can be helpful in interpreting water-entry phenomena and in developing water-entry theory. However, the transparency of water sometimes prevents clear photographs of the splash contours by obscuring the outline of the splash. To avoid this difficulty, a study using shadow photography was undertaken.

The splash contours formed in the vertical and oblique entires of 1- and 2-inch stainless-steel ball bearings were studied in a NUC Hydroballistics Laboratory tank about 10 by 20 by 5 inches deep and filled with water until the surface rose above the edges to form a negative meniscus. Shadowgraphs of the sphere water entries (Figure 12.1 and 12.2) were made by recording the images cast by a collimated spark beam upon a photographic film placed 5 inches behind the entry point and parallel to the entry trajectory. The spark, oriented so that its beam was normal to the plane of the film, was in front of the entry point and precisely aligned with the water surface. The spark was generated between two carbon electrodes with an 0.030-inch gap and had a duration of about 1 μs.

The spark flash timing sequence was initiated by a time-delay generator that was actuated when the falling sphere interrupted a photocell beam above the water; it was terminated immediately after the first half of the sphere crossed the water surface. Any amount of delay between 0 and 1 second could be introduced into the sequence in increments of 0.0001 second, allowing the sphere to be photographed at various penetrations and thus making it possible to follow the growth of the water-entry splash.

In the first series of tests, the steel sphere was held above the water by an electromagnet and dropped vertically by opening the magnet circuit. The height of the drop was varied to give several entry velocities. In the second series, the 2-inch diameter sphere entered the water at oblique angles. The sphere was suspended by a fine wire 13.5 feet long and swung into the water like a pendulum (Figure 12.3). Entry velocity was determined by measuring the distance traveled between two exposures recorded on a single film at an interval of 0.001 second. The deviation of the arc trajectory from a straight
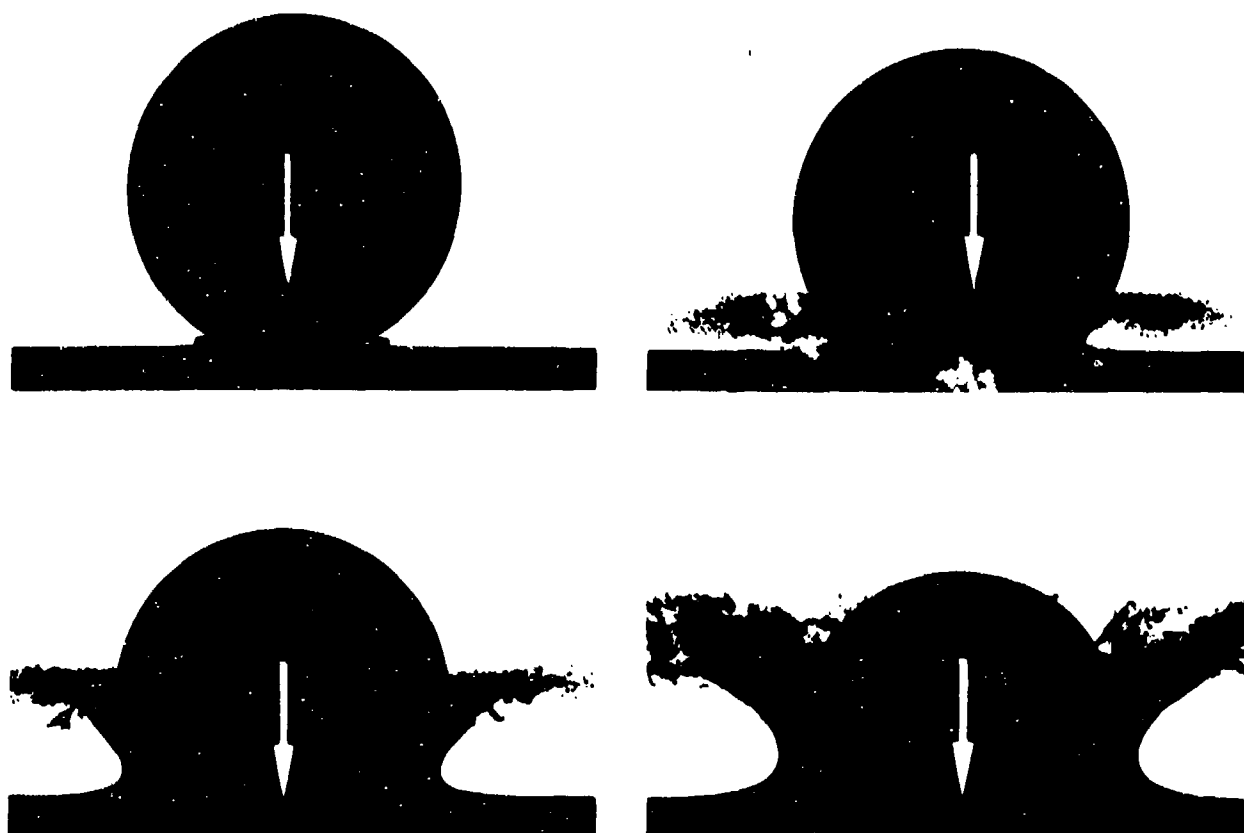
---

[1]Data taken from Reference 108.

217

Figure 12.1. Vertical water-entry shadowgraph of 2-inch sphere; $v_e = 22$ fps.

line was considered to be negligible over such a short trajectory. Oblique entry angles of 7, 12, 18, 24, and 47 degrees were used, with entry velocities varying from 16 to 30 fps.

The typical basket splash generated by the vertical entry of a sphere is shown in Figure 12.1. The splash has two distinct parts: the base, which extends from the original water level up to the zone of maximum splash contour constriction, and the sheath, which includes the layer of water about the sphere above the zone of maximum constriction and the spray of water leaving the sphere. The pressure of the sheath is practically atmospheric, and it is believed that the sheath has little effect upon the sphere since it is beyond the point of maximum pressure. In Reference 108, the curvature of the splash contour was found to approximate a parabola with its axis inclined to the horizontal. The equation of the parabola and associated parameters were experimentally derived as functions of the distance of penetration.

The sequence in Figure 12.2 shows a typical "sheath" splash produced by the vertical entry of a sphere at a low velocity. The splash resembles the one obtained by Worthington (Reference 112) under similar circumstances in his Series X photographs. The appearance of the splash at closure with its spray of droplets resembles the one in Figure 3.7 (Chapter 3), which also was reproduced from Worthington's work.

When a sphere enters water at an oblique angle (Figure 12.4), the forward splash is small and thin, the forward surface rise is less, and there is a relatively large rear surface rise that develops into a marked hump at low entry angles. The rear hump, as such, had not been noted previously, but can be seen vaguely in Figure 3.28 in Chapter 3 (taken from Reference 60). Photographs of the rear splash made from a point directly behind the sphere show two distinct types of rear-surface rise. At the lower entry velocities (16 fps), the hump rises as a single column at the first instant of water contact and persists until the sphere is completely immersed (top of Figure 12.5). At higher entry velocities (30 fps), two separate humps

218
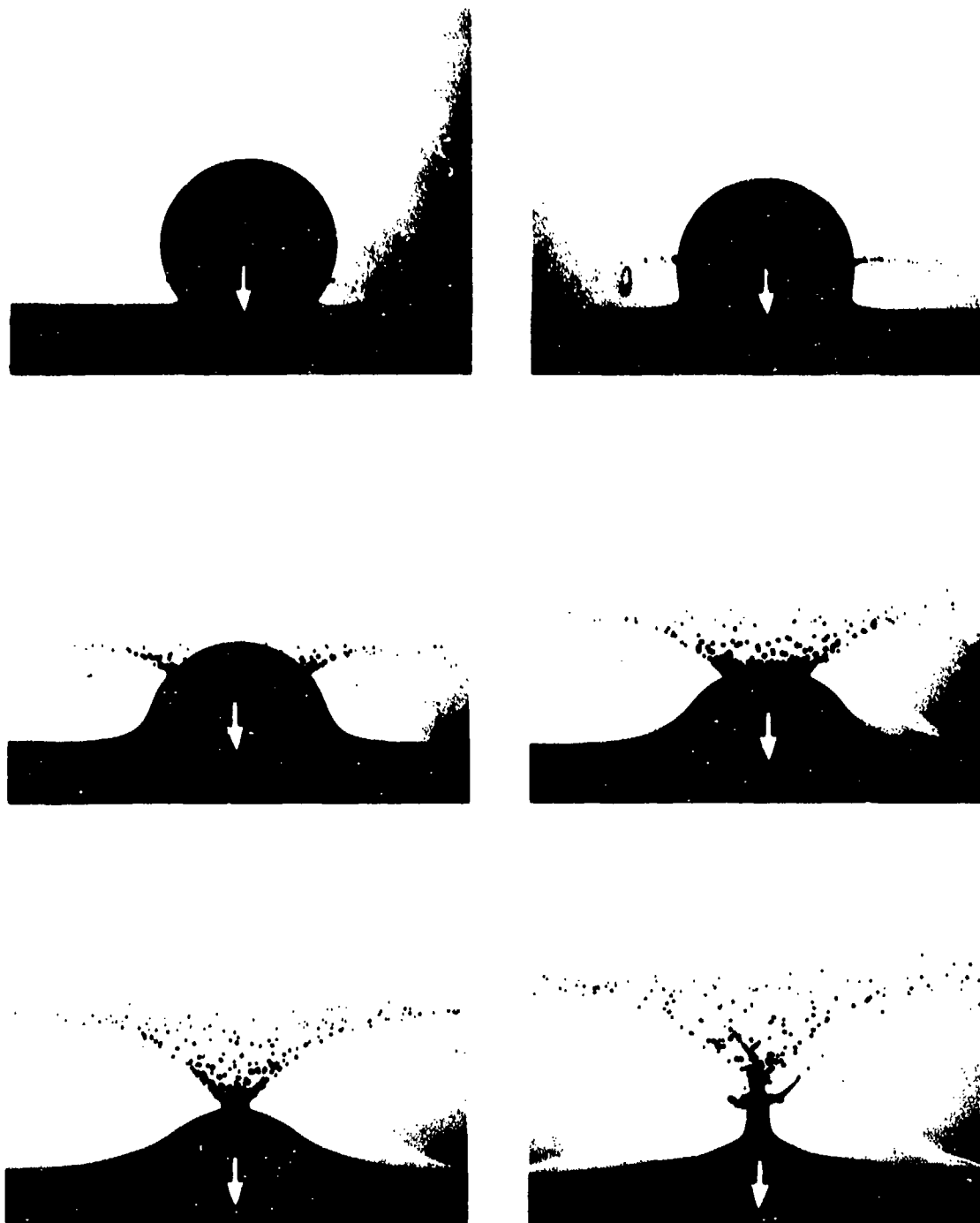
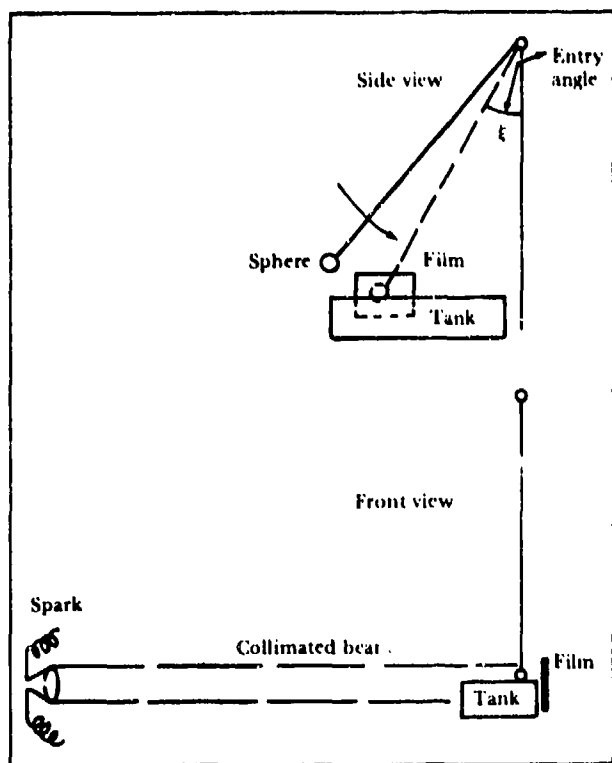Figure 12.2. Vertical water-entry shadowgraph of 1-inch sphere; v_e = 5.6 fps.

Figure 12.3. Oblique water-entry shadowgraph apparatus (not to scale).

form (bottom of Figure 12.5), move toward each other, coalesce, and finally rise together in a single column as at the lower velocity.

Photographs of the front of the sphere (Figure 12.6) show that very little water was thrown off to the sides during water entry and that no discontinuity existed in the front surface of the splash contour. The sideview shadowgraph thus is seen to represent a true cross-section of the splash through the center of the sphere. All shadowgraph records are sequences of single exposures, each obtained from a different launching.

Reference 108 compares experimental vertical-entry splash contours and theoretical approximations. A comparison is also made of experimental forward splash contours obtained in oblique water entry of spheres and approximate theory developed for the oblique entry of cylinders.

The shadowgraph method is more advantageous than conventional photography in the recording of actual splash contours. However, it should not be assumed that a central cross-sectional view is being obtained without supporting evidence from front and rearview photographs.
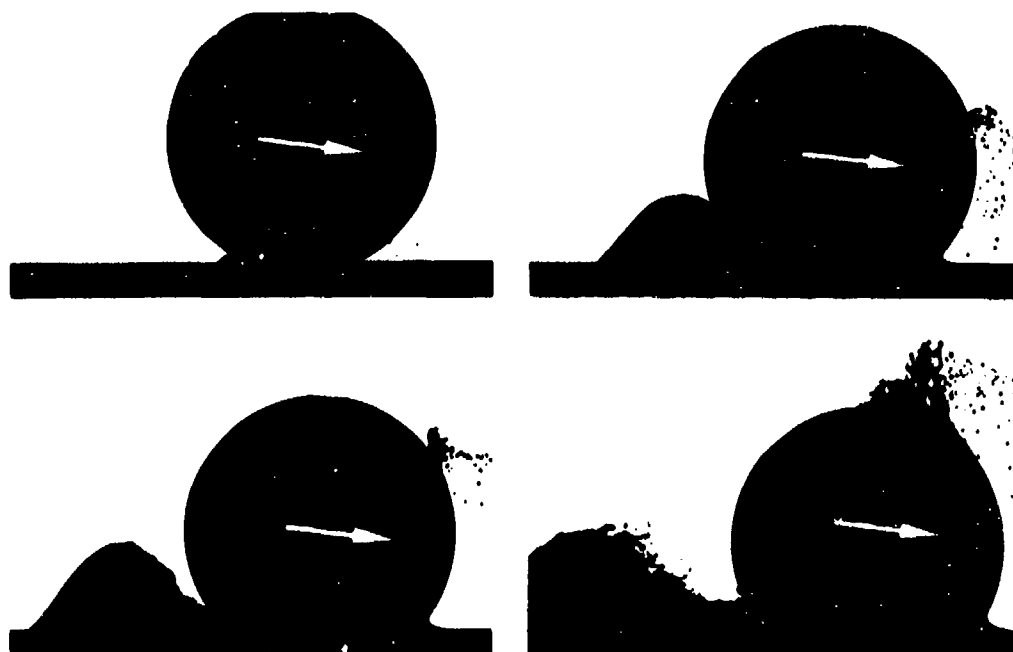
Figure 12.4. Oblique water-entry shadowgraph of 2-inch sphere ; v_e = 20 fps, ξ = -7°.

220

$v_c = 16$ fps

$v_c = 30$ fps
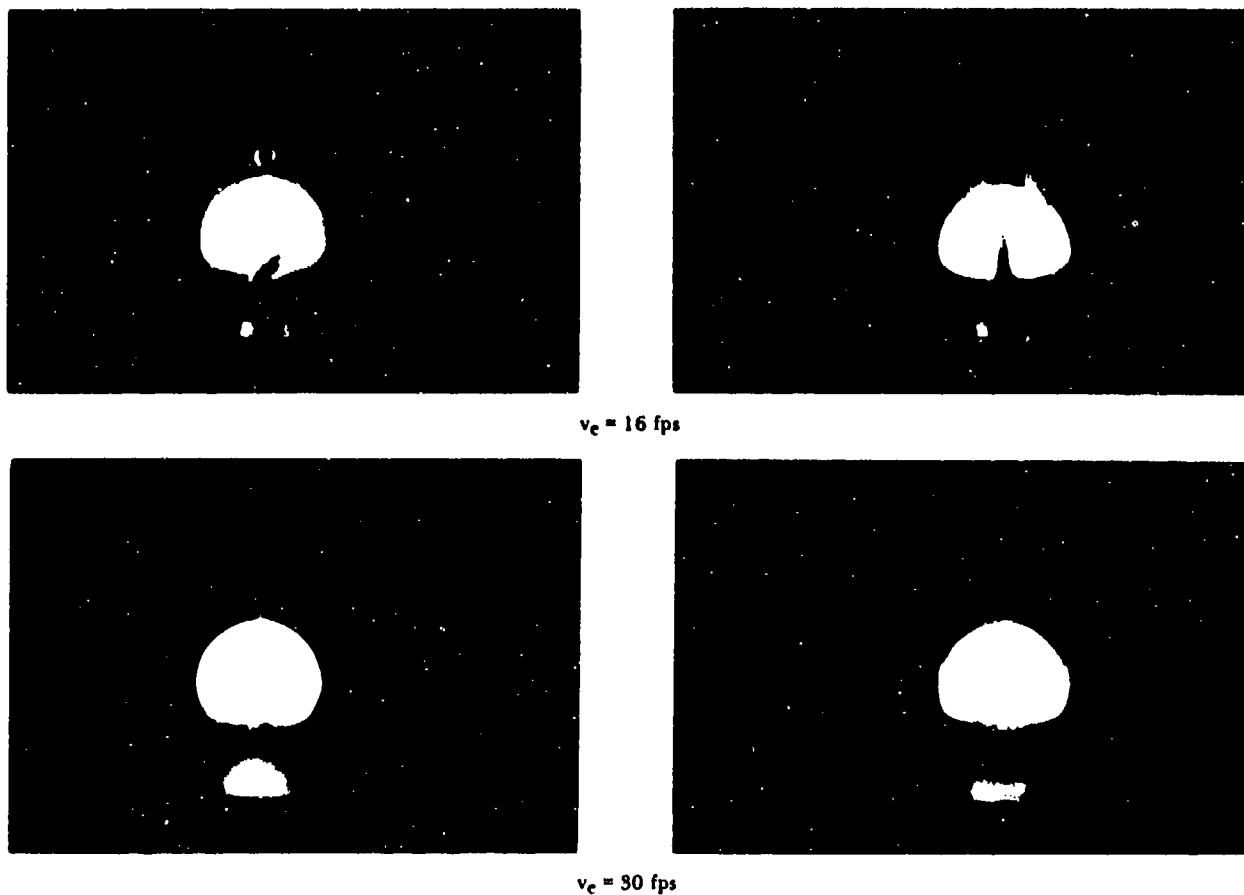
Figure 12.5. Two distinct types of rear-surface hump formed during oblique water entry, $\xi = -10^\circ$. Photographed by view camera directly behind 2-inch sphere.

Figure 12.6. Oblique water entries photographed by view camera in front of 2-inch sphere; $v_c = 20$ fps, $\xi = -14^\circ$.

221

CHAPTER 13

WAKE FORMATION

When a body moves through a fluid under fully wetted flow, a wake of turbulent fluid is formed. The turbulence arises from vortices generated in fluid that has passed near the surface of the body, i.e., the boundary layer, as well as from vortices that may be formed at the after end of the body, particularly if it is blunt. Since the wake contains momentum that is not recovered by the body, there will be a body drag, and the extent of the wake is an index of the drag. Skin friction forces and pressure reduction at the after end of the body cause the drag. In addition, vortex shedding may cause the flow about the body to become perturbed, resulting in fluctuations in the pressure distribution, which in turn can cause fluctuations in the missile direction of travel, velocity, and orientation.

Extensive studies have been made of the wake under conditions of fully wetted flow, but very little is known regarding its formation and behavior as a missile crosses an air-water interface. The speed of most air-to-water missiles is sufficiently high that water entry takes place under conditions of cavitation. The shape of the cavity is known to affect missile performance, and in some cases re-entrant jets are known to have formed, which could impinge on the after end of the missile, thereby deflecting it and possibly damaging it. Thus, the character of the water-entry cavity can be influenced by wake formation and behavior.

The hydrodynamic flow about a missile can be studied to advantage through the use of an oil-water interface. The presence of oil eliminates the water-entry splash and renders the flow more visible. The kinematic viscosity of the oil can be adjusted to that of air so that the flow in the neighborhood of a missile will simulate that obtained in an air-water interface insofar as

effects governed by the Reynolds number are concerned.

The experimental technique not only delineates the flow at the interface but marks the flow during the underwater flight by entrained oil. Photographs of vortex and jet formation obtained by this technique add to the understanding of these complex phenomena.

The studies described here were conducted at the NUC Hydroballistics Laboratory in the Liquid Interface Tank (Part V). A description of the apparatus and experimental techniques involved is given in Reference 90.

A 1-inch-diameter steel sphere and a 0.75-inch-diameter steel plate cylinder with circular cross section were launched in the water-filled tank topped with a layer of high-grade mineral oil having a kinematic viscosity of approximately 75% of that of air. The oil was dyed red for contrast.

The physical properties of the two liquids were as follows:

	Water	Oil
Relative density	0.996	0.837
Viscosity, lb/(ft sec)	0.54×10^{-3}	6.4×10^{-3}
Kinematic viscosity, ft^2/sec	0.87×10^{-5}	12.2×10^{-5}
Vapor pressure, torrs	31.8	0.5
Temperature, $^\circ$C	30	30

The missiles started from rest beneath the surface of the oil and traveled through the interface. Velocities ranging from 30 to 244 in/sec at the interface and ambient pressures of 737 and 25 torrs absolute resulted in both fully wetted and cavitating flows.

As a solid body traverses a liquid, at all except creep velocities, i.e., at Reynolds numbers much less than 1, the flow separates behind

222

the moving body and a wake is formed, the nature of which is determined by the Reynolds number of the flow as well as by body shape. The change in wake with increase in Reynolds number follows the same general pattern for cylinders, spheres, and other blunt bodies, the actual wake pattern associated with a particular Reynolds number being influenced by body shape, general turbulence level of the flow, etc.

The first appearance of the wake occurs as the streamlines broaden about the body, separating to allow a volume of disturbed fluid to form immediately behind it. Separation begins near the point where the velocity of flow around the body is decreasing most rapidly. In the case of the circular cylinder (Figure 13.1), separation begins near the rear stagnation point A. As the Reynolds number increases, the separation zone BB' moves forward to an almost stationary position, allowing the streamlines BC and B'C that bound the wake to broaden further. The flow within the wake then becomes apparent.

An inflow exists along the axis of symmetry of the wake and an outflow exists in the other portions. The circulatory motion produces a vortex configuration in the wake. The fluid in the wake is isolated from the main flow by layers of vorticity generated in the streamline bounding the body. The vorticity diffuses partially into the main flow but feeds primarily into the wake, causing it to elongate as the Reynolds number increases until the wake becomes unstable. Vorticity is then discharged periodically into the main stream, where it is dissipated by turbulent mixing. When the Reynolds number has increased sufficiently to cause a turbulent boundary layer on the body, the separation zone shifts to the rear and the streamlines
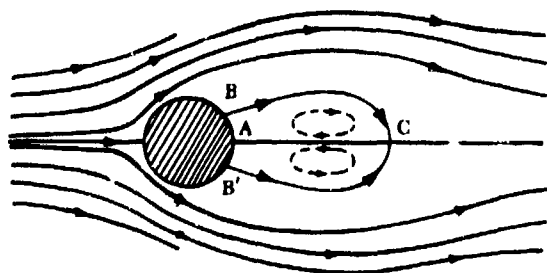
bounding the wake narrow abruptly. At these higher Reynolds numbers, the wake is characterized by completely turbulent flow; periodicity or pattern has vanished. Further increase in Reynolds number causes little apparent change in the wake until the onset of cavitation, although a slight and gradual broadening of the wake may occur if the separation zone creeps forward.

In the quasi-two-dimensional wake formed by long, thin bodies (cylinders, airfoils, etc.) oriented with their long axes normal to the flow, the vortex pattern within the wake is quite regular. At the onset of wake formation, the circulatory flow forms a vortex pair. The stationary vortex pair is permitted to exist behind the body by unstable equilibrium; any disturbance that spoils the symmetry of flow will cause the vortex pair to shed. As the Reynolds number increases, the vortex pair elongates in the direction of motion until it becomes unstable. Then a series of vortices is shed from alternate sides of the body, forming the well-known Kármán vortex street in the wake downstream (References 4 and 70). The frequency of vortex shedding increases with Reynolds number until the wake becomes so disturbed that the pattern is lost. For a circular cylinder normal to the flow, periodicity disappears from the wake above Reynolds numbers of approximately 10^5.

Extrapolation of the two-dimensional case suggests that a vortex ring will form within the wake of an axisymmetric body. Experimental data substantiate this, but the vortex ring either within the wake itself or in a shed array appears to be much less stable than the two-dimensional vortex pair or Kármán vortex street (References 24, 35, and 70). Observation of the wake formed by a circular disk (Reference 24) proved it to be composed of distorted loops of vorticity arranged with some symmetry. The flows reported in Chapter 14 also indicate a periodicity in the discharge of vorticity in the wake of a three-dimensional body.

The growth of a vortex configuration in a wake can be seen behind the sphere in Figure 13.2. Rotation of the fluid within the wake is indicated by arrows in Figure 13.3. The vortex appears to be a somewhat irregular ring stationary within the wake.

The vortex soon elongates in the direction of the main stream, probably because of the abrupt change in Reynolds number that occurs

Figure 13.1. Wake behind a circular cylinder at a low Reynolds number ($R < 50$).

223

35.0

39.2

43.3

47.5

Approximate time, ms

Figure 13.2. Growth of vortex in wake. Conditions: v (crossing oil-water interface) = 30 in/sec; p_a = 737 torrs; F = 1.5; R x 10^{-4} = 0.17 for oil and 2.4 for water; σ = 406 for oil and 326 for water.

224

a Sheath splash of oil narrows as
  sphere drops. Flow within splash
  appears to impinge on surface.
  Splash finally separates; upper
  portion flows back into oil layer,
  lower portion is shed from sphere.

b Sphere is followed by turbulent wake
  of oil that lengthens and is finally shed
  in strands and droplets. Wake appears
  to move upward in outer area and down-
  ward in inner area.

Oil-water interface

Motion of sphere
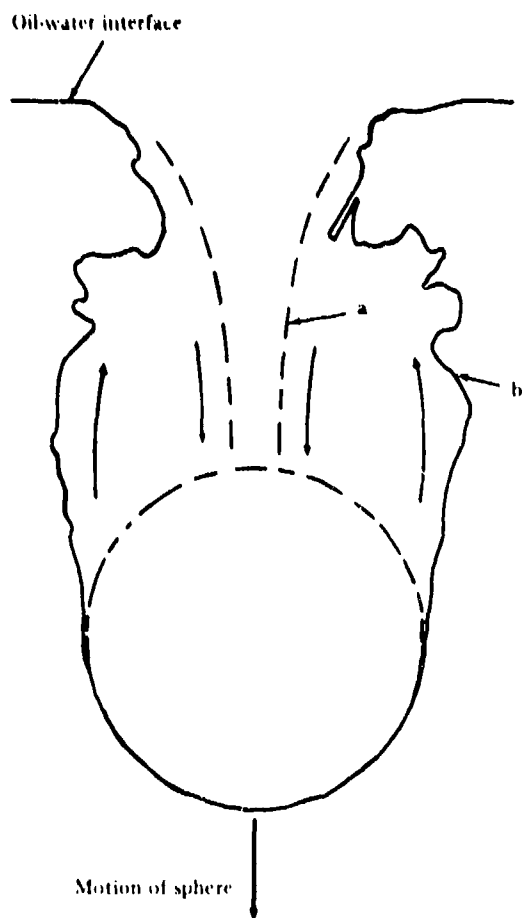
Diagram of flow
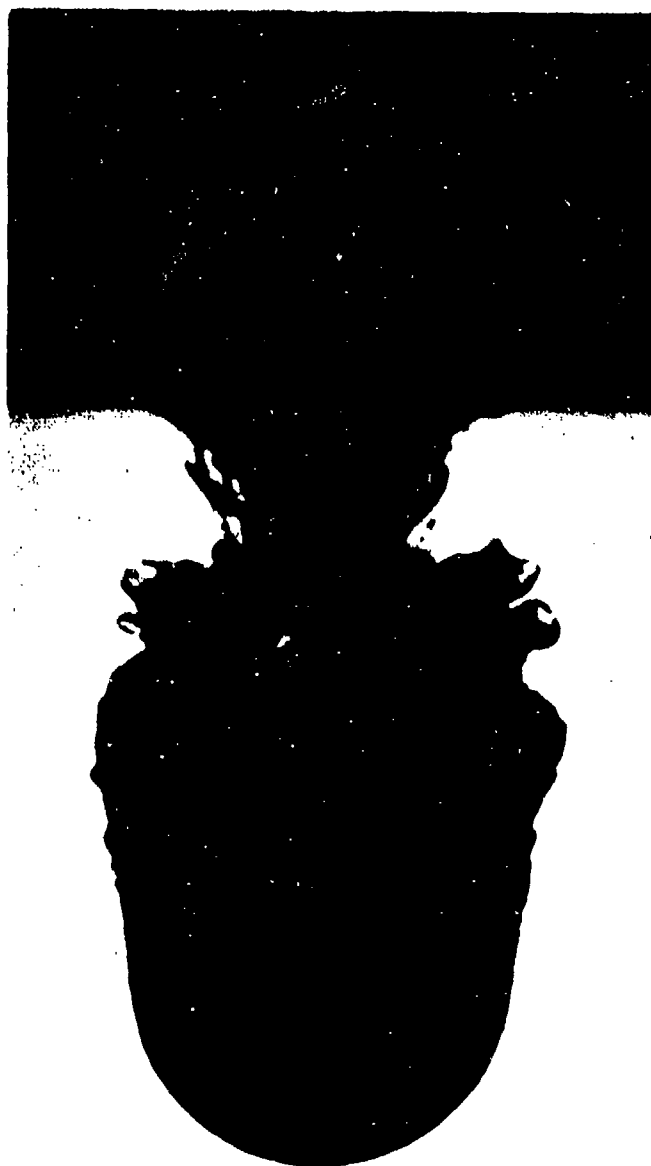
Colored oil-water wake

Figure 13.3. Direction of flow within wake.

at the interface. With the Reynolds number 0.17×10^4 in oil and 2.4×10^4 in water, the external configuration of the wake would be changed, even though the flow in the oil entrapped in the wake would remain at the lower R. The Reynolds number of the flow where the two liquids meet is not well defined. Since a vortex ring is unusual in a wake composed entirely of water, the presence of oil may increase the stability of the vortices. However, the growth, shedding, and subsequent decay of a cavitation vortex formed on a sphere started impulsively from rest in water (Figure 13.4) differs little from that of the oil vortex. Both initially approximate a torus and subsequently decay into irregular loops. The cavitation vortex, being of lesser mass and also of vaporized fluid, decays more rapidly.

225

Figure 13.4. Cavitating vortex from a steel sphere started impulsively from rest under water.

More prominent vortices appear at higher velocities (Figure 13.5). A large vortex configuration forms in the wake and is subsequently shed, the momentum imparted by the shedding vortex causing the sphere to deviate noticeably from its trajectory.

Vorticity diffuses into the main flow from the streamline bounding the wake, resulting in a "pineapple top" wake configuration (Figure 13.6). Fragments of fluid peel from the wake into the main flow soon after it separates from the sphere, travel along the streamline bounding the wake until, at the upstream end, they separate and move away with the main flow instead of recirculating in the wake.

Figures 13.2 and 13.7, of sphere launchings at 30 and 158 in/sec, respectively, show the behavior of the interface soon after passage of the sphere and its wake. Studies with the plate-cylinder missile (Figure 13.8) show that a slight angle of attack introduces a marked asymmetry into the flow. Vorticity can be seen in the larger wake area, and the ragged bits of oil peeling from the wake appear to be small fragments of vorticity trapped in the main flow.

Once a fully turbulent wake has formed, further increase in Reynolds number causes little change in the wake until the onset of cavitation.

Cavitation will occur in the region of separation when the ambient pressure falls below the vapor pressure of the fluid medium.

The first evidence of cavitation is not a visible change in the flow, but rather an abrupt increase in the flow noise. The first visible sign of cavitation (incipient cavitation) is the tiny bubbles along the streamline bounding the wake (Figure 13.9 from Reference 28), which are believed to occur at minute centers of vorticity; a dye was used to delineate the shear layer. As the stream velocity increases further, cavitation grows in the wake until the entire wake area is occupied, as shown in CIT water-tunnel tests of a torpedo model (Figure 13.10 from Reference 31). The size of the cavity is, of course, influenced by missile shape but is primarily determined by the cavitation number, which thus replaces the Reynolds number as the index of flow.

At the downstream end[1] of a cavity, the flow in the streamlines in and near the cavity wall may reverse direction and turn inward to form a re-entrant jet through the cavity opposing the direction of the main flow (Figure 13.11). Such a jet has been observed in the cavitation-number regime from 0.15 to 0.30 (Reference 10) and has been known to exist for

---

[1] Commonly called the base, a term that seems contradictory when referred to a vertical cavity.

226

0

8.3

16.7

33.3

Approximate time, ms
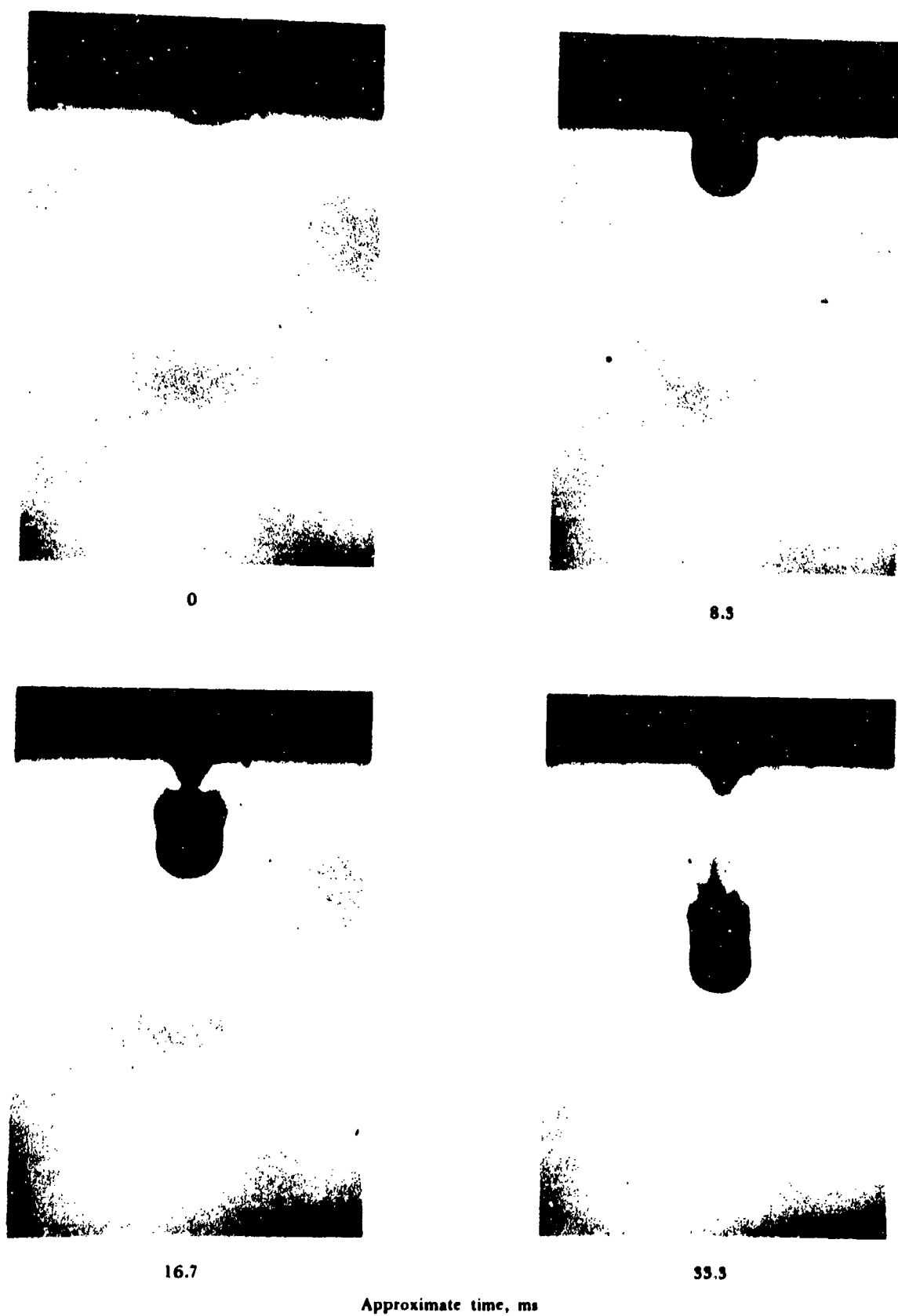
Figure 13.5a. Vortex shedding from fully wetted sphere. Conditions: v (crossing oil-water interface) = 96 in/sec; p_a = 737 torrs; F = 4.9; R x 10^{-4} = 0.55 for oil and 7.7 for water; σ = 39 for oil and 32 for water.
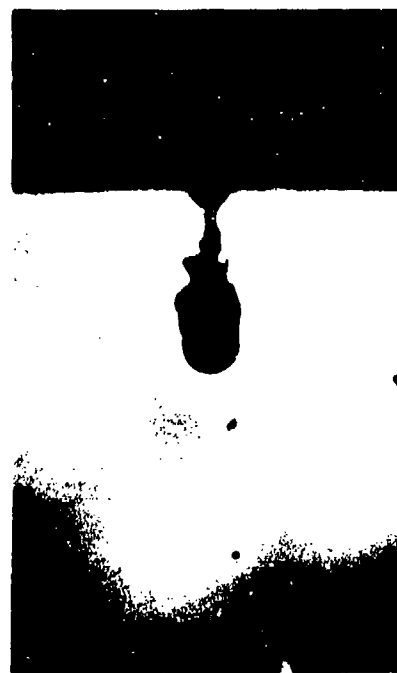
227
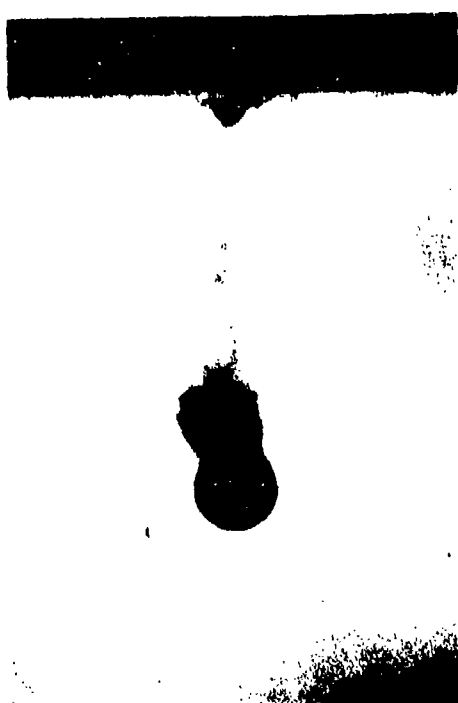
50.0

58.4

66.7

83.3

Approximate time, ms

Figure 13.5b. Vortex shedding from fully wetted sphere. Conditions: v (crossing oil-water interface) = 96 in/sec; p_a = 737 torrs; F = 4.9; R x 10^{-4} = 0.55 for oil and 7.7 for water; σ = 39 for oil and 32 for water.

228

10.8
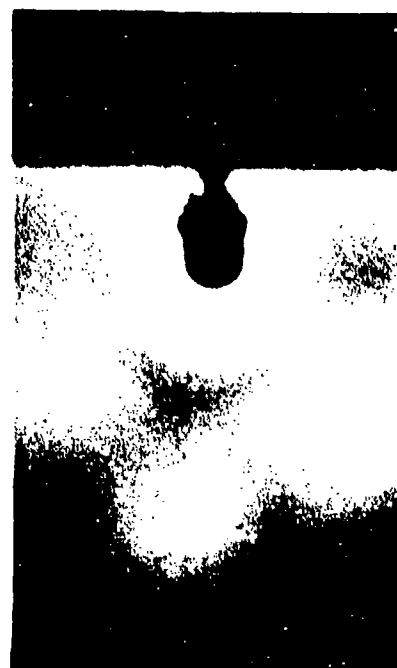
13.3

17.5

20.0

Approximate time, ms

Figure 13.6. Diffusion of vorticity into free stream. Conditions: v (crossing oil-water interface) = 158 in/sec; p_a = 737 torrs: F = 8.0; R x 10^{-4} = 0.9 for oil and 12.6 for water; σ = 15 for oil and 12 for water.

229

6.7

7.5

8.5

10.0

Approximate time, ms
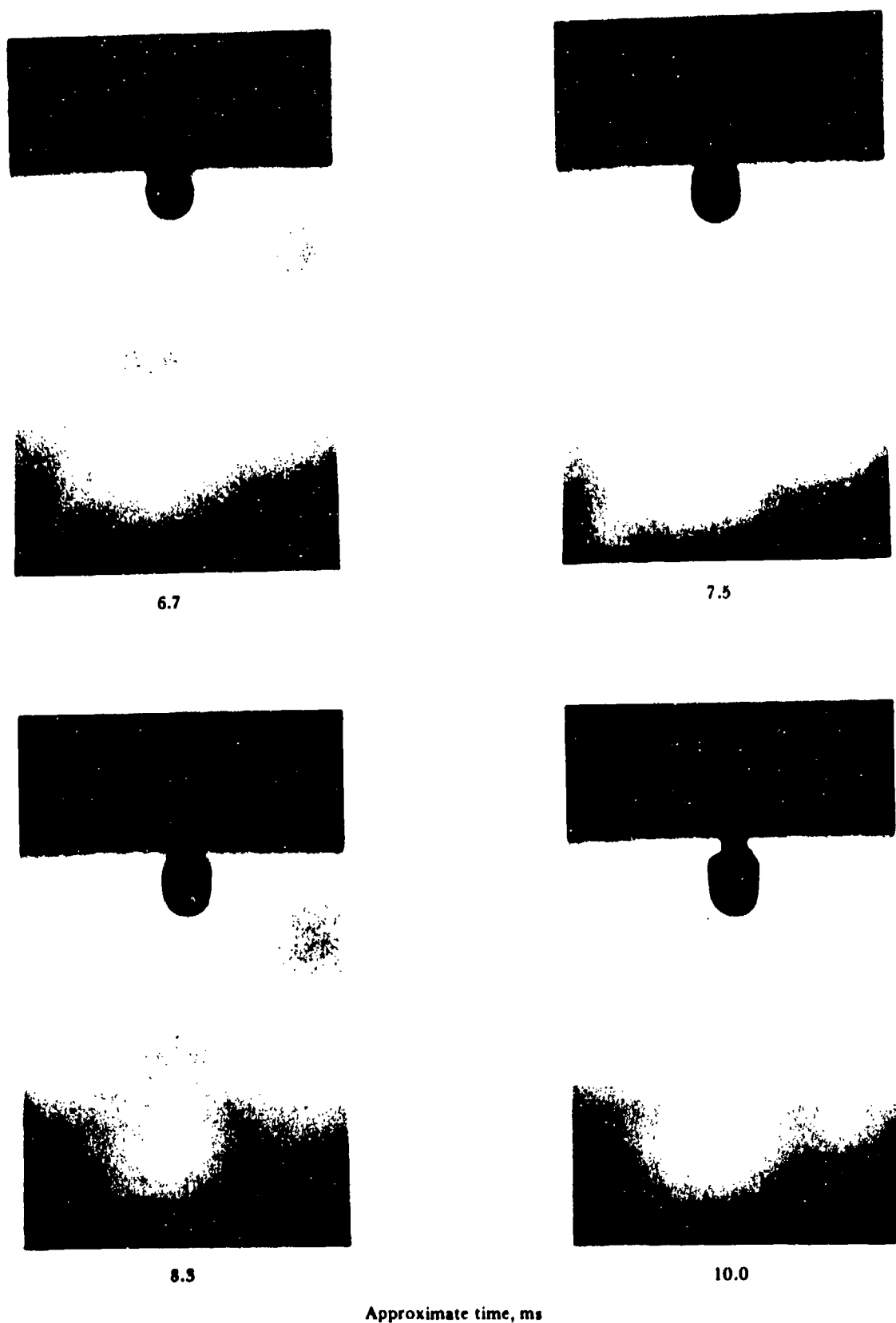
Figure 13.7. Change in interface with time. Conditions: v(crossing oil-water interface) = 158 in/sec; p_a = 737 torrs; F = 8.0; R x 10^{-4} = 0.9 for oil and 12.6 for water; σ = 15 for oil and 12 for water.

230

16.7

58.4

83.3

104.2

Approximate time, ms

Figure 13.8. Fully wetted plate cylinder crossing oil-water interface. Conditions: v (crossing oil-water interface) = 30 in/sec; p_a = 737 torrs; F = 1.8; R x 10^{-4} = 0.13 for oil and 1.8 for water; σ = 406 for oil and 326 for water.
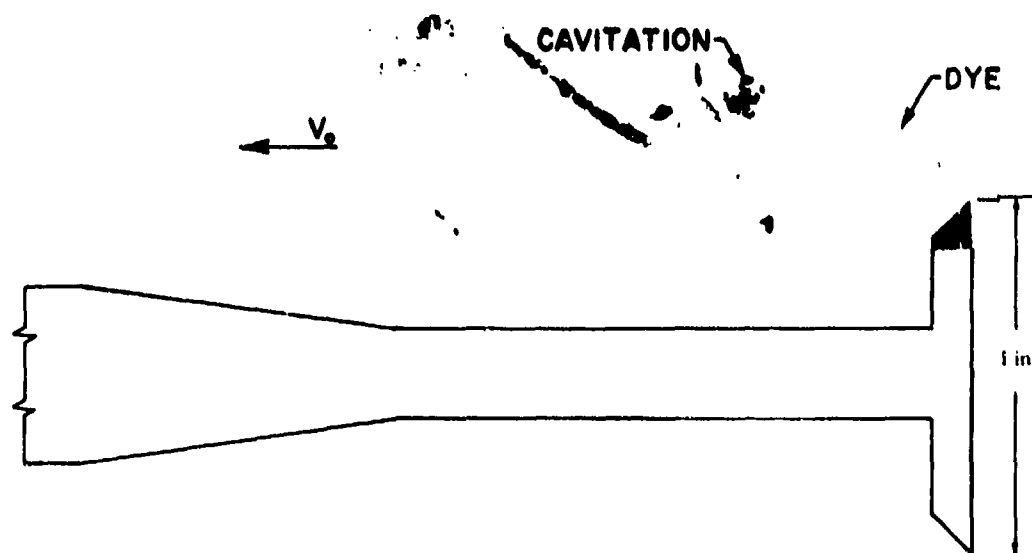
Figure 13.9. Shear layer and cavitation delineated by dye.

some time, but it is an experimentally elusive thing that has been little photographed. Either the downstream end of the cavity is opaque or, if translucent, the contrast between the jet and the main flow is too vague to resolve photographically. At still lower cavitation numbers, the cavity has been observed to terminate in a pair of hollow vortex tubes trailing from the base of the cavity (Figure 13.12, from Reference 82).

During the NUC studies of a sphere and a plate cylinder crossing an oil-water interface, the difference in vapor pressures of the oil and water caused the cavitation number in the oil to be higher than that in the water; at any given velocity and submergence, the cavity formed in oil was shorter and slimmer than the water cavity. The size difference became apparent when the base of the cavity, which had been traveling downward through the oil, remained stationary in the interface while the cavity lengthened. After the cavity had elongated sufficiently to achieve equilibrium at the ambient cavitation number, the cavity base again traveled downward. Cavity elongation illustrates the response of the cavity to sudden changes in cavitation number.

Photographs of sphere launchings made under conditions of cavitating flow show re-entrant jets, revealing not only their formation but the interaction between the jet and the

missile and cavity. In Figure 13.13 (the cavitating sphere crossing the interface), the jet had formed while the sphere was still in the oil. At about the time the base of the cavity crossed the interface, the jet had begun to impinge upon the sphere. A short time later, the impinging jet splashed from the sphere and distorted the cavity wall. The distortion continued to grow radially after the sphere and impinging jet had passed, but below the point of distortion the cavity soon assumed normal diameter, indicating that the jet was no longer splashing against the cavity wall. At approximately 50 ms after the missile reached the interface, a deep closure began just beneath the portion disturbed by the jet. After deep closure, the re-entrant jet re-formed at the base of the cavity.

In a second sphere launching at higher velocity under conditions of cavitating flow (Figure 13.14), a re-entrant jet again formed while the sphere was still in the oil. Later the jet deviated from the vertical and struck the cavity wall. A deep closure occurred at the contact point between the jet and cavity wall, the upper portion of the cavity collapsing about the jet and rebounding.

Figures 13.15 and 13.16 show a similar launching of the plate-cylinder missile. The sharp discontinuity at the leading edge produced a cavity so clear that the jet could be photographed as it overtook and then engulfed the
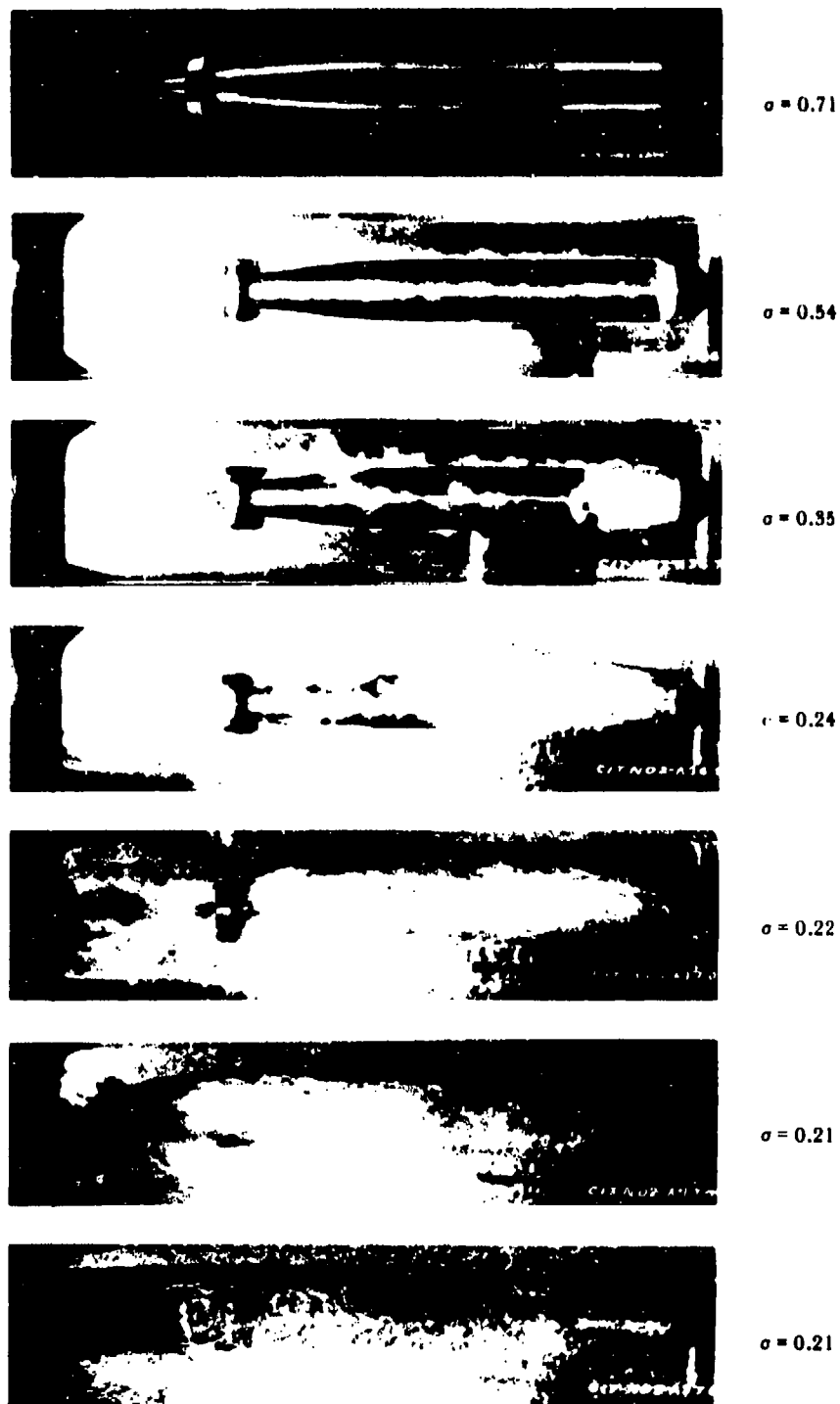
232

σ = 0.71

σ = 0.54

σ = 0.35

σ = 0.24

σ = 0.22

σ = 0.21

σ = 0.21

Figure 13.10. Increase in cavitation with decrease in σ. Torpedo model with hemisphere head.
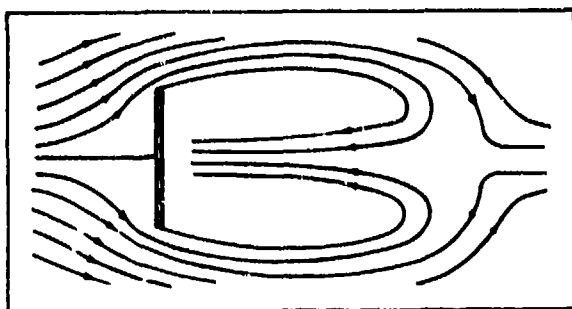
233

Figure 13.11. Re-entrant jet formation in cavitating flow behind a plate.

missile. The jet created a small disturbance near the interface before it struck the missile. In the motion pictures that were taken, the jet flow appeared to be pulsing. The cavity produced by this shape was so broad that the jet had almost reached the leading edge of the missile before the cavity became distorted.

A second disturbance in the cavity wall with its characteristic bulge appeared soon after the first, again suggesting pulsing or some other irregularity in the jet flow. In Figure 13.16 the collapse and rebound of the cavity after the missile had passed from the camera field can be seen. Study of the motion pictures of the cavitating flow leads to the belief that in the higher cavitation-number range immediately

preceding cavity collapse, a vortex ring may form at the base of the cavity.

The delineation of the flow when a missile crosses an interface from colored oil into water (the oil having approximately the same kinematic viscosity as that of air) provides information on wake behavior in missile air-to-water entry. The results show that wake formation and behavior are very complex. In fully wetted flow at low velocities, vorticity appears in the wake with subsequent vortex shedding and decay. At higher velocities, more prominent vortices appear; a large vortex configuration forms in the wake and is subsequently shed, the momentum imparted by the shedding vortex causing missile trajectory deviation. In cavitating flow, the flow in the streamlines in and near the cavity wall reverse and turn inward to form a re-entrant jet that passes through the cavity and opposes the direction of the main flow. This jet either impinges on the rear of the missile and is deflected into the side of the cavity or it strikes the side of the cavity directly. Later, deep closure may occur, with final cavity collapse and rebound.

The features of this study that may affect missile design are (1) vortex shedding, which may perturb the missile trajectory and permanently deflect it, and (2) the re-entrant jet, which can not only cause missile deflection but structural damage and malfunctioning in missiles which exhaust gases from the rear.
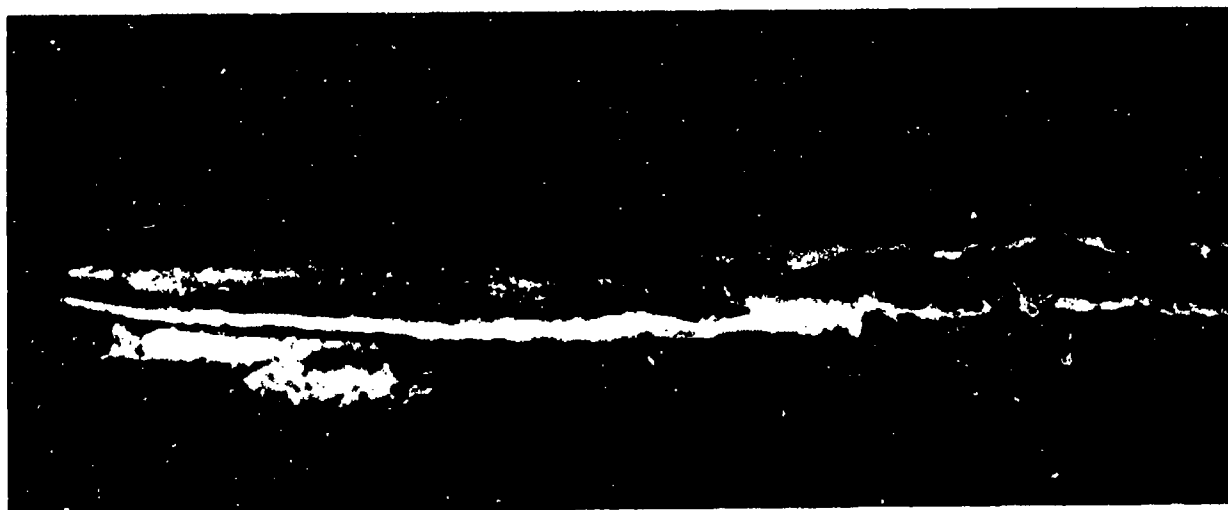
Figure 13.12. Vortices trailing from cavity.

234

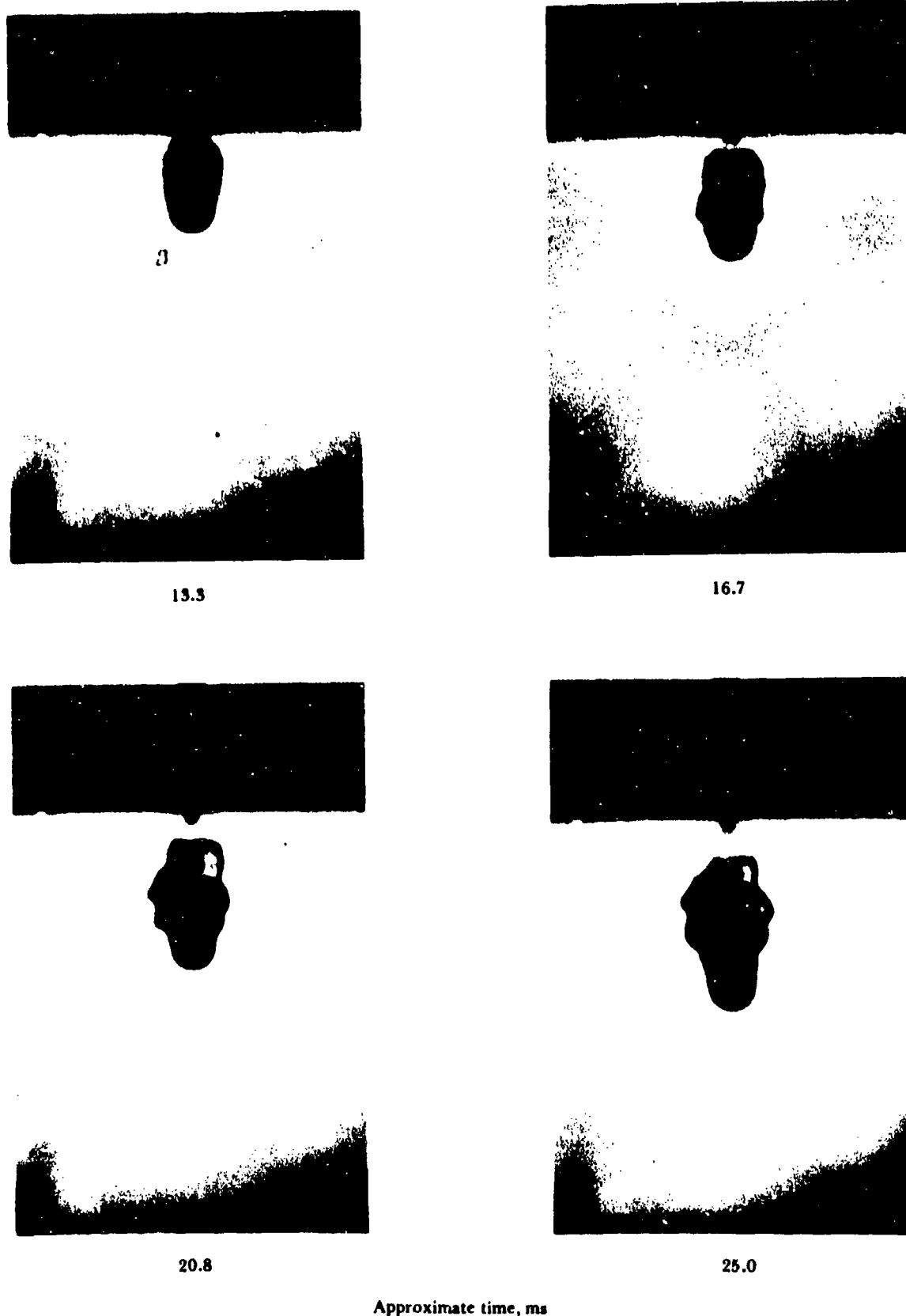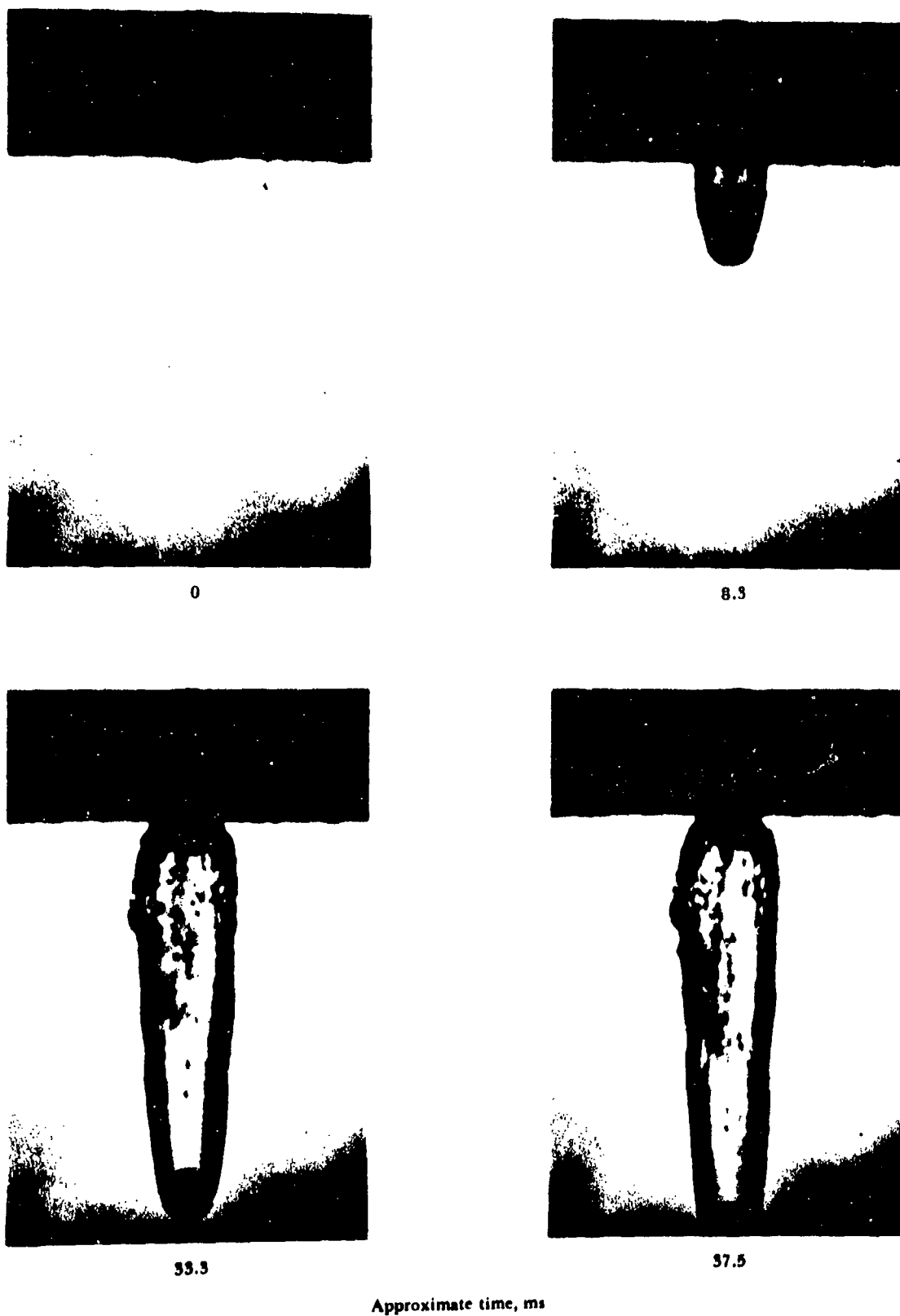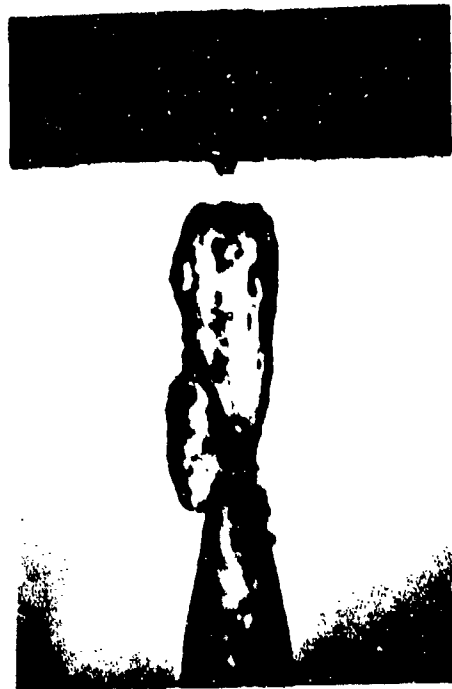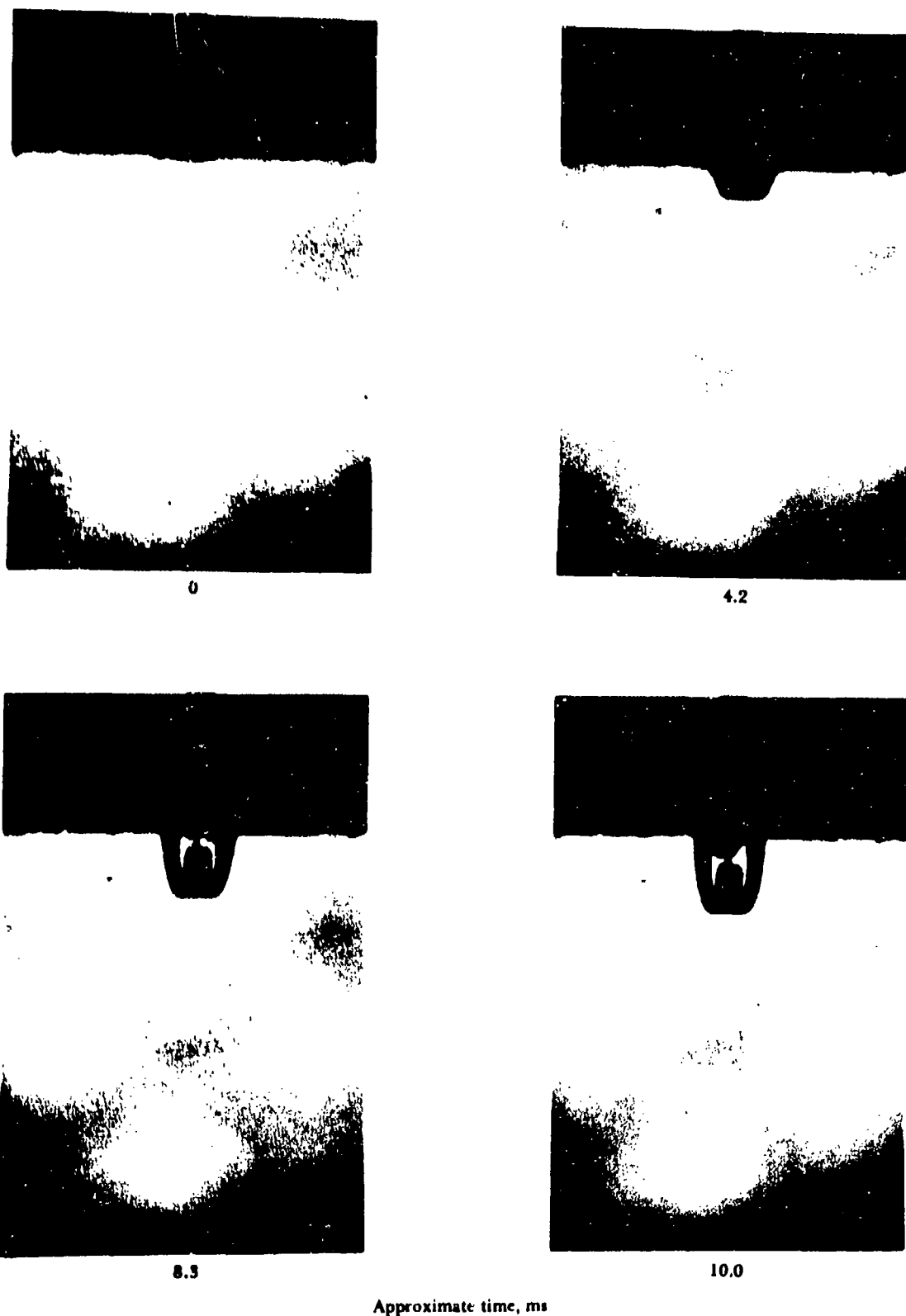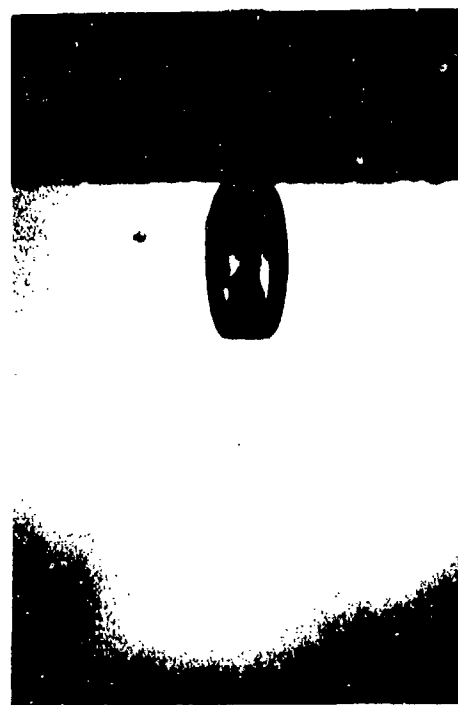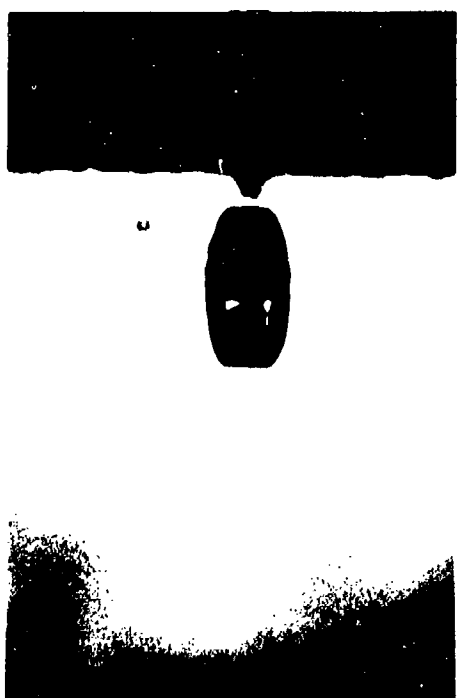0 8.3

10.0 11.7

Approximate time, ms
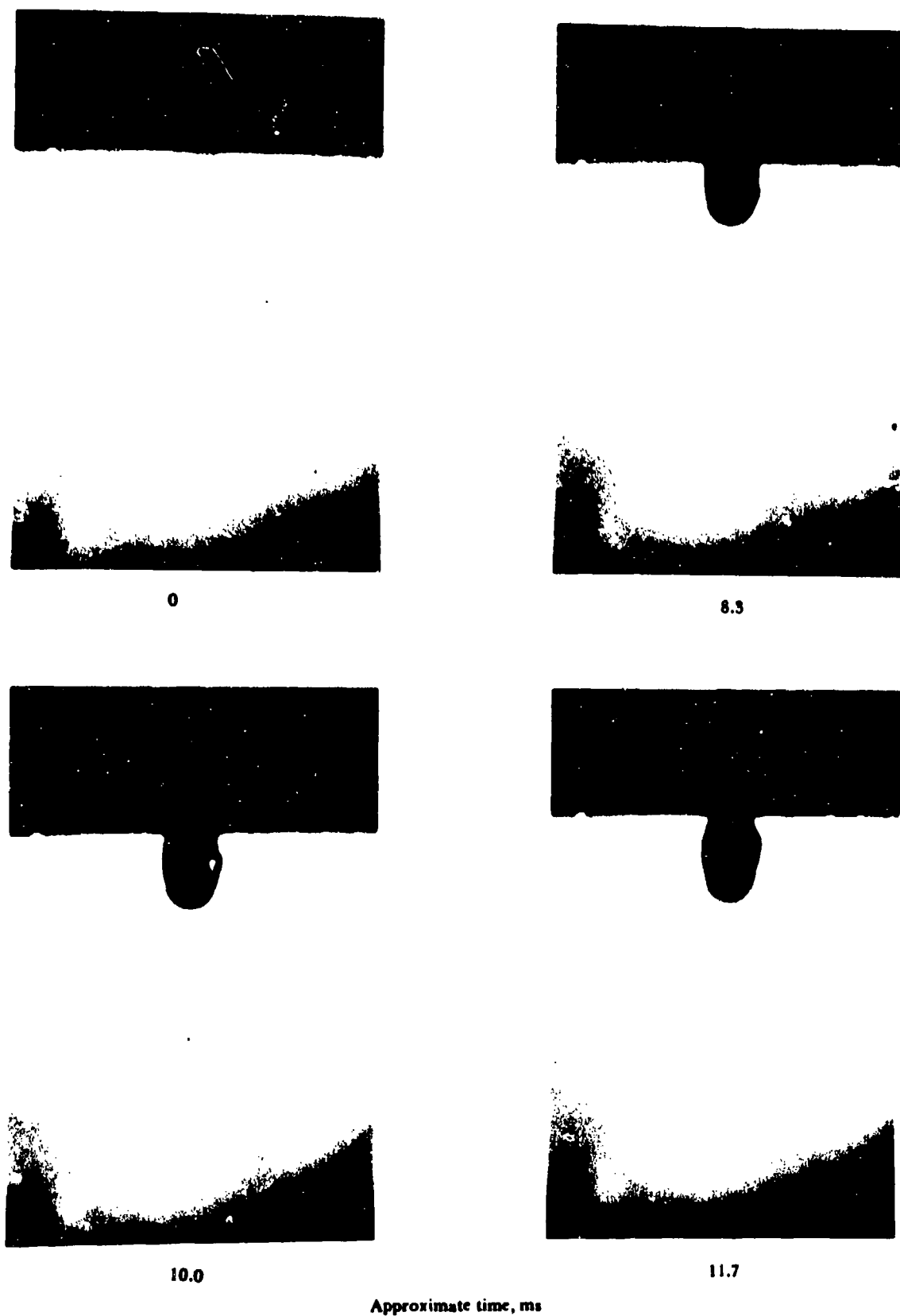
Figure 13.13a. Cavitating sphere crossing oil-water interface. Conditions: v (crossing oil-water interface) = 159 in/sec; P_a = 25 torrs; F = 8.1; R x 10^{-4} = 0.91 for oil and 12.7 for water; σ = 0.7 for oil and 0.1 for water.
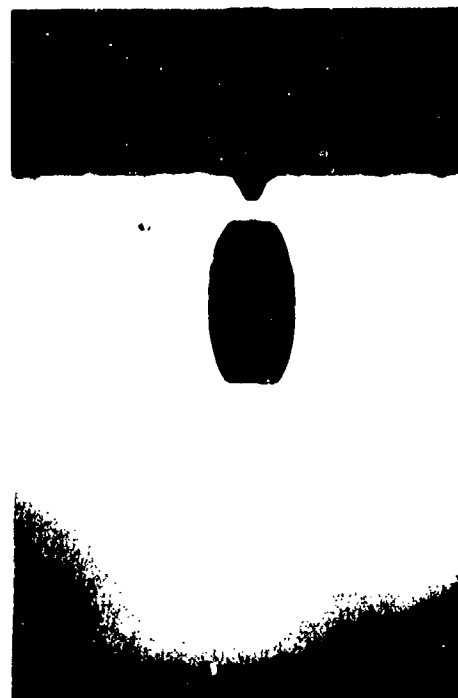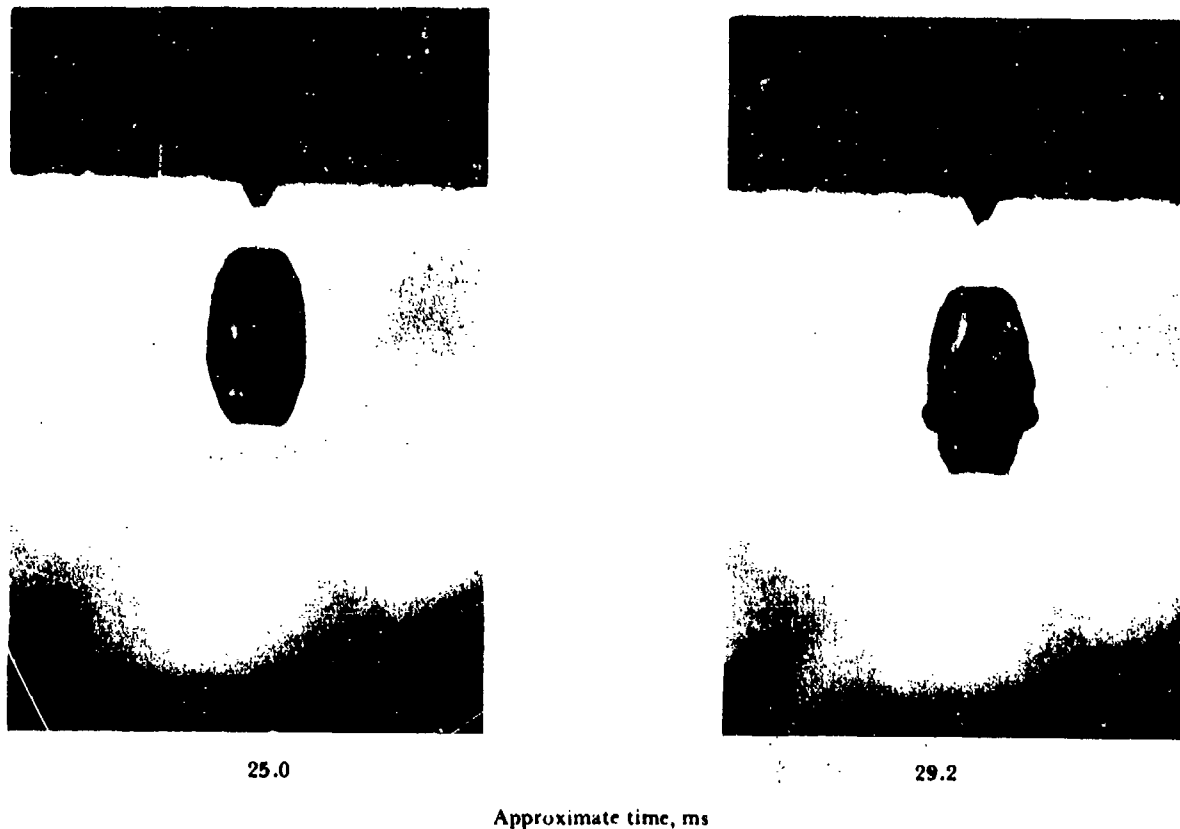
235

a

13.3

16.7

20.8

25.0

Approximate time, ms

Figure 13.13b. Cavitating sphere crossing oil-water interface. Conditions: v (crossing oil-water interface) = 159 in/sec; p_a = 25 torrs; F = 8.1; R x 10^{-4} = 0.91 for oil and 12.7 for water; σ = 0.7 for oil and 0.1 for water.

236

0

8.3

33.3

37.5

Approximate time, ms

Figure 13.14a. Cavitating sphere crossing oil-water interface. Conditions: v (crossing oil-water interface) = 244 in/sec; p_a = 22 torrs; F = 12.4; R x 10^{-4} = 1.4 for oil and 19.5 for water; σ = 0.3 for oil and 0.02 for water.

237

50.0   66.7

75.0   100.0

Approximate time, ms

Figure 13.14b. Cavitating sphere crossing oil-water interface. Conditions: v (crossing oil-water interface) = 244 in/sec; p_a = 22 torrs; F = 12.4; R x 10^{-4} = 1.4 for oil and 19.5 for water; σ = 0.3 for oil and 0.02 for water.

238

0

4.2

8.3

10.0

Approximate time, ms

Figure 13.15a. Cavitating plate-cylinder missile crossing oil-water interface. Conditions: v (crossing oil-water interface) = 150 in/sec; p_a = 25 torrs; F = 8.8; R x 10^{-4} = 0.64 for oil and 9.0 for water; σ = 0.8 for oil and 0.1 for water.

239

13.3

16.7

20.8

22.5

Approximate time, ms

Figure 13.15b. Cavitating plate-cylinder missile crossing oil-water interface. Conditions: v (crossing oil-water interface) = 150 in/sec; p_a = 25 torrs; F = 8.8; R x 10^{-4} = 0.64 for oil and 9.0 for water; σ = 0.8 for oil and 0.1 for water.

240

25.0   **29.2**

Approximate time, ms

Figure 13.15c. Cavitating plate-cylinder missile crossing oil-water interface. Conditions: v (crossing oil-water interface) = 150 in/sec; p_a = 25 torrs; F = 8.8; R x 10^{-4} = 0.64 for oil and 9.0 for water; σ = 0.8 for oil and 0.1 for water.

241
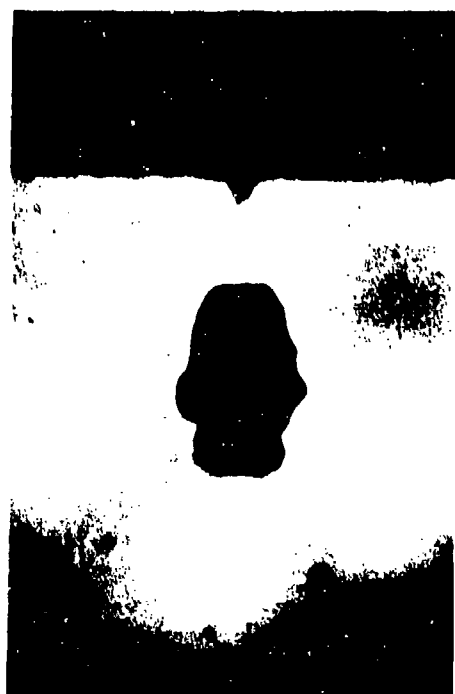
33.3
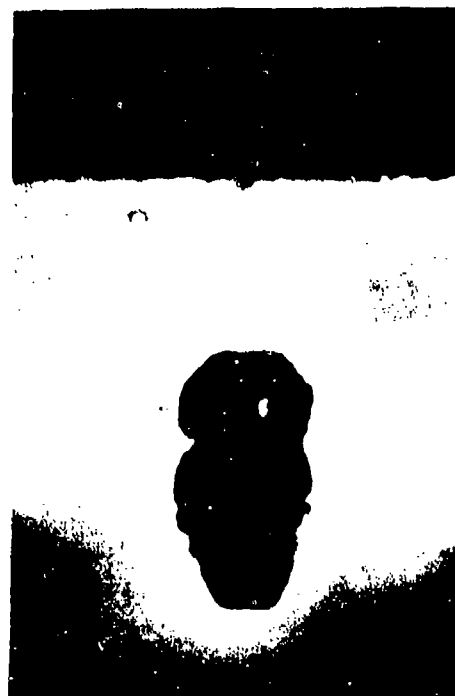
50.0

66.7

75.0

Approximate time, ms

Figure 13.16a. Collapse and rebound of cavity in latter part of launching shown in Figure 13.15.

242

91.7   100.0

116.7   133.3

Approximate time, ms

Figure 13.16b. Collapse and rebound of cavity in latter part of launching shown in Figure 13.15.

243

CHAPTER 14
WAKE EFFECTS

The fine structure or rapid fluctuation of the flow around a missile tail is important in wake studies because of the vibration it induces. In a large vehicle, the result may be metal fatigue and personnel discomfort. In a small missile, the tail may be so perturbed that missile orientation and velocity are somewhat affected. The large wake fluctuations reported in the sphere studies of Chapter 13 showed that a shed vortex resulted in trajectory deflection.

Studies of the fully wetted flight of a research missile (Basic Finner, Reference 80 and Figure 14.1), revealed an additional small pitching motion superimposed on the major motion with a frequency of about 15 Hz at a missile velocity of 7.5 fps. This frequency approximates that predicted by theory[1] for Kármán vortex street shedding (18 per second). Since a shedding vortex exerts a force normal to the missile motion, it was suspected that vortices were shedding from the base of the missile at a comparable frequency, and the observed small pitching motion was caused by interaction between the missile fins and the shedding vortices.

To determine whether vortex shedding could have produced such a pitching motion, tests were conducted in the large NUC Open Launching Tank (Part V). The experimental procedure was as follows:

1. The missile was trimmed to be nose-heavy and its specific gravity was adjusted so that a sinking velocity range of 1 to 6 fps could be studied when the missile was released vertically at the water surface.

2. A thin layer of nigrosine (black water-soluble dye) paste was applied either on the missile base near the intersection of fins and body cylinder or on the after edges of the fins.

3. The missile was held vertically nose down, partially submerged, with the dyed area just above the water surface, and released. It was held at least 15 inches away from the tank sides to avoid wall effects.

---

[1] From theory (Reference 24, page 570), the frequency of vortex shedding behind a cylinder with axis normal to the flow is

$$\frac{Nd}{U_0} = 0.198 \left(1 - \frac{19.7}{R}\right)$$

where N is the number of vortices shed per unit time, U_0 is the velocity of the undisturbed fluid with respect to the cylinder, d is the cylinder diameter, and R is the Reynolds number with respect to the cylinder diameter. For two-dimensional plates of width d normal to the flow

$$\frac{Nd}{U_0} = 0.16$$

where 0.16 is an average of values found by several investigators. The Reynolds number based on a velocity of 7.5 fps, a missile length of 10 inches, and a water temperature of 20°C is 5.79×10^5, which corresponds to transition on the missile body; thus the flow about the fins was probably turbulent.
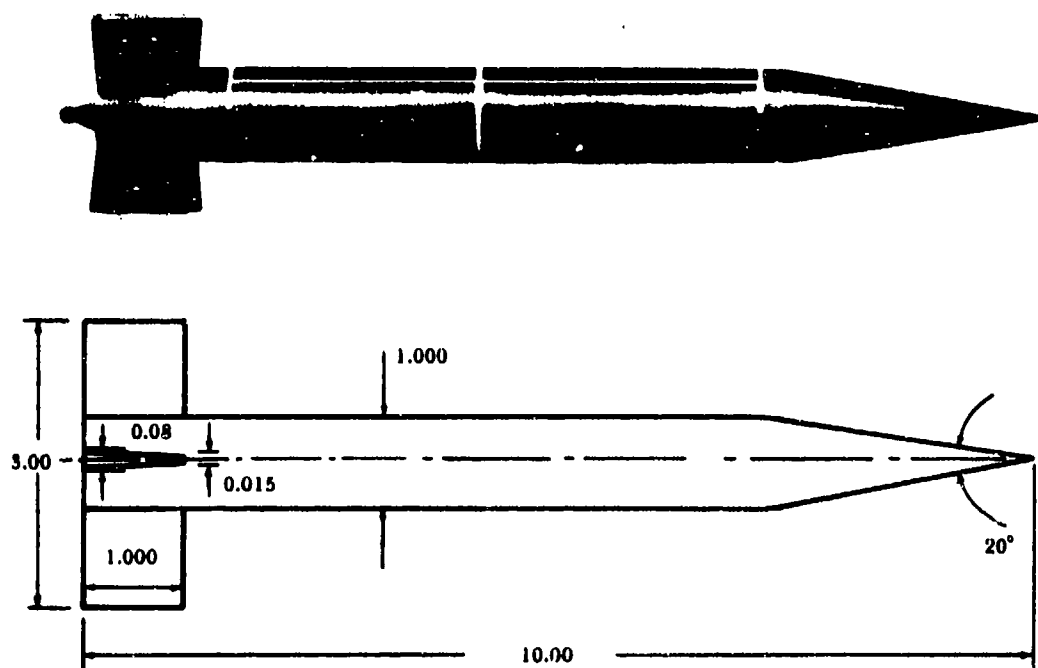
Figure 14.1. Basic Finner missile. Dimensions in inches.

4.   The sinking missile and the dye trail were photographed with the rotating disk camera (Part V).

5.   This procedure was repeated several times to assure typical performance.

The experimental results are illustrated in Figures 14.2 to 14.6. Figure 14.2 shows dye-trace photographs of vortices trailing from the missile base at velocities of 1.0 to 1.2 fps. Theory predicts that at 1.1 fps the vortex shedding frequency should be between two and three per second; data measurements showed this frequency to be about three. The missile acceleration over the velocity range studied was about 0.2 ft/sec^2, which is small. It is doubtful that acceleration significantly affected the results.

A velocity fluctuation at the frequency of vortex shedding (Figure 14.3) was observed from the data of Figure 14.2. It could have been caused by the fluctuating drag that resulted from vortex shedding (Reference 23, pp. 59-65 and Reference 24, pp. 556-562). Figure 14.4 illustrates tests made to determine whether the velocity fluctuation was caused by shedding vortices. A fairing was added at the

missile base to suppress vortex formation by reducing or eliminating the surface discontinuity at the base. A small cone was installed first, but it was completely enveloped in the disturbance at the missile base; vortices still formed and there were corresponding velocity fluctuations. A second afterbody consisting of an approximate 3.5-to-1 streamlined form was substituted. With this fairing, which eliminated surface discontinuity at the base, no large vortices were shed and no velocity fluctuation was noted. The dye-trace data indicate that the minor pitch fluctuations and velocity fluctuations were caused by vortex shedding at the missile base.

Figure 14.5 shows small high-frequency vortex shedding from the missile fins at approximately 25 per second and an average velocity of 1.1 fps. This is in excellent agreement with 26 per second predicted by theory (footnote 1 of this chapter, second equation) where a fin base thickness of 0.08 inch is used in the calculations. Enlarged photographs of fin vortices from the missile with and without the streamlined afterbody are shown in Figure 14.6. The predicted vortex shedding frequency at 1.0 fps missile velocity was 24 per second; the actual vortex shedding frequency was 25 per second. The predicted vortex shedding frequency at 2.8 fps was
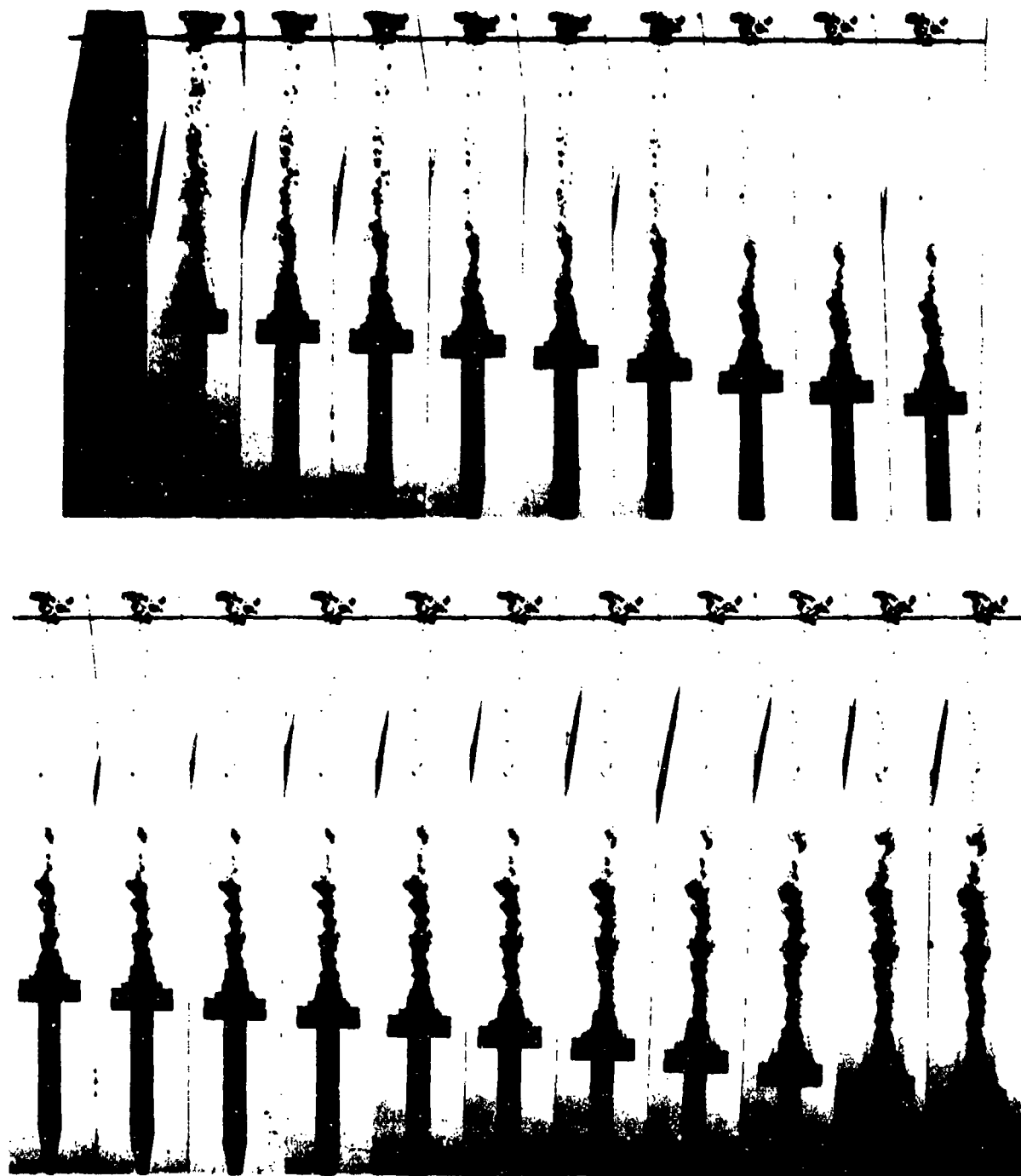
245

Figure 14.2. Vortices shedding from base of missile (0.04 sec between photographs).
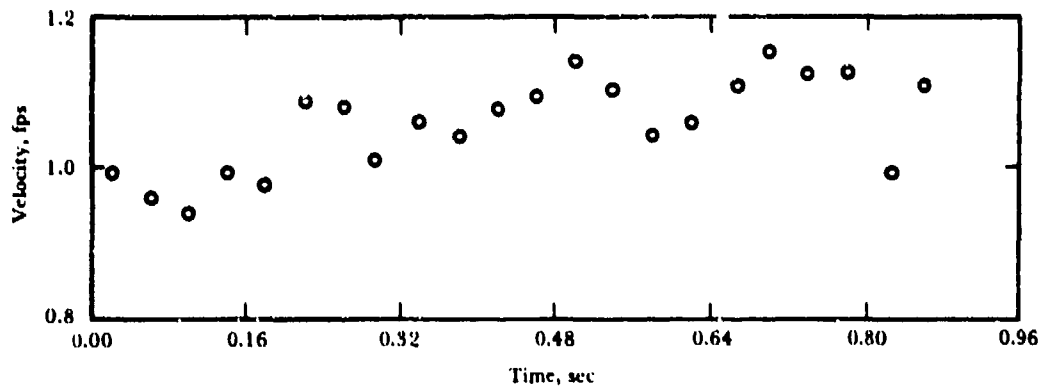
246

Figure 14.3. Missile velocity versus time during vortex study of Figure 14.2.

67 per second; the actual vortex shedding frequency at 2.7 fps and 2.9 fps was 65 per second. The vortex frequencies are approximately proportional to the linear velocity and agree with the values predicted by theory.

The effect of vortex shedding on missile behavior is illustrated in Chapter 13 (Figure 13.6), which shows the deviation in the direction of travel of a steel sphere in fully wetted flow after shedding a vortex. It is evident that in designing a missile or vehicle, care should be taken to avoid or to suppress the generation of vortices that could give rise to undesirable effects. In this connection, the elaboration of theory for vortex generation and shedding in the three-dimensional case would be helpful.

Missile alone,
v = 1.0 fps

Missile with cone,
v = 1.2 fps

Missile with streamlined
afterbody, v = 2.7 fps

Figure 14.4. Disturbances in flow behind missile.

v = 1.2 fps
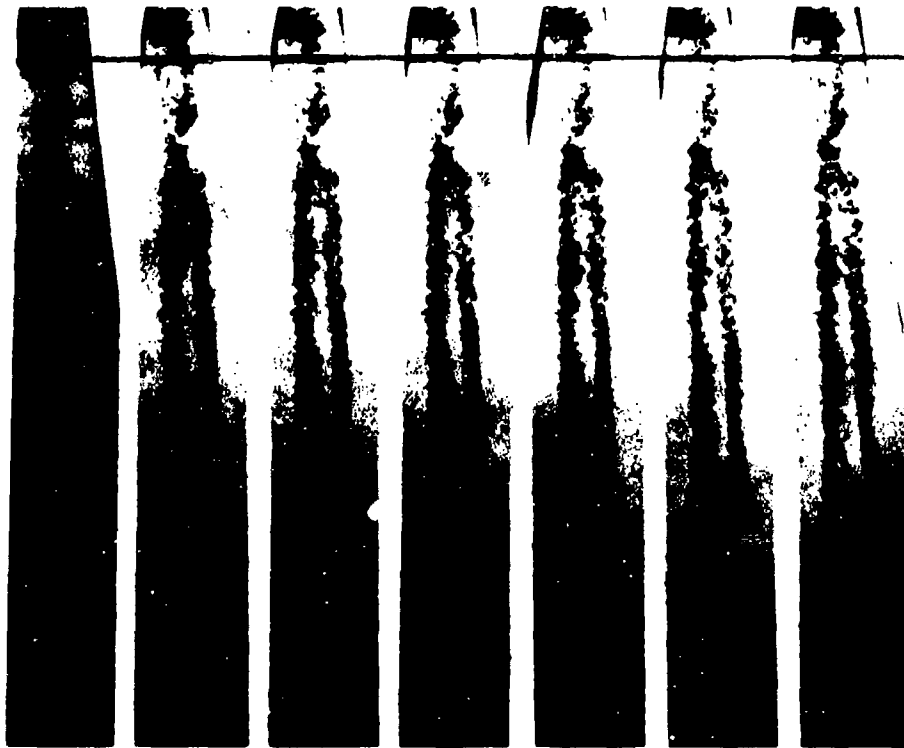
v = 1.0 fps

Figure 14.5. Vortices shedding from missile fins (0.04 sec between photographs).

249

Missile alone,
v = 1.0 fps

Missile with streamlined
afterbody, v = 2.7 fps

Missile with streamlined
afterbody, v = 2.9 fps

Figure 14.6. Enlargements of vortices shedding from fins.

CHAPTER 15
WATER-ENTRY CAVITIES OF SPINNING SPHERES

When a body moves through a real fluid, the generated boundary layer gives rise to skin friction drag. Under certain conditions, the flow in the immediate neighborhood of a wall becomes reversed, causing the boundary layer to separate from it and eddies to be formed in the wake of the body. Thus the pressure distribution is changed and differs markedly from that in a frictionless stream. This deviation is the cause of form drag and is detrimental in application in that it increases the body drag. In addition, boundary-layer growth as it affects pressure distribution must also affect fluid separation and hence cavity flow. Cavity flow, in turn, can give rise to control problems in the case of a missile in a completely enveloping water-entry cavity.

When a sphere is dropped vertically into water with a sufficiently high velocity, a cavity of air follows the body for some distance below the surface (Reference 112). The cavity wall appears to be tangent to the sphere at the point of separation, and is transparent. If the sphere is spun about an axis parallel to its direction of motion, the character of the cavity is basically unchanged for small spin velocities; the principal effect is merely to wrap any irregular striations around the cavity with a pitch corresponding to the forward speed and spin of the sphere (Figure 15.1 taken from Reference 51).

From Figure 15.1 it is apparent that

$$\tan \epsilon = \frac{v}{\omega r'} \qquad (15.1)$$

where

ω = rate of spin of sphere in radians per second about an axis parallel to its direction of motion

Figure 15.1. Cavity surrounding a 2-inch sphere spinning at 24 rps, v_e = 24.5 fps.

ϵ = angle that striations make with a plane normal to the direction of sphere travel

r' = radius of cavity bubble in region where ϵ is measured, ft

v = velocity of sphere, fps

251

If the spin velocity is increased sufficiently, a marked change in the character of the cavity wall and the separation angle takes place. The wall becomes frothy and opaque and the direction of separation is no longer tangent to the sphere at the separation point. For intermediate velocities, complex spiral cavities occur (Figure 15.2).

Since the body drag in cavity motion is loosely correlated with the maximum diameter of the cavity, it should be expected that a marked difference in drag will occur between low and high spin velocities. Studies made in the NUC Hydroballistics Laboratory (Reference 107) dealt with the effect of spin on the type of separation and on the drag.

The experiments were performed in the Open Launching Tank (Part V). Magnetic stainless-steel ball bearings of 1-, 1.5-, 2-, 2.5-, 3-, and 4.5-inch diameters were used. A few drops were also made with an 8.5-inch-diameter plastic bowling ball. The balls were dropped from 10.2 and 5.3 feet above the water level, corresponding to entry velocities of approximately 25 and 17 fps. A magnetic release was used; the steel ball was held to a conical seat in the end of a steel rod by an electromagnet and released by interrupting the current in the solenoid. The bowling ball was suspended by a non-twisting string and dropped by cutting the string. As the falling ball approached th water surface, it interrupted a photoelectric light beam that tripped the timing circuit for flash-lamp photography.

Before it was dropped, the steel ball was spun on the rod by a variable-speed motor mounted with its shaft in a vertical position. The motor was brought up to the desired speed, the speed was checked stroboscopically, and the ball was released. A small dot painted on the ball made it possible to determine photographically the exact rotative speed. The lights were flashed and photographs taken at 0.005-second intervals. Figure 15.3 is a typical photographic record.

| zero spin | 40-rps spin | 60-rps spin | 80-rps spin |

Figure 15.2. Types of cavity motion, 3-inch-diameter sphere, $v_e = 25$ fps.

252
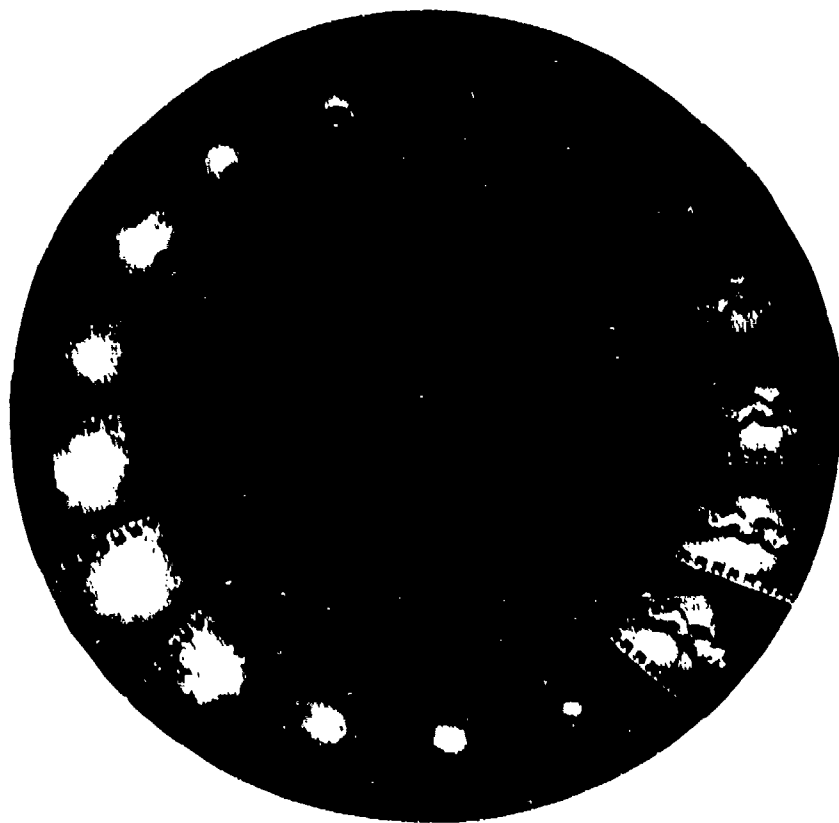
Figure 15.3. Disk camera photography used for measurements.

Figure 15.2 shows the types of separation that occurred as the spin velocity was increased. A 3-inch-diameter sphere with zero spin and 25-fps entry velocity shows separation of the cavity well forward of the equator, with transparent cavity walls. With a spin velocity of 40 rps, striations due to slightly irregular separation are wrapped around the cavity, but the general character is unchanged. A further increase in spin velocity to 60 fps shows two distinct regions of separation, with the section of the larger cavity from the forward region wrapped around the smaller cavity in the after region. When the spin rate is increased to 85 rps, the separation takes place only aft of the equator, and the cavity wall is completely opaque. This shift in separation position appears closely analogous to laminar-turbulent transition above the critical Reynolds number. Similar effects have been found with rotating spheres in wind tunnels.

If the shift in character of the cavity and the separation point for water entry of a spinning sphere is due to a transition from laminar to turbulent boundary layer, it should be possible to correlate this transition with a Reynolds number that takes into account the size of the sphere, entry velocity, and spin velocity. Luthander and Rydberg (Reference 41) defined a "Reynolds number" velocity for any point on the sphere as the relative velocity between that point and a fluid particle lying just outside the boundary layer and hence moving with potential flow uninfluenced by spin. The characteristic length is taken as the length of the path of the projection on the sphere surface of a point moving in the water just outside the boundary layer from the upstream pole along a meridian. In the case of zero spin, this reduces to the distance along a meridian to the point at which R is being evaluated.

253

If the change in character of the separation is due to transition from a laminar to a turbulent boundary layer, this transition must take place ahead of the point of separation of the type shown in the first panel of Figure 15.2, which was observed to occur between colatitude angles of 70 and 90 degrees, measured from the upstream pole of the sphere. By choosing a colatitude angle of 78 degrees, it can be shown that

$$R = \frac{4r}{3} \frac{r^2 \omega^2 + (1.5 v_e)^2}{1.5 v_e \nu} \qquad (15.2)$$

where

R = "Reynolds number" for spinning spheres

r = sphere radius, ft

v_e = velocity of sphere at water surface just before entry, fps

ν = kinematic viscosity of water, $ft^2 sec^{-1}$

For nonspinning spheres, Equation 15.2 reduces to the usual definition of Reynolds number for a sphere.

$$R = \frac{2r v_e}{\nu} \qquad (15.3)$$

Values obtained from this arbitrarily defined Reynolds number for spinning spheres cannot be compared with those for non-spinning spheres, or, in general, with each other; equal values of these Reynolds numbers do not necessarily indicate geometrical similarity of flow and therefore mechanical similarity on which the Reynolds number is based. This anomaly is apparent in the extraordinarily high transition Reynolds number (1 to 2 x 10^6) obtained for spinning spheres. Transition for spheres usually occurs at a Reynolds number of 2 × 10^5.

Figure 15.4 shows separation points plotted against the Reynolds number of Equation 15.2 for 52 drops in which separation was well defined, ignoring such corkscrew cases as the one in Figure 15.2. Most of these data were taken from drops with 2-, 2.5-, and 3-inch-diameter spheres with entry velocities of 17 and 25 fps and spin velocities of approximately 0, 40, 80, 120, and 200 rps. The two lowest
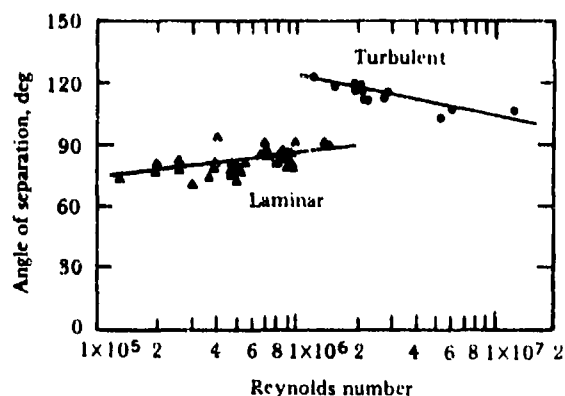
Figure 15.4. Separation angle as a function of Reynolds number.

Reynolds numbers were obtained with 1.5- and 2-inch spheres at 17 fps and zero spin. No consistent trends were found to be associated with ball size, height of drop, or spin velocity.

In corkscrew drops, two clearly defined types of separation (laminar and turbulent) are unmistakable. They are shown in Figure 15.5, along with some drops in which boundary-layer turbulence was induced by roughening the nose (the upstream surface) of the sphere. The solid lines of Figure 15.4, showing separation angle as a function of Reynolds number for non-corkscrew cavities, are repeated in Figure 15.5 for comparison.

The pairs of points designated by "O" and joined by dashed lines represent the upper and lower limits of separation for corkscrew cavities. The upper values form a group distinct from the lower values, although both sets are below the solid line representing single separation at the same Reynolds number. Such a difference is not surprising, however, since the shape of the cavity is certain to affect the pressure distribution in the surrounding water.

Since all the turbulent separations had occurred with spin, these data were insufficient to separate centrifugal effects from boundary-layer transition effects. To this end, a 25-fps zero spin drop was made with the 3-inch-diameter sphere with a 1-inch-diameter patch on the nose artificially roughened by cementing sand to it. An irregular separation occurred, but the upper and lower limits were well defined and are plotted as points "c" in Figure 15.5. To reach higher Reynolds numbers without spin, the 4.5-inch-diameter steel sphere was also
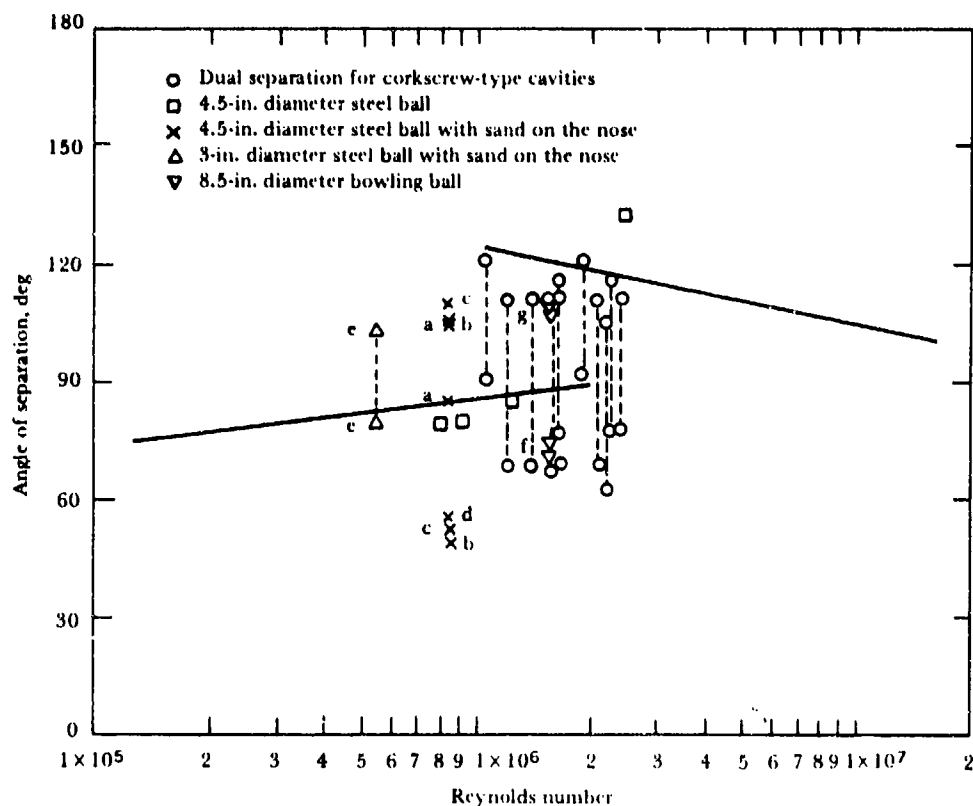
254

Figure 15.5. Separation angle as a function of Reynolds number for corkscrew cavities and induced turbulence.

sanded. The pair of points "a" represent the upper and lower limits of separation for a patch of sand about 2.3 inches in diameter. When still more sand was added, the lower separation occurred on the sand and the upper separation limit agreed well with case a. Points b and c were obtained for a patch with a chord diameter of about 3.4 inches. Point d resulted when the diameter of the patch was increased to 3.7 inches and the separation took place entirely from the sand. All the 4.5-inch-diameter drops were made at 25 fps.

Still higher Reynolds numbers were obtained with no spin by using an 8.5-inch-diameter bowling ball. Two 25-fps drops were made, with results plotted as point f. The character of the separation is shown at the left of Figure 15.6. A sand patch about 4 inches in diameter was cemented to the ball; the separation point moved sharply aft, as shown at the right of Figure 15.6 and plotted as points g for two drops in Figure 15.5. The position of the separation, the shape of the cavity, and the character of the cavity all indicate that this is

the same basic phenomenon as that obtained with spin. The quantitative difference between the turbulent separation point for a nonspinning sphere and for a spinning sphere at the same Reynolds number is probably due to the manner in which R is defined. In order to improve this definition, the actual velocity distribution just outside the boundary layer should be ascertained.

In the water entry of spheres, the transition from laminar to turbulent boundary layer, with a consequent reduction in the size of the wake, is accompanied by a marked reduction in drag, as it is in air. The drag coefficient is plotted in Figure 15.7 against Reynolds number for the same set of drops that were used to determine the separation point. A marked lowering of drag is apparent with the shift from laminar to turbulent separation.

At the low speeds involved in these studies, a turbulent boundary layer can inhibit separation and hence reduce the cavity size and the drag, much as in ordinary flow. The transition from laminar to turbulent flow is probably the most important factor in determining the nature

255

Figure 15.6. Effect of sand patch cemented to 8.5-inch-diameter bowling ball, v_c = 25 fps.

of the separation. The Reynolds number as defined in these studies for spinning spheres is not an adequate criterion for mechanical similarity under the action of inertia and viscosity. Further consideration of the actual velocity distribution about spinning spheres is in order.
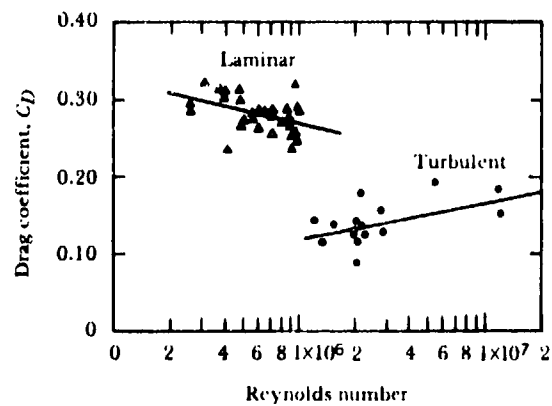

Figure 15.7. Effect of laminar and turbulent separation on drag coefficient.

256

CHAPTER 16
EFFECTS OF GRAVITY ON THE ENTRY CAVITY

Water-entry cavity behavior is a major factor in determining the underwater trajectory of a missile (Chapter 3) and, in turn, cavity closure affects cavity behavior because it terminates external gas flow into the cavity, thereby limiting its size. If the forces acting to close the cavity are sufficiently large, the cavity is repressed.

Cavity closure occurs either at the water surface (surface closure) or below (deep closure), the nature of the closure being influenced by both ambient and launching conditions and by the configuration and velocity of the missile (Chapter 3).

Surface closure appears to be the more complex and is the major factor in controlling cavity formation (Reference 22). Interplay among the many factors influencing surface closure has obscured its mechanism although it has been studied at length (Reference 8, 22, 46 and 112). Modeling studies (Chapter 9) in which the minimum entry velocities were 60 fps indicate that one-to-one Froude-number, cavitation-number, and gas-density scaling are adequate for water-entry cavity modeling but this scaling does not always model surface closure at lower entry velocities (Reference 45), indicating that some other force or forces may also be significant. During the early stages of missile penetration at low velocities, the most prominent force is probably fluid adhesion to the missile surface (Reference 112). Later, after the splash has formed, surface tension may assume a more dominant role in splash seal and surface closure. The increased kinematic viscosity of the atmospheric gas brought about by reduced pressure scaling may also delay fluid separation from the missile (Reference 8).

A better understanding of the forces affecting surface closure and thereby control of cavity formation could be advantageous in developing scaling techniques for hydroballistics modeling at low entry velocities. It is possible that the altered surface closure pattern resulting from the elimination of hydrostatic pressure may aid in the interpretation of these forces.

Deep closure can be explained satisfactorily in terms of forces generated by missile inertia tending to open the cavity and hydrostatic forces tending to close it. It would be expected, then, that deep closure would be inhibited in a zero-gravity system where the hydrostatic pressure tending to close the cavity does not exist.

The hydrostatic pressure produced by gravitational force can be nullified in the laboratory by launching a missile in a free-fall system. The gravitational force acts equally upon all elements of the system instead of only upon the missile and the disturbed liquid surface, reducing the net effect of gravity to zero. Free-fall conditions can be achieved by releasing the bottom of a tank filled with water immediately prior to missile water entry. The NUC Vertical Drop Tanks (Part V) were used for a series of such tests. Spheres and plate-cylinder missiles were dropped vertically at low velocities in the range from 12 to 22 fps. Since, in the case of spheres, it is known (References 46 and 112) that at these low velocities the surface condition affects cavity formation, the tests were made with precision-ground, highly polished stainless-steel spheres that had been given a thin durable hydrophobic coating of silicone to minimize water adhesion forces.[1] The plate-cylinder missiles consisted of cylindrical steel rods of

---

[1]The spheres were cleaned and placed in polymethylsiloxane, DC-500, 70 centistokes, for two days at 150 to 160°C. This produced a yellowish coating, the thickness of which is less than the wavelength of light.

different diameters that were undercut near the leading end to provide a clean line of cavity separation.

Figure 16.1 shows the vertical water entry of a 1½-inch-diameter sphere at atmospheric pressure traveling at 21 fps with respect to the water surface. The first sequence shows entry occurring in the normal gravitational field and is typical of that observed many times. The splash is of the normal "basket" type, and the cavity is glassily smooth with striated walls. The cavity necks off and closes beneath the water surface in a typical manner. In the second sequence, gravity is nullified by free fall of the water and a sheath-type splash occurs. The cavity has glassy, striated walls, but because of the absence of hydrostatic pressure, and therefore buoyancy forces, it follows the sphere down and there is no deep closure.

The most striking differences in water-entry behavior associated with removal of gravitational effects were noted in the cavity closures. Figure 16.2 shows water-entry cavities of a 1-inch-diameter sphere at ambient conditions during the first 0.055 second after water entry. Within the time span recorded, surface closure was almost complete, and incipient necking indicated that deep closure was in progress in the gravitational field. Without gravitational effects, the surface had completely closed and the cavity pulled away, but there was no tendency toward deep closure.

Figure 16.3 shows water-entry cavities of a 1-inch-diameter sphere at 16.1 fps entry velocity. Freon 12 (dichlorodifluoromethane) at 2 atmospheres pressure was used over the water surface, thereby providing a gas density eight times greater than that which would obtain with ambient air. Thus earlier surface closure should be expected in both fields (Chapter 3). In the gravitational field, a dome-like splash occurred and surface closure took place with pullaway from the surface, but buoyancy prevented the cavity from following the sphere downward. Without gravitational effects, cavity closure occurred earlier, with a smaller cavity that did follow the sphere. As predicted, both cavities were markedly smaller than the comparable cavities formed at ambient conditions.

In the gravitationless field the splash was more cusp-like in shape, as illustrated in Figure 16.4, which shows water-entry cavities of a 1-inch-diameter sphere under ambient atmospheric

conditions 0.036 second after entry. The slope of the splash as it separated from the sphere was measured from the photographic data of Figure 16.1 over approximately one sphere diameter of water penetration (0.007 second). For this purpose, the first 20 frames after water contact, taken at 2900/second, were measured (the sphere moved about one diameter in 17 frames) and the angles of separation on either side of the sphere were determined with respect to coordinates fixed in the water. The results are shown in Figure 16.5. The difference in slope between the two splashes was more than 10 degrees.

Interplay between gravitational and surface tension forces may initially determine the splash. A sheath of water rises around a sphere at water entry. As noted by Worthington (Reference 112), whether the rising sheath leaves the sphere or follows it depends upon the efficiency of fluid adhesion. For spheres with a hydrophobic coating (as used in these studies), adhesion forces are small, but the surface tension of the sheath will act at all times in favor of adhesion to the sphere (Figure 16.6), and the resulting small capillary pressure may have some effect. Below the sphere equator, the gravitational force will tend to bring about separation of the sheath from the sphere. Hence, removal of the gravitational forces should delay separation, resulting in a more vertical splash slope and a sheath-type splash. Such a splash, having a smaller throat and greater curvature, should be more susceptible to surface tension and gas dynamic underpressure forces, resulting in earlier cavity surface closure. These observations are substantiated by the photographic data.

Three vertical launchings of a 0.168-inch-diameter plate-cylinder rod made with an entry velocity of 14.9 fps show the effects of the gravitational field upon the cavity (Figure 16.7). The first sequence shows a launching in the normal gravitational field; in the other two sequences, the field is gravitationless. The ambient pressures were close to the vapor pressure of water, ranging from 24 to 35 torrs. The differences in deep closure are readily apparent. In the normal gravitational field, the cavity closes about the rod; without gravity it remains open for the duration of the photographic record. However, both zero-gravity cavities evidence necking in two places, indicating that two later deep closures will occur in spite of the absence of hydrostatic pressure. Cavity

258

Normal gravitational field

Gravitationless field

Figure 16.1. Vertical entry of sphere, v_e = 21 fps. Camera speed 290 frames/sec.

259

Normal gravitational field,
v_e = 14.4 fps
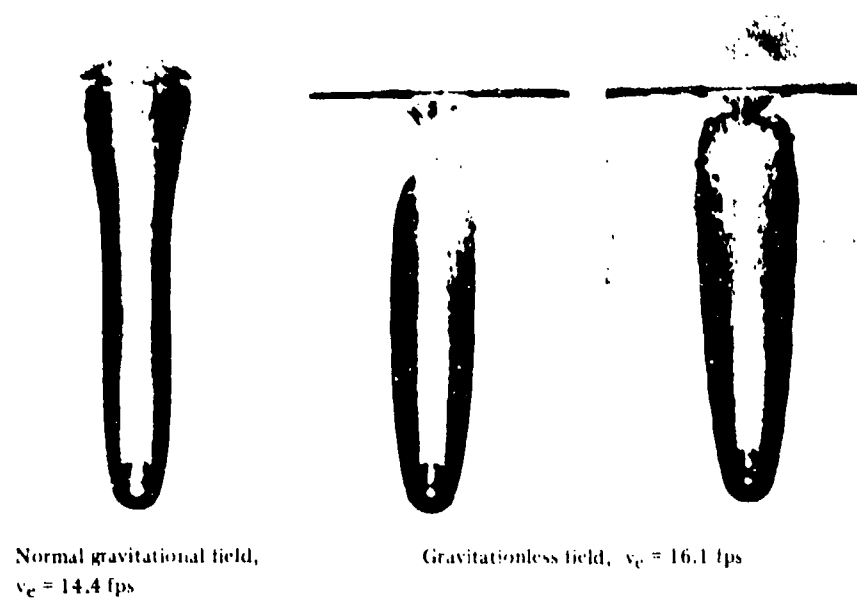
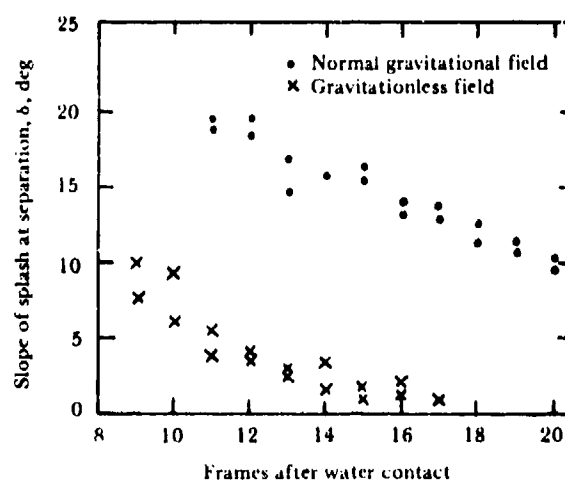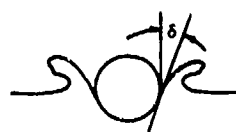Gravitationless field, v_e = 16.1 fps

Figure 16.2. Effect of gravity on cavity closure.

Normal gravitational field

Gravitationless field

Figure 16.3. Effect of gravity on surface closure, v_e = 16.1 fps. Time between photographs 0.004 second.

Normal gravitational field,
$v_c = 14.4$ fps

Gravitationless field,
$v_c = 16.1$ fps

Figure 16.4. Effect of gravity on splash.

Figure 16.5. Effect of gravity on slope of sphere splash;
$v_c = 21$ fps.

261
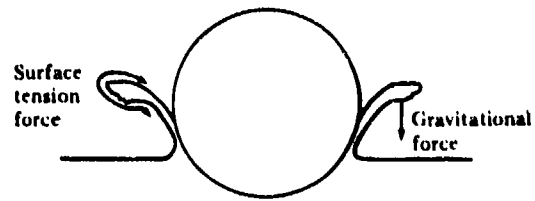
Figure 16.6. Action of surface tension and gravitational forces on splash.
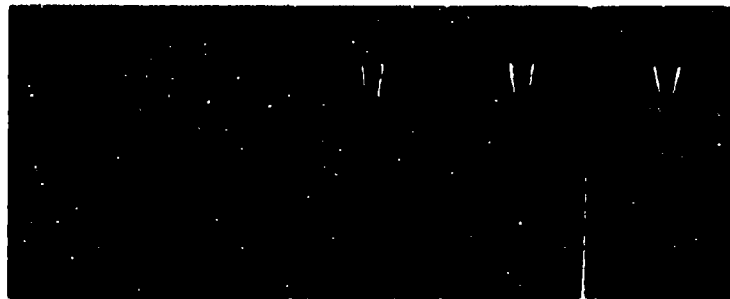
Normal gravitational field
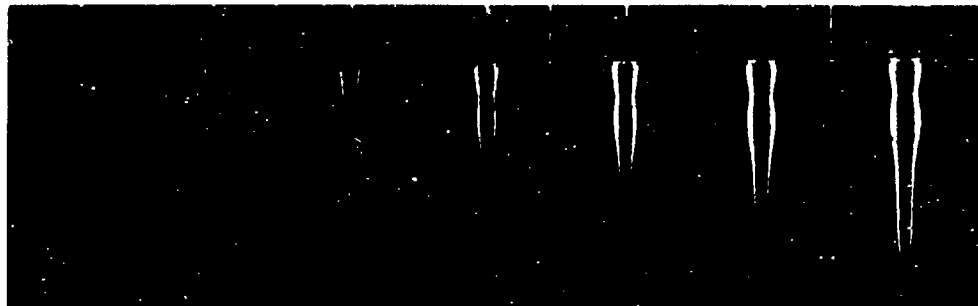
Gravitationless field

Gravitationless field

Figure 16.7. Effect of gravitational field on cavity, v_e = 14.9 fps. Time between photographs 0.008 second.

262

Figure 16.8. Cavity necking in gravitationless field.

necking in the gravitationless field is also illustrated in Figure 16.8 (0.070-inch-diameter rod entering water at 14.9 fps and 40-torr air pressure).

Consideration of the forces acting upon the cavities shown in Figures 16.7 and 16.8 suggests that the observed necking is a surface tension effect. The pressure force due to surface tension is of the order 10^{-2} psi immediately behind the plate; the gas dynamic pressure reduction force is considerably less, being of the order 10^{-4} psi. In addition, the suggestion of periodicity in the necking indicates the action of surface-tension forces[2]. An indication of deep necking was observed with some of the spheres tested, but their diameters were greater than the plate diameters; therefore their cavity diameters would be larger and surface tension effects less significant.

Enlarged frames of Figure 16.7 are presented in Figure 16.9 to show details of the splash. The zero-gravity splash formed by the rods is less cusplike than that formed by the spheres (Figures 16.1 and 16.4), but is definitely smaller and less domelike than the splash of the rod in the normal gravitational field.

Launchings of a 0.252-inch-diameter plate-cylinder rod were made to study the effects upon the zero-gravity cavity of change in atmospheric pressure. The tank pressures were 35 and 90 torrs; the entry velocity was 14.9 fps. The cavities increased in size with reduction in atmospheric pressure (Figure 16.10). The results illustrate the sensitivity of cavity closure to small changes in gas dynamic pressure reduction.

Removal of gravitational force effects provides a useful technique for studying water-entry cavity phenomena. The complex interaction of the forces affecting cavity behavior are not yet fully understood, especially at lower water-entry velocities where the surface adhesion and tension forces that affect surface closure (and therefore cavity formation) become more significant. It is believed that further water-entry studies that show splash and closure phenomena in fine detail will aid in interpreting the forces affecting the water-entry cavity and may be useful in extending hydroballistics modeling techniques to lower water-entry velocities.

---

[2]A fluid column is known to become unstable, neck, and break into droplets when surface-tension forces in the column boundary exceed internal column pressure (Reference 112). Here an air column is involved, but surface-tension forces would tend to constrict and break the column into separate bubbles.

Normal gravitational field, air pressure 30 torrs

Gravitationless field, air pressure 35 torrs
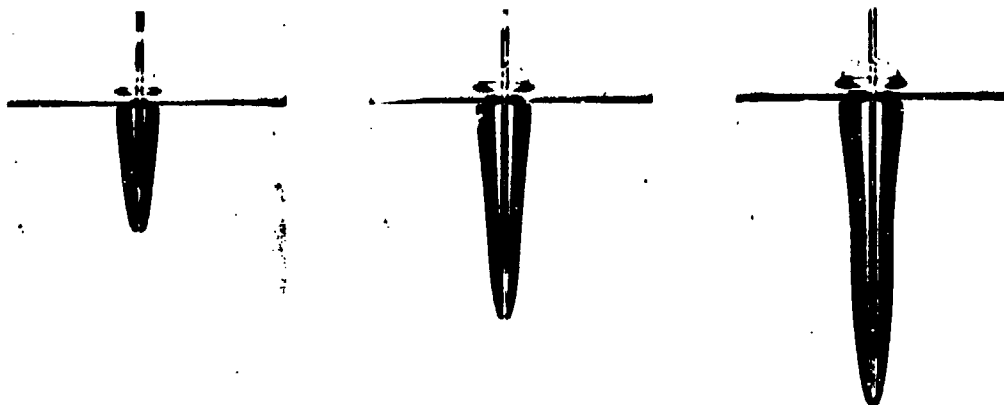
Gravitationless field, air pressure 24 torrs

Figure 16.9. Details of splashes shown in Figure 16.7.

264
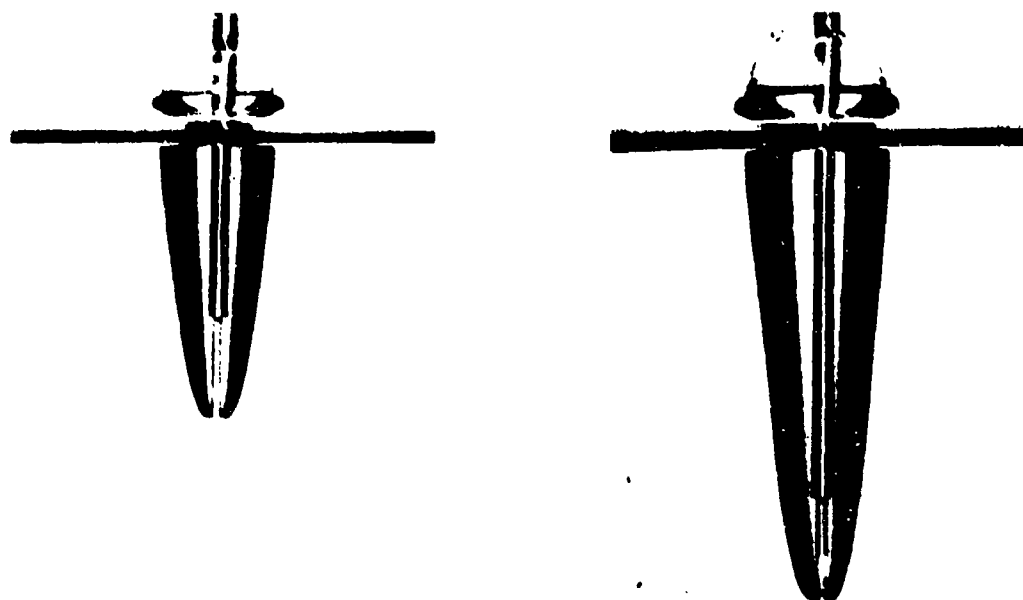
Air pressure 35 torrs
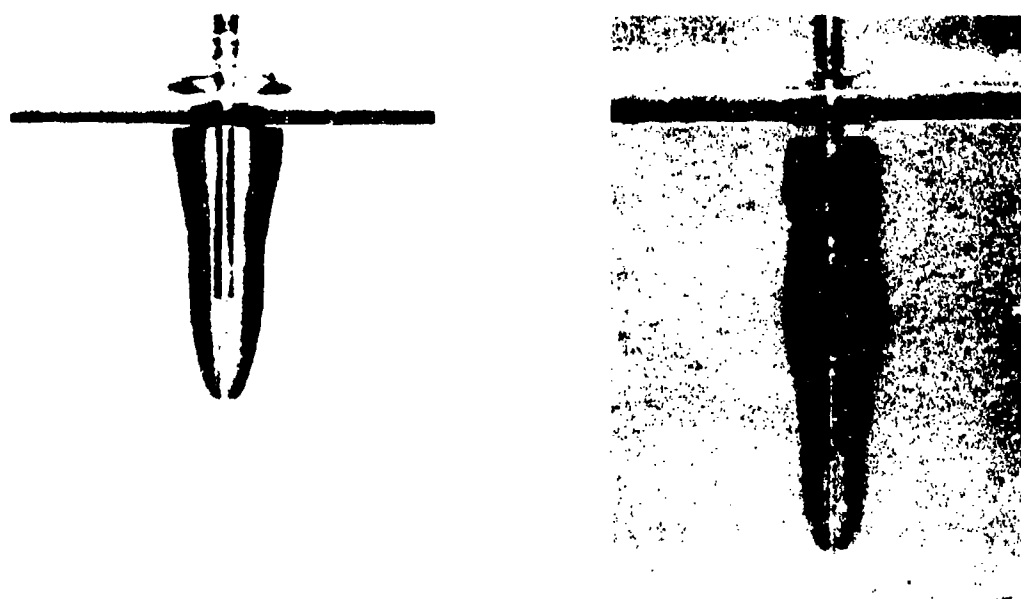
Air pressure 90 torrs

Figure 16.10. Effect of atmospheric pressure on water entry cavity in gravitationless field, $v_e = 14.9$ fps.

265

PART V.
SPECIAL EXPERIMENTAL TECHNIQUES AND HYDROBALLISTICS FACILITIES

CHAPTER 17
FACILITIES AND EQUIPMENT

Most of the data originating from this study of hydroballistics modeling were obtained at the Naval Undersea Research and Development Center (NUC)[1] either in the Hydroballistics (Model) Labor ory in Pasadena, California, or at the pro otype launching site at the Morris Dam Torpedo Range. The rest of the model data resulted from tests in the Hydrodynamics Laboratory at the California Institute of Technology (CIT). Those test facilities and equipment that are individually unique are described below.

VARIABLE-ANGLE VARIABLE-PRESSURE LAUNCHING TANK

The VAVP tank at NUC (Figures 17.1 and 17.2 and Reference 89) is a facility designed for studies of the water-entry, water-exit, and underwater-trajectory behavior of momentum-propelled missiles for varied trajectory angles, missile velocities, and conditions of cavitation. It was built primarily for research into the importance of scaling parameters (Froude, Reynolds, and cavitation numbers, gas-density

ratio, etc.) in water-entry and underwater-trajectory modeling, and to develop, if feasible, scaling techniques that provide similitude within the accuracies established as acceptable.

The steel tank is 3 feet wide by 3 feet deep by 8 feet long, with windows of 1-1/4-inch-thick tempered clear glass on three sides, a dome 2 feet high on the top, and a well 1 foot in diameter and 1 foot deep below. The windows are 24 inches wide by 69 inches long. The dome, well, and tank centerlines are coincident. A pit below the tank provides space for underwater-launching equipment.

The tank, mounted on curved tracks with a 46-inch radius so that it can be rotated from 5 to 90 degrees with respect to the horizontal, is driven by a hand-operated worm gear through a double sprocket and a 150-inch-long chain system attached to the tracks.

Missiles up to 2 inches in diameter and 1-1/4 pounds in weight can be launched in the tank with maximum velocities of 120 fps at water entry and 80 fps at water exit. The air (or gas) pressure in the tank can be varied from the

---

[1]At the time, the U.S. Naval Ordnance Test Station (NOTS).

267

Preceding page blank

Figure 17.1. Variable Angle Variable Pressure Launching Tank, oblique water-entry position. (From Reference 89.)
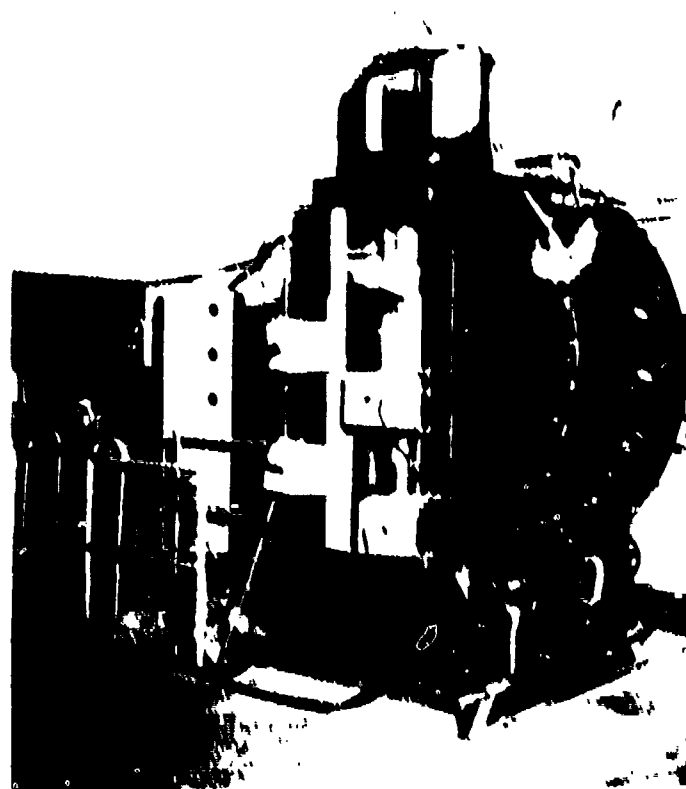
Figure 17.2. Variable Angle Variable Pressure Launching Tank.

vapor pressure of water to 1.5 atmospheres absolute. For metric photography, electronically operated Edgerton-type stroboscopic lamps of 1- to 2-μs flash duration illuminate the missile airflight, water-entry, water-exit, and underwater trajectory, as well as the associated cavity phenomena. Missile water-entry velocities, accurate to 0.1 fps, are immediately obtained from a photo-electric timer record taken during airflight. In addition, an optical whip recorder (described below) can be used to obtain highly accurate data on missile orientation during airflight and water entry.

The tank water as supplied from high-pressure city mains is supersaturated with air. The water was deaerated to a repeatable equilibrium condition for all launchings (Chapter 18) so that diffusion of air into the missile cavity was minimized, and water-vapor or very nearly water-vapor cavitation obtained. The air content of the water was determined with a Van Slyke-Neill manometric gas-analysis apparatus (Reference 62). The same water was used throughout a single series of launchings. The high degree of clarity necessary for metric stroboscopic photography was maintained by filtering the water through diatomaceous earth for about an hour each morning before tests were begun.

Water temperatures as low as 10°C (for reduced water-vapor pressure studies) can be obtained in about 2 hours by circulating the tank water through a refrigerator, and water temperatures as high as 80°C (for reduced water kinematic viscosity studies) can be obtained by circulating the tank water through a 24-kw electric heater for about 2 hours.

A single launcher projected missiles along the tank axis and served for both water-entry and water-exit studies. For water entry, it was mounted on the dome of the tank, and for water exit, on the well cover. The missile was held by slight friction in a ventilated sleeve-type carriage mounted on the end of a piston extending into the tank through a watertight and gas-tight seal. Upon actuation, the piston was impelled by a pneumatic system outside of, and sealed off from, the interior of the tank. After the acceleration stroke, the piston was stopped by a hydraulic buffering system; the momentum-propelled missile emerged from the carriage to continue in free flight. With missiles 1 foot long,

the free airflight before water entry was at least 2 feet; the free water flight before water exit was at least 1 foot, the actual length of the flight path being determined by the water level selected. The system was designed to launch the missile with no yaw or angular velocity and to minimize air (or water) flow due to launcher action.

For water-entry launchings, the missile was loaded through an access port (Figure 17.1) in the side of the tank dome. The missile was inserted into the carriage with the impelling piston forward and the launcher was cocked by pushing the piston back. For water-exit launchings, the missile was loaded through a port in the center of the dome (Figure 17.2). The missile, held in a close-fitting cylindrical carriage on the end of a long wooden pole, was pushed into the launcher by a piston in the pole carriage; the entire launcher system was then pushed down into launching position. A flared skirt on the pole carriage simplified alignment with the launcher carriage.

After prelaunching operations had been completed the pressure and density of the tank atmosphere were adjusted with either a large vacuum pump or compressed air or gas as required to satisfy the scaling condition constraints, and the density of the tank atmosphere was determined gravimetrically.

At the same time, the air pressure in the pneumatic missile launcher was adjusted to give the predetermined missile velocity, and the cameras were brought up to speed. With the laboratory in complete darkness, the missile was launched, and photographs taken with electronically timed Edgerton-type stroboscopic lamps, or, when the optical whip recorder (described below) was used, by electronically timed sparks. Sideview pictures of the missile and of the underwater cavity could be obtained in the pitch plane (the vertical plane that contains the trajectory) for all trajectory angles, but only 70- to 90-degree trajectories were visible in the vertical plane normal to the pitch plane.

Missile flight was terminated by a heavy nylon fabric backstop that is impervious to moisture and to the action of bacteria or molds. After launching, the missile was retrieved through the dome access port with a remotely operated clamp on the end of a pole.

269

Rotating-Disk Camera

The camera (Figure 17.3) and Reference 94 was designed and built at NUC for sideview photography. It has some advantages over a strip camera when only a few exposures are required: the larger frames permit closer detail and greater metric accuracy and there is no film waste. It is a 5-by-7-inch view camera (with back removed) mounted on a housing containing a rotating disk with a circularly cut 11-inch-diameter photographic film clamped to its surface. An adjustable triangular slot in the disk cover plate limits the photographic exposure to a sector for each flash of the stroboscopic lamps. The disk is rotated at any speed up to 3400 rpm ±0.5% of set speed with a General Electric Thymotrol controlled-speed motor. The speeds are set with a revolution counter and a stop watch for low speeds and with a stroboscope for high speeds. A Bausch and Lomb Tessar f/4.5, 11-7/8-inch focal-length lens was used for the tests described here, but any lens suitable for a 5-by-7-inch view camera can be used.

Before launching, the field of photographic coverage, the number of exposures, and the time interval between exposures were determined. From this information, the slot opening and disk speed were derived and the electronic apparatus was set to give the preassigned number of lamp flashes (exposures) at the desired frequency. By properly gating the number of flashes, the complete disk can be covered with exposures. The range of missile positions over the exposure sequence can be set with a time-delay generator, adjustable to 1 μs, that triggers the flash lamps at the appropriate moment after launcher actuation.

Optical Whip Recorder

The optical whip recorder, or whip camera (References 54 and 89), is used in water-entry studies to measure changes in the angular velocity of a missile at water entry, especially in pitch, although some changes in yaw may also occur. Because the change in pitch velocity is often impulsive, it is referred to as the "whip" of the missile.

The apparatus consists of a light source and a camera housed on the tank-dome lid (Figure 17.1). The light source (Figure 17.4) is an intense spark electronically timed to synchronize with the stroboscopic flash lamps. The position of the spark is stabilized by a small hole in a ceramic insulator that guides the spark from a tantalum electrode to the aperture in a disk-shaped phosphor bronze or brass electrode. A collimating lens converts the light into a beam of accurately parallel rays directed along the expected path of the missile.

Two small mirrors (0.08 inch square) mounted on the missile tail (Figure 17.5) intercept a bundle of collimated rays and reflect them to the whip camera (Figure 17.6), which is focused to receive such light and concentrate it

Figure 17.3. Rotating-disk camera open for loading. (From Reference 94.)

Aperture disc: brass or phosphor bronze, 0.010 in. thick, aperture 0.006- to 0.010-in. diameter

Tantalum electrode 8,000 volts to ground 0.060-in. diameter

Brass case at ground potential

Spark guide "Lavite," hole 0.006- to 0.010-in. diameter
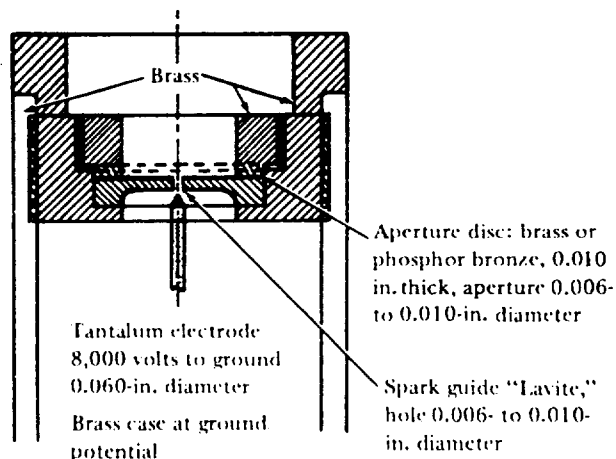
Figure 17.4. Light source for optical whip recorder. (From Reference 89.)
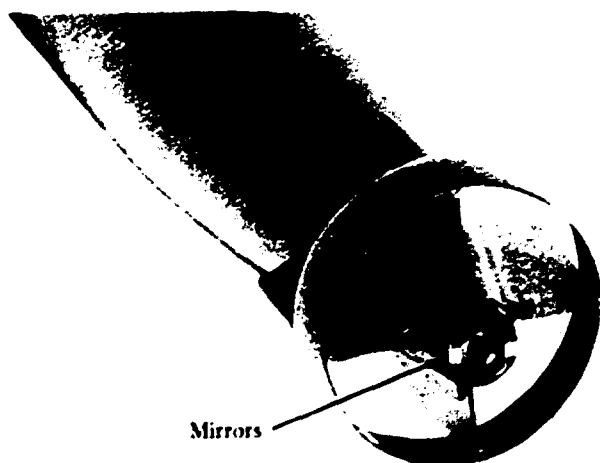
Figure 17.5. Mirrors on missile tail to reflect light to whip camera. (From Reference 89.)
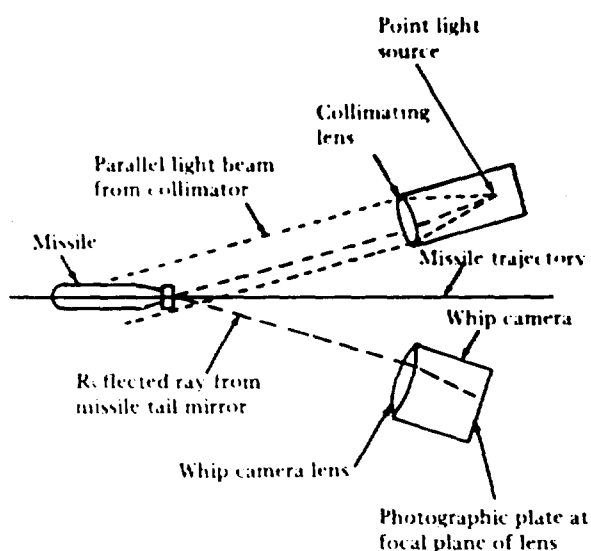
Figure 17.6. Optical whip recorder system. (From Reference 89.)

Figure 17.7. Operation of optical system. (From Reference 89.)

in a point image on the camera plate. A ray striking any portion of the lens is focused at the same point as any other ray coming from the same direction. If the ray changes its direction, the spot image shifts on the camera plate. Both the spark-source assembly and the whip camera are sealed off from the tank interior by optically flat plate-glass windows that do not affect the direction of the rays and hence the image position.

The operation of the optical system is shown in Figure 17.7. When a missile with a

mirror that is normal to the axis is traveling in the path of the parallel beam from the light source, the mirror orientation will remain constant and all reflected rays will be parallel and focused upon the plate at the same spot, as long as the missile does not rotate. Such will be the case regardless of transverse motion of the reflected light rays across the face of the lens caused by the mirror motion on an oblique path. If the mirror is not normal to the axis and the missile rotates or rolls, its orientation relative to the lens will change and the position of the point image will shift. The recorder is sensitive only to angular motion of the missile and not at all to translation.

Since the reflected rays subtend small angles with the camera axis, missile orientation change is nearly proportional to point-image displacement. Change in missile pitch and yaw may thus be obtained directly from vertical and horizontal point displacements of the precalibrated plate. If the possibility of roll is suspected, a second mirror with slightly different

271

orientation can be mounted on the missile, and roll can be determined from the relative position of synchronous dots on the two traces.

Time measurement is supplied by flashing the spark at accurately controlled intervals as small as 0.00025 second, resulting in a succession of dots on the photographic record that fall on top of each other if there is no angular motion and are spread out if there is. The use of a low flash rate during airflight minimizes overlapping of the dots when the angular velocity is small. To facilitate identification of synchronous dots from the two mirrors, the flashes are so generated that every tenth flash is omitted.

Figure 17.8 shows schematically a typical record obtained from the optical whip recorder. At the left, each dot is separated from its neighbor by an oblique distance whose vertical component represents change in pitch angle and whose lateral component represents change in yaw angle. These measurable changes occurred in the known time interval between the two dots; curves can readily be plotted to show change of angle versus time in both pitch and yaw.

The trace at the right of Figure 17.8 is an auxiliary record made to measure the roll of the missile. The dots are images reflected from a second mirror mounted on the missile tail at a different orientation, the rays differing slightly in direction and focusing at a different spot on the photographic plate. As the missile rolls, the
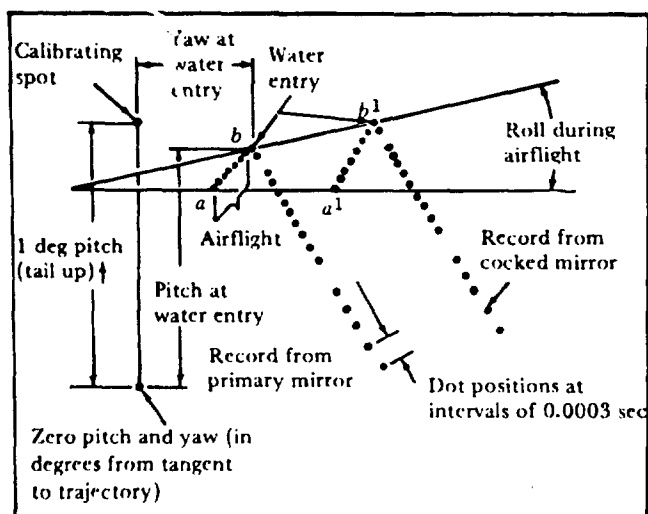
image from the second mirror rotates about that from the first. Hence, when lines are drawn connecting any two pairs of corresponding points (such as aa' and bb', Figure 17.8), the angle between these lines represents missile roll during the interval.

To calibrate the whip-camera plate, the missile is placed in a jig whose optical system duplicates that of the whip recorder and then is accurately oriented to a position corresponding to zero pitch and yaw along the air trajectory. The wax holding the mirrors is warmed and softened so that the mirrors can be oriented to give suitably positioned dot images on a white screen corresponding in size and position to the whip-camera plate. The plate is then substituted for the screen and calibrated by exposing it to point images from the mirrors corresponding to zero and 1-degree positive or negative missile pitch with zero yaw. (Calibration spots are shown in Figure 17.8). The calibrated plate is then used to obtain whip data.

Figure 17.9 reproduces typical records from the optical whip recorder, the missiles having heads of slightly different shapes. The record at the left shows a slight tail-up rotation of the missile in airflight, accompanied by considerable angular motion in yaw. Immediately upon impact, the tail started down while the yaw continued in the original direction. The record at the right shows practically no angular motion prior to impact, with a sharp reversal in direction from tail-down to tail-up shortly after impact. Comparators were used to measure the records, with a precision corresponding to a missile orientation of 0.0005 degree.

Simultaneous Whip and Sideview Camera Data

Initially, whip and sideview camera data could not be obtained simultaneously because the light used to illuminate the model tank for the sideview camera fogged the whip-camera record. Separate launchings to determine whip and trajectory were necessary, and a one-to-one correspondence between missile trajectory position and orientation was impossible to obtain. The use of light of different wavelengths for the two cameras solved the problem (References 53 and 89). Blue filters were placed over the flash lamps that furnished illumination for the sideview cameras and a red filter was placed over the whip-camera lens. The whip camera picks up the red component of light from the spark source,
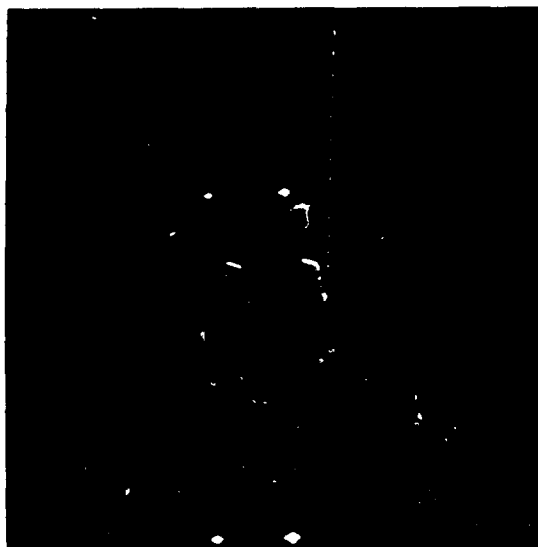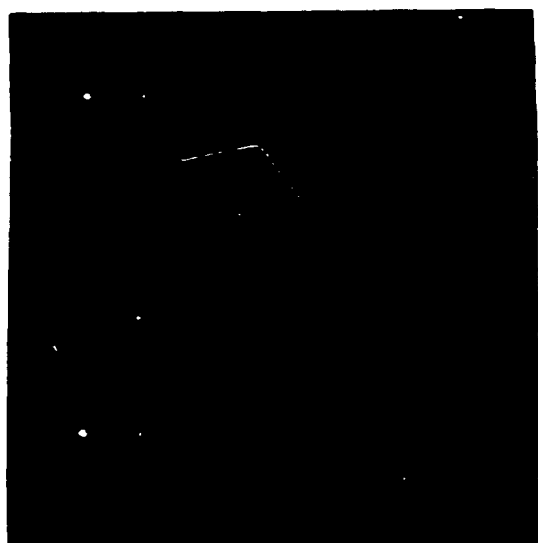

Figure 17.8. Typical record, optical whip recorder. (From Reference 89.)

Optical Comparators

The NUC Hydroballistics Laboratory data consist largely of photographic records. To determine time-position, attitudes, cavity characteristics, etc., the data were measured with micro- or optical comparators that read directly in microns (cm x 10^{-4}) and could be adapted to 35-mm and 16-mm motion-picture film, slides, or cut film.

One comparator used in these studies (Figure 17.10) was made by David W. Mann of Lincoln, Mass. (Reference 94). The stage is set horizontally and the microscope is mounted at an angle, with a prism to bend the line of sight. The overall magnification obtainable is about 6 to 1. This instrument has a measurement capability of 200 mm in the horizontal (abscissa) and 30 mm in the vertical (ordinate) directions. The stage and cross hairs may be rotated, and both are provided with circular vernier scales that read to 1 minute of angle.

CONTROLLED-ATMOSPHERE LAUNCHING TANK

The Controlled-Atmosphere Launching Tank (Reference 30) at CIT is used primarily to study the hydrodynamic problems involved as a free-flying body enters water from air, and for

Figure 17.9. Whip records of two missiles. (From Reference 89.)

but its red filter does not permit the filtered blue light of the flash lamps to fog the whip film.

The system used a tantalum rod (whose spectrum contains red lines) for the spark source, a Wratten No. 24 red filter over the whip-camera lens, and Wratten No. 67A blue filters over the General Electric FT 125 or EG and G FX-2 flash lamps. Kodak Royal Pan or Super Panchro-Press Sports Type B film (sensitive to blue) was used in the sideview camera and Kodak Super Panchro-Press Sports Type film (sensitive to red) in the whip camera.

Figure 17.10. The Mann comparator. (From Reference 94.)

273

associated studies, such as underwater explosions. Figure 17.11 is an artist's overall view and Figure 17.12 is a cutaway drawing showing the launching end of the tank. For normal operation, the tank is about three-fourths filled with water, leaving an air space above. A centrifugal device, mounted on the underside of a large hatch cover, launches the model at any trajectory angle from vertical downward to horizontal, with any attack angle up to ±10 degrees, and at any speed up to 180 fps. A battery of high-speed motion-picture cameras record the path of the model during both airflight and underwater travel. The cameras operate without shutters; exposures are made by intermittent illumination of the tank interior with Edgerton-type flash lamps. The fields of view of adjacent cameras overlap by 60%, and with the stereoscopic span thus obtained, the path of the model can be recreated step by step with analyzing equipment. The flash lamps that illuminate the tank interior are installed in six Lucite tubes that pass through the tank above and below the underwater cameras.

The tank is a large horizontal welded steel cylinder, 13 feet in diameter and 29 feet long.

Empty, it weighs about 40 tons; with water to a depth of 10 feet, its weight is about 150 tons. To provide adequate distance between the launching plane and the data-recording cameras, a section of a smaller cylinder is attached to one side. The large rectangular hatch opening is located off-center on the top near the far end of the tank. The entire launching mechanism is mounted on the hinged cover, which has an O-ring pressure seal and heavy C-clamp frames to hold it in place during launchings. The tank was designed to withstand an external pressure of a full atmosphere and an internal pressure of 40 psi. It provides a clear launching plane 25 feet long with a water depth of 10 feet.

A high degree of water clarity is essential for underwater photography. With both lamps and cameras on the same side of the tank, the light must travel 24 feet from the lamps to the model and back to the cameras. Even a slight amount of color, fine suspension, or micro-organisms in the water could absorb or scatter the light before it reached the cameras. The interior of the tank was designed not only to prevent corrosion of the steel tank, to provide a dark background, and to minimize the possibility of damage to models from striking tank
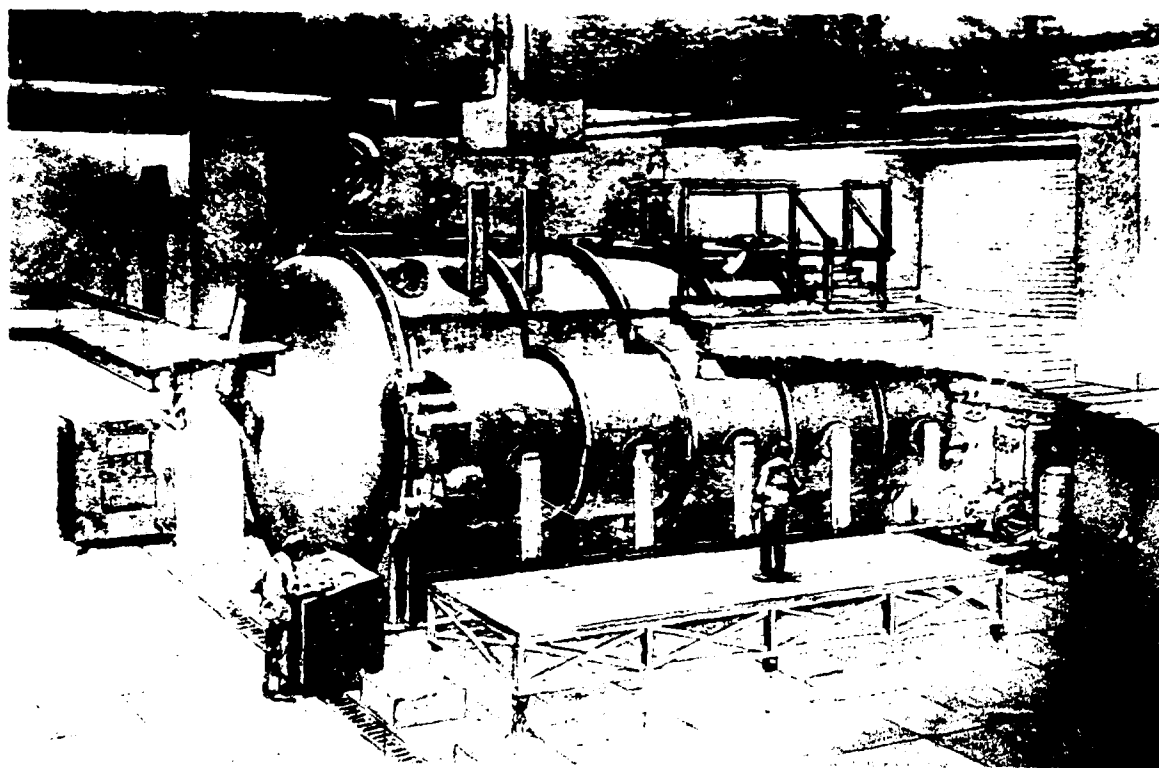
Figure 17.11. Controlled-Atmosphere Launching Tank at California Institute of Technology. (From Reference 30.)

274
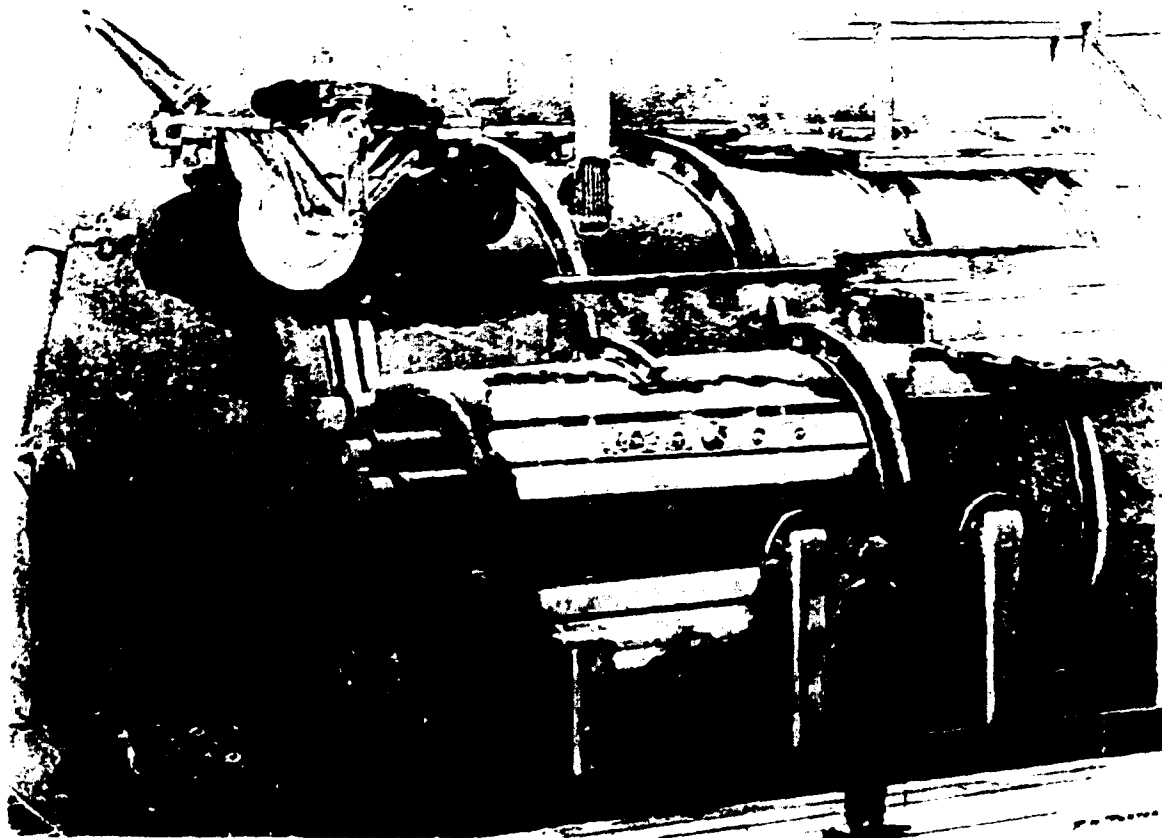
Figure 17.12. Cutaway view of launching end of CIT tank. (From Reference 30.)

walls, but to avoid any contamination of the water that might impair its optical properties. To meet these diverse and stringent requirements, a polyvinyl chloride plastic (Koroseal), in sheets 3/32 inch thick, was cemented over the entire interior, the seams being heat-sealed with strips of similar material. Commercial sand and alum filters remove suspended materials from the water, a row of germicidal ultraviolet lamps along the ceiling prevent bacterial growth, and a vacuum pump controls the atmospheric pressure.

When the local water supply happens to contain traces of yellow matter in solution that cannot be removed by filtration, the water absorbs the blue and violet light of the flash lamps. For this reason, distilled water was used in the tank.

The Launcher

The centrifugal launcher consists of a rotating wheel that carries the model near its periphery, with a planetary-gear system to keep the model from rotating about a transverse axis as it goes around with the wheel, and with a mechanism for releasing the model at any predetermined point along a 90-degree arc.

The hatch cover is hinge-mounted so that the launcher can swing down into the hatch (shown covered in Figure 17.13). A model is shown in place in the chuck. Figure 17.14 is a multiple-exposure photograph showing the fixed orientation of the model on the wheel. The wheel, a heavy steel plate having sufficient mass to insure uniform velocity, is supported on a stainless-steel shaft mounted on four preloaded precision ball bearings, assembled in a quill to form an accurately aligned unit. The launcher is driven by a 10-hp DC motor whose speed is controlled electronically. The control is activated by a selsyn generator driven by chain from the launcher shaft.

The model is counterbalanced by a movable weight on a screw in the plane of rotation of the model and displaced from it by 180 degrees. No provision is made for shifting

275
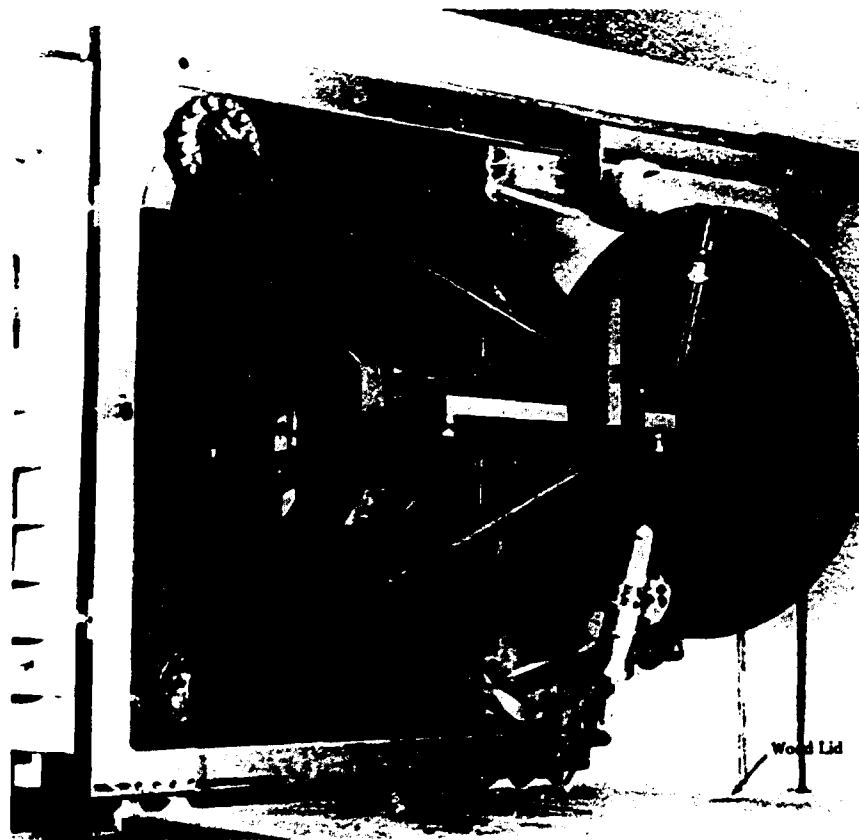
Figure 17.13. Launcher with model in chuck. Wood cover over hatch opening. (From Reference 30.)
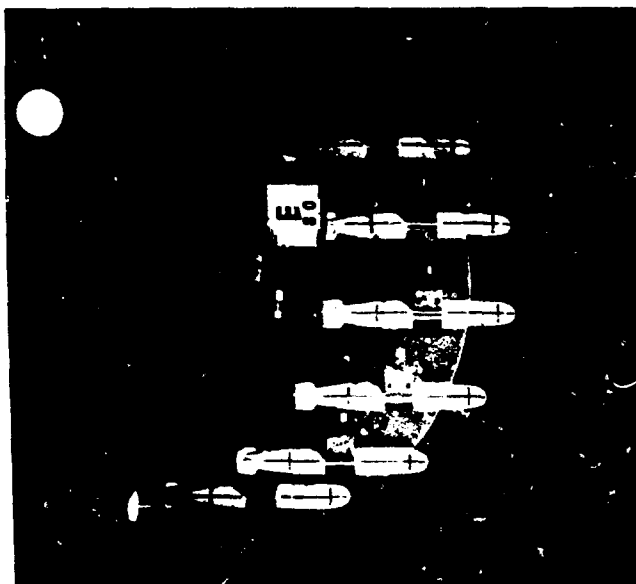
Figure 17.14. Multiple-exposure photograph of model in chuck.

this counterbalance after the model is released because the structure is massive, and a slight imbalance is not critical once the model is free.

The chuck (Figure 17.15) is shown with a steel ribbon in place. The visible end of the ribbon is fitted into an adapter in the cylindrical section of the model (Figure 17.16) and holds the model in place (Figure 17.17). Launching is accomplished by hitting the ribbon at the notched end with a rapidly moving knife in the chuck assembly, actuated by a release arm tripper (Figure 17.18). The model moves along a tangential path, and the chuck, continuing its circular motion, gradually lifts away from it. The rigidity of the model seat reduces to a minimum the energy stored in it that might affect the motion of the model at release. The entire chuck mechanism is mounted on ball bearings.

Figure 17.18 also sketches the opposite face of the wheel with the planetary-gear system

276
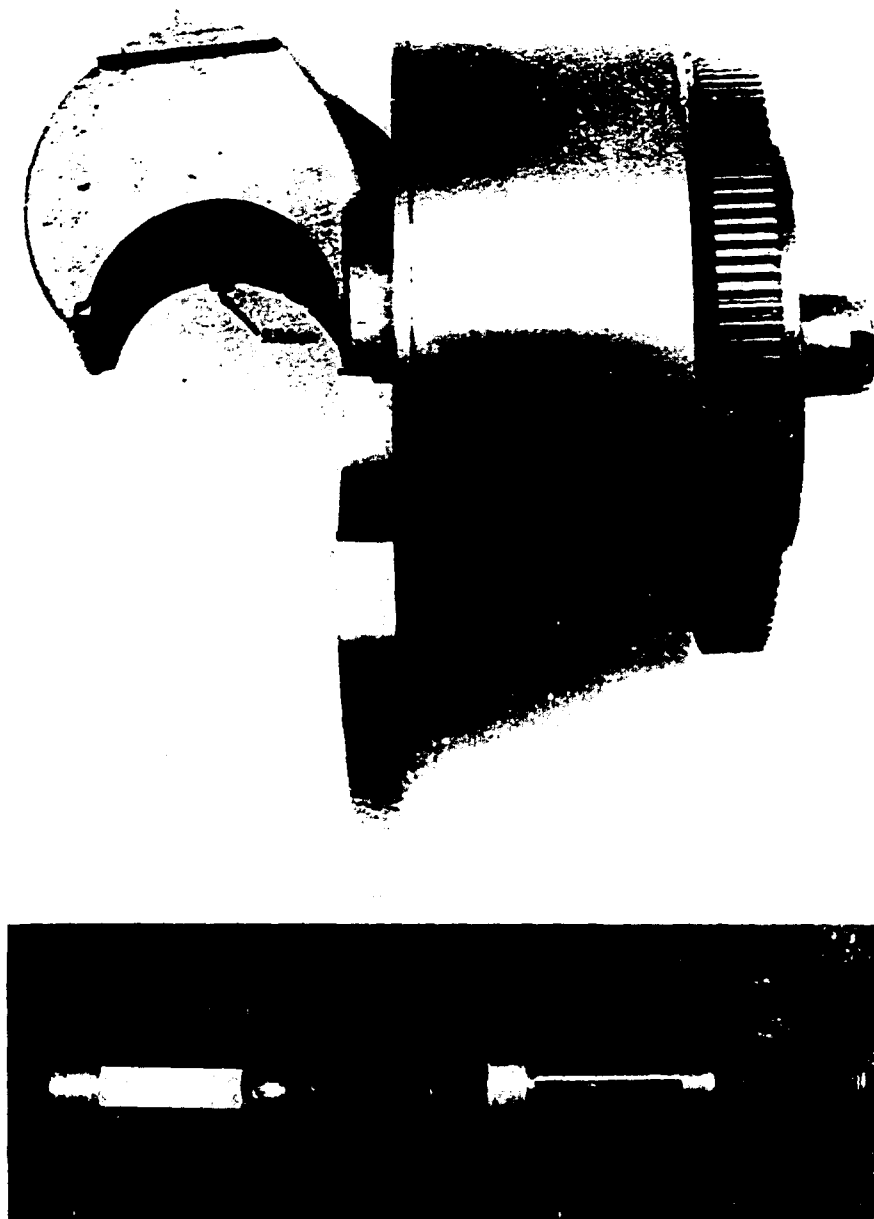
Figure 17.15. Launcher chuck with steel ribbon suspension.

and launching controls. The gear train, composed of specially cut fine-pitch precision gears, prevents the chuck from rotating around its own axis. To insure smoothness of operation and to prevent backlash, its idler gear is made in three layers. The central layer is integral with the spokes and hub; the two outer layers are ring gears, loaded against the central layer by small tangential coil springs in the rim. The central layer and one outer layer mate with the hub gear; the central layer and the other outer layer engage the chuck gear. The hub and chuck gears are equal in diameter.

Two levers or arms are bearing-mounted on the wheel shaft and prevented by clamps from rotating. The trajectory-angle arm clamps to the trajectory-angle scale, has a 90-degree adjustment, and is integral with the release arm, which carries the solenoid-operated tripper. The attack angle arm, attached to the central gear of the

277
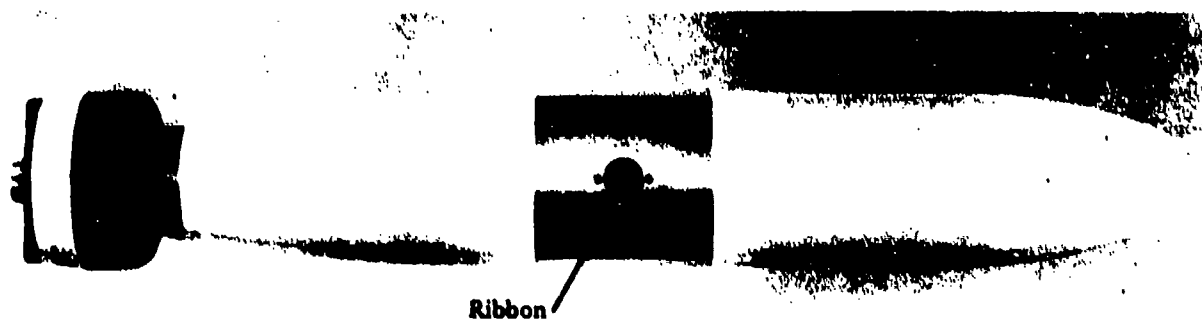
Figure 17.16. Adapter in cylindrical section of model.
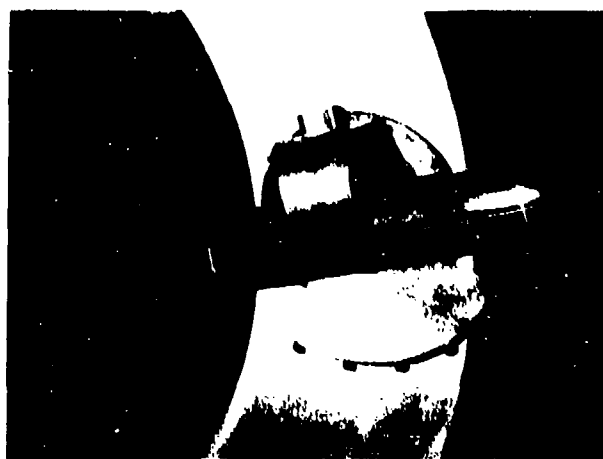
Figure 17.17. Model held in chuck.

planetary system, is clamped to the trajectory-angle arm with an adjustment of ±10 degrees on the attack-angle scale.

When the trajectory-angle arm is set at zero, the release arm hangs vertically in position to release the model on a horizontal trajectory. If, at the same time, the attack-angle arm is set at zero, the axis of the model will be horizontal (i.e., parallel to the tangent at the point of release) and the model flies with zero attack angle.

On the trajectory-angle arm, on the side facing the wheel, there is a light source and a photocell. A small mirror mounted on the wheel reflects light into the photocell at every revolution when the chuck is about 20 degrees ahead of the launching point. A signal is thus transmitted to the electronic interlocks that synchronize the operation of the tripper with that of the cameras and the lights.

Trajectory-Recording System

The cameras and flash lamps are described in Reference 29. The cameras are used as precision measuring instruments; many of their special features were designed to meet this requirement. The camera system should completely cover the underwater volume of the tank as well as the trajectory from launcher to water surface. The duration of a test run is 1 second or less; photographs were taken at rates between 500 and 3000 per second, depending upon the launching speed and the anticipated accelerations.

The synchronized high-speed motion-picture cameras used standard 35-mm film. The main bank of five recorded the underwater trajectory; two or three additional cameras recorded the air trajectory. In the launching plane, the adjacent camera fields had a 60% overlap; in the vertical direction the field of view covered the entire water depth (Figure 17.19). Such multiple coverage makes it possible to use a stereoscopic technique to measure six components of motion.

Each camera was attached to a flanged opening in the tank shell, looking in through a small window. The front nodal point of the underwater camera lens was at the center of curvature of the optically ground spherical window. All primary rays passed through the air-water interface at an angle of 90 degrees without refraction; there was no distortion or reduction of

278
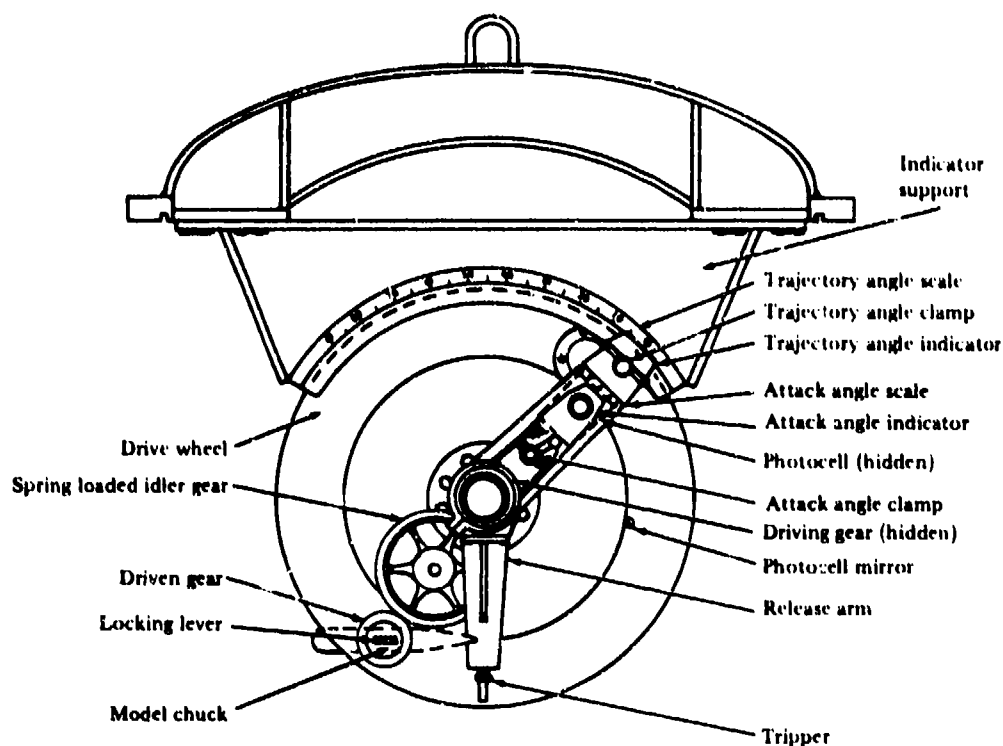
Figure 17.18. Launcher controls. (From Reference 30.)
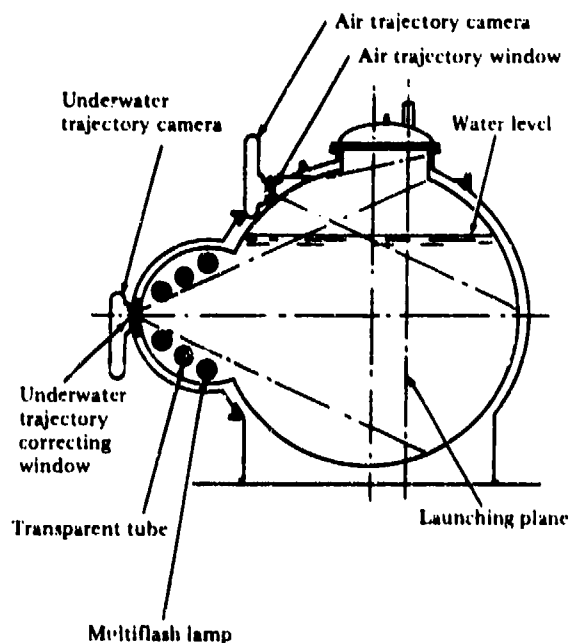
Figure 17.19. Camera field of view in vertical direction.
(From Reference 30.)

field. The curved water surface was a negative lens that increased the effective focal length of the system and shifted the focal plane, causing a field reduction of 4%, compared to a field reduction of 29% with a plane window.

A continuously moving film was required in order to provide the desired frame height and to meet the design requirement of 3000 frames per second, maximum. The selected speed of 31.25 fps gave a standard 35-mm frame height of 3/4 inch at 500 frames per second, requiring the extremely short exposures (on the order of 2 μs) that can be obtained from Edgerton-type flash lamps.

Figure 17.20 shows one of the underwater cameras, with film magazine, spherical window, and mounting flange. The lens is a 1-inch, f/2.3, Bausch and Lomb Baltar. To prevent friction, the film is guided through the focal plane by rollers instead of the usual pressure-plate arrangement. The film magazine can be detached from the camera and tilted to a horizontal position for loading. A 32-foot length of film, sufficient for a single run, is stored in

279
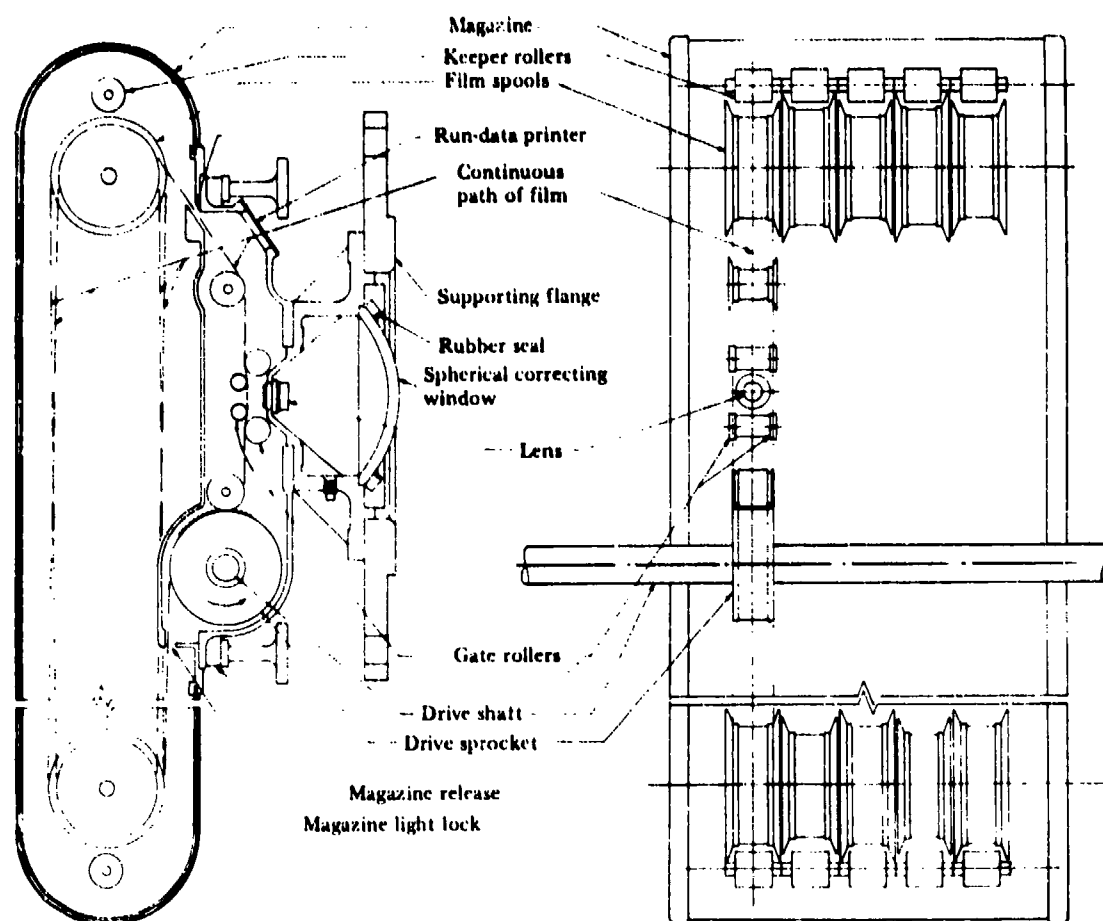
Figure 17.20. High-speed recorder camera. (From Reference 30.)

the magazine in a number of passes over the two sets of idler spools. The ends of the film, which extend through the light locks, are spliced to form a slack loop about 2 feet long outside the magazine.

The loading operation is completed by tilting the magazine into the vertical position and threading the loop over the guide rollers and drive sprocket of the camera. With the film in a continuous belt, it is possible to bring it up to speed gradually, expose it, and slow it down again without wasting film or using long leaders.

All cameras are driven through line shafting by a single synchronous motor (Figure 17.21). To provide gradual acceleration and deceleration of the film, the motor housing rotates in trunnion bearings; power is brought in through slip rings on the left-motor face. Two electrically operated brakes stop the shaft and the housing. To start the motor, the shaft brake is clamped,

the housing brake is released, and power is applied. The housing begins to rotate, comes up to speed, and is synchronized. The shaft brake is then released and the housing brake is applied gradually. As the housing slows down, the shaft takes up the difference between the synchronous speed and the housing speed, and when the housing stopped, the shaft was running at synchronous speed. By means of time-delay relays, this sequence of events proceeded automatically when the motor power was turned on. To slow and stop the film, the sequence was reversed.

The film travel was synchronized with the instant of launch so that the short strip of film exposed during loading did not pass through the camera during the actual recording period. A microswitch, actuated by a cam driven by a reduction gear from the camera shaft, made one contact for every pass of the film belt. In

280
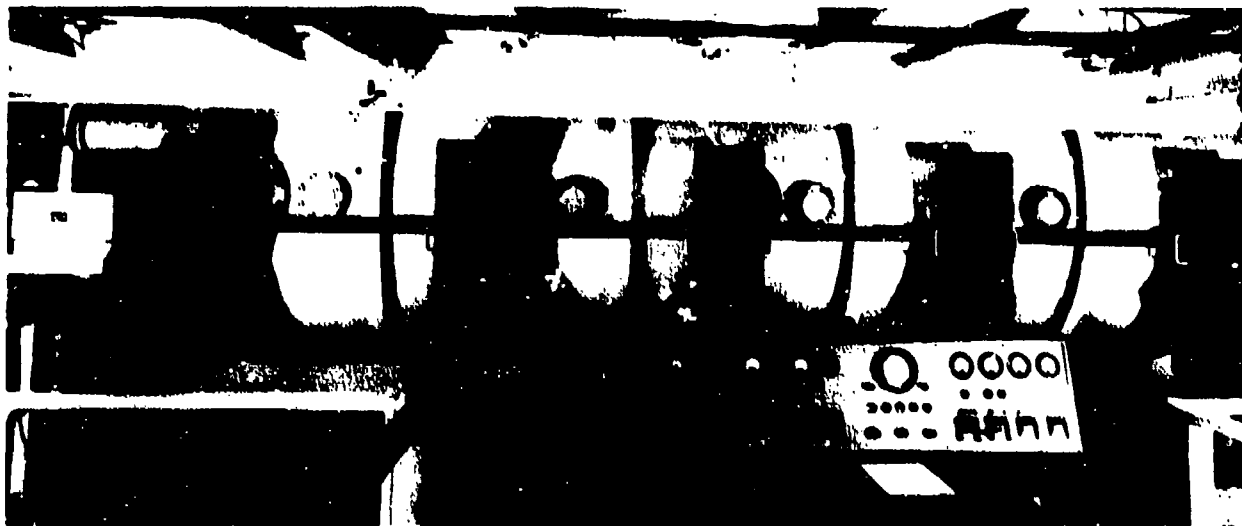
Figure 17.21. Underwater cameras and driving motor. (From Reference 30.)

operation, the camera shaft was first rotated manually until the microswitch closed; then all the films were threaded into their respective cameras, thus aligning the position of the splice with the microswitch. When the camera drive was running, the microswitch signaled each passage of the splices through the cameras and controlled the operation of the launcher release. Two other switches, activated by the same cam, controlled the operation of the flash lamps. To insure that the splices remained synchronized throughout the run, all the film belts had to be of exactly the same length, i.e., having the same number of sprocket holes. A film-loading device measured out the required length.

The cameras are operated with lenses continuously open, and exposures are made by intermittent illumination of the tank interior with flash lamps. A system consisting of from 30 to 42 Edgerton-type flash lamps, all operated simultaneously, was constructed. The individual lamps are synchronized with each other within less than $1/4\,\mu s$. Each lamp is a quartz tube about 8 inches long, filled with xenon, hydrogen, and a trace of radium bromide, with two metallic electrodes sealed into the ends of the tube. Two types of lamps are used: one a straight tube with an aluminized Lucite reflector (Figure 17.22), the other a helical tube in a headlight-type sealed-beam reflector with a smooth lens (Figure 17.23).

The power for each light is carried through an individual coaxial cable running to the

Figure 17.22. Lamp with Lucite reflector. (From Reference 30.)

control panel. Each is operated through an individual surge circuit that receives 4,000 volts of DC power from a large rectifier, and operates at twice this value through a voltage doubler. The power consumption is approximately 0.8 joules per flash; at 3,000 flashes per second, the battery of 30 lamps requires a continuous input of approximately 80 kw. The lights were operating only about 1/200 of the time, making the rate of power input during illumination more than 16,000 kw. The heat generated in the tubes

281
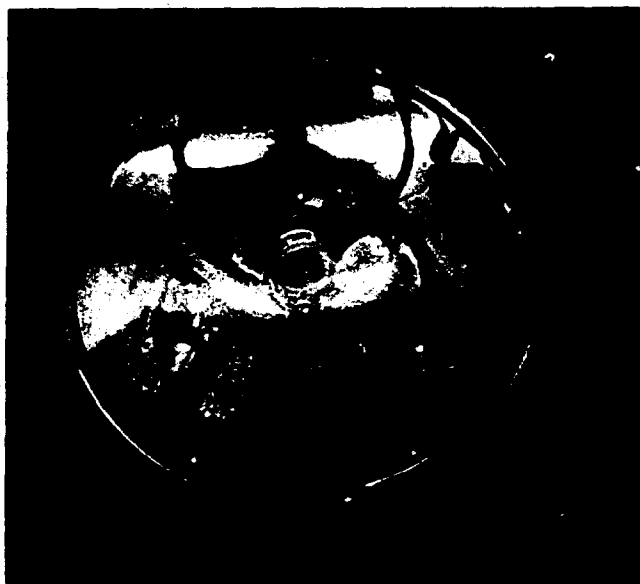
Figure 17.23. Headlight-type lamp. (From Reference 30.)

themselves limited the length of operation. The maximum for successful high-speed operation is 3600 flashes per run.

The steps in the photography of a typical model launching were as follows.

The camera magazines were loaded and the model was installed in the launcher, which was set for the desired trajectory and pitch angles before the hatch cover was closed. Then air pressure was adjusted, the launcher brought up to speed, and the camera motor was turned on.

The automatic launch sequence was started by the operation of the first of three interlocks. The second interlock was actuated by the microswitch on the camera drive immediately after the exposed film splices passed through the focal plane of the camera. The third and final interlock, which trips the model and launches it, was actuated on the next revolution of the launching wheel. The flash lamps began to function simultaneously with the release of the model and continued to flash until the entire length of film was exposed, at which time the lamps cut off and the equipment was automatically shut down in the reverse order of the starting sequence.

The camera motor runs at a constant speed. When the launcher runs at any multiple of that speed, the passage of the film splice through the camera and the passage of the model past the launching point occur with a fixed phase relation between them and may never coincide, in

which case it would be impossible to launch the model. Provision is made therefore to change the phase relationship by slowly rotating the camera-motor housing with a small electric motor geared to the housing brake.

Data-Analyzing System

The data-analyzing system was essentially a duplicate of the recording system. Projectors took the place of cameras and a movable screen replaced the model. All the films from one run in the launching tank were placed in the analogous projectors with the film strips synchronized so that the corresponding frames taken at the same time would be projected at the same time. Once the film strips were synchronized, they remained so during the projection of the entire run because the film drive of the projectors was a continuous shaft (Figure 17.24).

There was only one position in this space in which the two images could coincide. The exploring screen of the analyzer was adjusted until the two images fused into one, the movements being transferred to a battery of counters. When the screen registered precise image fusing, the counters indicated the projectile position in space corresponding to the pair of photographs. The analyzer was built to a scale of one half that of the tank.

The projectors (Figure 17.25) are precision instruments. Lenses were procured in matched pairs, one for the camera and the other for the
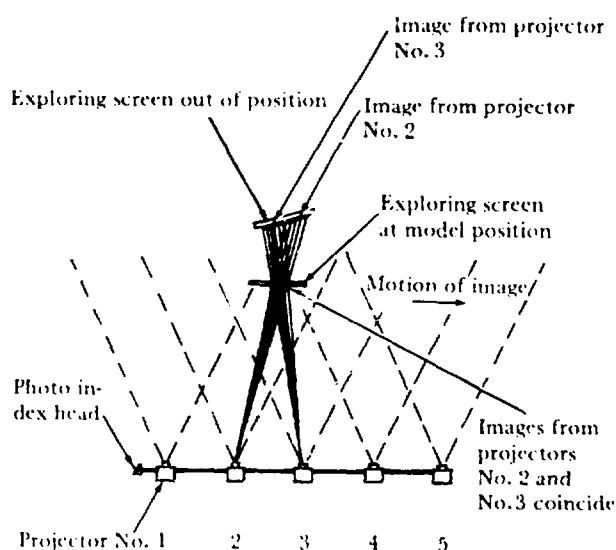
Figure 17.24. Data-analyzing system. (From Reference 30.)

282

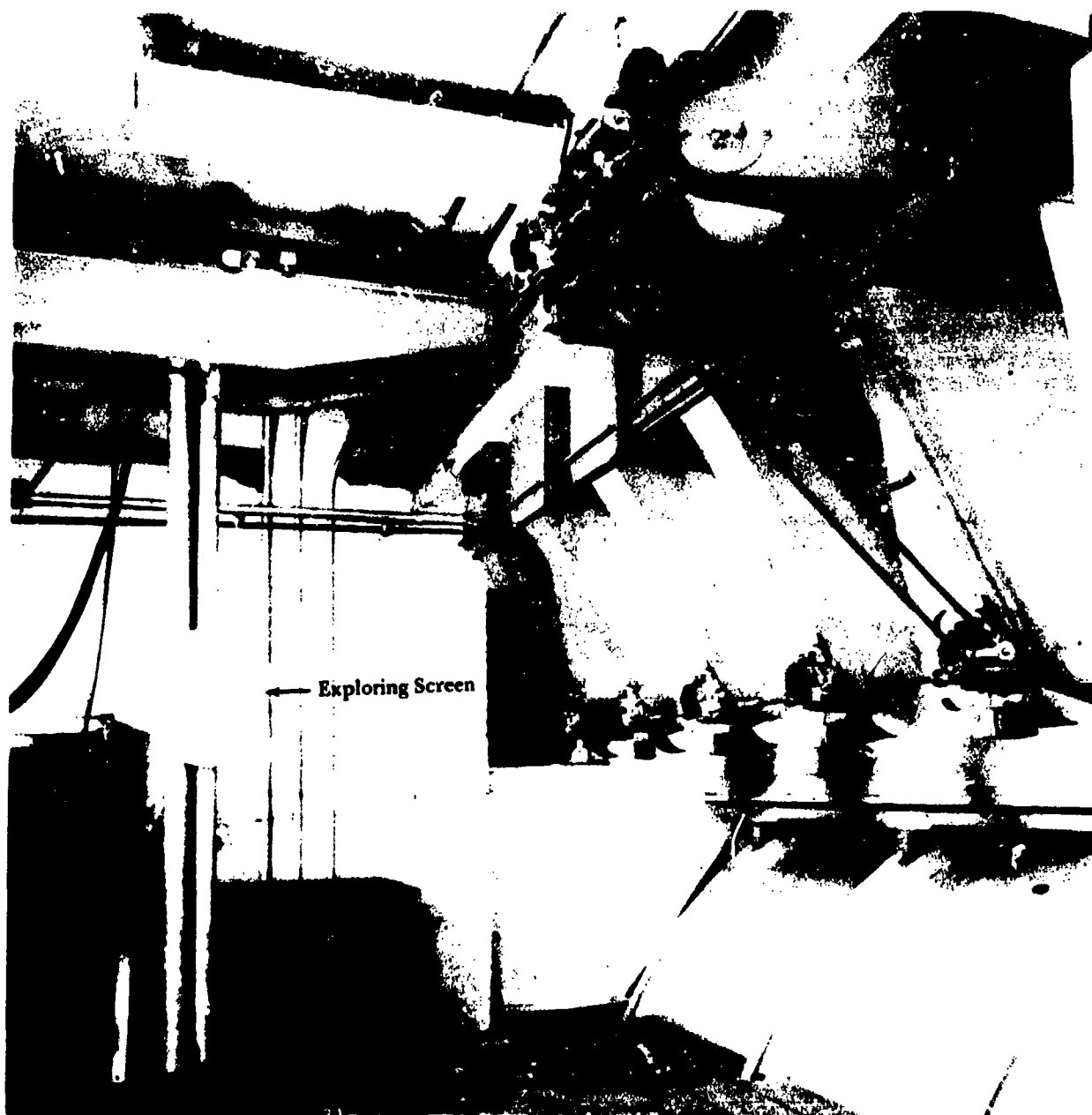Exploring Screen

Figure 17.25. Data-analyzing equipment. (From Reference 30.)

corresponding projector. The gate mechanism held the film exactly in the focal plane. The light source was kept as low in intensity as feasible for accurate readings in order to eliminate the heat that can affect both film and optical-system dimensions. Water cells and air cooling were also used to control temperature. Reference marks on the back wall of the launching tank and on a background screen at the rear of the analyzer were aligned before each measurement.

The exploring screen was a small disk with a half-model attached to it (Figure 17.25) so that the final projection was on a curved surface similar to the one photographed. The circular exploring screen was carried on a mechanical transport that provided three linear and two angular motions. A sixth motion was achieved

by rolling the half-model about its longitudinal axis. A carriage spanning the length of the room rode on overhead rails and transported a smaller carriage on a pair of transverse rails. Both carriages had rack-and-pinion drives. A pair of vertical guide tubes with a screw drive, suspended from the transverse carriage, could be rotated in azimuth to provide the second of three angular motions, the third being obtained by rotation of the circular screen in its own plane. Selsyn repeaters and mechanical counters functioned as position indicators to transmit the image-position information to the operator's desk. Roll was read directly from a scale on the screen.

PROTOTYPE LAUNCHING FACILITIES AT NUC

The NUC Morris Dam Torpedo Range near Azusa, Calif., provides facilities to launch proto-type missiles from air into water under controlled conditions of attitude and velocity and to measure water entry and subsequent behavior. The Fixed-Angle Launcher (FAL) and the Variable-Angle Launcher (VAL) are installed on a peninsula approximately 1000 yards upstream from the dam. The mild climate of the

district permits work throughout the year. A simplified map of the range area showing the principal facilities appears as Figure 17.26.

Projectiles launched from the VAL have a clear range 1000 yards long and at least 200 yards wide into water that varies in depth from 150 to 190 feet. Surrounding mountainsides provide excellent locations for detail and general-view camera stations. Both the FAL and the VAL ranges are instrumented with hydrophones and nets to record underwater trajectory data. The short airflight precludes studies of aerodynamic behavior or air stabilization.

Fixed-Angle Launcher

The FAL is a blowgun, 22.5-inch inside diameter and 300 feet long, that uses compressed air as a motive power. The whole system is mounted at an angle of 19 degrees with the horizontal. Plan and elevation views are given in Figure 17.27 and the hydrophone array in Figure 5.12 in Chapter 5. The launcher is anchored rigidly at its breech end and is supported along its length in such a way that it is free to expand lengthwise and yet is held in alignment. A keyway the length of the tube can be used to keep the torpedo from rolling. A
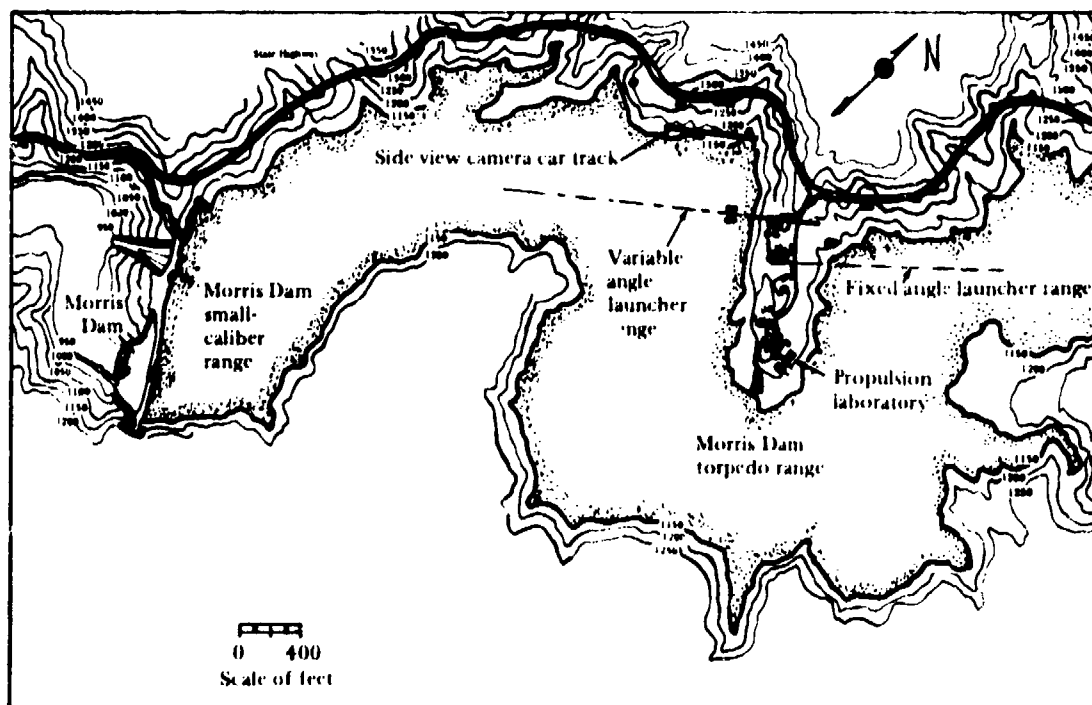

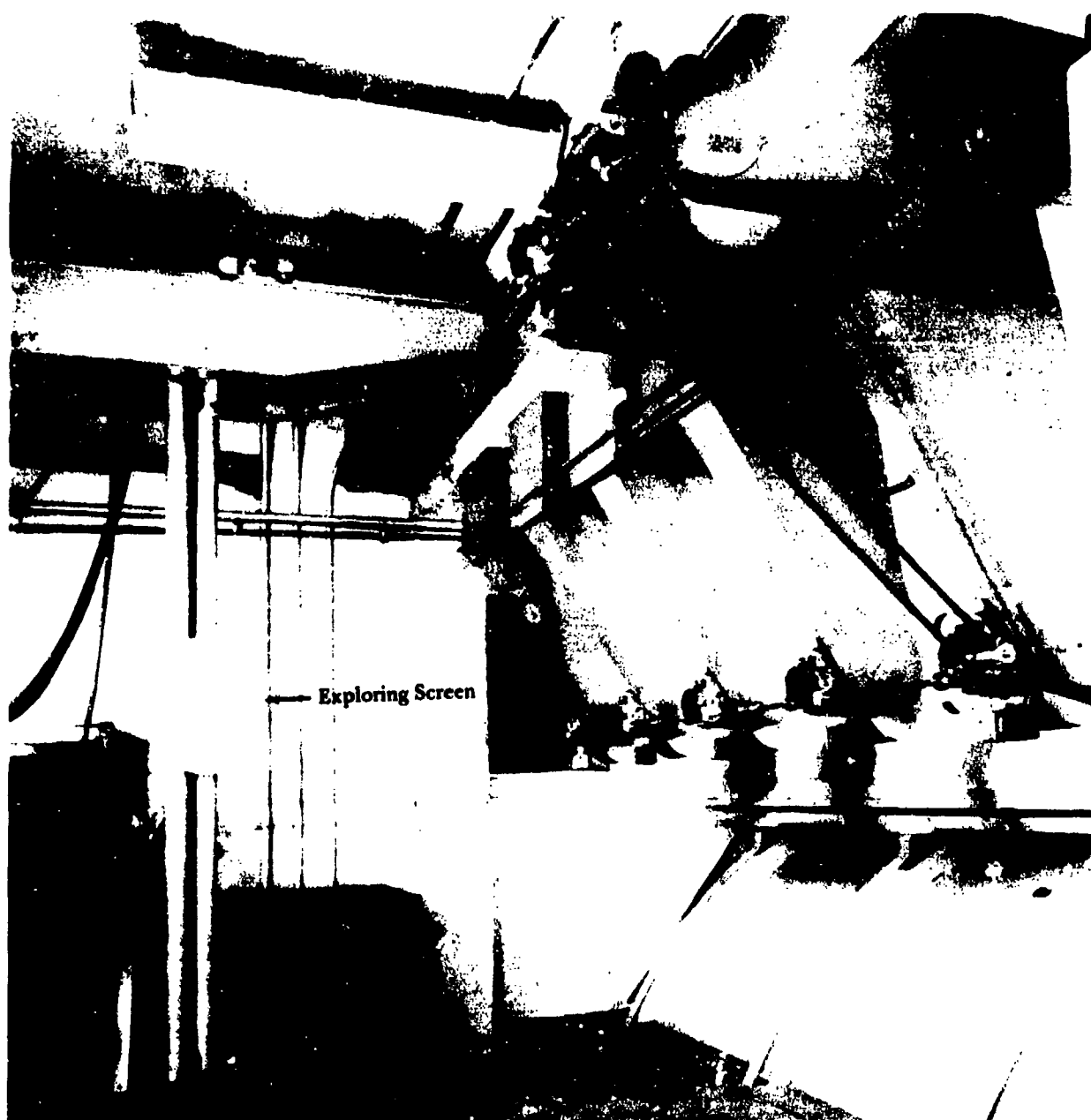Figure 17.26. Morris Dam Torpedo Range facilities.

284

Figure 17.25. Data-analyzing equipment. (From Reference 30.)

corresponding projector. The gate mechanism held the film exactly in the focal plane. The light source was kept as low in intensity as feasible for accurate readings in order to eliminate the heat that can affect both film and op ical-system dimensions. Water cells and air cooling were also used to control temperature. Reference marks on the back wall of the launching tank and on a background screen at the rear of the analyzer were aligned before each measurement.

The exploring screen was a small disk with a half-model attached to it (Figure 17.25) so that the final projection was on a curved surface similar to the one photographed. The circula exploring screen was carried on a mechanical transport that provided three linear and two angular motions. A sixth motion was achieved

283

by rolling the half-model about its longitudinal axis. A carriage spanning the length of the room rode on overhead rails and transported a smaller carriage on a pair of transverse rails. Both carriages had rack-and-pinion drives A pair of vertical guide tubes with a screw drive, suspended from the transverse carriage, could be rotated in azimuth to provide the second of three angular motions, the third being obtained by rotation of the circular screen in its own plane. Selsyn repeaters and mechanical counters functioned as position indicators to transmit the image-position information to the operator's desk. Roll was read directly from a scale on the screen.

PROTOTYPE LAUNCHING FACILITIES AT NUC

The NUC Morris Dam Torpedo Range near Azusa, Calif., provides facilities to launch prototype missiles from air into water under controlled conditions of attitude and velocity and to measure water entry and subsequent behavior. The Fixed-Angle Launcher (FAL) and the Variable-Angle Launcher (VAL) are installed on a peninsula approximately 1000 yards upstream from the dam. The mild climate of the

district permits work throughout the year. A simplified map of the range area showing the principal facilities appears as Figure 17.26.

Projectiles launched from the VAL have a clear range 1000 yards long and at least 200 yards wide into water that varies in depth from 150 to 190 feet. Surrounding mountainsides provide excellent locations for detail and general-view camera stations. Both the FAL and the VAL ranges are instrumented with hydrophones and nets to record underwater trajectory data. The short airflight precludes studies of aerodynamic behavior or air stabilization.

Fixed-Angle Launcher

The FAL is a blowgun, 22.5-inch inside diameter and 300 feet long, that uses compressed air as a motive power. The whole system is mounted at an angle of 19 degrees with the horizontal. Plan and elevation views are given in Figure 17.27 and the hydrophone array in Figure 5.12 in Chapter 5. The launcher is anchored rigidly at its breech end and is supported along its length in such a way that it is free to expand lengthwise and yet is held in alignment. A keyway the length of the tube can be used to keep the torpedo from rolling. A
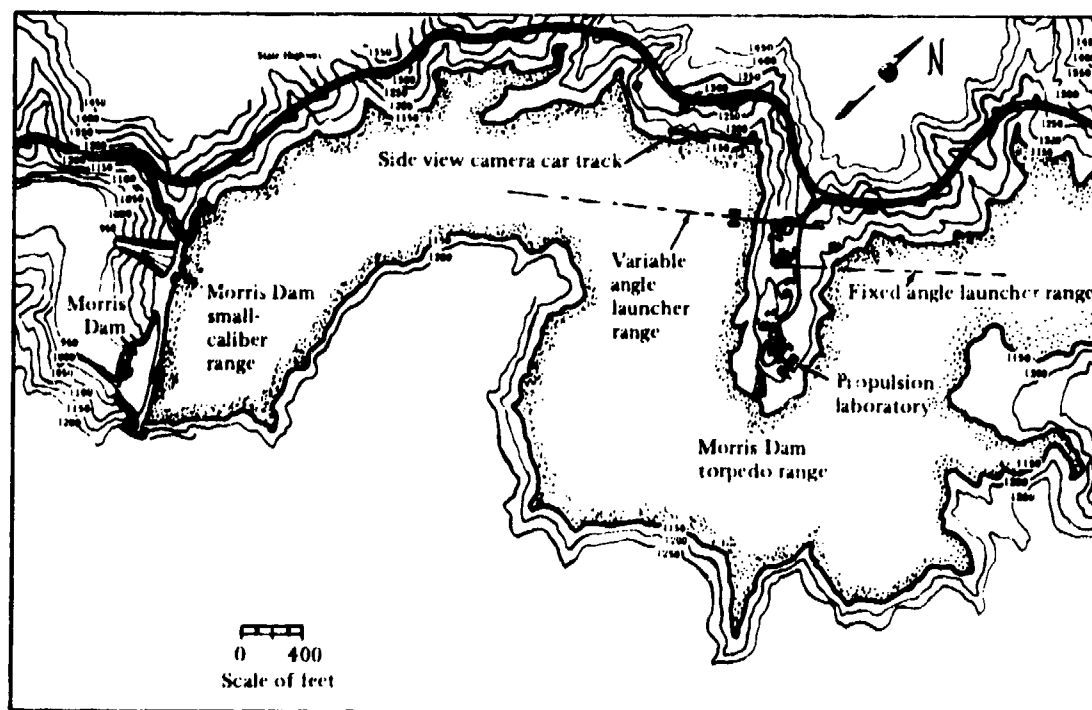

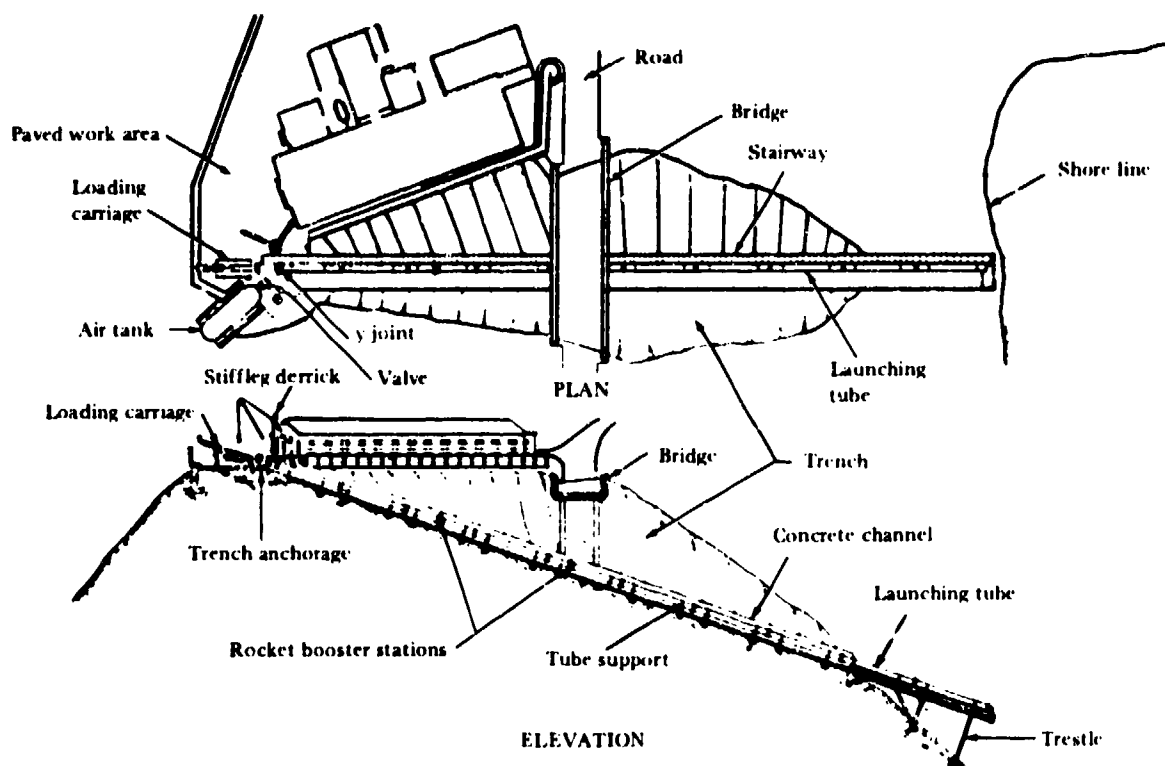Figure 17.26. Morris Dam Torpedo Range facilities.

Figure 17.25. Data-analyzing equipment. (From Reference 30.)

corresponding projector. The gate mechanism held the film exactly in the focal plane. The light source was kept as low in intensity as feasible for accurate readings in order to eliminate the heat that can affect both film and optical-system dimensions. Water cells and air cooling were also used to control temperature. Reference marks on the back wall of the launching tank and on a background screen at the rear of the analyzer were aligned before each measurement.

The exploring screen was a small disk with a half-model attached to it (Figure 17.25) so that the final projection was on a curved surface similar to the one photographed. The circular exploring screen was carried on a mechanical transport that provided three linear and two angular motions. A sixth motion was achieved

283

by rolling the half-model about its longitudinal axis. A carriage spanning the length of the room rode on overhead rails and transported a smaller carriage on a pair of transverse rails. Both carriage had rack-and-pinion drives. A pair of vertical guide tubes with a screw drive, suspended from the transverse carriage, could be rotated in azimuth to provide the second of three angular motions, the third being obtained by rotation of the circular screen in its own plane. Selsyn repeaters and mechanical counters functioned as position indicators to transmit the image-position information to the operator's desk. Roll was read directly from a scale on the screen.

PROTOTYPE LAUNCHING FACILITIES AT NUC

The NUC Morris Dam Torpedo Range near Azusa, Calif., provides facilities to launch prototype missiles from air into water under controlled conditions of attitude and velocity and to measure water entry and subsequent behavior. The Fixed-Angle Launcher (FAL) and the Variable-Angle Launcher (VAL) are installed on a peninsula approximately 1000 yards upstream from the dam. The mild climate of the

district permits work throughout the year. A simplified map of the range area showing the principal facilities appears as Figure 17.26.

Projectiles launched from the VAL have a clear range 1000 yards long and at least 200 yards wide into water that varies in depth from 150 to 190 feet. Surrounding mountainsides provide excellent locations for detail and general-view camera stations. Both the FAL and the VAL ranges are instrumented with hydro phones and nets to record underwater trajectory data. The short airflight precludes studies of aerodynamic behavior or air stabilization.

Fixed-Angle Launcher

The FAL is a blowgun, 22.5-inch inside diameter and 300 feet long, that uses compressed air as a motive power. The whole system is mounted at an angle of 19 degrees with the horizontal. Plan and elevation views are given in Figure 17.27 and the hydrophone array in Figure 5.12 in Chapter 5. The launcher is anchored rigidly at its breech end and is supported along its length in such a way that it is free to expand lengthwise and yet is held in alignment. A keyway the length of the tube can be used to keep the torpedo from rolling. A

Figure 17.26. Morris Dam Torpedo Range facilities.

Figure 17.27. Fixed-Angle Launcher (FAL).

1-ton projectile can be launched into the water at velocities of 400 to 500 fps. The FAL (Reference 59) was extensively used until the more versatile VAL was constructed.

Variable-Angle Launcher

The VAL can be adjusted to angles between 0 and 40 degrees with respect to the horizontal (Figure 17.28) and is designed to launch a 1500-pound missile at velocities up to 1000 fps. Tests can be carried out under accurately controlled conditions over a range of velocities and entry angles. The missile entry point can be predicted with sufficient precision that cameras and other instruments can be used at short range, either from land-based or anchored stations, enabling missile orientation, angular and linear velocities, and deceleration to be measured during water entry. Detailed entry photographs show the establishment of flow around the missile nose; broach and re-entry are also recorded photographically. The underwater

trajectory can be measured for almost 1000 yards. Instruments inside the torpedo measure missile attitude as a function of time or record its operation and that of its components. The projectile is recovered either by mechanical devices or by divers.

The main launcher ramp is constructed on a natural 45-degree slope on the downstream side of the peninsula; a counterweight track runs down a natural 30-degree slope on the upstream side (Figure 17.29).

The VAL is a blowgun, 22.5-inch inside diameter, and 300 feet long. It is supported within a movable bridge that was designed to accommodate additional tubes[2] ranging in diameter from 8 to 21 inches. Figure 17.30 shows the tube muzzle and the bays available for other tubes. The movable launcher bridge is supported at the outer end on two pontoons connected by a 95-foot-span and at the shore end by a carriage traveling on a 45-degree ramp (Figure 17.31). The inclination of the launcher

[2]The large tube can be used for subcaliber launchings; the subcaliber missile rests in a sectioned wooden sabot that separates from the missile during airflight.

285

Figure 17.28. Variable-Angle Launcher (VAL).
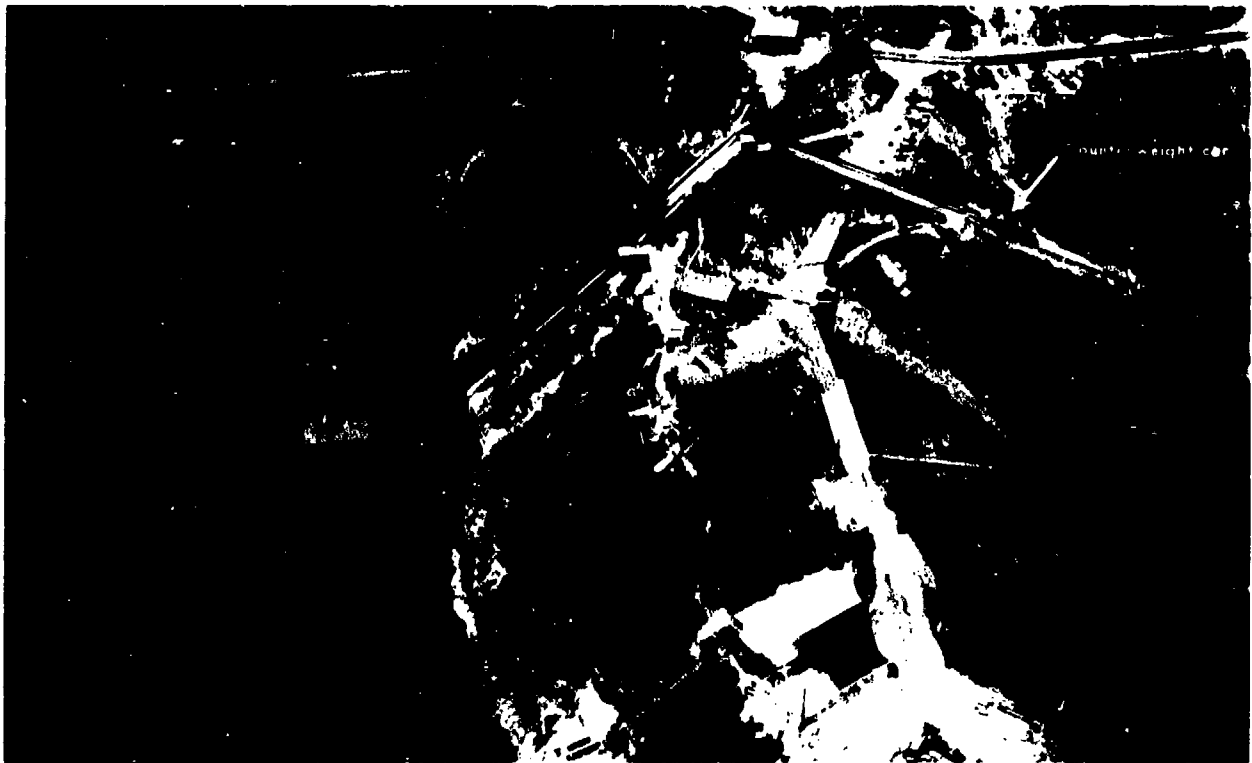
Figure 17.29. VAL operative equipment, including counterweight car.

286
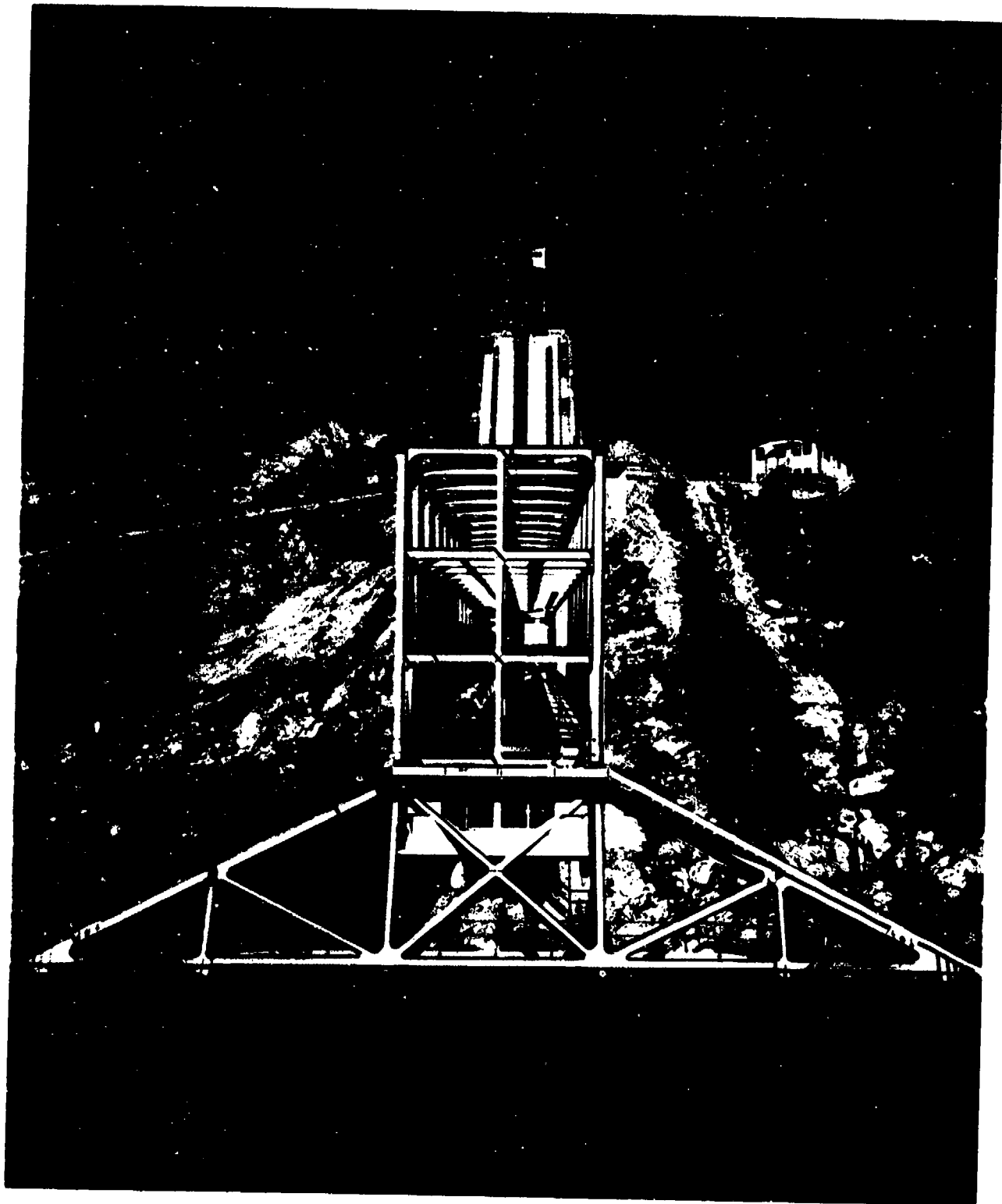
Figure 17.30. VAL launching tube and bays for additional tubes.

287
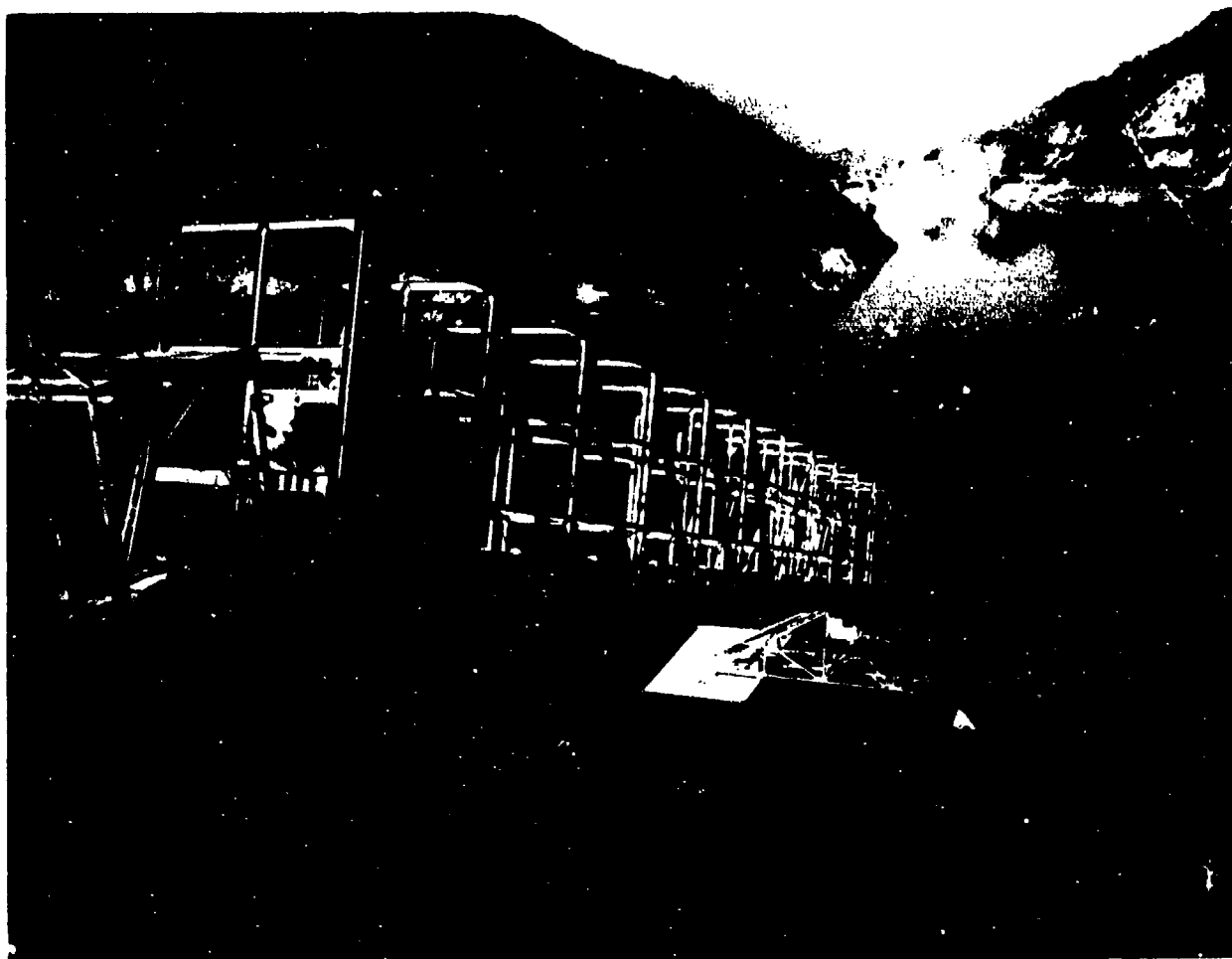
Figure 17.31. VAL on supporting pontoons.

bridge is adjusted by shifting the carriage up or down the ramp (Figure 17.29), the weight of the bridge and carriage being balanced by a counterweight car on the back slope of the hill. The bridge is moved by a motor drive acting on cables connecting the bridge support carriage to the counterweight car. The launcher bridge is noteworthy in that it was, when built, the longest all-welded steel span in the United States (300 feet long, 22 feet wide, and 35 feet high).

The carriage supporting the inner end of the launcher bridge moves on special rails weighing 1200 lb/yd, or about 10 times the weight of a standard railroad rail. The carriage is secured to the rails by four 7-inch-diameter pins to resist the recoil of the launcher. The 600-ton

counterweight car runs on a track of standard railroad rail laid over reinforced Gunite paving.

A large concrete structure supporting the launcher rails and the counterweight track was built over the ridge between the launcher and counterweight car (Figure 17.32). The rails for the carriage and counterweight car are continued to the top level of the cellular structure on slabs integral with the side walls and webs. The space within this structure houses electronic control and recording equipment, operating machinery, etc. In all, there are seven levels; the uppermost carries the main-drive machinery by which the bridge is moved.

A 40-foot steel tower was erected at the top of the concrete structure (Figure 17.32) to

288
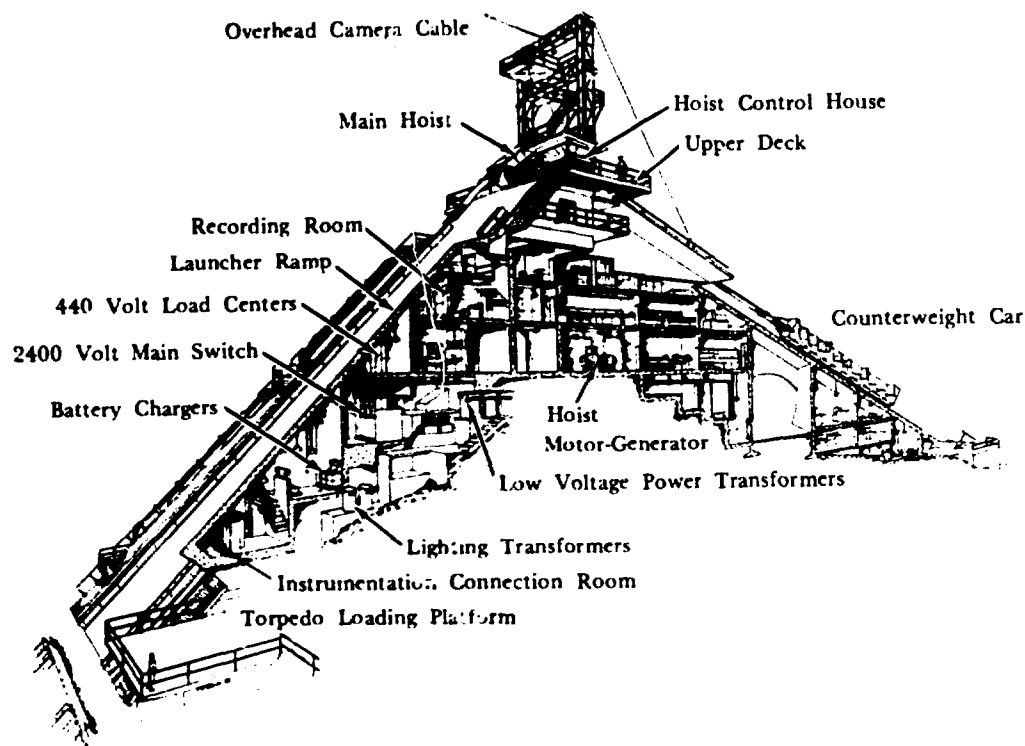
Figure 17.32. Concrete structure of VAL.

provide a vantage point for photography and to support an overhead cableway for a camera car.

Further details concerning the construction and instrumentation of the VAL can be found in References 27 and 78.

instrumentation[3]

Because a prototype launching needs precision instrumentation for assessment of results, a variety of instruments and techniques was developed for the Morris Dam Torpedo Range. Because a missile's underwater trajectory is influenced by the motions it has experienced during airflight and water entry, accurate measurements must be made of entry velocity, attitude, trajectory angle, angular velocity and acceleration in both pitch and yaw, and linear deceleration during the early phase of water entry.

The velocity and acceleration of the torpedo in the launching tube were determined from data recorded by the torpedo position interferometer (Reference 64), an electronic device that records the time the torpedo passes stations spaced 24 inches apart. A coupling loop

on the inside of the launching tube breach door was connected to a radio frequency oscillator, the launching tube itself acting as a cavity resonator. A 394-MHz signal caused resonance to occur every 24 inches as the projectile progressed down the tube.

Flare Camera

This camera is installed on the sideview camera car that can be moved to a position opposite the entry point (References 12 and 27). The track for the camera car is parallel to the center line of the range and 456 feet away on the west bank (Figures 17.26 and 17.33). The entry velocity, angular velocity and acceleration in a vertical place, and linear deceleration before the tail of the missile entered the water were measured precisely from the flare-camera records. Two brilliant pyrotechnic flares attached to the missile tail were photographed at a rate of 1000 exposures per second at an exposure time of about 0.0003 second. A solenoid-operated shutter controlled the exposure time.

---

[3]Described more fully in References 27, 59, 78, and 106.
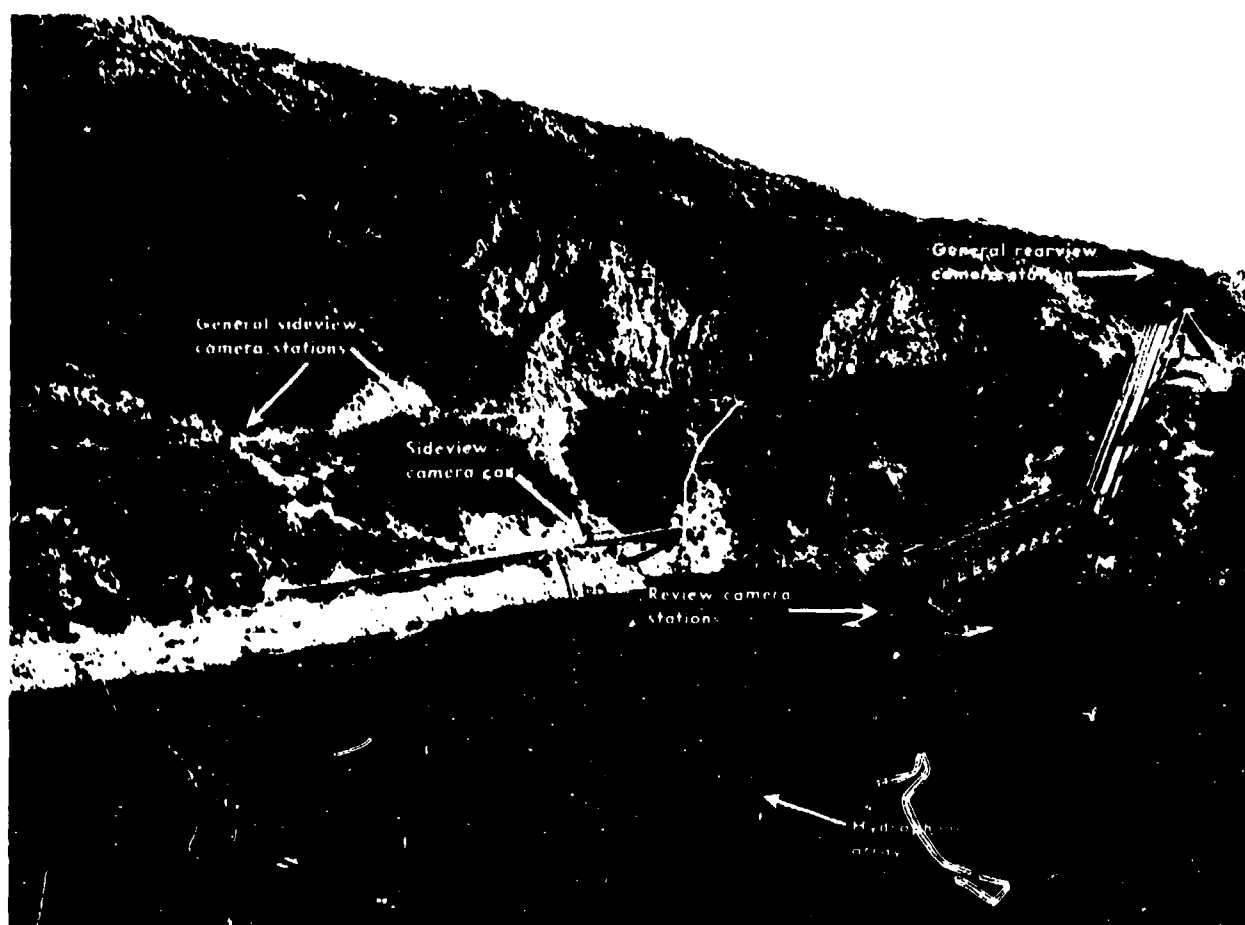
Figure 17.33. VAL camera stations and hydrophone array.

The optical system prevented blurring of the image by compensating for the forward velocity of the projectile (Figure 17.34). The photographic plate was stationary in the camera and the image of the flares was focused on it by a specially designed achromatic meniscus lens of 70-inch focal length and 1-inch aperture. An accurate plane-parallel plate mounted in a rotating spindle between the lens and the photographic plate rotated at 30,000 rpm, and refraction of light held the image stationary during each flare exposure. The retainers holding the plane-parallel plate in the spindle were shaped to give an intermittent shutter action with light transmitted during 47 degrees of spindle rotation. Plate thickness was determined by missile velocity and spindle speed. It is feasible to use a single plate during a series of launchings because satisfactory definition occurs over a usable velocity range.

Because the path of the projectile, as seen by the rotor, must be normal to the axis of the rotating spindle, two movable reflecting prisms were used to accommodate the various trajectory angles instead of rotating the camera about its optical axis. Adjustment of the prisms also accommodates the camera to changes in lake level. The exact speed of the rotor, which must be known in order to determine the time interval between individual exposures of the flare images, was determined by comparing pulses from a variable-reluctance pulse generator built into the spindle drive with a time scale from the master time base. Both traces were recorded on a single oscillograph record.

The flare images appear on the photographic plate as a series of regularly spaced marks approximately at right angles to the missile trajectory. The spacing between successive images of the flares represents the speed of

290
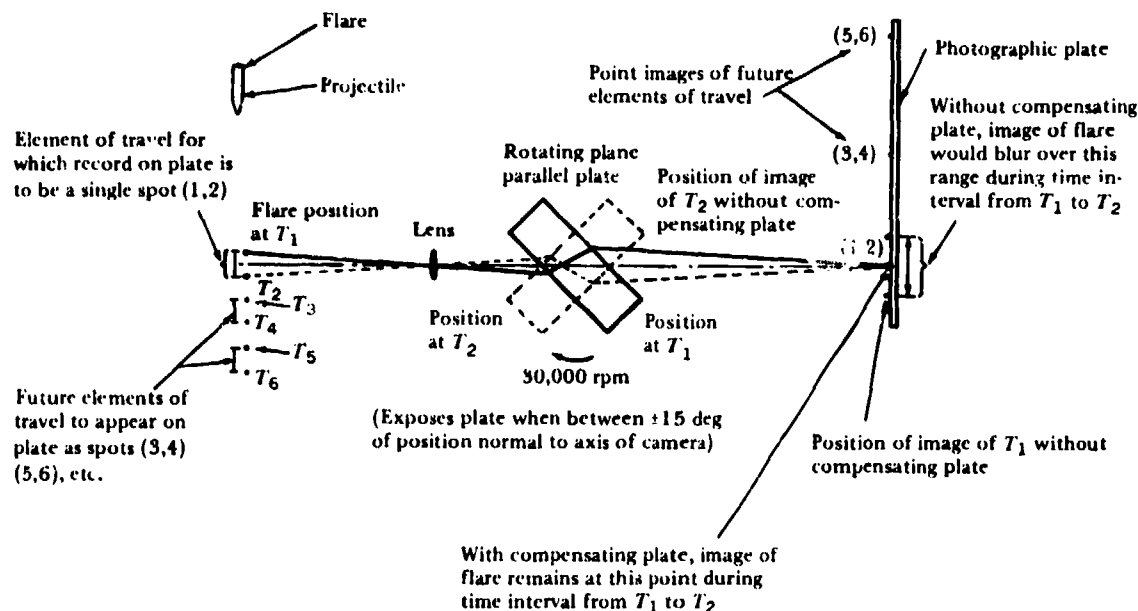
Figure 17.34. Optical system of flare camera.

In the figure, the following labels appear:

- Flare
- Projectile
- Point images of future elements of travel
- (5,6)
- (3,4)
- Photographic plate
- Without compensating plate, image of flare would blur over this range during time interval from T_1 to T_2
- Element of travel for which record on plate is to be a single spot (1,2)
- Rotating plane parallel plate
- Position of image of T_2 without compensating plate
- Flare position at T_1
- Lens
- T_2 T_3
- T_4
- T_5
- T_6
- Position at T_2
- Position at T_1
- Future elements of travel to appear on plate as spots (3,4) (5,6), etc.
- 30,000 rpm
- (Exposes plate when between ±15 deg of position normal to axis of camera)
- Position of image of T_1 without compensating plate
- With compensating plate, image of flare remains at this point during time interval from T_1 to T_2

the torpedo, providing an accurate determination of velocity during free flight and of deceleration during water entry. A typical flare-camera photograph is shown in Figure 17.35. The complement of the angle made by lines joining synchronous flare-image pairs with the torpedo line of flight gives the angle of attack. If the line of flight does not change perceptibly, the rate of change in angle of attack is equal to the rate of change in pitch. A carefully positioned moored spar provides a horizontal reference for pitch determination as well as a scale factor for distance determination. The flare images are straight line segments and synchronous images lie in a superimposed straight line.

The plates were measured on the comparators that were used for the model data. The scale of the plate was determined by fiducial marks on the spar. The range position of a missile can be measured to within 0.01 inch from a good flare image and projectile attitude in the pitch plane can be measured to within 0.1 degree.

Motion-Picture Cameras

High-speed Mitchell motion-picture cameras recorded the airflight, linear and angular water-entry motion, and splash of the missile. Its wake, broach, and re-entry were also recorded. The cameras were not synchronized with each other; time from the master time base was recorded on each frame in each camera to correlate the data.

Three 70-mm Mitchell cameras mounted at stations along the road bordering the west bank of the reservoir operated at 32 frames per second, jointly covering the first 1000 feet of the range. The last two cameras can be pivoted to follow the projectile still farther down range.

Two 35-mm Mitchell cameras operating at 120 frames per second recorded the details of water entry. One was set up on the sideview camera car (Figures 17.26 and 17.33) and the other was suspended directly above the entry point on an overhead cableway. A 16-mm Mitchell camera operating at 64 frames per second can be mounted on the connecting bridge below the muzzle of the launcher to give a close-up rear view of the water entry, and a general rearview camera (Army K-25 operating at about 1 frame per second) on top of the tower supporting the camera cableway can also photograph the trajectory and the wake.

Underwater Trajectory

Recording the underwater trajectory of a missile is a difficult yet essential procedure. Data concerning the path of the missile and its velocity and orientation along the trajectory were obtained in several ways.

291

Figure 17.35. Typical flare camera record.

The hydrophone array (Figure 17.33) recorded missile position at several known times during the underwater trajectory. Sound pulses, produced by the timed explosion of blasting caps inside the missile, were picked up by the hydrophones, amplified, and recorded on an oscillograph. In an array 75 feet deep, 150 feet wide, and 750 feet long, 24 hydrophones were held in position by buoys and anchor lines in five 150-foot-long bays. For one launching, 12 hydrophones recording on a 16-channel oscillograph were usually selected. The cap explosion times were tallied with an accurate time scale on the oscillograph record. Torpedo positions were determined by time differences, reduced to equivalent distances in feet, and set into the scale board of a computer (Figure 17.36). The position of a missile could be determined within ±1 foot on each coordinate, and the average velocity between points on the trajectory to within ±1%.

Magnetic loops were sometimes used instead of hydrophones during the early part of the underwater trajectory because of the high noise level from the cavity, turbulence, pieces of sabot striking the water, and reflected noises from the launching. A magnetic loop marks the time at which a magnetized missile passed through it, but does not define missile position or orientation.

The loops, each 25 feet square and consisting of 80 turns of copper wire, are hung vertically at selected positions across the range. The passage of the magnetized missile produced a pulse of current to operate the galvanometer of a high-speed oscillograph. The pulses were strong enough to require no amplification.

Nets (Reference 11) give a direct means of locating points on the trajectory. Twine nets (similar to fish nets but made with non-slip knots) were used for this purpose. The hole torn by passage of the missile provided the coordinates of a point on the trajectory, but could not record time and missile orientation.

Electric nets have also been used. No. 20 copper wires are stretched at 9-inch intervals horizontally across one face of a frame and vertically across the other, with a 1-inch space between the two arrays. Passage of the torpedo forces one set of electrified wires against the

292
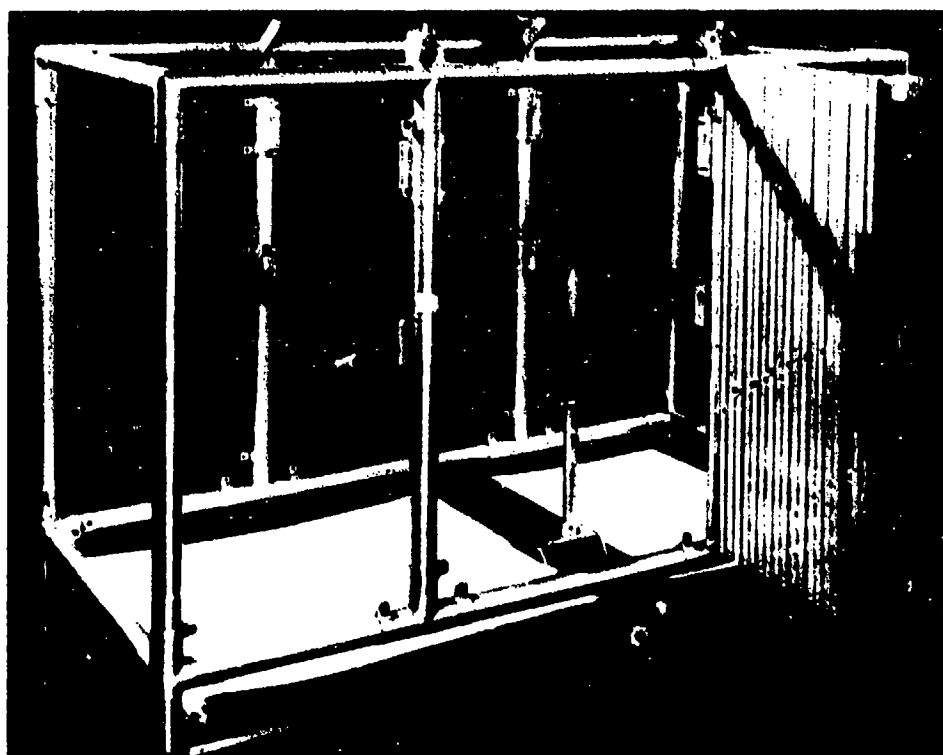
Figure 17.36. Computer for reducing hydrophone range data.

other, thereby closing a cir uit to record time of passage. The broken wires marked the position of torpedo passage, but these positions were less accurate than those determined by nets made of twine.

Internal gyroscopic instruments were developed to record missile attitude during air and underwater flight (Reference 63). Ordinarily, two gyroscopes were used so that orientation about three axes could be determined from the recorded data. The gyroscopes were equipped with commutators that indicated angular motion in 1/2-degree steps. A bank of miniature neon lights connected to the commutator flashed in sequence during angular motion of the gyro gimbals and exposed a continuously moving 16-mm film to form a series of dashes indicating direction and angle of rotation.

It is important to the success of hydroballistics testing that a precise time base be recorded on each photographic and oscillograph record for coordination of the results from the several instruments and for use in velocity calculations. Some instruments have to be started at a predetermined instant in order to

record a particular time interval. A master time base correlates launching records from oscillographs by supplying the same time indications to all records, obviating the need for individual synchronized recording units. It was governed by a fork-controlled oscillator used in conjunction with frequency-divider networks. Consistently high accuracy was achieved by compensating for temperature changes.

Each motion-picture camera photographed a cluster of seven 2-inch cathode-ray tubes (Figure 17.37) that record the launching number and the time as generated by the master time base. A chronograph attachment on the Mitchell motion-picture cameras focused the image of these tubes onto one corner of each frame. Three of the cathode-ray tubes recorded launching number and four indicated the time by a decade system (Figure 17.38). The spot on the first tube moved clockwise around the tube face in ten steps at 1-second intervals, those of the second and third tubes moved at 0.1-second and 0.01-second intervals, respectively, and the spot on the fourth tube moved continuously in a circle, completing one revolution every 0.01

293
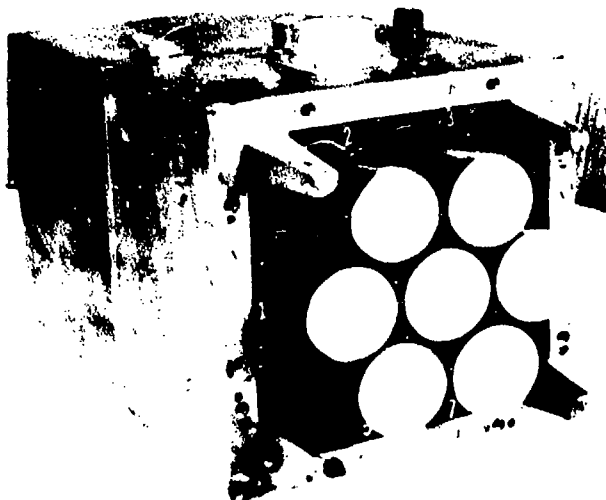
Figure 17.37. Master time base unit.
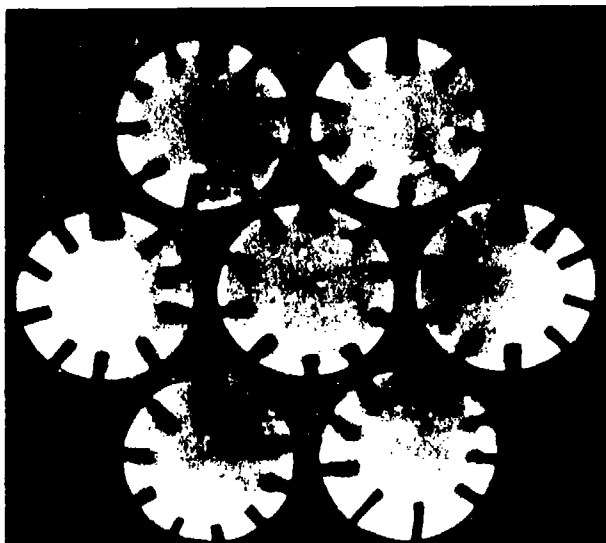
Figure 17.38. Master time base record showing time 1.533 seconds.

second. The precision was 0.001 second when the trace on the fourth tube was read to 0.1 revolution. A time scale from the master time base was also recorded on a channel of each recording oscillograph.

The launching-valve mechanism, the oscillographs in the recording station, and the cameras at the various remote stations can be operated either manually or by an automatic-sequencing system. The equipment performs three functions:

1. A pulse generator and a group of selector units start and stop the launching controls and instruments at any time during a 10-second interval after the launching operator has started the pulse generator (timing from the pulse generator is accurate to 0.1 second).

2. Precision electronic timers accurate to 0.01 second are started by the initial motion of the projectile to give time delay and function durations of up to 2 seconds.

3. Auxiliary motor-driven timers sequence functions requiring more than 10 seconds of operation.

Starting times were selected so that motion-picture cameras and oscillographs were at operating speed prior to launching. The sequencing system can control launching mechanism and instruments; any desired combination of automatic or manual operations can be achieved. It can also turn off each instrument at the end of the test.

Instruments can also be started by switches or break-rods actuated by passage of the torpedo through the launching tube or by motion of some part of the launching mechanism. A channel of the sequencing system was usually included in the circuit so that time delay and duration of operation could be controlled, as well.

Missile underwater photography in open ranges (e.g., the Morris Dam Torpedo Range) is described in References 13 and 79; it is far more complicated than underwater photography in model tanks.

OTHER MODEL FACILITIES IN NUC LABORATORY[4]

Open Launching Tank

The large model tank measuring 25 feet long by 52 inches high by 54 inches wide, with

----

[4]Further details are in Reference 54.

an inside width of 44 inches, is shown with its catapult-launching arrangement in Figures 17.39 and 17.40. The glass section nearest the launcher was 47 inches high by 66 inches long by 3/4 inch thick so that the top rail did not obstruct the photographic view. Glass panes 3/4 inch thick, 40 inches high, and 66 inches long comprised the other three sections, separated by U-frame columns 6 inches wide. No tie bars crossed the width of the tank; the columns supported the entire hydrostatic load (40 inches of water). The section nearest the launcher was also able to withstand shock loads arising from missile water entry.

The tank contained 2,200 gallons of water continuously filtered to remove particles as small as 0.5 micron. Commercial sodium hypochlorite was added to the water (approximately 1 gallon to the tankful) to prevent the formation of algae. Sufficient clarity was achieved to allow excellent photography.

Diving models were stopped by strips or rolls of rubber cushion along the bottom of the tank; canvas and felt blankets suspended above the water down range caught broaching models.

The launcher is a 5-foot cross bow (Figure 17.40). The wire-rope bow string is attached to the ends of two cantilever springs, each consisting of eight leaves of 3- by 3/8-inch spring steel. The combined spring constant is 443 lb/in, which, at the safe working stress of 100,000 psi, develops about 900 ft-lb of energy. At the maximum 18-inch draw, the bow develops about 3,500 pounds of pull so that a 3/16-inch bow cable is required. A 2-inch-diameter model weighing 1.1 pounds can be launched at about 140 fps.

The whip camera and optical accessories are mounted on the launcher carriage, together with the pickup for a photoelectric device used to determine launching velocity. A double rail guides both the launcher carriage, which is attached to the draw rope, and the electrically operated draw-screw trip mechanism. Scales and adjustable-limit switches are mounted on the guide rails so that the bow can automatically be
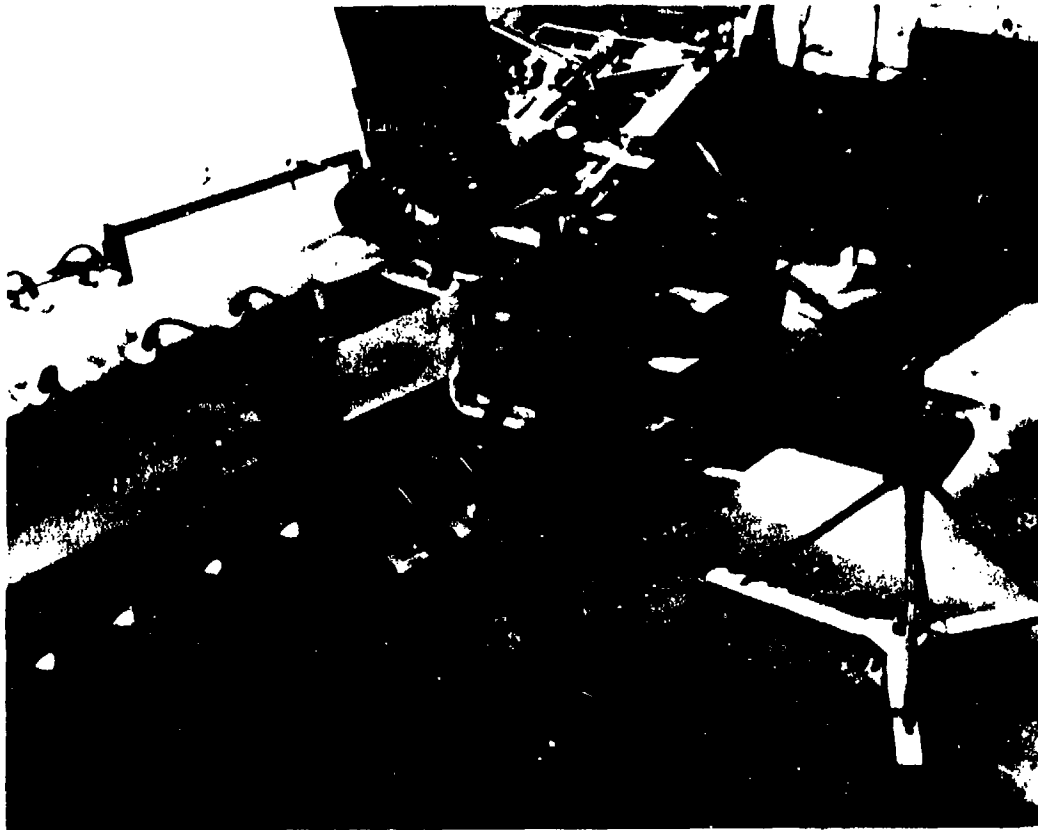
Figure 17.39. Open Launching Tank.

295
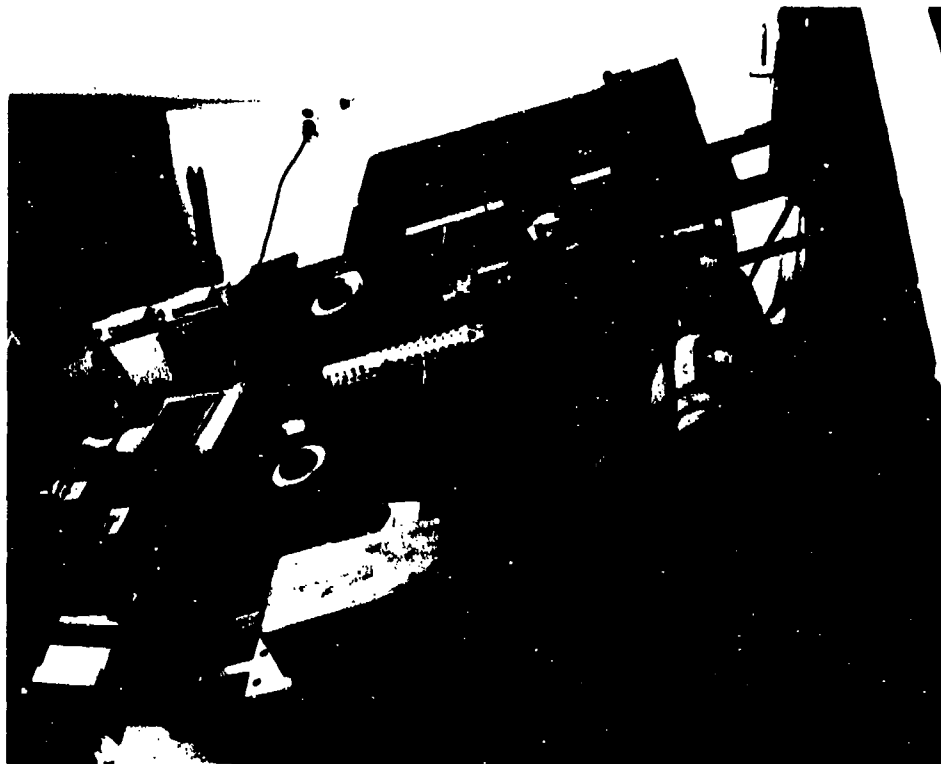
Figure 17.40. Catapult launcher for Open Launching Tar ..

set for a predetermined velocity, and so that timing sequences can be initiated by carriage movement.

A cable lift rotates the launcher carriage about a horizontal axis through the water-impact point, maintaining a constant free air-flight distance and constant entry point for all launching angles from 3.5 to 45 degrees. The launcher is raised or lowered by a hand crank on a double-drum hoist winch and can be clamped at any angle between the 3.5- and 45-degree limits. It is possible to launch missiles with angles of attack up to 10 degrees.

Liquid-Interface Tank

This tank permits the study of water-entry phenomena as a projectile passes into water from another liquid rather than from air (Chapter 13). The presence of the second liquid eliminates splash and other conditions that hamper observation of water-entry phenomena. In this tank, a missile can also be propelled from a standing start under the surface of the liquid, thus eliminating the entry cavity.

The tank measures 46 inches high, 15 inches square, and has 0.75-inch-thick plate-glass

windows at the front and rear (Figure 17.41). The absolute pressure in the tank can be varied from 2 atmospheres to a value corresponding to the vapor pressure of the liquid within the tank.

Mineral oil, slightly colored with a red dye for contrast with the water, is used for the second liquid (Figure 17.41). The interface between the two liquids can be cleaned by skimming and filtering. The tank is equipped with fittings for thermometers and gages, and a vertical notched scale mounted inside the tank provides the necessary fiducial marks.

Projectiles can be dropped from the top of the tank above the oil surface or started from beneath the surface by an impulse launcher designed to impel hardened-steel balls of 1.5- or 2-inch diameter downward from a starting position in the oil layer. The launcher was developed to meet the need for a device that would not entrain air in the liquid or impart turbulence to it and would not affect the pressure in the tank.

The impulse launcher is mounted on top of the tank (Figure 17.41). A steel ball of high magnetic permeability is held lightly on the lower end of the impulse rod by the magnetic field from a solenoid (Figure 17.42). A stud
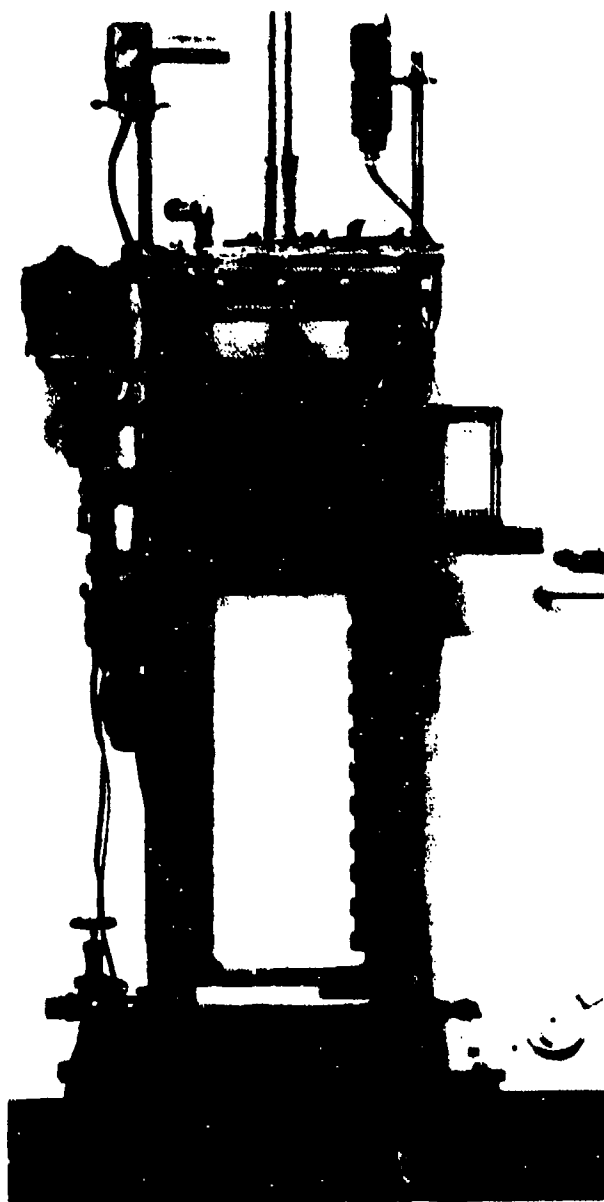
Figure 17.41. Liquid-interface tank.

Figure 17.42. Impulse launcher.

restraining a weight at the top of the tube is withdrawn magnetically and the weight falls, imparting an impulse to the rod that overcomes the slight magnetic restraint from the solenoid-holding coil at the bottom of the plunger and impels the ball downward. A velocity of 17 fps can be obtained at the interface.

A second impulse launcher was designed to launch spinning and nonspinning projectiles at higher velocities. In basic design, the launcher was similar to the first, but provision was made to rotate the impulse rod in an airtight bearing

and to impel the falling weight at higher velocities with compressed air.

Vertical-Drop Tanks

Two tanks with fallaway bottoms permit study of water-entry phenomena in the absence of gravity (Chapter 16). One tank measures 11-3/4 inches by 14 inches internal cross section and is 18-3/4 inches deep. Smooth internal walls and plate-glass windows have no internal obstructions or projections to induce circulation in the water. The bottom of the tank is held in place with two clamps that can be released simultaneously by powerful solenoids on the same energizing circuit. This vertical-drop tank was mounted above the open launching tank (Figure 17.43). The left part of Figure 17.44

297

The other vertical-drop tank, measuring 7 by 7 inches internal cross-section and 20 inches deep, was mounted in the liquid-interface tank (Figure 17.45) for studies of water entry under conditions of varying gas pressures and densities.

Sectional Tank

This tank was constructed for study of two-dimensional water-entry flow which would, in theory, be produced by the oblique entry of an infinitely wide flat plate. Two heavy sheets of plate glass measuring 2 feet high by 3 feet long are held accurately parallel and 2 inches apart by spacers (Figure 17.46). A rectangular flat plate 2 inches wide is impelled obliquely into the water. Continuous contact between the plate and the tank walls prevents flow around the ends of the plate and the effect, so far as flow is concerned, is similar to a sectional view of the flow induced by water entry of a flat plate of infinite width (Chapter 6, Figure 6.2).

The plate is impelled into the water with a rod driven by a pinion gear engaging a rack mounted on the side of the rod. A heavy flywheel is brought up to speed and suddenly coupled to the pinion gear by a quick-acting electric clutch. The rod with the attached plate is propelled forward at a relatively constant velocity by the energy stored in the flywheel. After about 1.5 feet of travel, the end of the rack runs off the pinion and the flywheel idles to a stop. The rod moves a short distance forward under its own momentum.

The impeller may be adjusted to give water-entry angles from about 5 degrees to

shows a plate-cylinder projectile entering while the water is held stationary, and the right part shows the same projectile entering while the water is freely falling. Studies indicated that the acceleration of the falling water was very nearly gravitational, and circulation of the water due to release or wall effect was negligible.

Figure 17.44. Plate-cylinder projectile entering stationary water (left); freely falling water (right).

298

Figure 17.45. Vertical-drop tank in liquid interface tank.

vertical. Water-entry velocities of about 15 fps have been attained.

Hydroballistics Range

A hydroballistics range (HBR) was established in the NUC laboratory to measure hydrodynamic coefficients of fully wetted missiles during free flight. The data-recording techniques developed can be utilized in any facility where fully wetted motion is to be observed, but the technique of multiple-exposure photography is not suitable for recording cavity motion.

For the deduction of usable hydrodynamic coefficients by fitting an equation to the free-flight trajectory data, the missile position must be determined to a high degree of accuracy (References 80 and 81). The simple but precisely aligned and instrumented HBR (Figure 17.47) was established in three bays of the open launching tank in the NUC Hydroballistics Laboratory. Here, horizontal and vertical distances in the trajectory plane and angles of pitch and roll can be measured (4 degrees of freedom). Distances can be measured to within ±0.001 feet, the pitch angle to ±2 minutes, and roll angle to within ±4 degrees.
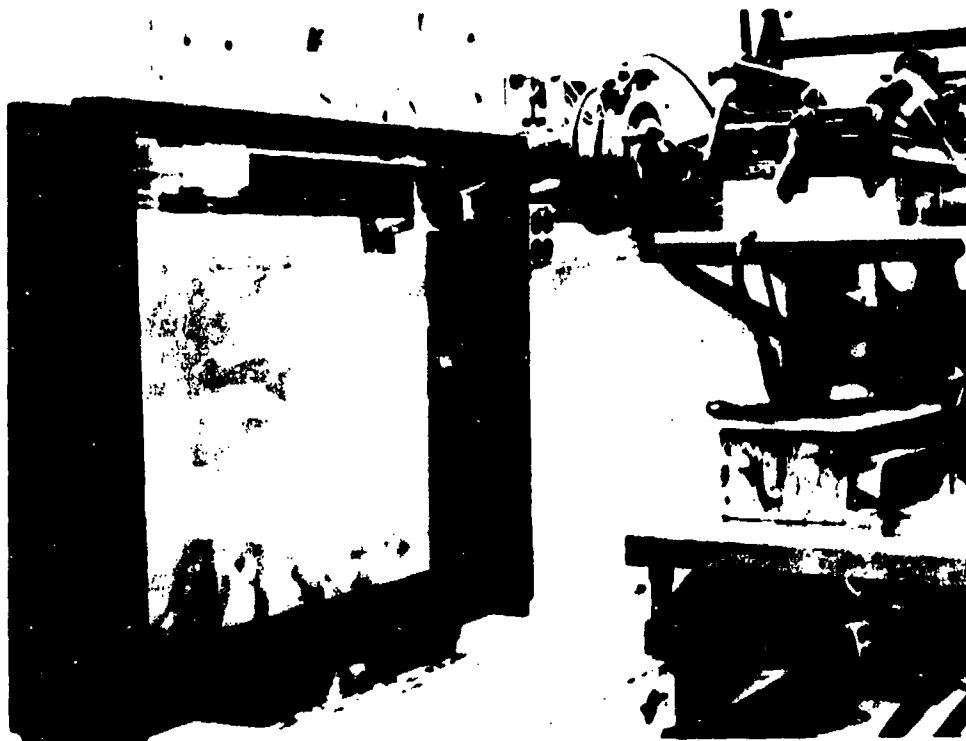
Figure 17.46. Sectional tank with plate-propulsion apparatus.
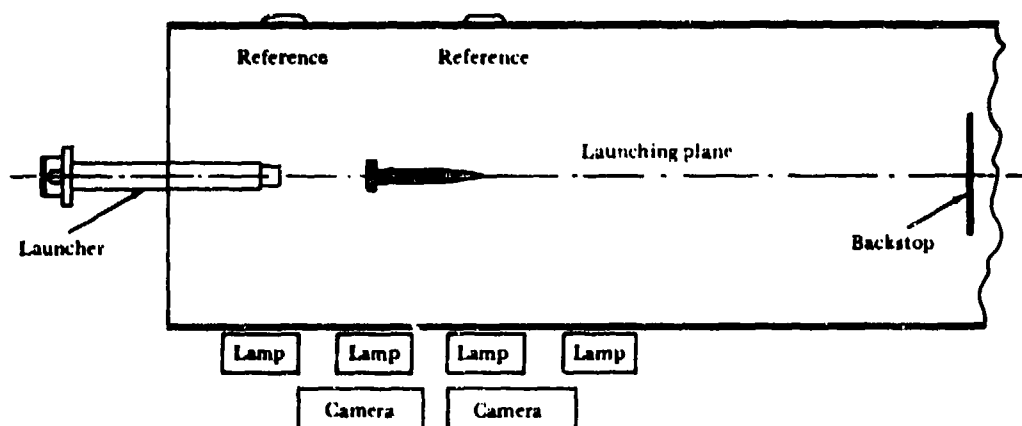
Figure 17.47. Hydroballistics range (plan view).

The portion of the tank in which the HBR was established is 4 by 4 by 18 feet. Three 3/4-inch-thick glass panes with clear spans of 5 by 5-1/2 feet between the structural-steel supporting ribs are mounted in the two sides. Panes can be adjusted with leveling screws to be vertical and coplanar to within less than 2 minutes of angle. The bulge in the glass caused by hydrostatic pressure is such that the maximum deviation of the glass surface from its reference plane is approximately 3 minutes of angle. A dull black cloth hung over the glass wall farthest from the cameras provides a suitable background for multiple-exposure photography.

The two precision cameras were positioned as shown in Figure 17.47; 4-by-5-inch ultraflat glass photographic plates (Chapter 18) were selected because film is too flexible for accurate positioning in the cameras. The cameras located the plates to within 0.001 inch of their focal planes and held the angular orientation of the plates normal to their axes to within 1 minute of angle. The plates themselves were flat to 0.0007 inch/linear inch. The cameras were rigidly mounted on surface plates equipped with threaded position and leveling adjustments. Cross-hair telescope sights attached to the cameras were used for their accurate alignment with respect to precision markers on the tank. Controlled development procedures minimized migration of the exposed silver grains and bleeding of the images during processing of the photographic plate (Reference 49 and Chapter 18).

To estimate distortions caused by the HBR optical system, a precision stadia rod with 1-inch graduations was photographed in several horizontal and vertical positions in the trajectory plane, and the distances between images of the graduations are measured with an optical comparator. In view of the variation in the horizontal image distance, individual magnification factors were determined for each missile image.

Since valid data can be obtained from the HBR only if the missile remains in the launching plane, a backstop was hung normal to the launching plane approximately 8 feet beyond the launcher, with the intersection of the launching plane marked on it. The missile flew into the backstop and remained hanging there until retrieved. Trajectories yawing more than 0.2 degree from the theoretical trajectory plane were disregarded. A mirror mounted above the water surface directly over the trajectory plane was used to verify that the plan view of the trajectory was a straight line, the position of the trajectory plane being established by the image of a white line on the bottom of the tank. The mirror was included in the field of view of the cameras, allowing this information to be recorded simultaneously with the position of the missile. No roll in excess of 5 degrees was detected in any of the missile launchings.

The HBR is illuminated by four Edgerton-type flash lamps that can be flashed at pre-selected frequencies and can be programmed to give several frequencies during a single launching, preventing overlap of images near the end of

300

the trajectory by decreasing the flash rate of the lights as the missile decelerates. The flash frequencies of these lamps are accurate to 0.01% of the set frequency.

The superposition technique of recording photographic data requires that a flat-black missile bearing small, white fiducial marks be photographed against a flat-black background. The data then consist of traces left by successive images of the white fiducial marks. The number of marks should be kept to a minimum and they should be so located that a minimum of interference occurs among their traces. It is also advantageous to make each mark different in shape or orientation so that each trace can be readily identified on the photographic records. Figures 17.48 and 17.49 show two different types of photographic record from the HBR.

Figure 17.48. Photographic record of Basic Finner with fiducial marks as shown in Figure 14.1, Chapter 14.
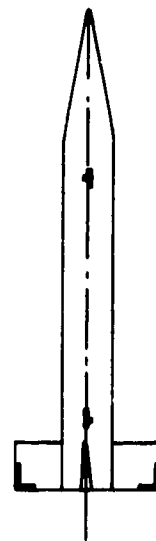
Figure 17.49. Photographic record of Basic Finner with fiducial marks as shown in inset

CHAPTER 18
EXPERIMENTAL TECHNIQUES

ENVIRONMENTAL FACTORS

Sharply defined underwater photography requires clear water. Ordinary tap water contains suspended material that reduces light transmissivity and blurs the image if the light path is long. Furthermore, some light-absorbing substances such as yellow-brown dyes resulting from the accumulation of organic vegetable matter in reservoirs are not removed by ordinary filtration. Distilled water is preferable for underwater photography, but cost prohibits its use in large hydroballistics tanks. A technique employing diatomaceous earth filters has been developed to clarify water for long-distance photography (Reference 45), and is now being used in the NOL Hydroballistics Facility (Reference 75).

Both tap and distilled waters require almost constant filtration and skimming to remove dust; air and gases in contact with the water surface should also be filtered. Underwater equipment and the experimental tank itself should be both noncorrosive and clean. Materials that are to be left in contact beneath the water (steel and brass, for example) should be so selected that electrolysis is not a problem.

Most tap and distilled waters carry an excess of dissolved or entrained air, which does not perceptibly affect the shape of a stable cavity. If, however, the concentration of air exceeds its equilibrium value at the experimental air pressure, the cavity wall roughens. Excess air in the water influences an existing unstable cavity separation and alters the inception of cavitation. In sufficient quantity, air can diffuse into the cavity and change the cavitation number. Deaerated water was used in the NUC experimental studies.

The amount of dissolved air in equilibrium with water at any given temperature decreases

with ambient pressure. The tank water can be deaerated by maintaining reduced atmospheric pressure within the tank while a stream of air is bubbled through the water. The agitation of the bubbling air removes excess air from the water and equilibrium is attained. This technique has been found to ensure repeatability. Air content can be measured with a Van Slyke-Neill manometric gas analysis apparatus (Reference 62).

The maximum possible atmospheric pressure within a facility is determined by the strength of the pressure vessel, the lower pressure limit being set by the vapor pressure of the liquid. The vapor pressure of lubricants or sealing compounds used within the tank can also add to the minimum pressure. The vapor pressure of the liquid can be controlled to some degree by adjusting the liquid temperature; e.g., the vapor pressure of water varies from 9 to 760 torrs over the temperature range of 10 to 100°C, offering a possibility of adjusting water vapor pressure for gas-density scaling in a model system.

Froude number scaling requires that the model velocity scale according to Equation 1.18, the addition of cavitation number scaling requires that the gas pressure scale according to Equation 1.23, and the further addition of gas-density scaling requires that the gas density scale according to Equation 1.24. In the absence of cavitation-number scaling, gas density is scaled simply by using air at the same pressure as in the model system, but the constraint of cavitation-number scaling requires the use of heavy gases for gas-density scaling. In this case, metered quantities of one or several gases were introduced into the tank after the air and water vapor had been reduced to a predetermined amount. These quantities, calculated from Equations 2.12, 2.13, and 2.14, were metered into

303

the tank with a manometer, making use of Equation 2.5. They were then mixed with a fan, and the tank atmosphere mixture brought to the desired launching density and pressure. Immediately before a test model was launched, a gas sample was drawn into a calibrated gas-density balloon and the gas density determined gravimetrically.

If a maximum or minimum density is required, the air must be removed as completely as possible from the tank. The evacuation process is hastened and the degree of air removal possible with ordinary equipment is increased when the tank is "rinsed" several times with the working gas.

The range of gas densities possible within a tank can be extended by chilling the liquid to reduce its vapor pressure. For example, the decrease in vapor pressure from 17.52 to 9.2 torrs occurring when the water temperature is reduced from 20 to 10°C increases the maximum gas-density coefficient obtainable at 1/11 atmosphere with Freon 114B2 (dibromotetrafluoroethane) from 0.69 to 0.79 (Reference 67).

It is sometimes desirable or necessary to operate models at velocities that do not cause turbulent flow in the boundary layer, thereby violating the requirement (Chapter 1) that both model and prototype velocities be above the critical Reynolds number for turbulent flow to obtain and for viscosity effects to be neglected. Turbulence can be induced artificially either by devices attached to the model or by slight modifications of the model shape. Devices used to induce turbulence either increase the surface roughness ahead of the normal transition zone or introduce a discontinuity in the missile shape where boundary-layer transition would normally occur.

There are a number of techniques for calculating boundary-layer parameters and the critical height or critical roughness which causes transition in the boundary layer, as, for example, Equation 8.1. Roughness can be increased by attaching grains of graded sand to the surface of the missile (as shown in Figure 8.3 of Chapter 8) but when the missile is forcibly halted by collision with a backstop, the grains of sand often dislodge and gouge the missile surface. A softer substitute such as poppy seeds, hollow plastic Ecco spheres, or microballoons (obtainable from Emerson and Cuming, Inc.,

Canton, Mass.) might be more suitable. To achieve roughness in this manner, each grain is placed individually in a preset pattern to insure a constant model configuration, and the grain pattern is replaced or at least repaired after each launching, which is a time-consuming procedure. Instead the grain pattern can be installed on the model and copper roughness caps electroplated from the impression (Figure 18.1). Duplicate caps can be installed on the model nose in a matter of minutes. Each cap lasts through several launchings.

Turbulence can also be induced by installing a wire ring around the missile nose at the zone of separation, by cutting a groove in the model nose (as shown in Figure 11.1), or by altering the model contour slightly to introduce a discontinuity in the curvature of the model surface where separation should occur. Valuable test data have resulted from the use of these and other techniques to induce turbulence artificially, but there is always the possibility that the system may be disrupted to the point where erroneous data occur.

Turbulence can obviously be induced by increase of the Reynolds number. If the velocity within the model system is fixed, the Reynolds number can be increased only by changing the liquid properties. Survey of the literature indicates that no liquid exists that can practicably be substituted for water in the model system, but it is possible that in the future, aqueous polymer solutions can be used advantageously.
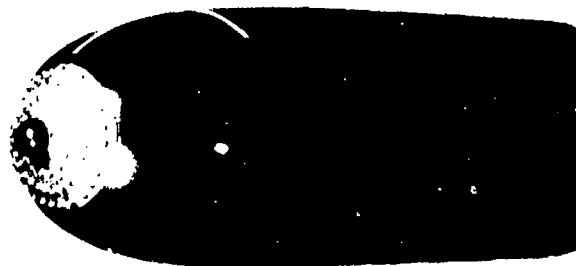
Figure 18.1. Electroplated copper roughness cap on CIT model nose.

Their action is imperfectly understood at the present time.

The density of water is almost constant from 0 to 100°C, but the viscosity varies from 1.792 to 0.284 centipoises. Heating water offers some increase in Reynolds number and under some circumstances may be adequate to shift the flow from the transitional regime to full turbulence. At the higher temperatures, water-vapor pressure becomes increasingly important in determining the cavitation number and gas density.

PREPARATION OF MODELS

Models should be accurately scaled to the prototype, and if several models of the same shape are used in a single test program, they should be as nearly alike as possible; for 2-inch-diameter models a tolerance of ±0.001 inch on external contours is desirable. Models made from the same templates can be within a few ten thousandths of an inch of each other in size.

Model design requirements, besides specifying the external contour and satisfying the structural demands imposed by launcher acceleration and dynamic forces, should also include the scaled dynamic properties of the prototype. The CG and moments of inertia of all model components should be calculated or estimated as the design progresses because only minor adjustments can be made with the trim weights. Designing a small model to be both strong enough and of specified dynamic parameters can be difficult because weight scales down as the cube of the linear dimension and moment of inertia as the fifth power (Equations 1.11 and 1.12).

Model weight can be determined with an ordinary precision balance, but special procedures are needed for determining CG and moment of inertia. Two combination CG balance fixtures were used (Figures 18.2 and 18.3). To determine the moment of inertia, the NUC system (Figure 18.4) compared the angular acceleration of the missile about a transverse axis through the CG upon application of a known torque to the angular acceleration of a calibration rod. In the CIT system, models and calibration rods were clamped at the CG in a torsional balance (Figure 18.5) and oscillation times were measured.

Both NUC and CIT torpedo models were made of hollow Dural or stainless-steel sections
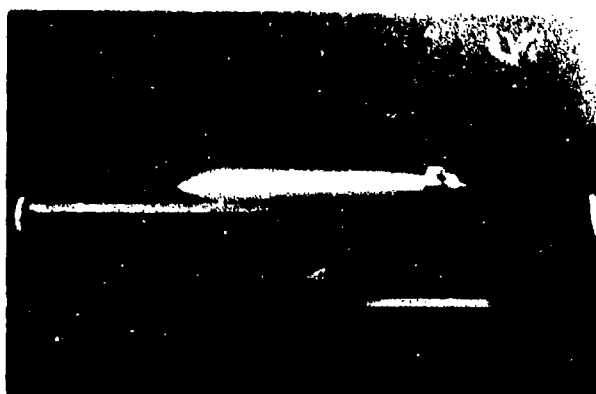
Figure 18.2. NUC model CG balance.
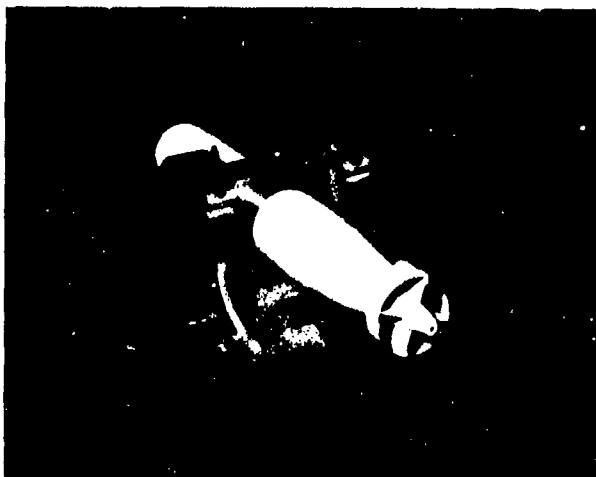
Figure 18.3. CIT model CG balance.

that could be combined in many ways. Threaded internal weights allowed adjustment of total weight, CG location, and moment of inertia. The adjustable internal arrangement of the models could be adapted to the different structural requirements imposed by the launchers in the two laboratories.

The NUC model's slip-fit joints were held together by an internal tie rod threaded along its length (Figure 18.6). The trim weights on the tie rod permit large adjustments in model trim. Model materials included stainless steel, Dural, Lucite, and nylon.

The gripping pressure of the chuck in the CIT launcher required a stronger model (Figure 18.7) made with aluminum-alloy nose and tail sections screwed into a heavy stainless-steel center section. The cycling acceleration force

305
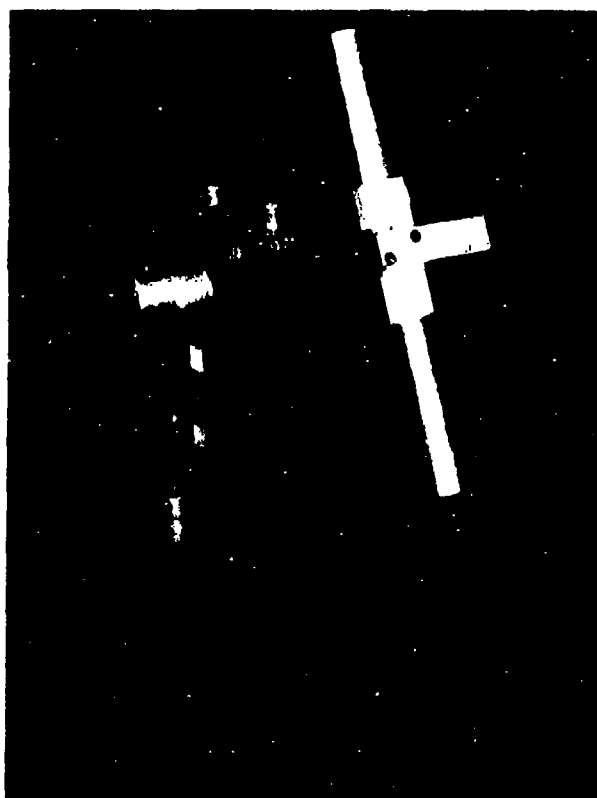
With calibration rod

With model

Figure 18.4. NUC rotational inertia balance.

With calibration rod
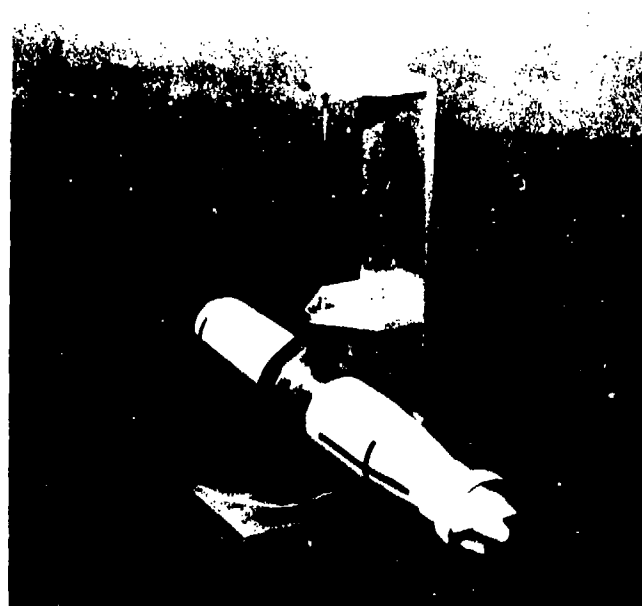
Wit' model

Figure 18.5. CIT torsional inertia balance.

306
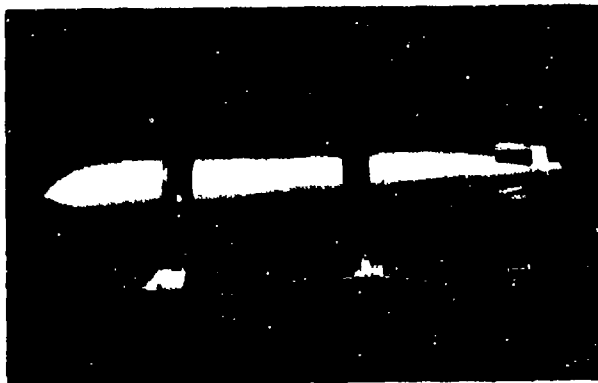
Figure 18.6. NUC model.
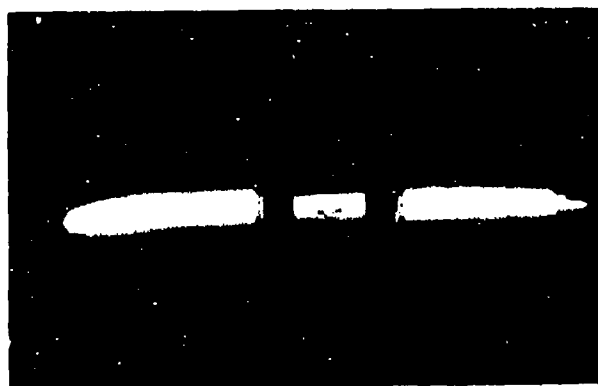
Figure 18.7. CIT model.

produced by rotation of the launching wheel precluded the use of Lucite or nylon nose or tail sections. Trim weights were screwed into tapped

holes in the nose and tail. Trimming was more difficult than it was with the NUC models because less weight remained to adjust the trim after the structural demands had been met, and the tapped holes allowed less choice of weight position than the tie rod did. A high moment of inertia was also difficult to achieve with so much of the weight concentrated near the CG.

Models cannot be permanently sealed against water leakage because the trim weights must be accessible for alteration and because it is sometimes expedient to combine different head and afterbody sections. The slip joints in the NUC models were sealed with dental wax and had to be resealed several times during a series of launchings. The CIT models were sealed with special buttress threads coated with Permatex; one section was heated and the other chilled before the models were assembled. They rarely leaked but were so tight they were difficult to disassemble. The models were weighed before and after each launching to ascertain that no leakage had occurred.

The model's tail-fin assembly poses special leakage problems. If the entire fin structure is made of stainless steel, the joints can be sealed with silver solder (top of Figure 18.8), but these joints tend to crack during usage. If the shell is thick enough, the fins can be inserted into external slots (bottom of Figure 18.8), but this method is not always feasible in the light of structural and weight requirements.

The condition of the model surface is known to affect cavity separation (Chapters 3,

Removable steel tail with silver-soldered joints
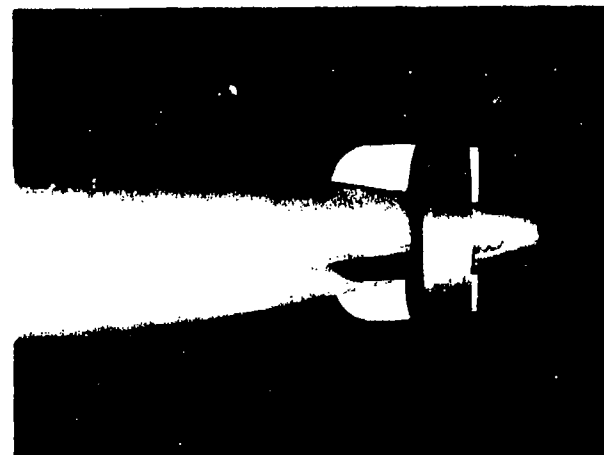
Tail with embedded fins

Figure 18.8. CIT model tails.

4, and 16). It was difficult to explain this surface effect (References 43 and 112) because model surfaces were not sufficiently reproducible. Tests in the NUC laboratory revealed that different cavities could form during apparently duplicate launchings of a polished steel sphere that was (1) normally handled, (2) rinsed in ether, or (3) greased.

Washing the model in a solvent such as ether and then wiping it with a paper tissue does not guarantee a clean surface. Stainless steel models, if chemically inert, can be further cleaned by dipping them into a hot saturated solution of potassium dichromate in concentrated sulfuric acid and then rinsing them in distilled water before they are dried. Hot water directly from the still is preferable. This technique is not practical for use with chemically reactive metals or plastics.

The models should not be handled after being cleaned, and the water surface and the portions of the launcher that come in contact with the model should also be cleaned. For assurance of a completely grease-free water surface, the water must be allowed to overflow.

A reasonably hydrophobic and durable coating was applied to stainless-steel spheres in the NUC laboratory by placing clean spheres (i.e., solvent-washed) in polymethylsiloxane, DC-500, 70 centistokes, for 2 days at 150 to 160°C. The resulting coating caused a yellowish discoloration but its thickness was less than the wavelength of visible light. The spheres were subsequently handled with paper tissues and cleaned with ether before being launched.

Such procedures are appropriate in studying the effects of surface condition, but in normal field work and in laboratory work, they are undesirable because completely hydrophobic or hydrophilic surfaces do not occur. A reproducible, uniform surface that is neither hydrophobic nor hydrophilic is better for routine model testing. Before each launching in the NUC laboratory, the model was dipped in ether and carefully rinsed by pouring ether[1] over it, always wiped with the same brand of paper tissue, and then handled for several minutes with

normally clean hands during the routine prelaunch procedure that includes model trim and loading the model into the launcher. Oil from the skin provided a mild and uniform contaminant on the model surface.

Merely washing the model in a container of solvent is not adequate because particles of grease will be redeposited during withdrawal. Rinsing minimizes this condition but manual handling is still necessary to distribute the remaining isolated grease formations and insure that a light film of grease covers the entire surface.

Some kind of visible marks should be applied to the models for contrast and clarity in photography, especially when light is limited, when photographic images are small, or when metric data are required.[2] A white model with black marks provides the greatest contrast against a black background.

Black anodizing provides an excellent, inexpensive surface finish for aluminum models. Models of other materials can be given a 0.001-inch coat of lacquer or painted with enamel and baked. Because a glossy surface may produce highlights that obscure fiducial marks, the CIT models were lightly blasted with 200-mesh sand before being coated.

Fiducial marks should be flush with the model surface. At CIT, after the models were painted, masking tape was applied to the entire surface except for the fiducial marks and then the models were sandblasted. The indentations made by sandblasting were filled with a contrasting color of paint and rubbed until smooth and flush with the model surface (Figure 18.9). Another method involves applying the fiducial marks over the paint and rubbing until the edges fair into the surface. For accurate interpretation of the photographic data, the width of the fiducial marks should be constant and the edges sharply defined.

Adequate fiducial marks were easy to achieve in the small Variable-Angle Variable-Pressure facility at NUC. In the large tank at CIT (Chapter 17), however, the photographic image was very small and the light was limited.

---

[1] Ethyl and petroleum ether are highly flammable. The use of dichloromethane, a nonflammable solvent, is recommended.

[2] Whip measurements made with the optical whip recorder (Chapter 17) depend upon images of one or more small mirrors mounted on the missile tail instead of fiducial marks painted on the model.

Figure 18.9. CIT model with inset fiducial marks.

Initially, fiducial marks were hung along the center line of the tank between the cameras and the launching plane, but they not only proved time-consuming to maintain in proper position but were a hazard to the models.

New fiducial marks, consisting of Edgerton-type flash lamps bent into right-angle configurations, were housed in watertight boxes and bolted to the tank walls opposite the CIT cameras. Threaded adjusting screws allowed these markers to be placed on the cameras' projected optical axes. Power was supplied from the same units that operate the regular flash lamps and, therefore, the markers flashed in unison with the tank lights. The marker images were so bright that several could be operated by a single pulsing unit. The five underwater trajectory cameras were spaced close enough (with 60% overlap at the launching plane) that three fiducial marks were visible in the fields of all except the two end cameras. As the metric analysis became more refined, fiducial marks were added to the top and bottom of each photographic frame for accurate positioning during projection.

At least one fiducial mark should always be visible to each data-recording camera and, if possible, the vertical should be marked with a plumb bob. In a multiple-camera system, at least one of the fiducial marks seen by each camera should also be seen by one other camera. If projected images are to be measured, several fiducial marks should be located near the extremes of the field of view so that the film can later be aligned as it was during exposure.

The brilliance of the fiducial marks is important when several images are recorded on the same film or plate; the image must be readable against the repeatedly exposed, yet not overexposed, background.

Fiducial marks could not be used during one series of water-exit tests in the Variable-Atmosphere Wave Tank at CIT (Chapter 19 and Reference 93). The motion of highly polished 1-inch-diameter precision-ground steel spheres was measured over distances of a few inches and, at the same time, photographic data on associated hydrodynamic phenomena such as water-surface deformation were obtained. Any rotation of the sphere would have introduced error into the data obtained from a fixed fiducial mark on the sphere surface. Sphere positions measured from photographs by setting the cross hairs of a comparator (Chapter 17) on the curved edge of a sphere image lacked the required degree of precision. A technique described in References 90 and 94, using the virtual image or highlight produced in a sphere by a stroboscopic point-light source, obtained accurate sphere position-time measurements.

By suitable placement of the light and camera with respect to the trajectory of the sphere, the projections of the highlights on the object plane can be made to coincide with the positions of the sphere center except for a slight lateral offset perpendicular to the motion of the sphere. Moreover, the rotation of a precision-ground sphere does not measurably affect the position of the highlight.

Highlight photographs permit precise centering of the cross hairs of a measuring microscope, and thus precise measurement of highlight (i.e., sphere) positions. The intensity of the highlight permits many exposures to be made on a single stationary film. Displacements of the sphere can be measured directly, and data reduction involves fewer measurements than when each exposure is recorded on a separate frame.

Use of the highlight technique in air is illustrated in Figure 18.10. A camera and a stroboscopic point-light source, L, were so positioned that the trajectory of the sphere center, C, lay in the object plane of the camera; points along the trajectory were equidistant from the light source and camera lens node, N. For a ray of light from the point-light source to be reflected from the sphere (assumed to be moving

309
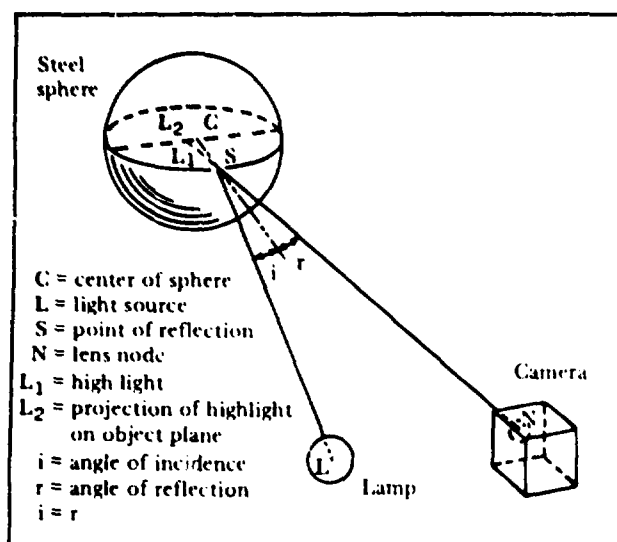
Figure 18.10. Optical setup for highlight method of photography. (From Reference 94.)

C = center of sphere
L = light source
S = point of reflection
N = lens node
L_1 = high light
L_2 = projection of highlight on object plane
i = angle of incidence
r = angle of reflection
i = r

Commercial Ektar f/6.3, 8-1/2-inch focal-length lens and a Polaroid Land camera back were used with Polaroid 3000 Speed/Type 47 film to obtain highlight data.

A Kodak Wratten No. 25(A) red-gelatin film filter cemented between circles of optical glass mounted in front of the camera lens reduced the light wavelength range (and hence light dispersion due to tank-wall prismatic effects), resulting in sharper highlight images.

Both the camera lens node and the lamp were 8 inches from the Lucite tank wall. The trajectory of the 1-inch-diameter sphere was vertical, parallel to and 9 inches from the tank wall. The magnification factor for highlight photographs was about 1.1 and the camera lens stop between f/32 and f/45.

To focus the camera, a sphere was positioned so that its center was in the object plane at some point in the trajectory. A zirconium concentrated arc lamp (Sylvania C2/DC/S) was placed just in front of and in line with the stroboscopic lamp and the sphere. The room was then darkened and the camera, with lens fully open, was focused on the highlight. The range and number of sphere positions to be observed over the exposure sequence was adjusted by setting the frequency and by gating the number of flashes. For data acquisition, the room was darkened and a time-delay generator, adjustable

vertically) into the camera lens, it was necessary that the incident and reflected rays lie in the plane LCN. Then the point of reflection, S, would lie in LCN, as would the virtual image (highlight), L_1, which was midway between the surface and the center of the sphere. The projection of L_1 on the object plane is L_2 and would be at the same height as C, displaced slightly to one side of it.

The highlight accurately represents the sphere center and can be used for vertical distance, velocity, and acceleration measurements. It can also be used to measure the sphere's lateral deviation in the object plane, if the deviation is small; the relation of the projection of the highlight to the center of the sphere does not change significantly. Precision-ground spheres up to a diameter of 1-5/16 inch with a sphericity tolerance of 0.000025 inch are available commercially.

The highlight technique for acquisition of data is also applicable to a sphere immersed in water. Here, in addition to the optical setup shown in Figure 18.10, it is necessary that the sphere trajectory be parallel to the plane surface of the water-tank window and that the point-light source and lens node be equidistant from the window (Figure 18.11). For studies at CIT, a PEK X-81 xenon short-arc lamp of about 1-μs flash duration (PEK Labs, Inc., Sunnyvale, California) was used as the point-light source. A Graphic View II camera fitted with a Kodak

EGG FX-2 strobe lamp with parabolic reflector
Kodak Wratten No.58 filter
Tracing paper for light diffusion
Sphere
Kodak Wratten No.25(A) filter
Lucite tank
PEK X-81 xenon short-arc strobe lamp in metal box
Rotating-disk camera
Graphic view camera

Figure 18.11. Optical setup for rotating disk and highlight methods of photography. (From Reference 94.)

to 1μs, triggered the flash sequence at the proper instant. Calibration of the highlight system consisted of photographing, without change in focus adjustment, a scale in the object plane.

Figure 18.12 shows a typical highlight film with 55 highlight images as indicated by an electronic counter. The images are clear and sharp, except those obtained during the initial motion as the sphere slowly started from rest. As many as 100 exposures have been taken without noticeable loss of contrast with the background. The images are round and the cross hairs of a measuring microscope can be centered on them with a precision of ±5 microns for good highlights and ±2 microns for very good highlights.

A combination of highlight and rotating-disk camera techniques was used to obtain synchronous photographs of the sphere position and perturbation of the water surface as the sphere moved toward it. The rotating-disk camera was so positioned that its lens axis was normal to the water-tank window and lay in the plane of the undisturbed water surface (Figure 18.13). An E G and G (Edgerton, Germeshausen, and Grier) FX-2 stroboscopic lamp of about 1-μs flash duration provided diffused background illumination for silhouette

photographs of the water surface. A Kodak Wratten No. 58 green filter in front of the FX-2 lamp and the Kodak Wratten No. 25(A) red filter in front of the highlight camera lens prevented fogging of the highlight film by light from the FX-2 lamp. The PEK X-81 lamp light did not adversely affect rotating-disk camera photography and no additional light filtering was needed. Both stroboscopic lamps were pulsed simultaneously to obtain synchronous data.

A series of rotating-disk camera photographs using Kodak Royal Pan film is shown in Figure 18.13. The image of the X-81 lamp can be seen as a highlight in the sphere.

PHOTOGRAPHY

In metric photography, the densest image of the greatest contrast obtained with the fastest film may not always be the most easily measured. Under a microscope, a grainy image is too amorphous to position accurately. The edge of the image, which should be sharp and clear, resembles the broken edge of a macadam highway. A dense image tends to bleed into the surrounding background, thus adding to the irresolution. A slower, fine-grained emulsion will produce a thinner image that may appear less

Figure 18.12. Highlight film of sphere moving upward, 1 ms between exposures. (From Reference 94.)
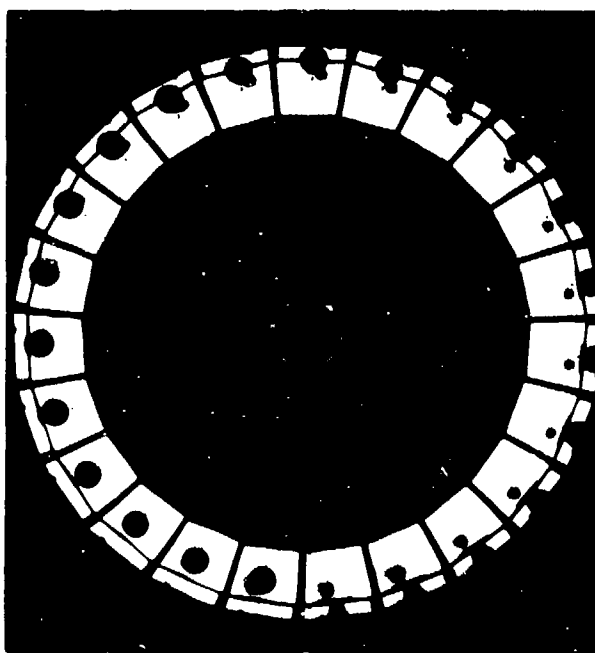
Figure 18.13. Rotating disk camera photograph, 1 ms between exposures. (From Reference 94.)

311

desirable to the naked eye but will be far more readable under the microscope.

Manufacturers' film-speed ratings do not apply to film exposed with Edgerton-type flash lamps; the reciprocity relationship that determines film speed breaks down for extremely short, high-intensity exposures (Reference 49). Individual emulsions should be tested in the actual model system.

Special emulsions sensitive to narrow light-frequency bands have been developed for astronomers' use. They are available coated on "ultra-flat" glass plates (i.e., flat to 0.0007 inch per linear inch) or even on optically flat glass plates for precise photographic measurements (Reference 34).

Precision photography is dependent upon controlled developing. Minimum developing time, a fine-grain developer, and controlled temperature and agitation are necessary, even the position of the plate in the developer can be significant. Faulty developing can cause the exposed silver halide grains to migrate within the gelatinous base, or unexposed grains adjacent to a heavily exposed area can be erroneously developed, introducing error into the photographic measurement.

Color film enhances the value of cavity photographs, seeming almost to add an extra dimension to the experimental data.

Shadowgraphs have been successful for recording entry splash (Reference 112 and Chapter 12). A tank, filled with water to the top so that its surface formed a negative meniscus with the sides, stood between the camera and the spark light source. The spark and the camera were positioned so that the spark lay on the extended optical axis of the camera, which crossed the water in the plane of the water surface. The moving missile was usually used to trigger an adjustable, preset time delay in the spark circuit.

FLOW–MARKING TECHNIQUES

In 1893, a French experimenter, Marey, used silvered wax-rosin spheres whose specific gravity approximated that of water, to mark the flow of a liquid (Reference 42), in 1904 Prandtl used flakes of mica (Reference 66), and in 1900 Worthington and Cole (Reference 113) published a paper describing a bubble-marking technique that rendered flow in water more visible.

Worthington and Cole used a network of minute bubbles generated by electrolysis. So long as the water was still, the bubbles rose uniformly from the bottom of the tank. When the liquid was in motion, the bubbles were carried with it, the bubble velocity being equal to the sum of the water velocity and the velocity induced by buoyancy. Slichter added the elements of time and multiple exposure to the bubble-tracer technique by photographing his experiments with Edgerton flash lamps (Chapter 4), and in 1947, Birkhoff and Caywood took high-speed Edgerton photographs of missiles traveling in a metric-bubble field (Chapter 4).

Care is required in the generation of a metric-bubble field. Ideally, the bubbles, tiny and of uniform size and spacing, lie within the launching plane and have a specific gravity of just less than one (about 0.85) so that they rise slowly to the water surface. The surface tension of the fluid comprising the bubble should be less than that of water, its index of refraction greater, and its compressibility approximately equal. Benzene (sp. gr. 0.69) can be mixed with carbon tetrachloride (sp. gr. 1.60) to a density giving the desired bubble velocity. The major problem lies in generating equally spaced bubbles of equal size.

Birkhoff and Caywood worked with bubble networks of both air and hexane. The air-bubble network arose from a punctured gum rubber tube lying along the intersection of the launching plane with the tank bottom. The tiny holes in the tube were of uniform size, and the rate of bubble emission was controlled by applying tension to the tube. The hexane was introduced into the water through a line of hypodermic needles. The rate of bubble generation was determined by the pressure applied to the needle plungers; uniformity was achieved by driving them with a common fluid pressure source.

Flows have also been marked by soluble dyes introduced into the flow by the model. The dyes can be coated on the model surface, implanted in grooves, or ejected from within the model through holes in the skin (Chapters 11, 13, and 14). Dyes are particularly helpful in studying boundary-layer flow but their use is somewhat limited because the very presence of the dye influences the flow to some unknown degree; the error is minimized when the specific gravity of the marking fluid equals that of water.

Flows on clean surfaces can be marked with powdered aluminum, as in the classic photographs of Prandtl and Tietjens (Reference 66), with talc, lycopodium powder, etc. Prandtl and Tietjens tested the surface condition by blowing directly down on a little powder that had been sprinkled on the water surface. The powder spread out in all directions, leaving a cleared circular area in the center. If the powder remained spread after being blown, the surface was sufficiently clean; if the cleared circle closed, the surface was contaminated.

A thin coating of paraffin on stationary models that are partially submerged will prevent capillary action from influencing the flow near the fluid boundary.

CHAPTER 19
HYDROBALLISTICS FACILITIES DESIGN

Many hydroballistics model facilities were designed during World War II to model the water-entry behavior of air-launched torpedoes that entered the water at relatively low velocities and of mines that were dumped from moving ships or propelled from deck launchers. These early facilities were open to ambient air, but theory and experiment indicated the need to scale (control) the gas pressure and possibly the gas density over the water surface in order to model missile water-entry behavior.

Postwar studies with pressure-vessel modeling facilities confirmed the need to scale gas pressure and density and also demonstrated that models larger than 2 inches in diameter (as used at NUC and CIT) would be required in order to minimize the effect of unscaled forces (viscosity, surface tension, etc.), and to provide adequate internal space for instrumentation and mechanisms for missile control, propulsion, etc.

Interest in water-to-air missiles and the effect of waves on both missile water-entry and water-exit behavior required facilities with underwater launching and wave-making capabilities. To meet the need for larger and more versatile modeling facilities, the Variable-Atmosphere Tank (VAT) at NUC, the Lockheed Underwater Missile Facility (LUMF), and the NOL Hydroballistics Facility were constructed.

Reference 45 provides an extensive description of research into the problems involved in the design of a large modeling facility. A basic design requirement is that the facility be able to be evacuated to the vapor pressure of water so that the cavitation-number and gas-density scaling requirements can be met. It should also be able to withstand the positive pressure incurred in the simulation of deep submergence. If the modeling facility is expected to investigate

the effect of waves, the wave channel must be rectangular in section. The testing area should be at least twice (preferably three times) the water depth away from the wave generator in order that free or gravity waves can be achieved. The wave channel should also include an artificial beach to absorb wave energy and thereby prevent wave reflection from the channel end. The design of wave tanks, wave generators, and wave absorber- is thoroughly discussed in References 71 and 109.

The stringent requirement that the launcher introduces no perturbations in the model system becomes increasingly difficult to meet as the energy imparted to the model becomes greater. The mass of the model increases as the scale factor λ^3, and in a Froude-scaled system the velocity of the model increases as $\lambda^{1/2}$. Thus the needed energy increases as λ^4, and absorption of the energy remaining in the launcher without disturbing the modeling system becomes more difficult as the model size increases; the launcher itself may become prohibitively large.

For some applications, a self-powered missile may be more feasible than a momentum-propelled missile. The small, high-speed turbine engines and miniature storage batteries now available make such an approach more attractive. For studies at supersonic velocities, smaller models are satisfactory because the inertial forces are great enough to obscure the gravitational force, and the modeling thus becomes independent of Froude scaling.

Instrumentation of the model is becoming more important. Telemetry has been used with a model 1.25 inches in diameter and 7.4 inches long (Reference 57) to transmit data on water-entry accelerations. It appears feasible, if larger

314

models are used, to include apparatus that will transmit data on missile accelerations and attitude and on both cavity and missile pressures. Such data are difficult to obtain photographically; in fact, photographic determination of the missile attitude in completely enveloping cavitation and missile pressures cannot at present be accomplished, and estimation of cavity pressure is questionable. Data verification through comparison of missile velocities determined photographically (by differentiating missile displacement with respect to time) and telemetry (by integrating missile accelerations with respect to time) should be possible. The telemeter, although increasingly useful, cannot entirely replace the camera to record the time history of cavity formation and behavior.

The factors important to success in underwater photography are adequate light, low light attenuation, an efficient optical system, and fast film response. Edgerton-type flash lamps (Chapters 17 and 18) can put out 1 joule/flash at repetition rates ranging from 1 to more than 5000 per second. They can be combined in banks to illuminate wide areas, but their physical size limits the amount of light that can be made available at any given point. The laser now offers unlimited possibilities for superior illumination (Reference 19).

The attenuation of light is determined by the length of the light path through the water and by the water clarity. As a beam of light passes through water, its forward intensity decreases according to Lambert's law (Reference 17)

$$I = I_0 e^{-kx} \qquad (19.1)$$

where I is the light intensity at any position x measured along the direction of the beam, k is the absorption coefficient, and I_0 is the intensity at x = 0. A measure of the transparency of the medium may be defined by assuming a unit distance (i.e., setting x = 1). Let I_1 be the intensity at this distance. Then

$$I_1/I_0 = e^{-k} \qquad (19.2)$$

The ratio I_1/I_0 is the transmissivity of the water and may be expressed in terms of a foot, a yard, or a meter. Water clarity in larger modeling

facilities becomes a critical factor in photography; for a distance of 10 meters from light source to missile to camera, the light intensity at the camera in terms of that of the light source for various transmissivities is as follows:

Percent light transmissivity per meter	Light intensity at camera
95	0.60
90	0.35
85	0.20
80	0.11

It is evident that the light intensity at the camera decreases rapidly with a slight decrease in transmissivity. For light in the visible region of the spectrum, a transmissivity of 95%/meter corresponds to that of distilled water and 90%/meter corresponds to that of very clear water. A transmissivity of 93%/meter can be achieved by filtration through diatomaceous earth filters (Chapters 17 and 18 and Reference 45). An extensive transmission bibliography is given in Reference 18.

Water contamination results from corrosion of the tank and submerged equipment and from biological growths. The specific details of the corrosion problem depend upon whether distilled, tap, or seawater is used, the type of filter system, and the composition of the tank and other surfaces in contact with the water. Sea water, because of its abundance of dissolved salts, is considerably more corrosive than distilled or tap water. Materials are ordinarily selected to prevent electrolytic action (i.e., corrosion), but electrolysis can sometimes be used to advantage: magnesium plates are installed in the NUC tanks (tap water filtered through diatomaceous earth) to protect materials of lower electromotive force (e.g., iron, steel) from electrolytic action. Experience at the CIT tank with distilled water filtered through aluminum hydroxide precipitated on graded sand showed the following materials to be of satisfactory corrosion resistance: 18-8 stainless steel (Types 302 and 304), brass (some nautical brasses and Tobin bronze are suitable), Monel, nylon, Tygon, Tygon paint, polyvinyl chloride plastics, Lucite, and fiber glass. The following materials were not satisfactory for use in the tank: 18-8 stainless steel (Type 303 or 416);

galvanized steel; aluminum with or without standard anodizing; various wax and tar coatings; cadmium; copper; copper nickel; and copper nickel chromium plates. Corrosion also affects water turbidity and hence light transmissivity; the corrosion effect of various materials is discussed in Reference 45.

As a launching tank construction material, stainless steel has many advantages over ordinary steel, which requires down time and expense to maintain linings, paints, and coatings. An epoxy coating provides noncorrosive, biologically inert, pinhole-free tank lining that will adhere to a steel vessel through repeated pressure and temperature cycles, and is less expensive than stainless steel. All external plumbing should be as corrosion-free as the tank itself.

Before installation, a proposed tank lining should be tested by subjecting it to the prevailing conditions: distilled, tap, or seawater, plus all possible additives such as chlorine, rust inhibitors, etc. The water should have been circulated through the filter because some filters introduce additional ions. The condition of the water should be tested photographically in the actual test setup using the camera, film emulsion, light source, and exposure time involved. If the lining material meets the photographic requirements, it should be subjected to pressure and temperature cycling representative of the various scaling conditions to be used.

Model-tank water must be continuously filtered. Generous filter capacity should be provided; it is difficult to maintain a filter performance at the efficiency level assumed by manufacturers. The filter system should be designed to prevent accidental dumping of the filter bed or cake into the tank when power failures or some other untoward conditions occur. An efficient skimmer should also be included.

The water-circulation system should prevent, as far as is reasonably possible, stagnant regions from forming in the tank and should provide a constant flow of water across viewing windows, camera ports, and other submerged points struck by external light, where biological growths are likely to occur. Chlorination of the water or the addition of copper sulfate as algicides have been found to decrease the light transmissivity markedly; therefore, avoidance of

unnecessary lighting of the tank to deter algal growth is recommended (Reference 45).

All exposed windows and ports should be closed when the tank is not in use, and the use of ultraviolet lamps to control biological growths above the water should be considered. Good circulation was attained in the CIT tank by locating the tank outlet in a standpipe running the entire depth of the tank. Ports were spaced about a foot apart and sized to be inversely proportional to the ambient static head.

Filters on all air inlets should be used to screen out airborne contaminants. Filters are particularly necessary in the inlet line that is used to return the tank to normal atmospheric pressure after evacuation.

The moisture that condenses on instruments mounted within enclosed launching tanks when tank pressure is reduced can be avoided by heating the instruments slightly above ambient temperature.

In designing an optical system for a launching tank, the number of cameras should be carefully weighed against the resultant image size. Too few cameras can be false economy; the data's worth is measured by the resolution of the photographic image. The size of the photographic image should be as large as practicable. Provision should be made for both metric and view photography with both direct and silhouette lighting.

The following are possible metric photography techniques:

1. A metric camera installation similar to that developed for the CIT tank (Chapter 17) to record high-speed stereoscopic motion pictures of any action in the launching tank. It can measure six degrees of freedom and can also record the details of the hydrodynamic flow pattern as delineated by wake, cavity, and splash. (The use of 70-mm film should be considered.)

2. An installation of precision-plate cameras similar to that developed for the hydroballistics range at NUC (Chapter 17) to record position data only. It can easily measure four degrees of

316

freedom and, if a device such as an aerial-mapping machine[1] is used to measure the photographic plates, six degrees of freedom should be measurable.

Both systems give time-position data of sufficient accuracy that excellent first differences are possible but second differences give only a reasonable estimate of acceleration.

Several large plate-glass windows would be useful to allow pictorial records to be made of events within the tank (e.g., cavity fluctuations, flow separation). The rotating-disk camera used in the NUC Hydroballistics Laboratory (Chapter 17) is especially valuable in cavity studies. Plate cameras of several sizes, and high-speed, portable motion-picture cameras should also be provided (Chapter 17 and Reference 76).

Selection of photographic film is influenced by the wave length and intensity of the light source, and by the duration of the light flash. The reciprocity relationship between exposure and image density provided by film manufacturers and determined for general photographic work is not necessarily valid for the short, high-intensity Edgerton flash. With limited illumination, position data of greater accuracy can be measured from the thin fine-grained image of slower emulsions than from the darker, larger-grained image formed by faster films (Chapter 18).

The Polaroid process can be used to provide immediate verification of system operation and to measure quantities important in establishing the conditions for the subsequent launching.

In designing a new facility, existing ones should be studied for valuable features that should be retained. The aim should be simple, adaptable equipment with mechanized data systems. Whenever possible, the tank should be bolted instead of welded together to facilitate future modification.

A large facility could profitably be built first in pilot size. Many design, instrumentation, and operation problems could be met and solved, the operating personnel could be trained while the large facility is under construction, and the small facility would remain a valuable tool in its own right. It would allow close observation of detailed phenomena and would

also permit relatively inexpensive, rapid surveys of many areas of a test program, materially reducing the number of expensive tests in the larger tank. Much useful information was obtained in preliminary research studies conducted in pilot tanks (Reference 45) which were built prior to the construction of the NOL Hydroballistics Facility (Reference 75).

Precision instruments and new materials developed in other fields should be used when applicable. All new techniques and devices should be examined to make certain that loss of data accuracy is not the price of greater speed or ease of operation.

RECENT DEVELOPMENTS IN TANK DESIGN

The NUC Variable-Atmosphere Tank

The Variable-Atmosphere Tank (VAT) at NUC, a steel pressure vessel designed for water-exit studies (Figure 19.1), is a cylinder 12 feet in diameter and 39 feet high. The bottom of the cylinder rests at ground level and a steel skirt extends 10 feet below to support the tank and to form a subterranean housing for a hydraulic lift and other machinery. At present, the VAT is instrumented to observe the water exit of relatively large (11-inch diameter) models (Reference 77).

The pressure within the tank can be varied from approximately 0 to 1 atmosphere absolute. The vacuum pump can reduce the tank pressure to the vapor pressure of water in about 15 minutes.

The water system, designed to maintain clarity at all times, includes a noncorrosive lining in the tank, continuous filtration of all water, and surface skimming. Algae growths are controlled by window-washing devices and ultraviolet lamps at the water surface.

A vertical row of five observation windows measuring 28 inches wide and 76 inches high gives complete coverage of the tank interior. There are 45 observation and illumination ports in vertical rows, 15 ports in each row. One row of ports is directly behind the observation windows; the other two rows are 45 degrees to each side (90 degrees to each other), to accommodate an orthogonal stereoscopic camera system for gathering metric data. The observation

---

Figure 19.1. Variable-Atmosphere Tank (VAT) at NUC.

and outside the tank for handling such large loads as missiles and launchers (Figure 19.3). When the tank is in operation, the monorail is withdrawn and the door is closed. A flat circular platform moved by a telescoping hydraulic lift transports the launcher, launching equipment, and missile between the access door and the tank bottom, where it remains to support the launcher during operation. The maximum depth of water above the surface of the lowered platform is 24-1/2 feet.

A cushion in the top of the tank stops missiles and a funnel-shaped net hanging from the padding and extending into the water has a catcher net at the bottom that is programmed to close after an upward-traveling model has passed. The net is fastened to the top of the tank when it is not needed.

Underwater launchers designed to launch missiles 11 inches in diameter have been used in the VAT. An entire launcher assembly can be mounted on rails and driven across the platform tank by a hydraulic system to simulate cross-flow. Lateral velocities up to 1 fps have been used. In addition, the launcher can be tilted to simulate the rolled condition of a submarine.

The internal instrumentation for models used in the VAT varies with the objective of each test. Various equipment for model instrumentation, such as pressure transducers, accelerometers, and oscillographs, are available. However, photographic coverage of a test in the VAT is the primary source of data. The VAT was expanded to include a vertical water tunnel (Reference 77), at the same time retaining its hydroballistics capabilities.

The Lockheed Underwater Missile Facility

The Lockheed Underwater Missile Facility (LUMF) at Sunnyvale, Calif., was constructed to study the water exit of 11-inch-diameter missiles in the presence of waves operating in Froude – cavitation-number scaled systems. The LUMF (Figure 19.4) was subsequently enlarged to give it towing capabilities.

The tank itself is made of reinforced concrete and is a wave channel 15 feet wide, 17 feet deep, and 180 feet long, with an operating water depth of 15 feet. It has a 17-foot-high piston-type wave generator capable of generating waves 0 to 4 feet crest to trough, with periods from 1.07 to 5.37 seconds and a beach-type wave absorber. Two basins 25 and 37 feet deep

windows and parts are shown in Figure 19.2. The entire interior of the tank can be covered photographically with cameras at the observation windows and at corresponding alternate port holes on each side of the main windows. Ports used for camera coverage can be equipped with spherical windows to remove distortion caused by light refraction. Either photoflood or Edgerton-type stroboscopic flash lamps provide illumination. Silhouette photography is achieved by lighting the field from the rear ports.

A side access door about 25 feet above the tank floor is equipped with a monorail and hoist of 1/2-ton capacity that can be extended inside

318

Figure 19.2. Interior of VAT, with launcher at bottom.

provide underwater launching capabilities for missile water-exit studies. An underwater launcher is available for testing the 11-inch-diameter missiles and a missile catcher is installed above the water surface.

The tank's tow system provides controlled speeds of 5 to 50 fps in both directions and continuous accelerations from 1 to 8 fps. A pressure shell 27.5 ft in diameter is mounted over the tank, and the air pressure above the water surface can be varied from ambient to 0.73 psia. Instruments installed inside the pressure shell include recording oscillographs, flight recorders, high-speed cameras, and transducers. A Van-Slyke gas analyzer (Reference 62) is used to determine the air content of the water. The design and operation of this versatile facility are described in Reference 87.

The NOL Hydroballistics Facility

A tank measuring 100 by 35 feet and 75 feet deep was constructed in the Hydroballistics Laboratory at the Naval Ordnance Laboratory, White Oak, Md. (References 69 and 75) to allow study of relatively large models entering, leaving, and passing through the water at high speeds (Figure 19.5). Gun launchers both above and below the water surface propel the models into the tank.

The tank occupies the central portion of a nine-story building resting on a concrete mat foundation, 36 inches thick, laid on solid rock. Four stories of the building are below grade. The bottom of the tank is a prestressed concrete slab 24 inches thick; the top, a concrete slab 42 inches thick; and the walls, supported outside by vertical and horizontal reinforced concrete ribs, are 14 inches thick.

The structural ribs serve also as the partitions and floors of the observation cubicles (Figure 19.5), 23 of which are equipped for remote operation of recording cameras and instrumentation in the test tank. There are 124 observation ports (16 inches in diameter and 1-1/4 inches thick) in the walls, top, and bottom of the tank for coverage of missile launchings and underwater trajectories.

Fifteen 36-inch-diameter gunports in the top, bottom, and north end of the tank accommodate the launchers. Monorail hoists handle the launcher equipment outside the tank, and an overhead-travel crane of 6-ton capacity,

319

Figure 19.3. VAT access doorway.

remotely controlled from the cubicles, handles the equipment inside the tank.

Special water-treatment equipment supplies the 1,750,000 gallons of clear water for high-speed photography. To eliminate all possible sources of contamination, the entire tank is lined with 1/8-inch-thick stainless-steel plate, and all accessories in the tank, including the overhead travel crane, are of stainless steel and other noncorrosive materials. Water drained out to change the level or to empty the tank is discharged through a 36-inch-diameter stainless-steel pipe into a storage container having an interior specially coated to prevent contamination.

The tank is virtually airtight to allow control of atmospheric conditions, being evacuated by steam-ejector equipment on the roof of the building. The structure was designed to withstand a differential pressure of 14.7 lb/in.^{2} with a water depth of not less than 35 feet.

The CIT Variable-Atmosphere Wave Tank

Small, pilot-type facilities are needed for exploration of the hydroballistic phenomena
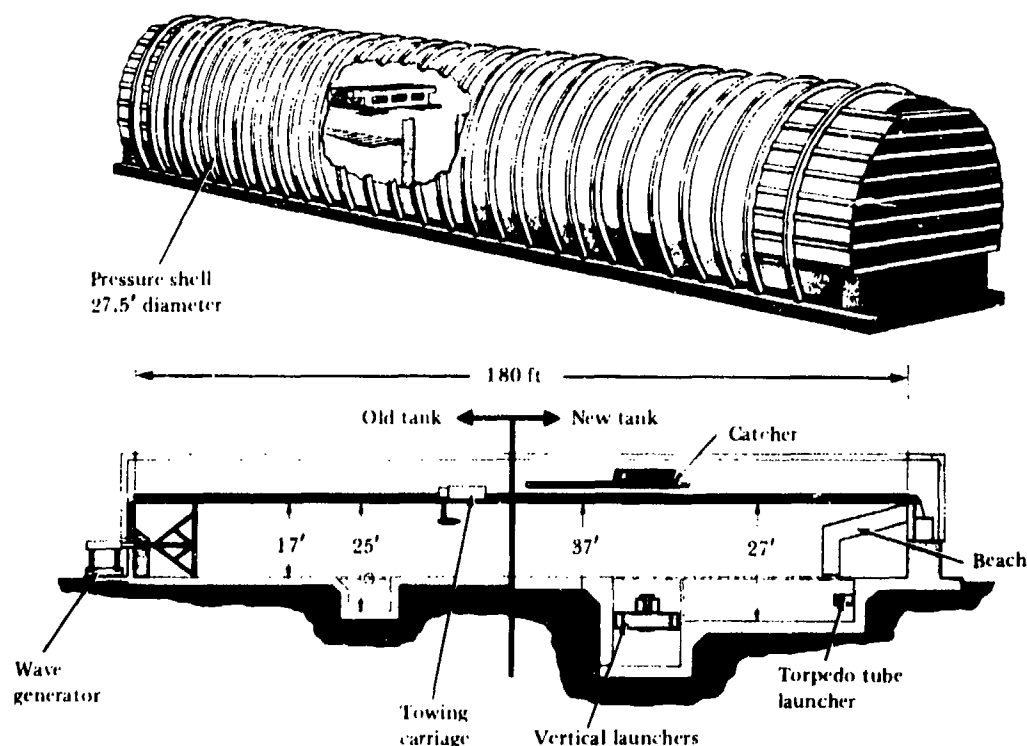
Figure 19.4. Lockheed Underwater Missile Facility (LUMF).
(From Reference 87.)

320
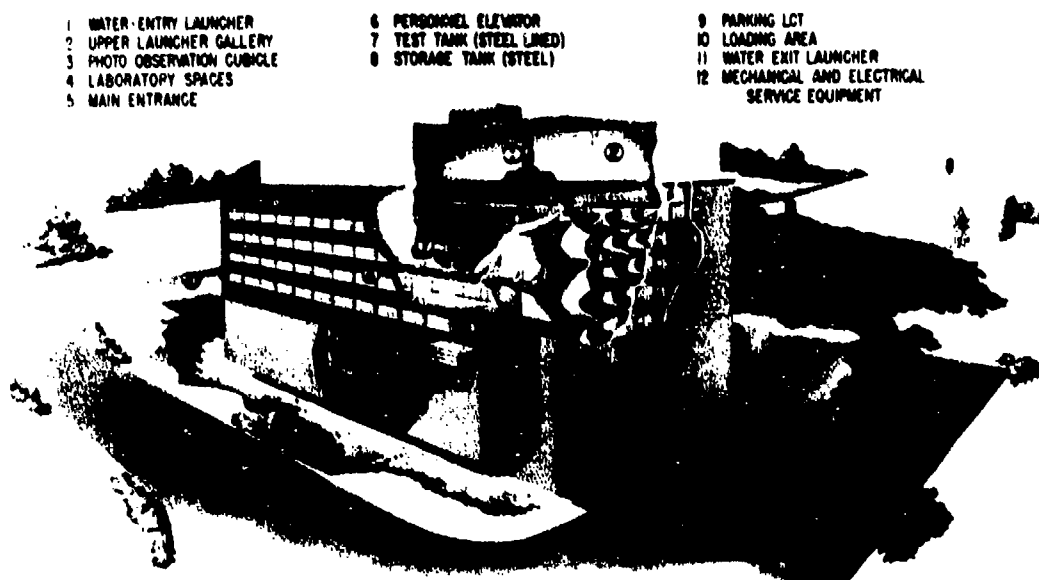
Figure 19.5. Hydroballistics Facility at NOL.

predicted by hydroballistic theory and for detailed observations that might be useful in extending the theory itself. Such a facility is the Variable-Atmosphere Wave Tank at CIT (Reference 93), designed for the study of the water-entry, water-exit, and underwater-trajectory behavior of small momentum-propelled missiles for varied trajectory angles, missile accelerations and velocities, wave fields, and conditions of cavitation.

The wave tank is shown in Figures 19.6 and 19.7. It is a reduced-pressure vessel constructed almost entirely of 2-inch-thick Lucite sheeting, its three flanged sections bolted together with nylon bolts and sealed with O-rings: a wave-generation section, a test section, and a wave-absorption section. The tank rests on four supports equipped with screws for height adjustment and leveling. The two inner supports are heavy laminated wood piers with fiber-impregnated plastic bases and adjusting screws. The two outer supports are made of steel, and the tank end-plate associated with the wave-generation equipment is made of stainless steel. The floor of the tank is about 3 feet from ground level.

There are access ports with O-ring fitted covers in the wave-generation and absorption sections. Tank air pressure can be lowered to the vapor pressure of water, providing a wide range of cavitation numbers within the tank. Water of the high clarity necessary for metric strobo-scopic photography is maintained with a Millipore filter.

The 5.6-foot-long test section (Figures 19.6 and 19.7) has a turret 2 feet high, with a removable cover for missile loading and recovery. In the floor of the test section there are three 1-foot-diameter holes for mounting missile launchers. One hole is directly beneath the turret for vertical or near-vertical launchings; the other two are on either side for oblique launchings into the turret. The missile may be launched either into the advancing wave or away from it. A nylon fabric backstop is used to terminate missile flight. When not in use, the holes are covered from underneath by plates so constructed that the holes are filled and the channel bed is smooth and uniform.

A major feature of the wave tank is its magnetic propulsion system that operates on the principle of an accelerating coil. A magnetically permeable sphere is placed on the axis of a wire coil whose radius is large compared both to the sphere and to the coil-winding cross section. A current pulse passing through the coil when the sphere is on axis but not centered in the coil causes the sphere to be drawn toward the coil center with a force proportional to the spatial gradient of the energy in the magnetic field. The

321
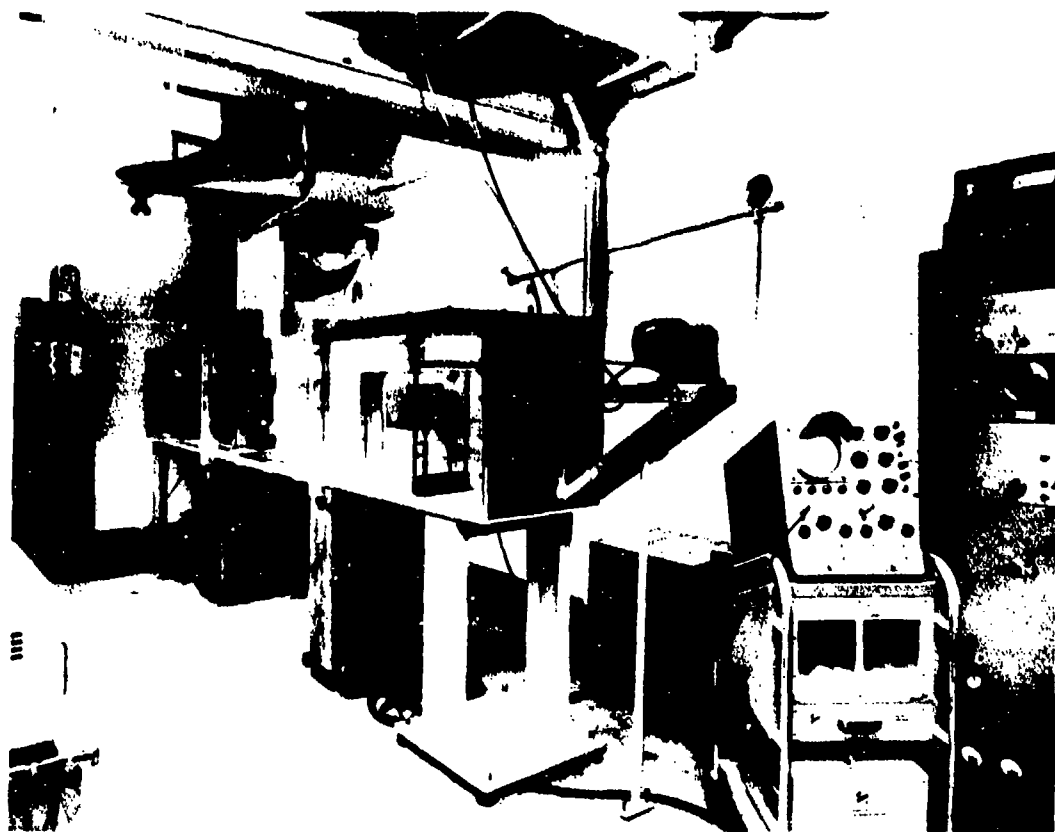
Figure 19.6. Variable-atmosphere wave tank at CIT. (From Reference 93.)
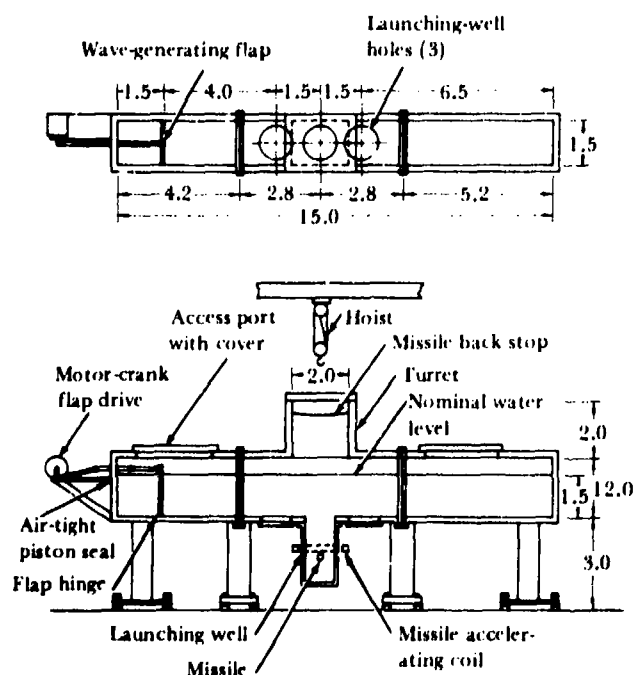
Figure 19.7. Detail of variable-atmosphere wave tank.
(From Reference 93.)

field energy is proportional to the square of the current. If the current terminates just before the sphere reaches the coil center, the sphere continues in its path along the coil axis without being decelerated by magnetic forces. Propulsion is thus achieved without introducing extraneous hydrodynamic disturbances. An example of an accelerating coil launching is shown in Figure 19.8.

The wave tank and the coil holder are constructed of nonmagnetic and nonconducting materials to obviate reaction force on the coil. Thus, the force on the coil is equal and opposite to the propelling force applied to the missile. If the coil is instrumented externally, it may be possible to measure the force directly without missile attachments or telemetering. The data so obtained can be combined with data from displacement-time photographs to provide information on virtual mass and drag under conditions of suddenly accelerated motion (Reference 92).

The propulsion force on the magnetic sphere, being a true body force rather than a

322
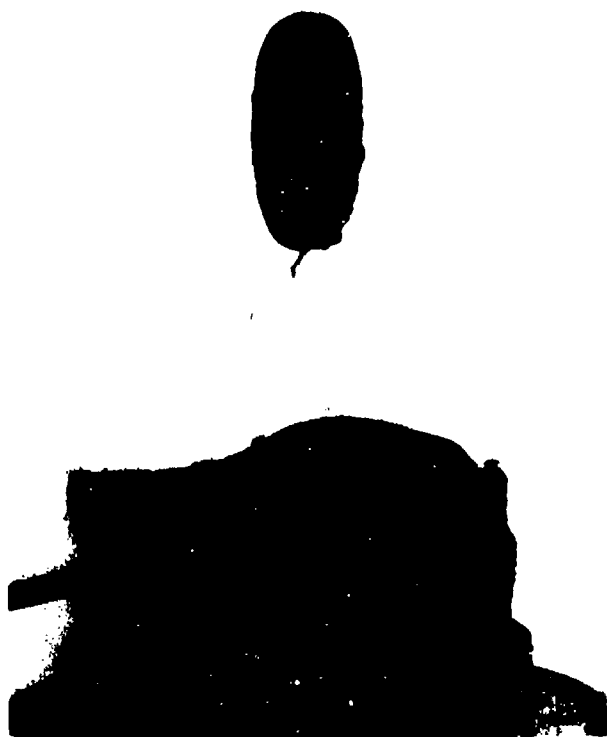
Figure 19.8. Steel sphere launched vertically upward by submerged accelerating coil. (From Reference 93.)

contact force, prevents the generation of elastic waves within the sphere itself that might interfere with an analysis of the hydroelastic effects under study.

Using this magnetic propulsion system, a 1-inch-diameter stainless-steel sphere attained an underwater velocity of about 50 fps in 2 inches of travel from rest for an expenditure of 20,000 watt-seconds of electrical energy when an 8-inch ID coil was used. With a 1-1/2-inch ID coil, about 90 fps was attained for about 1,500 watt-seconds of energy. The reduction in efficiency with increase in coil size was expected. The period of missile acceleration can be varied by adjustments in the electrical circuit and, if desired, the missile may even be made to describe oscillations.

The tank wave channel (Figure 19.6) is 15 feet long, 1-1/2 feet wide, and 2 feet high, with a maximum undisturbed water level for wave studies of about 1-1/2 feet. A rigid flap, hinged at the bottom of the channel and actuated by an adjustable crank and controlled-

speed gear-motor system, is used to generate progressive waves from 1 to 3 feet in length and up to 3 inches in amplitude. The flap is 1-1/2 feet from the end of the channel so that fluctuation in water level behind it is moderate and less than flap height for all flap amplitudes. The distance from the wave generator to the center of the test section is 5-1/2 feet, almost four times the maximum wave depth. Theory indicates (Reference 109) that the extraneous disturbances of the water at the wave generator become negligible in two or three wave depths of travel; hence essentially free gravity waves should exist in the test section.

This method of generating waves was chosen because the longest wave contemplated for study is about 3 feet in length, relatively short in comparison with the water depth, and theory shows (Reference 71) this type of generator to be suitable for producing such waves. Moreover, the inertia of the generator is not large, the generator is easily regulated, and the flap motion required to produce a desired wave is calculable.

No wave absorber is presently used because the wave channel, extending 8 feet beyond the center of the test section, is long enough for four of the longest waves (3 feet) to pass the center of the test section before the reflected waves return. It is believed that the wave train will stabilize and that tests can be completed during this interval. Tests of longer-duration waves may require a wave absorber.

ARL Controlled Atmosphere Tank

A rectangular, glass-front, steel tank (Figure 19.9) was constructed at the Alden Research Laboratories,[2] Worcester Polytechnic Institute, Worcester, Mass., for water-entry, water-exit, and underwater trajectory studies of small models (Reference 3). The rubber-lined interior of the tank measures 9 feet in length by 4 feet high by 4-1/2 feet wide. There are three hatches, two on top and one on the end, where a launcher may be mounted for studies of water entry, water exit at low velocities, and underwater trajectories.

For observation or photography, a 1-1/4-inch-thick tempered glass plate 9 feet by 4 feet is mounted as one side of the tank. A 70-mm strip camera with Edgerton-type flash

---

[2]Formerly the Alden Hydraulic Laboratory.

lamps is used. With the present electronic equipment, these lamps have a maximum rate of 1100 flashes per second. The gas pressure in the tank can be varied from atmospheric pressure to 0.06 atmosphere. Evacuation of the tank to 0.06 atmosphere, when operating at normal water elevation, takes about 20 minutes. With heavy gases, both the pressure and density of the atmosphere above the water surface can be varied.

The tank's carbon dioxide powered launcher of the plunger type (Figure 19.10) is mounted on a hollow drum and can be rotated to vary the launching angle. The missile, attached to the plunger by means of small springs, is directed by a set of guides during its launching phase and is in free flight after 2 feet of guided travel. With this arrangement, models up to 2 inches in diameter can be launched at velocities up to 150 fps. No variation in tank pressure results from this launching technique. Missile launchings at entry angles from 0 to 90 degrees, exit angles up to 30 degrees, and underwater trajectories can be studied.
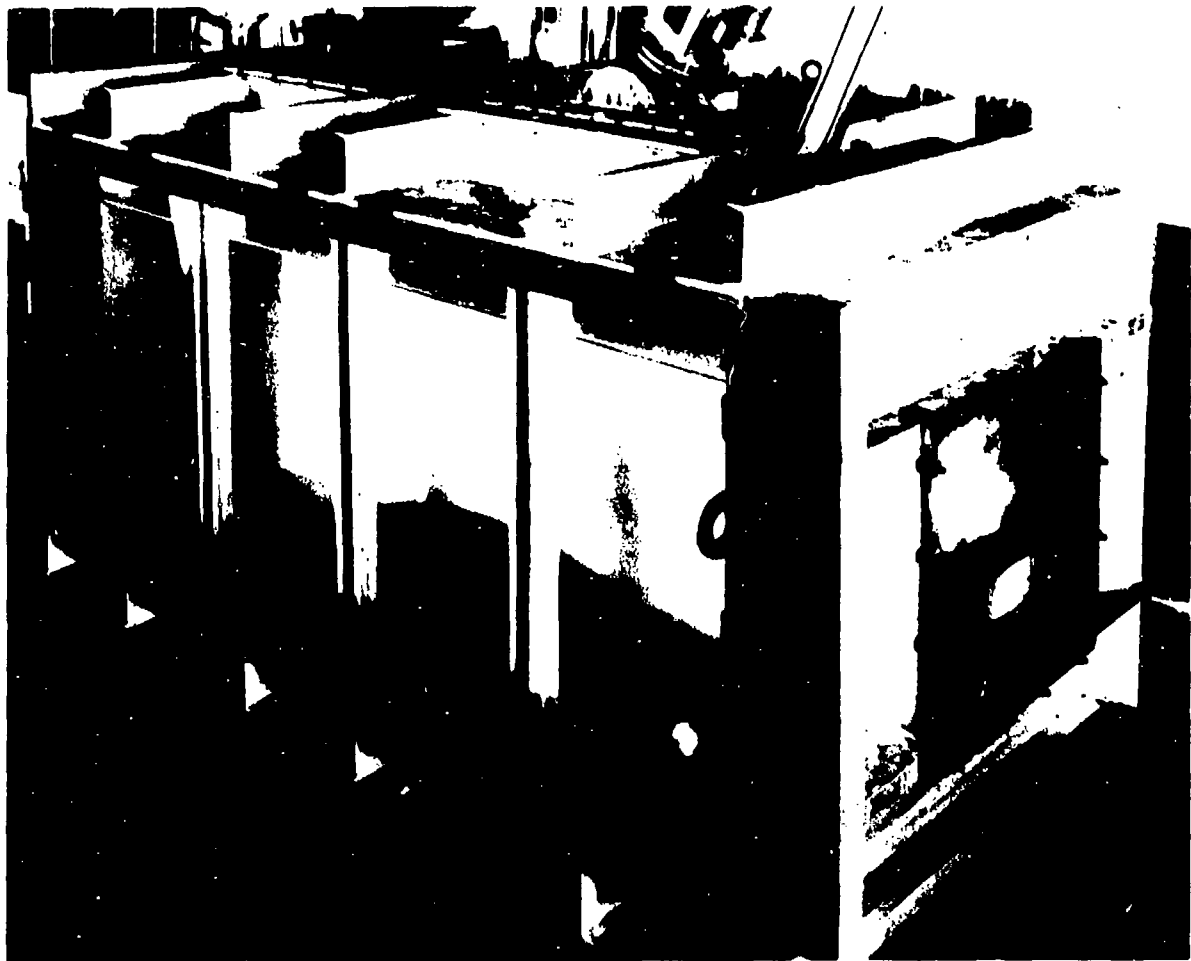
Figure 19.9. Controlled atmosphere tank at Alden Research Laboratories.
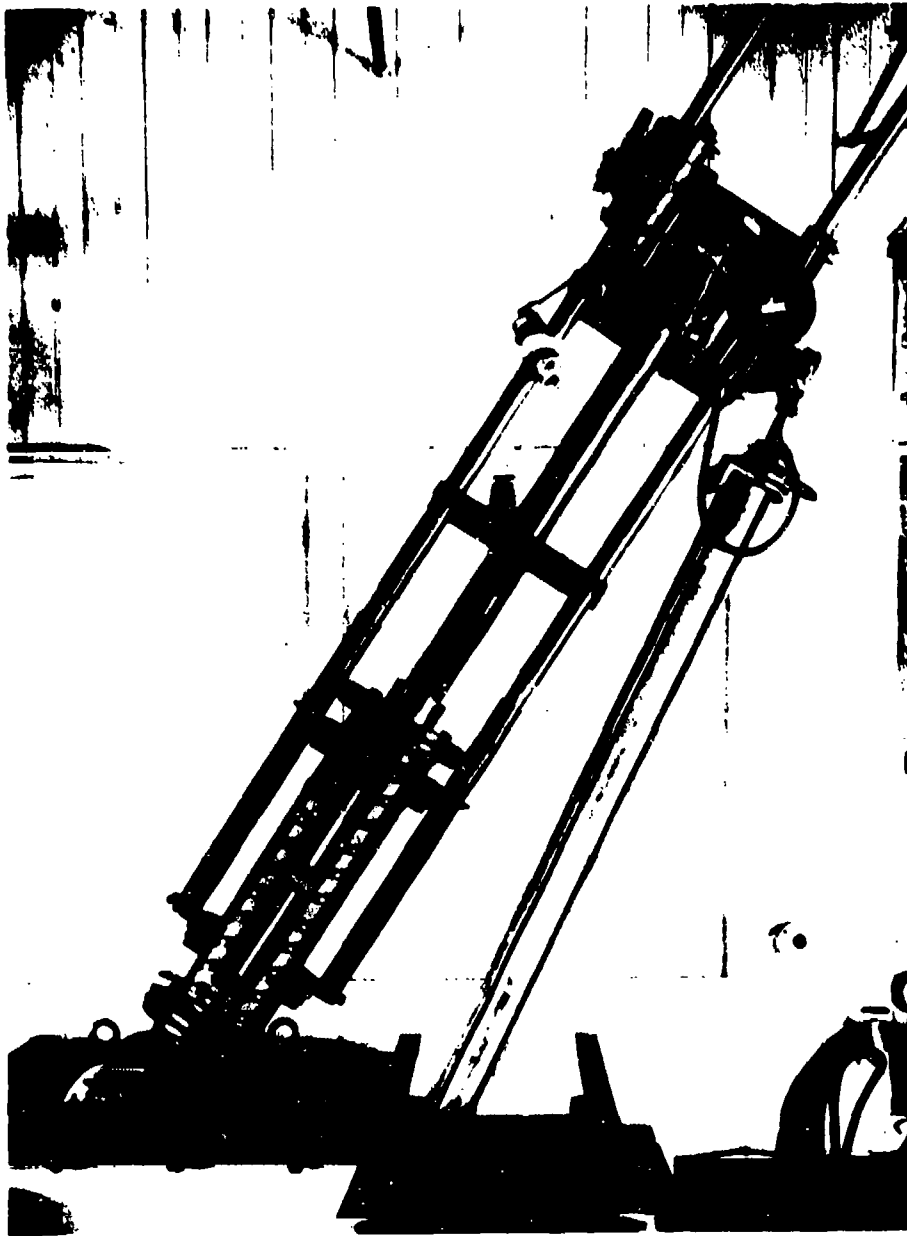
Figure 19.10. Launcher on Controlled Atmosphere Tank.

PART VI.
THE CHANGING STATUS OF MODELING

CHAPTER 20
THE CHANGING STATUS OF MODELING

Present-day knowledge of modeling is at best only partial and, certainly, the state of the art does not permit any dogmatic assertions regarding the reliability of existing techniques. Modeling has persisted as an art rather than as a well-ordered science because there is no infallible way to measure the relative significance of the physical forces in a model system The order of numerical magnitude usually used in engineering as a measure of significance is inadequate because the resultant of the large forces determining a phenomenon may be nearly zero. Understanding of the phenomena to be modeled and past experience with similar modeling systems help in evaluating the physical forces involved, yet unexpected results sometimes occur. Such modeling failures can be of subtle origin.

Experimental studies of water entry have produced a set of empirical design criteria applicable to a few specific problems but little information of a general or systematic nature has evolved and design data are lacking in many areas. When scaling conditions are known, experimental modeling studies can be programmed to obtain general or specific design data, but in many areas the actual scaling conditions are yet to be established or confirmed.

The effects of sea state upon missile behavior need to be investigated. Wave and wind action of a highly variable nature exists at the air-water interface. Knowledge of the flow about a missile operating immediately beneath the surface is lacking, and little is known about the effects of deep submergence on the cavitation characteristics of missiles and on the various power plants that are dependent upon external exhaust. Variations within the sea water as introduced by salinity, thermal layers, etc., may also trigger irregular cavity behavior. Effects such as these must be recognized before missile behavior can be predicted with confidence.

It is almost certain that very high pressures, many times greater than stagnation pressure, are present at impact; but these pressures, never fully evaluated at lower entry velocities, are virtually unexplored in the sonic regime (References 52, 83, and 84). They are important structural design criteria, particularly as the entry velocities approach the transonic (4000 – 5000 fps) range. At these velocities, the pressure surge will probably be important in determining the trajectory and may also affect the entry

cavity. Compressibility is a factor that requires consideration in all media.

Mitigation of water-entry shock will be a major problem at the higher entry velocities. Frangible nose caps have been used to cushion water-entry shock, and a step-nose[1] has been considered, but usually the issue has been avoided by deploying a parachute to decelerate the missile prior to entry. Study of the high-velocity regime should also include the modeling of ricochet characteristics.

The scaling laws required to determine a Mach-modeling system have not yet been formulated. Were it possible to create an ideal system of perfect fluids and frictionless, rigid solids, these scaling laws could be easily established; in a system of real materials, the physical phenomena must be described and the significant forces identified first.

Extrapolation of the vast library of water-tunnel data to the entry cavity is attractive, but the steady-state cavity occurring in a water tunnel differs from the transient cavity at water entry (Reference 101). The importance of secondary forces in determining cavity separation might profitably be studied in a water tunnel, however, or a controlled, transient cavity might be generated there after greater knowledge is gained of the pressure variation in a typical water-entry cavity.

A record of cavity pressure as a function of time, and a special pressure distribution to describe gas flows within the cavity would increase understanding of cavity growth, shape, and dissipation; knowledge of cavity pressure at the critical points of missile-cavity separation would aid in evaluating the forces in equilibrium. A meaningful study of the relationship between the surface condition of the missile and cavity formation might then be possible.

Little is known of cavity attrition — how little might be measured by the fact that the disappearance of the water-entry cavity is often mistakenly termed "cavity collapse." The water-entry cavity, being partially of a noncondensable gas, does not — indeed cannot — collapse.

Instead, it is shed or progressively entrained in a variety of ways by the flowing water. It is known that the flow at the base of the cavity sometimes terminates in re-entrant jets directed upstream, but the exact flow conditions producing these jets are not known, even though the jets are sometimes of sufficient strength to interfere with missile performance. The momentum exchange between the missile and the water might be determined by observing the motion of a water-entry cavity after the generating missile has been stopped suddenly.

The phenomena of water exit requires further study. Some theoretical study and a great deal of particular water-exit information have been generated by the Navy's Polaris and Poseidon programs, but it is recognized that much more investigation is needed. Existing experimental data show that the exit phenomena are at least as sensitive to secondary forces as are those of entry.

Pre-exit flight is of major importance in determining the linear and angular velocities retained by the missile following water exit. Transient-flow phenomena arising from random turbulence in the boundary layer and asymmetric flow patterns caused by irregular cavities[2] can produce a great variety of exit angles and velocities in successive launchings even though the missiles have been launched under presumably equal conditions. The possibility of stabilizing performance by bolstering a weak or fluctuating cavity with exhaust material from an internal propulsion system is attractive. Cavity life might also be extended artificially by introducing wetting agents into the boundary layer ahead of the separation point, effectively reducing the surface tension in the boundary layer, thereby reducing the cavity-closure force.

The release of hydrodynamic forces occurring as the missile becomes airborne will in general be asymmetric and can easily be large, increasing the probability of significant perturbation of missile motion at water exit.

The first investigations of water exit should be directed toward control of the pre-exit flight;

---

[1] Effective, because at entry it generates a series of progressively larger cavities, thus dividing the total entry shock into several smaller shocks. The step-nose appears promising from the standpoint of shock mitigation, but other problems will inevitably arise from its use.

[2] Observation of cavities formed by missiles exiting at low velocities suggests that the large vortex rings shed from the base of the cavity must influence the exit perturbation (Chapter 11).

328

then the effects of the launcher, the missile power plant, and the sea state should be examined.

If the problems of hydroballistics have a common denominator, it is the cavity; inevitably, cavity behavior is examined first as a measure of any new effect. Undesirable cavity behavior can disrupt missile performance completely, yet this same cavity offers a promising possibility of missile control. It is evident from several experimental studies (Chapters 8 and 11, for example) that under some circumstances the cavity imparts a highly desirable stability to missile performance. It is not now possible to produce a stabilizing cavity upon demand; to be able to do so would be of great advantage.

The shape of the cavity will affect missile control in many ways. Too large a cavity will not only increase drag but will make large changes in missile orientation possible within the cavity. The separation of too slender a cavity is inherently unstable (Chapters 3 and 8). The possibility of using the interaction between the jet exhaust and the cavity wall as a means of missile control offers an attractive way to influence the trajectory of a quasi-steady, cavity-running projectile that has only its nose in contact with the water.

The rate of cavity dissipation and the cavity shape as dissipation occurs can be critical factors in missile performance; a sudden shift in the cavity introduces a rudder effect that can alter both the trajectory and the missile orientation and can also affect the operation of the sensing equipment within the missile. Under some circumstances, there might be some benefit in jettisoning the cavity artificially by suddenly slowing the missile with a parachute device.

Many of the experimental techniques and design criteria discussed in Chapters 18 and 19 are now in common use; they represent the state of the art. This was not true when the techniques and criteria were evolved, nor are they necessarily familiar now to those not intimately concerned with experimental hydroballistics. It is hoped that the studies reported here, most of them conducted at the Naval Undersea Research and Development Center, Pasadena Laboratory, will provide a basis for assessing the present state of the modeling art, a springboard for future experiments, and a guide for extending the modeling technique to other phases of hydroballistics.

Much remains to be done to advance and refine the techniques of hydroballistics. Cameras, telemeters, pressure-sensing devices, and small power plants presently available place the suggested studies within the realm of possibility, although challenging development of both instrumentation and experimental techniques still lies ahead.

NOMENCLATURE

A	Maximum cross-sectional area of missile, ft^2
a	Water-entry deceleration of missile, g
C_D	Drag coefficient of missile $\left[C_D = D/(1/2)\rho_w v^2 A\right]$
C_L	Lift coefficient of missile $\left[C_L = L/(1/2)\rho_w v^2 A\right]$
C_p	Molecular heat at constant pressure, cal (mole $^oC)^{-1}$
C_v	Molecular heat at constant volume, cal (mole $^oC)^{-1}$
c	Velocity of sound in water, ft sec^{-1}
D	Drag of missile, lb; force exerted on missile in a direction parallel to line of travel
d	Diameter of missile, in.
E	Bulk modulus of elasticity of water, lb ft^{-1} sec^{-2}
F	Froude number; ratio of inertial and gravitational forces $[F = v/(dg)^{1/2}]$
f	Flexure number; ratio of inertial and flexural forces $\left(f = v^2/n_o^2\ell^2\right)$
g	Gravitational acceleration, ft sec^{-2}
h	Depth of missile below water surface, in., ft, missile diameters
I	Moment of inertia of missile about any transverse axis through CG, slug ft^2 or lb in^2; light intensity in forward direction (Equation 19.1)
k	Light absorption coefficient (Equation 19.1)
L	Lift of missile, lb. Component in vertical plane of force exerted on missile in direction normal to line of travel

Preceding page blank

ℓ	Distance from missile nose to CG, in. (Equation 1.10); beam or missile length in flexure number scaling, ft (Equation 1.7); generalized measure of length in Table 3.2
M	Molecular weight
m	Mass of missile, lb
n	Moles of gas
n_o	Fundamental transverse frequency of missile, Hz (Equation 1.7)
P	Flat plate radius $(P = R_p - R_o$, Figure 5.2)
p_a	Atmospheric pressure (gas pressure over water surface), atm., torrs, lb in^{-2}
p_c	Sum of gas and vapor pressures in cavitation bubble acting to keep bubble open, atm., torrs, lb in^{-2} $(p_c = p_g + p_v)$
p_g	Gas pressure (exclusive of vapor pressure) in cavitation bubble acting to keep bubble open; gas pressure in missile underwater launching system, atm., torrs, lb in^{-2}
p_v	Fluid vapor pressure, atm., torrs, lb in^{-2}
Q	Parameter used to present ogive-plate-ogive data $[Q = 1/(1 + p_o \cdot R_p)]$
R	Reynolds number; ratio of inertial and viscous forces $(R = vd/v)$; spherical cap radius (Figure 5.2)
R '	Gas constant $[R' = 1.987$ cal $($mole $^oC)^{-1}]$
R_o	Ogival radius (Figure 5.2)
R_p	Missile radius (Figure 5.2)
r	Sphere radius
r '	Radius of cavity bubble in region where striation angle, ϵ, is measured (Figure 15.1)
S	Surface tension of fluid, dynes cm^{-1}
s	Missile water penetration measured along trajectory from point of water entry, in., ft, missile diameters
T_g	Temperature of gas, ^oC
T_w	Temperature of fluid, ^oC
t	Time, sec; measured from instant of missile water contact or emergence
V	Volume of gas in missile underwater-launching system or cavity bubble

v	Missile velocity, ft sec^{-1}
v_g	Gas velocity, ft sec^{-1}
W	Work performed by gas expansion in missile underwater-launching system
α	Missile angle of attack in pitch, deg; angle in vertical plane between missile axis and direction of motion, positive in sense of nose-up rotation (Figure 1.1); half-sphere angle (Figure 5.2)
γ	Gas specific heat ratio ($\gamma = C_p/C_v$)
$\Delta\dot\theta$	Whip of missile, deg sec^{-1}; change in missile pitch velocity at water entry over impact and flow-formation phases
δ	Slope (deviation from vertical) of water-entry splash at point of separation from sphere, deg (Figure 16.5)
ϵ	Angle between water-entry cavity striations and plane normal to direction of travel of sphere, deg (Figure 15.1)
ζ	Generalized angle; used in Equations 1.20, 1.21, and 1.22 to represent pitch angle, θ, trajectory angle, ξ, angle of attack, α, yaw, ψ, or roll, ϕ.
η	Surface tension of fluid, dynes cm^{-1}; used in Table 3.2
θ	Missile angle of pitch, deg; angle between missile axis and horizontal plane, positive in sense of nose-up rotation (Figure 1.1)
$\dot\theta$	Pitch velocity, deg sec^{-1}
ι	Missile angle of inclination, deg; projection of missile pitch angle on vertical plane containing the trajectory; positive in sense of nose-up rotation (Figure 9.5)
λ	Modeling scale factor; ratio of the model and prototype missile diameters used for convenience ($\lambda = d_m/d_p$)
μ	Viscosity of fluid, lb ft^{-1} sec^{-1}
ν	Kinematic viscosity of fluid, ft^2 sec^{-1}
ξ	Missile trajectory angle, deg; path angle of missile CG with respect to horizontal plane, positive in climb (Figure 1.1)
ρ	Density of gas, slug ft^{-3} or in terms of the density of a "standard atmosphere" (see definition of ρ')
ρ	Gas-density coefficient; ratio of gas density in the model system to density of air at 20°C and 740 torrs.
ρ_w	Density of fluid, slug ft^{-3}

σ Cavitation number; ratio of the static and dynamic pressures $\left[\sigma = (p_a + \rho_w gh - p_g - p_v)/(1/2)\rho_w v^2\right]$

τ Weber number; ratio of the inertial and surface tension forces $\left[\tau = v/(S/\rho_w d)^{1/2}\right]$

ϕ Missile angle of roll, deg; angle through which missile rotates about its longitudinal axis, positive in clockwise direction as viewed from the rear

ψ Missile angle of yaw, deg; angle between missile axis and vertical plane containing trajectory, positive when missile tail is to the right as viewed from rear

ω Empirical cavity closure parameter (Equation 9.1); rate of spin of sphere about an axis parallel to its direction of motion, rad sec^{-1} (Equation 15.1)

Subscripts

e   Water-entry or exit conditions

m   Model conditions

p   Prototype conditions

o   Initial condition

1   Final or end condition

BIBLIOGRAPHY

1. Abelson, H. I. Cavity Shapes at Vertical Water Entry: a Comparison of Calculated and Observed Shapes. White Oak, Md., U.S. Naval Ordnance Laboratory, January 23, 1967. (NOL Technical Report 67-31.)

2. *Aerosol Wetting Agents.* New York, N.Y. American Cyanamid Co., 1946.

3. Alden Hydraulic Laboratory. Controlled Atmosphere Tank. Worcester, Mass., Worcester Polytechnic Institute, 1958-59. (Contract NORD 15520.)

4. Birkhoff, Garrett. "Formation of Vortex Streets," in Journal of Applied Physics, Vol. 24, No. 1 (1953), pp. 98-103.

5. ——————. *Hydrodynamics: a Study in Logic, Fact and Similitude.* Princeton, N.J., Princeton University Press for University of Cincinnati, 1950. 186 pp.

6. ——————. *Hydrodynamics: a Study in Logic, Fact and Similitude.* Princeton, N.J., Princeton University Press, 1960. Revised edition, 184 pp.

7. Birkhoff, Garrett, and Thomas E. Caywood. "Fluid Flow Patterns," in Journal of Applied Physics, Vol. 20, No. 7 (1949), pp. 646-59.

8. Birkhoff, Garrett, and Robert Isaacs. Transient Cavities in Air-Water Entry. Washington, Navy Department, January 1951. (NAVORD Report 1490.)

9. Birkhoff, Garrett, and E. H. Zarantonello. *Jets, Wakes, and Cavities.* Vol. 2 of *Applied Mathematics and Mechanics.* New York, N.Y., Academic Press, 1957, 353 pp.

10. Burt, F. S. "New Contributions to Hydroballistics," in *Advances in Hydroscience.* Vol. 1, Ven Te Chow, ed. New York, N.Y., Academic Press, 1964. Pp. 182-280.

11. Christie, William H. Determination of the Underwater Trajectories of Missiles by the Use of Nets. Inyokern, Calif., U.S. Naval Ordnance Test Station, November 25, 1949. (NAVORD Report 1200.)

12. ————. The Rotating Plane-Parallel Plate Flare Camera. Inyokern, Calif., U.S. Naval Ordnance Test Station, April 17, 1950. (NAVORD Report 1209.)

13. ————. Underwater Photography, Its Application to High-Speed Missiles. China Lake, Calif., U.S. Naval Ordnance Test Station, December 15, 1950. (NAVORD Report 1247.)

14. Cooper, E. P. Theory of Water Entry of Missiles with Flat Noses. Inyokern, Calif., U.S. Naval Ordnance Test Station, April 26, 1949. (NAVORD Report 1154.)

15. Dergarabedian, Paul. Compressibility Effects During Water Entry. China Lake, Calif., U.S. Naval Ordnance Test Station, June 23, 1955. (NAVORD Report 3523.)

16. Dodge, Barnett F. *Chemical Engineering Thermodynamics.* 1st ed. New York, N.Y., McGraw-Hill Book Co., 1944. 680 pp.

17. Dorsey, N. Ernest. *Properties of Ordinary Water-Substance.* New York, N.Y., Reinhold Publishing Corp., 1940, 673 pp.

18. DuPré, Elsie F., and Leo H. Dawson. Transmission of Light in Water: an Annotated Bibliography. Washington, Naval Research Laboratory, April 1961. (NRL Bibliography No. 20.)

19. Ellis, A. T., and M. E. Fourney. "Application of a Ruby Laser to High Speed Photography," in Proceedings of the Institute of Electrical and Electronics Engineers, Vol. 51, No. 6 (1963), pp. 942-3.

20. Fabula, A. G. "Ellipse-Fitting of Two-Dimensional Normal Symmetric Impact of Rigid Bodies on Water," in Proceedings of the Fifth Midwestern Conference on Fluid Mechanics, April 1 and 2, 1957. Ann Arbor, Mich., the University of Michigan Press, 1957. Pp. 299-315.

21. Fabula, A. G., and I. D. Ruggles, Vertical Broadside Water Impact of Circular Cylinder: Growing Circular-Arc Approximation. China Lake, Calif., U.S. Naval Ordnance Test Station, October 12, 1955. (NAVORD Report 4947.)

22. Gilbarg, David, and R. A. Anderson. "Influence of Atmospheric Pressure on the Phenomena Accompanying the Entry of Spheres into Water," in Journal of Applied Physics, Vol. 19, No. 2 (1948), pp. 127-39.

23. Goldstein, S., ed. *Modern Developments in Fluid Dynamics.* Vol. I. Oxford, Great Britain, Oxford University Press, 1938. Pp. 1-330.

24. ————. *Modern Developments in Fluid Dynamics.* Vol. II. Oxford, Great Britain. Oxford University Press, 1938. Pp. 331-702.

25. *Handbook of Chemistry and Physics.* 48th ed. Cleveland, Ohio, Chemical Rubber Publishing Co., 1967-68.

26. Hoover, W. R., and V. C. D. Dawson. Hydrodynamic Pressure Measurements of the Vertical Entry of a Sphere. White Oak, Md., U.S. Naval Ordnance Laboratory, October 26, 1966. (NOL Technical Report 66-70.)

336

27. Jennison, James H. The Variable-Angle Launcher for Air-to-Water Missiles. Inyokern, Calif., U.S. Naval Ordnance Test Station, May 15, 1950. (NAVORD Report 1180.)

28. Kermeen, R. W., and B. R. Parkin. Incipient Cavitation and Wake Flow Behind Sharp-Edged Disks. Pasadena, Calif., California Institute of Technology, August 1957. (Engineering Division Report No. 85-4.)

29. Knapp. R. T. "Special Cameras and Flash Lamps for High-Speed Underwater Photography," in Journal of the Society of Motion Picture Engineers, Vol. 49, No. 1, (1947), pp. 64-82.

30. Knapp. R. T., and Joseph Levy, J. P. O'Neill, and F. B. Brown. "The Hydrodynamics Laboratory of the California Institute of Technology," in Transactions of the American Society of Mechanical Engineers, Vol. 70, No. 5 (1948), pp. 437-57.

31. Knapp, Robert T. Entrance and Cavitation Bubbles. Pasadena, Calif., California Institute of Technology, December 27, 1944. (Hydraulic Machinery Laboratory Report No. ND-31.)

32. ————. Hydrodynamic Force Resulting from Cavitation on Underwater Bodies. Pasadena, Calif., California Institute of Technology, July 21, 1945. (Hydrodynamics Laboratory Report No. ND-31.2.)

33. ————. Nose Cavitation: Ogives and Spherogives. Pasadena, Calif., California Institute of Technology, January 18, 1945. (Hydraulic Machinery Laboratory Report No. ND-31.1.)

34. *Kodak Plates and Films for Science and Industry.* Rochester, N.Y., Eastman Kodak Co., 1967. (Kodak Publication No. P-9.)

35. Lamb, Horace. *Hydrodynamics.* 6th ed. New York, N.Y., Dover Publications, 1945. 738 pp.

36. Levy, Joseph. On Modeling the Oblique Entry into Water of Air Launched Missiles. Pasadena, Calif., California Institute of Technology, August 1956. (Hydrodynamics Laboratory Report No. E-12.19.)

37. Levy, Joseph, and John Kaye. Investigations of Water Entry Phenomena: Preliminary Studies of Effect of Atmospheric Pressure on Trajectory of 2-Inch Correlation Model of Mark 13-6 Torpedo. Pasadena, Calif., California Institute of Technology, March 1, 1948. (Hydrodynamics Laboratory Report No. M-59.)

38. ————. Studies of Water Entry: Effect of Atmospheric Pressure on Entry Behavior of Models of Mark 13-6 Torpedo With Standard Head (Head F) and One Finer Head (Head I). Pasadena, Calif., California Institute of Technology, January 1949. (Hydrodynamics Laboratory Report No. N-59.)

39. Levy, Joseph, and Donald A. Price, Jr. Free-Body Modeling of the Stability and Control of Submarines. Pasadena, Calif., California Institute of Technology, May 1956. (Hydrodynamics Laboratory Report No. E-27.2.)

40. Loeb, Leonard, The Kinetic Theory of Gases. New York, N.Y., McGraw-Hill Book Co., 1934. 687 pp.

41. Luthander, S., and A. Rydberg. "Experimentelle Untersuchung uber den Luftwiderstand bei einer um eine mit der Windrichtung parallele Achse rotierenden Kugel," in Physikalische Zeitschrift, Vol. 36, No. 16 (1935), pp. 552-8.

42. Marey, M. "Le Mouvement des Liquides: Etudie par la Chronophotographie," in Comptes Rendus de l'Academie des Sciences, Vol. 116 (1893), pp. 914-24.

43. May, Albert. "Effect of Surface Condition of a Sphere on Its Water-Entry Cavity," in Journal of Applied Physics, Vol. 22, No. 10 (1951), pp. 1219-22.

44. ————. The Influence of the Proximity of Tank Walls on the Water-Entry Behavior of Models. White Oak, Md., U.S. Naval Ordnance Laboratory, October 3, 1951. (NAVORD Report 2240.)

45. ————. Research for Design of a Hydroballistics Tank. White Oak, Md., U.S. Naval Ordnance Laboratory, August 30, 1963. (NOL Technical Report 63-119.)

46. ————. "Vertical Entry of Missiles into Water," in Journal of Applied Physics, Vol. 23, No. 12 (1952), pp. 1362-72.

47. May, Albert, and Jean C. Woodhull. "Drag Coefficients of Steel Spheres Entering Water Vertically," in Journal of Applied Physics, Vol. 19, No. 12 (1948), pp. 1109-21.

48. ————. "The Virtual Mass of a Sphere Entering Water Vertically," in Journal of Applied Physics, Vol. 21, No. 12 (1950), pp. 1285-89.

49. Mees, C. E. Kenneth. The Theory of the Photographic Process. 3rd ed., T. H. James, ed. New York, N.Y., the Macmillan Co., 1966. 591 pp.

50. Mosteller, G. G. Axial Deceleration at Oblique Water Entry of 2-Inch-Diameter Models with Hemisphere and Disk-Cylinder Noses. China Lake, Calif., U.S. Naval Ordnance Test Station, February 12, 1957. (NAVORD Report 5424.)

51. ————. Spin Rate of Spheres Under Water as Determined from the Direction of Striations on the Cavity Formed at Water Entry. Inyokern, Calif., U.S. Naval Ordnance Test Station, April 1948. (NAVORD Report 1012.)

52. ————. Water-Entry Acceleration: an Annotated Bibliography. China Lake, Calif., U.S. Naval Ordnance Test Station, December 19, 1956. (NAVORD Report 5397.)

53. Mosteller, G. G., and H. I. Scribner. Improved Instrumentation for Water-Entry Modeling: Simultaneous Whip and Sideview Photography. China Lake, Calif., U.S. Naval Ordnance Test Station, May 19, 1955. (NAVORD Report 3499.)

54. Mosteller, G. G., and J. G. Waugh. Laboratory Facilities for Model Studies. Inyokern, Calif., U. S. Naval Ordnance Test Station, November 14, 1949. (NAVORD Report 1198.)

55. National Defense Research Committee. Mathematical Studies Relating to Military Physical Research. Vol. 1 of Summary Technical Report of the Applied Mathematics Panel, NDRC. Washington, NDRC, 1946.

56. ————. Torpedo Studies. Vol. 21 of Summary Technical Report of Division 6, NDRC. Washington, NDRC, 1946.

57. Neale, Lawrence C., Alfred H. Barrett, and James A. Wentworth. Development of a Telemetry System for Water-Entry Missiles. Worcester, Mass., Worcester Polytechnic Institute, December 1965. (Alden Hydraulic Laboratory Report No. 58.)

58. Nisewanger, C. R. Experimental Determination of Pressure Distribution on a Sphere During Water Entry. China Lake, Calif., U.S. Naval Ordnance Test Station, October 27, 1961. (NAVWEPS Report 7808.)

59. Office of Scientific Research and Development. Aircraft Torpedo Development and Water Entry Ballistics. Pasadena, Calif., California Institute of Technology, 1946. (OSRD Report No. 2550.)

60. ————. Photographic Studies in Underwater Ballistics. Pasadena, Calif., California Institute of Technology, November 15, 1945. (CIT Morris Dam Report 153; CIT IPC 81.)

61. ————. Water Entry and Underwater Ballistics of Projectiles. Pasadena, Calif., California Institute of Technology, 1946. (OSRD Report 2551.)

62. Peters, J. P., and D. D. Van Slyke. Quantitative Clinical Chemistry. Vol. II, Methods. Baltimore, Md., Williams and Wilkins, 1932. Pp. 267-74.

63. Pitzer, R. L., J. A. DeJulio, R. A. Nielsen, H. C. Riggins, and Gardner Wilson. A Digital Instrumentation System Developed at the Naval Ordnance Test Station. China Lake, Calif., U.S. Naval Ordnance Test Station, May 25, 1954. (NAVORD Report 3332.)

64. Pitzer, Robert L. The Torpedo Position Interferometer. Inyokern, Calif., U.S. Naval Ordnance Test Station, November 17, 1949. (NAVORD Report 1217.)

65. Plesset, Milton S., and Philip A. Shaffer, Jr. "Drag in Cavitating Flow," in Reviews of Modern Physics, Vol. 20, No. 1 (1948), pp. 228-31.

66. Prandtl, L., and O. G. Tietjens. Applied Hydro- and Aeromechanics. New York, N.Y., McGraw-Hill Book Co., 1934. 311 pp.

67. Properties and Applications of the Freon Fluorocarbons. Wilmington, Del., E. I. DuPont de Nemours and Co., 1966. (Freon Technical Bulletin B-2.)

68. Richardson, E. G. "The Impact of a Solid on a Liquid Surface," in Proceedings of the Physical Society of London, Vol. 61, Part 4 (1948), pp. 352-66.

69. Richter, Victor J. "NOL's Hydroballistics Laboratory," in Naval Research Reviews, Vol. 18, No. 7 (1965), pp. 23-25.

70. Rosenhead, L. "Vortex Systems in Wakes," in Advances in Applied Mechanics. Vol. III. New York, N.Y., Academic Press, 1953. Pp. 185-95.

71. Ross, James, and C. E. Bowers. Laboratory Surface Wave Equipment. Minneapolis, Minn., University of Minnesota, 1953. (St. Anthony Falls Hydraulic Laboratory Project Report No. 38.)

72. Rouse, Hunter. Cavitation and Pressure Distribution: Head Forms at Angles of Yaw. Iowa City, Iowa, State University of Iowa. 1962. (Studies in Engineering Bulletin 42.)

73. Rouse, Hunter, and John S. McNown. Cavitation and Pressure Distribution: Head Forms at Zero Angle of Yaw. Iowa City, Iowa, State University of Iowa, 1948. (Studies in Engineering Bulletin 32.)

74. Schlichting, Dr. Hermann. *Boundary Layer Theory.* 6th ed. New York, N.Y., McGraw-Hill Book Co., 1968. 744 pp.

75. Seigel, A. E. The Hydroballistic Facility at NOL. White Oak, Md., U.S. Naval Ordnance Laboratory, August 1, 1966. (NOL Technical Report 66-125.)

76. Shaftan, Kenneth, and Dean Hawley. *Photographic Instrumentation: Techniques, Equipment, Applications.* Redondo Beach, Calif., Society of Photographic Instrumentation Engineers, 1962, 330 pp.

77. Smith, H. D. The Hydroballistics Laboratory at NOTS. China Lake, Calif., U.S. Naval Ordnance Test Station, April 1966. (NAVWEPS Report 9035.)

78. Smith, J. A. Design and Construction of the Variable-Angle Launcher. China Lake, Calif., U.S. Naval Ordnance Test Station, January 16, 1952. (NAVORD Report 1327.)

79. Stanton, J. S., and W. G. Weigel. Investigation of Certain Problems of High-Speed Photography Under Water. Inyokern, Calif., U.S. Naval Ordnance Test Station, January 20, 1949. (NAVORD Report 1063.)

80. Stubstad, G. W. Pure Pitching Motion of the Basic Finner. China Lake, Calif., U.S. Naval Ordnance Test Station, October 1, 1958. (NAVORD Report 6417.)

81. Stubstad, G. W., and J. G. Waugh. Drag Coefficient of Fully Wetted Basic Finner Missile. China Lake, Calif., U.S. Naval Ordnance Test Station, June 7, 1956. (NAVORD Report 5269.)

82. Swanson, W. M., and J. P. O'Neill. The Stability of an Air-Maintained Cavity Behind a Stationary Object in Flowing Water. Pasadena, Calif., California Institute of Technology, September 5, 1951. (Hydrodynamics Laboratory Memorandum Report No. M-24.3.)

83. Szebehely, Victor G., and Michel K. Ochi. "Hydrodynamic Impact and Water Entry," in *Applied Mechanics Surveys.* Washington, Spartan Books, 1966. Pp. 951-57.

84. Tate, Dr. Manford B., compiler. Proceedings of the Naval Ordnance Laboratory Water Entry Symposium. White Oak, Md., U. S. Naval Ordnance Laboratory, December 1, 1955. (NAVORD Report 4180.)

85. Trilling, Leon. "The Impact of a Body on a Water Surface at an Arbitrary Angle," in Journal of Applied Physics, Vol. 21, No. 2 (1950), pp. 161-70.

86. von Kármán, Th. The Impact of Seaplane Floats During Landing. Washington, National Advisory Committee for Aeronatics, 1929. (Technical Note No. 321.)

87. Waid, Robert L. "Cavitation Research Capabilities of the Lockheed Underwater Missile Facility," in *Cavitation Research Facilities and Techniques.* New York, N.Y., American Society of Mechanical Engineers, 1964. Pp. 127-31.

88. Waugh, J. G. Underwater Launch and Trajectory Modeling Scaling Techniques. China Lake, Calif., U.S. Naval Ordnance Test Station, March 15, 1960. (NAVORD Report 7029.)

89. ------. "The Variable-Angle Variable-Pressure Launching Tank," in *Cavitation Research Facilities and Techniques.* New York, N.Y., American Society of Mechanical Engineers, 1964. Pp. 118-26.

90. ————. "Water-Entry Study with Two Liquids," in Proceedings of the Seventh Underwater Ballistics Conference. Part I, Unclassified Sessions. Washington, Office of Naval Research, 1948. Pp. 43-51.

91. ————. Water-Entry Whip and Deceleration of Eight Full-Scale Torpedo Models with Ogive and Spherogive Heads. Inyokern, Calif., U.S. Naval Ordnance Test Station, March 2, 1950. (NAVORD Report 1223.)

92. Waugh, J. G., and A. T. Ellis. "Fluid-Free-Surface Proximity Effect on a Sphere Vertically Accelerated From Rest," in Journal of Hydronautics, Vol. 3, No. 4 (1969), pp. 175-9.

93. ————. "The Variable-Atmosphere Wave Tank," in *Cavitation Research Facilities and Techniques.* New York, N.Y., American Society of Mechanical Engineers, 1964. Pp. 114-17.

94. Waugh, J. G., A. T. Ellis, and o. B. Mellsen. "Techniques for Metric Photography," in Journal of the Society of Motion Picture and Television Engineers, Vol. 75, No. 1 (1966), pp. 2-6.

95. Waugh, John G. Underwater Trajectories of Fourteen Full-Scale Unpowered Torpedo Models with Ogive, Spherogive, Plate-Ogive, and Modified Cone Heads. China Lake, Calif., U.S. Naval Ordnance Test Station, February 5, 1953. (NAVORD Report 2012.)

96. ————. "Water-Entry Pitch Modeling," in Journal of Hydronautics, Vol. 2, No. 2 (1968), pp. 87-92.

97. ————. Water-Entry Whip and Deceleration of Four Full-Scale Torpedo Models with Modified Cone Heads. China Lake, Calif., U.S. Naval Ordnance Test Station, October 9, 1950. (NAVORD Report 1262.)

98. Waugh, John G., and Raymond W. Ager. Water-Entry Whip and Deceleration of Six Full-Scale Torpedo Models with Ogive and Plate-Ogive Heads. China Lake, Calif., U.S. Naval Ordnance Test Station, April 20, 1951. (NAVORD Report 1308.)

99. Waugh, J. G., G. G. Mosteller, and Raymond W. Ager. Effect of Underpressure of the Water Entry Whip of 2-Inch-Diameter Missiles with Vented Disk-Cylinder Heads. China Lake, Calif., U.S. Naval Ordnance Test Station, June 28, 1954. (NAVORD 3342.)

100. ————. Effect of Underpressure on the Water-Entry Whip of a 22.4-Inch-Diameter Missile with Plate-Cylinder Head. China Lake, Calif., U.S. Naval Ordnance Test Station, November 3, 1952. (NAVORD Report 1995.)

101. Waugh, John G., and G. W. Stubstad. Water-Entry Cavity Modeling: Part 1, Vertical Cavities. China Lake, Calif., U.S. Naval Ordnance Test Station, October 8, 1956. (NAVORD Report 5365, Part 1.)

102. ————. Water-Entry Cavity Modeling: Part 2. Oblique Cavities. China Lake, Calif., U.S. Naval Ordnance Test Station, December 4, 1957. (NAVORD Report 5365, Part 2.)

103. ————. Water Exit Behavior of Missiles: Part 1, Preliminary Studies. China Lake, Calif., U.S. Naval Ordnance Test Station, May 11, 1961. (NAVWEPS Report 7735, Part 1.)

104. ――――――. Water-Exit Behavior of Missiles: Part 2, Effect of Cavitation and Exit Angle. China Lake, Calif., U.S. Naval Ordnance Test Station, April 1964. (NAVWEPS Report 7735, Part 2.)

105. ――――――. Water-Exit Behavior of Missiles: Part 3. Macroscopic Effects of the Hydrodynamic Flow Pattern. China Lake, Calif., U.S. Naval Ordnance Test Station, April 1964. (NAVWEPS Report 7735, Part 3.)

106. Wayland, Harold. Scale Factors in Water Entry. Inyokern, Calif., U.S. Naval Ordnance Test Station, April 18, 1947. (NAVORD Report 978.)

107. Wayland, Harold, and Frank G. White. Boundary Layer Effects on Spinning Spheres. Inyokern, Calif., U.S. Naval Ordnance Test Station, October 25, 1949. (NAVORD Report 1190.)

108. White, Frank G. Photographic Studies of Splash in Vertical and Oblique Water Entry of Spheres. Inyokern, Calif., U.S Naval Ordnance Test Station, April 24, 1950. (NAVORD Report 1228.)

109. Wiegel, Robert L. Oceanographical Engineering. Englewood Cliffs, N.J., Prentice-Hall, Inc., 1964. 532 pp.

110. Wilcox, G. M., and J. G. Waugh. Water-Entry Study of the Mk 25 Torpedo with 3.5-Calibre 70-Degree Spherogive Head. Pasadena, Calif., California Institute of Technology, May 1953. (Hydrodynamics Laboratory Report No. E-12.12.)

111. Wilcox, Genevieve M. The Effects of Atmospheric Pressures upon the Water Entry Behavior of a Missile Having a Hemispherical Nose and Flared-Cone Tail. Pasadena, Calif., California Institute of Technology, July 15, 1952. (Hydrodynamics Laboratory Memorandum Report EM-12.8.)

112. Worthington, A. M. *A Study of Splashes*. New York, N.Y., the Macmillan Co., 1963.

113. Worthington, A. M., and R. S. Cole. "Impact with a Liquid Surface Studied by the Aid of Instantaneous Photography," in Philosophical Transactions of the Royal Society (London), Vol. 194A (1900), pp. 175-200.